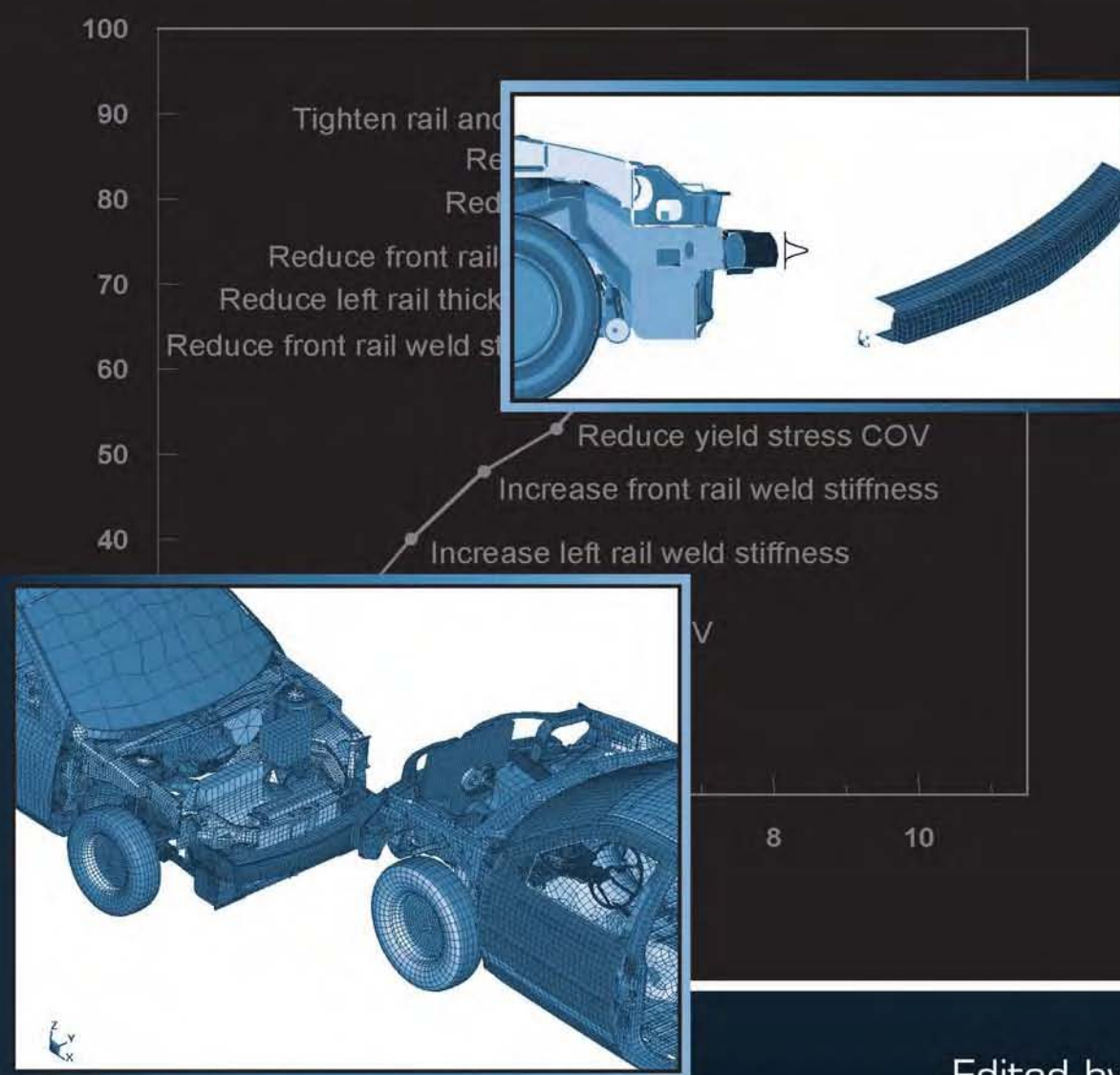


# ENGINEERING DESIGN RELIABILITY APPLICATIONS

For the Aerospace, Automotive,  
and Ship Industries



Edited by  
Efstratios Nikolaidis  
Dan M. Ghiocel  
Suren Singhal

# **ENGINEERING DESIGN RELIABILITY APPLICATIONS**

For the Aerospace, Automotive,  
and Ship Industries



# ENGINEERING DESIGN RELIABILITY APPLICATIONS

For the Aerospace, Automotive,  
and Ship Industries

Edited by

**Dr. Efstratios Nikolaidis**

Professor, Mechanical, Industrial and Manufacturing Engineering Department  
The University of Toledo, Toledo, Ohio, USA

**Dr. Dan M. Ghiocel**

President, Ghiocel Predictive Technologies Inc., Rochester, New York, USA  
Adjunct Professor with Case Western Reserve University, Cleveland, Ohio, USA

**Dr. Suren Singhal**

Assistant Manager, Materials, Processes, and Manufacturing Department,  
NASA Marshall Space Flight Center, MSFC, Alabama, USA



**CRC Press**

Taylor & Francis Group

Boca Raton London New York

---

CRC Press is an imprint of the

Taylor & Francis Group, an informa business

CRC Press  
Taylor & Francis Group  
6000 Broken Sound Parkway NW, Suite 300  
Boca Raton, FL 33487-2742

© 2008 by Taylor & Francis Group, LLC  
CRC Press is an imprint of Taylor & Francis Group, an Informa business

No claim to original U.S. Government works  
Printed in the United States of America on acid-free paper  
10 9 8 7 6 5 4 3 2 1

International Standard Book Number-13: 978-1-4200-5132-2 (Hardcover)

This book contains information obtained from authentic and highly regarded sources. Reprinted material is quoted with permission, and sources are indicated. A wide variety of references are listed. Reasonable efforts have been made to publish reliable data and information, but the author and the publisher cannot assume responsibility for the validity of all materials or for the consequences of their use.

No part of this book may be reprinted, reproduced, transmitted, or utilized in any form by any electronic, mechanical, or other means, now known or hereafter invented, including photocopying, microfilming, and recording, or in any information storage or retrieval system, without written permission from the publishers.

For permission to photocopy or use material electronically from this work, please access [www.copyright.com](http://www.copyright.com) (<http://www.copyright.com/>) or contact the Copyright Clearance Center, Inc. (CCC) 222 Rosewood Drive, Danvers, MA 01923, 978-750-8400. CCC is a not-for-profit organization that provides licenses and registration for a variety of users. For organizations that have been granted a photocopy license by the CCC, a separate system of payment has been arranged.

**Trademark Notice:** Product or corporate names may be trademarks or registered trademarks, and are used only for identification and explanation without intent to infringe.

---

**Library of Congress Cataloging-in-Publication Data**

---

Nikolaïdis, Efstratios.

Engineering design reliability applications : for the aerospace, automotive, and ship industries /  
Efstratios Nikolaïdis, Dan M. Ghiocel, Suren Singhal.

p. cm.

Includes bibliographical references and index.

ISBN 978-1-4200-5132-2 (alk. paper)

1. Engineering design. 2. Reliability (Engineering) I. Ghiocel, Dan M. II. Singhal, Suren. III. Title.

TA174.N55 2007

629.04--dc22

2007017923

---

Visit the Taylor & Francis Web site at  
<http://www.taylorandfrancis.com>

and the CRC Press Web site at  
<http://www.crcpress.com>

# Dedications

---

*To my parents George Nikolaidis and Theopisti Nikolaidis*

**Efstratios Nikolaidis**

*To my father Professor Dan Ghiocel, President of the Romanian Academy of Technical  
Science, Civil Engineering Division*

**Dan M. Ghiocel**

*To my parents, my wife Adesh, and children Rashi and Sara, and to all-too-important  
mentors, colleagues, and friends*

**Suren Singhal**

*If one does not reflect, one thinks oneself master of everything; but when one does reflect,  
one realizes that one is a master of nothing.*

**Voltaire**

# Contents

---

1	Applications of Reliability Assessment for Aerospace, Automotive, Bioengineering, and Weapons Systems <i>David S. Riha, Ben H. Thacker, Luc J. Huyse, Mike P. Enright, Chris J. Waldhart, W. Loren Francis, Daniel P. Nicolella, Stephen J. Hudak, Wuwei Liang, and Simeon H.K. Fitch</i> .....	1-1
2	Reliability Assessment of Aircraft Structure Joints Under Corrosion-Fatigue Damage <i>Dan M. Ghiocel and Eric J. Tuegel</i> .....	2-1
3	Selected Topics in Probabilistic Gas Turbine Engine Turbomachinery Design <i>James A. Griffiths and Jonathan A. Tschopp</i> .....	3-1
4	Applications of Reliability-Based Design Optimization <i>Robert H. Sues, Youngwon Shin, and (Justin) Y.-T. Wu</i> .....	4-1
5	Probabilistic Progressive Buckling of Conventional and Adaptive Trusses <i>Shantaram S. Pai and Christos C. Chamis</i> .....	5-1
6	Probabilistic Analyses of High-Speed Civil Transport (HSCT) Combustor Liner Components <i>Shantaram S. Pai and Pappu L.N. Murthy</i> .....	6-1
7	Probabilistic Analysis and Design in the Automotive Industry <i>Zissimos P. Mourelatos, Jian Tu, and Xuru Ding</i> .....	7-1
8	Integrated Computer-Aided Engineering Methodology for Various Uncertainties and Multidisciplinary Applications <i>Kyung K. Choi, Byeng D. Youn, Jun Tang, Jeffrey S. Freeman, Thomas J. Stadterman, Alan L. Peltz, and William (Skip) Connon</i> .....	8-1



<b>9</b>	<b>Reliability Assessment of Ships</b>	
	<i>Jeom Kee Paik and Anil Kumar Thayamballi</i> .....	<b>9-1</b>
<b>10</b>	<b>Reliability Analysis of Composite Structures and Materials</b>	
	<i>Sankaran Mahadevan</i> .....	<b>10-1</b>
<b>11</b>	<b>Micromechanics Modeling and Reliability Analysis of Carbon Nanocomposite Structures</b>	
	<i>Srikanth Pilla, Aaron Hammitt, and Efstratios Nikolaidis</i> .....	<b>11-1</b>
	<b>Index</b> .....	<b>I-1</b>

# Preface

In today's competitive business environment, design decisions involve significant uncertainty. Manufacturers strive to meet customer expectations for high performance, large product variety, and low cost. Deterministic approaches often yield inefficient designs because they use empirical tools, such as safety factors or worst-case scenarios, to accommodate uncertainty (Figure 1a). Use of deterministic methods to reduce cost or weight may result in systems that are vulnerable to variability and uncertainty because they operate on very tight margins (Figure 1b). To succeed in this environment, one should replace traditional deterministic design approaches with a new risk-based approach that uses rigorous models to quantify uncertainty and assess reliability (Figure 1c).

Reliability methods are becoming increasingly popular in the aerospace, automotive, civil, defense, and power industries because they help design safer and more reliable products at lower cost than traditional deterministic approaches. These methods have helped companies such as General Electric, United Technologies, General Motors, Ford, DaimlerChrysler, Boeing, Lockheed Martin, and Motorola improve dramatically their competitive position and save billions of dollars in engineering design and warranty costs. Although reliability design methods are being implemented in the industry, researchers are making important advances on various fronts including development of advanced reliability methods for complex practical systems, reliability design, and decision under uncertainty.

Companies need to educate their designers and managers about the advantages and potential of probabilistic methods. Professors need to educate their students about nondeterministic methods and increase the awareness of administrators about the importance and potential of these methods. Excellent books are available on reliability analysis and design and on decision under uncertainty; yet a comprehensive, detailed documentation of successful applications of these methods on complex real-world

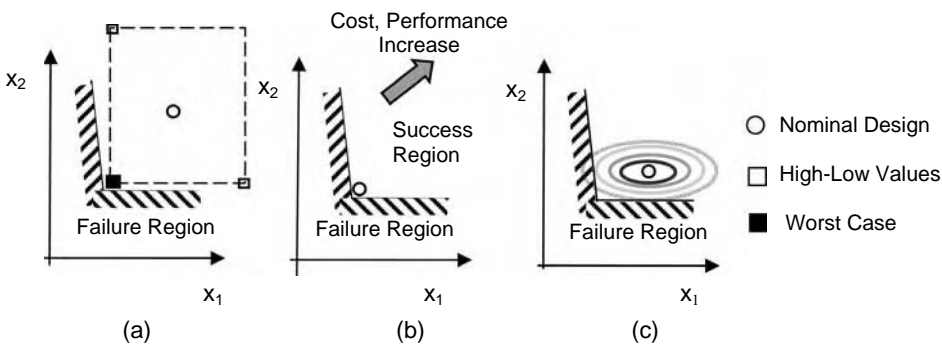


**FIGURE 1** Deterministic design may produce overly expensive (a) or unsafe designs (b). Probabilistic methods yield more economical and safer designs (c). Ellipses are regions containing some fixed percent of realizations.

systems is badly needed. To respond to this need, this book presents a collection of successful applications of reliability design in the aerospace, automotive, ship, and defense industries. These applications involve advanced systems such as space shuttle, aerospace propulsion, nanocomposite structures, and bioengineering systems. The benefits of reliability designs are quantified in these applications.

This book is for engineers, technical managers, and consultants in the aerospace, automotive, civil, and shipbuilding engineering industries who want to use, or are already using, reliability methods for product design. Professors and students who work on reliability methods will find this book useful, too.

The book consists of 11 chapters. The first chapter explains the need for accurate assessment of the reliability of complex, large-scale systems. Then, it presents two computer programs for reliability analysis, and demonstrates these programs on aircraft engines, structures used for testing explosives, and medical and automotive systems. Chapter 2 to Chapter 6 focus on aircraft and space systems, including lap joints, gas turbines, and actively controlled space structures. Chapter 7 and Chapter 8 present analytical tools for reliability analysis, design optimization, and sensitivity analysis of automotive systems. Analytical tools that help reduce tests in design and increase robustness are also given in these chapters. Chapter 9 shows a general methodology for reliability assessment of ship structures. This methodology includes methods for setting reliability targets, assessing the ultimate strength, computing the limit states of all important failure modes, and developing load models. The methodology is demonstrated on reliability assessment of a double-hull tanker and a bulk carrier. Chapter 10 and Chapter 11 focus on reliability analysis of composite materials and structures. Methods for computing the limit states of important failure modes and system reliability analysis of composite materials are presented and demonstrated in Chapter 10. Chapter 11 presents a methodology for probabilistic analysis of carbon nanofiber composite materials and reliability analysis of structures made of these materials.

Seven of the above chapters (2, 3, 4, 5, and 7 to 9) were extracted from the *Engineering Design Reliability Handbook*<sup>1</sup> that was published by the same editors. Chapter 1, Chapter 6, Chapter 10, and Chapter 11 are new or substantially updated versions of chapters published in the above handbook.

<sup>1</sup> *Engineering Design Reliability Handbook*, E. Nikolaidis, D. Ghiocel, S. Singhal (Eds.), CRC Press, Boca Raton, FL, December 2004.

# The Editors

---

**Efstathios Nikolaidis** is a professor of mechanical, industrial, and manufacturing engineering at the University of Toledo, Ohio. His research has focused on reliability-based design optimization of aerospace, automotive, and ocean structures; theories of uncertainties; and structural dynamics. Dr. Nikolaidis has published one book, three book chapters, and more than 100 journal and conference papers, mostly on nondeterministic approaches.

**Dan Ghiocel** is the chief engineering scientist of Ghiocel Predictive Technologies, Inc., in Rochester, New York, a company specializing in nondeterministic modeling for high-complexity engineering problems. Since 2001, Dr. Ghiocel has also been an adjunct professor at Case Western Reserve University, in Cleveland, Ohio. He has accumulated extensive experience in probabilistic approaches for civil, nuclear facility, and jet engine systems. He is a member holding various responsibilities in several prestigious technical committees and professional working groups, including the AIAA, SAE, and ASCE. Since 2002, he has been a fellow of the North American Academy of Sciences and Arts.

**Suren Singhal** is a nationally and internationally recognized leader in the field probabilistic methods and technology. Dr. Singhal has initiated new committees, panels, and forums in nondeterministic and probabilistic approaches. He has led the development of state-of-the-art probabilistic technology and documents dealing with diverse aspects such as cultural barriers and legal issues.



# Contributors<sup>\*</sup>

---

**Christos C. Chamis**  
NASA Glenn Research Center  
Cleveland, Ohio

**Kyung K. Choi**  
The University of Iowa  
Iowa City, Iowa

**William (Skip) Connon**  
US Army Materiel Systems  
Analysis Activity  
Aberdeen Proving Ground  
Aberdeen, Maryland

**Xuru Ding**  
General Motors Corporation  
Warren, Michigan

**Mike P. Enright**  
Southwest Research Institute  
San Antonio, Texas

**Simeon H. K. Fitch**  
Mustard Seed Software  
Charlottesville, Virginia

**W. Loren Francis**  
Southwest Research Institute  
San Antonio, Texas

**Jeffrey S. Freeman**  
The University of Tennessee  
Knoxville, Tennessee

**Dan M. Ghiocel**  
Ghiocel Predictive  
Technologies Inc.  
Pittsford, New York

**James A. Griffiths**  
General Electric Company  
Evendale, Ohio

**Aaron Hammit**  
The University of Toledo  
Toledo, Ohio

**Stephen J. Hudak**  
Southwest Research Institute  
San Antonio, Texas

**Luc J. Huyse**  
Southwest Research Institute  
San Antonio, Texas

**Wuwei Liang**  
Southwest Research Institute  
San Antonio, Texas

**Sankaran Mahadevan**  
Vanderbilt University  
Nashville, Tennessee

**Zissimos P. Mourelatos**  
Oakland University  
Rochester, Michigan

**Pappu L. N. Murthy**  
NASA Glenn Research Center  
Cleveland, Ohio

**Daniel P. Nicolella**  
Southwest Research Institute  
San Antonio, Texas

**Efstratios Nikolaidis**  
The University of Toledo  
Toledo, Ohio

**Shantaram S. Pai**  
NASA Glenn Research Center  
Cleveland, Ohio

**Jeom Kee Paik**  
Pusan National University  
Pusan, South Korea

**Alan L. Peltz**  
US Army Materiel Systems  
Analysis Activity  
Aberdeen Proving Ground  
Aberdeen, Maryland

**Srikanth Pilla**  
The University of Wisconsin  
Madison, Wisconsin

**David S. Riha**  
Southwest Research Institute  
San Antonio, Texas

**Youngwon Shin**  
Applied Research Associates Inc.  
Raleigh, North Carolina

**Thomas J. Stadterman**  
US Army Materiel Systems  
Analysis Activity  
Aberdeen Proving Ground  
Aberdeen, Maryland

**Robert H. Sues**  
Applied Research Associates Inc.  
Raleigh, North Carolina

*\*Disclaimer:* The views and opinions expressed in this book are strictly those of the contributors and the editors, and they do not necessarily reflect the views of their companies, their organizations, or the government.

**Jun Tang**  
University of Iowa  
Iowa City, Iowa

**Ben H. Thacker**  
Southwest Research Institute  
San Antonio, Texas

**Anil Kumar Thayamballi**  
Chevron Shipping  
Company LLC  
San Francisco, California

**Jonathan A. Tschopp**  
General Electric Company  
Evendale, Ohio

**Jian Tu**  
General Motors Corporation  
Warren, Michigan

**Eric J. Tuegel**  
Air Force Research Laboratory  
Wright-Patterson Air Force Base  
Dayton, Ohio

**Chris J. Waldhart**  
Southwest Research Institute  
San Antonio, Texas

**(Justin) Y.-T. Wu**  
Applied Research Associates, Inc.  
Raleigh, North Carolina

**Byeng D. Youn**  
University of Iowa  
Iowa City, Iowa

# 1

## Applications of Reliability Assessment for Aerospace, Automotive, Bioengineering, and Weapons Systems

---

David S. Riha

Ben H. Thacker

Luc J. Huyse

Mike P. Enright

Chris J. Waldhart

W. Loren Francis

Daniel P. Nicolella

Stephen J. Hudak

Wuwei Liang

*Southwest Research Institute*

Simeon H.K. Fitch

*Mustard Seed Software*

1.1	Introduction .....	1-1
1.2	Overview of NESSUS.....	1-3
1.3	Overview of DARWIN.....	1-6
1.4	Application Examples .....	1-9
	Gas Turbine Engine Rotor Risk Assessment • Stochastic Crashworthiness • Probabilistic Shuttle Debris Transport Modeling • Los Alamos Dynamic Experiment Containment Vessel • Cervical Spine Impact Injury Assessments • Fracture Reliability of Space Shuttle Main Engine Flowliner	
1.5	Conclusions .....	1-29
1.6	Acknowledgments .....	1-30
	References .....	1-30

### 1.1 Introduction

---

Continuing programs of national significance are pushing numerical simulation to new levels. These include the Federal Aviation Administration (FAA) Turbine Rotor Material Design program aimed at reducing the risk of rotor fracture, the Nuclear Regulatory Commission (NRC) program to assess the long-term safety of the nation's first underground high-level radioactive waste repository, the Department of Energy (DOE) Stockpile Stewardship program to replace underground nuclear testing with computationally based full weapon system certification, and the reactivation of the NASA space shuttle return-to-flight efforts. The common denominator of all these program areas is the need to compute—with high confidence—the reliability of complex, large-scale systems involving multiple physics, nonlinear behavior, and uncertain or variable input descriptions.

Probabilistic analysis, in addition to being applied to systems in which serious consequences are attached to failure (safety-driven systems), is also employed to predict the reliability of engineered systems and identify important design and manufacturing variables for (1) one or few-of-a-kind high-cost systems



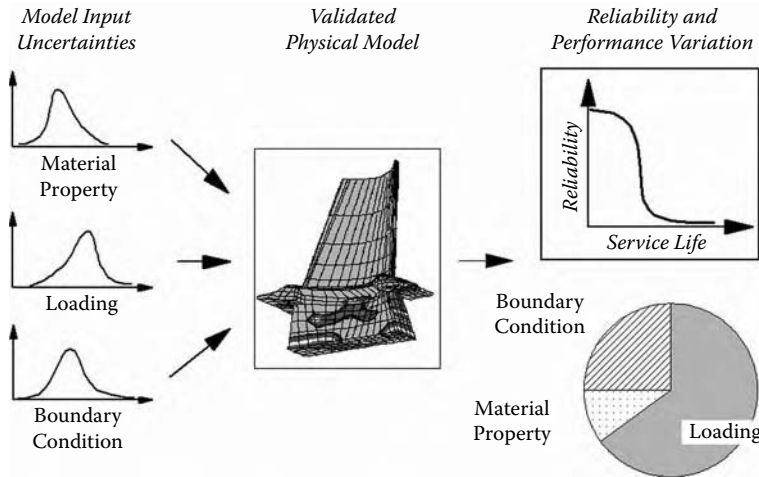


FIGURE 1.1 Basic process of input uncertainty propagation.

on which there will be little or no full-system testing, (2) products that are manufactured in large numbers and whose warranty costs are prohibitive or unacceptable, and (3) products that are manufactured in large numbers where small changes in the manufacturing process can lead to large cost savings.

The basic problem being addressed by probabilistic analysis is illustrated in Figure 1.1. Model inputs are represented as random variables leading to corresponding uncertainty in the model responses, which are usually related to some performance measure, e.g., fatigue life. In addition, the probabilistic analysis identifies which input variables contribute the most (and the least) to the computed reliability.

Uncertainties enter a complex simulation from a variety of sources: inherent variability in input parameters, lack of or insufficient input data, human errors, model simplification, and lack of understanding of the underlying physics. In general, all uncertainties can be categorized as being either inherent (irreducible) or epistemic (reducible). Epistemic uncertainty can, in principle, be reduced by gathering additional data, implementing more rigorous quality control, or by using more sophisticated or higher-fidelity analysis. Although it is well accepted that probabilistic methods are appropriate for characterizing inherent uncertainties, it is not as widely accepted to use a probabilistic approach to represent epistemic uncertainty. In many instances, however, a probabilistic approach can be justified, especially if a variable is truly random, but only limited data or expert opinions are available [1,2]. The use of probability to represent epistemic uncertainty is supported by the subjective or personalistic view of probability. According to this view, probability is considered as representing a decision maker's degree of belief that a system will adopt a certain state [3].

To support the need for more accurate simulations, analysts are developing higher-fidelity models that more closely represent the actual behavior of the system. Finite element models in excess of 1 million elements are not uncommon, and often also involve multiple coupled physics such as solid mechanics, structural dynamics, hydrodynamics, heat conduction, fluid flow, transport, chemistry, and acoustics. Even with the remarkable advances in computer speeds seen recently, simulations performed with these high-fidelity models can take hours or days to complete for a single deterministic analysis. Because probabilistic analysis methods, regardless of the particular method employed, require repeated deterministic solutions, efficient methods continue to be needed.

Beginning with the development of the NESSUS® (Numerical Evaluation of Stochastic Structures Under Stress) probabilistic analysis computer program [4], Southwest Research Institute (SwRI) has been addressing the need for efficient probabilistic analysis methods for nearly 25 years. Recently, SwRI has also focused on improving the NESSUS software to reduce the time required to define complex probabilistic problems [5], improve support for large-scale numerical models (greater than 1 million elements) [6], improve the robustness of the underlying probabilistic algorithms [7,8], and address approaches for

vague or lack of data and expert/corporate knowledge [9]. NESSUS can be used to simulate uncertainties in loads, geometry, material behavior, and other user-defined random variables to predict the probabilistic response, reliability, and probabilistic sensitivity measures of systems. Some of the applications currently being addressed by NESSUS users include aerospace structures, automotive structures, biomechanics, gas turbine engines, geomechanics, nuclear waste disposal and packaging, offshore structures, pipelines, rotordynamics, and weapon systems.

The NESSUS framework allows the user to link probabilistic algorithms with analytical equations, external computer programs (including commercial finite element codes), and general combinations of the two to compute the probabilistic response of a system. NESSUS includes a hierarchical model capability that allows the user to link different analysis packages and analytical functions. This capability provides a general relationship of physical processes to predict the uncertainty in the performance of the system. The powerful NESSUS Java-based graphical user interface (GUI) is highly configurable and allows tailoring to specific applications.

In 1995 SwRI initiated development of the DARWIN® probabilistic analysis software. As compared to NESSUS, which is a general-purpose probabilistic analysis code, DARWIN (Design Assessment of Reliability With INspection) is a tailored code for performing probabilistically based damage tolerance analysis of gas turbine engine rotor disks [10–12]. The software integrates finite element stress analysis, fatigue crack growth life assessment, material anomaly data, probability of detection (POD) by nondestructive evaluation, and inspection schedules to determine the probability of fracture of disks as a function of applied operating cycles. The program also identifies the regions of the disk most likely to fail, and the risk reduction associated with inspections. DARWIN is currently being used by at least seven major aircraft engine companies worldwide, and several of these companies have already used DARWIN in support of FAA certification activities. In recognition of DARWIN's technology and acceptance by industry, the code received an R&D 100 award as “one of the 100 most technologically significant new products of the year” in 2000.

DARWIN includes tailored probabilistic methods adapted from NESSUS technology and an integral fracture mechanics module that includes NASGRO [13] technology. These sophisticated technology elements are integrated within a powerful custom GUI that makes the code extremely easy to use. DARWIN also permits ANSYS models and ANSYS stress results to be directly input and displayed within the software. This, in turn, facilitates the rapid and highly efficient extraction of relevant geometry and stress information to support the probabilistic damage tolerance calculations. DARWIN currently considers random variations in key input variables including the initial defect size and frequency, NDE POD as a function of damage size, time of inspection, crack growth material properties, and applied stresses.

In the remainder of this chapter, an overview of the NESSUS and DARWIN codes is presented followed by a series of application problems. Further information on the probabilistic methods employed in NESSUS and DARWIN can be found in the references.

## 1.2 Overview of NESSUS

NESSUS is a general-purpose tool for computing the probabilistic response or reliability of engineered systems. SwRI researchers initially developed the software to help NASA assess uncertainties in critical space shuttle main engine components [14]. The NESSUS framework allows the user to link traditional and advanced probabilistic algorithms with analytical equations, external computer programs including commercial finite element codes, and general combinations of the two. Eleven probabilistic algorithms are available, including traditional methods such as Monte Carlo simulation and the first-order reliability method (FORM) as well as advanced methods such as the advanced mean value (AMV) and adaptive importance sampling (AIS). In addition, NESSUS provides a hierarchical modeling capability that can link different analysis packages and analytical functions. Once the probabilistic response is quantified, the results can be used to support risk-informed decisions regarding system reliability. A summary of the NESSUS capabilities is shown in Figure 1.2. NESSUS was awarded the R&D 100 award in 2004 because of the numerous enhancements allowing practical application of probabilistic methods to real problems.

### Inputs

- Java-based graphical user interface
- Free format keyword interface
- Ten probability density functions
- Correlated random variables
- Users/Theory/Examples manual

### Outputs

- Cumulative distribution function
- Prob. of failure given performance
- Performance given prob. of failure
- Probabilistic sensitivity factors wrt  $\mu$  and  $\sigma$
- Confidence bounds
- Empirical CDF and histogram

### Results Visualization

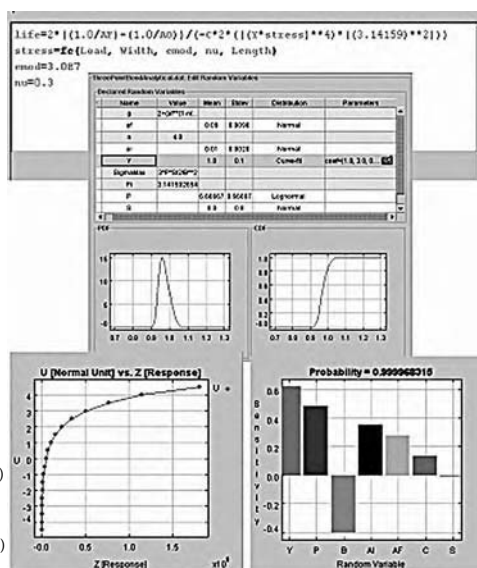
- XY, bar, pie charts
- Comparison of multiple solutions
- 3D model visualization

### Deterministic Analysis

- Parameter variation analysis
- Design of Experiments (DOE)

### Probabilistic Analysis Methods

- First-order reliability method (FORM)
- Second-order reliability method (SORM)
- Fast probability integration (FPI)
- Advanced mean value (AMV+)
- Response surface method (RSM)
- Automatic Monte Carlo simulation (MC)
- Importance sampling (ISAM)
- Latin hypercube simulation (LHS)
- Adaptive importance sampling (AIS)
- Hybrid method (AMV+/AIS2)
- Probabilistic fault-tree (PFTA)



### Applications

- Component/system reliability
- Reliability-based optimization
- Reliability test planning
- Inspection scheduling
- Design certification
- Risk-based cost analysis
- MVFO probability contouring
- Model validation

### Performance Functions

- Analytical (Fortran)
- Analytical (direct)
- Numerical (FEM, CFD, other)
- Failure models (Fortran, ext. models)
- Hierarchical failure models

### Interfaces

- ABAQUS/Standard/Explicit
- MSC. NASTRAN
- ANSYS
- NASA/GRC-FEM
- PRONTO
- DYNA/PARADYN
- LS-DYNA
- MAD YMO
- NASA analysis modules
- NASGRO
- User-defined
- MATLAB
- CTH
- WCN

### Other

- Automated restart
- Batch processing
- Distributed processing support

### Hardware

- PC (NT4, W2000, XP)
- Unix workstations (HP, Sun)
- Linux

FIGURE 1.2 Summary of NESSUS 8.4 capabilities.

In the NESSUS GUI, an outline structure is used to define the required elements for the problem set-up and execution. The user navigates through the nodes of the outline to set up the problem, define the analysis, and view the results. The outline structure for a typical problem is shown in Figure 1.3.

A powerful feature of NESSUS is the ability to link models together in a hierarchical fashion. In the problem statement window, each model is defined in terms of input/output variables and mathematical operators. This canonical description improves readability, conveys the essential flow of the analysis, and allows complex reliability assessments to be defined when more than one model is required to define the system performance. A problem statement for a simple problem is shown in Figure 1.3. The performance is life (number of cycles to failure) given by an analytical stress versus cycles crack model, which requires input from other models. In this case, two stress quantities from an ABAQUS® finite element analysis (FEA) are used in the life equation. Functions are also supported (ABAQUS in this example) and are defined in a subsequent screen. The function can be defined by a numerical model, preprogrammed subroutine, or regression model. This hierarchical model capability provides a general equation form to define the performance by linking results from numerical analysis programs and analytical equations.

Most engineering structures can fail owing to multiple events including multiple failure modes and/or components in which the nonperformance of one or a combination of events can lead to system failure. System reliability considers failure of multiple components of a system and/or multiple failure modes of a component. System reliability assessment is available in NESSUS via a probabilistic fault tree analysis (PFTA) method [15]. System failure is defined through the fault tree by defining bottom (failure) events and their combination with AND and OR gates. Each bottom event considers a single failure (component reliability) and can be defined by a finite element model or analytical function. An example of a fault tree defined in the NESSUS GUI is shown in Figure 1.4.

NESSUS includes a sophisticated Java-based GUI, three-dimensional probability contouring and results visualization, capabilities for performing advanced design of experiments and sensitivity analysis, a probabilistic input database, and state-of-the-art interfaces to many new third-party codes such as

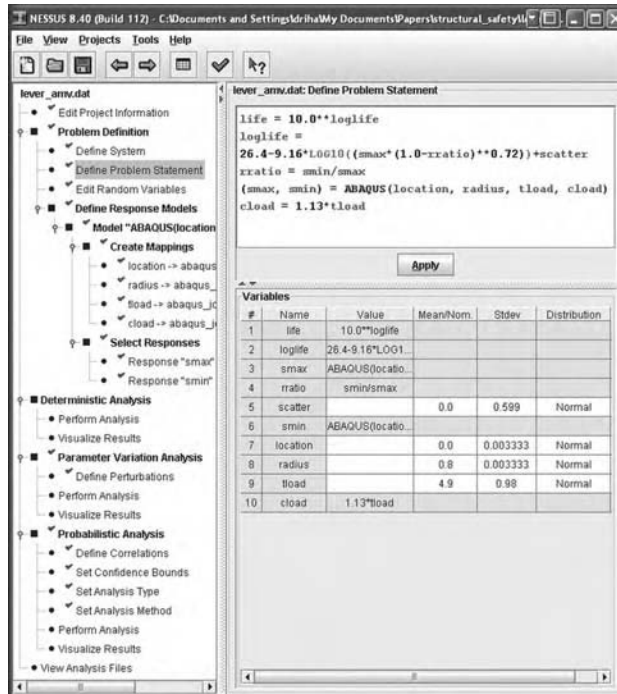


FIGURE 1.3 The NESSUS GUI provides an outline structure on the left that guides the user through the problem setup, analysis, and results visualization. Each model is defined in terms of input/output variables and mathematical operators in the problem statement window. This canonical description improves readability, conveys the essential flow of the analysis, and allows complex reliability assessments to be defined when more than one model is required to define system performance.

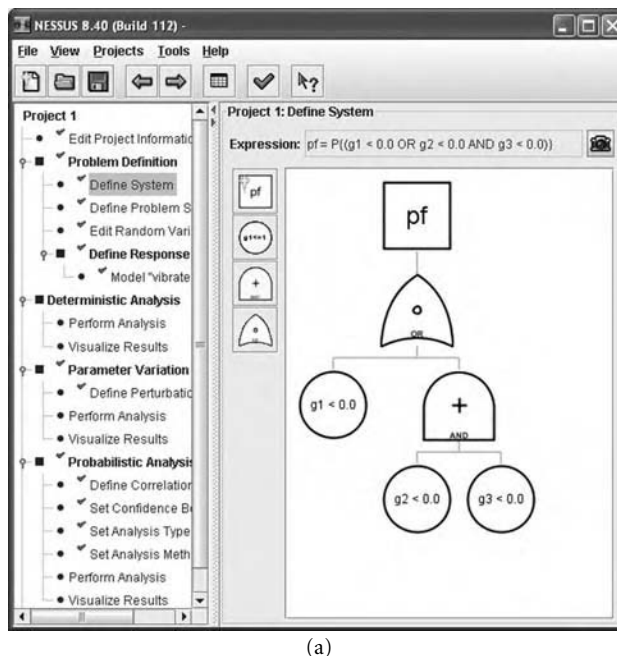
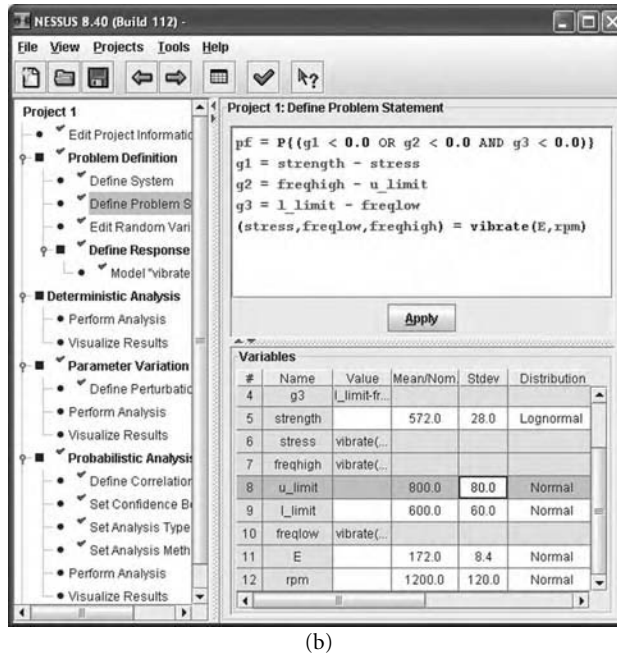


FIGURE 1.4 NESSUS fault definition screens (a) and problem statement (b) for a two-gate three-event system.



(b)

FIGURE 1.4 (Continued).

ABAQUS, ANSYS®, LS-DYNA®, MATLAB®, MSC.NASTRAN®, NASGRO®, and ParaDyn [5]. The NESSUS GUI is highly configurable, allows tailoring to specific applications, and provides capabilities for commercial or in-house developed codes to be easily integrated into the NESSUS framework.

### 1.3 Overview of DARWIN

Rotating components of aircraft gas turbine engines may occasionally contain anomalies introduced during the manufacturing process that are not representative of nominal conditions. These anomalies may occur anywhere within a billet and may change shape during the forging process. If undetected during manufacturing or subsequent field inspections, they can ultimately lead to catastrophic events such as loss of life and loss of the aircraft [16].

A recent FAA Advisory Circular (AC 33.14-1 [17]) provides guidance on the assessment of the risk of fracture associated with inherent anomalies in high-energy rotating components. It describes a probabilistic damage tolerance process that can be used to predict the probability of fracture associated with titanium rotors and establishes a design target risk (DTR) for this event. AC 33.14-1 recommends the consideration of a number of variables for a probabilistic risk assessment of disk fracture, including initial anomaly size, component stress and volume, material properties, crack propagation life, inspection POD, and shop visit time. This document was developed for titanium materials with hard alpha anomalies.

A probabilistic fracture mechanics code called DARWIN® [18] has been developed to predict the risk of fracture associated with rotors and disks containing material anomalies [19,20]. It addresses the influences of the primary random variables such as initial anomaly size, applied stress, and fracture mechanics-related material variables. DARWIN was originally developed for titanium materials, where anomalies are relatively rare and are assumed to form growing cracks during the first cycle of the applied load. A summary of the random variables in DARWIN is provided in Figure 1.5. DARWIN was recently extended to address materials with relatively higher anomaly occurrence rates compared to those found in premium-grade titanium alloys [21]. It provides treatment for anomalies with unequal crack formation periods that may be present in nontitanium materials.

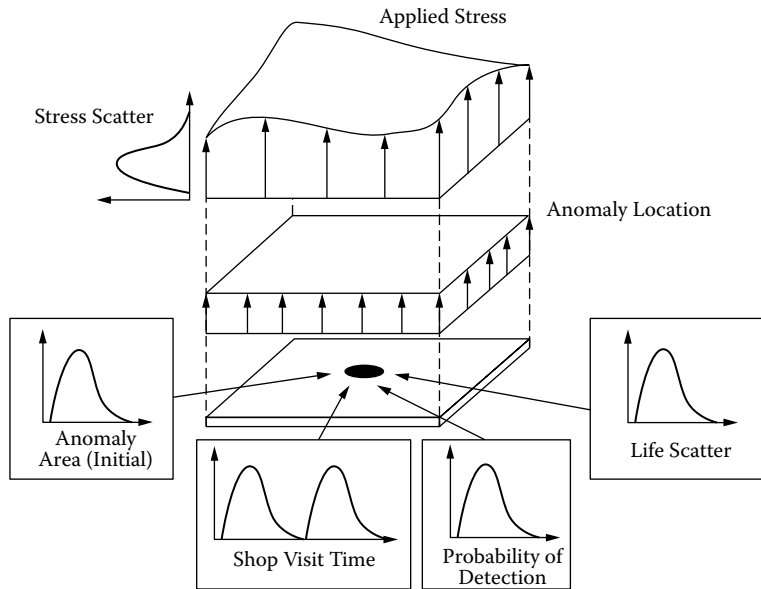


**FIGURE 1.5** Summary of the random variables associated with DARWIN risk assessment.

The computation time associated with a probabilistic fracture mechanics-based risk assessment may be nontrivial. To improve the efficiency of risk computations, an approximate solution is used to address the uncertainty associated with the location of the anomaly. As shown in Figure 1.6, the disk is subdivided into regions of approximately equal risk, called *zones*. The volume of material contained in a single zone will experience similar stresses and inspection schedules, and has similar material properties and POD. Therefore, anomalies located within a zone will exhibit similar crack growth life values. The crack propagation life is estimated using stress intensity factor solutions for cracks in rectangular plates [22] and cracks at holes that approximate the actual component geometry and stress distributions, illustrated in Figure 1.7.

In addition to inherent anomalies, engine disks may also be subjected to induced anomalies. These anomalies are introduced during manufacturing and handling operations, and are typically found on machined surfaces. In contrast with inherent anomalies in which fracture risk is based on the volume of

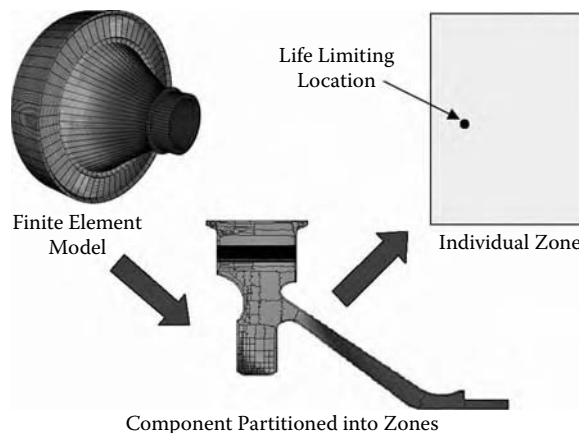


**FIGURE 1.6** DARWIN uses a zone-based approach for risk assessment in which a component is partitioned into subregions of approximately equal risk.

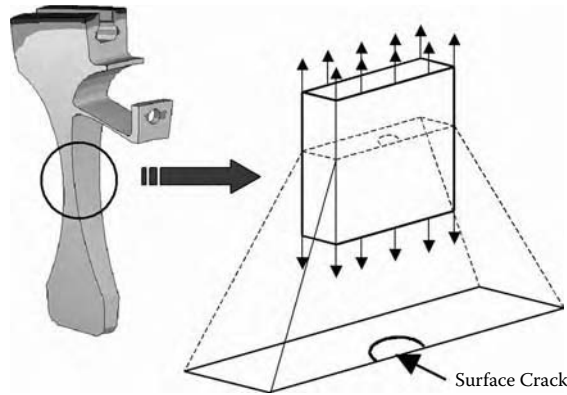


**FIGURE 1.7** In DARWIN, crack propagation life is estimated using stress intensity factor solutions associated with cracks in rectangular plates and cracks at holes.

a component, the fracture risk for induced anomalies is based on the surface area associated with specific features such as bolt holes.

There are many similarities in the risk assessment of components with inherent and induced anomalies. Most of the random variables are identical for these anomaly types (e.g., applied stress, crack growth life variability, inspection time, and POD). Life prediction for both anomaly types requires descriptions of crack geometry and associated boundary conditions, applied stresses on the crack plane, and fatigue crack growth properties. The crack growth process is often very similar for these two anomaly types. Therefore, a general probabilistic approach is used in DARWIN to assess the risk of both anomaly types.

A summary of the general probabilistic approach is shown in Figure 1.8 [23]. It incorporates features that are common to these anomaly types into a general probabilistic framework, and addresses the

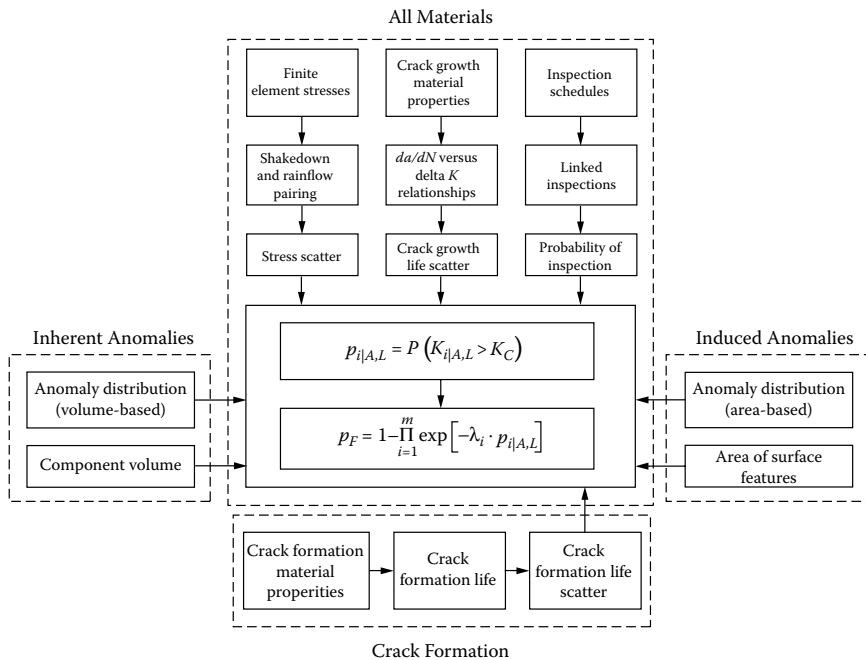


**FIGURE 1.8** The DARWIN general probabilistic framework for risk prediction of components with inherent and induced material anomalies.

additional variables associated with nonzero crack formation times. The major advantage to this approach is that it reduces the number of redundant computational algorithms that must be developed and maintained to support risk computations.

The announcement of FAA Advisory Circular 33.14-1 (Damage Tolerance for High Energy Turbine Engine Rotors) [17] adds a new probabilistic damage tolerance element to the existing design and life management process for aircraft turbine rotors. Use of DARWIN is an acceptable method for complying with AC33.14-1, and has the potential to reduce the uncontained rotor disk failure rate and identify optimal inspection schedules.

## 1.4 Application Examples

The NESSUS and DARWIN software have been used to predict the probabilistic response for a wide range of problems. Several problems are presented in this section to illustrate probabilistic modeling approaches, solution strategies, and results use and interpretation. Sufficient detail is provided for the reader to understand the modeling approach and results, and additional information is available in the references. Each application is also concluded by a short summary that highlights the main features and results of the specific analysis approach.

### 1.4.1 Gas Turbine Engine Rotor Risk Assessment

Consider the aircraft rotor disk shown in Figure 1.6. The design life of the disk is 20,000 flight cycles. Internal stresses and temperatures are identified using FEA based on operational loading conditions. Five primary random variables are considered for probabilistic analysis. The main descriptors for three of these variables (stress scatter, life scatter, and inspection time) are indicated in Table 1.1. For the remaining two variables (defect area, POD), empirical distributions (AIA POST95-3FBH-3FBH defect distribution, #3 FBH 1:1 Reject Calibration POD Curve) found in AC33.14-11 [17] were used for probabilistic fatigue life predictions. A total of 44 zones were used to model the disk. Additional details regarding the selection of random variables and associated distributions can be found in the literature [18,25].

Failure probability results from DARWIN are shown in Figure 1.9 (100 samples per zone). It can be observed that the mean disk failure probability is below the target risk value specified by the FAA Advisory Circular 10 ( $1 \times 10^{-9}$ ). However, the upper confidence bound result (no inspection) is well above the target risk, so variance reduction is needed. As shown in Figure 1.10, the desired variance reduction can be achieved by increasing the number of samples in each zone to 100,000. However, this requires a total of over 4 million samples for the disk.

In Figure 1.11, a comparison of the confidence bounds against the number of disk samples is shown for three sample allocation approaches: uniform (i.e., same number of samples in all zones), RCF (risk contribution factor), and optimal (see Reference 25 for further details). For a specified number of samples it can be observed that, compared to the uniform approach, the confidence bounds are narrower for the RCF and optimal approaches. The target risk can be achieved with the RCF and optimal approaches with approximately 40,000 disk samples (over 4 million disk samples are required for the uniform approach). It is interesting to note that the optimal method converges only slightly faster than the RCF approach.

This example illustrates the application of probabilistic methods to fracture mechanics-based life assessment. It demonstrates the inverse relationship among the number of Monte Carlo samples and the numerical accuracy associated with sampling-based failure probability predictions. In addition, it illustrates the computational advantages associated with variance reduction techniques.

**TABLE 1.1** Titanium Aircraft Rotor Application Example—Random Variables

Random Variable	Median	COV(%)	Distribution
Stress scatter	1.0	20	Lognormal
Life scatter	1.0	40	Lognormal
Inspection time	10,000 cycles	20	Normal



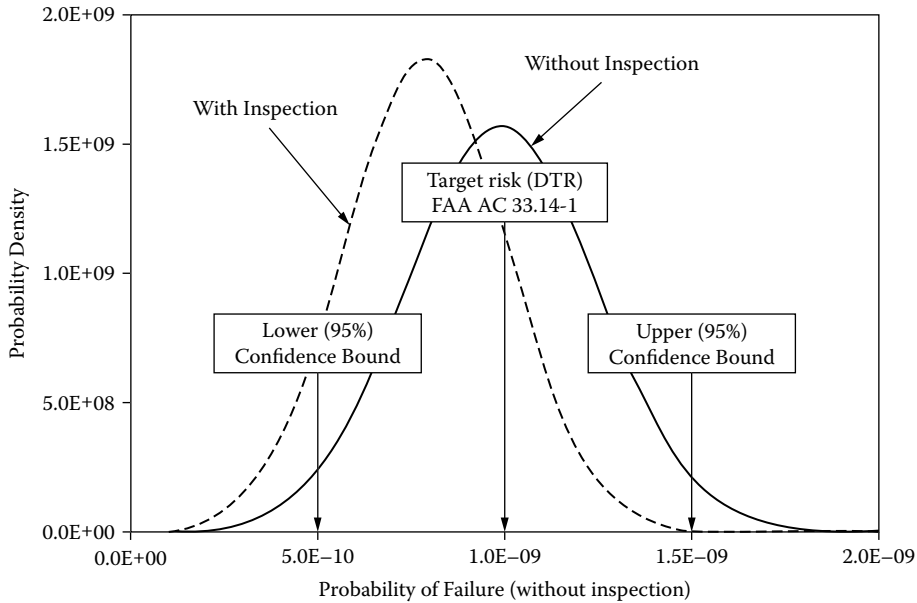


**FIGURE 1.9** Upper confidence bounds on disk risk results for a fixed number of zones initially do not satisfy FAA target risk. (From Enright, M.P. and Millwater, H.R., Optimal Sampling Techniques for Zone-Based Probabilistic Fatigue Life Prediction, in *Proceedings of 43rd Structures, Structural Dynamics, and Materials Conference, Non-Deterministic Approaches Forum*, AIAA/ASME/ASCE/AHS/ASC, Denver, CO, 2002. With permission.)

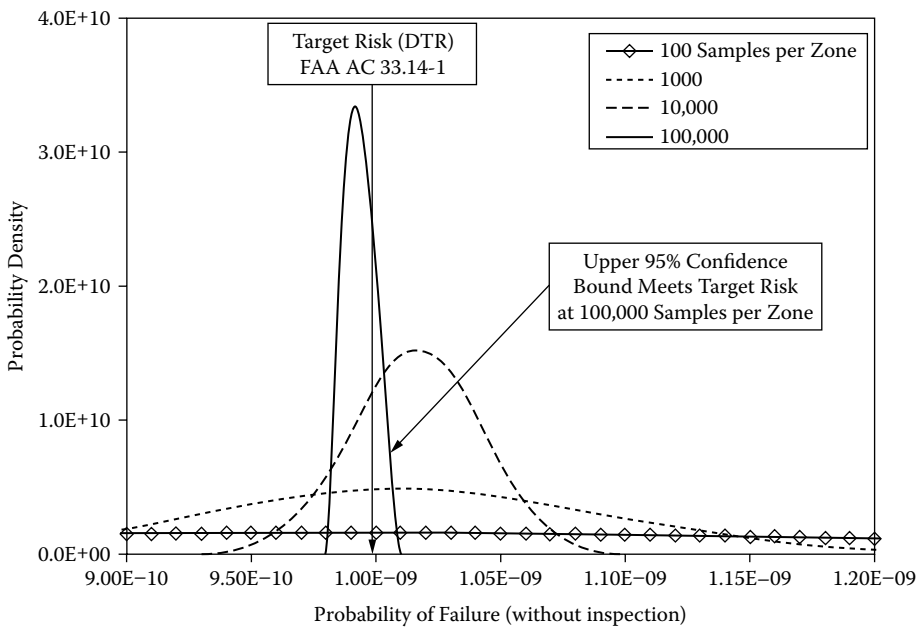


**FIGURE 1.10** Increasing the number of zone samples reduces variance but is computationally expensive. (From Enright, M.P. and Millwater, H.R., Optimal Sampling Techniques for Zone-Based Probabilistic Fatigue Life Prediction, in *Proceedings of 43rd Structures, Structural Dynamics, and Materials Conference, Non-Deterministic Approaches Forum*, AIAA/ASME/ASCE/AHS/ASC, Denver, CO, 2002. With permission.)

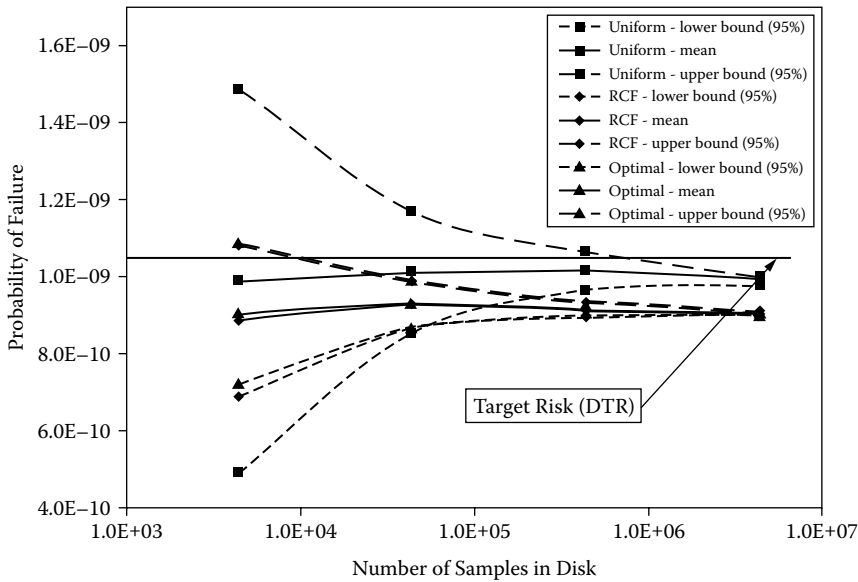


**FIGURE 1.11** Comparison of three disk variance reduction techniques (uniform, RCF, and optimal). (From Enright, M.P. and Millwater, H.R., Optimal Sampling Techniques for Zone-Based Probabilistic Fatigue Life Prediction, in *Proceedings of 43rd Structures, Structural Dynamics, and Materials Conference, Non-Deterministic Approaches Forum*, AIAA/ASME/ASCE/AHS/ASC, Denver, CO, 2002. With permission.)

### 1.4.2 Stochastic Crashworthiness

Vehicle reliability usually entails comparing analysis results to those of a design guide, or for the case of safety and crash, NHTSA requirements. This approach does not take into account (in a quantifiable manner) the fact that there is inevitably some element of uncertainty in the basic design parameters, such as material properties, tolerances, and loadings. Crashworthiness characteristics quantify the safety of a vehicle and have a direct correlation to quality. Measures of quality are widely publicized in magazines, news reports, and Web sites. In many cases, these are heavily depended on by consumers in making vehicle choices and therefore have direct impact on revenue. The crashworthiness characteristics are generally determined by one or at most a few crash tests. These tests are expensive, and low scores by an independent testing organization can have serious revenue consequences. Therefore, a model that can predict the reliability of vehicle safety can reduce expensive crash testing, quantify the reliability, and enable a designer to perform manufacturing/material cost and crashworthiness metric trade-offs.

NESSUS was used to identify the most effective design changes to improve reliability of a small vehicle during an impact with a larger vehicle [26]. The developed approach and models can be applied to different impact scenarios and vehicle types. The stochastic crashworthiness model is based on an LS-DYNA finite element model of a vehicle frontal offset impact and a MADYMO model of a 50th percentile male Hybrid III dummy to predict the system performance metrics. The LS-DYNA finite element model used in this analysis was built by the National Crash Analysis Center (NCAC) and is shown in Figure 1.12. It consists of over 250,000 nodes and 240,000 elements and was analyzed using LS-DYNA version 960 on SGI and HP parallel platforms. The analysis time was approximately 30 CPU hours using eight processors. In this study, the influence of parameters such as uncertainty in weld quality (stiffness, failure strength), uncertainty in various material properties (yield, ultimate strength, strain hardening), uncertainty in local thickness of stamped parts, and, finally, imperfections due to actual assembly processes were used as input variables. The uncertainty in the bumper installation location is one random variable that requires that the nodal coordinates of the model be changed for each value of the installation location

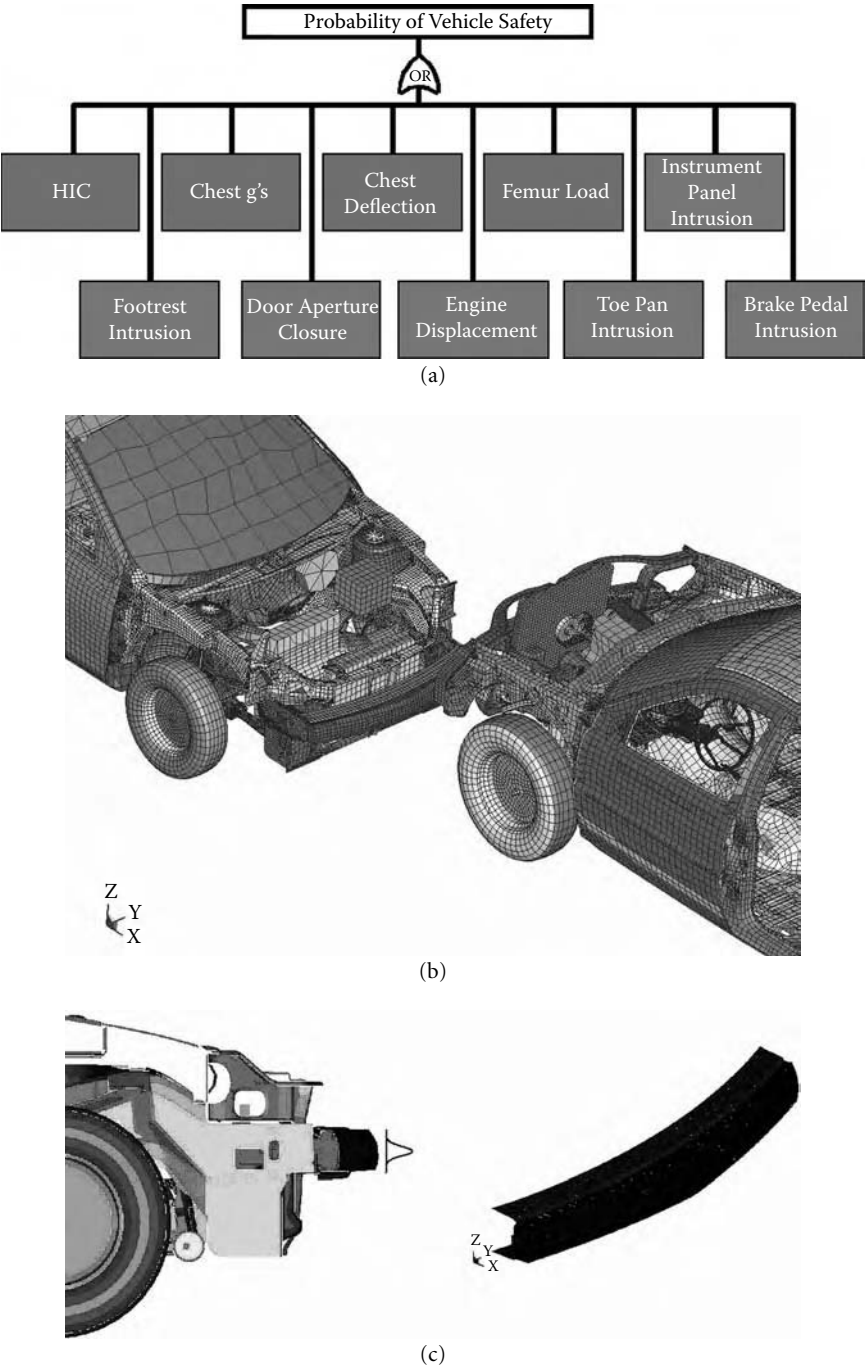


**FIGURE 1.12** Crashworthiness fault tree definition (a), LS-DYNA finite element model (b), and the random variable modeling the uncertainty in the bumper installation height (c).

required by the probabilistic algorithms. The portion of the finite element model changed by this random variable is shown in Figure 1.12.

Response quantities from the models were used to define four occupant injury acceptance criteria and six compartment intrusion criteria. MADYMO was used to predict the head injury criteria (HIC), chest

acceleration, chest deflection, and femur load. The limit states for each of these failure criteria are developed using limiting values from federal motor vehicle safety standards (FMVSS). The six compartment intrusion criteria are computed from LS-DYNA displacement values and limiting values provided by guidelines from the Insurance Institute of Highway Safety. An acceleration history from the LS-DYNA vehicle model is used as the crash pulse input to the occupant injury model in MADYMO. These ten acceptance criteria were used as events in a probabilistic fault tree to compute the overall system reliability (Figure 1.12).

NESSUS was used to compute the reliability of each acceptance criterion and the system reliability by combining all acceptance criteria events into a probabilistic fault tree. A response surface model was developed for each acceptance criterion to facilitate the probabilistic analysis and vehicle design trade-off studies. A redesign analysis was performed using the computed probabilistic sensitivity factors to direct design changes. These sensitivities were used to identify the most effective changes in model parameters to improve the reliability.

Probabilistic redesign increased reliability from 23 to 86% and improved the NCAP star rating from 4 to 5 stars. Major reliability improvements for occupant injury and compartment intrusion can be realized by certain specific modifications to manufacturing tolerances and supplier material quality. The reliability improvement and specific design changes are shown in Figure 1.13. The star rating probability uses the HIC and chest acceleration failure modes and yields a 5-star rating even when the system reliability using the additional failure modes is approximately 40%. Including the other failure modes through the probabilistic fault tree correctly accounts for correlated events and provides the sensitivity factors of the system-level failure probability. This information enables a designer to apportion the system reliability among the different failure modes in an optimal way to design a safer vehicle.

A system reliability analysis is critical to the correct evaluation of the vehicle performance, especially for evaluating the probabilistic sensitivity factors at the system level for redesign analysis. Certain parameters such as stiffness/strength parameters can improve reliability for compartment intrusion performance measures but may be detrimental to the crash pulse attenuated to the vehicle occupant. The system model correctly accounts for events with common variables (correlated events) and thus correctly identifies the important variables on the system level.

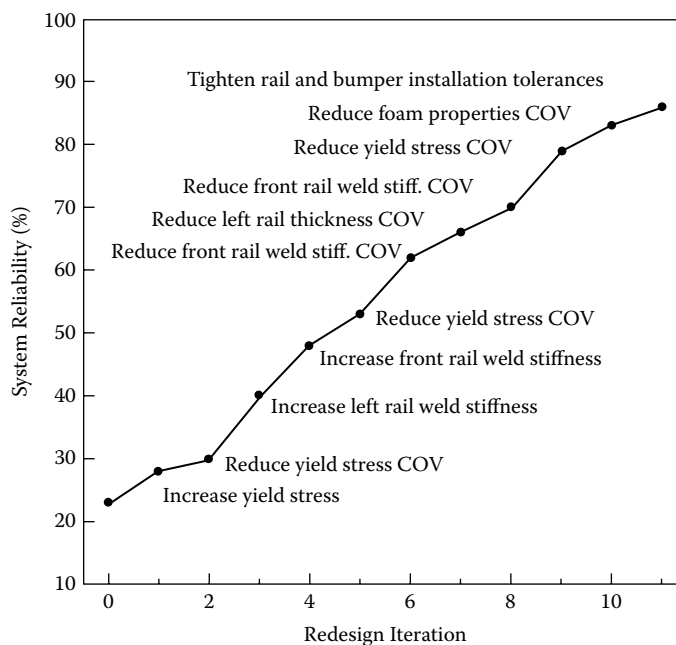


FIGURE 1.13 Vehicle system reliability improvement study performed with NESSUS.

In summary, this application demonstrates how the results of a probabilistic analysis considering complex dynamics, nonlinear material behavior, and large-scale contact and material deformations can be used to improve the crashworthiness of a vehicle and the safety of the vehicle for its occupants. Specifically, by making a series of 11 specific design changes shown in Figure 1.13, the occupant safety is increased from under 30 to nearly 90%. The combination of high-fidelity numerical models and efficient probabilistic methods with fast-running approximate performance models provides a practical approach to the probabilistic design of complex systems.

### 1.4.3 Probabilistic Shuttle Debris Transport Modeling

As a result of the conclusion that debris impact caused the damage to the left wing of the Columbia Space Shuttle Launch Vehicle (SSLV) during ascent, the Columbia Accident Investigation Board [27] recommended that an assessment be performed of the debris environment experienced by the SSLV during ascent. Eliminating the possibility of debris transport is not feasible; therefore, a flight rationale based on probabilistic assessment is required for the SSLV's return to flight. The assessment entails identifying all potential debris sources, their probable geometric and aerodynamic characteristics, and their potential for impacting and damaging critical shuttle components.

The analysis objective was to convert existing NASA analysis models and computer codes into an end-to-end probabilistic analysis tool for the assessment of external tank debris release, impact, and damage to the orbiter [28]. Although the focus was mostly on the development of an analysis approach, a reliability assessment tool was built using the existing NESSUS code. NESSUS allows the user to perform probabilistic analysis with both analytical models and external computer programs such as NASA's debris transport codes.

The debris impact and damage mechanism is governed by the following events:

- $E_1$ : A piece of foam breaks off.
- $E_2$ : Debris travels down to and impacts the shuttle.
- $E_3$ : Impact is of sufficient force to damage the shuttle beyond acceptable limits.

In this probabilistic modeling, a failure occurs if and only if these three events occur concurrently; mathematically this can be expressed as:

$$\begin{aligned}\Pr(\text{failure}) &= \Pr(E_1 \cap E_2 \cap E_3) \\ &= \Pr(E_1)\Pr(E_2 | E_1)\Pr(E_3 | E_1 \cap E_2)\end{aligned}$$

This expression generally tracks the breakdown of the debris analysis into the several subdisciplines involved: debris modeling, CFD analysis, and impact modeling. Note that most of the discipline-specific models are conditional in nature. For example, the CFD analysis used to predict the kinetic energy (event  $E_2$ ) of a divot inherently assumes that a divot has broken off ( $E_1$ ). In other words, the CFD model does not so much model the event  $E_2$  but the conditional event  $E_2|E_1$ .

Figure 1.14 describes how the conditional models are nested within each other due to the conditioning of each event upon the other events. It is worthwhile mentioning that the analysis of an in-flight debris release event, for which the release conditions are fairly well known (from image analysis), can be achieved by considering only the events  $E_2$  and  $E_3$ . In each of the subsequent sections the current state of the modeling will be described. The probability  $\Pr(E_1 \cap E_2 \cap E_3)$  gives the probability of unacceptable damage at a given time of release.

- *Debris release  $E_1$* : Time-dependent probability density functions were fitted to the external tank debris tables generated by the Shuttle Program at the NASA Michoud Assembly Facility. A different release table must be created for each location of interest.
- *Debris transport and impact  $E_2$* : During transport, lift forces act to disperse the debris about their idealized, or zero-lift, trajectories. Therefore, the farther downstream the debris travels before

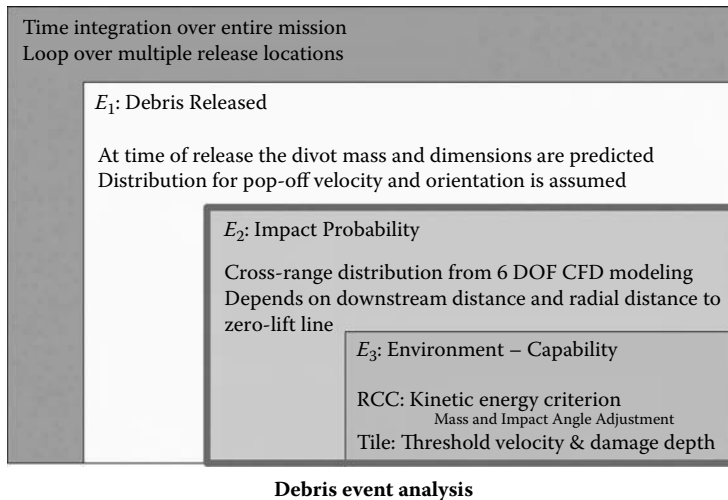


**FIGURE 1.14** Functional outline of the probabilistic debris transport analysis.

impact, the greater the cross-range or dispersion. A rotationally symmetric cross-range distribution was modeled using 6 DOF CFD results generated by NASA Ames and ELORET at Mach 2.5. Depending on the foam shape and initial rotation rate, either a Weibull, lognormal, or truncated normal distribution provides the best fit to the CFD results. This cross-range distribution is overlaid on top of the orbiter geometry to determine the probability of impact (Figure 1.15).

- *Damage to orbiter  $E_3$* : A probabilistic capability model for both the reinforced carbon-carbon (RCC) wing leading edge and the orbiter tile has been implemented. A different distribution is used depending on the nature of the impact: two types of foam and ice are considered. A normal distribution is used for RCC, and a Gumbel-min distribution is used for tile. The local incidence angle is an important driver for the RCC panel capability: the capability increases as the incidence angle becomes shallower.

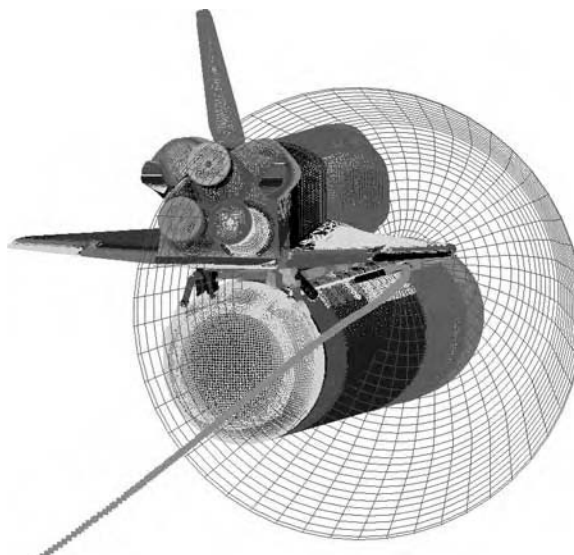


**FIGURE 1.15** Zero-lift line and 3-sigma cone for PAL ramp release location.

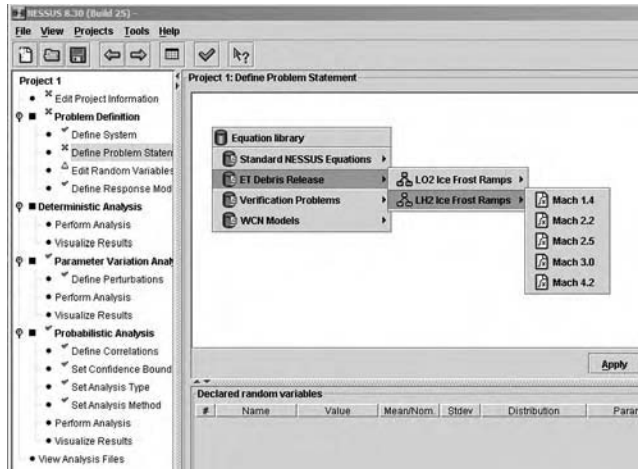
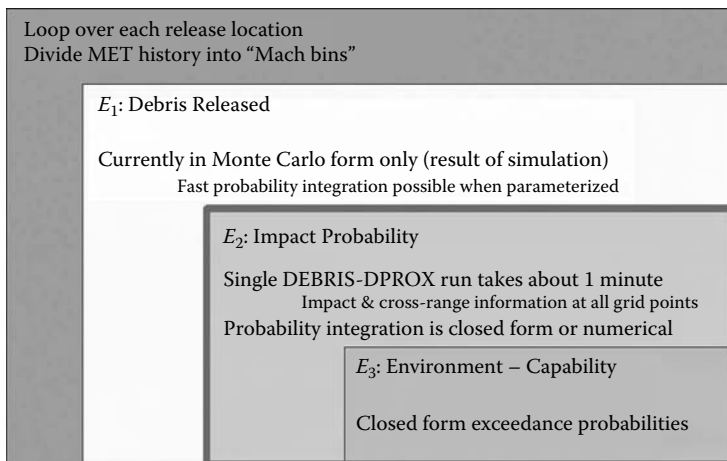


FIGURE 1.16 A right-mouse click in the NESSUS problem statement window activates the DTA equation database.

Various uncertainties affect the debris transport process. For instance, debris pieces travel downstream along a somewhat erratic path; advanced 6 DOF CFD results were used to develop a stochastic model of this cross-range. Statistical descriptions of the RCC panel and tile zone capability were derived directly from experimental impact results. In addition to the highly stochastic nature of the release and transport of debris, uncertainties exist in the atmospheric conditions, mission profile, impact conditions, and material properties.

The deterministic and probabilistic models were embedded in the NESSUS software and predict the probability of impact and damage to the space shuttle wing leading edge and thermal protection system components. A right-mouse click inside the problem definition window activates the Debris Transport Analysis (DTA) equation database (Figure 1.16). By simply clicking on the debris release location and time of interest, the appropriate model and variable definition are created.

The analysis tool is configured to enable quick analysis of any potential debris release event that may be recorded during the orbiter's ascent into space. The conditional probabilistic analysis of a debris release can be performed very quickly (see Figure 1.17). For such an event the release conditions are—at least approximately—known, and the probability  $\Pr(E_2 \cap E_3 \mid E_1)$  is readily assessed.



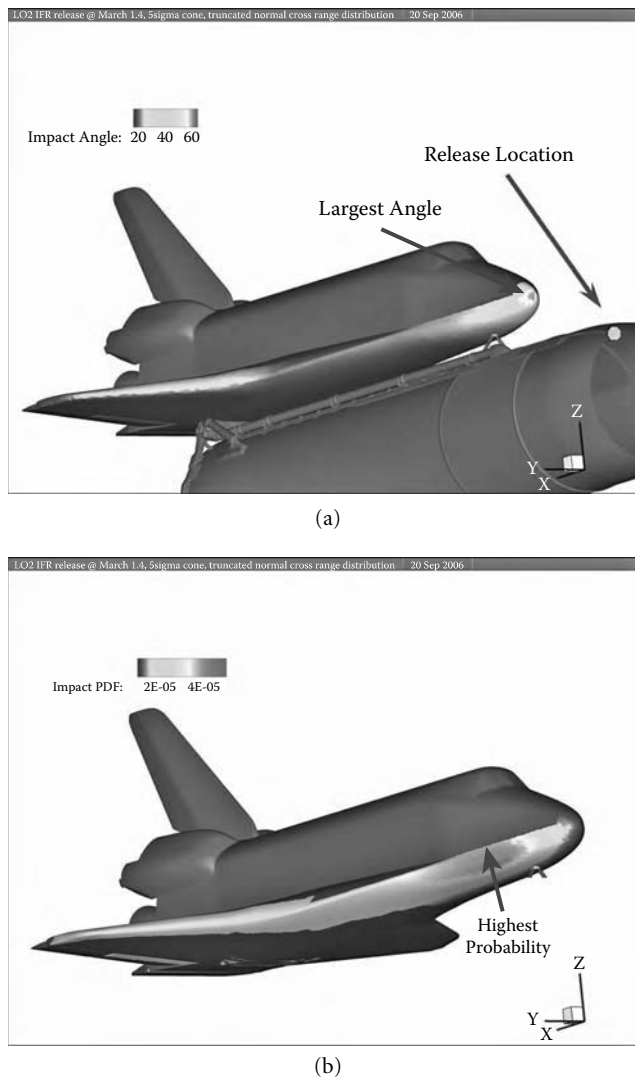
Debris event analysis

FIGURE 1.17 Overview of computational aspects in current debris transport model.

In addition to the probability  $\Pr(E_2 \cap E_3 \mid E_1)$ , the code also generates plots of the sensitivity to a variety of distribution parameters such as the cross-range distribution. This is particularly of interest as the cross-range distribution type is dependent on an unknown initial rotation rate of the debris. These sensitivities point to the key drivers in the problem and were used to guide the allocation of further modeling and analysis efforts.

Among other parameters, the likelihood of unacceptable damage depends on the time of release (Mach number of the orbiter) and the divot mass as well as the impact velocity and impact angle. A typical result is depicted in Figure 1.18. Probability of impact and damage, as well as the sensitivities thereof with respect to the distribution assumptions, can be computed and visualized at each point on the orbiter or summarized per wing panel or tile zone.

In summary, the probabilistic debris transport and damage analysis illustrates approaches to modeling conditional events. The probability of damage is mitigated by including the conditions under which the debris is released and impact occurs. Accounting for all events in the sequence provides an accurate risk of failure.



**FIGURE 1.18** Typical result showing (a) a possible release location and the impact angle and (b) probability of impact to both the RCC panels and thermal protection shield on the space shuttle orbiter.



The probabilistic debris transport analysis specifically decoupled the release, transport, and damage events to evaluate either the probability of damage over the entire mission and orbiter, or to evaluate a specific release condition with a known release location, debris size, and Mach number.

#### 1.4.4 Los Alamos Dynamic Experiment Containment Vessel

Over the past 30 years, Los Alamos National Laboratory (LANL) has been conducting confined high-explosion experiments utilizing large, spherical, steel pressure vessels (Figure 1.19). These experiments are performed in a containment vessel to prevent the release of explosion products to the environment. Design of these spherical vessels was originally accomplished by maintaining that the vessel's kinetic energy, developed from the detonation impulse loading, be equilibrated by the elastic strain energy inherent in the vessel. Within the last decade, designs have been accomplished utilizing sophisticated and advanced 3D computer codes that address both the detonation hydrodynamics and the vessel's highly nonlinear structural response. Additional details of this analysis can be found in References 29 and 30.

The containment vessel is a spherical vessel with three access ports: two 16-in. ports aligned in one axis on the sides of the vessel and a single 22-in. port at the top of the vessel. The vessel has an inside diameter of 72 in. and a 2 in. nominal wall thickness. The vessel is fabricated from HSLA-100 steel, chosen for its high strength, high fracture toughness, and no requirement for postweld heat treatment. The vessel's three ports must maintain a seal during use to prevent any release of reaction product gases or material to the external environment. Each door is connected to the vessel with 64 high-strength bolts, and four separate seals at each door ensure a positive pressure seal.

A series of hydrodynamic and structural analyses of the spherical containment vessel were performed using a combination of two numerical techniques. Using an uncoupled approach, the transient pressures acting on the inner surface of the vessel were computed using the Eulerian hydrodynamics code, CTH (Sandia National Laboratories), which simulated the high-explosive (HE) burn, the internal gas dynamics, and shock wave propagation. The HE was modeled as spherically symmetric with the initiating burn taking place at the center of the sphere. The vessel's structural response to these pressures was then analyzed using the DYNA3D explicit finite element structural dynamics code.

The simulation required the use of a large, detailed mesh to accurately represent the dynamic response of the vessel and to adequately resolve the stresses and discontinuities caused by various engineering features such as the bolts connecting the doors to their nozzles. Taking advantage of two planes of symmetry, one-quarter of the structure was meshed using approximately 1 million hex elements. The structural response simulation used an explicit finite element code called PARADYN (Lawrence Livermore National Laboratory), which is a massively parallel version of DYNA3D, a nonlinear, explicit Lagrangian FEA code for 3D transient structural mechanics. PARADYN was run on 504 processors of LANL's "Blue Mountain" massively parallel computer, which is an interconnected array of independent SGI (Silicon Graphics, Inc.) computers. The containment vessel model can be solved on the Blue Mountain computer

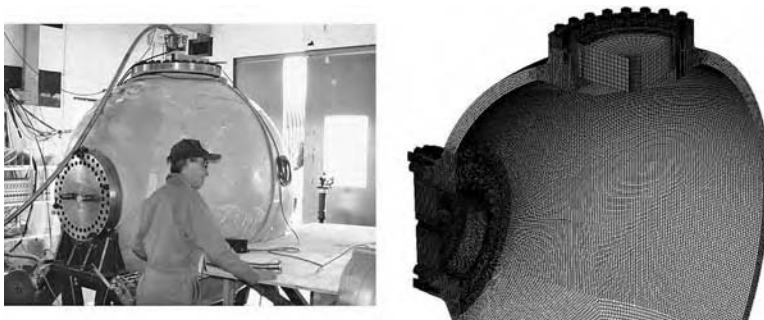


FIGURE 1.19 LANL 6-ft ID containment vessel and one-quarter symmetry mesh used for the structural analysis.

**TABLE 1.2** Probabilistic Inputs for the Containment Vessel Example Problem

Variable	PDF	$\mu$	$\sigma$	COV
Radius (in.)	Normal	37.0	0.0521	0.00141
Thickness (in.)	Lognormal	2.0	0.08667	0.04333
$E$ (lb/in. <sup>2</sup> )	Lognormal	29.0E + 06	1.0E + 06	0.03448
$S_y$ (lb/in. <sup>2</sup> )	Normal	106.0E + 03	4.0E + 03	0.03774

with approximately 2.5 hours of run time. The same analysis run on a single process would have required 35 days. The NESSUS restart and batch capability allowed multiple parallel analyses to be performed.

Four random variables were considered and are listed in Table 1.2: radius of the vessel wall (radius), thickness of the vessel wall (thickness), modulus of elasticity ( $E$ ), and yield stress ( $S_y$ ) of the HSLA steel. The properties for radius and thickness are based on a series of quality control inspection tests that were performed by the vessel manufacturer. The coefficients of variation for the material properties are based on engineering judgment. In this case, the material of the entire vessel, excluding the bolts, is taken to be a single random variable.

When the thickness and radius random variables are perturbed, the nodal coordinates of the finite element model change, with the exception of the three access ports in the vessel, which remain constant in size and move only to accommodate the changing wall dimensions. This was accomplished in NESSUS using the model mapping facility, where a vector of direction cosines and magnitudes is defined to describe how much and in what direction each nodal coordinate moves for a given perturbation in both thickness and radius. The NESSUS mapping procedure allows the perturbations in radius and thickness to be cumulative so these variables can be perturbed simultaneously. Once the scale factors are defined and input to NESSUS, the probabilistic analysis, regardless of method, is performed without further user intervention.

The response metric for the probabilistic analysis is the maximum equivalent plastic strain occurring over all times at the bottom of the vessel finite element model. This maximum value occurs well after the initial pulse and is caused by bending modes created by the ports.

The AMV+ method in NESSUS was used to calculate the CDF of equivalent plastic strain shown in Figure 1.20. Also, Latin Hypercube Simulation (LHS) was performed with 100 samples to verify the

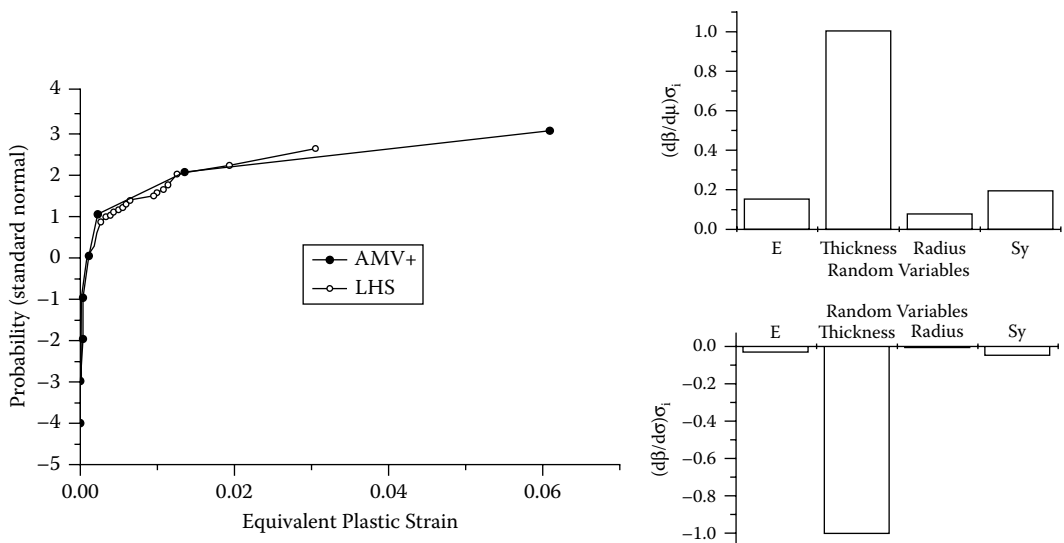


**FIGURE 1.20** Cumulative distribution function (CDF) of equivalent plastic strain plotted on standard normal scale (left) and probabilistic sensitivity factors in the form of normalized derivatives of the safety index with respect to mean (right top) and standard deviation (right bottom) for the CDF point at  $u = 3$  (standard normal unit).

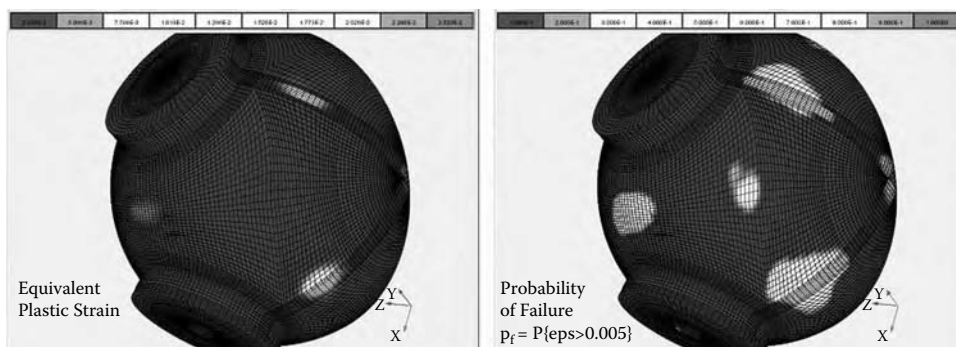


**FIGURE 1.21** Contours of equivalent plastic strain (left) and probability of equivalent plastic strain exceeding 0.5% (right). Light shades indicate higher strain and probability values.

correctness of the AMV+ solution near the mean value. As shown, the LHS and AMV+ results are in excellent agreement. However, in contrast to the LHS solution, the AMV+ solution predicts probabilities in the extreme tail regions with far fewer PARADYN model evaluations.

Probabilistic sensitivities are also shown in Figure 1.20 and are multiplied by  $\sigma_i$  to nondimensionalize the values and facilitate a relative comparison between parameters. The values are also normalized such that the maximum value is equal to one. It can be concluded that the reliability is most sensitive to the mean and standard deviation of the thickness of the containment vessel wall.

Because of the statistical variations in thickness and radius, and the time-varying wave propagations caused by the loadings, the probability of exceeding 0.5% plastic strain was also computed over the complete mesh domain using the NESSUS probability-contouring capability. The NESSUS restart capability allows the probability contours to be computed without any additional PARADYN runs. Contours displaying equivalent plastic strain (deterministic PARADYN results) are shown on the left in Figure 1.21; contours displaying the probability of exceeding 0.5% equivalent plastic strain are shown on the right of the figure. The difference between the two contour plots clearly shows the additional (and different) information the probabilistic results produce.

In summary, this analysis demonstrates the application of probabilistic methods to large-scale numerical models. The containment vessel model consisted of approximately 1 million elements and required a nonlinear solution taking several hours of execution time. The radius and thickness random variables required that the finite element geometry be recreated for each realization of these variables by the probabilistic algorithms (e.g., 100 different meshes were created for the LHS analysis). The NESSUS variable-mapping capabilities automatically create these different meshes. Advanced probabilistic methods such as AMV+ are capable of efficiently generating probability predictions and sensitivity factors for computationally intensive and nonlinear problems. In general, limited sampling is employed when feasible to increase confidence in the approximate method solutions. Probability contouring is essential for identifying critical failure locations when the performance is affected by random variables that vary spatially. The method is especially useful in nonlinear applications, in which the response changes due to variations in geometry and transient loads are usually not intuitive.

### 1.4.5 Cervical Spine Impact Injury Assessments

Cervical spine injuries occur as a result of impact or from large inertial forces such as those experienced by military pilots during ejections, carrier landings, and ditchings. Other examples include motor vehicle, diving, and athletic-related accidents. Reducing the likelihood of injury by identifying and understanding the primary injury mechanisms and the important factors leading to injury motivates research in this area.

Because of the severity associated with most cervical spine injuries, it is of great interest to design occupant safety systems that minimize the probability of injury. To do this, the designer must have

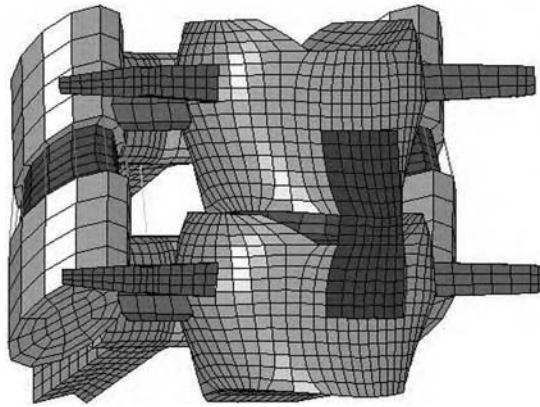


**FIGURE 1.22** C5–C6 motion segment finite element model.

quantified knowledge of the probability of injury due to different impact scenarios, and also know which model parameters contribute the most to the injury probability. Stress analyses play a critical role in understanding the mechanics of injury and the effects of degeneration as a result of disease on the structural performance of spinal segments, and FEA is the method of choice to conduct these analyses. However, in many structural systems, there is a great deal of uncertainty associated with the environment in which the spine is required to function. This uncertainty has a direct effect on the structural response of the system. Biological systems are an archetypal example: uncertainties exist in the physical and mechanical properties and geometry of the bone, ligaments, cartilage, joint, and muscle loads. Hence, the broad objective of this investigation is to explore how uncertainties influence the performance of an anatomically accurate, 3D, nonlinear, experimentally validated finite element (FE) model of the cervical spine.

Four FE models of the C5–C6 (cervical vertebrae numbers 5 and 6) motion segment were generated to represent large and small males and females. The geometry for those models was taken from computed tomography (CT) scans of healthy volunteers with ages ranging from 18 to 40 years. A parametric FE model was created that uses 35 independent dimension parameters that can be directly measured from CT scan images [31]. A total of 73 (23 female and 50 male) volunteers were scanned and measured. The parameter measurements were then averaged into the four different groups: small female (106–120 lb), large female (136–150 lb), small male (166–180 lb), and large male (226–240 lb). The four models were then generated using an all-hexahedral finite element mesh generation package (TrueGrid, v.2.4, XYZ Scientific, Livermore, CA) and analyzed in LS-DYNA®. A sample model is shown in Figure 1.22.

Five ligaments of the cervical motion segment were modeled: the anterior longitudinal ligament (ALL), the posterior longitudinal ligament (PLL), the joint capsular ligaments (JC), the interspinous ligament (ISL), and the ligament flavum (LF). Cross-sectional areas for the ALL and PLL are modeled with hexagonal elements using previously determined values. The JC, ISL, and LF are modeled with spring elements using experimental force-displacement data from the literature [32].

A Monte Carlo analysis was first performed on the FE models of the ALL and PLL to verify that the probabilistic dynamic response of the ligament model accurately simulated experimental results. The means, standard deviations, and distributions for the material parameters (Table 1.3) and ligament cross-section area (Table 1.4) were calculated from the experimental data and applied to the FE model. Variations of the bulk modulus ( $K$ ) and viscoelastic coefficients ( $G_2$ ,  $G_4$ ,  $G_{\infty}$ ), along with the associated correlations between these variables and the cross-sectional area were used to perform a 10,000-sample Monte Carlo analysis on the relaxation response of the ligaments using NESSUS. Lognormal distributions were assumed for all variables. By applying the calculated statistical variation to the FE model, we were able to simulate not only the mean response of the ligaments but also the variation in that response (Figure 1.23). The cumulative distribution function (CDF) for the maximum force during the relaxation experiment was plotted with the predicted CDF in Figure 1.24.

TABLE 1.3 Material Properties for the ALL and PLL

		$G_2$	$G_4$	$G_{\infty}$	$K$ (N/mm <sup>2</sup> )
ALL	Mean	0.107	0.613	0.279	104.4
	St Dev	0.032	0.083	0.079	46.0
PLL	Mean	0.111	0.641	0.248	114.7
	St Dev	0.030	0.082	0.083	44.2
Annulus—male	Mean	0.038337	0.743974	0.102088	15.13683
	St Dev	0.096347	0.196770	0.074908	22.95371
Annulus—female	Mean	0.049680	0.393058	0.235738	28.94731
	St Dev	0.064018	0.372591	0.178332	65.59087

TABLE 1.4 Ligament Cross-Sectional Area

	Mean	SD
C5–C6 ALL	12.4853	0.855137
C5–C6 PLL	15.0556	0.99509

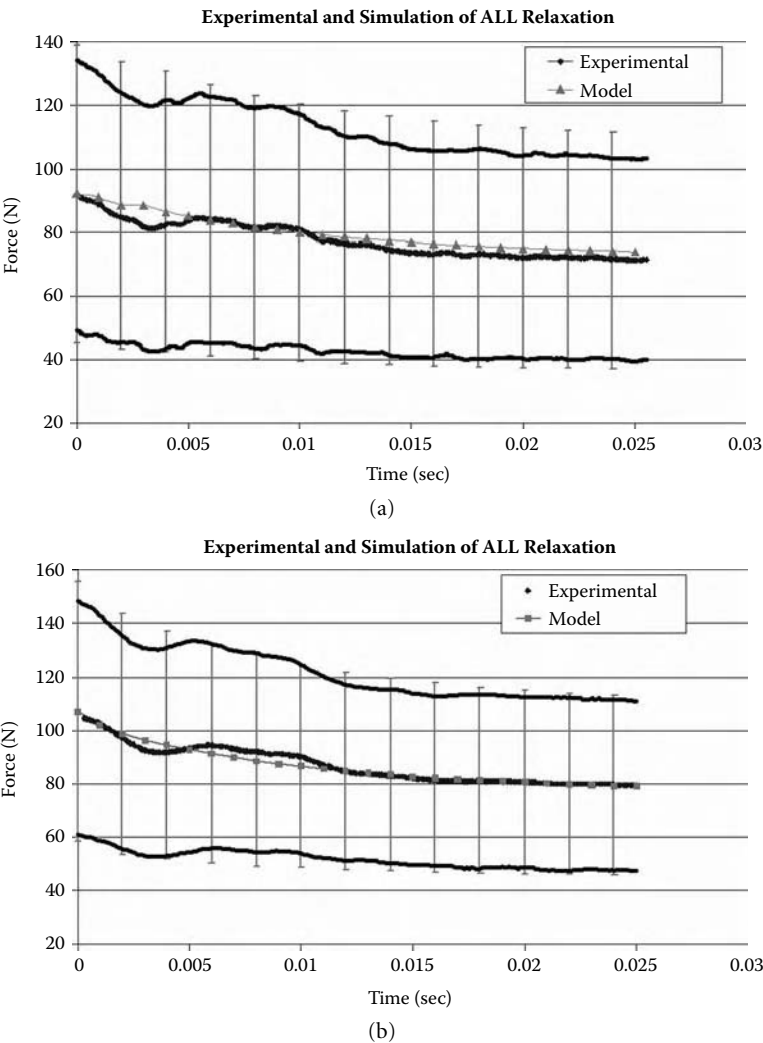
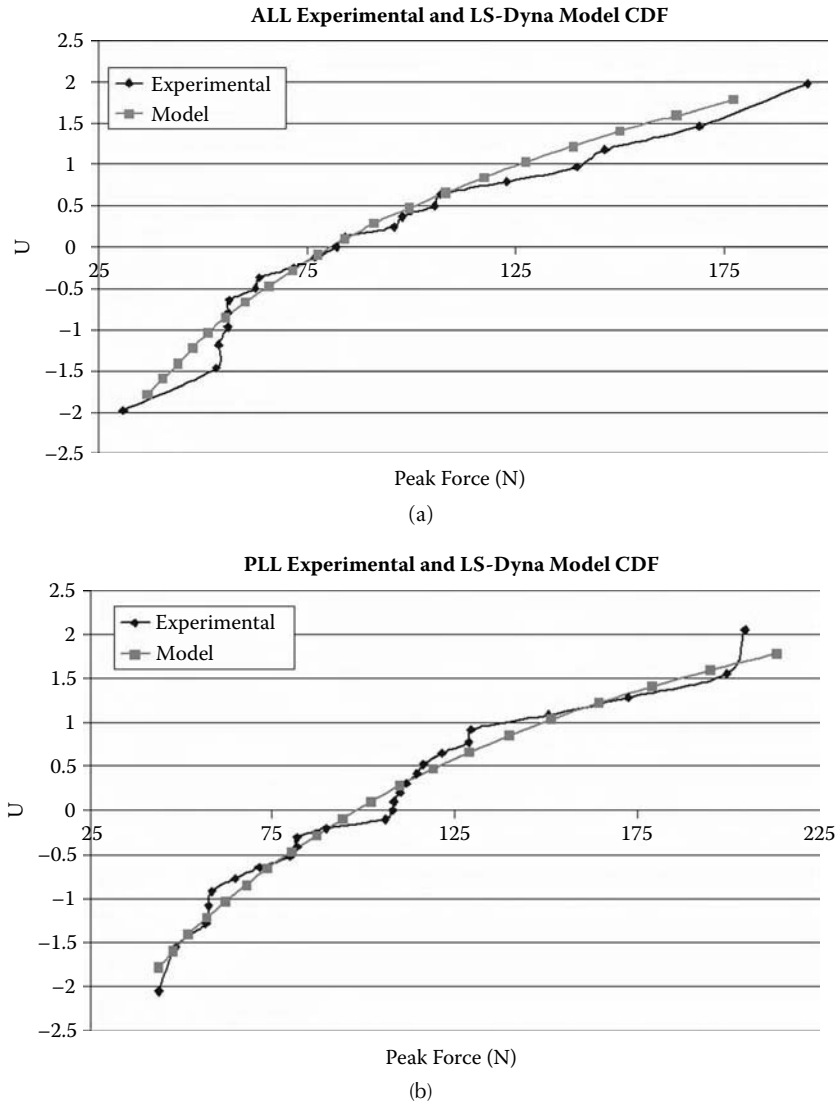
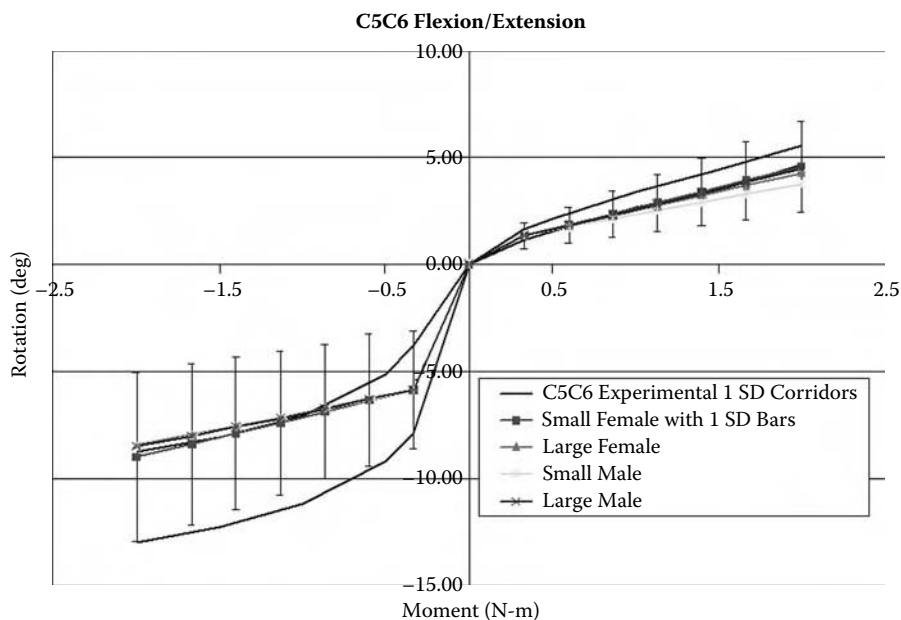


FIGURE 1.23 Experimental and model relaxation response of the ALL (a) and the PLL (b) with +/-1 standard deviation experimental and simulated corridors.



**FIGURE 1.24** Experimental and model CDFs for the maximum force during a 25% strain relaxation test for the ALL (a) and the PLL (b).

A probabilistic analysis of the C5–C6 motion segment was performed using the random variables that were generated for the ligaments' material properties, ligament areas, and disk material properties as shown in Table 1.3 and Table 1.4. For each motion segment of each gender and weight group, 100 Latin Hypercube Samples (LHSs) were used to determine the mean response and variation in quasi-static axial rotation, lateral bending, flexion, and extension under a 2 N-m moment. The variables for the LHS analysis included  $G_2$ ,  $G_4$ ,  $G_{\text{infinity}}$ , and  $K$  of the ALL, PLL, and annulus, as well as the ALL area, PLL area, ISL area, and joint capsule ligament areas. A lognormal distribution was used for all variables and a 10% COV was assumed for the ISL area and the joint capsule ligament area. NESSUS was used to predict the probabilistic response for the entire range of motion during the 2 N-m loading. Figure 1.25 shows the response for flexion/extension compared to experimental results from the literature [33] (similar results are available for axial and lateral bending). The results show that the models predict the response and variation well. The large experimental corridors illustrate the variability that exists in biological systems.



**FIGURE 1.25** Probabilistic response of a C5–C6 motion segment in flexion and extension shown with C5–C6 experimental data  $\pm 1$  SD.

The coefficient of variation (COV) of the maximum rotation for the small female, calculated from the probabilistic model, averaged approximately 42%, which reflects the variation shown in the experimental results.

In summary, the cervical spine impact injury assessment demonstrates the use of numerical models to predict the performance of a complex system when full-scale testing is not possible. The parametric models are being validated against motion segment experiments. Specific element tests such as the ligament behavior are being used to validate specific material models. These model validation studies increase confidence in the deterministic and probabilistic predictions. The probabilistic approach also provides a mechanism to account for the large variations and uncertainties in biological systems. Future work in this area should include development of a high-fidelity continuum cervical spine model for assessing the combined likelihood of vertebral fracture, ligament sprain, and disk rupture with the identification and classification of clinically relevant injury modes. Additionally, research is needed to integrate random process loading and random field representations of geometrical variations and initial configuration into the probabilistic model. To be directly useful in aircraft crew systems designs, the probabilistic methodology must be integrated into an occupant-safety design tool such that the sensitivity of design (controllable) parameters are related to probability of injury.

#### 1.4.6 Fracture Reliability of Space Shuttle Main Engine Flowliner

In May of 2002, three cracks were discovered in the flowliner of one of the orbiters near the interface with the low-pressure turbo pump. Cracking was identified as high-cycle fatigue due to flow-induced vibrations produced by the turbo pumps. Initial deterministic fracture mechanics analyses suggested that the fatigue cracks might lead to failure in a single flight. This result was believed to be conservative because of the inherent uncertainty in much of the input, which led to multiple worst-case assumptions in the deterministic analysis.

The feedline flowliners supply liquid hydrogen ( $LH_2$ ) fuel to the low-pressure hydrogen turbo pumps of the space shuttle main engines (Figure 1.26). Although repairs were made to the cracks, subsequent

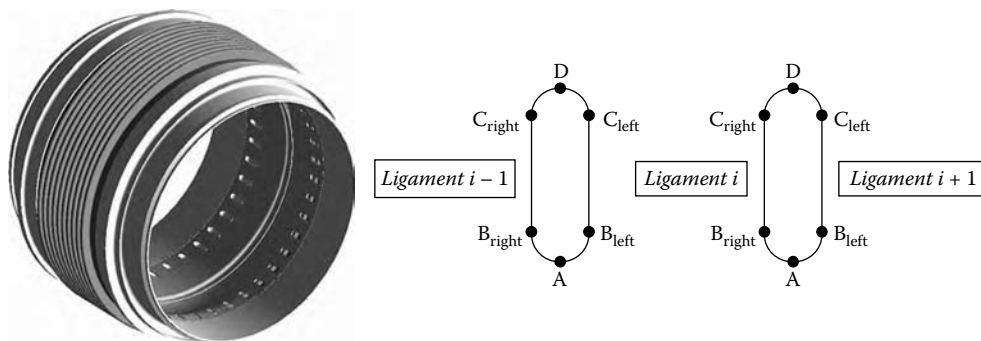


**FIGURE 1.26** Liquid hydrogen feedline showing bellows and flowliner containing slots along with schematic of designated crack locations at flowliner slots. Welds at either end of the feedline serve to connect the feedline to flanges (not shown).

hot-engine test data indicated the possibility of higher stresses in the flowliner than originally estimated. As illustrated in Figure 1.26, cracks can potentially be induced in various orientations (labeled A through D) at any of the 38 slots in the flowliner. However, not all locations exhibit cracking; in fact only 11 cracks were observed in the entire space shuttle fleet. To explore the effects of multiple compounding of conservative assumptions inherent to the existing deterministic fracture mechanics analysis of the flowliner, SwRI, as part of a NASA Engineering Safety Center (NESC) multidisciplinary Independent Technical Assessment (ITA) team, was tasked to conduct a detailed probabilistic fracture mechanics analysis [34,35].

Uncertainty in key input parameters in the initial deterministic analyses led to multiple conservative assumptions regarding (1) initial defect sizes due to uncertainties in inspection capability; (2) load/stress history due to uncertainties in fluid-structure interactions, transient thermal stress, and welding residual stress; and (3) rate of fatigue crack growth due to the uncertain influence of the cryogenic environment ( $\text{LH}_2$  at  $-423^\circ\text{F}$ ). In addition, uncertainties also existed in modeling of the crack-driving forces needed to predict the remaining fatigue life that resulted in conservative assumptions regarding crack shape, as well as other factors. The combined effect of these multiple conservative assumptions was predicted flowliner lives of less than one flight, or about 1.6 million flow-induced vibratory cycles. These conservative assumptions can be relaxed by (1) acquiring new data and knowledge, (2) explicitly accounting for the uncertainties by performing probabilistic analysis, or (3) by a combination of (1) and (2).

A high-fidelity probabilistic fracture mechanics analysis was performed by replacing conservative modeling assumptions with more rigorous analysis techniques. To properly treat the complex loading, geometrical features, and interaction effects, a code named Flowliner Fatigue Life (FFL) was developed. The stress intensity factors for the four-corner crack models are subject to bivariate stress fields and are calculated using a weight function method. The local stress field in ligament 4 for some of the dominant vibration modes is shown in Figure 1.27.

A probabilistic damage tolerance model was developed for the flowliner by integrating the deterministic FFL software with the NESSUS probabilistic analysis code. The probabilistic model treated the following uncertainties: magnitudes of the cyclic stress amplitudes for each flight stage, fatigue crack growth material properties, and defect distribution resulting from periodic in-service inspection as characterized by several candidate POD curves. Quantification of the uncertainty in the first two variables was based on measured data; uncertainty in the third variable (inspection POD) was based on expert opinion since data were not available.

A new model for treating uncertainty in fatigue crack growth rates was developed and implemented based on the three regimes of fatigue crack growth [35]. The form of the three-component model is better suited to probabilistic fatigue life calculations as it avoids problems often encountered with asymptotic models in statistical characterization of uncertainty in the near-threshold fatigue crack



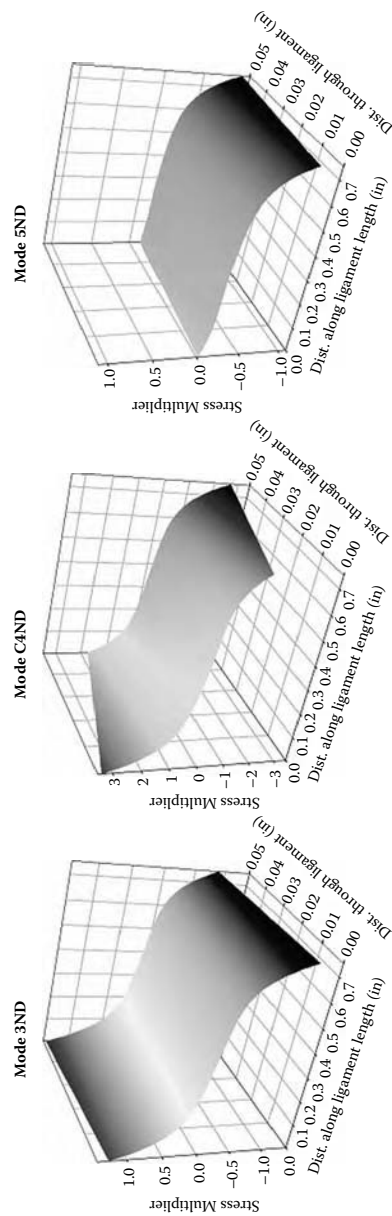


**FIGURE 1.27** Cyclic stress distributions at maximum and minimum loads and cyclic stress ranges for several vibration modes.

growth regime. The system risk assessment takes the variable loading on all 38 ligaments of the downstream flowliner into account. The most likely crack growth scenario is where the crack begins with a corner crack and transitions to a through-crack in response to the local stress gradient. NESSUS keeps track of the critical life as well as which ligament is the most critical. This approach allows the computation of the relative contribution of each slot to the total failure probability.

The probabilistic fracture analysis was carried out for multiple load cases and various input assumptions such as flight spectrum, POD curve, etc. The ITA team developed several different loading spectra for the alternating stresses in the flowliner. Probabilistic analyses were performed to examine similarities and differences among these spectra. These spectra and their origins are as follows:

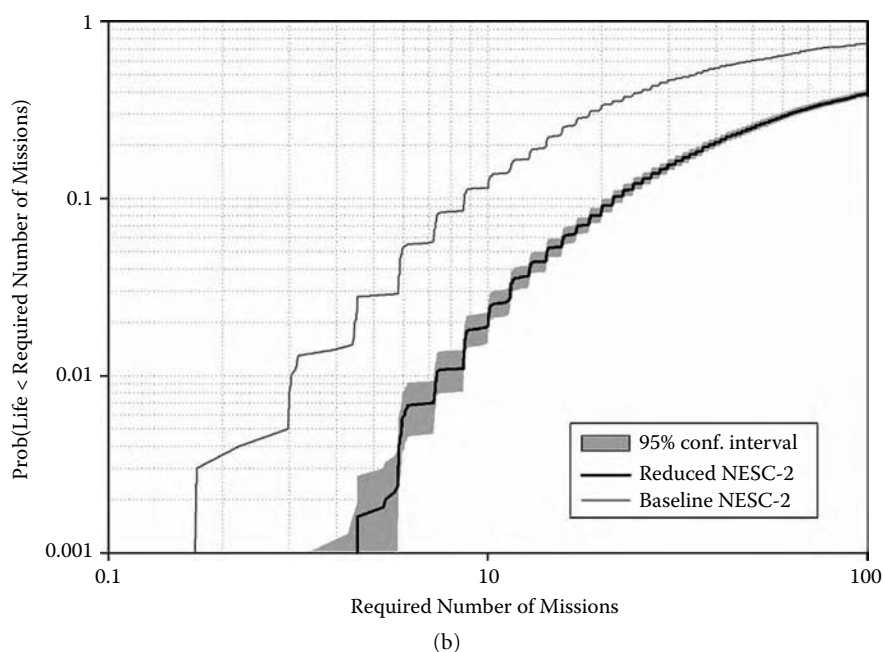
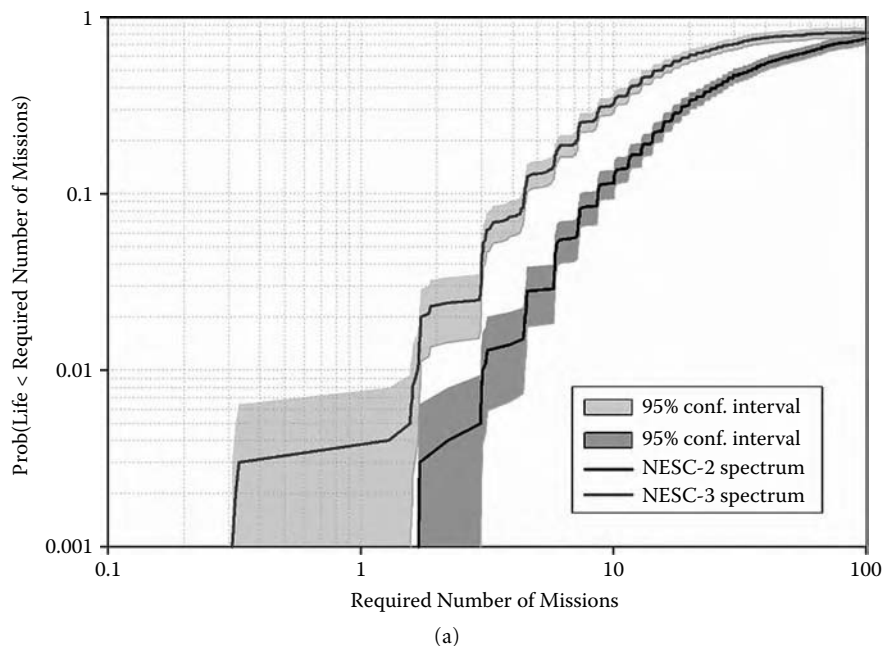
- NESC-2 spectrum: Derived by NASA LaRC on the basis of the Swales rainflow count from the B132 strain gauges from the flowliner test articles. All of the seven flight stages are assumed to be independent of each other.
- NESC-3 spectrum: This spectrum is to NESC-2 except for a multiplier (1.238) that applies to all strain levels because it was based on a gage with higher strain readings, and it contains more cycles in the high-stress regime. Each of the seven flight stages is assumed independent.
- Reduced NESC-2 spectrum: SwRI adjusted the NESC-2 spectrum by using median RMS strain levels instead of the maximum RMS strain levels used in NESC-2 that corresponded to the worst time window of the worst test. All seven flight stages are assumed independent.
- Certification spectra: The Shuttle Program Office developed several certification spectra, including those designed to represent various fault conditions that might be encountered during launch. Probabilistic analyses were performed on several of these spectra that were identified as being particularly damaging based on preliminary deterministic analyses with the FFL code.

Figure 1.28a compares the probabilities of not meeting various numbers of missions with the NESC-2 versus NESC-3 spectra. These results, obtained using 5000 Monte Carlo simulations, assumed a POD with a median flaw size of 20 mils to model the initial flaw size distribution, and fatigue crack growth scatter. In these plots, fractional missions are counted on the basis of number of completed load steps. The stair-step nature of these curves is due to the fact that damage was computed within a given flight stage by sorting cycles from high to low values of alternating stress (rainflowed order and not chronological order). As can be seen in Figure 1.28a, the probabilities that the flowliner fatigue life does not exceed four missions are approximately 1.4% and 7.5% for the NESC-2 and NESC-3 spectra. For NESC-3 the probability of failure during a single mission is approximately 1/300. The CDF of 95% sampling confidence intervals for the failure probability estimates are also shown in Figure 1.28a.

The probabilistic load modeling can justifiably remove some of the overconservatism in the previously developed load spectra (NESC-2 and NESC-3) while explicitly accounting for the variability of the loads. Results for the reduced NESC-2 spectrum are shown in Figure 1.28b, where they are compared with those from the original NESC-2 spectrum. As can be seen, the reduced spectrum results in a probability of not achieving four missions of approximately 0.0004 compared to that of 0.017 for the original worst-case NESC-2 spectrum, which is about a 40× decrease in the probability of not achieving four missions.

Results for the “Engine #3 Out” spectrum versus that for the reduced NESC-2 spectrum are compared in Figure 1.29. This load spectrum is characterized by an initial load step with about half a million cycles (about 1/3 of the total number of cycles) at a relatively high stress level. In spite of the use of median values and uncertainty modeling, the probability of failure for one mission is about 25%, and the probability of failure within four missions is 80%. However, it is important to note that these results are conditional probabilities; that is, they are conditional upon failure of engine #3. To achieve a total failure probability value that can be compared with the previously discussed probabilities, this conditional probability must be multiplied by the probability of losing a single engine.

Probabilistic sensitivity factors were computed to rank the relative importance of the input random variables on the flowliner failure probability. The magnitudes of the cyclic stress amplitudes were found to be by far the most important variable; in particular, the probability of failure (POF) was found to be very sensitive to changes in both the mean and standard deviation of the cyclic stress amplitude for Flight



**FIGURE 1.28** Probability of not meeting various numbers of missions: (a) compares conservative NESC-2 versus NESC-3 loading spectra, and (b) compares conservative NESC-2 spectra with conservative high-load level in baseline NESC-2.

Stage 6. Crack detection was the second most important variable; crack growth rate material properties and loading Stages 1 through 4 were of lesser importance, and their relative importance could not be differentiated from each other. Other probabilistic sensitivity studies assisted in identifying that one of the greatest potentials for reducing the probability of flowliner failure is to increase the POD from 50% at 75 mils (99% at 280 mils) to 50% at 20 mils (99% at 75 mils) for a given load spectrum.

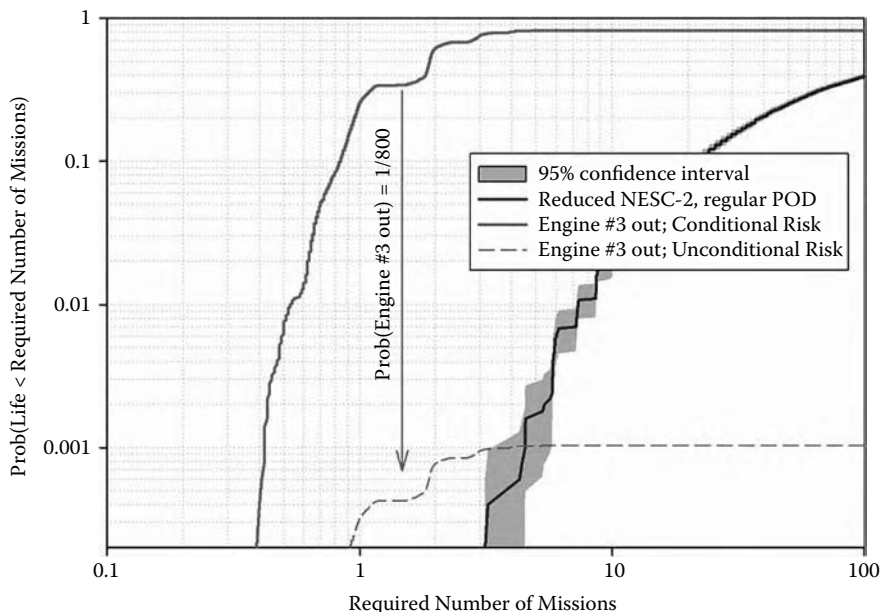


FIGURE 1.29 Flowliner failure probability results using two for “Engine #3 Out” and “reduced NESC-2” spectra.

In summary, the original deterministic life predictions for flowliner cracking estimated lifetimes less than one flight. The predictions made using the common practice of employing compounding conservative assumptions in this case did not support a flight rationale. Several of these conservative assumptions were removed by accounting for the uncertainties explicitly in a probabilistic analysis. The probabilistic modeling approach quantified the reliability and identified the important variables that drive the flowliner reliability to support more informed decision making.

## 1.5 Conclusions

Probabilistic analysis using analytical approaches or advanced analysis packages such as NESSUS and DARWIN in general provide more realistic information for decision making than traditional deterministic approaches. The probabilistic approach quantifies the reliability and identifies the design, manufacturing, and environmental parameters that have the most impact on the reliability. The important parameters can then be used to identify areas for design changes, inspection intervals, or environment restrictions. In addition, modeling actual variability of model parameters such as loads may allow removal of overly conservative assumptions and provides a means to evaluate the reliability of a system that does not pass requirements based on a traditional design approach.

Several probabilistic analyses were presented that demonstrated different modeling approaches and use of probabilistic results. The advanced and efficient probabilistic analysis methods employed in the case studies allow for using high-fidelity, multiphysics models to define the structure or system even when each deterministic analysis may take several hours to run. The use of probabilistic modeling to replace conservative assumptions in a systematic way allows the analyst to quantify the reliability and identify important parameters affecting the performance. In the application problems presented, the probabilistic results revealed additional information that would not have been available if traditional deterministic approaches were used.

## 1.6 Acknowledgments

The authors wish to acknowledge the support provided for the NESSUS and DARWIN probabilistic computer programs. NESSUS was supported by the National Aeronautic and Space Administration Lewis Research Center (now the Glenn Research Center at Lewis Field); the Los Alamos National Laboratory, Southwest Research Institute Internal Research; and many others sources too numerous to mention. The Federal Aviation Administration under Cooperative Agreement 95-G-041 and Grant 99-G-016 supported DARWIN. The ongoing contributions of the Industry Steering Committee are also gratefully acknowledged. The 2000 DaimlerChrysler Challenge Fund; Naval Air Warfare Center Aircraft Division; and Los Alamos National Laboratory, the NASA Engineering and Safety Center (NESC) are also acknowledged for their support for the applications problems summarized in this chapter.

## References

1. Thacker, B.H. and Huyse, L.J., Probabilistic assessment on the basis of interval data, in *Proceedings of 43rd Structures, Structural Dynamics, and Materials (SDM) Conference*, AIAA/ASME/ASCE/AHS/ASC, Denver, CO, 2003, on CD.
2. Oberkrampf, W., Helton, J., Joslyn, C., Wojtkiewicz, S., and Ferson, S., Challenge Problems: Uncertainty in System Response Given Uncertain Parameters, technical report, Sandia National Laboratories, Albuquerque, NM, 2002.
3. De Finetti, B., *Theory of Probability*, John Wiley, New York, Vol. 1 (1974), Vol. 2 (1975).
4. Southwest Research Institute, NESSUS Reference Manual, ver. 8.4, 2006.
5. Thacker, B.H., Riha, D.S., Fitch, S.K., Huyse, L.J., and Fleming, J.B., Probabilistic Engineering Analysis Using the NESSUS Software. *Structural Safety*, Vol. 28, No. 1–2, pp. 83–107, January–April 2006.
6. Thacker, B.H., Rodriguez, E.A., Pepin, J.E., and Riha, D.S., Application of probabilistic methods to weapon reliability assessment, in *Proceedings of 42nd Structures, Structural Dynamics, and Materials (SDM) Conference*, AIAA 2001-1458, AIAA/ASME/ASCE/AHS/ASC, Seattle, WA, 2001, on CD.
7. Thacker, B.H., Riha, D.S., Millwater, H.R., and Enright, M.P., Errors and uncertainties in probabilistic engineering analysis, in *Proceedings of 42nd Structures, Structural Dynamics, and Materials (SDM) Conference*, AIAA 2001-1239, AIAA/ASME/ASCE/AHS/ASC, Seattle, WA, 2001, on CD.
8. Riha, D.S., Thacker, B.H., and Fitch S.H.K., NESSUS capabilities for ill-behaved performance functions, in *Proceedings AIAA/ASME/ASCE/AHS/ASC 45th structures, structural dynamics, and materials (SDM) conference*, AIAA 2004-1832, AIAA/ASME/ASCE/AHS/ASC, Palm Springs, CA, 2004.
9. Huyse, L.J., Thacker, B.H., Fitch, S.K., Riha, D.S., Pepin, J., and Rodriguez, E., A Probabilistic Treatment of Expert Knowledge and Epistemic Uncertainty in NESSUS®, in *Proceedings of 47th Structures, Structural Dynamics, and Materials (SDM) Conference*, AIAA 2006-1994, AIAA/ASME/ASCE/AHS/ASC, Newport, RI, 2006.
10. Leverant, G.R. et al., A Probabilistic Approach to Aircraft Turbine Rotor Material Design, in *Proceedings of ASME International Gas Turbine and Aeroengine Congress*, 97-GT-22, ASME, New York, NY, 1997.
11. Southwest Research Institute, Allied Signal, General Electric, Pratt and Whitney, Rolls-Royce Allison, and Scientific Forming Technologies, Turbine Rotor Material Design: Final Report, DOT/FAA/AR-00/64, Federal Aviation Administration, Washington, DC, 2000.
12. Leverant, G.R., McClung, R.C., Millwater, H.R., and Enright, M.P., A new tool for design and certification of aircraft turbine rotors, *ASME Journal Engineering Gas Turbines Power*, 126(1), 155–159 (2003).
13. Southwest Research Institute, NASGRO Reference Manual, ver. 5.0, 2006.
14. Southwest Research Institute, Probabilistic Structural Analysis Methods (PSAM) for Select Space Propulsion System Components, Final Report, NASA contract NAS3-24389, NASA Lewis Research Center, Cleveland, OH, 1995.

15. Torng, T.Y., Wu, Y.-T., and Millwater, H.R., Structural System Reliability Calculation Using a Probabilistic Fault Tree Analysis Method, in *Proceedings of 33rd Structures, Structural Dynamics, and Materials (SDM) Conference*, Part 2, AIAA/ASME/ASCE/AHS/ASC, Dallas, TX, 1992, pp. 603–613.
16. National Transportation Safety Board, Aircraft Accident Report: United Airlines Flight 232 McDonnell Douglas DC-10-10 Sioux Gateway Airport, Sioux City, Iowa, July 19, 1989, NTSB/AAR-90/06, NTSB, Washington, DC, 1990.
17. Federal Aviation Administration, Advisory Circular—Damage Tolerance for High Energy Turbine Engine Rotors, AC 33.14-1, U.S. Department of Transportation, Washington, DC, 2001.
18. Southwest Research Institute, DARWIN™ User's Guide, ver. 6.0, 2006.
19. Leverant, G.R., McClung, R.C., Millwater, H.R., and Enright, M.P., A new tool for design and certification of aircraft turbine rotors, *Journal of Engineering for Gas Turbines and Power*, ASME, Vol. 126, No. 1, pp. 155–159, 2003.
20. McClung, R.C., Enright, M.P., Millwater, H.R., Leverant, G.R., and Hudak, S.J., A software framework for probabilistic fatigue life assessment, *Journal of ASTM International*, Vol. 1, No. 8, 2004, Paper ID JAI11563. Also published in *Probabilistic Aspects of Life Prediction*, ASTM STP 1450, pp. 199–215, 2004.
21. Enright, M.P. and Huyse, L., Methodology for probabilistic life prediction of multiple anomaly materials, *AIAA Journal*, AIAA, 44 (4), pp. 787–793, 2006.
22. McClung, R.C., Enright, M.P., Millwater, H.R., Leverant, G.R., and Hudak, S.J. (2004). A software framework for probabilistic fatigue life assessment, *Journal of ASTM International*, 1 (8) Paper ID JAI11563. Also published in *Probabilistic Aspects of Life Prediction*, ASTM STP 1450, 199–215.
23. Enright, M.P., McClung, R.C., and Huyse, L. (2005). A Probabilistic Framework for Risk Prediction of Engine Components with Inherent and Induced Material Anomalies, in *Proceedings 50th ASME International Gas Turbine & Aeroengine Technical Congress*, ASME, GT2005-68982, Reno, NV, 2005.
24. Aerospace Industries Association Rotor Integrity Subcommittee, The Development of Anomaly Distributions for Aircraft Engine Titanium Disk Alloys, in *Proceedings of 38th Structures, Structural Dynamics, and Materials Conference*, AIAA/ASME/ASCE/AHS/ASC, Kissimmee, FL, 1997, pp. 2543–2553.
25. Enright, M.P. and Millwater, H.R., Optimal Sampling Techniques for Zone-Based Probabilistic Fatigue Life Prediction, in *Proceedings of 43rd Structures, Structural Dynamics, and Materials Conference, Non-Deterministic Approaches Forum*, AIAA/ASME/ASCE/AHS/ASC, Denver, CO, 2002.
26. Riha, D.S., Hassan, J.E., Forrest, M.D., and Ding, K., Stochastic Approach for Vehicle Crash Models, in *Proceedings of SAE 2004 World Congress & Exhibition*, 2003-01-0460, Detroit, MI., March 2004.
27. Report of the Columbia Accident Investigation Board. Vol. 1, DC, Government Printing Office; Washington, DC, 2003.
28. Huyse, L., Waldhart, C.J., Riha, D.S., Larsen, C.E., Gomez, R.J., and Stuart, P.C., Probabilistic Modeling of Space Shuttle Debris Impact, in *Proceedings 18th ASCE Engineering Mechanics Division Conference*, Blacksburg, VA, 2007.
29. Rodriguez, E.A., Pepin, J.W., Thacker, B.H., and Riha, D.S., Uncertainty Quantification of A Containment Vessel Dynamic Response Subjected to High-Explosive Detonation Impulse Loading, in *Proceedings AIAA/ASME/ASCE/AHS/ASC 43rd Structures, Structural Dynamics, and Materials (SDM) Conference*, AIAA 2002-1567, Denver, CO, April 2002.
30. Thacker, B.H., Rodriguez, E.A., Pepin, J.E., and Riha, D.S., Uncertainty Quantification of a Containment Vessel Dynamic Response Subjected to High-Explosive Detonation Impulse Loading, in *Proceedings IMAC-XXI: Conference & Exposition on Structural Dynamics*, No. 261, Kissimmee, FL, 2003.
31. Nicoletta, D.P., Francis, W.L., Bonivitch, A.R., Thacker, B.H., Paskoff, G.R., and Shender, B.S., Development, Verification, and Validation of a Parametric Cervical Spine Injury Prediction Model, *Proceedings of 47th Structures, Structural Dynamics, and Materials (SDM) Conference*, Newport, RI, 2006.
32. Yoganandan, N., Kumaresan, S., and Pintar, F.A., Geometric and mechanical properties of human cervical spine ligaments, *Journal of Biomechanical Engineering*, Vol. 122, 2000.

33. Wheeldon, J.A., Pintar, F.A., Knowles, S., and Yoganandan, N., Experimental flexion/extension data corridors for validation of finite element models of the young, normal cervical spine, *Journal of Biomechanics*, Vol. 39, No. 2, pp. 375–380, 2006.
34. Hudak, S.J. Jr., Huyse, L., Chell, G., Lee, Y.-D., Riha, D.S., Thacker, B.H., McClung, R.C., Gardner, B.M., Leverant, G.R., Unruh, J., and Pleming J.B., Probabilistic Fracture Mechanics Analysis of the Orbiter's LH2 Feedline Flowliner, *Final Contractor Report, NASA CR-2005-213585*, 2005.
35. Hudak, S.J. Jr., Huyse, L., Chell, G., Lee, Y.-D., Riha, D.S., Thacker, B.H., McClung, R.C., Gardner, B.M., and Pleming J.B., A Probabilistic Return-to-Flight Assessment of the Orbiter's LH2 Feedline Flowliner, in *Proceedings of 47th Structures, Structural Dynamics, and Materials (SDM) Conference*, Newport, RI, 2006.

# 2

## Reliability Assessment of Aircraft Structure Joints Under Corrosion- Fatigue Damage

---

2.1	Introduction .....	2-1
2.2	Current Engineering Philosophy .....	2-2
	Deterministic Approach • Risk-Based Approach	
2.3	Corrosion-Fatigue Damage Modeling .....	2-8
	Fatigue Damage • Corrosion Damage • Corrosion-Fatigue Damage	
2.4	Reliability of Aircraft Structure Joints Including Maintenance Activities.....	2-35
	Risk/Reliability-Based Condition Assessment	
2.5	Illustrative Examples .....	2-39
	Probabilistic Life Prediction Using Different Corrosion-Fatigue Models • Risk-Based Maintenance Analysis of a Lap Joint Subjected to Pitting Corrosion and Fatigue	
2.6	Concluding Remarks.....	2-55
	References .....	2-56

Dan M. Ghiocel

*Ghiocel Predictive Technologies Inc.*

Eric J. Tuegel

*Air Force Research Laboratory*

### 2.1 Introduction

---

A continuing challenge in the aviation industry is how to keep aircraft safely in service longer with limited maintenance budgets. Probabilistic methods provide tools to better assess the impact of uncertainties on component life and risk of failure. Application of probabilistic tools to risk-based condition assessment and life prediction helps managers to make better risk-informed decisions regarding aircraft fleet operation and airworthiness. In addition to assessing aircraft reliability, probabilistic methods also provide information for performing an analysis of the cost of continuing operation based on risks and their financial consequences.

Corrosion and fatigue, separately or in combination, are serious threats to the continued safe operation of aircraft. As a result, the U.S. Air Force, the U.S. Navy, the Federal Aviation Administration (FAA), and the European Joint Aviation Authorities (JAA) have guidelines on how aircraft should be designed and maintained to minimize the risk of failure from fatigue damage [1–5]. Although corrosion has a deleterious impact on structural integrity, the airworthiness regulations and requirements have limited instructions regarding corrosion, noting that each part of the aircraft has to be “suitably protected against deterioration or loss of strength in service due to any cause, including weathering, corrosion and abrasion” [6, 7]. The ability to assess the impact of future



corrosion on structural integrity, alone or acting in concert with fatigue, is difficult. A framework to assess the effects of corrosion in combination with fatigue on structural integrity has been under development [8].

The parameters of primary interest to aircraft fleet managers are:

- Risk of failure for a single component on a single aircraft
- Failure risk of an individual aircraft (the sum of risks for all components)
- Hazard failure rates for individual aircraft and the aircraft fleet
- Cost-effectiveness of maintenance actions in reducing failure risk for individual aircraft and the fleet

The purpose of this chapter is to review key aspects of assessing the quantitative risk to airframe structures from concurrent corrosion and fatigue damage. Both the current engineering practice and new research developments are reviewed. The physics-based stochastic damage models necessary to make this risk assessment as well as the statistical data needed to construct these models are discussed. The emphasis is on physics-based stochastic modeling of corrosion-fatigue damage. Lack of data and engineering understanding of the physics of a damage process are highlighted. At the end of the chapter, various probabilistic results computed for different physics-based stochastic damage models and different corrosion severity conditions are illustrated for a typical aircraft lap joint.

## 2.2 Current Engineering Philosophy

---

Aircraft-structure joints are the most fatigue- and corrosion-susceptible areas on an aircraft. Loads are transferred from one structural detail to another through fasteners, with the attendant stress-concentrating holes making this a prime location for fatigue cracks to form. The tight fit of details and fasteners can trap moisture in the joint. Relative movement between the structural details and the fasteners, as well as the stress concentrations, can cause corrosion protection systems (anodize, primer, and topcoat) to crack and wear, allowing moisture to reach the aluminum parts and start the corrosion process. A typical example structure is a longitudinal skin joint on the pressurized fuselage of a transport aircraft (Figure 2.1). The loading of longitudinal skin joints, particularly those on or near the horizontal neutral axis of the fuselage, is simply the pressurization of the fuselage, which is approximately constant amplitude with a stress ratio (ratio between minimum over maximum stress) of zero. For illustration purposes, we assume that there is only a single pressurization stress cycle per flight.

### 2.2.1 Deterministic Approach

In the current USAF practice, when the aircraft is designed, a crack-growth analysis is performed for each critical location assuming a discrete 1.27-mm (0.05 in.) flaw or crack (Figure 2.2). This conservative assumption protects against the possibility of a rogue flaw at any one of the critical locations resulting in the loss of an aircraft or its crew. Different assumptions are allowed if the critical location is a cold-worked hole or interference-fit fastener. But for illustration, we will work with the 1.27-mm crack. The existence of a 1.27-mm (0.05-in.) flaw is a rare event that happens less than one in a million based upon back calculations from full-scale fatigue-test crack data [9].

Each critical location is to be inspected at half the component life, determined by the crack-growth analysis, after approximately 11,000 pressurization cycles for the example in Figure 2.2. In principle, half the life was chosen in order to cover scatter from the “mean” life given by the analysis. The condition of the structure in terms of amounts and severities of cracking, corrosion, fretting, etc., is determined with nondestructive inspections (NDI). The inspection should be accomplished with an NDI method capable of finding a crack less than or equal to the analytical crack length at half the component life from a 1.27-mm flaw.

The capability of NDI to find cracks, or other types of damage, is expressed in terms of the probability of detection (POD) curve. POD curves for fatigue cracks in standard geometries have been developed and compiled in handbooks [10–12] for a variety of NDI methods. An example of a POD curve for eddy-current inspection of a Boeing 737 lap joint is shown in Figure 2.3. Note that 1.27-mm fatigue cracks in the joint were found only about 5% of the time with this particular NDI setup. The USAF philosophy is to assume

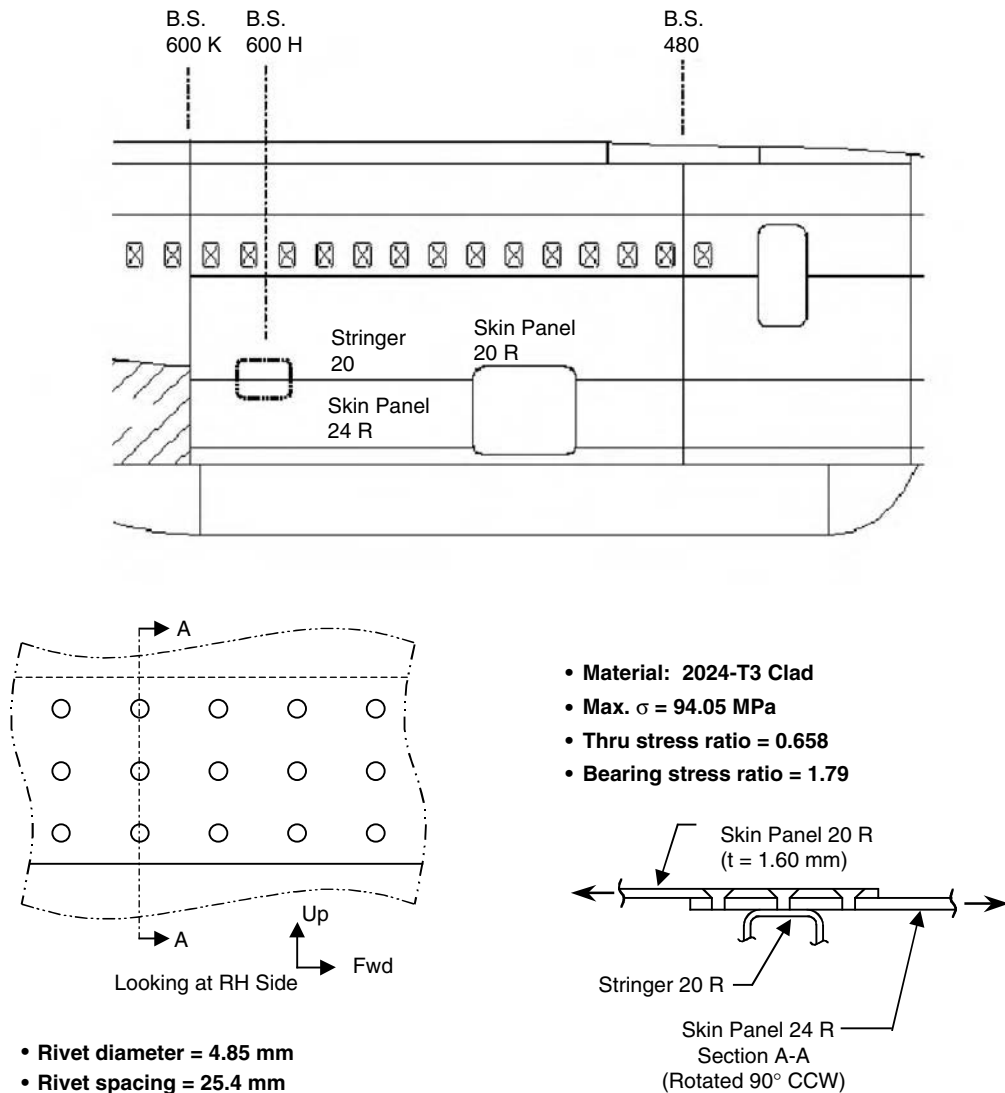


FIGURE 2.1 Details of joint selected as example.

after an inspection that there is a crack at the location just below the 90% detection with 95% confidence limit, denoted 90/95 value. For the aircraft splice joint in Figure 2.1, the 90/95 value of crack size is 2.39 mm, which would be adequate to find the almost 4-mm crack predicted for 1.27-mm starting crack at 11,000 hours (Figure 2.2). From the crack-growth analysis in Figure 2.2, it would take approximately 16,000 pressurization cycles for a 2.93-mm crack to grow to failure. Thus, if no cracks were found in the lap joint during the first inspection using the above eddy-current technique, the second inspection would need to be 8,000 cycles later, or after approximately 19,000 pressurization cycles. The times for subsequent inspections at this location are determined using this same procedure until a crack is found and repaired, or the aircraft is retired. After a repair, inspection intervals will be determined by the characteristics of the repair and its ability to prevent further damage and degradation to the structure. As an aircraft fleet becomes older, inspections can be required more frequently. These inspections can be a real burden to the maintainers and to the operators.

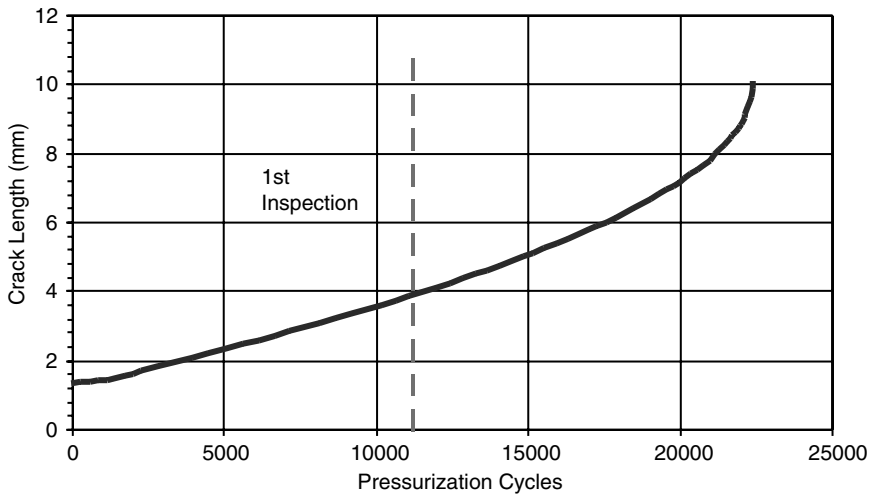


FIGURE 2.2 Example of crack-growth analysis and time to the first inspection.

Recent work has sought to quantify the capabilities of several NDI methods to find corrosion [13]. The major concern with NDI for corrosion is detecting corrosion that is buried between layers of a built-up structure. Corrosion on a visible surface is best found visually in adequate lighting; however, this method does not reveal how deeply the corrosion penetrates. When looking for corrosion, the measured quantity is part thickness that is converted to thickness loss from the design specification. In general, eddy current and ultrasound are capable of determining the thickness of a part with reasonable accuracy when the accessible surface is uncorroded. A roughened surface due to corrosion creates difficulties for surface-contacting probes or probes that need an accurate standoff from the surface. X-rays can be used to measure part thickness with corrosion on either surface, provided that there is access to both sides of the part. The ability of any method to detect corrosion depends upon the size of the corroded area vs. the size of the area over which the NDI signal is averaged.

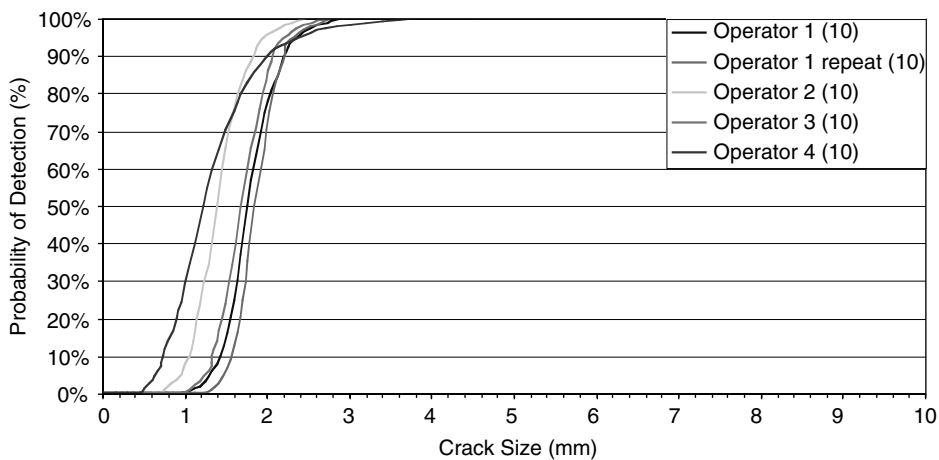


FIGURE 2.3 Results of probability-of-detection study for eddy-current inspection with 200-kHz probe of the fasteners in an unpainted 737 aluminum aircraft splice joint.

Multiple site damage (MSD) or widespread fatigue damage (WFD) should also be considered when evaluating failure risks of structural components. The above approach to aircraft maintenance was developed for discrete source damage, before the risks posed by MSD were fully recognized. The MSD scenario typically assumed when considering damage tolerance is a long, detectable crack emanating from a critical location with small, undetectable cracks at many of the adjacent fastener holes. These small cracks provide a low-energy path for the long crack to follow during fast fracture, much like perforations in paper make it easier to tear a sheet in a specific spot. This scenario cannot be identified with NDI. And the likelihood of MSD existing cannot be reliably estimated analytically because good models for estimating the distribution of small cracks in a structure do not exist. The issue of MSD will be left for another time, when it can be dealt with more thoroughly.

### 2.2.2 Risk-Based Approach

Typically, in order to determine the failure risk of an aircraft component, three pieces of information are needed:

1. The current “damage” condition of the component
2. The material capacity associated with the progressive “damage” mechanism, i.e., residual strength, or critical crack size, or fracture toughness
3. A predictive model of how the current “damage” condition will develop with continued usage

The maximum frequency of a structural failure leading to the loss of the aircraft acceptable to the USAF is  $10^{-7}$  event occurrences per flight [14, 15].

#### 2.2.2.1 Risk-Based Condition Assessment

In a risk-based or risk-quantified approach to aircraft management, a distribution of crack sizes would be estimated, either analytically or based upon previous inspection experience, for a structure prior to an inspection. The crack size distribution would be modified after the inspection based upon the POD for the NDI method and the subsequent maintenance actions performed on the detected cracks.

Lincoln [15] discussed the utility of probabilistic approaches for assessing aircraft safety and for solving key reliability problems faced in practice, such as:

1. Potential cracking problems are revealed, and the aircraft is beyond its deterministic damage-tolerance limits.
2. Aircraft cracking has occurred to the extent that the deterministic-damage-tolerance derived inspection intervals need to be shortened in order to preserve safety.
3. Aircraft have been designed to be fail safe, but (widespread) fatigue damage has degraded the aircraft structure such that the fail safety of the structure has been compromised.

One of the difficulties in managing aircraft fleets is tracking data from past aircraft inspections to refine the assessment of the current condition of each aircraft or the entire fleet. A good knowledge of the current state of a component or aircraft is important for accurately determining the risk of failure. Electronic databases make storing the data easier. The challenge is getting the data into the database.

Over the last decade, the USAF has developed the probability of fracture (PROF) software to compute the probability of a component fracturing during a single flight [16, 17]. Inputs to the program are based upon data that are readily available as a result of the USAF aircraft structural integrity program (ASIP). These inputs include: material fracture toughness, predicted crack size vs. flight hours for the usage spectrum, normalized stress intensity vs. crack length for the location of interest, distribution of crack sizes at that location throughout the fleet at some previous time, and the distribution of extreme loads the aircraft will experience.

PROF computes the single-flight probability of failure  $P_f$  by incorporating two independent failure events: (1) failure occurs when the effective crack size is larger than a prescribed maximum crack size (the residual strength of the component becomes unacceptably low), or (2) failure occurs when the

effective crack size is smaller than critical size,  $a_c$ , but the maximum stress intensity factor is larger than material fracture toughness,  $K_c$ :

$$P_f = \int_0^a f(a)[1 - \text{Prob}(K(a) \leq K_c)] da + [1 - \text{Prob}(a \leq a_c)] \quad (2.1)$$

where  $f(a)$  is the crack-size distribution function and  $a_c$  is the critical crack size.

The USAF is continuing to improve the methods used to determine the probability of fracture and risks associated with operational aircraft fleets.

### 2.2.2.2 Local Failure Criteria

The effect of selecting different local failure criteria on the stress–strain curve is shown in Figure 2.4. Since the material toughness can be related to a critical crack size at failure for a given stress, the two failure criteria in PROF can be plotted together on the crack size–stress plane as in Figure 2.5. The residual strength of the component defines the limit of a component’s ability to carry load [18] and can be simplistically thought of as a limit surface in the stress vs. crack-size plane described by the minimum of the yield and fracture curves in Figure 2.5. When the structure is new and the sizes of any cracks are small, the net section stress must be less than the yield strength of the material. For a longitudinal lap splice subjected to only pressurization loading (Figure 2.1), the maximum net section stress is  $\sigma/(1 - nd/W)$ , where  $W$  is the width of the panel,  $d$  is the diameter of the fastener holes, and  $n$  is the number of fasteners in a row. As the component is fatigued, cracks form and grow. The residual strength of the component is the stress required to cause fracture. For a single crack, based on linear elastic fracture mechanics (LEFM), the local stress at the crack tip that defines the residual stress can be simply computed by the relationship

$$\sigma_c = \frac{K_c}{\beta\sqrt{\pi a}} \quad (2.2)$$

where  $K_c$  is the critical stress intensity factor or fracture toughness that causes material to fracture,  $\beta$  is the stress intensity geometry factor for the given crack, and  $a$  is the crack size.

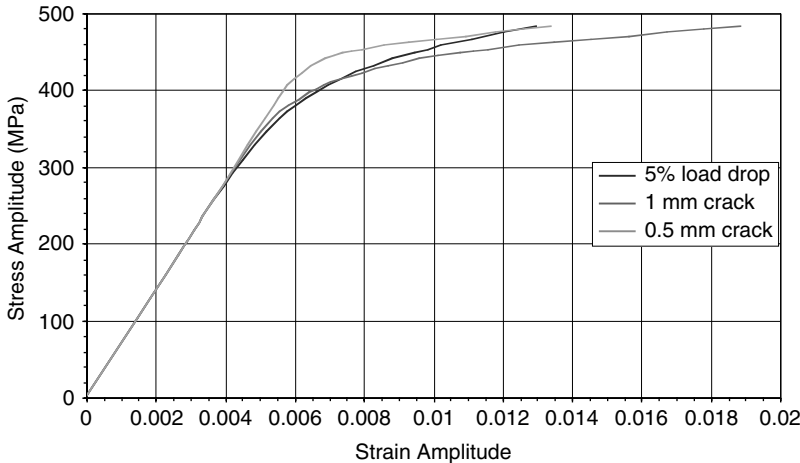


FIGURE 2.4 Cyclic stress–strain curve for 2024-T3 sheet.

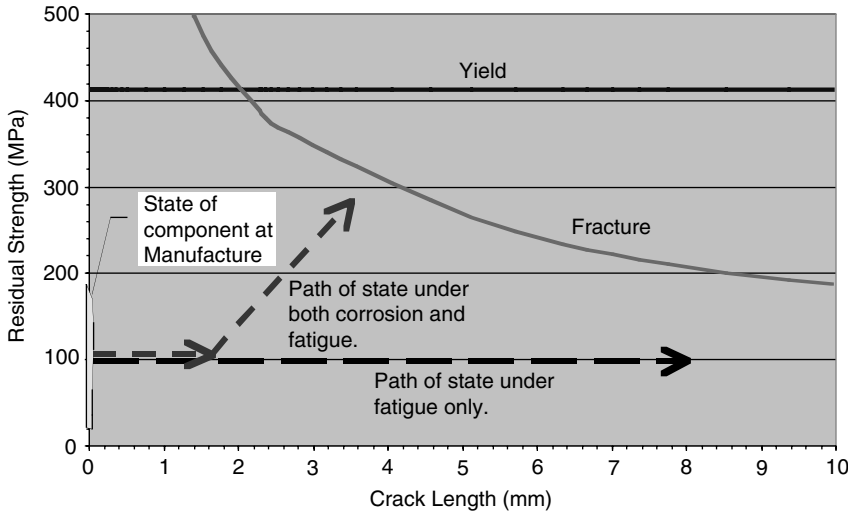


FIGURE 2.5 Pictorial description of residual strength space.

If the structure is designed such that load can be redistributed from the cracked component, or area of the component, to other components or areas, the determination of the critical stress for failure of the component is harder. As the component cracks, it becomes more compliant. Load redistributes to stiffer intact structure nearby, reducing the stress intensity at the crack and the likelihood that fast fracture will occur. Such a structure is said to be fail safe.

Yield strength and  $K_{Ic}$  are variable from lot to lot and even locally within a given component; the limits in Figure 2.5 become zones of constant-probability contours. The values for yield strength used in aircraft design are based upon the A- or B-basis allowable in Mil-Hdbk-5 [19]. An A-basis allowable is the lower value of either a statistically calculated number or the specification minimum. The statistically calculated number indicates that at least 99% of the population is expected to equal or exceed the statistically calculated mechanical property value, with a confidence of 95%. A B-basis allowable indicates that at least 90% of the population of values is expected to equal or exceed the statistically calculated mechanical property value, with a confidence of 95%.

Plane-strain fracture toughness,  $K_{Ic}$ , is treated as being normally distributed, with mean values and standard deviations calculated on a rather small data set. However, the critical fracture toughness for a part,  $K_{Ic}$ , is dependent upon the thickness of the material. A number of  $K_{Ic}$  values are compiled by Skinn et al. [20] for a 2024-T3 aluminum sheet. However, of over 140 tests reported, there were only 3 where the net section stress in the specimen did not exceed 80% of the yield strength and could be considered to have met the requirements of linear elastic fracture mechanics. The average of those three tests on 1.5-mm-thick sheets was  $119.6 \text{ MPa} \sqrt{\text{m}}$ , with a standard deviation of  $9 \text{ MPa} \sqrt{\text{m}}$ .

### 2.2.2.3 Uncertainty in Failure Criteria

In the above discussion of residual strength, failure is considered as a stepwise change of system state—from having structural integrity to having no structural integrity. In reality, the transition from a sound state to a “failed state” is smooth; the changes in system integrity occur gradually with small changes in time. It is difficult to define a distinct instant when “failure” occurred. Thus there is a lack of distinctness, or uncertainty, to the failure criteria. Several researchers have proposed using nondeterministic approaches, using either probabilistic or fuzzy approximation, to describe fatigue damage and subsequent failure [21, 22]. This approach has a certain appeal to it, but it still requires more development before being applied to practical situations.

## 2.3 Corrosion-Fatigue Damage Modeling

At low homologous temperatures, fatigue damage accumulates with applied load cycles, regardless of how fast or slowly the cycles are applied. On the other hand, corrosion develops as a function of time, regardless of whether the structure is loaded or not. Putting these two mechanisms into the same model is challenging because of the different “time” scales at which “damage” develops.

### 2.3.1 Fatigue Damage

Fatigue changes crack size distribution as a result of applied loading only. A new structure starts out with few, if any, cracks. New cracks form at stress concentrations with applied loading as a result of local plasticity and microplasticity. Many microscopic cracks may form, but only a few become visible, macroscopic cracks. The portion of the fatigue life until the formation of a detectable crack, which is considered here to be about 2 mm, is denoted as crack nucleation. The portion of the fatigue life after a detectable crack is formed until the component fails is denoted as crack propagation or growth. Different mathematical models are used to analyze these two phases of the fatigue life, though it is likely that a single physical mechanism operates throughout the entire fatigue life [23].

#### 2.3.1.1 Crack Initiation

A common model for estimating the load cycles until the development of a detectable crack is currently the semiempirical local strain-life approach [24–26]. The local strain-life method models the stress–strain history at the “root” of a stress concentration, or notch, from the cyclic stress–strain curve of the material and the notch (local plasticity) analysis. The number of constant-amplitude stress–strain (closed) cycles that is accumulated until the detectable crack size is reached is determined based on the strain-life curve of the material adjusted for the nonzero mean stress effects. For variable-amplitude cycle loading, the cumulative damage defined by crack size is then computed using the kinetic damage equation. To count stress–strain cycles, rainflow counting or other methods can be used. The growth and linkup of small cracks are included in crack initiation when the models are calibrated to the detection of a suitably long crack, so models for small crack growth are not needed.

The material for the aircraft structural joint shown in Figure 2.1 is a 2024-T3 aluminum sheet. Examples of cyclic stress–strain curves for this material, found by putting a curve through tips of the stable hysteresis loops obtained during strain-controlled fatigue tests of smooth specimens, are shown in Figure 2.4. The differences between the curves are partially the result of using different failure criteria for the fatigue tests, which results in the hysteresis loops being defined as stable at different times [27]. Hysteresis loops are considered stable at half the cycles to failure. However, an alloy like 2024-T3, which is cold-worked prior to aging, can cyclically soften, i.e., the extreme stresses experienced at the extreme strain points decrease with increasing number of load cycles throughout the entire test, making the determination of the stable hysteresis loop somewhat imprecise.

The curve can be modeled using the Ramberg-Osgood equation

$$\frac{\Delta\epsilon}{2} = \frac{\Delta\sigma}{2E} + \left( \frac{\Delta\sigma}{2K'} \right)^{\frac{1}{n'}} \quad (2.3)$$

where  $\Delta\epsilon/2$  is the strain amplitude,  $\Delta\sigma/2$  is the stress amplitude,  $E$  is the elastic modulus,  $K'$  is the cyclic strain hardening coefficient, and  $n'$  is the cyclic strain hardening exponent. The values of  $K'$  and  $n'$  for the different curves are provided in Table 2.1 [27].

For the aircraft lap joint shown in Figure 2.1, a detailed analysis of the load transfer indicates that the most critical location is the first row of fasteners in the outer skin. It has the largest bypass, or through, stress, 61.9 MPa, and the largest bearing stress, 168.3 MPa. Applying the respective stress concentration factors for a hole in a plate [28] and adding the components together gives the maximum  $K_t\sigma = 417.4$  MPa. The local stress–strain history can be determined by a finite-element analysis, which can be very time

**TABLE 2.1** Cyclic Strain Hardening Coefficients and Exponents for Curves in Figure 2.4

Curve (Failure Criterion)	$K'$ (MPa)	$n'$
5% load drop	843	0.109
1-mm crack	669	0.074
0.5-mm crack	590.6	0.040

consuming if the load history has a large number of load levels in it, or by using Neuber's equation,  $K_t^2 = K_\sigma K_\epsilon$ , where  $K_\sigma$  is the stress concentration factor,  $\sigma_{\text{notch}}/\sigma_{\text{global}}$ , and  $K_\epsilon$  is the strain concentration factor at the hole,  $\epsilon_{\text{notch}}/\epsilon_{\text{global}}$ . Solving for the maximum notch stress and strain yields the results in Table 2.2 for each of the cyclic stress-strain curves.

The strain amplitude and mean stress (or the maximum stress) are used to estimate the time to a detectable crack. First, the strain-life curve, determined with data from  $R = -1$  (completely reversed) strain-control testing, is needed. The standard strain-life curve expresses alternating strain as a function of cycle life:

$$\epsilon_a = \frac{\Delta\epsilon}{2} = \frac{\sigma'_f}{E}(2N_f)^b + \epsilon'_f(2N_f)^c \quad (2.4)$$

Values of the coefficients and exponents for 2024-T3 using the three failure criteria above are listed in Table 2.3 [27]. The first term in Equation 2.4 characterizes high-cycle fatigue when macroscopic plastic deformation is not evident, while the second term characterizes low-cycle fatigue associated with macroscopic plastic deformation. The resulting strain-life curves are compared in Figure 2.6. The abscissa of the strain-life curves represent the number of applied load cycles at which 50% of the specimens tested at that strain amplitude would have failed.

The strain-life curves are for completely reversed loading with a zero mean stress. The loading for the fuselage lap joint has a stress ratio of zero, i.e., a mean stress of  $\Delta\sigma/2$ . So the strain-life curves need to be adjusted for a nonzero mean stress.

For evaluating the probabilistic crack initiation life, a local strain-life approach with randomized strain-life curve parameters can be used. Thus, the four parameters,  $\sigma'_f$ ,  $b$ ,  $\epsilon'_f$ , and  $c$ , are random material parameters. It is expected that the first pair of parameters that influences the short lives is statistically independent with respect to the second pair of parameters that influences the long lives. Within each of the two pairs of parameters, there is expected to be a certain level of statistical dependence.

The most popular numerical procedures used to correct the strain-life curve for the nonzero mean stress effects are [29]:

1. Morrow correction (MC): mean-stress effect in the elastic term

$$\epsilon_a = \frac{\sigma'_f}{E} \left( 1 - \frac{\sigma_m}{\sigma'_f} \right) (2N_f)^b + \epsilon'_f(2N_f)^c \quad (2.5)$$

**TABLE 2.2** Notch Stress and Strain History for the First Row of Fasteners in the Joint of Figure 2.1

Curve (Failure Criterion)	$\sigma_{\text{max}}$ (MPa)	$\Delta\epsilon/2$	$\sigma_{\text{mean}}$ (MPa)
5% load drop	388.7	0.00276	194.4
1-mm crack	392.3	0.00279	196.2
0.5-mm crack	412.8	0.00294	206.4



**TABLE 2.3** Strain-Life Equation Coefficients and Exponents for 2024-T3 Sheet

Strain-Life Curve (Failure Criterion)	$\sigma'_f$ (MPa)	$B$	$\epsilon'_f$	$c$
5% load drop	835	-0.096	0.174	-0.644
1-mm crack	891	-0.103	4.206	-1.056
0.5-mm crack	1044	-0.114	1.765	-0.927

2. Modified Morrow correction (MMC): the mean-stress effect in the elastic and plastic strain terms

$$\epsilon_a = \frac{\sigma'_f}{E} \left( 1 - \frac{\sigma_m}{\sigma'_f} \right) (2N_f)^b + \epsilon'_f \left( 1 - \frac{\sigma_m}{\sigma'_f} \right)^{\frac{c}{b}} (2N_f)^{\frac{c}{b}} \quad (2.6)$$

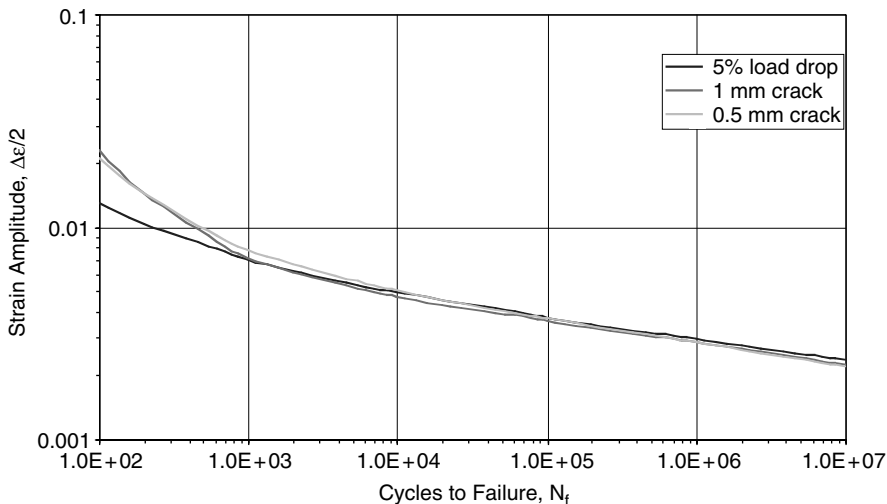
3. Smiths-Watson-Topper (SWT) approach changes the strain-life curve expression by

$$\sigma_{\max} \epsilon_a = \frac{(\sigma'_f)^2}{E} (2N_f)^{2b} + \sigma'_f \epsilon'_f (2N_f)^{b+c} \quad (2.7)$$

The mean and maximum stresses are denoted by  $\sigma_m$  and  $\sigma_{\max}$  in the above equations. It should be noted that the selection of the mean-stress correction procedure has a large impact on the computed component lives.

For the 2024-T3 sheet material, the adjusted strain-life curves using the MC procedure are compared in Figure 2.7. The range of strain amplitudes in Table 2.2 produces estimates of the time to 50% of the fastener holes in the first row having a detectable crack as 100,000 to 150,000 pressurization cycles.

If the loading stress history is variable amplitude instead of constant amplitude, then rainflow, range pair, or other cycle-counting procedures can be used to break the local stress-strain history into applied closed stress-strain cycles of different strain amplitudes,  $\Delta\epsilon/2$ , and mean stresses,  $\sigma_m$ .

**FIGURE 2.6** Strain-life curves for 2024-T3 sheet.

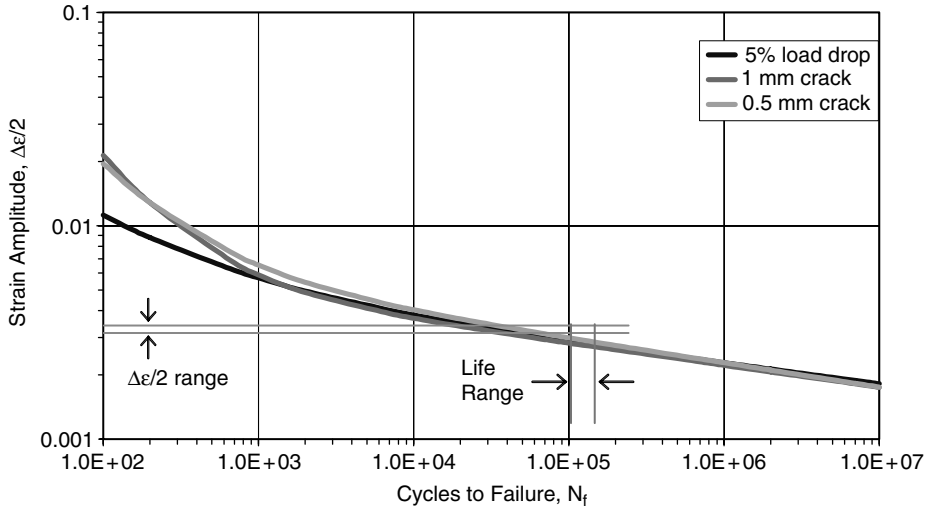


FIGURE 2.7 2024-T3 sheet strain-life curves adjusted for  $R = 0$  loading with Morrow's equation.

For every cycle in the history, the number of cycles to failure of a smooth specimen under constant-amplitude loading is determined by solving Morrow's equation for  $N_f$ . Then, the cumulative damage is computed by solving the first-order differential kinetic damage equation of the form:

$$\frac{dD}{dN} = f(D, N, N_f(\epsilon_a, \sigma_m), p) \quad (2.8)$$

where the letter  $p$  denotes the physical parameters of the cumulative damage model.

The total accumulated damage,  $D_T$ , due to cyclic loading can be directly computed by the convolution of the damage function,  $D(X_{\min}, X_{\max})$ , with cycle counting distribution  $N_T(X_{\min}, X_{\max})$ :

$$D_T = \int_T d(t) dt = \sum_{i \text{ for } v \leq u} D(v_i, u_i) = - \iint_{v \leq u} N_T(v, u) \frac{\partial^2 D(v, u)}{\partial v \partial u} dv du \quad (2.9)$$

The integral value is the summation of all elementary damages produced by the sequence of closed stress-strain hysteresis loops.

It was proven experimentally by Halford [30] that for a sequence of cycles with constant alternating stress and mean stress, the cumulative damage curve, the crack initiation life,  $N_f(\epsilon_m, \sigma_m)$ , can be accurately constructed based only on two experiments for the extreme amplitude levels, i.e., maximum and minimum life levels. The greater the ratio between the (two) extreme life levels, the more severe damage interaction there is and the greater deviation from the linear-damage rule.

### 2.3.1.1.1 Linear-Damage Rule

The popular linear-damage rule (LDR) has the mathematical form:

$$D = \sum \frac{n_i}{N_i} = \sum r_i \quad (2.10)$$

where  $D$  is the damage,  $n_i$  is the number of cycles of  $i$ th load level,  $N_i$  is the fatigue life according to the  $i$ th load level, and  $r_i$  is the cycle ratio of the  $i$ th load level. In the linear-damage rule, the damage is measured by the cycle ratio. Failure occurs when the damage reaches unity.

The shortcoming of the popular linear-damage rule (LDR) or Miner's rule is its stress independence or load-sequence independence; it is incapable of taking into account the interaction of different load levels. There is substantial experimental evidence that shows that the LDR is conservative under completely reversed loading conditions for low-to-high loading sequences,  $\sum r_i > 1.0$ , and severely underconservative for high-to-low loading sequences,  $\sum r_i < 1.0$ . It should be noted that for intermittent low-high-low-high- ... -low-high cyclic loading, the LDR severely underestimated the predicted life, as indicated by Halford [30].

#### 2.3.1.1.2 Damage Curve Approach

The damage curve approach (DCA) was developed by Manson and Halford [30]. The damage curve is expressed in the following form:

$$D = \left( \frac{n}{N} \right)^q = \left( \frac{n}{N} \right)^{\left( \frac{N}{N_{\text{ref}}} \right)^\beta} \quad (2.11)$$

where  $D$  is the accumulated damage,  $n$  is the number of cycles, and  $N$  is the fatigue life for the corresponding strain amplitude and mean stress.  $N_{\text{ref}}$  is the *reference* fatigue life. Parameter  $\beta$  is set equal to 0.40 for many alloys.

#### 2.3.1.1.3 Double Damage Curve Approach

The double damage curve approach (DDCA) was developed by Manson and Halford by adding a linear term to the DCA equation [30]. The DDCA is defined by the relationship:

$$D = \left( \frac{n}{N} \right) \left[ q_1^\gamma + (1 - q_1^\gamma) \left( \frac{n}{N} \right)^{\gamma(q_2-1)} \right]^{1/\gamma} \quad (2.12)$$

where

$$q_1 = \frac{0.35 \left( \frac{N_{\text{ref}}}{N} \right)^\alpha}{1 - 0.65 \left( \frac{N_{\text{ref}}}{N} \right)^\alpha}, \quad q_2 = \left( \frac{N}{N_{\text{ref}}} \right)^\beta$$

The parameters  $\alpha$  and  $\beta$  are set to equal 0.25 and 0.40, respectively, for many alloys. Parameter study shows that the value of  $\gamma$  can be set at 5.00, which makes the DCA a sufficiently close fit to the DDCA. From the equations of DCA and DDCA, it can be seen that the exponent  $q$  in DCA and the parameters  $q_1$  and  $q_2$  are all stress-level dependent, and the interaction between different stress-levels can be adequately considered.

#### 2.3.1.1.4 Stochastic Variability in Crack Initiation

Cracks nucleate in aluminum alloys at coarse slip bands inside large grains, with primary crystallographic slip planes oriented favorably to the applied loading so that there is microplastic deformation around large, hard constituent particles (or other phases), or at grain boundaries [31–38]. Variability in grain orientations and sizes and in particle sizes leads to variability in the time to nucleate a crack.

One source of data for crack nucleation in 2024-T3 is the results of the AGARD round cooperative test program for short-crack growth-rate data [32]. The number of cycles until a through crack developed was reported for many of the specimens. The specimens were 2.3 mm thick. The size is consistent with the definition of crack initiation stated earlier, so these data can provide an estimate of the scatter in the time to form a 2-mm crack. Single-edge notched tension (SENT) specimens shown in Figure 2.8 were used.

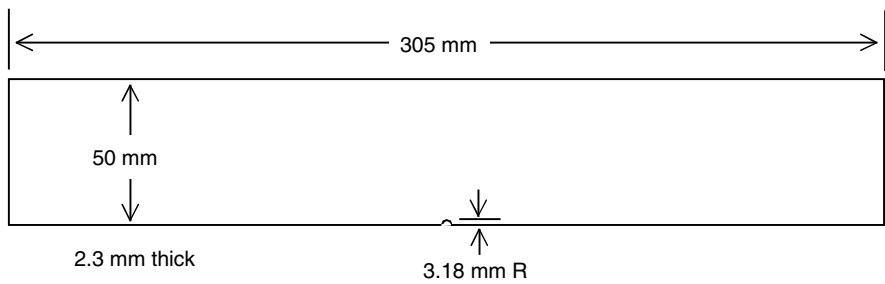


**FIGURE 2.8** Single-edge notched tension specimen used in AGARD short-crack cooperative test program. (From Newman, J.C., Jr. and Edwards, P.R., Short-Crack Growth Behaviour in an Aluminum Alloy: an AGARD Cooperative Test Programme, AGARD R-732, 1988. With permission.)

Tests were conducted with constant-amplitude loading at three different maximum stress levels for each stress ratio,  $R$ , of  $-2$ ,  $-1$ ,  $0$ , and  $0.5$ . In addition, tests were carried out at three reference stress levels for two different load spectra: FALSTAFF (a standardized spectrum representative of the load-time history in the lower wing skin near the root of a fighter aircraft) and a Gaussian-type random load sequence. An example of the data along with cycles to initiation estimates using the three strain-life models is shown in Figure 2.9 for the constant-amplitude  $R = 0$  tests.

Another useful data set for the variation in crack initiation time was done at Boeing in the 1970s [39]. The goal of the study was to develop sufficient fatigue data to identify the form of the life distributions, so that a probabilistic fatigue design method could be explored. Eight 2024-T3 panels, 914.4 mm wide by 3.18 mm thick, with 110 holes measuring 4.76 mm in diameter, were fatigue-tested under two different load spectra. The panels came from three different heats of material. A conductive-paint crack-detection circuit was used to detect cracks on the order of 0.5 mm from each hole. When a hole cracked, it was oversized to 9.53-mm diameter and cold-worked to inactivate that hole as a future crack site. Testing was continued until 10% to 20% of the holes had cracked, though in two instances testing continued until 50% of the holes cracked. The number of spectrum load points until crack detection during these tests is shown in Figure 2.10. The number for spectrum load points to cracking predicted with the strain-life

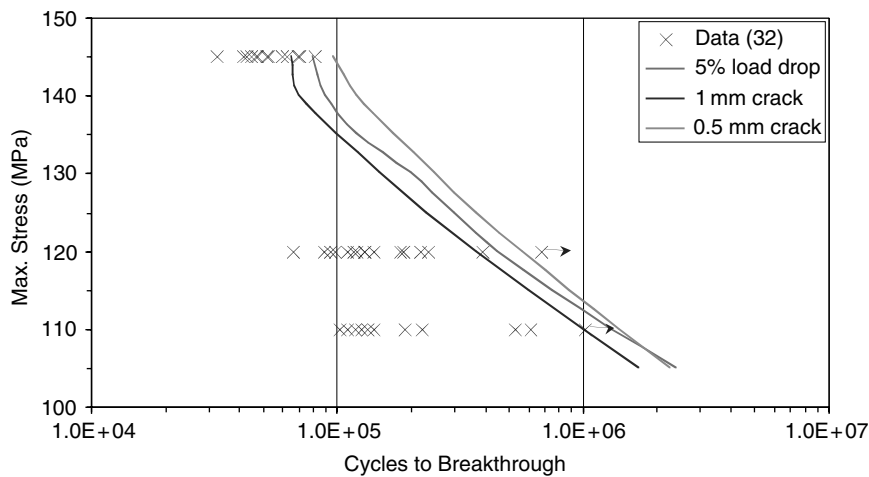


**FIGURE 2.9** Cycles to development of a through-thickness crack in SENT specimens of 2024-T3.

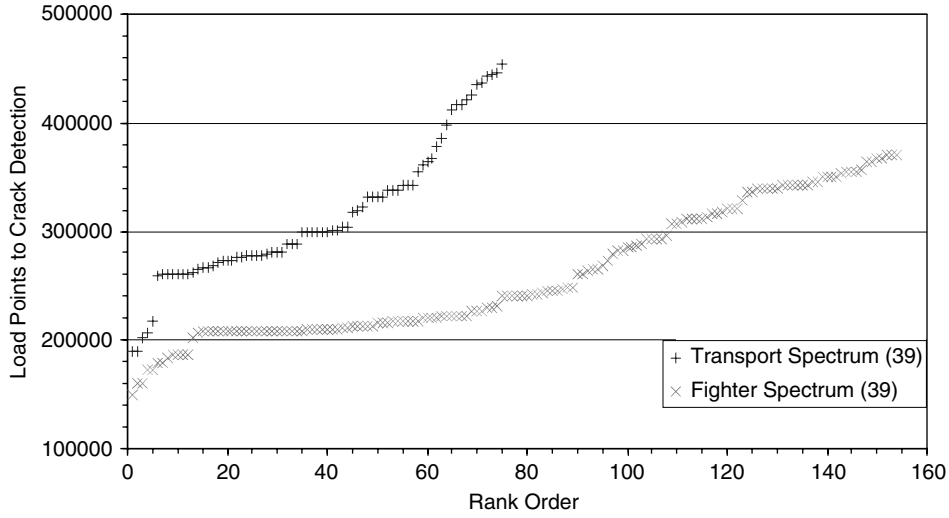


FIGURE 2.10 Cycles to detection of a crack at holes in 2024-T3 panels.

models presented earlier is approximately 1 million for the transport spectrum and about 440,000 for the fighter spectrum.

It should be noted that the most important source of uncertainty in probabilistic crack initiation life prediction comes from the strain-life curve uncertainty. The uncertainty in the shape of the damage curve model is of secondary significance in risk predictions.

### 2.3.1.2 Crack Propagation

Usually, in practice, the fatigue-crack-propagation models are based on linear elastic fracture mechanics (LEFM) theory. The limitation of the crack-propagation models based on LEFM theory is that they are applicable only to the propagation of long cracks. The small-crack growth below a given stress-intensity-range threshold is totally ignored. In fact, this is not true. Cracks nucleate at a microscale within the grains in plastic slip bands, and then, by accumulating strain energy, they penetrate the grain boundaries and start growing much faster. At each grain boundary there is potential for different crystallographic grain orientations in adjoining grains. If there is a significant difference in orientation, the small crack will stop until it can reform in the next grain. When many grains are penetrated and the crack is 1 to 2 mm, the crack becomes a long crack. Or in other words, a macrocrack was initiated. In the small-crack stage, the LEFM theory is not applicable, since the crack tip plastic zone occupies a large volume in comparison with the crack dimensions.

In this section, small-crack-growth modeling is covered by the cumulative damage models described earlier for crack initiation. No further discussion on the small-crack growth using micro- and meso-mechanics models is included here.

The rate of growth for long cracks,  $da/dN$ , is modeled as a function of the stress intensity range,  $\Delta K$ , and some material behavior parameters. Crack size is denoted by its length,  $a$ , such that the current intensity of growth is uniquely defined by the increment per cycle or the crack growth rate,  $da/dN$ , expressed by a functional relationship of the form

$$da/dN = f(\Delta K, K_{\max}, K_c, \Delta K_{\text{th}}, E, \nu, \sigma_Y, \sigma_U, \epsilon_d, m) \quad (2.13)$$

where independent variables  $\Delta K$  and  $K_{\max}$  define the stress intensity range and maximum stress intensity, respectively; and  $E$  (elastic modulus),  $\nu$  (Poisson's ratio),  $\sigma_Y$  (yield strength),  $\sigma_u$  (ultimate

**TABLE 2.4** Forman Equation Parameters for 2024-T3 Sheet

$K_c$ (MPa $\sqrt{\text{m}}$ )	$C$ (mm/cycle)	$m$	$n$	$p$	$Q$
97.7	$1.47 \times 10^{-4}$	0.39	1.66	0.93	0.54
$R$	0	0.5	0.7	-1	
$\Delta K_{\text{th}}$	3.0	1.75	1.18	5.85	

strength),  $\varepsilon_d$  (ductility),  $m$  (hardening exponent),  $K_c$  (fracture toughness), and  $\Delta K_{\text{th}}$  (threshold level) define the material properties. Several curve fits have been used to model empirical crack propagation.

### 2.3.1.2.1 Forman Model

One of the popular crack-propagation models is the generalized Forman fatigue-crack-growth model [40]:

$$\frac{da}{dN} = \frac{C(1-R)^m (\Delta K - \Delta K_{\text{th}})^p (\Delta K)^n}{((1-R)K_c - \Delta K)^q} \quad (2.14)$$

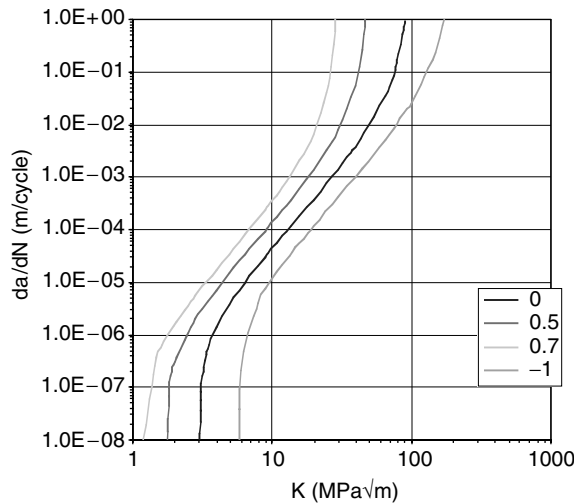
where  $R$  is the stress ratio,  $\sigma_{\text{min}}/\sigma_{\text{max}}$ ;  $K_c$  is the critical stress intensity to cause fracture;  $\Delta K_{\text{th}}$  is the threshold stress intensity as a function of the stress ratio; and  $C$ ,  $m$ ,  $n$ ,  $p$ , and  $q$  are parameters used to fit the data. The values of the parameters for a 2024-T3 sheet, based on data from 1.6- to 2.29-mm-thick sheets tested in lab air, dry air, or humid air, are given in Table 2.4, and the resulting crack growth-rate curves are shown in Figure 2.11.

The generalized Forman model describes the crack-growth behavior in all of the growth-rate regimes. In the Region II, the above reduces to a linear equation in log-log space (Paris law).

The stochastic crack-growth model considers all the parameters as random quantities, but will include also two additional random factors for modeling uncertainties in the regions of low and high values of the rate  $da/dN$  in Regions I and III [40]:

$$\frac{da}{dN} = \frac{C(1-R)^m \Delta K^n (\Delta K - \lambda_{K_{\text{th}}} \Delta K_{\text{th}})^p}{[(1-R)\lambda_{K_c} K_c - \Delta K]^q} \quad (2.15)$$

The threshold random factor can be adjusted to simulate the uncertain small-crack growth.

**FIGURE 2.11** Corrosion rates for 2024-T3 sheet (1.63 mm thick) at four sites.

### 2.3.1.2.2 Hyperbolic Sine Model

The hyperbolic sine equation (SINH) model was developed by Pratt and Whitney Aircraft [41] to interpolate the crack-growth-rate data over a range of the four test variables:  $T$  (temperature),  $R$  (stress ratio),  $F$  (frequency), and  $t_h$  (hold times). The SINH equation, which provides the basic sigmoidal shape and the constants to vary the shape of the curve and the inflection point, is given by the expression

$$\log(da/dN) = C_1 \sinh\{C_2[\log(\Delta K) + C_3]\} + C_4 \quad (2.16)$$

where  $da/dN$  is the crack growth rate per cycle, and  $\Delta K$  is the stress-intensity-factor range. Parameters  $C_1$  and  $C_2$  are shape factors that “stretch” the curve vertically or horizontally, respectively, while  $C_3$  and  $C_4$  locate the inflection point horizontally and vertically, respectively. The slope of the curve at the inflection point is found to be  $C_1 C_2$ . The parameter  $C_1$  is normally set to be 0.5 for many materials.

### 2.3.1.2.3 Modified Sigmoidal Model

The modified sigmoidal equation (MSE) model was developed by General Electric Company [41]. The basic MSE model is expressed as

$$\frac{da}{dN} = e^B \left( \frac{\Delta K}{\Delta K^*} \right)^P \left( \ln \left( \frac{\Delta K}{\Delta K^*} \right) \right)^Q \left( \ln \left( \frac{\Delta K_c}{\Delta K} \right) \right)^D \quad (2.17)$$

where  $da/dN$  is the crack growth rate per cycle, and  $\Delta K$  is the stress intensity range. The equation has the general sigmoidal shape, with the lower asymptote  $\Delta K^*$  representing the threshold value of  $\Delta K$ . The equation involves six parameters,  $\Delta K^*$ ,  $\Delta K_c$ ,  $B$ ,  $P$ ,  $Q$ , and  $D$ . The parameter  $B$  controls the vertical motion of the entire curve. The parameter  $P$  provides the control of the slope at the inflection point of the sigmoidal curve. The vertical location of the inflection point is controlled by a combination of  $B$ ,  $P$ , and  $\Delta K^*$ .

### 2.3.1.2.4 Crack-Closure Model

A crack-propagation model based on crack-closure concepts was implemented in the FASTRAN code by Newman [42]. FASTRAN has been used to model small-crack propagation as well as long-crack propagation. However, the FASTRAN model does capture the effects of material microstructure on small cracks, e.g., the grain boundary effects on small-crack growth rates and orientation at the tip. FASTRAN has, however, been successfully used by different researchers to assess the fatigue life of aircraft components, starting from the initial size of a constituent particle to the final fatigue failure [43, 44].

The analytical crack-closure model is used to calculate crack-opening stresses ( $S_0$ ) as a function of crack length and load history. Based on the value of the crack-opening stress, the effective stress-intensity-factor range is computed, and consequently the crack growth rates are determined. The crack-propagation equation in FASTRAN [44] is

$$\frac{dc}{dN} = C_1 \Delta K_{\text{eff}}^{C_2} \frac{1 - \left( \frac{\Delta K_0}{\Delta K_{\text{eff}}} \right)^2}{1 - \left( \frac{K_{\text{max}}}{C_5} \right)^2} \quad (2.18)$$

where

$$\Delta K_0 = C_3 \left( 1 - C_4 \frac{S_0}{S_{\text{max}}} \right) \quad K_{\text{max}} = S_{\text{max}} \sqrt{\pi c} F \quad \text{and} \quad \Delta K_{\text{eff}} = (S_{\text{max}} - S_0) \sqrt{\pi c} F$$

The crack-opening stress,  $S_0$ , is calculated from the analytical closure model.  $\Delta K_{\text{eff}}$  is called the effective stress intensity.  $\Delta K_0$  is the effective threshold stress-intensity-factor range. One of the advantages of using effective stress intensity is that the constants do not change at different stress ratios.

### 2.3.1.2.5 Stochastic Variability in Crack Propagation

The variability of fatigue-crack growth rate (FCGR) in aluminum alloys arises from changes in crystallographic texture along the crack path, the presence of microcracking at second-phase particles ahead of the crack, and the amount of transgranular vs. intergranular cracking. A significant data set for determining the variability in FCGR of 2024-T3 was produced by Virkler et al. [45]. Sixty-eight center-crack panels, 558.8 mm long by 152.4 mm wide, were cut from 2.54-mm-thick 2024-T3 sheets. Cracks were nucleated at a 2.54-mm-long electrodischarge-machined notch in the center of the panel and grown to 9.00 mm under controlled loading and environment. The number of cycles to reach specific crack lengths was then recorded for each panel under constant-amplitude ( $R = 0.2$ ) loading with a maximum load of 23.4 kN at 20 Hz. Crack-length vs. cycles data from a few select panels are presented in Figure 2.12 so that the individual curves can be identified more easily. The crack-growth curves spread out as the cracks get longer, but they also cross each other in many places as a result of sudden increases and decreases in the growth rates. The corresponding FCGR data are plotted in Figure 2.13.

These data were generated at a single stress ratio; the scatter in crack growth rate data at other stress ratios may be different. In addition, the material was from a single lot. Lot-to-lot variations cannot be determined from these data. An estimate of the variation possible between different batches of materials can be made by comparing data collected from different test programs. Even then, the comparison is only over a limited range of stress intensities for a few stress ratios, and there are typically only a handful of specimens tested at each condition in any given program. An example of the data available from different test programs is compared with the curve given by the Forman equation in Figure 2.14 for  $R = 0$  loading, which is of the most interest for the fuselage joint example.

It should be noted that, in Figure 2.12, the curves for crack length vs. load cycles have slightly different shapes, since the curves cross over. This indicates that an accurate probabilistic modeling would need to consider the random variation of the crack-size evolution shapes. Typical stochastic crack-growth models [46]

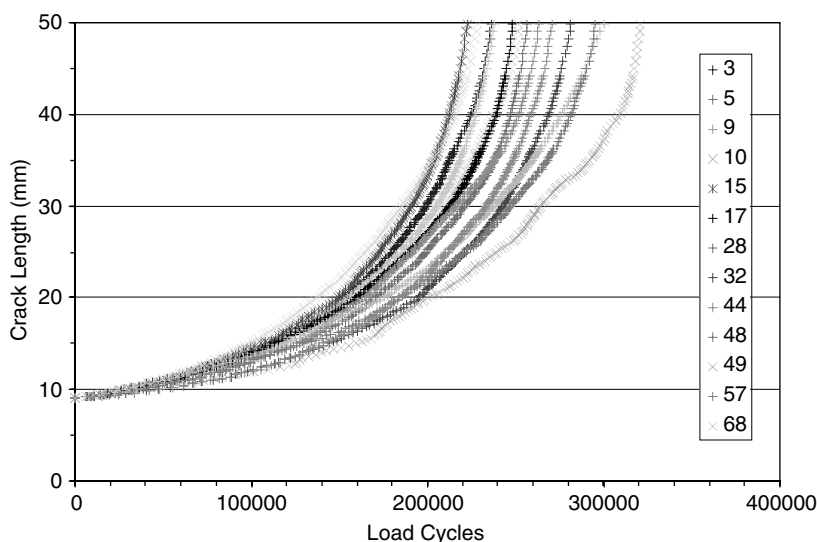


**FIGURE 2.12** Crack length vs. load cycles for 2024-T3 sheet;  $R = 0.2$ ,  $P_{\text{max}} = 23.4$  kN. (Data from Virkler, D.A., Hillberry, B.M., and Goel, P.K., The Statistical Nature of Fatigue Crack Propagation, AFFDL-TR-78-43 [also DTIC ADA056912], 1978.)



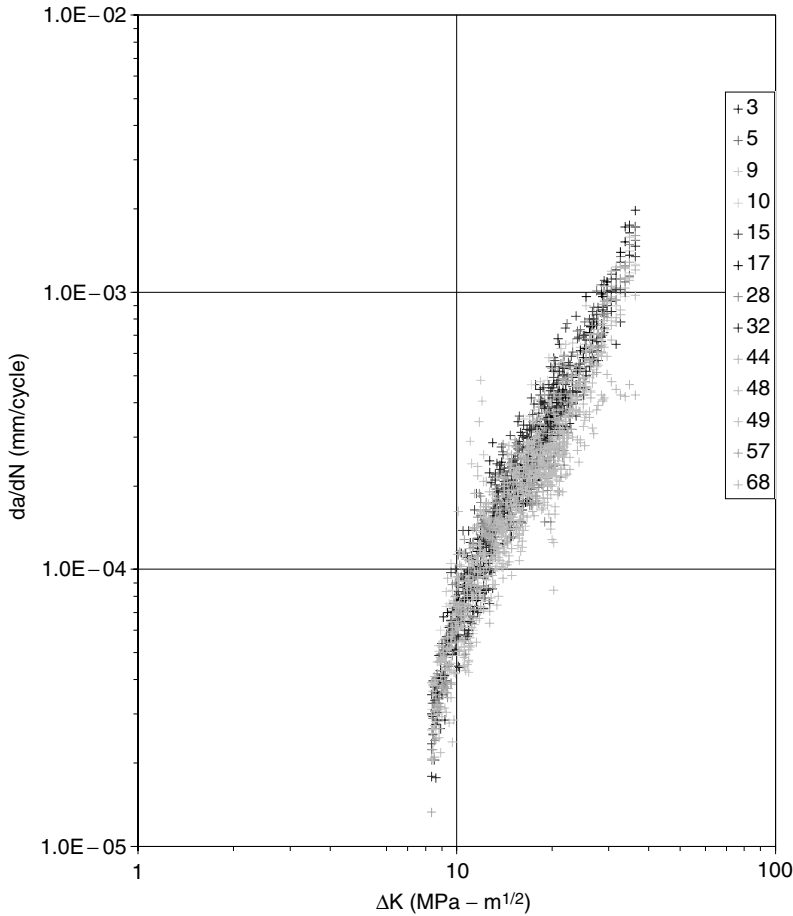


**FIGURE 2.13** Fatigue-crack-growth rate from curves in Figure 2.12.

assume that stochastic crack growth is composed of a median growth curve scaled by a positive random factor, neglecting the random fluctuating variations around the median shape. However, for a refined stochastic modeling, the crack growth process has to be idealized by a stochastic-process model rather than a random-variable model. The random shape variations indicate that the crack-growth process has a finite correlation length. Correlation length is the distance for which the correlation between two points becomes lower than a threshold value. An infinite correlation length corresponds to a random-variable model.

Table 2.5 shows the statistics of number of cycles for four levels of crack sizes: 9.2 mm (close to initial flaw size of 9 mm), 14 mm, 29 mm, and 49.8 mm (considered critical crack size).

As shown in Table 2.5, between the random number of cycles measured for a 9.2-mm crack size and that measured for a 49.8-mm crack size, there is a correlation coefficient as low as 0.31. This indicates a relatively large departure from the usual perfect correlation or, equivalently, the infinite correlation length assumption.

Figure 2.15 shows the histograms from the Virkler data of the number of cycles at which the specified crack length was reached for two selected crack lengths. The numbers of cycles for two specimens are marked on the histogram plots with circles. It should be noted that the two specimens have crack evolutions that are quite different than other statistical crack evolutions. The position of the first specimen moves within the histogram of the crack population from a value in the far right tail at 9.2-mm crack size to a value close the mean at 49.8-mm crack size. The position of the second specimen moves from a value close to the mean at 9.2-mm crack size to a value in the far left tail at 49.8-mm crack size (it is the

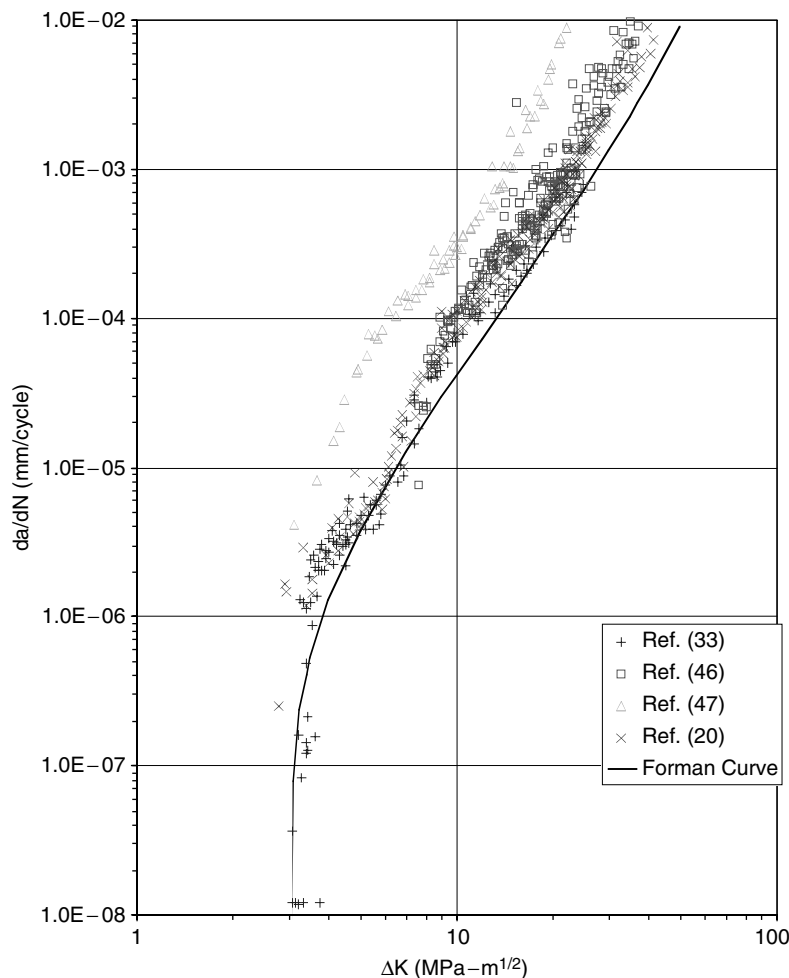


FIGURE 2.14 2024-T3 FCGR lot-to-lot variability,  $R = 0$  loading.

shortest-life crack path within the 68-specimen population). If there was a real perfect correlation between the random number of cycles measured at different crack lengths, then the two marked crack trajectories should maintain their position within the histogram of the crack population without migrating from one location to another.

The fact that the correlation for length of the crack-growth process is not infinite adds more complexity to stochastic modeling of crack-propagation physics. For a constant-amplitude stress-cycle loading, the changes in the shape of the crack-growth curve are a consequence of the local nonhomogeneities in the

TABLE 2.5 Statistics for the Number of Cycles for a Given Crack Size

Crack Size	Mean	Standard Deviation	C.O.V.	Correlation w/9.2 mm	Correlation w/14.0 mm	Correlation w/29.0 mm	Correlation w/49.8 mm
9.2 mm	7,304	1,560	0.210	1.00	0.52	0.38	0.31
14 mm	105,976	9,863	0.093	0.52	1.00	0.87	0.78
29 mm	212,411	14,252	0.067	0.38	0.87	1.00	0.96
49.8 mm	257,698	18,850	0.073	0.31	0.78	0.96	1.00

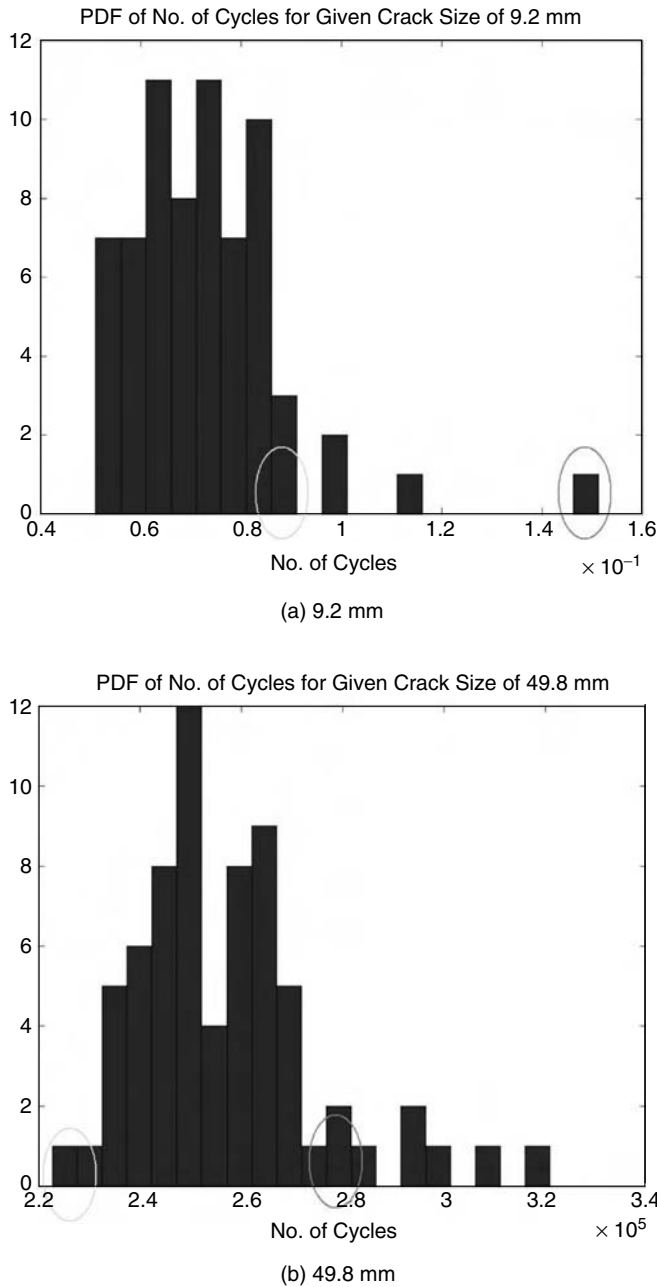


**FIGURE 2.15** Histograms of number of cycles for given crack lengths: (a) 9.2 mm; (b) 49.8 mm.

material properties and resistance against crack growth. For random-amplitude loading, the changes in the shape of the crack-growth curve are larger, since they also include the effects of the random fluctuation of the stress amplitude. The random effects due to material nonhomogeneity and variation in loading history are statistically independent.

Another key aspect for getting an adequate stochastic crack-growth model is to accurately consider the statistical correlation between the estimation of the fatigue-model parameter. For example, for a Paris-law model for the Virkler data shown in Figure 2.12, the absolute value of statistical correlation coefficients

between the estimate of the model coefficient and the estimate of the model exponent is as high as 0.90. Assuming statistical independence between the two random parameters of the Paris-law model produces significant modeling error that can affect the computed fatigue-failure risks by an order of magnitude.

### 2.3.2 Corrosion Damage

Corrosion in aluminum alloys can be broadly characterized into three types: pitting, general, and intergranular [47, 48]. The development of corrosion and its subsequent growth is less well described than is fatigue.

Pitting is a form of localized corrosion that takes the form of cavities on the surface of a metal. Pitting starts with the local breakdown of protective surface films. Pitting may cause the perforation of thin sections, as well as creating stress concentrations that may trigger the onset of fatigue cracking or other types of corrosion. Simplistic models for the progression of pitting corrosion are widely available.

Corrosion of aluminum alloys generally starts with pitting. Isolated pits are difficult to detect, but they have a significant effect on the fatigue life. Pits can occur on boldly exposed surfaces or on the faying surfaces of joints. Pits are stress concentrations where cracks can form; deep, narrow pits are essentially cracks. Even mild levels of pitting can significantly decrease the fatigue life of laboratory specimens. As pitting becomes widespread, a large area of material can become thinner, resulting in higher stress in that location. This increase in stress is generally less than the stress concentration at an isolated pit, but it is over a larger volume of material than with an isolated pit. These thinned regions will cause long cracks to grow faster, while pits will cause cracks to nucleate faster.

General corrosion is when pitting becomes so widespread that individual pits can no longer be identified. As a result, a significant area of the structure becomes thinner, resulting in higher stress at that location. This increase in stress is generally less than the stress concentration at an isolated pit, but it is over a larger volume of material than with an isolated pit. As a result, unless the structure is lightly loaded or used infrequently, cracking due to the interaction of fatigue and corrosion occurs well before general corrosion develops. If general corrosion occurs within a joint, the trapped corrosion products may cause bulging in the joint. Models for how general corrosion progresses are not readily available.

Intergranular corrosion develops out of pits as a result of preferential attack of the grain boundaries, as shown in Figure 2.16 [49]. Exfoliation and stress corrosion cracking (SCC) are special types of

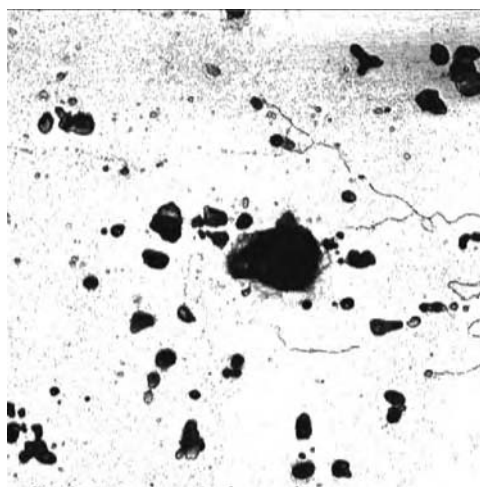


**FIGURE 2.16** Photomicrograph of pits with intergranular corrosion on the surface of a 2024-T3 sheet (4 mm thick) after 4 h of exposure to 3.5% NaCl solution with no load applied (specimen PG-11). (From Bell, R.P., Huang, J.T., and Shelton, D., Corrosion Fatigue Structural Demonstration Program, Lockheed-Martin final report for AFRL/VASM, 2004, [49]. With permission.)

intergranular corrosion that occur in materials with directional grain structures (exfoliation) or under the influence of sustained tensile loads (SCC). The growth of intergranular corrosion is highly dependent upon chemical and metallurgical conditions and is not easily predicted.

### 2.3.2.1 Corrosion Pitting

In this subsection, two of the most accepted pitting models are described.

#### 2.3.2.1.1 Power-Law Pit Model

For a boldly exposed surface, the depth of the deepest pit,  $a$ , as a function of exposure time,  $t$ , is typically described by a power law [50],

$$a = At^{1/n} \quad (2.19)$$

where  $A$  and  $n$  are empirically determined parameters, with  $n$  usually having a value between 2 and 4. This relationship does not mean that any one pit grows at this rate. Pits develop, sometimes rapidly, stagnate, and new pits begin. Rather, this equation represents how the maximum of the distribution of pit depth changes with time. An example of laboratory pitting data for 2024-T3 sheets in 3.5% NaCl solution is shown in Figure 2.17. The least-squares fit of the power-law equation to the data results in  $n$  equal to 2.52 and  $A$  equal to  $20.07 \mu\text{m}$ . These pit depths were measured with either an optical microscope or a confocal microscope from the surface of the specimen. If the pit tunneled, as in Figure 2.18, this could not be determined until after the specimen was broken open.

#### 2.3.2.1.2 Wei Pit Model

A spatial pit-growth model was proposed by Wei [51, 52]. This pit-growth model assumes that the pit shape is a hemispherical shape and that its size grows at a constant volumetric rate,  $dV/dt$ , given by

$$\frac{dV}{dt} = 2\pi a^2 \frac{da}{dt} = \frac{MI_{p0}}{nF\rho} \exp\left(-\frac{\Delta H}{RT}\right) \quad (2.20)$$

By integrating the above equation, the pit depth  $a$  at a given time  $t$  is given by

$$a = \left\{ \left[ \frac{3MI_{p0}}{2\pi nF\rho} \exp\left(-\frac{\Delta H}{RT}\right) \right] t + a_0^3 \right\}^{1/3} \quad (2.21)$$

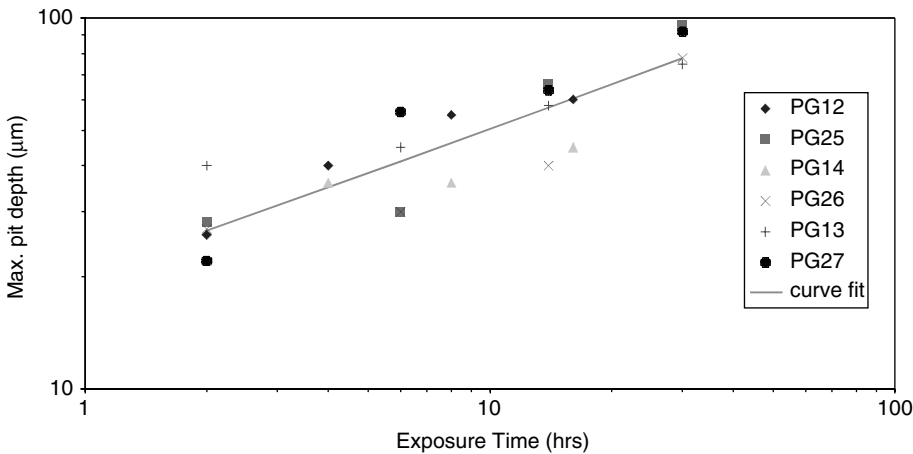


**FIGURE 2.17** Maximum pit depth vs. time in 3.5% NaCl solution for 2024-T3 sheets (1.6 mm thick). (From Bell, R.P., Huang, J.T., and Shelton, D., Corrosion Fatigue Structural Demonstration Program, Lockheed-Martin final report for AFRL/VASM, 2004, [49]. With permission.)

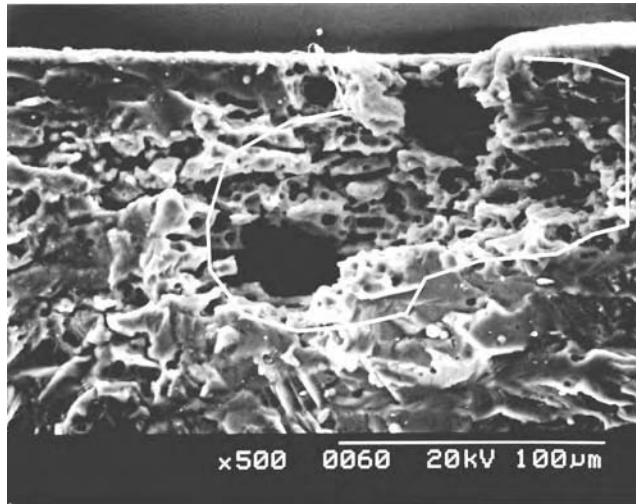


**FIGURE 2.18** Example of pit that tunneled (specimen PG14). The pit is outlined by the white curve. (From Bell, R.P., Huang, J.T., and Shelton, D., Corrosion Fatigue Structural Demonstration Program [51]. With permission.)

where  $a_0$  is the initial pit radius,  $M$  is the molecular weight of the material,  $n$  is the valence,  $F = 96,514$  C/mole is Faraday's constant,  $\rho$  is density of the material,  $\Delta H$  is the activation energy,  $R = 8.314$  J/mole-K is the universal gas constant,  $T$  is the absolute temperature, and  $I_{p0}$  is the pitting current coefficient.

In the Wei model, the assumption of a hemispherical shape of the pits introduces a significant modeling uncertainty. Pit shape is quite an important aspect. The pit depth alone does not adequately describe the stress concentration at a pit. Pit shapes are quite variable and can change with continuing corrosion. Pit shape is influenced by the microstructure of the material that developed as a result of prior thermomechanical processing, the environment (both mechanical and chemical), and the corrosion protection system. More sophisticated models of pitting corrosion are clearly needed.

### 2.3.2.2 Stochastic Variability of Corrosion in Aluminum Alloys

#### 2.3.2.2.1 Field Studies

Several long-term studies have been done to determine the statistical effects of environmental exposure on 2024-T3 aluminum materials [53, 54]. The first study [53] was conducted under the direction of the Atmospheric Exposure Test Subcommittee of ASTM Committee B-7 on Light Metals and Alloys. Several magnesium and aluminum alloys, including bare and clad 2024-T3 sheets (1.63 mm thick), were exposed at five test sites for periods of  $1/2$ , 1, 3, 5, and 10 years. The specimens included riveted joints as well as single-piece panels. The principal measurement in this test program was the change in tensile strength as a result of the exposure.

The second test program [54] involved four test sites for periods of 1, 2, and 7 years. The four test sites represented rural marine (Kure Beach), industrial marine (Corpus Christi, TX), moderate industrial (Richmond, VA), and industrial (McCook, IL) areas. In this test program, pit depths, mass loss, and changes in tensile strength were recorded. A plot of maximum pit depth vs. exposure time is presented in Figure 2.19. The results indicate that while corrosion in a seacoast environment may start more quickly, there is not much additional corrosion with continued exposure. After 7 years, all the panels had about the same maximum pit depth. The corrosion rate at each of the locations was determined from the total mass loss per unit area divided by the total days of exposure and reported as milligrams lost per square decimeter per day, mdd (Figure 2.20). It is interesting to note that while the marine environments initially had deeper pits than the industrial environments, the industrial environments had higher corrosion rates. The locations with higher

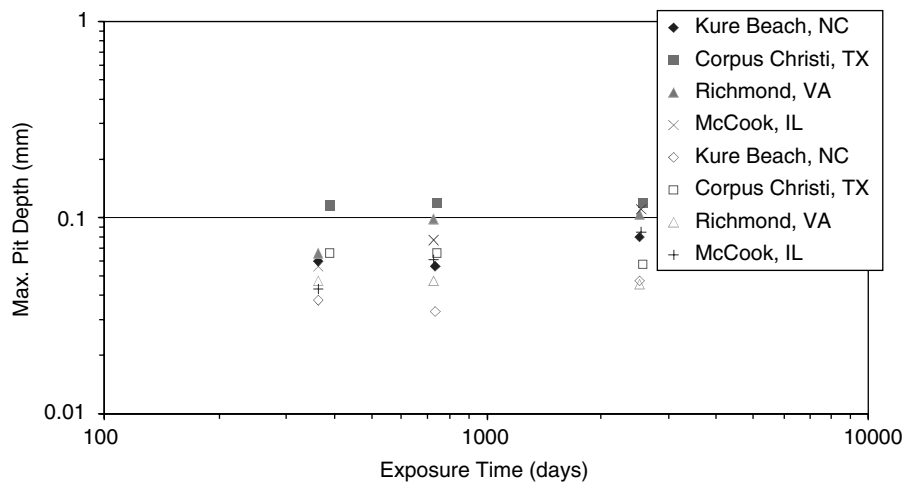


**FIGURE 2.19** Maximum pit depths on exposed 2024-T3 sheets (1.63 mm thick). (Solid symbols are maximum depths; open symbols represent average of the deepest four pits.) (From Ailor, W.H., Jr., Performance of aluminum alloys at other test sites, in *Metal Corrosion in the Atmosphere*, ASTM STP 435, ASTM, 1968, pp. 285–307. With permission.)

corrosion rates likely had more pits per unit area, or there was more tunneling of the pits. These corrosion rates are for “boldly” exposed material.

In practical applications, the goal of a stochastic corrosion model is to obtain either the distribution of corrosion damage at any service time or the distribution of service times to reach any given level of corrosion. Different distributions may be required for corrosion on exposed surfaces and for corrosion in occluded areas such as joints. However, data on corrosion in occluded areas are just now becoming available.

**2.3.2.2.2 Laboratory Studies**

Numerous laboratory studies with accelerated protocols have looked at the distribution of corrosion pit sizes [55–57]. Pitting on exposed surfaces is primarily a function of the dispersion of constituent

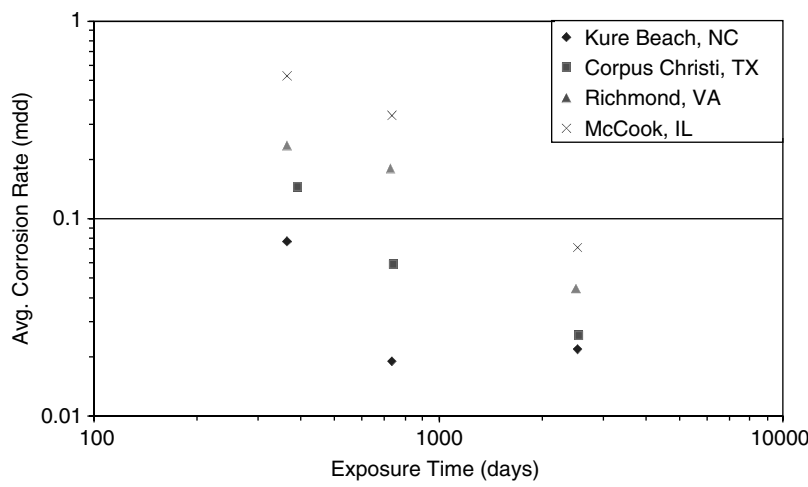


**FIGURE 2.20** Corrosion rates for 2024-T3 sheets (1.63 mm thick) at four sites. (From Ailor, W.H., Jr., Performance of aluminum alloys at other test sites, in *Metal Corrosion in the Atmosphere*, ASTM STP 435, ASTM, 1968, pp. 285–307. With permission.)

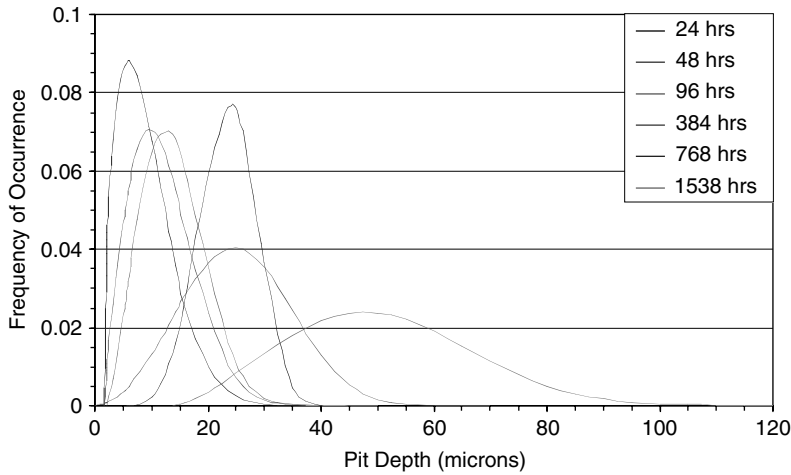


**FIGURE 2.21** Three-parameter Weibull distributions of pit depth as a function of exposure time for 7075-T6.

particles in the material microstructure and not the environment. The stochastic descriptions of pitting developed during accelerated laboratory programs should be applicable to pitting on exposed surfaces in natural environments.

Sankaran et al. [55] estimated the distributions of pit dimensions on 7075-T6 as a function of time exposed per ASTM G85 Annex 2 from 200 randomly selected pits at each exposure time (Figure 2.21, Figure 2.22, Figure 2.23). The progression of these distributions with time exhibited a ratcheting behavior. This can be seen in the sequence of pit-depth distributions from 96-h exposure to 1538-h exposure shown in Figure 2.21.

In the studies of pitting on 2024-T3 [56, 57], statistics are reported on the projected area of the pits perpendicular to the loading direction. The Gumbel extreme-value distribution was used to describe the projected areas of the largest pits (Figure 2.24). Note that the area of these pits at 192 h of exposure is an order of magnitude greater than was the area of the pits in the 7075-T6 tests [55].

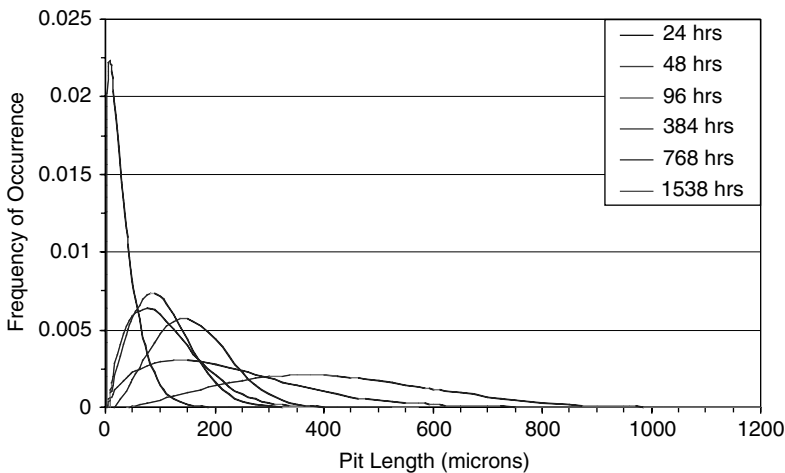


**FIGURE 2.22** Three-parameter Weibull distributions of pit length (in rolling direction of sheet) as a function of exposure time for 7075-T6.



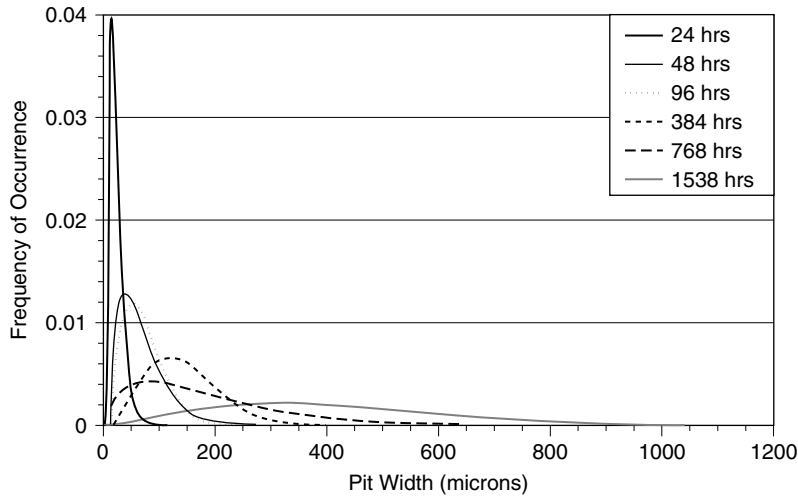


**FIGURE 2.23** Three-Parameter Weibull distributions of pit width (perpendicular to rolling direction of sheet) as function of exposure time for 7075-T6.

This is probably the result of the different severities of the environments and not any inherent material characteristics.

In subsequent fatigue analyses, the pits in the 2024-T3 materials were treated as semicircular surface cracks with a depth-to-width ratio of 0.5 and of equivalent area, which is the most severe case for these small “cracks.” Data from the 7075-T6 tests demonstrate that a constant depth-to-width ratio is not realistic, as illustrated by the Weibull distributions shown in Figure 2.25. The nonanalytical estimated bivariate joint probability distribution of pit depth size and pit width is plotted in Figure 2.26. Engineering experience shows that the impact of ignoring the pit aspect ratio in fatigue-crack growth analyses is to potentially overestimate the stress intensity by about a factor of 2, which could lead to overestimating the crack growth rate by an order of magnitude or even more.

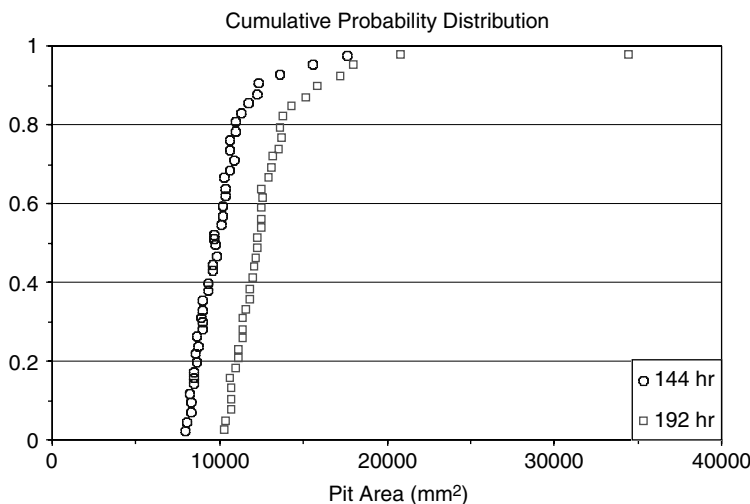


**FIGURE 2.24** Extreme-value plots of pit area for largest 10% pits in 2024-T3 material. LT plane exposed to 3.5% salt water in alternate immersion for 144 h and 192 h. Pit area measured on ST plane.

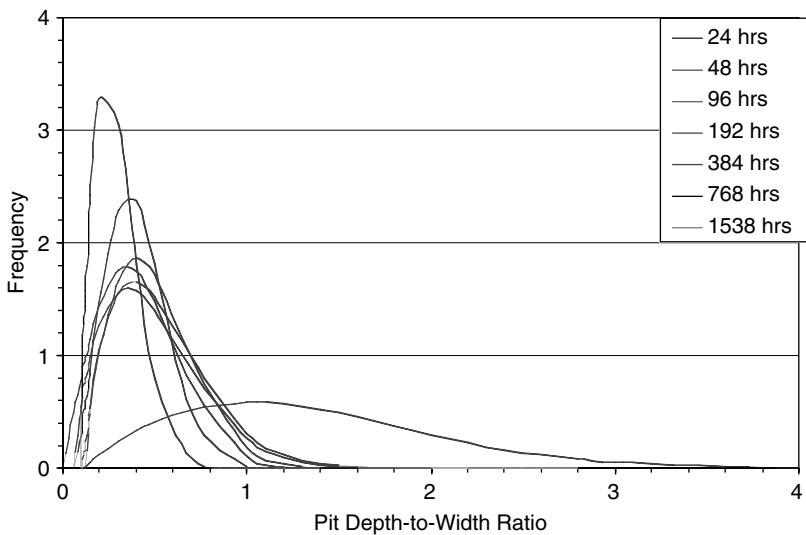


FIGURE 2.25 Three-parameter Weibull distribution of the pit depth-to-width ratio as a function of exposure time for 7075-T6.

2.3.2.2.3 Corroded Surface Topography

Corroded surface topography can have significant influence on corrosion progression and fatigue resistance due to its influence on the local stresses and stress intensity factors. Corroded surface topography incorporates all the key stochastic aspects of the random corrosion progression. At a global scale, in an average sense, the corrosion topography is defined by the general thickness loss, while at a local scale the corrosion topography is defined by the pitting geometry. The corrosion starts as pits on the surface at the boundaries between the aluminum matrix and constituent particles, and then grows with a rough spatial profile due to highly variable growth rates for individual pits. Finally the surface becomes slightly smoother as the pits broaden and link up to form a general corroded surface. Data on

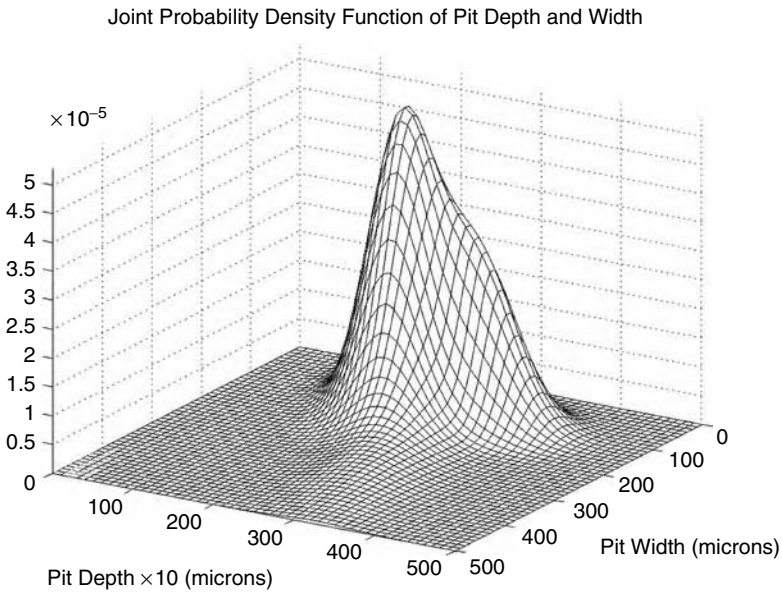


FIGURE 2.26 Joint PDF of pit depth and width after 768 h.

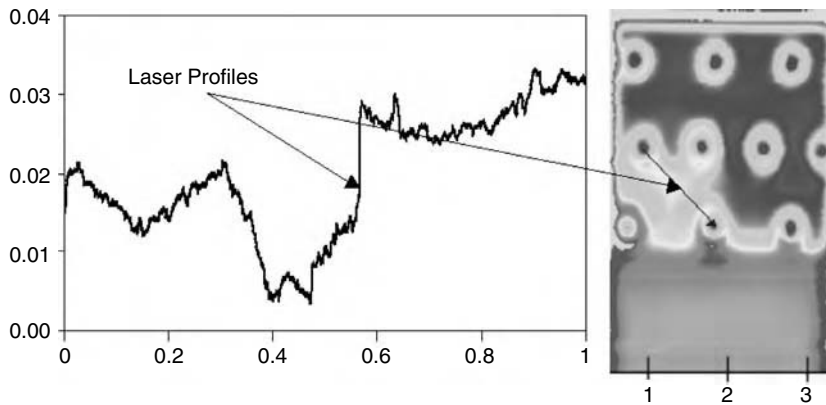


FIGURE 2.27 Thickness map of corroded surface and fine-detail line scan.

the time progression of corroded surfaces through these phases are lacking. Corrosion topography influences both the local stresses (through local pitting) and far-field stresses (through general thickness loss). A typical corroded surface and a cut-line (laser) profile through it are shown in Figure 2.27. Mathematically, stochastic corrosion surfaces can be handled using stochastic field-expansion models such as proper orthogonal decomposition or Karhunen-Loeve series expansion [58, 59].

### 2.3.3 Corrosion-Fatigue Damage

In this section the effects of corrosion of both crack initiation and propagation stages are discussed. Then, three corrosion-fatigue damage models are presented. These models are the Wei corrosion-fatigue (WCF) model [53, 54], the crack-closure corrosion-fatigue (CCCF) model [42], and the simultaneous corrosion-fatigue (SCF) model [8]. The WCF model replaces the crack-initiation model with a corrosion-pitting model, and after a crack is initiated, the corrosion has no effect on the fatigue cracking. The CCCF and SCF models incorporate the corrosion effects on fatigue cracking during both the crack-initiation and the crack-propagation stages.

Corrosion effects are of two kinds: (1) a local increase in stress near a corrosion pit and (2) a general increase of the far-field stress due to component thickness loss. Pitting can dramatically reduce component life, but it is only significant during the crack-initiation phase. General thickness loss has a less dramatic effect on the time to form a crack, but the increased stress can speed up the growth of existing cracks.

Pitting corrosion usually shortens the time for cracks to form, in some cases eliminating the crack nucleation phase altogether. The reduction in the nucleation portion depends on the amount of corrosion, which in turn depends upon the length of exposure to the corrosive environment and the severity of the corrosive environment in relation to the rate at which load cycles are applied. It is difficult to simulate the effect of natural environments in the laboratory because of the time scale involved (20 to 30 years), and currently the relationship between the time scales in accelerated corrosion tests to the natural environment has not been established. So synchronizing the rate at which load cycles are applied with corrosion rate is impossible.

In the laboratory, cracks grow faster in aggressive environments. It is not clear how significant the environmental effects on crack growth are for aircraft structures. Many of the fatigue loads are applied when the aircraft is flying high, where conditions are cold and relatively dry. There can be condensation of moisture inside a transport aircraft. This creates at most a humid environment, so crack growth in humid air may be appropriate. Takeoff and landing loads can be applied in a warm and humid external environment, but this is a small fraction of each flight, unless the aircraft is used for short hops. Recent data gathered from coupons mounted in the wheel wells and vertical tails indicate that most corrosion

in USAF transport aircraft occur-while the aircraft is on the ground [60]. In general, crack-growth rates in high-humidity air should be used for crack-propagation assessments on USAF aircraft.

Local corrosion, such as pitting, on the surface of a part does not greatly affect the growth of long cracks. Because the crack is “sampling” through the thickness of the material, small stress fluctuations at the surface affect only a small local portion of the crack. Not until corrosion becomes so widespread that there is a general loss of part thickness is crack growth affected. Then the crack-growth rate increases because stress increases in the part.

### 2.3.3.1 Wei Corrosion-Fatigue (WCF) Model

The Wei model was developed over a period of several years [51, 52]. As described above, the Wei models assume two stages of corrosion-fatigue damage growth. The first stage is the corrosion stage due to initial pitting, which continues until a threshold level is reached (threshold corresponds to an equal growth rate of pit depth and crack depth, after which crack growth takes over). The second stage is the fatigue stage that ends with the material failure. The Wei models include two fatigue-crack stages, a surface-crack stage and then a through-crack stage. The surface-crack-fatigue part of the Wei model is based on simple Paris-law, with a  $\Delta K_{th}$  of 3 MPa  $\sqrt{m}$  for 2024-T3 aluminum. Thus, in the Wei model, corrosion is just the initiator of fatigue damage due to crack growth. After fatigue takes over (crack-depth growth rate is larger than pit-depth growth rate), corrosion has no further effect. This is a different concept than the SCF model that is presented in this section.

The time to failure,  $t_f$ , is given by

$$t_f = t_{ci} + t_{ic} + t_{cg} \quad (2.22)$$

where,  $t_{ci}$  is the time required for a nucleated pit to grow and for a surface crack to initiate from it;  $t_{ic}$  is the time required for the surface crack to grow into a through crack; and  $t_{cg}$  is the time for a through crack to grow to a prescribed critical length, given as a part of a failure criterion.

Using the pit-growth equation given by Wei, the time for the pit to grow to  $a_{ci}$  is given by

$$t_{ci} = \frac{2\pi nF\rho}{3MI_{p0}} \left( a_{ci}^3 - a_0^3 \right) \exp\left( \frac{\Delta H}{RT} \right) \quad (2.23)$$

The pit radius at which a crack is initiated,  $a_{ci}$ , can be expressed in terms of the threshold driving force  $\Delta K_{th}$  via the crack-growth mechanism. For the sake of simplicity and computational expediency, the surface crack remains semicircular in shape, and the stress-intensity-factor range is given by

$$\Delta K_s = \frac{2.2}{\pi} K_t \Delta \sigma \sqrt{\pi a} \quad (2.24)$$

where  $\Delta \sigma$  is the far-field stress range,  $K_t$  is the stress concentration factor resulting from the circular rivet hole, and the factor of  $2.2/\pi$  is for a semicircular flaw in an infinite plate. Again, the surface crack is assumed to nucleate from a hemispherical corrosion pit when  $\Delta K_s$  increases to  $\Delta K_{th}$ . The corresponding crack length that satisfies this condition is easily found to be

$$a_{ci} = \pi \left( \frac{\Delta K_{th}}{2.2 K_t \Delta \sigma} \right)^2 \quad (2.25)$$

The expression for  $t_{ci}$  can be found by substituting Equation 2.25 into Equation 2.26. The material parameters of the Wei corrosion model for 2024-T3 aluminum are shown in Table 2.6.

Within the Wei corrosion-fatigue model, a standard Paris law is assumed for crack propagation:

$$\left( \frac{da}{dN} \right)_c = C_C (\Delta K)^n \quad (2.26)$$

**TABLE 2.6** Parameters Used in the Pit-Growth Model for 2024-T3

Parameters	2024-T3	Parameters	2024-T3
Density, $\rho$ (gm/m <sup>3</sup> )	$2.7 \times 10^6$	Initial pit radius, $a_0$ (m)	$2 \times 10^{-5}$
Molecular weight, $M$	27	Pitting current constant, $I_{p0}$ (C/sec)	0.5
Valence, $n$	3	Threshold, $\Delta K_{th}$ (MPa√m)	3.0
Activation energy, $\Delta H$ (J/mole)	50,000	Applied stress, $\Delta\sigma$ (MPa)	90
Temperature, $T$ (K°)	293	Stress concentration factor, $K_t$	2.6

The driving force  $\Delta K$  is considered to be of two different forms, according to whether the crack is a surface crack or a through crack. For a surface crack,  $\Delta K$  equals  $\Delta K_s$  given in Equation 2.24, and it remains so until the crack can be modeled as a through crack. When the crack becomes a through crack,  $\Delta K$  is assumed to be equal to  $\Delta K_{tc}$ , which has the following form:

$$\Delta K_{tc} = F_{tc} \left( \frac{a}{r_0} \right) \Delta \sigma \sqrt{\pi a} \quad (2.27)$$

where  $r_0$  is the radius of the rivet hole. For ratios of  $a/r_0$  in the interval from 0 to 10, inclusive, for an infinite plate under uniaxial tension containing a circular hole with a single through crack emanating from the hole perpendicular to the loading axis, the function  $F_{tc}(a/r_0)$  can be numerically evaluated by

$$F_{tc} \left( \frac{a}{r_0} \right) = \frac{0.865}{(a/r_0) + 0.324} + 0.681 \quad (2.28)$$

The remaining question concerning the driving force  $\Delta K$  is that of the transition from a surface crack to a through crack. It is assumed that the transition occurs at the crack length  $a_{tc}$ , which is defined by equating the geometry-dependent function from Equation 2.24 and Equation 2.28. Thus, the transition crack length  $a_{tc}$  is the solution of

$$F_{tc} \left( \frac{a_{tc}}{r_0} \right) = \frac{2.2}{\pi} K_t \quad (2.29)$$

which is easily found to be

$$a_{tc} = r_0 \left[ \frac{0.865}{(2.2/\pi)K_t - 0.681} - 0.324 \right] \quad (2.30)$$

The final computation to be completed is for  $t_{tc}$  and  $t_{cg}$ . First consider the computation for the time between crack initiation and transition to a through crack,  $t_{tc}$ . Substituting Equation 2.24 into Equation 2.26 yields a simple differential equation in that the variables  $a$  and  $N$  can be separated, and an explicit solution can be found. Assuming that  $N = vt$ , where  $v$  is the loading frequency, then

$$t_{tc} = \frac{2(\sqrt{\pi})^{n_c} [(\sqrt{a_i})^{2-n_c} - (\sqrt{a_{tc}})^{2-n_c}]}{v(n_c - 2)C_c(2.2K_t\Delta\sigma)^{n_c}} \quad (2.31)$$

if  $n_c \neq 2$ . For aluminum alloys, typically  $n_c$  is not equal to 2.

The time between the through-crack initiation time and the final failure time is

$$t_{cg} = \int_{a_{tc}}^{a_f} \frac{1}{vC_c(\Delta\sigma\sqrt{\pi})^{n_c}} \left( \frac{0.324r_0 + a}{1.086r_0\sqrt{a} + 0.681(\sqrt{a})^3} \right)^{n_c} da \quad (2.32)$$

**TABLE 2.7** Parameters Used in the Crack Growth Model for 2024-T3

Parameters	2024-T3	Parameters	2024-T3
Fatigue coefficient, $C_c$ (m/cycle)	$3.3 \times 10^{-10}$	Final crack size, $a_f$ (mm)	3.0
Crack growth exponent, $n_c$	3.0	Frequency, $\nu$ (cycles/day)	2, 10
Radius of rivet hole, $r_o$ , (mm)	3.0	Threshold, $\Delta K_{th}$ (MPa $\sqrt{m}$ )	3.0

Source: Ailor, W.H., Jr., Performance of aluminum alloys at other test sites, in *Metal Corrosion in the Atmosphere*, ASTM STP 435, ASTM, 1968, pp. 285–307.

where  $a_f$  is the final crack size. In most cases, the  $t_{cg}$  can only be calculated by numerical integration. The parameters for crack growth that are shown in Table 2.7 are from the literature [52].

### 2.3.3.2 Crack-Closure Corrosion-Fatigue (CCCF) Model

The crack-closure fatigue model [42] was modified to include the effect of corrosion pitting on the local stress intensity. To include corrosion pit effects the effective-stress-intensity range,  $\Delta K_{eff}$ , is amplified by a pitting factor as follows:

$$\Delta K'_{eff} = \psi(t) \Delta K_{eff} \quad (2.33)$$

The pitting factor  $\psi(t)$  depends on pit size and crack size:

$$\psi(t) = \sqrt{1 + \frac{a_{pit}(t)}{a_{crack}(t)}} \quad (2.34)$$

Equation 2.33 and Equation 2.34 are equivalent to an additive corrosion-fatigue-damage model that superimposes linearly the corrosion damage, pit size, fatigue damage, and crack size in the stress-intensity analytical expression. Since, practically, there is no corrosion during flights, only the ground time is considered for evaluating the corrosion pit growth. The pit growth, Equation 2.34, is computed using Wei pit model Equation 2.21.

### 2.3.3.3 Simultaneous Corrosion-Fatigue (SCF) Model

The SCF model describes corrosion-fatigue damage occurring simultaneously [8]:

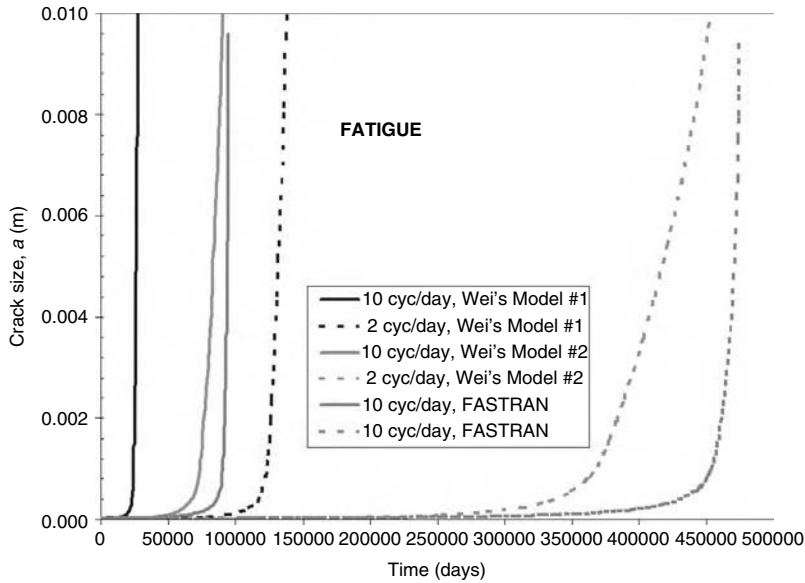
1. Cracks form during the crack nucleation phase. The time to form a crack can be decreased by corrosion that occurs during the crack nucleation phase.
2. Cyclic loading is interspersed with periods of pit growth, which increases the local stress concentration factor.
3. If load cycles are applied infrequently, pitting may transition to general corrosion and thickness loss, leading to an increase in the global stress.
4. Once a crack is formed, only the thickness loss due to general corrosion and the associated stress increase affect the growth rate of the crack.

The SCF model is implemented as follows: (1) for crack initiation, an additive incremental total damage model that linearly superimposes the pit-depth increment and the stress-concentration factor; and (2) for crack propagation, two time-variant corrosion-topography factors (pitting and thickness loss factors) that multiply the stress-intensity-factor range.

### 2.3.3.4 Comparative Results

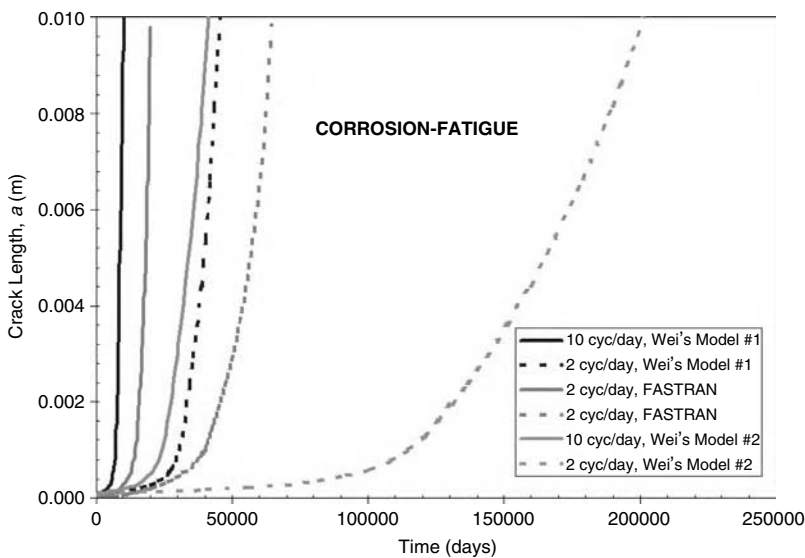
In this subsection, computed results obtained using the deterministic corrosion-fatigue models described above are compared.

Figure 2.28 and Figure 2.29 compare the WCF model and the CCCF model for a plate with a hole [51]. The plate is 90 mm wide and 1.3 mm thick. The hole has a 3-mm radius and is located in the center of the plate. The initial pit size, corresponding to the size of the constituent particle from which



**FIGURE 2.28** Results of the WCF and CCCF models (using FASTRAN) for pure fatigue.

the pit starts, is  $20\text{ }\mu\text{m}$ . The constituent particle shape was assumed to be hemispherical. Two aircraft operating scenarios are considered here: (1) 10 load cycles/day, assuming 15-h flight and a 9-h stay on ground (for same location); and (2) 2 load cycles/day, assuming 3-h flight and 21-h stay on ground (for same location). The stress range was 90 MPa at temperature, and the notch factor was  $K_t = 2.6$ . The material was 2024-T3 aluminum. The fatigue coefficient,  $C_c$ , and the exponent,  $n_c$ , were assumed to be  $3.95\text{ E-}11$  and  $3.55$  for Wei model 1 [52] and  $1.86\text{ E-}11$  and  $3.15$  for Wei model 2, respectively.



**FIGURE 2.29** Results of WCF and CCCF models (using FASTRAN) for corrosion fatigue.

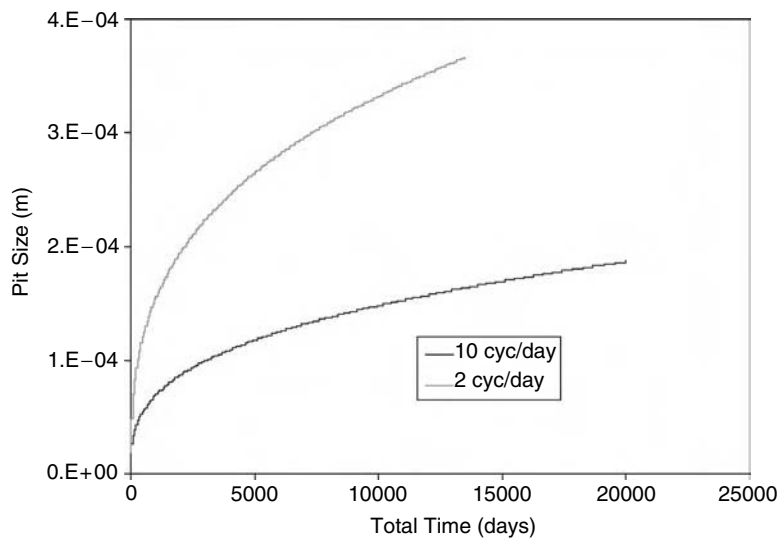


FIGURE 2.30 Pit-depth curves for the two operating scenarios for aircraft.

The pit-growth and the pitting-factor curves for the two corrosion scenarios are plotted in Figure 2.30 and Figure 2.31, respectively. The pit-growth curves are the same for the WCF and CCCF models. The pitting factors are applied only in conjunction with the CCCF model (Equation 2.33 and Equation 2.34).

Figure 2.28 shows the pure-fatigue lives computed for the WCF models and the CCCF model assuming 10 cycles/day and 2 cycles/day, respectively. Figure 2.29 shows the corrosion-fatigue lives using the same models. Only the time on ground was considered for corrosion growth. The computed lives are also included in Table 2.8.

It should be noted from Figure 2.28, Figure 2.29, and Table 2.8 that the range of results of the WCF model 1 and model 2 include the CCCF results. For pure fatigue, there is a poor matching between the lives computed using Wei model 1 and CCCF. The Wei model 2 matches quite well the FASTRAN results

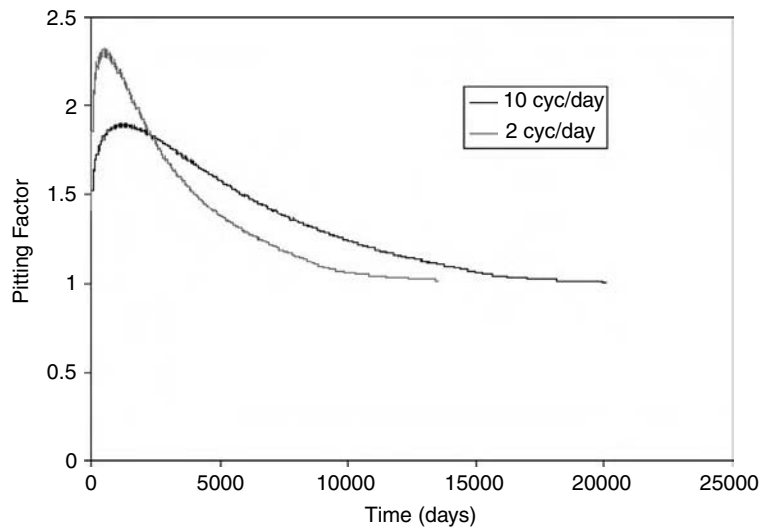
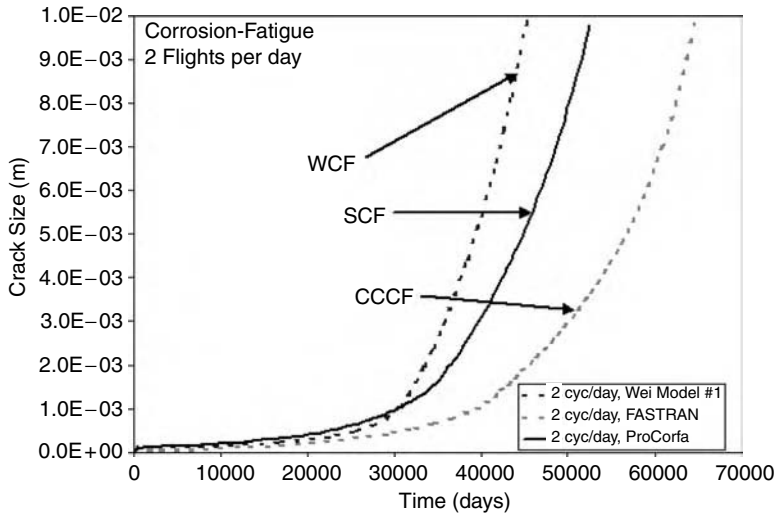


FIGURE 2.31 Pitting corrosion factor for the two operating scenarios for aircraft.



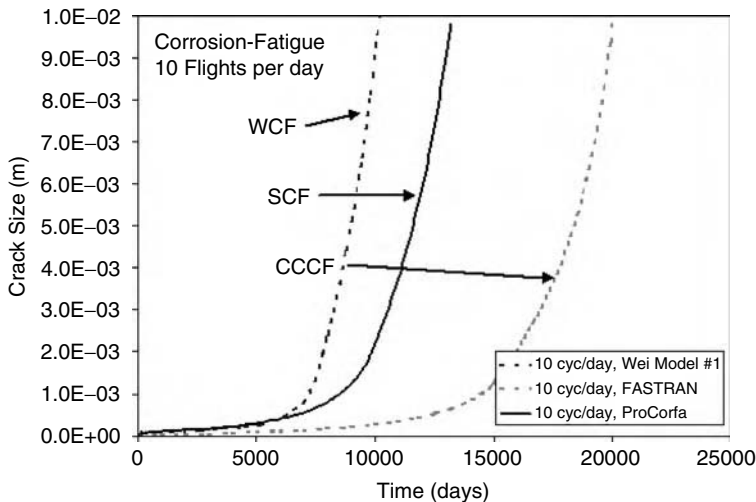
**TABLE 2.8** Comparative Life Results Using WCF Model and CCCF Model

Investigated Case	WCF-Wei Model 1	WCF-Wei Model 2	CCCF
Fatigue, 10 cycles/day	27,560 days	90,647 days	94,905 days
Fatigue, 2 cycles/day	137,802 days	453,239 days	474,850 days
Corrosion fatigue, 10 cycles/day	10,185 days	41,320 days	20,018 days
Corrosion fatigue, 2 cycles/day	45,370 days	201,046 days	64,951 days

**FIGURE 2.32** Comparative life predictions for 2 cycles/day using WCF model, SCF model, and CCCF model.

for pure fatigue, while the Wei model 1 agrees better than the Wei model 2 with CCCF results for the largest corrosion damage, namely, the 2-cycles/day case (21 h/day stay on ground).

Figure 2.32 and Figure 2.33 compare the WCF, CCCF, and SCF models for the two previous corrosion-fatigue scenarios. In this comparison, the SCF model uses the LDR for crack initiation combined with the

**FIGURE 2.33** Comparative life predictions for 10 cycles/day using WCF model, SCF model, and CCCF model.

Forman model for crack propagation (Table 2.3 and Table 2.4). The main differences between the WCF model results and the SCF model results are due to the different fatigue-crack-propagation models used. WCF uses a truncated Paris-law model, and SCF uses the Forman model. The crack-growth threshold,  $\Delta K_{th}$ , was taken equal to  $3 \text{ MPa}\sqrt{\text{m}}$ . The Paris-law model was truncated at this threshold value.

## 2.4 Reliability of Aircraft Structure Joints Including Maintenance Activities

The reliability analysis concept is illustrated in Figure 2.34. It can be seen in the figure that the effect of corrosion on fatigue life is to increase the time-variant failure risk and to produce unscheduled maintenance events. In Figure 2.34, notation SME stands for scheduled maintenance events, and notation UME stands for unscheduled maintenance events. In the figure, the probability distributions of the crack-size population before and after the inspections are also shown. The result of inspection is the replacement (or repair) of the components with larger cracks, which are most likely to be detected by inspections.

### 2.4.1 Risk/Reliability-Based Condition Assessment

Component risk/reliability-based condition assessment is usually based on three risk/reliability metrics: (1) instantaneous probabilistic failure risk that expresses the risk at any given time or damage level, (2) component remaining life (when no maintenance activity is included), and (3) future probabilistic failure risk that expresses the risk in the next time interval (this future interval is associated with a maintenance interval).

#### 2.4.1.1 Physics-Based Reliability Engineering Approach

The physics-based reliability engineering approach integrates the structural reliability theory with the reliability engineering theory. The basic relationship that links the two theories is the relationship between

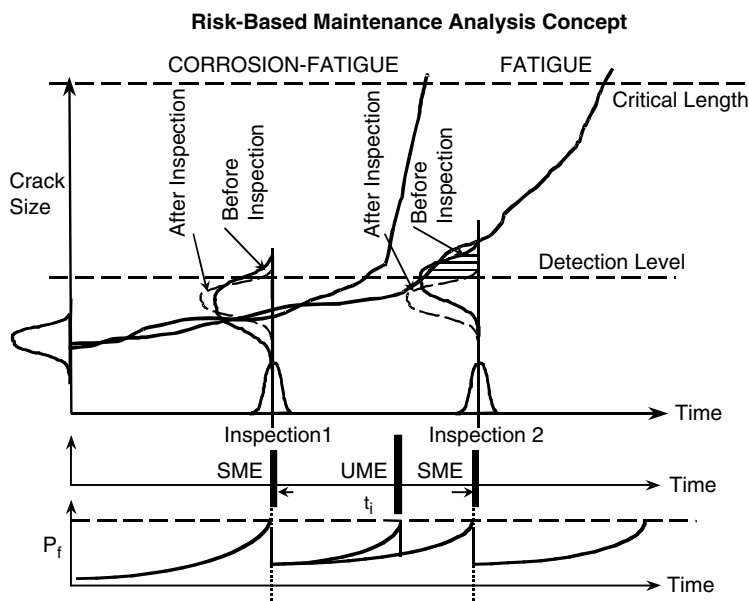


FIGURE 2.34 Risk/reliability-based maintenance analysis concept.

the computed instantaneous failure probability and the hazard failure rate at any given time:

$$\text{Prob}[T_f \leq t + \Delta t | T_f > t] = P_f(t) + [1 - P_f(t)] \exp \left[ - \int_t^{t+\Delta t} h(x) dx \right] \quad (2.35)$$

The above equation expresses the failure probability within a time interval that defines the probability distribution of a component life, in terms of the instantaneous failure probability computed at the starting time of the interval,  $P_f(t)$ , and the variation of the hazard failure rate,  $h(x)$ , in the interval. Then, the reliability engineering metrics, such as MTBF (mean time between failures), that are required for maintenance cost analysis can be computed by integrating the reliability function (defined by unity minus the failure probability):

$$\text{MTBF} = \int_0^{\infty} [1 - P_f(t)] dt \quad (2.36)$$

Statistics and reliability metrics that are of interest to engineers and decision makers are:

1. Crack-length statistics evolution with no or multiple inspection intervals
2. Failure risk evolution with no or multiple inspection intervals
3. Reliability index evolution with no or multiple inspection intervals
4. Hazard failure rate evolution with no or multiple inspection intervals
5. Average hazard failure rates per inspection intervals
6. Number of failures (removals) per inspection intervals
7. PDF of the parent crack length population after each inspection
8. Equivalent Weibull failure (life) models
9. Posterior probability density function of life via Bayesian updating to incorporate failure data
10. Posterior PDF of crack size via Bayesian updating to include inspection data

An adequate risk/reliability-based condition assessment of an aircraft component with corrosion-fatigue damage needs to include the following analysis and modeling steps:

1. Stochastic modeling of operational loading condition and environmental conditions
2. Stochastic modeling of component loading, environmental surface conditions, and material and structural properties (This step may also include modeling of the component surface boundary conditions, such as contact-surface constraint effects, material property variations, manufacturing deviations from the baseline geometry, etc. These last aspects are not discussed here.)
3. Stochastic component stress/strain analysis to compute the stress/strain state in the component for given operating conditions that are time dependent
4. Stochastic modeling of component stress and strain histories at critical locations (This step includes the construction of principal-, component-, and equivalent-stress histories.)
5. Component reliability analysis or risk analysis for initial no-usage conditions (no deterioration due to progressive damage mechanisms) (This initial risk is due to stochastic variations in component design parameters, including manufacturing geometry deviations, material fabrication defects, assembly errors, etc. This time-invariant reliability problem is not discussed here.)
6. Reliability/risk-based condition assessment and life prediction (effect of maintenance is not included) based on stochastic damage models for both the crack-nucleation and crack-propagation stages
7. Reliability/risk-based maintenance analysis, including the effects of maintenance uncertainties on present failure risks, defined instantaneous failure risks, and future failure risks during the some time interval, typically selected to be the next inspection interval
8. Optimal-cost reliability/risk-based maintenance cost analysis, including the computation of overall maintenance costs vs. the component removal time based on reliability analysis results accounting for both scheduled maintenance events (SME) and unscheduled maintenance events (UME). (These postreliability analysis aspects are not discussed here.)

Two reliability analysis options are possible: (1) for a defined maintenance schedule and inspection techniques, the time-variant component risk/reliability (and unscheduled maintenance rates) can be computed; or (2) for a selected reliability level and selected inspection techniques, the required (scheduled) maintenance intervals can be determined.

#### 2.4.1.2 Equivalent “Physics-Based” Weibull Failure Models

For practical purposes, equivalent Weibull component life models are determined based on the computational results of the physics-based reliability analysis. These equivalent “physics-based” Weibull life models have the advantage that they can be easily compared with the existing Weibull models developed from field failure data.

To compute the two parameters of the Weibull distribution, a least-squares error minimization technique is used to fit the random sample life data [61]. Before performing the least-squares fitting, a transformation of the coordinates is performed so that the Weibull distribution points are shown along a straight line.

For the equivalent Weibull model, the instantaneous failure probability is computed by

$$P_f(t) = 1 - e^{-\left(\frac{t}{\theta}\right)^\beta} \quad (2.37)$$

where  $\beta$  and  $\theta$  are the shape and scale parameters of the Weibull distribution.

The Weibull hazard failure rate at time  $t$  is expressed by

$$h(t) = \frac{1}{\theta\beta\left(\frac{t}{\theta}\right)^{\beta-1}} \quad (2.38)$$

For a shape factor equal to unity, the Weibull distribution reduces to an exponential distribution that has a constant mean hazard failure rate.

#### 2.4.1.3 Maintenance Inspection Uncertainties

To maintain an acceptable reliability level for a mechanical component, two strategies are available: (1) to design the component for a long life so that there is no need for any maintenance during service life, or (2) to allow maintenance through inspections during the component service life, with repairs as required. It is known that the second strategy corresponds to a more cost-effective approach and can help to extend the component service life. The key aspect for implementing such a strategy is to be able to accurately predict and control the evolution of the component’s failure risk, including all maintenance activities and their associated uncertainties.

##### 2.4.1.3.1 Nondestructive Inspection (NDI) Techniques

Inspection routines are adopted to detect and remove cracks with sizes larger than a rejection limit, resulting in the improvement of reliability toward an acceptable level. For a particular NDI technique, several factors randomly affect the inspection results. For aircraft components, the most important influencing factors are those related to the precision of the type of NDI used and the operator skill.

The detection probability is defined as the number of times a crack of size  $a$  has been detected, divided by the number of trials, with each trial being performed by a different inspector or inspection team using the same inspection technique. Crack sizing errors include a significant statistical uncertainty. The literature includes some outstanding references on the subject [62–64].

The rejectable crack size  $a_R$  is also an important parameter for component maintenance. This limit size is specified based on safety and economic aspects. The rejectable crack size  $a_R$  (corresponding to repair or replacement) represents the limit for maintenance action on a detected crack of either accepting (leave) or rejecting (fix) it.

The rejectable crack size can be used to evaluate the following probabilities, where independence between additive sizing error and detection is assumed [62]:

1. The probability  $P_R(a)$  of rejecting a crack with size  $a$ , calculated as the product of the detection probability and the probability of sizing the detected crack larger than  $a_R$ :

$$P_R(a) = P_D(a)[1 - F_S(a_R - a)] \quad (2.39)$$

2. The probability  $P_A(a)$  of accepting a crack with size  $a$ , calculated as the product of the detection probability and the probability of sizing the detected crack smaller than  $a_R$ , added to nondetection probability:

$$P_A(a) = P_D(a)F_S(a_R - a) + [1 - P_D(a)] = 1 - P_R \quad (2.40)$$

In Equation 2.39 and Equation 2.40,  $F_S$  is the cumulative probability distribution of the statistical crack sizing errors. For a given crack size  $a$ , the sum of these two probabilities equals unity, since a crack must always be either rejected or accepted. For a particular case where  $a > a_R$ , the function  $P_R(a)$  is called the probability of correct rejection, while for  $a < a_R$ , the function  $P_A(a)$  is called the probability of correct acceptance. It should be observed that both  $P_R(a)$  and  $P_A(a)$  depend on the reliability of the inspection technique and on the specified rejection limit  $a_R$ . These definitions can be used to evaluate four additional parameters quantifying the global effect of an inspection procedure [62]:

1. The total probability of correctly rejecting a crack:

$$P_{CR} = \int_{a_R}^{-\infty} P_R(a)f_A(a)da \quad (2.41)$$

2. The total probability of incorrectly rejecting a crack:

$$P_{IR} = \int_0^{a_R} P_R(a)f_A(a)da \quad (2.42)$$

3. The total probability of correctly accepting a crack:

$$P_{CA} = \int_0^{a_R} P_A(a)f_A(a)da \quad (2.43)$$

4. The total probability of incorrectly accepting a crack:

$$P_{IA} = \int_{a_R}^{-\infty} P_A(a)f_A(a)da \quad (2.44)$$

Obviously, the sum of the above probabilities is unity,  $P_{CR} + P_{IR} + P_{CA} + P_{IA} = 1$ . The function  $f_A(a)$  is the probability density function of the crack-length population before inspection.

#### 2.4.1.3.2 Brief Description of NDE Inspection Types

Nondestructive evaluation (NDE) tests are used in maintenance to avoid loss of aircraft due to aging effects. They are also used in manufacturing to assure the quality of the components. Nearly every form of energy is used in nondestructive tests, including all wavelengths of the electromagnetic spectrum as well as mechanical vibration. These tests are divided into the following basic methods: visual, liquid penetrant, radiographic, ultrasonic, eddy-current, microwave, and infrared.

#### 2.4.1.3.3 Probability of Detection (POD) Curves

The capabilities of NDE techniques are typically quantified by plotting the probability of detection (POD) as a function of flaw size. Berens and Hovey [65] have shown that a lognormal formulation for the POD

curve provides a reasonable model for the observed behavior of NDE data. The lognormal POD can be expressed as

$$\text{POD}(x) = \int_0^x \frac{1}{\sigma u \sqrt{2\pi}} \exp\left[-\frac{(\ln(u) - \mu)^2}{2\sigma^2}\right] du \quad (2.45)$$

Studies have been conducted by various organizations to determine POD curves for various NDE techniques when applied to various selected aircraft components. Similar to the POD curves for crack detection, POD curves for thickness loss due to corrosion can be determined. Figure 2.3 shows the POD curve for detecting thickness loss using an eddy-current NDE inspection of an unpainted 737 aircraft splice joint. It can be noticed from that figure that the operator's skill can significantly affect the POD curve for a given eddy-current NDE technology.

#### 2.4.1.4 Probabilistic Modeling for Crack-Growth Process Including Multiple Inspections

Figure 2.35 shows the corrosion-fatigue-crack growth process with and without crack detection inspections. The plots show the time evolution of the PDF of crack length in an axonometric view and, using contour right-side plots, this corresponds to four NDE inspections at 4000 flight hours (FH) each. After each inspection, new cracks are born due to the repair or replacement of components with large cracks. The new crack populations are introduced by the removal of large cracks in the previous crack populations. An accurate stochastic modeling of the corrosion-fatigue-crack growth process, including inspections, has to include the presence of multiple statistical crack-size populations. A nonnormal probabilistic mixture model is used for the crack-size populations. For each crack-size population, a nonnormal probability distribution is assumed.

## 2.5 Illustrative Examples

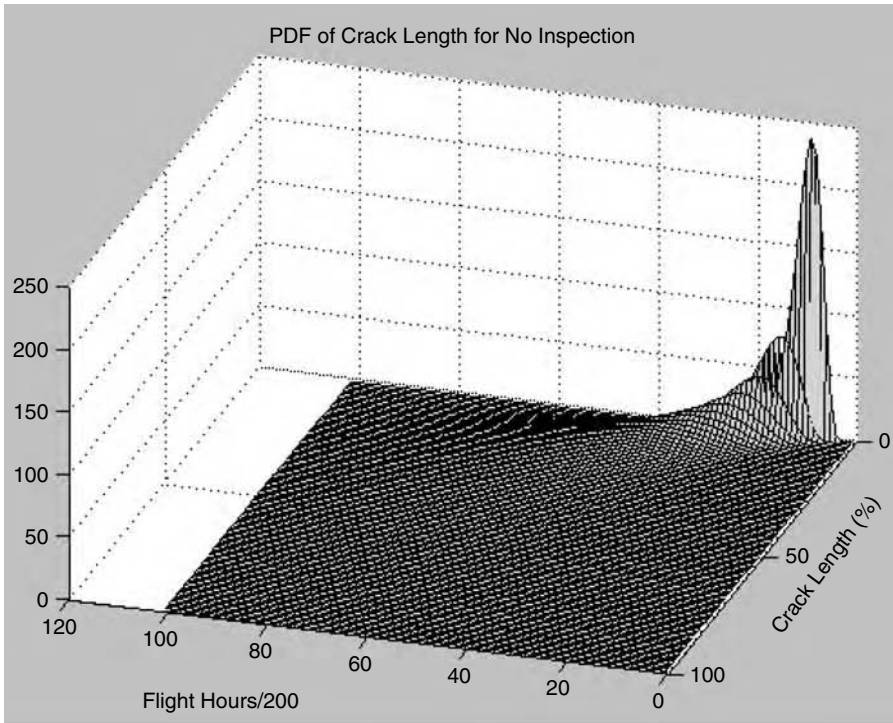
To keep the discussion simple, the illustrative examples presented in this section include only the effect of pitting corrosion on corrosion-fatigue life. The effects of other corrosion types, including intergranular corrosion in early stages or general thickness loss and pitting in later stages, are not considered. No cladding was assumed. Also, the multiple site damage (MSD) or widespread fatigue damage (WFD) that usually produces the ultimate lap-joint system failures is not included. Only the local failure in critical locations is considered. However, both MSD and WFD are real threats to aircraft structural integrity and therefore they must be considered when evaluating the risk of failure for an actual aircraft structure.

Several examples of probabilistic life prediction and risk-based maintenance analysis against corrosion-fatigue damage are shown in this section:

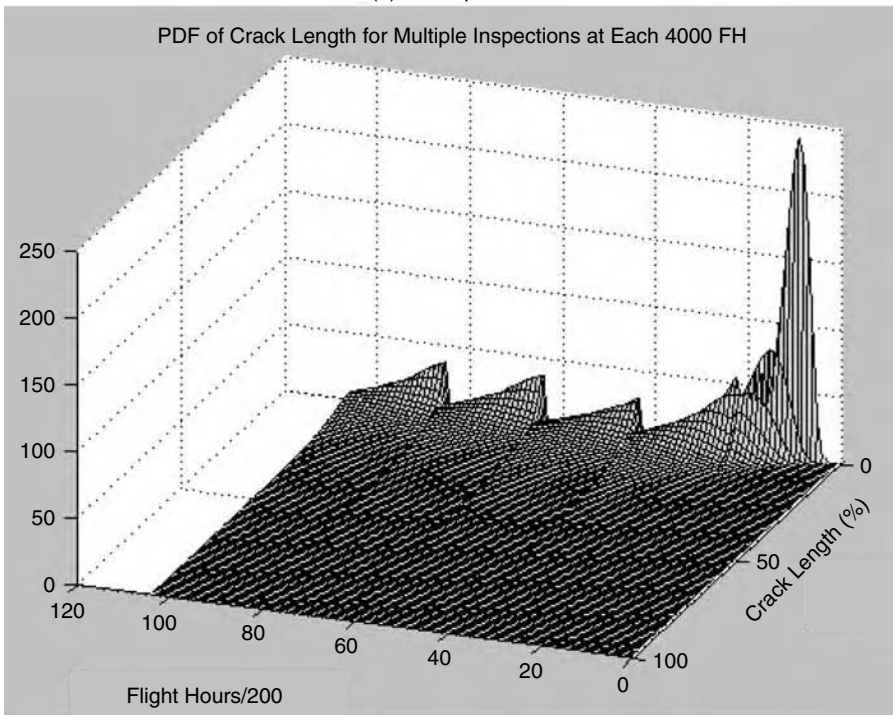
1. Probabilistic life predictions using the WCF, CCCF, and SCF models
2. Risk-based optimal cost analysis for a typical component
3. Risk-based maintenance analysis for a typical aircraft lap joint (Figure 2.1), including the effect of randomly rotating the aircraft to different airfields.

### 2.5.1 Probabilistic Life Prediction Using Different Corrosion-Fatigue Models

In the first example, the CCCF model (using a modified FASTRAN version) is used to compute the corrosion-fatigue life of thin 2024-T3 aluminum sheets [44]. The surface constituent particle size was statistically modeled using a lognormal probability distribution based on the results of Laz and Hillberry [44]. The simulated PDF of the particle size is plotted in Figure 2.36. Figure 2.37 shows the computed probabilistic fatigue life and corrosion-fatigue life assuming airport locations with different environmental severities. Figure 2.38 shows the fatigue life vs. the corrosion-fatigue life for all the airport locations



(a) No Inspection



(b) Multiple Inspections at Each 4000 FH

**FIGURE 2.35** Evolution of crack-length development: (a) no inspection; (b) multiple inspections at each 4000 flight hours.

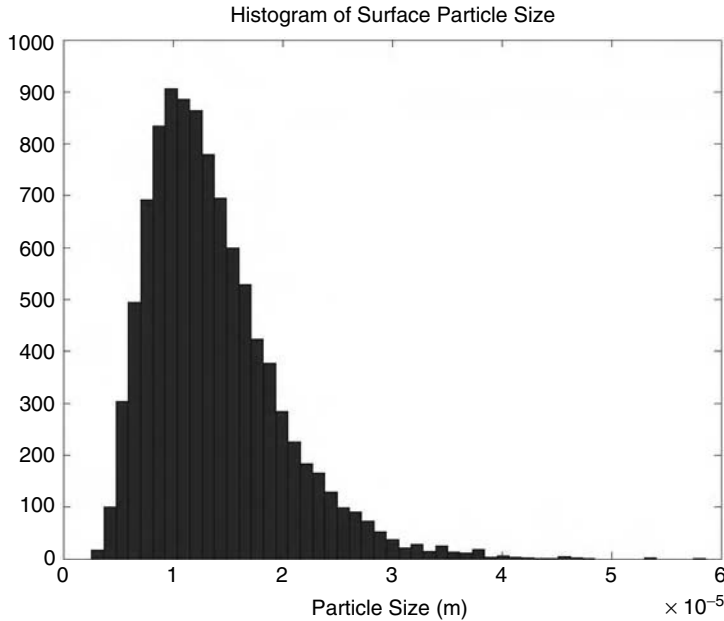


**FIGURE 2.36** Simulated PDF of the surface constituent particle size.

considered. It should be noted that the corrosion effects reduce the component fatigue life up to 10 to 15 times. Figure 2.39 shows the plot of the corrosion-fatigue life vs. the particle size. As shown, there is a relatively weak negative statistical correlation between corrosion-fatigue life and particle size. This indicates that particle size may not be a governing parameter for the corrosion-fatigue-life prediction (the random corrosion effects influence the life more significantly). This negative correlation is much stronger between pure fatigue life and particle size, as shown in Figure 2.40. Thus, for pure fatigue damage, the role of the particle size on the predicted life is significantly greater than for corrosion-fatigue damage.

The second example is a comparison between the WCF model and the SCF model for assessing the probabilistic corrosion-fatigue life of an aircraft component. The material considered is 2024-T3 aluminum. The constituent surface particle sizes, the threshold stress intensity range  $\Delta K_{th}$ , and the pit depth were assumed to be random variables for the probabilistic life prediction. The constituent particle size distribution is lognormal based on the data of Laz and Hillberry [43, 44], as shown in Figure 2.36. The stress-intensity-range threshold was modeled by a normal variable with mean of  $3 \text{ MPa}\sqrt{\text{m}}$  and a coefficient of variation of 0.10. The pit depth at any arbitrary time was modeled by a random scale factor between 1 and 21 applied to a mean  $I_{PO} = 0.5 \text{ C/sec}$ . The pit scale factor was introduced to simulate the different environmental severity conditions at various airport locations. The fatigue-crack-propagation models included in the WCF and SCF models are the truncated Paris-law crack-growth model and, respectively, the Forman crack-growth model. They are compared in Figure 2.41. From this figure it can be observed that for stress intensity ranges that are only slightly larger than the threshold of  $3 \text{ MPa}\sqrt{\text{m}}$ , the WCF model assumes much higher crack-growth rates than the SCF model. This behavior is expected to reduce the fatigue life computed with the WCF model.

Figure 2.42 and Figure 2.43 show the probabilistic corrosion-fatigue life computed for the two aircraft operating scenarios of two load cycles/day and ten load cycles/day, respectively, assuming that the mean duration of one cycle (flight) is 1.5 hours. The probabilistic life estimations indicate that the WCF model overestimates the statistical variability of the corrosion-fatigue life due to two modeling



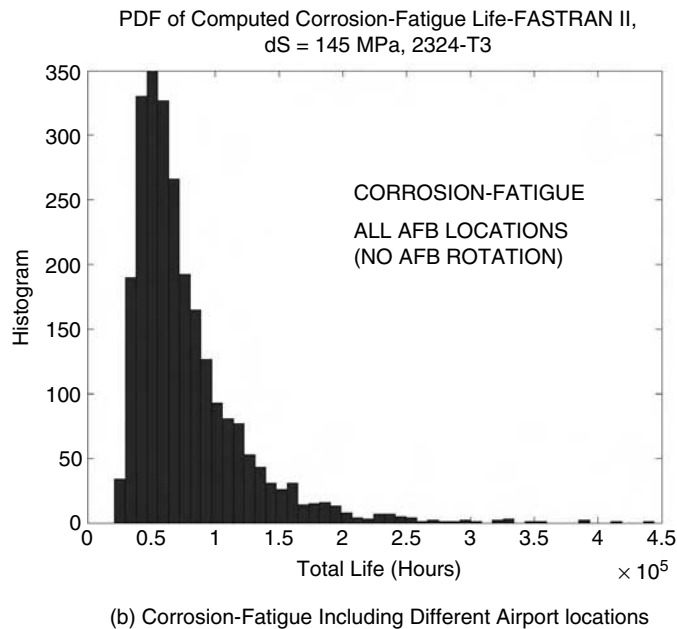
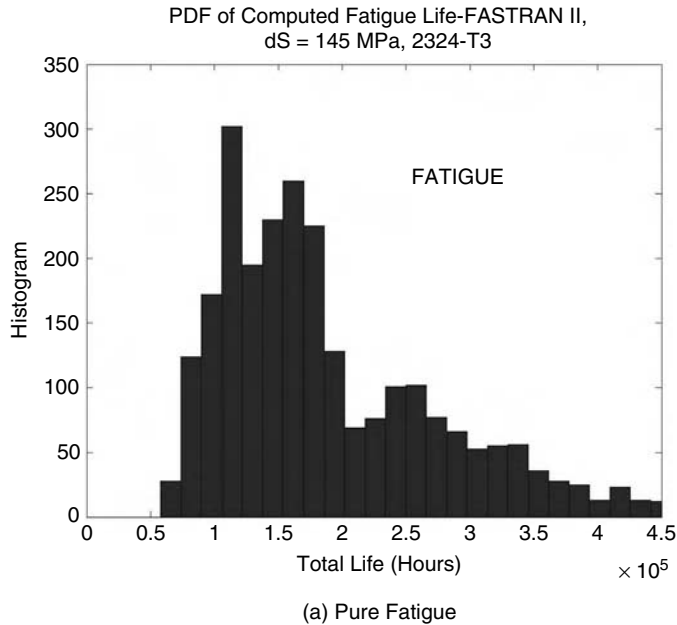


**FIGURE 2.37** Predicted-life PDF computed using CCCF model: (a) pure fatigue; (b) corrosion-fatigue including different airport locations.

effects: (1) it exaggerates the crack growth rates for  $\Delta K$  slightly above  $\Delta K_{th}$ , so that it produces a shorter life of some components; and (2) it does not include the effect of pitting on crack growth, so that it produces a longer life of some other components. The first effect, item 1, is stronger and more visible when the fatigue damage is greater, i.e., greater for ten cycles/day than for two cycles/day. The second effect, item two, is more visible when the *corrosion* damage is greater, i.e., greater for two cycles/day than for ten cycles/day.

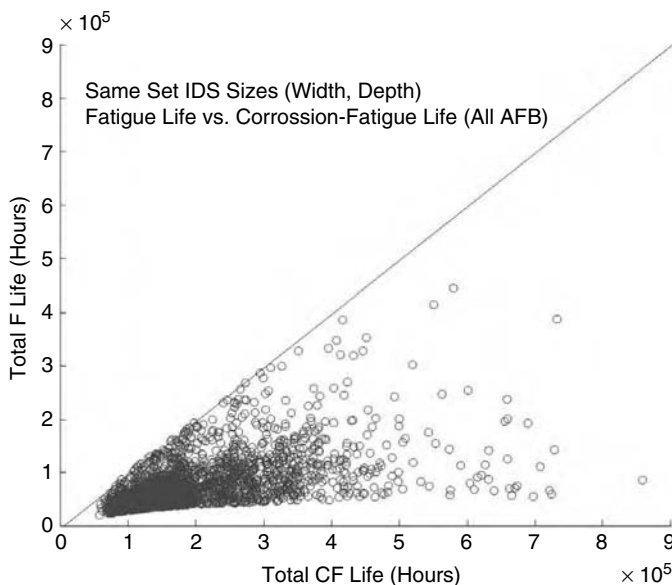


FIGURE 2.38 Fatigue life vs. corrosion-fatigue life.

### 2.5.2 Risk-Based Maintenance Analysis of a Lap Joint Subjected to Pitting Corrosion and Fatigue

The reliability analysis was performed for the aircraft lap joint shown in Figure 2.1. The major loading in the lap joint comes from the pressurization in the aircraft. Figure 2.44 shows the load transfer with the aircraft lap-joint components. The input random variables included in the reliability analysis are shown in Table 2.9.

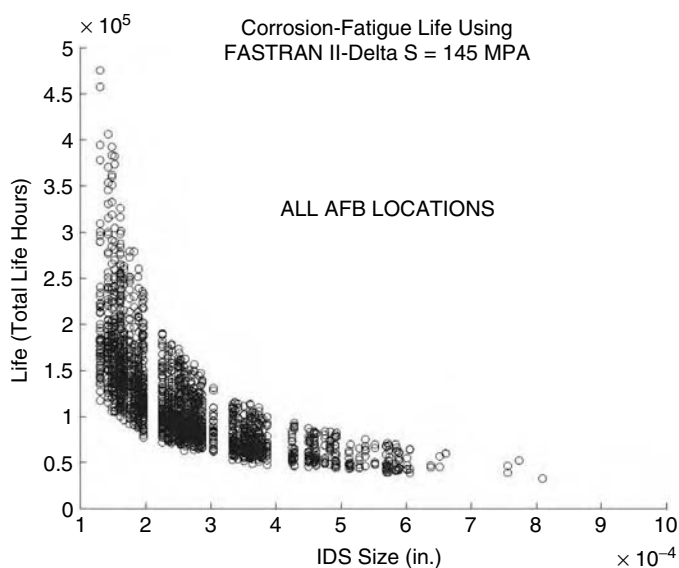


FIGURE 2.39 Corrosion-fatigue life vs. surface particle size.

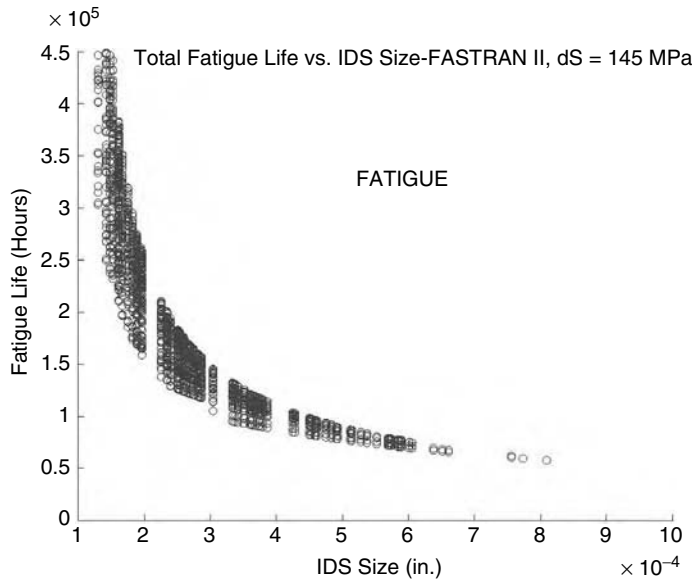


FIGURE 2.40 Pure fatigue life vs. surface particle size.

Figure 2.45 illustrates the stochastic history of pressure loading and environmental conditions of the aircraft. The elementary constituent of the stochastic history of the lap joint is the block that includes a single flight and a single stay on ground. It was assumed that the random pressure load is described by a single cycle for each flight. The environmental severity condition that drives corrosion was considered to randomly vary with the airport location. However, for the same location it was assumed that the environmental condition is a time-invariant quantity.

Figure 2.46 illustrates the simulated PDF of the pit growth volumetric rate based on the assumptions shown in Table 2.9. The surface particles were assumed to be the initiators of the pits and microcracks.

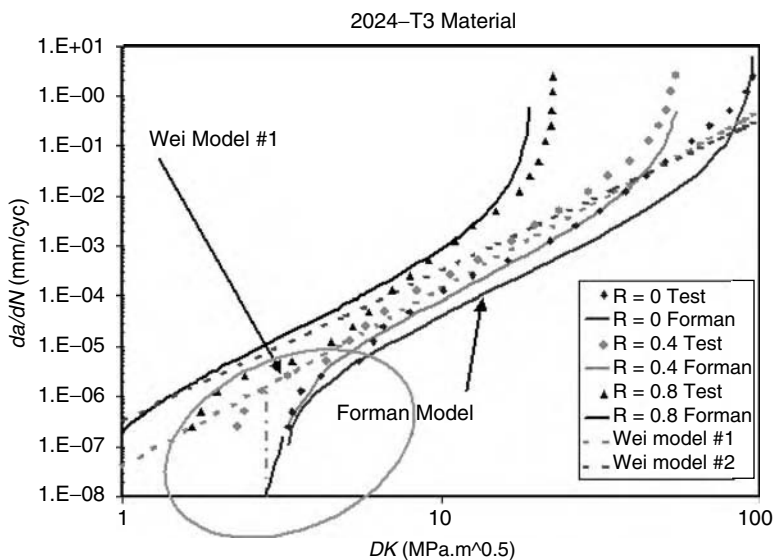


FIGURE 2.41 Comparison of fatigue-cracking models.

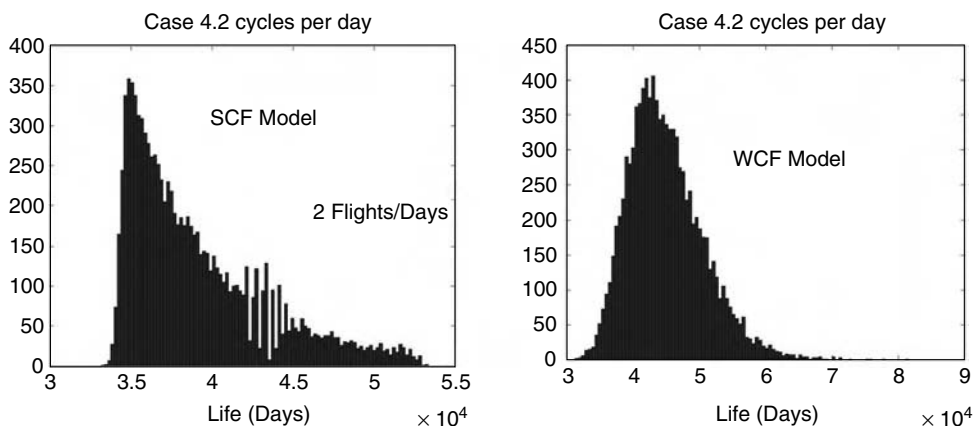


FIGURE 2.42 PDF of predicted life for the SCF and WCF models for two cycles/day.

From Figure 2.46, it should be noted that the environmental severity condition characterized by pit growth rate has a highly skewed probability distribution. Figure 2.46 indicates that the environmental severity conditions expressed by the pit growth rates are mild for most of the airport locations and severe for only a few locations. A truncated exponential distribution was used to fit the trend of the measured corrosion rate data at different airport locations [8, 60]. These large differences in values indicate that the crevice pits can grow up to ten times faster in some airport locations than in others.

Four flight scenarios were investigated for reliability analysis of the aircraft lap joint. The four scenarios were obtained by combining two aircraft operating scenarios with two flying scenarios. The two operating scenarios were (a) one flight/day and (b) three flights/day, and each of these was applied in two flying scenarios: (1) each aircraft flies from an airport location to the same airport location, without random rotation of the airport location; and (2) each aircraft flies randomly from an airport location to any other airport location, with random rotation of the airport location. In the last flying scenario, it was assumed that all airport locations are equally probable and that each individual aircraft can visit all airport locations. This is the ideal situation for reducing scatter of the corrosion effect, assuming a uniform distribution of the aircraft fleet across the airport location set.

To compute the probabilistic corrosion-fatigue life of the lap joint, both the crack-initiation and the crack-propagation stages were included. The stochastic strain-life curve and the stochastic Forman

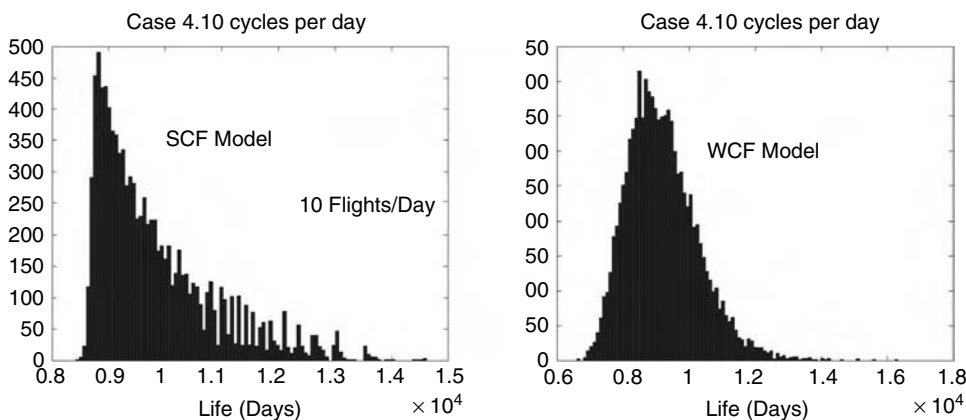


FIGURE 2.43 PDF of predicted life for the SCF and WCF models for ten cycles/day.

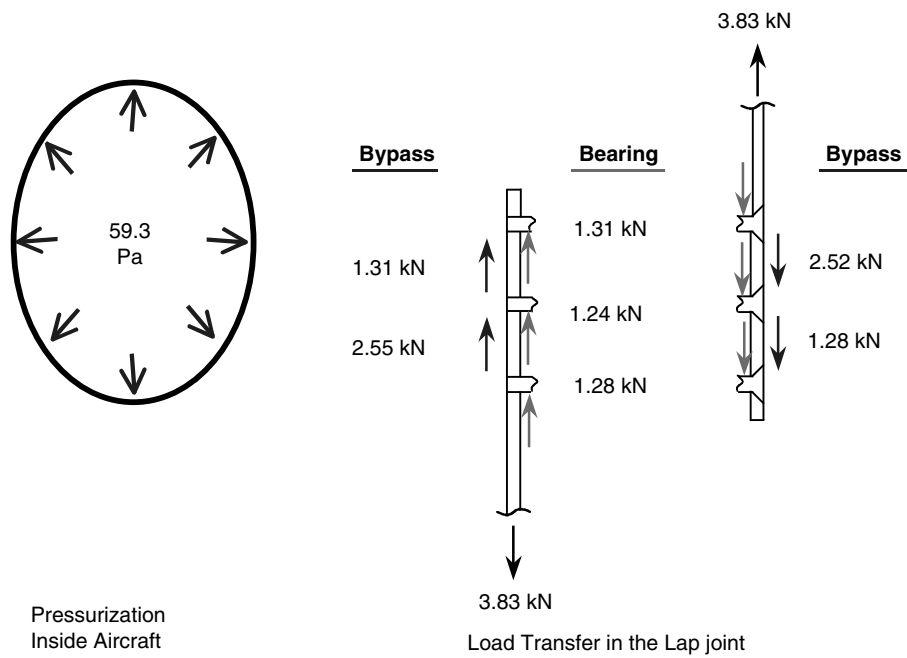


FIGURE 2.44 Pressure load transfer in the lap-joint components — fasteners and splices.

TABLE 2.9 Input Random Variables Included in the Reliability Analysis

Random Parameter	Mean	Standard Deviation	Probability Distribution
Uniform pressure inside aircraft, $p$ (Pa)	59.3	2.97	normal
Single flight duration, $d$ (h)	2.8	0.50	lognormal
Surface particle size, $a_0$ ( $\mu\text{m}$ )	13.66	6.02	Weibull (Figure 2.36)
Strain life curve exponents, $b$ and $c$	-0.114, -0.927	0.00114, 0.00927	normal, normal
Strain life curve parameters, $\sigma'_f$ (MPa) and $\epsilon'_f$	1044	20.88	normal
	1.765	0.0353	normal
Stress-intensity-range threshold, $\Delta K_{th}$ (MPa $\sqrt{\text{m}}$ )	3.00	0.15	normal
Toughness, $K_{Ic}$ (MPa $\sqrt{\text{m}}$ )	97.7	2.93	normal
Pit-growth parameter, $I_{PO}$ , in Wei model variation due to different environmental conditions for different airport locations (C/sec)	14.08	22.26	truncated exponential 0.1–100 C/sec(Figure 2.46)

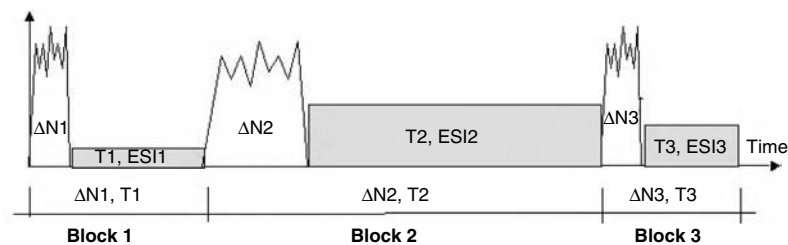


FIGURE 2.45 Stochastic history of loading and environmental conditions.

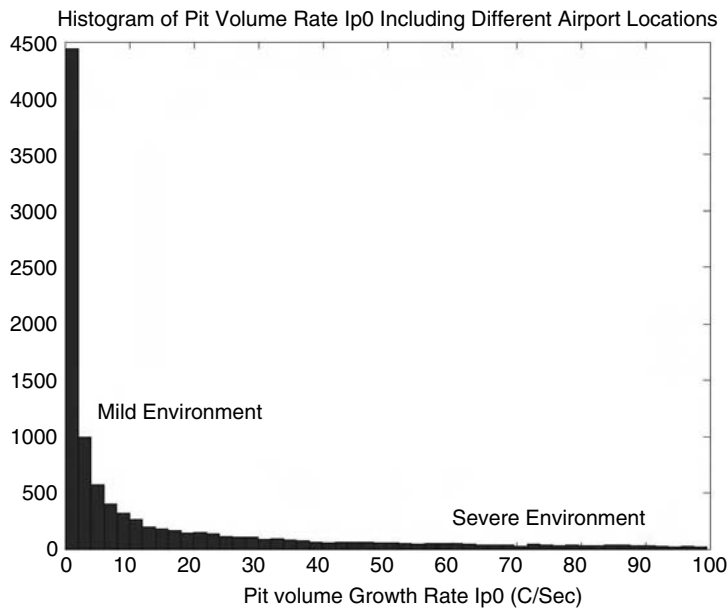


FIGURE 2.46 Simulated PDF of the pit-growth volumetric rate.

crack-propagation models were developed from the deterministic models based on the assumption that their parameters are random quantities, as shown in Table 2.9. To include the effect of pitting corrosion on the lap-joint fatigue life, a SCF model was employed.

Figure 2.47 and Figure 2.48 show the simulated pit-depth-growth curves for all airport locations assuming no rotation of airport locations. These pit curves were computed using the Wei pitting model

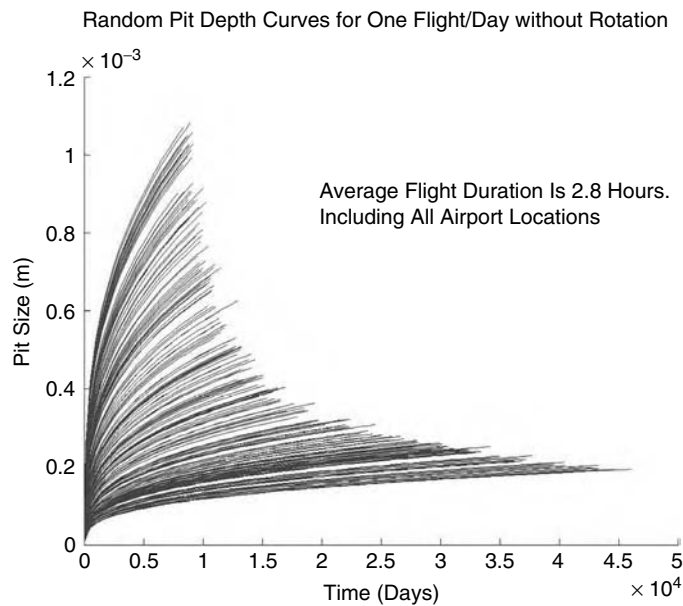
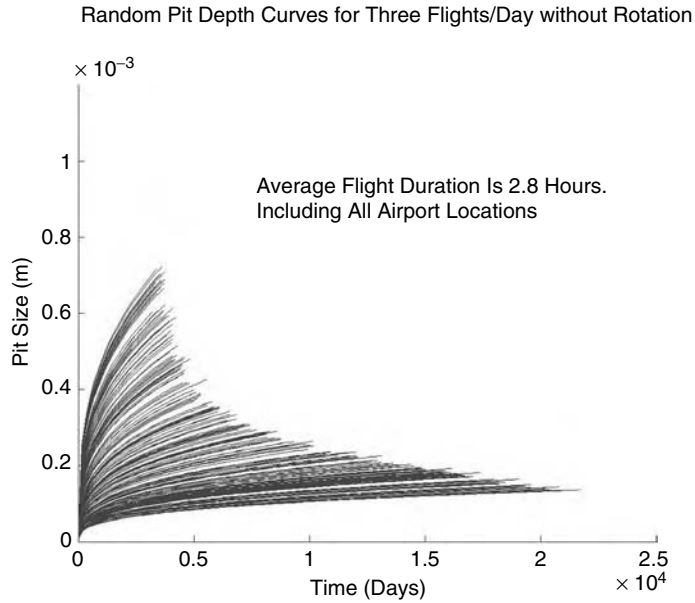
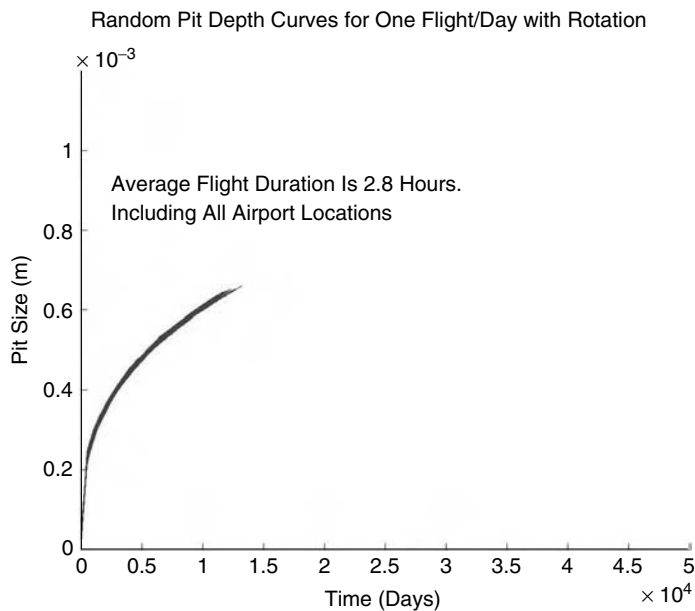


FIGURE 2.47 Simulated pit-growth curves for one flight/day without airport rotation.



**FIGURE 2.48** Simulated pit-growth curves for three flights/day without airport rotation.

(Equation 2.20). The pit-growth curves shown in the figures stop at the failure times. Figure 2.47 is for the one-flight/day scenario and Figure 2.48 is for the three-flights/day scenario, respectively. Figure 2.49 and Figure 2.50 show the pit-growth curves for the same two scenarios with a random rotation of aircraft location. It was assumed that each aircraft has an equal probability to fly to any airport location. This means there is a high probability that each airport will be visited about the same number of times by each aircraft. Therefore, for the scenario with the airport rotation, the scatter of the pit growth drops



**FIGURE 2.49** Simulated pit-growth curves for one flight/day with airport rotation.

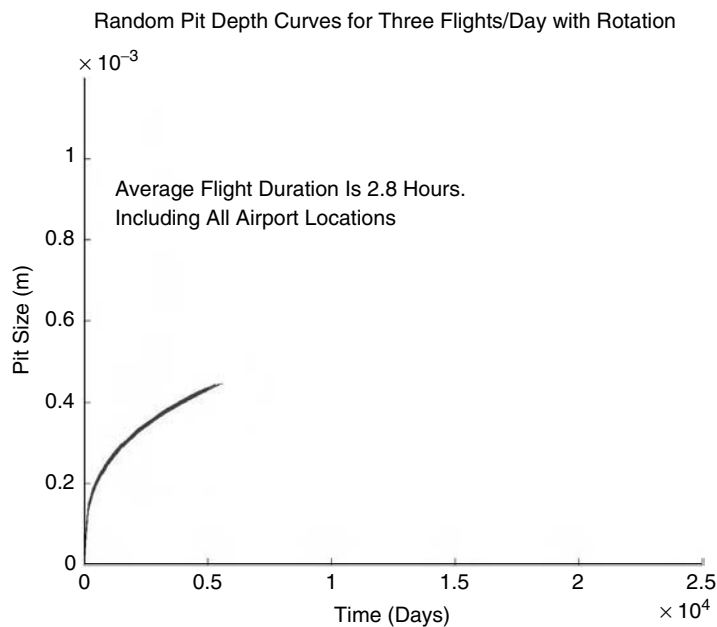


FIGURE 2.50 Simulated pit-growth curves for three flights/day with airport rotation.

significantly, converging in the limit to the (deterministic) mean pit growth for an infinite number of flights per aircraft.

The simulated crack-length curves are plotted in Figure 2.51 through Figure 2.54 for the four investigated scenarios. The computed histograms (with different incremental steps) of predicted corrosion-fatigue life of the four cases are shown in Figure 2.55. It should be noted that the mean

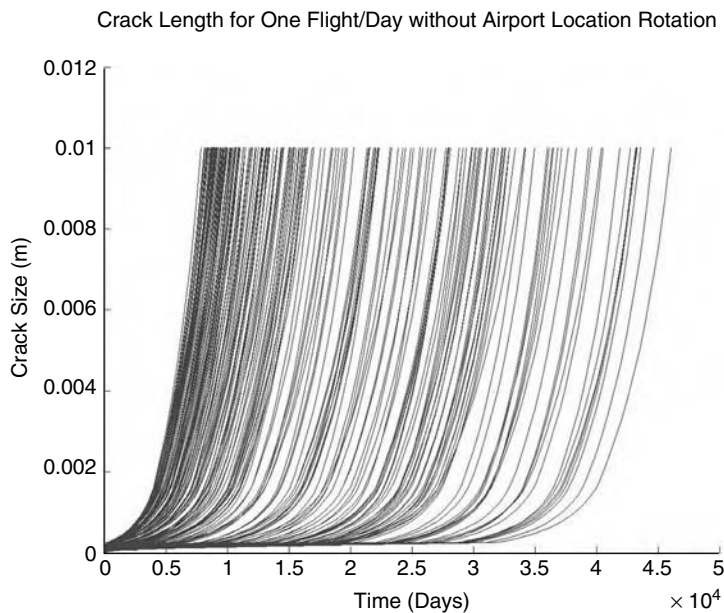


FIGURE 2.51 Simulated crack-size curves for one flight/day without airport rotation.



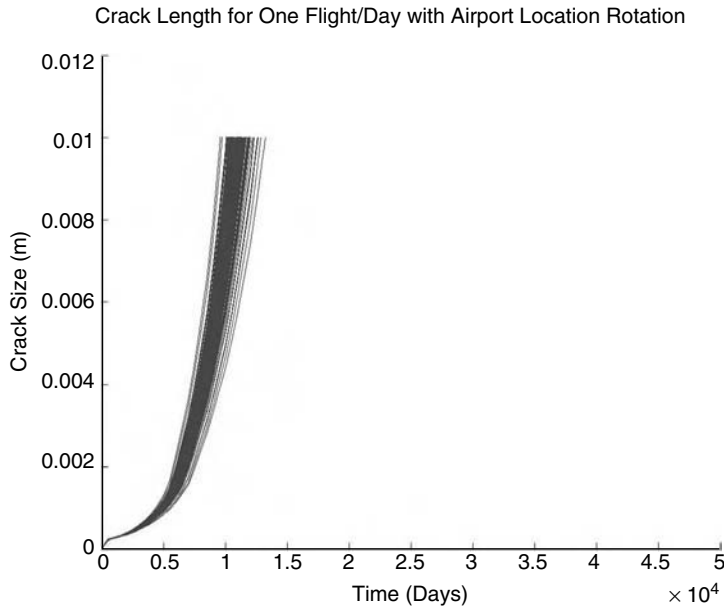


FIGURE 2.52 Simulated crack-size curves for one flight/day with airport rotation.

corrosion-fatigue life is about double for the one-flight/day scenario vs. the three-flights/day scenario. Figure 2.56 and Figure 2.57 illustrate the probability density of the time until a 5.0-mm crack length is reached for the one-flight/day scenario, without airport rotation and with airport rotation, respectively. The computed probability densities (PDF) are compared with analytical densities, namely, the lognormal and normal probability densities. It should be noted that for the case without rotation, the computed skewed density is far from the lognormal density, while for the case with rotation, the

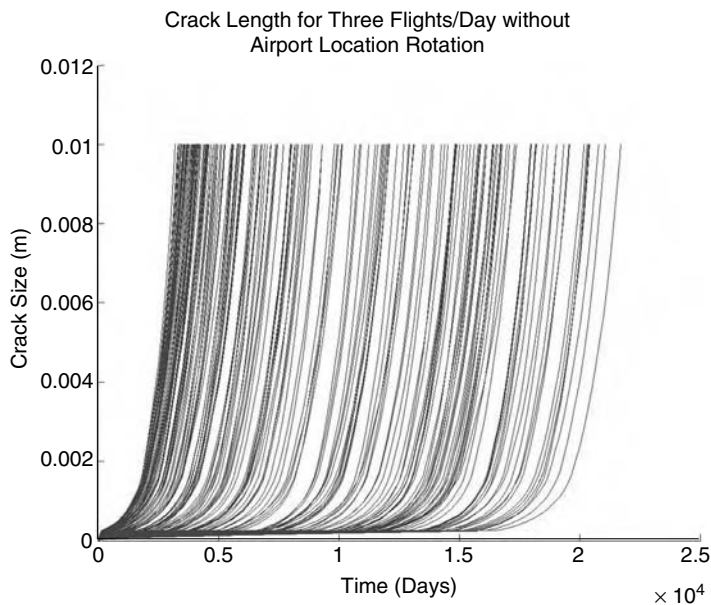


FIGURE 2.53 Simulated crack-size curves for three flights/day without airport rotation.

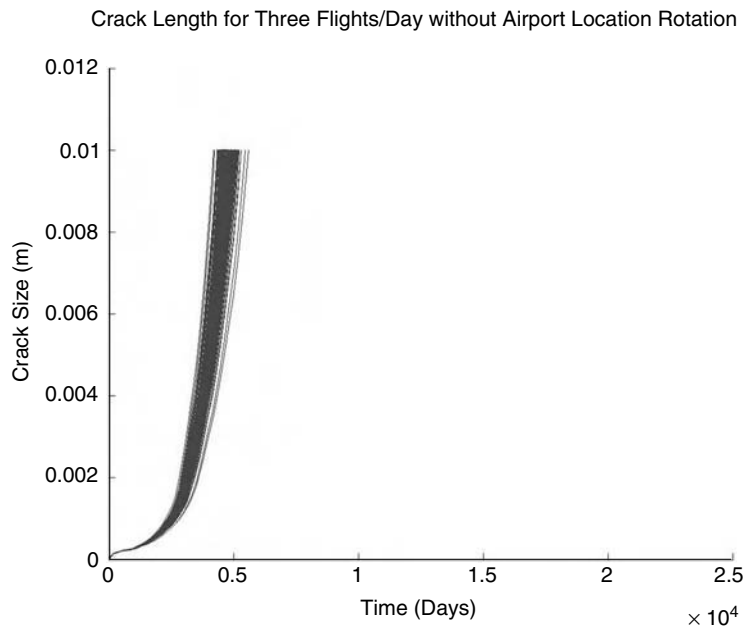


FIGURE 2.54 Simulated crack-size curves for three flights/day with airport rotation.

computed density is very close to normal density. For the former case, without rotation, the heavy right tail of the PDF shape is due to the fact that many airport locations have milder environmental-severity conditions, as indicated in Figure 2.46. For the latter case, the scatter of corrosion effects is reduced and the predicted-life probability density converges to the normal distribution in accordance with the central limit theorem.

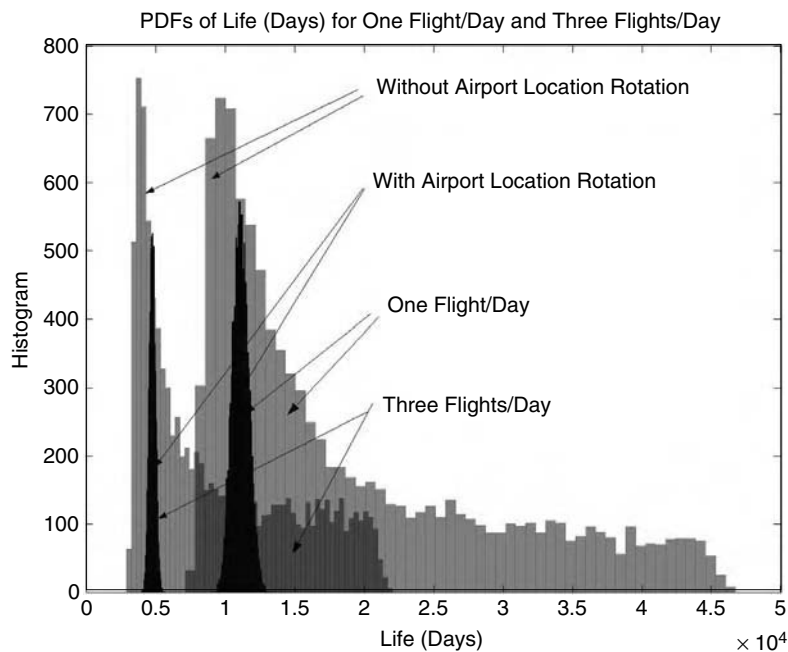


FIGURE 2.55 Corrosion-fatigue histograms (different steps) for the investigated scenarios.

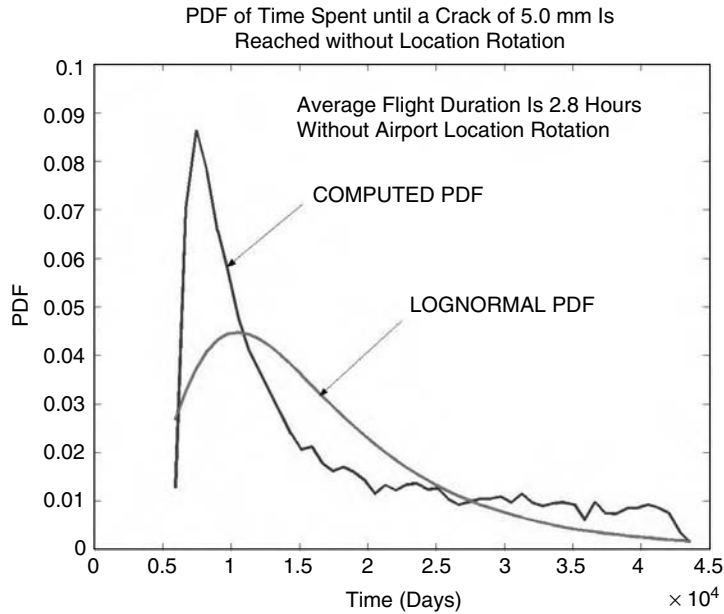


FIGURE 2.56 PDF of corrosion-fatigue life for one flight/day without airport rotation.

To consider the effect of maintenance, the uncertainties associated with the probability of crack detection for different standard NDE inspections were included using the appropriate POD curves. The eddy-current NDE technique with different operator skill classes was considered. The eddy-current POD curve was assumed to correspond to a lognormal distribution with a logarithmic mean and logarithmic standard deviation of (a)  $-4.73$  and  $0.98$  for the best operator, (b)  $-3.75$  and  $0.70$  for the average operator, and (c)  $-2.73$  and  $0.45$  for the worst operator. No crack-sizing error was included in addition to operator

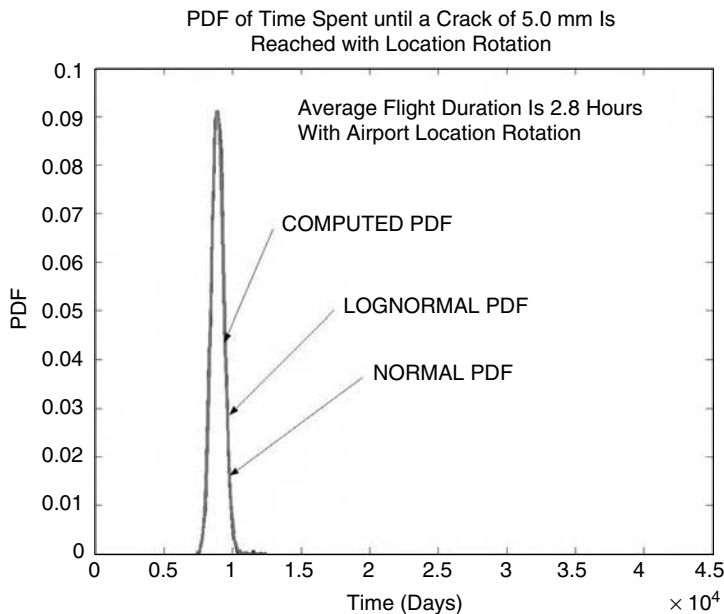
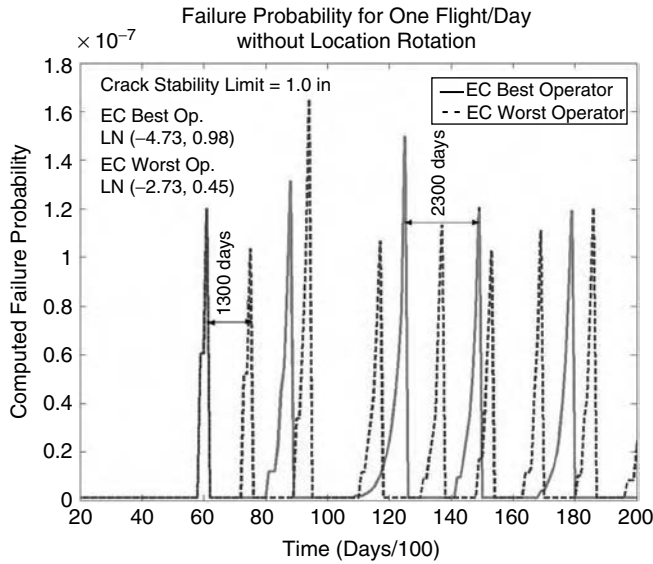


FIGURE 2.57 PDF of corrosion-fatigue life for one flight/day with airport rotation.



**FIGURE 2.58** Risk-based inspection times for one flight/day, without rotation, for a given target risk of  $2 \times 10^{-7}$ : effect of the operator's skill.

skill variation. At each inspection time, the statistical crack population was filtered through the POD curve. Based on the computed probabilities of acceptance or rejection, each crack was randomly accepted or removed by replacing the cracked component. The repair effects were not considered for this illustrative example.

Figure 2.58 through Figure 2.61 indicate the inspection schedule required over 20,000 days (about 60 years) for maintaining the corrosion-fatigue damage risk under a reliability target defined by an upper-bound failure probability of  $2 \times 10^{-7}$ . Figure 2.58 and Figure 2.59 show the results computed for the

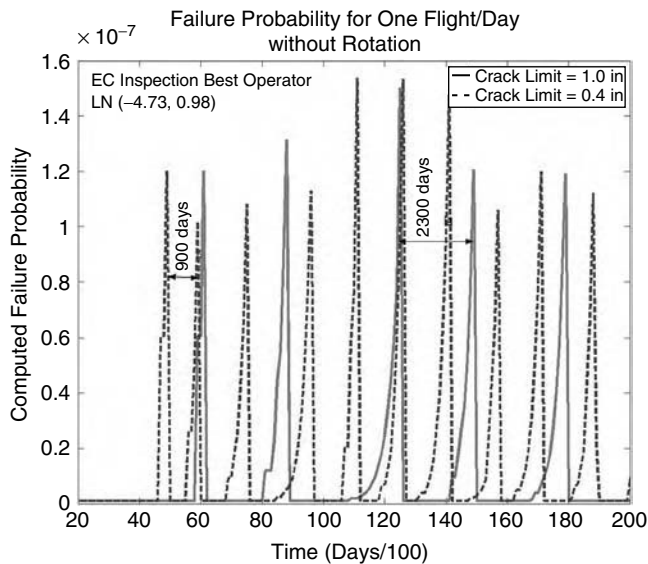


**FIGURE 2.59** Risk-based inspection times for one flight/day, without rotation, for a given target risk of  $2 \times 10^{-7}$ : effect of crack-limit criterion.

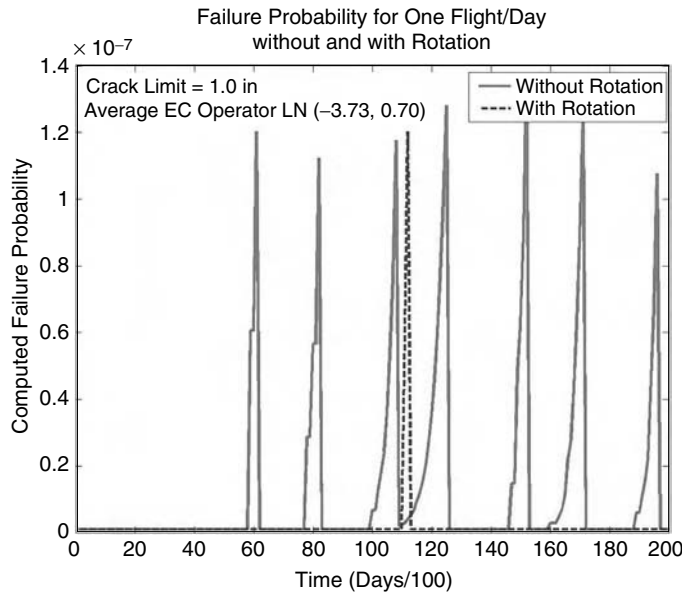


FIGURE 2.60 Risk-based inspection times for one flight/day without and with rotation.

one-flight/day scenario without airport rotation. Figure 2.58 compares results for different NDE operator skills (best operator vs. worst operator), while Figure 2.59 compares results for different failure limit criteria (crack limit of 1.0 in. vs. crack limit of 0.40 in.). It should be noted that the minimum inspection interval drops from 2300 days (6450 flight hours [FH]) to 1300 days (3640 FH) due to the NDE operator's skill, and from 2300 days (6540 FH) to 900 days (2520 FH) due to the crack-limit criterion considered.

Figure 2.60 and Figure 2.61 compare the required inspection schedules for the two cases, without and with airport rotation, including both the one-flight/day scenario and three-flights/day scenario, assuming the same reliability target, an average operator's skill, and a 1.0-in. crack-limit failure criterion.

Without the airport rotation, the required inspection intervals in real time are about two or three times longer for the one-flight/day scenario than for the three-flights/day scenario. However, if the inspection intervals are measured in effective FH instead of days, this observation is not true. The minimum inspection intervals are 1600 days (4480 FH) for the one-flight/day scenario and 600 days (5040 FH) for the three-flights/day scenario. The increase of the inspection intervals expressed in flight hours from the one-flight/day scenario to three-flights/day scenario indicates that the effects of corrosion are more severe for one-flight/day when the time spent by an aircraft on ground is longer.

With the airport rotation, the minimum inspection intervals are much longer than those computed without airport location rotation. The minimum inspection intervals are 11,200 days (31,360 FH) for the one-flight/day scenario and 4,600 days (38,640 FH) for the three-flights/day scenario. This large benefit effect of the random rotation of airport locations is mainly a result of the large reduction in the statistical scatter of corrosion effects as a result of the central limit theorem.

The exclusive use of *instantaneous* failure probabilities to characterize aircraft reliability is insufficient for setting the risk-based maintenance strategy. This is because, from a risk-based-maintenance point of view, one is interested in the aircraft's reliability over a period of time, not only at the critical instantaneous times. To illustrate the point, we can review the results in Figure 2.60. For the inspection schedule shown, the maximum risk is almost constant with a value of  $1.2 \times 10^{-7}$ . The maximum risk is bounded to  $1.2 \times 10^{-7}$  independent of the aircraft operating scenarios, without or with airport location rotation. However, the number of inspections is different, so that the number of times when the maximum failure

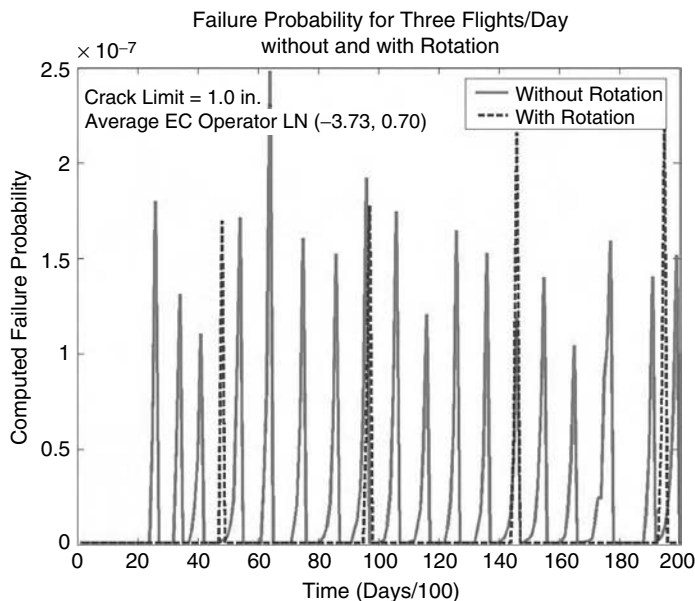


FIGURE 2.61 Risk-based inspection times for three flights/day without and with rotation.

risk is reached is different for the two operating scenarios. Thus, if the average hazard failure rates over a long period are computed, they are very different. For the results in Figure 2.60, if the average hazard failure rates are computed over the 20,000-day (about 60 years) period, these are  $1.04 \times 10^{-10}$  events/day and  $7.97 \times 10^{-12}$  for the cases without airport rotation and with rotation, respectively. This means that, in the long run, the average number of aircrafts having failures is about ten times higher for the case without airport rotation than the case with rotation, although the maximum instant risk is the same for the two cases. Thus, to maintain the same aircraft reliability for the two cases, it would be necessary to define different target instantaneous risks for the two cases, about an order of magnitude lower for the case without rotation, so that finally we end up with the same average hazard rates over the period of interest. Failure probabilities are good reliability metrics for time-invariant or instantaneous reliability problems, while average hazard failure rates are good reliability metrics for time-variant problems such as the risk-based maintenance problem.

The above discussion also indicates that the age distribution of the aircraft fleet plays an important role on the aircraft fleet reliability over a given period of time. Figure 2.60 shows that for different time periods, for example 7000 days (about 20 years), depending on the aircraft fleet age distribution and its variation in the selected periods, the individual aircraft risks can vary wildly. As a consequence of this, the average fleet hazard failure rates can vary about two orders of magnitude for different time periods and different fleet age distributions.

## 2.6 Concluding Remarks

This chapter presents an overview of the key engineering issues that are important for performing a reliability analysis of aircraft structure joints under corrosion-fatigue damage. The chapter focused on probabilistic modeling of stochastic cumulative damage due to corrosion fatigue. Different corrosion-fatigue models are reviewed in relative detail, and their results are compared. One model was then applied to the probabilistic life prediction and risk-based maintenance analysis of an aircraft fuselage lap joint. For this illustrative example, the loading stochasticity was limited to the small

variability of aircraft pressurization. Variability-related structural modeling and analysis, as well as the stochasticity of the loading and load transfer through the structure to the individual fasteners, were ignored in order to keep the example simple.

Computational risk-based maintenance using physics-based stochastic damage models, carefully calibrated with the appropriate empirical data, provides a quantitative process for simultaneously maximizing aircraft availability and reducing maintenance costs while maintaining safety and airworthiness. The physics-based stochastic modeling tools and computational reliability methods are sufficiently mature to approach the difficult problem of aircraft fleet maintenance from a probabilistic risk-based perspective.

An important practical aspect, not discussed herein, is that probabilistic models need to be implemented so that they can incorporate new information and statistical data coming from lab tests, depot maintenance, and service history. Refinement of the probabilistic models in this way will make risk predictions sharper by reducing their statistical confidence intervals (reducing uncertainties due to modeling and lack of data).

## References

1. U.S. Air Force, Aircraft Structural Integrity, AFD 63-10, US Air Force Publications Distribution Center, Baltimore, 1997. (also [www.e-publishing.af.mil](http://www.e-publishing.af.mil))
2. U.S. Air Force, Aircraft Structural Integrity Program, AFI 63-1001, U.S. Air Force Publications Distribution Center, Baltimore, 2002. (also [www.e-publishing.af.mil](http://www.e-publishing.af.mil))
3. U.S. Air Force, *General Guidelines for Aircraft Structural Integrity Program*, MIL-STD-1530B, Aeronautical Systems Center, Wright-Patterson Air Force Base, OH, 2004. (also [www.dodssp.daps.mil](http://www.dodssp.daps.mil))
4. Damage Tolerance and Fatigue Evaluation of Structure, Federal Aviation Regulation, Part 25, Airworthiness Standards: Transport Category Airplanes, Sec. 25.571.
5. Damage Tolerance and Fatigue Evaluation of Structure, Joint Aviation Requirements, Part 25 Large Aeroplanes, Section 25.571. (available at <http://www.jaa.nl>)
6. Protection of Structure, Federal Aviation Regulation, Part 25, Airworthiness Standards: Transport Category Airplanes, Sec. 25.609.
7. Protection of Structure, Joint Aviation Requirement, Part 25, Large Aeroplanes, Section 25. 609. (available at <http://www.jaa.nl>)
8. Brooks, C.L., ECLIPSE-Environmental & Cyclic Life Interaction Prediction Software, Aeromat 1999, Dayton, OH. (available at [http://www.apesolutions.com/frm\\_link.htm](http://www.apesolutions.com/frm_link.htm))
9. Gallagher, J.P., Giessler, F.J., Berens, A.P., and Engle, R.M. Jr., *USAF Damage Tolerant Design Handbook: Guidelines for the Analysis and Design of Damage Tolerant Aircraft Structure*, AFWAL-TR-82-3073 (ADA153161), Defense Technical Information Center, Ft. Belvoir, VA, May 1984, p. 1.4.3.
10. Rummel, W.D. and Matzkanin, G.A., *Nondestructive Evaluation (NDE) Capabilities Databook*, ADA286978, 3rd Ed., Defense Technical Information Center, Ft. Belvoir, VA, 1997.
11. Yee, B.G.W., Chang, F.H., Couchman, J.C., Lemon, G.H., and Packman, P.F., *Assessment of NDE Reliability Data*, NASA-CR-134991 (ADA321309), Defense Technical Information Center, Ft. Belvoir, VA, 1974.
12. Matzkanin, G.A. and Yolken, H.T., *A Technology Assessment of Probability of Detection (POD) for Nondestructive Evaluation (NDE)*, NTIAC-TA-00-01 (ADA398282), 2001.
13. Hoppe, W., Pierce, J., and Scott, O., *Automated Corrosion Detection Program*, AFRL-ML-WP-TR-2001-4162 (ADA406600), Defense Technical Information Center, Ft. Belvoir, VA, 2001.
14. U.S. Dept. of Defense, Joint Service Specification Guide: Aircraft Structures, JSSG-2006, Appendix A.3.1.2, Requirement Guidance, Dept. of Defense, Washington, D.C., 1998. (also [www.dodssp.daps.mil](http://www.dodssp.daps.mil))
15. Lincoln, J.W., Risk assessments of aging aircraft, in *Proc. 1st Joint DoD/FAA/NASA Conf. on Aging Aircraft*, Vol. 1, Air Force Wright Aeronautics Laboratory, Wright-Patterson Air Force Base, OH, 1997, pp. 141–162.

16. Berens, A.P., Hovey, P.W., and Skinn, D.A., *Risk Analysis for Aging Aircraft Fleets*, Vol. 1, *Analysis*, WL-TR-91-3066 (ADA252000), Defense Technical Information Center, Ft. Belvoir, VA, 1991.
17. Hovey, P.W., Berens, A.P., and Loomis, J.S., *Update of the Probability of Fracture (PROF) Computer Program for Aging Aircraft Risk Analysis*, Vol. 1, *Modifications and User's Guide*, AFRL-VA-WP-TR-1999-3030 (ADA363010), Defense Technical Information Center, Ft. Belvoir, VA, 1998.
18. Broeck, David, Residual strength of metal structures, in *ASM Handbook*, Vol. 19, *Fatigue and Fracture*, Lampman, S.R., Ed., ASM International, Materials Park, OH, 1996, pp. 427–433.
19. U.S. Air Force, *Metallic Materials and Elements for Aerospace Vehicle Structures*, Mil-Hdbk-5H, Defense Area Printing Service, Philadelphia, 2001. (also [www.dodssp.daps.mil](http://www.dodssp.daps.mil))
20. Skinn, D.A., Gallagher, J.P., Berens, A.P., Huber, P.D., and Smith, J., *Damage Tolerant Design Handbook: a Compilation of Fracture and Crack Growth Data for High Strength Alloys*, Vol. 3, WL-TR-94-4054 (ADA311690), Defense Technical Information Center, Ft. Belvoir, VA, 1994.
21. Mishnaevsky, L.L., Jr. and Schmauder, S., Damage evolution and heterogeneity of materials: model based on fuzzy set theory, *Eng. Fracture Mechanics*, 57(6), 625–636, 1997.
22. Moller, B., Graf, W., and Beer, M., Safety assessment of structures in view of fuzzy randomness, *Comput. Struct.*, 81, 1567–1582, 2003.
23. Mitchell, M.R., Fundamentals of modern fatigue analysis for design, in *ASM Handbook*, Vol. 19, *Fatigue and Fracture*, Lampman, S.R., Ed., ASM International, Materials Park, OH, 1996, pp. 227–249.
24. Socie, D.F. and Morrow, JoDean, Review of contemporary approaches to fatigue damage analysis, *Risk and Failure Analysis for Improved Performance and Reliability*, Burke, J.J. and Weiss, V., Eds., Plenum Publishing Corp., New York, 1980, pp. 141–194.
25. Dowling, N.E., Estimating fatigue life, in *ASM Handbook*, Vol. 19, *Fatigue and Fracture*, Lampman, S.R., Ed., ASM International, Materials Park, OH, 1996, pp. 250–262.
26. Socie, D.F., Dowling, N.E., and Kurath, P., Fatigue life estimation of notched members, in *Fracture Mechanics: Fifteenth Symposium*, ASTM STP 833, Sanford, R.J., Ed., ASTM, Philadelphia, 1984, pp. 284–299.
27. Bucci, R.J., Nordmark, G., and Starke, E.A., Jr., Selecting aluminum alloys to resist failure by fracture mechanisms, in *ASM Handbook*, Vol. 19, *Fatigue and Fracture*, Lampman, S.R., Ed., ASM International, Materials Park, OH, 1996, pp. 771–812.
28. Peterson, R.E., *Stress Concentration Factors*, John Wiley & Sons, New York, 1974.
29. Bannantine, J.A., Comer, J.J., and Handrock, *Fundamentals of Metal Fatigue Analysis*, Prentice Hall, Englewood Cliffs, NJ, 1990.
30. Halford, G.A., Cumulative fatigue damage modeling — crack nucleation and early growth, *Int. J. Fatigue*, 19(93), 253–260, 1997.
31. Lankford, J., The growth of small fatigue cracks in 7075-T6 aluminum, *Fatigue Eng. Mater. Struct.*, 5(3), 233–248, 1982.
32. Newman, J.C., Jr. and Edwards, P.R., *Short-Crack Growth Behaviour in an Aluminum Alloy — An AGARD Cooperative Test Programme*, AGARD R-732, National Technical Information Service (NTIS), Springfield, VA, 1988.
33. Edwards, P.R. and Newman, J.C., Jr., *Short-Crack Growth Behaviour in Various Aircraft Materials*, AGARD R-767, National Technical Information Service (NTIS), Springfield, VA, 1990.
34. Goto, M., Statistical investigation of the behaviour of small cracks and fatigue life in carbon steels with different ferrite grain sizes, *Fatigue Eng. Mater. Struct.*, 17(6), 635–649, 1994.
35. Pearson, S., Initiation of fatigue cracks in commercial aluminum alloys and the subsequent propagation of very short cracks, *Eng. Fracture Mech.*, 7, 235–247, 1975.
36. Kung, C.Y. and Fine, M.E., Fatigue crack initiation and microcrack growth in 2024-T4 and 2124-T4 aluminum alloys, *Metallurgical Trans. A*, 10A, 603–610, 1979.
37. Sigler, D., Montpettit, M.C., and Haworth, W.L., Metallography of fatigue crack initiation in overaged high-strength aluminum alloy, *Metallurgical Trans. A*, 14A, 931–938, 1983.
38. Li, P., Marchand, N.J., and Ilschner, B., Crack initiation mechanisms in low cycle fatigue of aluminum alloy 7075-T6, *Mater. Sci. Eng.*, A119, 41–50, 1989.



39. Butler, J.P. and Rees, D.A., Development of Statistical Fatigue Failure Characteristics of 0.125-inch 2024-T3 Aluminum Under Simulated Flight-by-Flight Loading, AFML-TR-74-124 (ADA002310), Defense Technical Information Center, Ft. Belvoir, VA, 1974.
40. Moore, N., Ebbeler, D. H., Newlin, L.E., Surtharshana, S., and Creager, M., An Improved Approach for Flight Readiness Certification — Probabilistic Models for Flaw Propagation and Turbine Blade Fatigue Failure, Volume 1, NASA-CR-194496, Dec. 1992.
41. Vanstone, R.H., Gooder, O.C., and Krueger, D.D., Advanced Cumulative Damage Modeling, AFWAL-TR-88-4146 (ADA218555), Defense Technical Information Center, Ft. Belvoir, VA, 1988.
42. Newman, J.C., FASTRAN-II, A Fatigue Crack Growth Structural Analysis Program, NASA TM-104159, National Aeronautics and Space Administration, Langley, VA, 1992.
43. Laz, P.J. and Hillberry, B.M., The Role of Inclusions in Fatigue Crack Formation in Aluminum 2024-T3, presented at Fatigue 96: 6th International Fatigue Congress, Berlin, Germany, 1996.
44. Laz, P.J. and Hillberry, B.M., Fatigue life prediction from inclusion initiated cracks, *Int. J. Fatigue*, 20(4), 263–270, 1998.
45. Virkler, D. A., Hillberry, B.M., and Goel, P.K., The Statistical Nature of Fatigue Crack Propagation, AFFDL-TR-78-43 (ADA056912), Defense Technical Information Center, Ft. Belvoir, VA, 1978.
46. Liao, M. and Xiong, Y., A risk analysis of fuselage splices containing multi-site damage and corrosion, presented at *41st Structures, Structural Dynamics, and Materials Conference*, AIAA-2000-1444, American Institute for Aeronautics and Astronautics, Reston, VA, 2000.
47. Hollingsworth, E.H. and Hunsicker, H.Y., Corrosion of aluminum and aluminum alloys, in *ASM Handbook*, Vol. 13, *Corrosion*, ASM International, Materials Park, OH, 1987, pp. 583–608.
48. Cole, G.K., Clark, G., and Sharp, P.K., The Implications of Corrosion with respect to Aircraft Structural Integrity, DSTO-RR-0102, DSTO Aeronautical and Maritime Research Laboratory, Melbourne, Australia, 1997.
49. Bell, R.P., Huang, J.T., and Shelton, D., Corrosion Fatigue Structural Demonstration Program, final report, Defense Technical Information Center, Ft. Belvoir, VA, to be published.
50. Szklarska-Smialowska, Z., Pitting corrosion of aluminum, *Corr. Sci.*, 41, 1743–1767, 1999.
51. Harlow, D.G. and Wei, R.P. Probability approach for prediction of corrosion and corrosion fatigue life, *AIAA J.*, 32(10), 2073–2079, 1994.
52. Wei, R.P., Corrosion and Corrosion Fatigue of Airframe Materials, DOT/FAA/AR-00/22, National Technical Information Service, Springfield, VA, 2000.
53. Brandt, S.M. and Adam, L.H., Atmospheric exposure of light metals, in *Metal Corrosion in the Atmosphere*, ASTM STP 435, ASTM, Philadelphia, PA, 1968, pp. 95–128.
54. Ailor, W.H., Jr., Performance of aluminum alloys at other test sites, in *Metal Corrosion in the Atmosphere*, ASTM STP 435, ASTM, Philadelphia, PA, 1968, pp. 285–307.
55. Sankaran, K.K., Perez, R., and Jata, K.V., Effects of pitting corrosion on the fatigue behavior of aluminum alloy 7075-T6: modeling and experimental studies, *Mater. Sci. Eng.*, A297, 223–229, 2001.
56. Zamber, J.E. and Hillberry, B.M., Probabilistic approach to predicting fatigue lives of corroded 2024-T3, *AIAA J.*, 37(10), 1311–1317, 1999.
57. Burynski, R.M., Jr., Chen, G.-S., and Wei, R.P., Evolution of pitting corrosion in a 2024-T3 aluminum alloy, in *Structural Integrity in Aging Aircraft*, AD-Vol. 47, ASME, New York, 1995, pp. 175–183.
58. Ghiocel, D.M., Combining Stochastic Networks, Bayesian Inference and Dynamic Monte Carlo for Estimating Variation Bounds of HCF Risk Prediction, presented at the *7th National Turbine Engine High Cycle Fatigue Conference*, Monterey, CA, April 16–19, 2003.
59. Ghiocel, D.M., Refined Stochastic Field Models for Jet Engine Vibration and Fault Diagnostics, presented at *International Gas Turbine & Aeroengine Congress, 2000 TURBO EXPO*, Munich, Germany, May 8–11, 2000.

60. Kinzie, R. Jr., Corrosion Suppression: Managing Internal & External Aging Aircraft Exposures, presented at *6th Joint FAA/DoD/NASA Conf. on Aging Aircraft*, Aircraft Structures Session 1A, San Francisco, 2002.
61. Abernethy, R.B., *The New Weibull Handbook*, R.B. Abernethy, 1993.
62. Liao, M, Forsyth, D.S., Komorowski, J.P., Safizadeh, M., Liu, Z., and Bellinger, N., Risk Analysis of Corrosion Maintenance Actions in Aircraft Structures, presented at ICAF 2003, *Fatigue of Aeronautical Structures As An Engineering Challenge*, Lausanne, 2003.
63. Rocha, M.M., Time-Variant Structural Reliability Analysis with Particular Emphasis on the Effect of Fatigue Crack Propagation and Non-Destructive Inspection, report 32-94, University of Innsbruck, Institute of Engineering Mechanics, 1994.
64. Koul, A.K., Bellinger, N.C., and Gould, G., Damage-tolerance-based life prediction of aeroengine compressor discs: II — a probabilistic fracture mechanics approach, *Int. J. Fatigue*, 12(5), 388-396, 1990.
65. Berens, A.P. and P.W., Hovey, Evaluation of NDE Reliability Characterization, AFWAL-TR-81-4160 (ADA114467), Defense Technical Information Center, Ft. Belvoir, VA, 1981.



# 3

## Selected Topics in Probabilistic Gas Turbine Engine Turbomachinery Design

---

3.1	Introduction .....	3-1
3.2	Traditional Reliability Engineering Approaches .....	3-2
3.3	Probabilistic Rotor Design/Fracture Mechanics .....	3-4
	Introduction • Probabilistic Life Analysis for New Parts • Field-Management Risk Assessments • Future Probabilistic Efforts	
3.4	Fan, Compressor, Turbine Blade Probabilistic HCF Design.....	3-7
	Introduction • Background • Geometry Variation • Blade Frequency — Probabilistic Campbell Diagram • Mistuning • Forced-Response Prediction • Material Capability • Failure Probability Calculation • Updating of Predictions • Field Effects • Summary	
3.5	Overall Summary .....	3-19
	References .....	3-20

James A. Griffiths

Jonathan A. Tschopp

*GE Transportation*

### 3.1 Introduction

---

The use of probabilistic methods in gas turbine engine design is a rapidly growing field, with wide applications in various design disciplines such as performance, aero, heat transfer, and mechanical design. For example, probabilistics can be used to obtain a better understanding of engine performance and to define robust engine cycles that provide specified levels of performance in the presence of component/hardware variation. Probabilistic models can also be used to support aircraft/engine integration studies to optimize customer-based parameters such as the direct cost of fleet operations. This chapter focuses on the use of probabilistics in structural design, in particular, the design of rotating parts within the engine. Figure 3.1 provides a cross section of a modern commercial turbofan engine. The focus of this discussion is on the rotating parts — the fan, compressor, and turbine — with particular attention paid to design issues involving damage tolerance and fatigue. Given the complexities of the overall problem, this chapter can only provide an overview of the probabilistic methods available. The discussion begins with a summary of traditional reliability engineering methods.

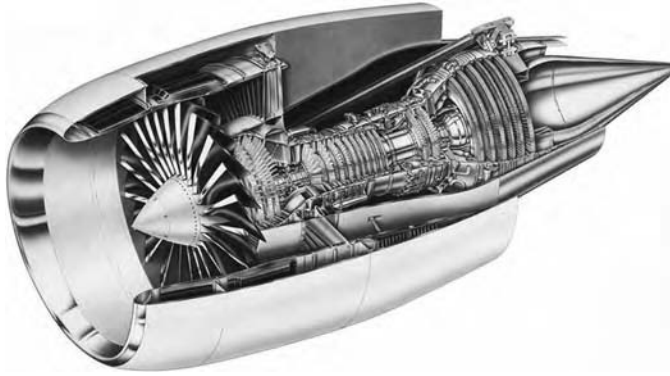


**FIGURE 3.1** Trimetric of the GE90-94B turbofan engine. The chapter focus is on turbomachinery design, with particular emphasis on damage tolerance and fatigue behavior of fans and compressors.

## 3.2 Traditional Reliability Engineering Approaches

Reliability is defined as the probability that an item will perform its intended function for a specified interval under stated conditions. Failure is defined as the inability of the item to perform its function within previously specified limits. In general, such a definition transcends structural reliability, the focus of this chapter, and pertains to all aspects of engine reliability. Failures can be categorized based on their potential impact or hazard to the system. Category I failure hazards will lead to death or severe injury to personnel or total loss of the system. Category II hazards may cause personal injury, including death, or major system damage, or may require immediate corrective action for personnel or system survival. Category III hazards can be controlled without injury to personnel or major system damage, while Category IV hazards are highly unlikely to result in personal injury or system damage. Typical reliability metrics include shop visit rate and in-flight shutdown rate for both military and commercial engines, unscheduled engine removal rate and delay/cancellation rate for commercial engines, line replaceable unit (LRU) removal rate, in-flight abort rate, and mean time between failures for military engines.

System-level reliability is determined by a rollup of subsystem reliabilities. During the design phase, targets for subsystem reliability are established by allocating goal reliabilities for each subsystem based on the overall desired system reliability. Often, these subsystem allocations are based on historical experience with similar equipment. Figure 3.2 illustrates a general subsystem structure used for such analyses as adopted by the Air Transport Association (ATA). As data are developed for the actual subsystems, product reliability is updated by calculating from the bottom up, and it is measured at various subsystem and system levels vs. the allocations. Reliability block diagrams are used to roll up the reliability. Individual elements are considered to be in series or in parallel and their reliabilities combined appropriately. For two subsystems in series, the system operates only if both subsystems operate successfully. Thus system reliability is the product of the individual subsystem reliabilities:

$$R_{\text{system}} = R_A * R_B \quad (3.1)$$

where  $R_{\text{system}}$  is the combined reliability level, and  $R_A$  and  $R_B$  are the individual elements in series.

For parallel subsystems, where only one subsystem needs to remain operational for the system to operate, the system reliability can be expressed as

$$R_{\text{system}} = 1 - (1 - R_A) * (1 - R_B) \quad (3.2)$$

where  $R_A$ ,  $R_B$ , and  $R_{\text{system}}$  are defined as above. Complex systems can be analyzed by using these series and parallel calculations in various combinations, leading to the system-level reliability.

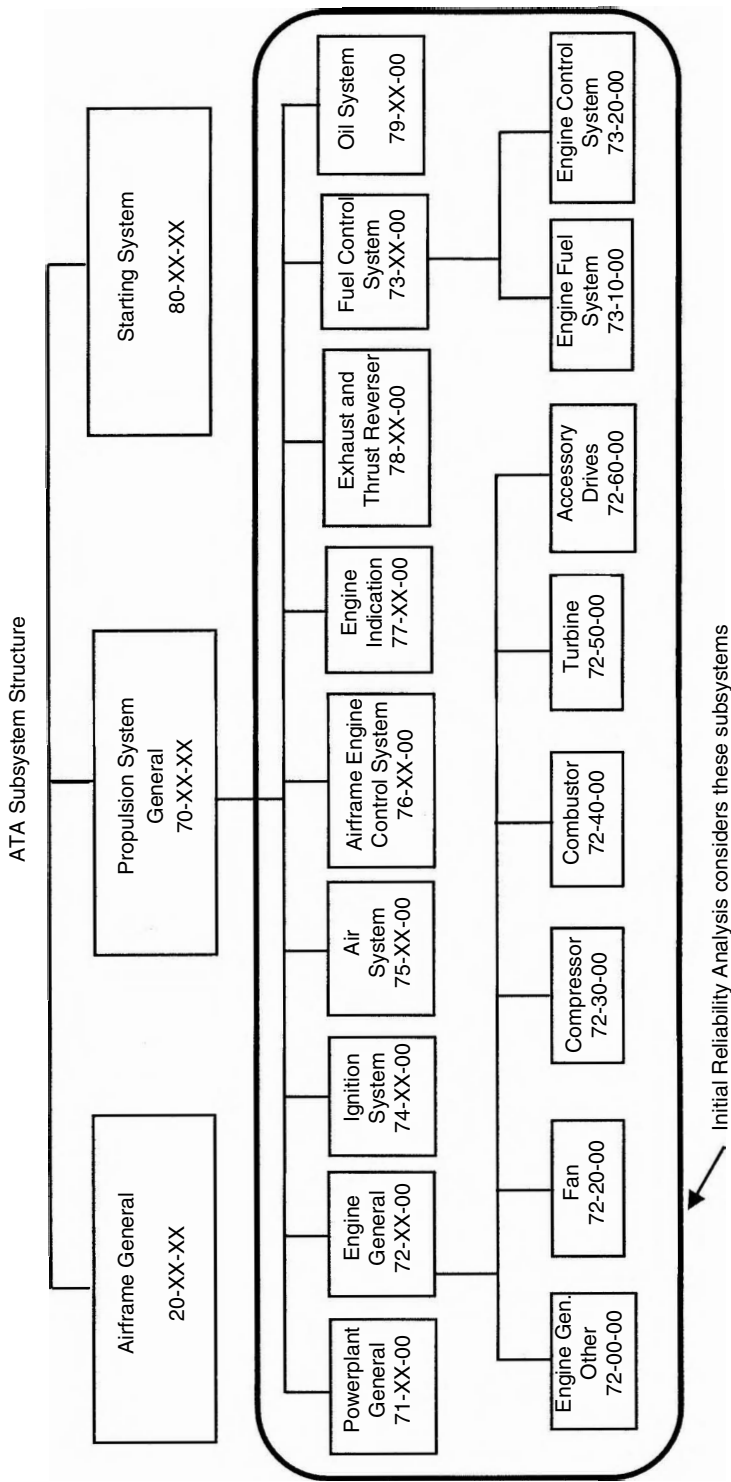


**FIGURE 3.2** Portions of the Air Transport Association (ATA) consensus structure used as the framework to conduct reliability allocations and rollout reliability model results for aircraft engine subsystems.

A bottom-up reliability rollup is based on failure modes effects and criticality analyses (FMECA). This is a detailed analysis of all potential failure modes, including description of the failure mode, its effects on the subsystem and engine, any compensating provisions, definition of failure detection method, hazard severity classification, and rate of occurrence. These analyses help identify high drivers of unreliability and serious hazards, and through the rollup process they help determine predicted reliability rates for the system.

System reliability typically improves over time as fixes to known failure modes are introduced to reduce their failure rate or as new failure modes are discovered and fixed. Often, reliability predictions are stated in terms of a “mature” rate, where maturity is defined at some amount of cumulative engine flight hours (EFH) for the fleet. Reliability growth can be characterized by plotting the cumulative number of failure events against cumulative EFH. Typically, a power function is fit to express the relationship between  $\log(\text{cumulative events})$  vs.  $\log(\text{cumulative EFH})$ . The first derivative of this function then is used to determine the instantaneous failure rate.

Weibull analysis is typically used to characterize the statistical distribution of component life. The shape parameter for the Weibull function helps to identify age dependency of the failure rate; these include the classical bathtub curve segments of infant mortality (shape parameter  $< 1$ ), random failures (shape parameter  $= 1$ ), and wear out (shape parameter  $> 1$ ). Commercial software is available for both Weibull and reliability growth analyses.

## 3.3 Probabilistic Rotor Design/Fracture Mechanics

---

### 3.3.1 Introduction

Two fundamental uses for probabilistic analyses on critical rotating components include design/life prediction of new parts and field-management risk assessments for fielded hardware. Field-management risk assessments are typically conducted to support development of field corrective-action plans in response to problems identified by either analytic predictions (a calculated life problem) or discovery of cracks in fielded components. Probabilistic methods used for field risk assessments can include Monte Carlo simulations for crack initiation and propagation lives, Weibull analysis of field experience, or probabilistic fracture mechanics assessments to address anomalies such as hard-alpha (nitrided titanium) in titanium components or alloy contaminants introduced during material processing.

Probabilistic analysis for the design of new rotating parts has evolved over time. Initially, probabilistic analyses were introduced to address specific issues that were determined to be best handled by a stochastic rather than a strict deterministic process. The primary introduction point for probabilistic analysis has been probabilistic fracture mechanics to address damage-tolerance criteria. Strategies have been developed limiting the use of random variables to only those variables thought to be key to the final results. Probabilistic fracture mechanics approaches typically focus on defect size and frequency as the primary random variables. The primary challenges have been understanding and modeling the fatigue behavior of the anomalies, development of the input anomaly size distribution, and validation and calibration to specimen data and field component experience. As these approaches mature, they are being applied earlier in the design process so that damage-tolerance considerations help shape the final design for the part rather than provide a postdesign assessment of damage risk.

Requirements for damage-tolerance analysis on commercial engines are described in the Federal Aviation Administration (FAA) Advisory Circular 33.14-1 [1]. The Rotor Integrity Subcommittee (RISC) of the Aerospace Industries Association (AIA) developed a strategy to address damage tolerance of critical titanium parts in response to the FAA Titanium Rotating Components Review Team Report in 1990 [2]. Key parts of this industry consensus strategy include (1) definitions of hard-alpha anomaly occurrence rates and size distributions in finished hardware, and (2) the definition of a design target risk (DTR) metric [3] to determine both the acceptability of new hardware designs as well as the appropriateness of proposed actions for fielded hardware. These methods are currently being extended to additional areas such as surface-anomaly damage tolerance and wrought nickel damage tolerance under the auspices of

the RISC. The U.S. Department of Defense's description of damage-tolerance design best practices for military engines is set forth in the MIL-HDBK1783B handbook (Engine Structural Integrity Program or ENSIP [4]).

### 3.3.2 Probabilistic Life Analysis for New Parts

In performing a probabilistic life assessment, the distribution of potential anomalies (size and frequency distributions) and the behavior of such anomalies during field service must be defined. Typically, anomaly distributions are described by an overall frequency expressed as the number of anomalies of all sizes per unit volume or weight and a separate probability density function of anomaly size.

Anomaly fatigue behavior is described by crack-growth curves, assuming the anomaly acts like a crack under cyclic loading. Growth is a function of the initial size of the anomaly, the local stress and temperature fields, the number and cyclic content of the flight missions, and the material crack-growth resistance. In addition, surface and embedded anomalies can differ in crack-growth behavior, with surface anomalies typically growing faster under the same cyclic loading conditions.

The fundamental metric of interest is probability of fracture (POF), where POF is the predicted probability of component rupture per unit time/cycle (rate) or for a given interval in time or cycles (typically the component service life). This in turn is a function of two things: the chance of having an inclusion (inclusion probability) and the chance that the initial inclusion is of sufficient size to cause fracture within the specified life of the component (crack probability). POF is, in its simplest sense, the product of these two underlying probabilities.

Inclusion probabilities are dependent on the material, its manufacturing processes, and the sensitivity of production inspections to the presence of anomalies as a function of size and shape (probability of detection as a function of defect area). The AIA RISC has developed baseline hard-alpha anomaly distributions for titanium alloys, accounting for the several manufacturing and inspection steps in the process to go from ingot to finished parts [3], similar to that shown in Figure 3.3. Details of the process to determine the baseline anomaly distributions are provided in this reference. These distributions are based on both analytical models of the manufacturing process and correlation with historical data for commercial engine experience, such as dimensional data from detected anomalies and inspection capabilities. Based on these distributions, inclusion probability is estimated by taking the product of the volume of the material and the anomaly frequency.

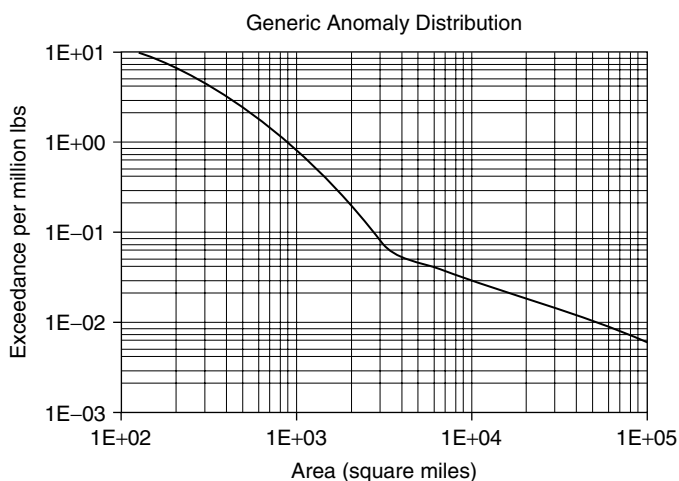
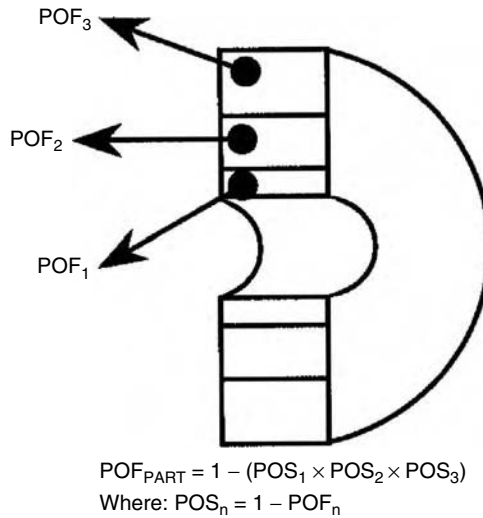


FIGURE 3.3 Generic anomaly size (area) distribution expressed as exceedance probability.





**FIGURE 3.4** Schematic of summation of part subvolume probability based on binomial model of failure for combining failure probability.

Crack probabilities are determined in two steps. First, given a life goal—cycles to failure under a specified cyclic loading and environment—a maximum crack size that will survive to the life goal is determined using fracture mechanics crack-growth analysis. Given the critical crack size, one minus the cumulative probability (or exceedance probability) of the critical size from the anomaly size distribution determines the crack probability.

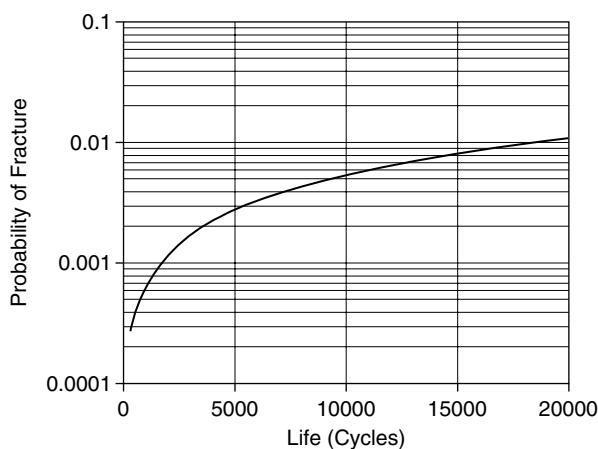
These analyses are conducted for a series of subvolumes within the component of interest to reflect the variation in stress, temperature, and geometry within the component and to reflect how crack-growth capability varies throughout the part. The part is divided into regions of near-constant life, and each region is analyzed. Probabilities of fracture are determined for each subvolume in the part, and these are subsequently combined statistically to get the total part probability of fracture schematically, as shown in Figure 3.4. These calculations are repeated for a range of service lives to create a part probability of fracture vs. life curve (predicted cumulative fracture probability distribution).

Figure 3.5 shows an example of a POF plot. The POF at the required service life from the curve is compared with the DTR, where DTR is an agreed upon standard (relative risk value) for accessing the acceptability of a calculated component POF. Typically, DTRs are validated against specimen data and component field experience. Parts with a calculated POF less than the DTR are considered acceptable. Parts that are predicted to exceed the DTR require action to reduce the POF below the DTR. Redesign and field inspection are the typical actions.

Much of this process has been automated in OEM specific analysis systems. In addition, the FAA has funded the Southwest Research Institute (SWRI) for development of a commercially available computer code (DARWIN) to conduct these calculations [5].

A very important step in the use of probabilistic methods is the validation/calibration of such methods with observed field experience. Adamson [6] and an AIA RISC paper [3] provide examples of such validation/calibration efforts.

Several general conclusions can be drawn concerning the relative sensitivity of POF to key variables. First, POF is approximately directly proportional to volume, all other factors being equal. Second, factors affecting residual life, such as local stress, have a more significant effect on POF. For example, it is not uncommon for a 10% change in stress to yield a 30 to 40% increase in risk. Finally, the frequency of anomalies influences the nature of the regions driving risk. For low-frequency anomalies such as hard-alpha in titanium, the POF is primarily driven by bulk stress regions in the part; large volumes of material



**FIGURE 3.5** Example of a probability-of-fracture curve in which probability of failure is expressed as a function of cumulative cycles.

at “moderate” stress levels contribute significantly more risk than very highly local stress-concentration features. The contrary is true for alloys that have small inclusions at high frequencies. Here, stress-concentration features can primarily drive risk due to the comparatively high likelihood of anomalies in these small regions.

### 3.3.3 Field-Management Risk Assessments

Field-management risk assessments can be undertaken for such reasons as premature component cracking problems, hard-alpha inspection programs, or preplanned in-service inspection intervals on military engines. Techniques similar to those described above for life analysis are used, although in this case the focus is on the probability of fracture over a fixed interval of time in hours or cycles between in-service component inspections. Critical to this analysis is the probability of anomaly detection for in-service component inspection methods. This ultimately determines the distribution (size and frequency) of the larger anomalies that go undetected and can propagate during the next inspection interval.

### 3.3.4 Future Probabilistic Efforts

Probabilistics can be extended to creep, fatigue, and burst design tasks. Efforts to develop physics-based models and appropriate distributional data for such models may be substantial. As a benchmark, significant efforts by industry went into developing and validating the probabilistic fracture mechanics approach for damage tolerance. Extension of probabilistic methods to these alternative failure mechanisms will also require significant engineering effort, largely due to the need for validating failure predictions with field experience, as was the case with the probabilistic fracture efforts described above.

## 3.4 Fan, Compressor, Turbine Blade Probabilistic HCF Design

### 3.4.1 Introduction

The focus of the remaining discussion is on resonant-mode vibration of fans, compressors, and turbine blades and vanes. Resonant-mode vibration is a dominant cause of blade failure in high-cycle fatigue (HCF). The USAF is currently funding industrywide research into probabilistic methods for HCF failure probability assessment as part of its HCF initiative [7]. In conjunction with this, future engine development programs will likely face probabilistic HCF failure rate requirements.

Current deterministic-based methods are briefly described first. Following this, progress to date and future development needs and direction for probabilistic methods will be outlined. The primary focus of the discussion will be fan and compressor blades; the complex geometries, thermal stresses, and high-temperature effects associated with turbine blades and vanes provide additional complications for probabilistic HCF assessment.

### 3.4.2 Background

Integral-order blade stimuli are caused by other vanes, blades, and by airflow distortion. Rotating blades pass through pressure fluctuations due to these excitation sources. The frequency of stimulus is therefore related to the engine speed and the number of struts or vanes or the spatial content of the airflow distortion pattern. The fundamental harmonic of the excitation equals the product of the speed and order of the excitation (e.g., number of upstream vanes).

Traditionally, components are designed to either avoid resonances in the operating speed range of the engine associated with known engine-order excitation sources or to place resonances in lower-speed regions and away from mission points in the cycle where sustained operation is expected. The Campbell diagram, Figure 3.6, is used to display the excitation frequencies due to known sources and compare those frequencies with the variation in vibratory frequencies of the blades with engine speed. Blade vibratory frequencies can change with engine speed due to temperature changes and centrifugal stiffening of the blade. The intersection of engine-order excitation lines and blade-frequency lines indicate resonance at the crossing engine speed.

Historically, frequency placement has been based on frequencies associated with nominal blade geometries. For modes outside the operating range, a set percentage margin in frequency with allowance for maximum engine overspeed is used to account for blade frequency and engine differences. For modes with resonances within the operating range of the engine, maximum permissible blade vibratory stresses are set using factors of safety applied to minimum material HCF capability. Guidelines for maximum nominal steady-state stresses are used early in the design process to provide adequate allowable vibratory stresses. These measures are taken to provide confidence that measured stresses in the aeromechanical

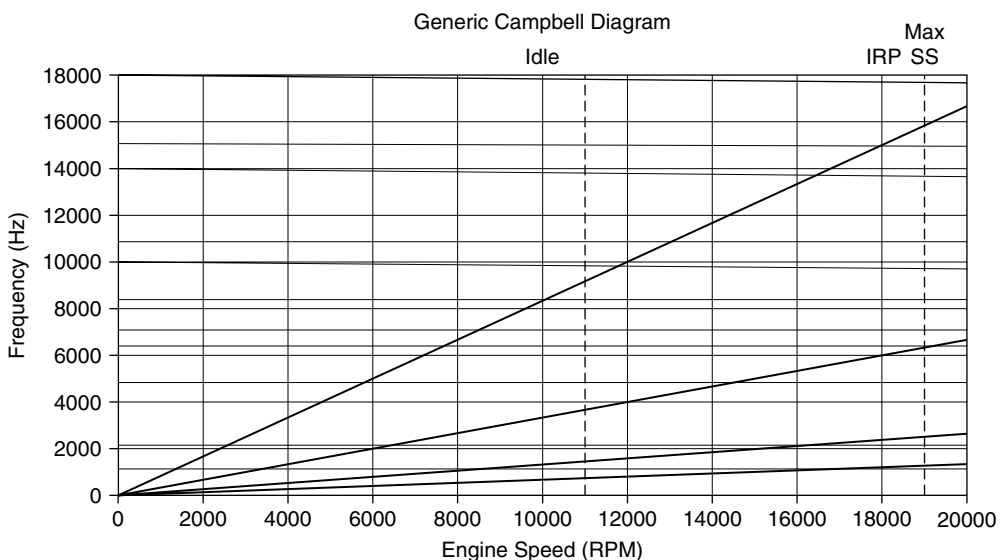


**FIGURE 3.6** The Campbell diagram identifies vibratory modes with resonances in the engine operating range. “Horizontal” lines are individual blade vibratory modes. Driver lines are integral per-rev excitation sources: distortion, upstream/downstream blade or vane count, etc.

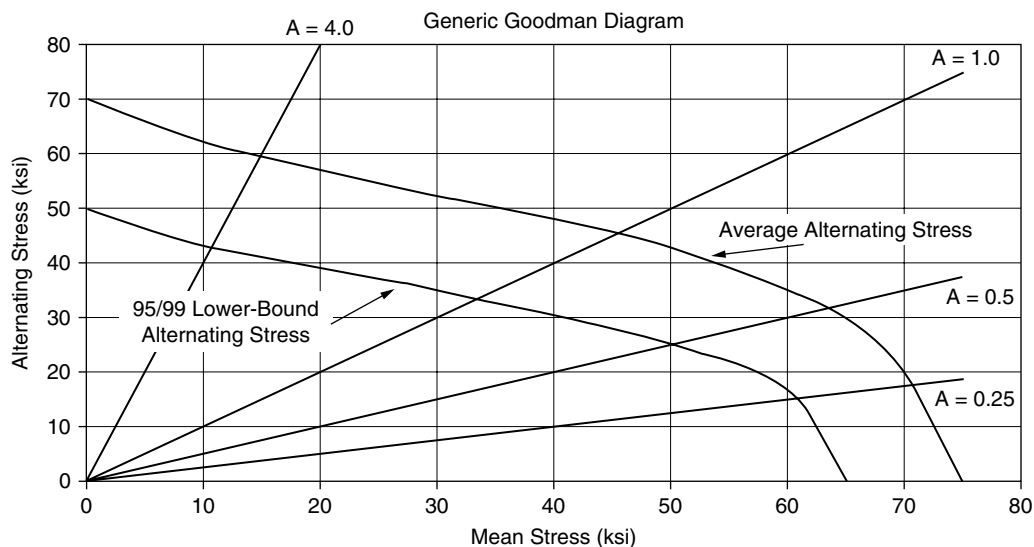


**FIGURE 3.7** The Goodman diagram describes HCF alternating-stress capability as a function of mean or steady-state stress for a given number of HCF cycles. Average (mean) and lower-bound (95% confidence/99% of population exceedance) capabilities are indicated. The A-ratio lines are constant alternating stress/steady-state stress ratios.

qualification engine test would ultimately be acceptably low. The design is qualified based on the measured vibratory stress levels, not the predicted analytic values of stress.

Allowable vibratory stresses are expressed as a function of the local steady-state stress in the Goodman diagram, Figure 3.7. Allowable vibratory stress decreases with increasing steady-state stress.

Strain gauges monitoring blade vibratory stress are typically limited in quantity due to restrictions on the number of instrumentation leads from the rotating structure. Thus, there is uncertainty in the maximum blade vibratory stress, and one cannot be sure that the maximum responding blade was instrumented. Second, one or, at most, a very modest number of engines are instrumented for aeromechanical qualification tests. Therefore, factors of safety to account for sampling of blade stresses and engine-to-engine variation are used. In addition, both engine deterioration and damage to hardware occur in the fleet, potentially increasing vibratory stress, reducing material capability, or both. Historic factors of safety for vibratory stress have been used in the past to address all these issues based on experiences from successful designs.

With the advent of probabilistic methods, predictions of probability distributions for quantities like blade frequency and stress are replacing fixed design margins based on the nominal blade geometry and material properties. Variation in blade geometry, mode shape and frequency, and vibratory stress response can all be addressed explicitly. A number of deterministic tools developed in connection with the U.S. government's HCF initiative are being applied probabilistically to address critical aspects of the problem such as mistuning [8–10] (variation in blade-to-blade response due to subtle blade geometry differences on a single rotor) and forced-response vibratory stress prediction. As shown in Figure 3.8, geometry variation influences blade frequencies and mode shapes that, in turn, influence forced response.

Another important aspect of the probabilistic assessment methodology is the ability to update predictions as more data become available. Such data may include new analytic predictions, component or engine test results, and field experience. Probabilistic HCF analyses can be an ongoing process over the life of the engine design as new data become available. Quantifying uncertainty in predicted failure probability is desired, and such uncertainty should diminish throughout the product life cycle as additional data and field experience become available. A schematic for tracking such predictions is shown in Figure 3.9. This schematic is similar to that suggested by Los Alamos National Laboratory and their PREDICT [11] system.

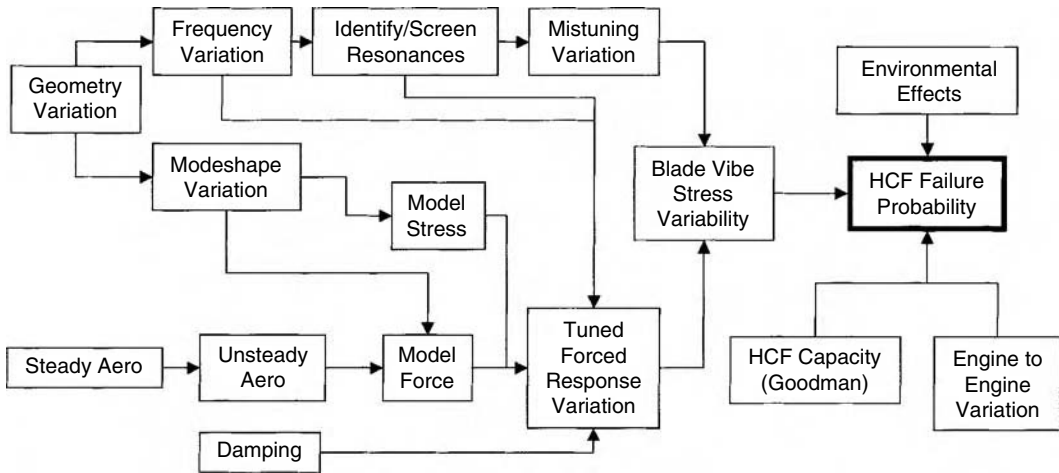


**FIGURE 3.8** High-level analysis flowchart for prediction of HCF failure probability. Geometry variations drive mode shape and frequency, which, in turn, drive forced-response variation and HCF failure probability.

### 3.4.3 Geometry Variation

Probabilistic assessments are grounded on an understanding of the geometric variability of the blades. From variation in geometry and material properties, mode-shape and frequency data are derived. These, in turn, have a strong influence on mistuning effects, aero damping, and forced response. This discussion focuses on solid-blade geometries; the presence of internal cooling-air passages for turbine blades, for example, significantly complicates characterization and analysis of geometry variation, although in principle the methods described below still apply.

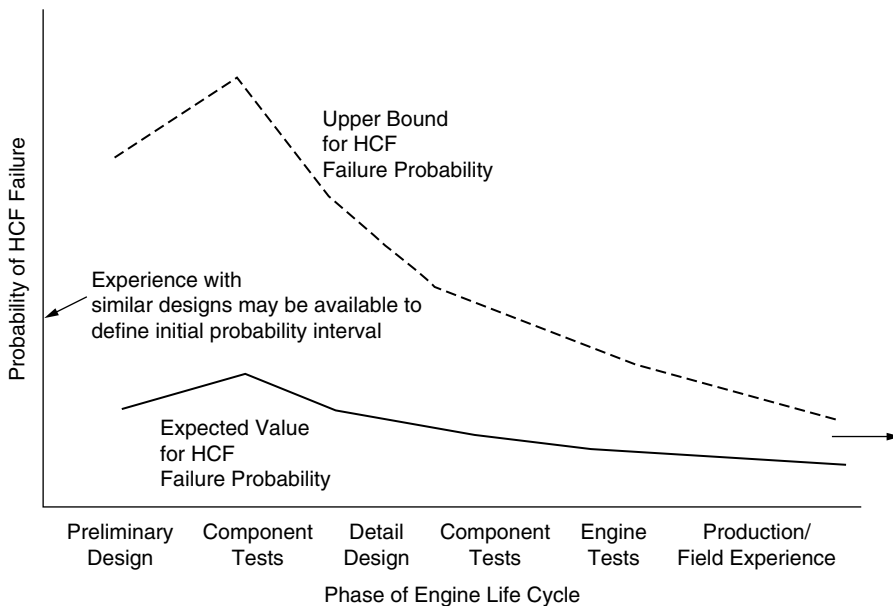


**FIGURE 3.9** Predictions of HCF failure probability can be conducted throughout the engine life cycle. Uncertainty in failure probability should diminish with time as additional data become available. A one-sided confidence interval is shown in this example because the upper limit is of primary interest.

Two well-documented methods for statistical analysis of data are currently under study or in use in characterizing blade geometry variation. The first method is principal components analysis (PCA) [12], and the second is spatial statistics analysis (SSA) [13, 14]. The former method is available in a number of commercial software packages and is a technique used to simplify analysis when considering a large number of quantified variables, such as detailed geometry measurements. The latter is a more specialized technique arising from the mining industry; commercial software code is available for some applications.

In PCA, the data for various geometric features are assembled as a vector in which individual quantities are typically correlated, e.g., individual thicknesses on a grid over the blade. PCA constructs a series of independent linear combinations of the individual geometry variables (called components), which, when taken all together, explain all the variance in the original data. Each component is uncorrelated with all previous ones, facilitating subsequent generation of simulated random blades; the amount of variance explained with each additional component diminishes. The intent is to capture most of the original variance in a relatively small set of components, enabling rapid simulation of new random blades. The linear coefficients for each PCA component for all measured blades define distributions from which new sets of coefficients can be drawn independently. When working with physical geometry parameters, distributions of these coefficients are generally non-Gaussian. One can either fit parametric models to individual-component coefficient distributions, or one can draw samples with replacement (bootstrap) if the database is sufficiently large. Due to the non-Gaussian nature of the coefficient distributions, a mixture model of Gaussian distributions can be used, for example, to approximate a bimodal coefficient distribution. Significant amounts of actual hardware measurements are necessary to implement this method effectively. Figure 3.10 illustrates the process.

In spatial statistics, geometry variables at two locations are assumed correlated by a function of the distance between the points, closer points being more highly correlated than those farther apart. This correlation function with distance is characterized using the correlogram or a related function, the variogram, which tracks variance, not correlation, as a function of distance between points. For example,

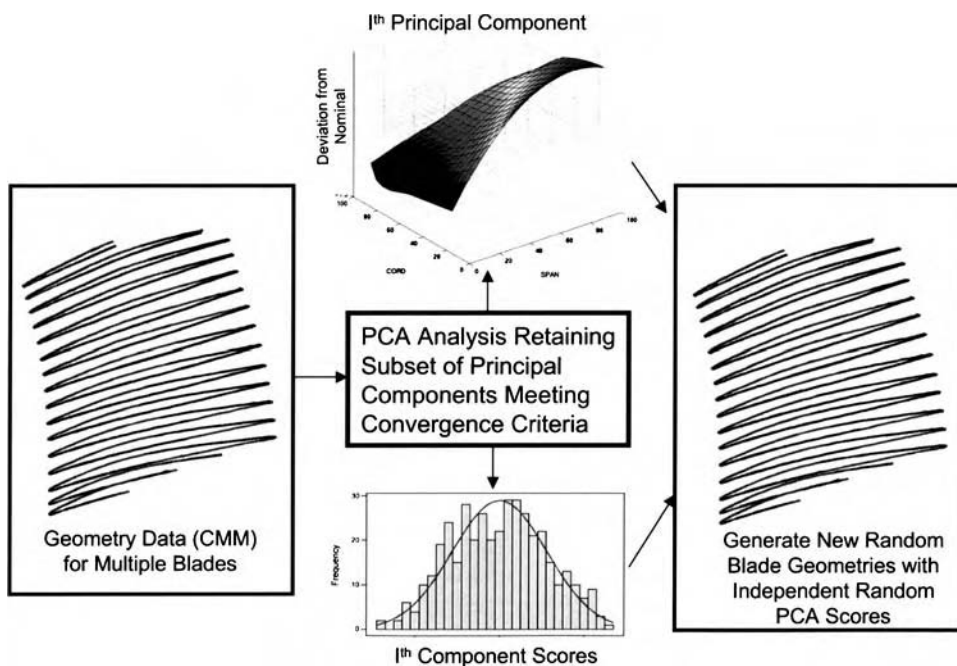


**FIGURE 3.10** Principal components analysis (PCA) defines components (“manufacturing modes”) containing most of the original variance in geometry and permits simple generation of new, random blade geometries.

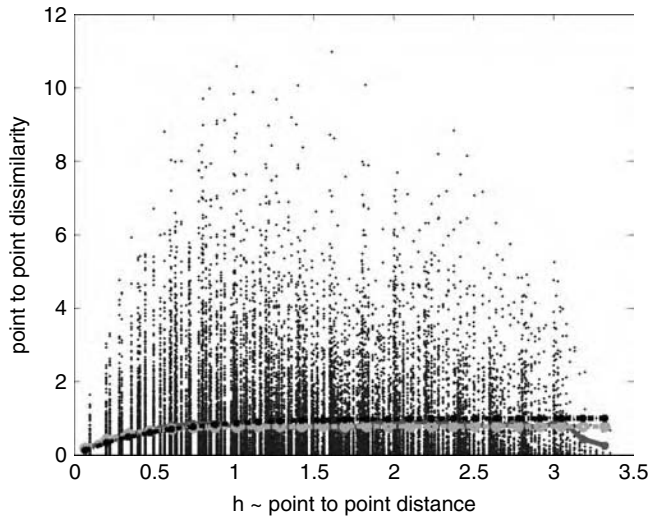


**FIGURE 3.11** Example of experimental variogram cloud with fitted exponential theoretical variogram. Original data were generated from a given variogram. Raw average variogram and least-squares-fit exponential variograms are also shown as dashed lines. Data points are individual squared error values for grid point pairs.

blade thicknesses would be more highly correlated at adjacent locations than they are when well separated across the blade. Isotropic spatial statistics models are used for simplicity; correlation or variance is expressed as a single function of distance applied across the full blade.

Measurements can be used to construct an experimentally based variogram; the collection of raw variance vs. distance data is known as a variogram cloud. In this case, distances between measurement points are then divided into a number of bins of similar distance, and the average squared differences of the measurements within each bin are used to define the variogram. A number of traditional variogram functions are available, each described by a limited number of parameters, which can be fit to the average bin data using least-squares methods to provide a theoretical variogram. Figure 3.11 shows an example variogram cloud as well as an associated variogram model fit.

Spatial statistics models can be used early in the design stage to define generic correlation functions before hardware is manufactured and measured geometry data are available for PCA analysis. In this case, additional random blade geometries are generated using an appropriate theoretical variogram, likely based on similarity to a previous blade design and manufacturing method. A covariance matrix is constructed based on the variogram and a grid of measurement points; random blade geometries are then calculated using Cholesky decomposition of the covariance matrix. Spatial statistics and PCA analyses can therefore be used to complement each other in various stages of design evolution.

### 3.4.4 Blade Frequency—Probabilistic Campbell Diagram

PCA or SSA geometry models can be used to generate a series of random blades. Finite element models of these random blades would then be used to predict frequency and mode-shape variation. This can be done by either (1) building an ensemble of individual blade models and conducting modal analysis on individual random finite element models or by (2) modeling the nominal geometry and determining frequency and mode-shape sensitivities to geometry variation. Once sensitivities are known, random sets of deviations from nominal geometry can be processed to estimate blade frequency and mode-shape changes by linear superposition. Blair and Annis [15] provide examples of the application of SSA to predicting variation in blade frequency.

As an example of probabilistic analysis, consider a family of blades with a particular vibratory mode from a specified engine-order excitation predicted to have resonance above the engine operating range

on the Campbell diagram. In the past, a factor of safety between redline engine speed (maximum overspeed) and nominal blade frequency would be used to avoid resonance for blades with lower-than-nominal frequency. Using the nominal blade frequency and frequency variations predicted by generating random blade geometries and frequencies about nominal by finite element or sensitivity analysis, one can now directly calculate the probability of lower blade frequencies resulting in a resonance at or below max speed. As opposed to a fixed-percentage frequency margin, this focuses attention on those modes for which blade frequency may be most sensitive to geometry variation and the variation in blade frequency is highest. By these techniques, one can produce a probabilistic Campbell diagram.

It is probable that some resonances will be within the engine operating range. Additional forced-response analyses can be used to assess the likelihood of potential HCF failure from these remaining modes. For these modes, the probabilistic Campbell diagram indicates the distribution of engine speed over which individual blades resonate.

### 3.4.5 Mistuning

Blades in a tuned system (all identical) share a common forced-response stress. However, blade geometric and material variations introduce structural dynamics effects known as mistuning, which result in variation in response from blade to blade. Responses of individual blades are coupled via the disk. In the extreme, energy can be localized in one or several blades, resulting in high response of those blade(s) substantially above the tuned response. Variation in blade response must be accounted for in predicting HCF failure probability. Mistuning analysis is used to predict the sensitivity of a stage's design to blade variation for a fixed excitation level.

It is not practical to build full rotor models repeatedly to determine mistuned responses. This has been done in isolated cases for single rotors to validate models, but it is not a practical design approach to characterize rotor-to-rotor variation. Reduced-order models [8–10] have been developed to provide a practical means of predicting blade-to-blade response variation on rotors due to blade differences. These models are based on cyclic-symmetry finite element models of the rotor. Cyclic-symmetry models reflect the fact that individual sectors (one blade plus associated share of the disk) on the rotor respond similarly, with a known phase relationship existing between the individual sectors based on the number of blades on the rotor and the excitation engine order. Mistuned modes of vibration may be described using linear combinations of tuned-system responses or blade-alone responses with constraint modes describing interactions with the disk at the blade–disk interface. The size of the reduced-order model is substantially smaller than the original number of degrees of freedom in the sector finite element model. Thus, reduced-order models, once built, can be used to rapidly characterize rotor-to-rotor variation.

Current advanced tools typically characterize blade differences with a frequency standard deviation parameter that is used to vary the stiffness of the individual mistuned sectors on the rotor. Stiffness varies with frequency squared. Individual rotor analysis provides blade-to-blade variability at a fixed excitation level. Monte Carlo simulations of a series of random rotors can also be conducted to determine the variability, engine to engine, due to mistuning structural dynamic effects at a constant modal force. Relative response of the maximum blade on each rotor, for example, is compared with a tuned rotor (all identical blades) and then typically displayed as a function of blade frequency standard deviation, as shown in Figure 3.12. However, the Monte Carlo simulations provide all blade responses for each rotor in the simulation, providing a wealth of information for subsequent probabilistic analysis.

Two methods can be used to store and use this full set of blade relative-response data in subsequent failure probability analyses. First, a parametric model can be selected for describing blade-to-blade vibratory stress variation on a single random rotor. Individual mistuned rotor stress variations can then be fit using the selected model, and distributions of the model parameters themselves can be captured for future use. There will be correlations between model parameters that must be accounted for in subsequent usage. Alternatively, one can retain a large sample of Monte Carlo-generated mistuned vibratory stress data and bootstrap random rotors from this ensemble of data. The former method requires less data storage but forces a specific upper-tail behavior on the data based on the chosen parametric model. The bootstrap



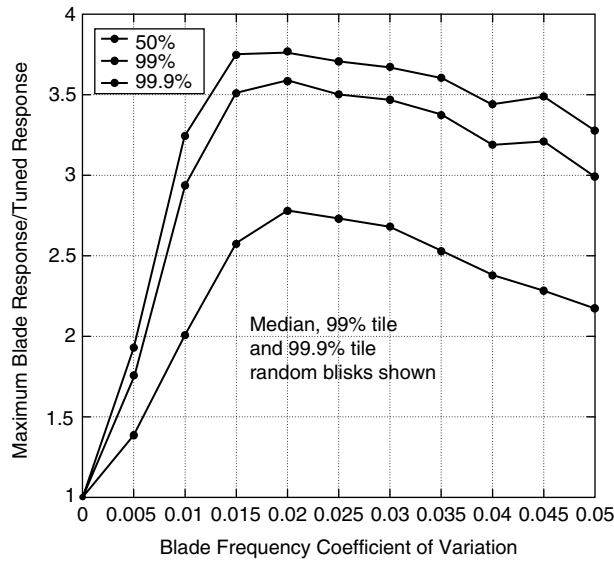


**FIGURE 3.12** Amplification factors (ratio of maximum blade response on mistuned-blisk to tuned-blisk response) shown for higher responding random blisks. Amplification ratio depends on level of blade mistuning as characterized by blade frequency coefficient of variation.

method requires that substantially more data be stored, but it does not impose a specific upper-tail structure on the blade-to-blade variability coming from the mistuning analysis.

Typically, the worst mistuning responses (highest maximum-to-average ratio of blade response) occur in regions where there are closely spaced blade and “disk” modes that can interact (known as a veering region). A “disk” mode is a mode with significant disk activity. A tuned cyclic-symmetry sector finite element model analysis, containing a single blade and its share of the disk, can be used to identify those modes and engine-order stimuli that most likely result in higher mistuned responses. One can then focus subsequent mistuning and forced-response analyses on those modes most likely to exhibit high variability in response.

### 3.4.6 Forced-Response Prediction

Blade resonant response can be expressed as

$$\sigma_v = \frac{MF * Q * \sigma_m}{(2\pi f)^2} \quad (3.3)$$

where  $\sigma_v$  is the blade vibratory stress,  $MF$  is the modal force normalized by modal mass,  $Q$  is a magnification factor (dependent on percent critical damping from aero and mechanical sources),  $\sigma_m$  is the modal stress at the location of interest, and  $f$  is frequency in Hz. Modal force is determined by the dot product of the unsteady pressure field with the mode shape of interest. Variations in frequency and mode shape have been determined by earlier geometry studies. Thus, variations in  $f$  and  $\sigma_m$  have been characterized. The additional complexities added for forced-response analysis are damping and unsteady pressure field variation. Both of these are challenging to characterize probabilistically.

Techniques are under development to predict the variation in unsteady pressure fields due to blade-geometry variation, with fixed boundary conditions on steady airflow. Adjoint methods [16, 17] can, in principle, be used to determine unsteady pressure variations due to blade-geometry variations characterized by methods described above. Although these methods would provide data concerning the variation

in unsteady pressure due to geometry changes of the blades under study, they do not fully address all sources of unsteady pressure field variation.

The unsteady pressure field is a complex function of a large number of variables including, to name a few, engine operating line, variable geometry schedule, clearances, bleed rates, corrected speed, profiles and distortion, and stage boundary conditions determined by other stages. Aeromechanical testing is conducted over a range of operating conditions to survey vibratory stresses. However, characterizing engine-to-engine variability beyond available engine test data will be difficult. Where specific sources of excitation are linked to critical resonance, component tests and computational fluid dynamics (CFD) analyses might be used to understand sensitivity to critical variables of interest, although such analyses are typically difficult and expensive to conduct. Thus, in general, defining methods for predicting probabilistic forced responses remains a critical research effort. Reliance on developing probability distributions for engine-to-engine variation in excitation levels will likely rely on distributions derived from expert opinion for the near future, augmented by test data and targeted analysis where feasible.

### 3.4.7 Material Capability

Allowable vibratory stress is determined using the Goodman diagram, where local mean stress is considered in setting allowable vibratory stress. Goodman diagrams can be linked to the traditional fatigue curve through the concept of equivalent stress. Equivalent uniaxial stresses [18, 19] can be defined for a given stress ratio,  $R$ , (minimum stress/maximum stress) or the related alternating stress ratio,  $A$ , (alternating stress/mean stress) for the test. Median and selected percentile uniaxial equivalent vibratory stress capabilities can be characterized by fitting a traditional fatigue curve. To be effective, such a fit generally requires substantial data covering a range of stress/life values and  $R$  (or  $A$ ) ratio values. The fatigue curves can be translated then to a Goodman diagram using various  $R$  or  $A$  ratios based on mean stress to calculate the corresponding vibratory stresses. A method for transforming fatigue-curve data to Goodman curves is outlined as follows (in this example, for fully elastic behavior):

1. Select an  $A$  ratio of interest (multiple  $A$  ratios are eventually used to create the Goodman diagram).
2. Calculate the corresponding  $R$  ratio:

$$R = \frac{1-A}{1+A} \quad (3.4)$$

3. Extract the equivalent uniaxial stress at various percentile levels from the fatigue curve and convert to maximum stress using a preferred model. For the Walker model [18] for equivalent stress in the fully elastic regime, this is expressed using a material-dependent Walker exponent,  $m$ , as follows:

$$S_{eq} = \frac{S_{max}}{2} * (1-R)^m \quad (3.5)$$

4. Convert the maximum stress to alternating stress and plot on the Goodman diagram:

$$S_{alt} = \frac{A}{A+1} * S_{max} \quad (3.6)$$

Figure 3.13 shows a schematic of the process used to construct a Goodman diagram. Modifications to this basic procedure are necessary for higher steady-state stresses ( $A$  near 0), where cyclic elastic-plastic behavior may be involved.

Pascual and Meeker [20] introduced the random fatigue-limit model to characterize fatigue behavior. In this model, specimen lives have a lognormal probability distribution, with the mean parameter (log life)

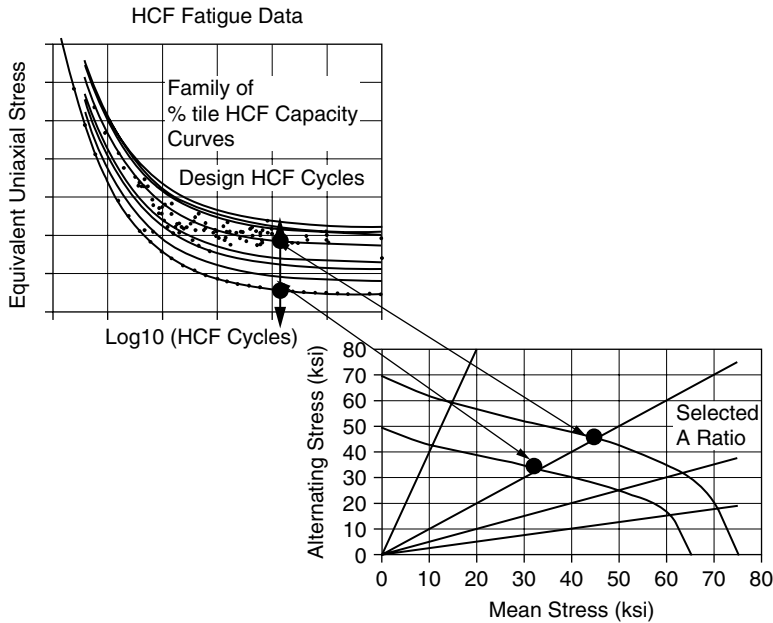


**FIGURE 3.13** Example of a process for constructing a probabilistic Goodman diagram in a fully elastic regime, where more HCF fatigue failures typically occur.

linearly related to the log of the difference between the applied stress and a random fatigue limit for each specimen. A selection of probability-density models is available for modeling the fatigue-limit stress itself. Comparisons with data sets of equivalent stress derived from a series of varying  $R$  ratio tests indicate that this model can be useful in describing behavior of materials with fatigue-limit behavior. In particular, the model may represent well the large variation in fatigue life at lower stress levels approaching the fatigue limit.

Traditional LCF lifing methods have focused on life variability at a given level of stress. As discussed previously in probabilistic rotor design, LCF-driven design criteria focus on life (cycles) and, for probabilistic fracture mechanics in particular, the margin in life between inspection intervals. In the HCF regime, as typified by the random fatigue-limit model, there are order-of-magnitude larger variations in life at a given stress compared with the LCF regime. HCF design necessarily focuses on stress margin, not life.

It is assumed that the component will ultimately be subjected to sufficient cycles to cause failure. Typically, engine specifications stipulate a controlling number of cycles for which allowable stresses are defined, and these typically range from  $10^7$  to  $10^9$  cycles. The failure probability calculation then reduces to the calculation of the probability that the applied vibratory stress exceeds the allowable stress at the specified number of cycles as determined by the Goodman diagram. Of course, suitable factors can be applied either to vibratory or allowable stress to account for field degradation effects to either the hardware itself or to operating conditions within the engine.

### 3.4.8 Failure Probability Calculation

The probability of individual blade failure is determined at the limiting spot on the blade where the vibratory stress is the maximum percentage of local HCF capability based on the local steady-state stress; this location is known as the critical location. The probability that the critical location vibratory stress for a random blade exceeds material HCF capability can be expressed as the integral:

$$P_f = \int_0^{\infty} f_{\text{app}}(x) * F_{\text{allow}}(x) dx \quad (3.7)$$

## Random Engine – Outer Loop

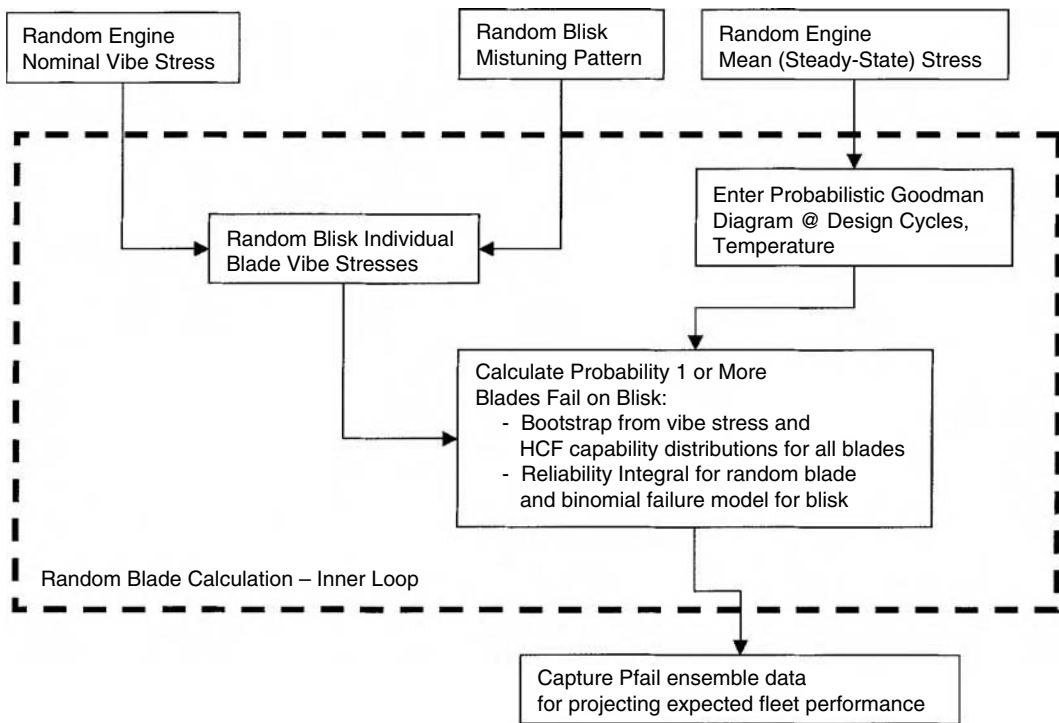


**FIGURE 3.14** High-level Monte Carlo process schematic for calculating HCF failure probabilities based on typical forced-response distributional data. More-primitive variables such as geometry, frequency, and mode shape ultimately dictate the higher-level forced-response distributions used here.

where  $f_{app}(x)$  is the probability density of critical location vibratory stress, and  $F_{allow}(x)$  is the cumulative probability function for material HCF capability at the local steady-state stress on which the vibratory stress is superimposed. Simplified solutions for this integral exist for some pairs of distribution types, e.g., normal or lognormal for both distributions [21]. Otherwise, numerical integration is required, or Monte Carlo simulation is used to predict it.

To date, Monte Carlo techniques have been used primarily to assess HCF failure probability. A typical, but simplified, Monte Carlo simulation sequence (excluding field effects for now) would include the following steps (Figure 3.14 illustrates this process):

1. Select a nominal value of blade vibratory stress from a probability distribution representing anticipated engine-to-engine variability in average vibratory stress and uncertainty in that stress.
2. Generate a random blade-to-blade relative vibratory stress distribution from mistuning data (parametric or bootstrap models) and multiply by the selected nominal vibratory stress to obtain the distribution of individual blade vibratory stresses for a random engine.
3. Select mean stress level at the controlling critical location from a suitable probability density distribution reflecting the operating conditions at which the resonance occurs.
4. Using a probabilistic Goodman diagram, calculate the parameters for the allowable stress distribution (for example, a set of lognormal distribution parameters,  $\mu$  and  $\sigma$ , can be calculated from the median and another specified lower-bound percentile curve on the Goodman diagram) based on mean stress from step 3.

5. Calculate the random blade failure probability in one of two ways:
  - a. For parametric models of blade-to-blade stress variability and HCF capability, use the reliability integral to calculate failure probability of a random blade,  $P_{\text{fRB}}$ . Probability of failure of one or more blades on the rotor,  $P_{\text{fRE}}$ , can then be calculated using the binomial model by:

$$P_{\text{fRE}} = 1 - (1 - P_{\text{fRB}})^{N_{\text{blade}}} \quad (3.8)$$

where  $N_{\text{blade}}$  is the number of blades on the rotor.

- b. For bootstrapped vibratory stress samples from the mistuning analysis, generate a random allowable stress for each blade on the rotor and compare it with the individual blade applied stress. One or more blades exceeding its allowable stress constitutes failure for the engine.
6. Collect ensemble data from the Monte Carlo simulation and interpret the results. For bootstrapped mistuning data, a count of the number of engines with failed blades provides an estimate of the failure probability of the fleet. With parametric models used for blade-to-blade mistuned stress, each random engine results in a failure probability for the random engine. The ensemble average of these engine-level failure probabilities is the expected value for fleet failure rate.

In the course of the Monte Carlo analysis, individual probability distributions may be scaled or additional variables defined as the product, sum, difference, or division of two random variables. Hahn and Shapiro [22] provide a ready reference for calculating such manipulations of independent random variables.

### 3.4.9 Updating of Predictions

Failure probability predictions can be updated with new information as it becomes available. Such data may include additional design analyses, component test results, engine test results, and field experience or failure data. At one extreme, distributions used previously can simply be ignored and new distributions defined based solely on the new data. An alternative and preferred approach is to reflect both old and new data in the latest predictions. Bayesian analysis [23, 24] is one well-known method of updating distributions where the final results reflect both the prior distributions (previous knowledge) and the new data.

To clarify, take a specific example. Assume, for convenience, that blade frequencies are normally distributed. Uncertainty in the actual population frequency distribution can then be expressed by probability distributions for the population mean and standard deviation themselves. Based on data to date, so-called “prior” distributions can be defined for the mean and standard deviation parameters themselves. Now assume that additional blades are tested. The likelihood of obtaining the actual test data can be expressed as a function of the normal distribution mean and standard deviation of the probability density function for the normal distribution. Posterior distributions for the parameters (combining previous knowledge and the new test data) are calculated using Bayes’ theorem, a statement of conditional probabilities:

$$P(\theta, x) = \frac{P_{\text{prior}}(\theta) * L(x, \theta)}{\int_{\theta} P_{\text{prior}}(\theta) * L(x, \theta) d\theta} \quad (3.9)$$

where  $P_{\text{prior}}(\theta)$  is the prior joint distribution for the parameters, and  $L(x, \theta)$  is the likelihood of obtaining the actual test data, given the parameters  $\theta$ . One issue with Bayesian techniques is the balance between prior knowledge and new data influencing the posterior distributions. The literature abounds with references to “noninformational priors” to let the test data speak for itself. In our case, however, we want prior data to influence the final results. However, prior distributions that are too restrictive can result in their overpowering the associated test data. The balance on how best to combine prior data and new knowledge remains a significant area of research for HCF probabilistics.

The integral in the denominator of Equation 3.9 can be a difficulty. So-called conjugate pairs for prior distribution and likelihood have historically been used where the posterior distribution is in the same form as the prior distribution with altered hyperparameters [23, 24]. Use of these conjugate pairs restricts

probability distributions used to model critical HCF data. More recently, Markov chain Monte Carlo methods [25, 26] have been developed, which eliminate the need to explicitly perform the integration in the denominator of Equation 3.9. The applicability of these methods for updating HCF-failure-related distributions is actively under investigation. Much effort remains to define best practices in updating distributions used for HCF analysis.

### 3.4.10 Field Effects

Alterations to both component hardware and engine operating conditions occur in the field. For example, engine temperatures may increase as the engine deteriorates. Physical damage can occur, such as foreign object damage (FOD), on leading edges of blades. The location, extent, and impact of such damage must be accounted for when making HCF reliability predictions. For example, in the case of FOD damage to the leading edge of blades on a fan, the rate at which FOD occurs, the distribution of FOD sites along the blade leading edge, and the geometry of the FOD site must all be described with suitable probability distributions. In addition, there must be analytic or empirical transfer functions relating FOD site location and geometry to a fatigue notch sensitivity factor,  $K_f$ , applied to the vibratory stress when calculating failure probability. Alternatively, a knockdown factor can be defined and applied to the HCF capability. FOD occurs on random blades, so the Monte Carlo simulation for FOD failure needs to address blade-to-blade stress variability as well. Griffiths and Kielb [27] provide an example of such a model considering FOD damage impact in calculating HCF failure probability for a generic fan blade design. Similar concerns exist for dovetail wear, LCF/HCF interaction, and other physical degradation mechanisms.

### 3.4.11 Summary

A logical progression of analyses culminating in the prediction of failure probability is presented. The intent is to identify those vibratory modes most likely to cause failure early on in the process using preliminary design tools whenever feasible, and then to concentrate the most intensive and expensive analyses on these modes of greatest concern.

Geometry variability is characterized, and variability in blade mode shape and frequency is derived. Potential resonance crossings for known engine excitation sources are then identified using the Campbell diagram, with the intent to place modes outside the operating range or at a relatively benign engine speed as much as possible. Historical experience and tuned-system modal analysis for a variety of engine orders of excitation can be used to screen for modes most likely to result in high stress due to structural dynamic effects known as mistuning.

Mistuning and forced-response analysis can then be used to predict nominal blade stresses for these most critical modes. Such analyses are used to characterize both blade-to-blade stress variability within an engine as well as from engine to engine due to structural dynamic considerations. Simulations of random rotors and engines are then conducted to generate random-engine applied and allowable vibratory stresses and assess failure probability.

The development of HCF probabilistics remains an exciting and ongoing area of research as an alternative design approach to fixed factors of safety applied to nominal designs. It is anticipated that, in the near term, both probabilistic methods and deterministic analysis with safety factors will be utilized together to assess designs, with eventual migration to probabilistic methods as the primary approach as confidence in and experience with such methods continue to grow.

## 3.5 Overall Summary

Probabilistic design methods for predicting component structural failures are proving, and will continue to prove, to be highly useful technologies for designing gas turbine engine components. Currently, probabilistic damage-tolerance methods, driven by industry and FAA development activities over the last decade, have a significant lead time over emerging probabilistic HCF failure prediction methods.

An industry and USAF initiative for developing HCF failure prediction methodologies is underway to mature those technologies. Confidence in the use of these tools will grow as they are used to make design predictions and such predictions are then validated by component test results, engine test results, and ultimately by field experience. Much effort remains to mature and validate these tools and also to extend probabilistic methods to other failure mechanisms.

## References

1. Damage Tolerance for High Energy Turbine Rotors, Advisory Circular (AC) 33.14-1, U.S. Dept. of Transportation, Federal Aviation Administration, Washington, DC, 2001.
2. Titanium Rotating Components Review Team Report, U.S. Federal Aviation Administration Aircraft Certification Service Engines and Propeller Directorate, Washington, DC, 1990.
3. Sub-team to the Aerospace Industries Association Rotor Integrity Subcommittee, The Development of Anomaly Distributions for Aircraft Engine Titanium Disk Alloys, American Institute of Aeronautics and Astronautics, Washington, DC, 1997.
4. Department of Defense, Engine Structural Integrity Plan (ENSIP), Department of Defense Handbook, MIL-HDBK-1783B, DOD, Washington, DC, 2002.
5. Wu, Y.-T., Millwater, H.R., and Enright, M.P., Probabilistic Methods for DARWIN™, paper presented at 4th Annual FAA/USAF Workshop, Application of Probabilistic Methods to Gas Turbine Engines, Jacksonville, FL, 1999.
6. Adamson, J.D., Validating the Pratt & Whitney Probabilistic Design System, paper presented at 6th Annual FAA/Air Force/NASA/Navy Workshop on the Application of Probabilistic Methods to Gas Turbine Engines, Solomon's Island, MD, 2003.
7. U.S. Air Force, High Cycle Fatigue (HCF) Science and Technology Program Annual Report, AFRL-PR-WP-TR-2001-2010, U.S. Air Force Research Laboratory, Dayton, OH, 2000.
8. Lim, S.-H., Bladh, R., Castanier, M.P., and Pierre, C., A compact, generalized component mode mistuning representation for modeling bladed disk vibration, AIAA 2003-1545, in *Proceedings of 44th Structures, Structural Dynamics, and Materials Conference and Exhibit*, AIAA/ASME/ASCE/AHS/ASC, Norfolk, VA, 2003.
9. Bladh, R., Pierre, C., Castanier, M.P., and Kruse, M.J., Dynamic response predictions for a mistuned industrial turbomachinery rotor using reduced-order modeling, *J. Eng. Gas Turbines Power*, 124 (2), 311–324, 2002.
10. Yang, M.-T. and Griffin, J.H., A Reduced Order Model of Mistuning Using a Subset of Nominal Modes, ASME 99-GT-288, presented at International Gas Turbine Institute Turbo Expo, Indianapolis, IN, 1999.
11. Meyer, M.A., Booker, J.M., Bement, T.R., and Kerscher, W.J., III, PREDICT: a new approach to product development, *R&D Mag.*, 41, 161, 1999.
12. Kshirsagar, A.M., *Multivariate Analysis*, Marcel Dekker, New York, 1972.
13. Cressie, N.A.C., *Statistics for Spatial Data*, rev. ed., John Wiley & Sons, New York, 1993.
14. Wackernagel, H., *Multivariate Geostatistics*, 2nd ed., Springer-Verlag, Berlin, 1998.
15. Blair, A. and Annis, C., Development of Probabilistic Methods for Campbell Diagram Frequency Placement, paper presented at 7th National Turbine Engine High Cycle Fatigue Conference, Palm Beach, FL, 2002.
16. Hall, K.C. and Thomas, J.P., Sensitivity Analysis of Coupled Aerodynamic/Structural Dynamic Behavior of Blade Rows, extended abstract for the 7th National Turbine Engine High Cycle Fatigue Conference, Palm Beach, FL, 2002.
17. Thomas, J.P., Hall, K.C., and Dowell, E.H., A Discrete Adjoint Approach for Modeling Unsteady Aerodynamic Design Sensitivities, IAAA 2003-0041, AIAA, Reston, VA, 2003.
18. Walker, K., The Effect of Stress Ratio during Crack Propagation and Fatigue for 2024-T3 and 7075-T6 Aluminum, ASTM STP 462, ASTM, Philadelphia, 1970.

19. Smith, R.N., Watson, P., and Topper, T.H., A stress-strain function for the fatigue of metals, *J. Mater. JMLSA*, 5, 767–778, 1970.
20. Pascual, F.G. and Meeker, W.Q., Estimating fatigue curves with the random fatigue-limit model, *Technometrics*, 41 (4), 277–289, 1999.
21. Dhillon, B.S., *Mechanical Reliability: Theory, Models, and Applications*, AIAA Education Series, American Institute of Aeronautics and Astronautics, Washington, DC, 1988.
22. Hahn, G.J. and Shapiro, S.S., *Statistical Models in Engineering*, John Wiley & Sons, New York, 1967.
23. Martz, H.F. and Waller, R.A., *Bayesian Reliability Analysis*, rev. ed., Krieger Publishing, Malabar, FL, 1991.
24. Gelman, A., Carlin, J.B., Stern, H.S., and Rubin, D.B., *Bayesian Data Analysis*, Chapman & Hall/CRC, Boca Raton, FL, 1997.
25. Robert, C.P. and Casella, G., *Monte Carlo Statistical Methods*, Springer-Verlag, New York, 1999.
26. Congdon, P., *Bayesian Statistical Modelling*, John Wiley & Sons, Chichester, U.K., 2001.
27. Griffiths, J. and Kielb, R., Monte Carlo Analysis Applied to HCF Failure Probability Prediction, paper presented at 7th National Turbine Engine High Cycle Fatigue Conference, Palm Beach, FL, 2002.





# 4

## Applications of Reliability-Based Design Optimization

---

Robert H. Sues

Youngwon Shin

(Justin) Y.-T. Wu

*Applied Research Associates, Inc.*

4.1	Introduction .....	4-1
4.2	Overview of Reliability-Analysis Methods .....	4-2
	Model Approximation Methods • Reliability Approximation Methods	
4.3	Review of RBDO Methods .....	4-5
4.4	RBDO Applications.....	4-5
4.5	Selected Aerospace Application Examples.....	4-6
	Shape Optimization of an Axial Compressor Blade • Shape Optimization of an Airplane Wing • Optimization of an Integral Airframe Structure Step Lap Joint • Transport Aircraft Wing Optimization	
4.6	Conclusions .....	4-21
	References .....	4-22

### 4.1 Introduction

---

Physics-based modeling combined with computer-aided design has increasingly become widely accepted by the design community to reduce product design and development time as well as testing requirements. To ensure high reliability and safety, uncertainties inherent to or encountered by the product during the entire life cycle must be considered and treated in the design process.

In general, there are three approaches to incorporate uncertainties into engineering design: reliability-based design, robust design, and safety-factor-based design. The RBDO (reliability-based design optimization) approach adopts a probability-based design optimization framework to ensure high reliability and safety. A typical formulation for reliability-based design is:

$$\begin{aligned} &\text{Minimize: } F(\mathbf{d}) \\ &\text{Subject to: } P[g_j(\mathbf{X}, \mathbf{d}) > 0] \geq R_j^*; \quad j = 1, J \\ &\quad \quad \quad d_k^l \leq d_k \leq d_k^u; \quad k = 1, K \end{aligned} \tag{4.1}$$

in which  $F(\mathbf{d})$  is an objective function such as weight or expected life-cycle cost;  $\mathbf{X}(i = 1, n)$  is a random variable vector;  $\mathbf{d}$  is a design (or decision) variable vector with lower bound  $\mathbf{d}^l$  and upper bound  $\mathbf{d}^u$ ;  $g_j(\mathbf{X}, \mathbf{d}) = 0$  defines design-limit states, with each  $g_j(\mathbf{X}, \mathbf{d}) > 0$  corresponding to a successful event associated with multiple failure modes; and  $R_j^*$  depicts target reliabilities (i.e.,  $1 - \text{allowable failure probabilities}$ ).

The multiple failure events can be statistically correlated due to common random variables. A more general system-reliability definition requires the use of union and intersection events, e.g.,  $R = 1 - P\{[(g_1 \leq 0) \cup (g_2 \leq 0)] \cap [(g_3 \leq 0) \cup (g_4 \leq 0)]\}$ .

Another useful formulation is to maximize reliability with resource constraints. A general RBDO formulation involves deterministic and probabilistic functions of multiple objective functions and multiple equality and inequality constraints. Design variables may be deterministic, e.g., tightly controlled geometry, or associated with random variables such as the mean value of a random variable.

The objective of robust design is to develop designs that are insensitive to input variations. An example formulation for robust design is:

$$\begin{aligned} \text{Minimize: } & \frac{d(\sigma_{\text{performance}})}{d(\sigma_i)} \\ \text{Subject to: } & d_k^l \leq d_k \leq d_k^u; \quad k=1, K \end{aligned} \quad (4.2)$$

While the concept recognizes and treats the uncertainties, it focuses on minimizing the performance variation, e.g., in the form of standard deviation, and does not explicitly address reliability requirements. The safety-factor approach treats uncertainties by adding safety/reliability margins in the design requirements and by attaching safety factors to the nominal values of the uncertainty variables. Even though the RBDO approach is more comprehensive and promises lower life-cycle cost, it has yet to become as widely used as the other two approaches, mainly because it requires more sophisticated analyses and skills with probabilistic analysis. RBDO may become more widely used when the methods are standardized and more commercial-grade, easy-to-use, RBDO design tools become available in the near future.

In addition to the need to generate probabilistic models, probabilistic analysis in RBDO generally requires a relatively larger number of deterministic analyses that may involve highly complicated and computationally time-intensive numerical models, such as finite element and CFD (computational fluid dynamics) models. Fortunately, with recent advances in computational mechanics and the remarkable increase in computational power, including the use of parallel computing, high-fidelity numerical modeling thought to be infeasible a decade ago is now available on the engineer's personal computer. Moreover, a large amount of research work on the development of efficient reliability calculation algorithms has greatly increased the efficiency of the overall RBDO algorithms.

The remainder of this chapter is organized as follows. Section 4.2 provides an overview of the reliability-analysis methods, focusing on efficient approximation methods, followed by an overview of the RBDO formulation and solution strategies in Section 4.3. Section 4.4 gives an overview of RBDO applications. Section 4.5 presents several detailed RBDO application examples based on aerospace structural systems. Finally, the conclusions are given in Section 4.6.

## 4.2 Overview of Reliability-Analysis Methods

A straightforward approach to solve an RBDO problem, such as the formulation in Equation 4.1, is to conduct a double-loop optimization process in which the outer loop iteratively selects feasible designs that approach the minimum objective, while the inner loop evaluates reliability constraints for each selected design. However, for complicated  $g$ -functions and objective functions, the repeated inner-loop reliability analysis can cause the RBDO to be prohibitively time consuming.

The following subsections will provide a brief overview of reliability-analysis methods, focusing on efficient analysis strategies to reduce the computational burden of probabilistic analyses within the RBDO analysis framework. Section 4.3 will review the overall RBDO analysis strategy.

### 4.2.1 Model Approximation Methods

An increasingly popular approach for RBDO is to replace the computationally time-intensive models, using instead approximate, fast-running models that allow the use of Monte Carlo simulation for the

entire RBDO analysis, thus reducing the user's need to learn advanced computational probabilistic analysis methods.

There are a wide variety of model approximation methods, including response surfaces, neural networks, and Taylor's series expansion approaches as well as various extensions or variations of these methods. For example, the versions of the response-surface approach include global, local (or moving), and hybrid global-local approximations, and Taylor's expansion method includes adding higher-order terms based on a few additional calculation points. Another useful and generic technique is to employ variable transformation methods to make the original function less nonlinear in the transformed variable space, before applying approximation methods.

Using the response-surface method, typically a design-of-experiment (DOE) approach is selected to define the layouts of the model-calculation points. There are many DOE methods to choose from, including Box-Benkehn, second-order central composite design, and factorial designs [1, 2]. The selection of the method depends on several factors, including the number of variables, the nonlinear behavior of the model, and the acceptable modeling errors/residuals. The selection of the DOE points depends on the ranges of the input variables as well as the range of the responses that are of interest to designers.

Since the approximation model is built based on the selected points, the errors tend to be small only in a limited region and potentially large in the regions of extrapolation, especially if the model is highly nonlinear relative to the approximation model. It is therefore essential to conduct goodness-of-fit tests and check the model adequacy, including the use of residual plots to compare the exact and the approximate models at selected error-checking points. In addition, after the optimal design has been obtained using the approximate model, it would be useful to conduct a model update to confirm or improve the result.

As an example of using approximation models, Fu et al. [3] evaluated several response-surface models for car crashworthiness studies and applied a second-order polynomial regression model and moving least-squares regression for crash safety design optimization. Li [4] evaluated polynomial models of different orders and found that the second-order polynomial response surface was sufficient for many crash safety applications.

## 4.2.2 Reliability Approximation Methods

The objective of the reliability approximation methods is to efficiently produce accurate reliability results without using time-consuming Monte Carlo (MC)-type simulations. Typically, the efficiency is measured in terms of the number of times the  $g$ -function needs to be computed to generate the result. Many approximation methods, summarized below, are based on the most-probable-point (MPP) concept and focused on calculating the probability of failure ( $= 1 - \text{reliability}$ ). For more details, see [5, 6].

The probability of failure can be expressed as:

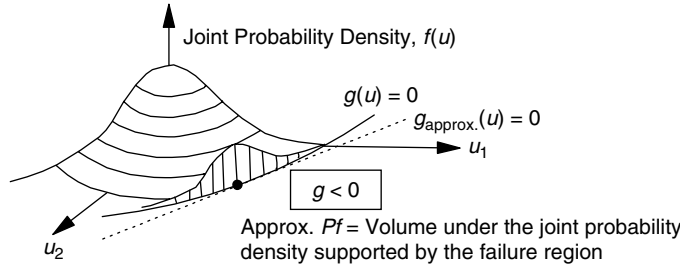
$$p_f = \int_{\Omega} \cdots \int_{\Omega} f_X(\mathbf{x}) d\mathbf{x} \quad (4.3)$$

in which  $f_X(\mathbf{x})$  is the joint probability density function (PDF), and the integration region is the failure domain, defined as  $\Omega = \{\mathbf{x} \mid g(\mathbf{x}) \leq 0\}$ .

The MC method computes  $p_f$  by drawing random samples of  $\mathbf{X}$  and using the following formulation:

$$p_f = \int_{\Omega} \cdots \int_{\Omega} I(\mathbf{x}) f_X(\mathbf{x}) d\mathbf{x} = E[I(\mathbf{x})] = \frac{1}{K} \left[ \sum_{i=1}^K I_i \right] \quad (4.4)$$

where  $I(\mathbf{x})$  is the indicator function (i.e.,  $I = 1$  if  $g(\mathbf{x}) \leq 0$ , otherwise  $I = 0$ ) and  $K$  is the number of samples. This procedure is straightforward and highly robust. The drawback is that the number of samples must be large to reduce the variance of the  $p_f$  estimate. In safety-critical systems where the probability of failure must be very small, a large number of samples is typically required. Efficiency issues prompted the development of reliability approximation methods.



- In the standardized-normal space, find the most-probable-point (MPP) on the limit state that has the highest probability of occurrence
- Replace complicated  $g$ -function by simple  $g$ -function around the MPP
- Compute probability-of-failure using the simplified  $g$ -function
- Analytical local probabilistic sensitivities also available
- Probability can be updated by local sampling around MPP

**FIGURE 4.1** The concept of MPP-based approximation.

The majority of the reliability approximation methods use the model approximation methods reviewed above combined with the idea of minimizing the model approximation errors in the high-risk region. These approximation methods are thus local, i.e., they focus around a point called the most probable point (MPP).

The standard MPP approach first transforms the original random variables to independent standard normal, or Gaussian, variables. As illustrated in Figure 4.1, in the transformed standard normal (reduced)  $u$ -space, MPP is the minimum distance point from the origin to the  $g = 0$  surface. The minimum distance  $\beta$  is called the *safety index*, and the MPP is also called the  $\beta$ -point or the *design point*.

A linear or quadratic approximate model is typically developed using the tangent and curvatures at the MPP or using MPP-centered DOE and regression analysis. The approximation can be developed in the original  $X$ -space or the transformed  $u$ -space, depending on which one provides a better approximation. The widely used first-order reliability method (FORM) solution is based on the tangent surface in the  $u$ -space with the corresponding failure probability of:

$$p_f = \Phi(-\beta) \quad (4.5)$$

which provides a first-order estimate if the original limit-state surface is not significantly nonlinear. A second-order version, SORM, also in the  $u$ -space, is available by adding the curvature information [5–7]. The FORM and SORM approaches have been extended to time-variant reliability [8] and to system-reliability problems involving multiple limit states and multiple MPPs [5].

Searching for the MPP is a constrained optimization problem where the objective is to minimize the distance subject to  $g = 0$ . Several tailored methods have been developed to speed up the search [5, 6, 9]. It should be cautioned, however, that multiple MPPs may exist. In such cases, not only the global minimum distance point must be correctly identified [10, 11], but the accuracy of using a single MPP-based approximation should also be questioned. To help ensure that the correct MPP has been found and the  $p_f$  estimate is reasonably accurate, an error-checking procedure, such as applying the importance-sampling methods to update the  $p_f$ , should be considered [10, 12–15].

As a rule of thumb, assuming that the derivatives are computed by numerical differentiation, experience suggests that the required number of  $g$ -function calculations is on the order of five times  $(n + 1)$  for FORM. For complicated models, the computation cost of the MPP approach depends on how many  $g$ -function calculations are needed to locate the MPP and how many additional runs are needed to develop approximate models. For problems with a large number of variables, variable screening methods should be considered to reduce the problem dimensions [3, 16].

Based on the above safety-index concept, a generalized safety index has been proposed using:

$$\beta_G = \Phi^{-1}(-p_f) \quad (4.6)$$

where  $p_f$  is the probability of failure calculated from any methods. In RBDO, sometimes the target reliabilities are defined using  $\beta$  or  $\beta_G$ .

### 4.3 Review of RBDO Methods

---

Even with the use of the above efficient methods, the double-loop procedure still demands a significant number of  $g$ -function evaluations, and the computation can be prohibitive when each function evaluation is computationally intensive. As a result, many approximate RBDO methods have been developed. Most of these methods are built on the MPP concept, the response-surface methodology, or a combination of both.

The most popular approach is perhaps to develop global response-surface models of the  $g$ -functions. With this approach, the reliability analysis can be conducted quickly using the methods in the previous section. While this approach is attractive, it is limited to well-behaved functions that can be well approximated by low-order polynomial regression models. More complicated response-surface models using multiple local surfaces may be more effective for highly nonlinear models, but the initial costs to develop the models could be much higher. It is a good practice to check the models using the methods mentioned in Section 4.2.1.

Yang and Gu [17] have reviewed several approaches that convert double loops to a single loop, including the single-loop–single-variable method by Chen et al. [18], the safety-factor approach by Wu et al. [19, 20], and the sequential optimization and reliability assessment (SORA) method by Du and Chen [21]. Another efficient single-loop approach based on adaptive response surfaces was developed by Sues et al. [22–24] and is described in Section 4.5. All of these methods simplify the reliability calculations.

### 4.4 RBDO Applications

---

Numerous examples of RBDO applications are available in the literature. An excellent reference that reviews such applications with emphasis on civil and aerospace structures is by Frangopol and Maute [25]. This section will provide additional examples of RBDO applications in the civil, aerospace, and mechanical engineering areas.

Davidson et al. [26] applied RBDO to the minimum weight designs of earthquake-resistant structures subjected to system-reliability constraints considering the uncertainties on the earthquake response spectra, the sizing design variables, and the material properties. Comparison was made between the optimal designs based on probabilistic response spectra and the design based on deterministic spectra that correspond to particular levels of the probability of system failure.

Feng and Moses [27] considered system-reliability constraints of both the damaged and original intact systems for statically indeterminate structures in which redundancy is added to increase the structural safety. Frames of several different configurations were optimized with sizing design variables.

Yang and Nikolaidis [28] applied RBDO to a preliminary design of the wing of a small commuter airplane subjected to gust loads that were modeled using probabilistic distributions. The system-reliability constraint considered the uncertainty in the material strengths, and the weight of the wing was optimized with the sizing design variables. The difference in the behavior of the reliability-based and the deterministic optimal designs was studied.

Pu et al. [29] applied RBDO to a typical frame of a small-waterplane-area twin-hull (SWATH) ship subjected to system-reliability constraints on structural failure criteria considering uncertainties on the loads and material strength. The influence of each sizing design variable to the system reliability was accessed by sensitivity information during RBDO, which recommended the most efficient way to improve the safety by identifying the critical design variable.

Stroud et al. [30] considered the probabilistic constraints of the material strength and the flutter speed in the design of a platelike wing. Finite element analysis and the doublet-lattice method were used to calculate the stresses and the aerodynamic loads for the flutter analysis under the presence of uncertainties in the thickness, flutter speed, load, and material strength. The study showed that improvement in the reliability was obtained in reliability-based optimal designs with a small weight increase relative to the deterministic optimal design.

In the design of an intermediate complexity wing model, Pettit and Grandhi [31] included the aileron-effectiveness constraint in addition to the constraints on the wingtip displacement and the natural frequencies. With the consideration of uncertainties on the sizing design variables, reliability-based optimal design produced a final design that satisfied the target reliabilities with a small weight penalty added to the deterministic optimal design.

Grandhi and Wang [32] applied optimization to minimize the weight of a twisted gas turbine blade subjected to a probabilistic constraint on natural frequency with the consideration of uncertainties in the material properties and the thicknesses distributions.

Yang et al. [33] applied reliability-based optimal design to the crashworthiness design of a full vehicle system in multicrash scenarios. Probabilistic constraints were imposed on the four impact modes: full frontal impact, roof crush, side impact, and offset impact. The optimization problem considered the uncertainties of the important design variables in local or global impact modes. They demonstrated that the weight could be reduced compared with a deterministic (baseline) design while satisfying the safety constraints.

## 4.5 Selected Aerospace Application Examples

In this section, selected application examples developed by the authors and their associates are presented along with details of RBDO formulations and solution strategies. The first three examples were solved using an in-house multidisciplinary stochastic optimization (MSO) shell code. The last example was solved using ProFES/MDO code, which was developed by Applied Research Associates (ARA).

An overview of the methodology implemented in the MSO shell is summarized in Figure 4.2 (for a complete description see Oakley et al. [24] or Sues et al. [34]). The methodology involves: (1) response-surface development for the objective and all the constraints; (2) stochastic optimization using the response

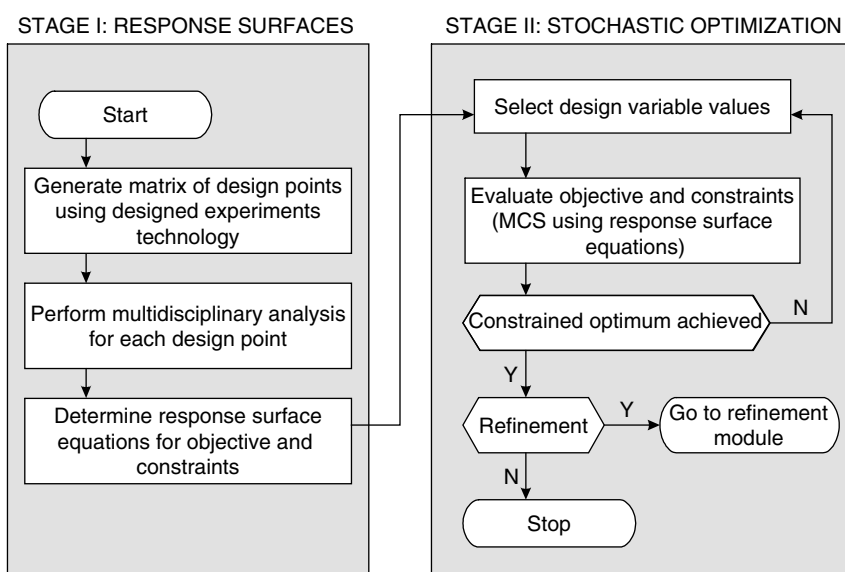


FIGURE 4.2 Flowchart of MSO shell.

surface, standard nonlinear programming, and Monte Carlo simulation; and (3) refinement of the response surfaces at the optimum for the objective and at the most probable failure points (MPPs) for each constraint. This process is repeated until convergence is achieved. The method is efficient because of the use of experimental design techniques for initial response-surface generation and the use of response surfaces for evaluation of system performance and constraints during the RBDO. The method is accurate because of the refinement procedure employed. Further, design and random variables are handled simultaneously so that the required number of  $g$ -function evaluations is a multiple of the number of design variables plus the number of random variables, as opposed to the number of design variables times the number of random variables. Unlike other typical reliability-based design optimization approaches wherein the goal is usually to minimize weight (or cost) for a structural configuration subject to a limiting weight, the MSO shell considers system performance based objective functions (e.g., cruise range, payload weight, revenue, etc.) and also considers aerodynamics and shape parameters. The MSO shell properly simulates the performance of a system that is a function of both single-occurrence and operational random variables via an efficient nested-loop algorithm. Single-occurrence random variables represent random conditions that occur only once during the lifetime of the system as well as random conditions that assume a fixed value once the system or component has been fabricated. Operational random variables represent the conditions that exhibit uncertain changes during operation of the system.

Figure 4.3 summarizes an overview of the methodology implemented in ProFES/MDO [35], which involves: (1) a multistage design-of-experiments variable-screening strategy to define the significant variable set; (2) probabilistic analysis using any of ProFES's probabilistic analysis methods and interaction with commercial CAE codes; (3) linearization of the constraints at the most probable failure points (MPPs) of each random variable, for each constraint; (4) development of a second-order response surface for the objective function at the mean values of all design variables; (5) nonlinear programming to find the optimum design using the response surfaces (via a public domain or commercial optimizer); and (6) updating of the MPPs for the current active constraint set using new values of the design variables. As shown, the process is repeated until convergence is achieved.

### 4.5.1 Shape Optimization of an Axial Compressor Blade

The MSO shell has been used to perform a multidisciplinary stochastic shape optimization of an axial compressor blade [24, 34]. The overall goal is to determine a reliable design in which the blade twist and thickness distribution minimize cost as a function of the blade weight and of the expected efficiency during cruise conditions. Uncertainties in geometry, material properties, modeling error, operational rotor speed, and extreme off-design rotor speed conditions are considered, and reliability constraints against exceeding tip clearances, fatigue life, and yield stress at the blade root are imposed.

The entire geometry of the axial compressor is defined using Bézier curves. A Bézier curve is made of two endpoints and two control points. The hub and shroud geometry are simple surfaces of revolution from four-point Bézier curves, as illustrated in Figure 4.4, in which each curve's slopes at the two endpoints are tangent to the lines from the endpoints and the corresponding control points in the middle. In the figure, the four Bézier points are connected by straight lines.

The compressor blade is a skinned surface that is defined by a family of airfoil sections. At each radial station from hub to shroud, the airfoil section of the blade is defined by chord length, maximum thickness, twist angle, and leading-edge position. The airfoil section shape is based on a standard NACA (National Advisory Committee for Aeronautics) profile. The value of chord length, thickness, twist, and leading-edge position is defined by three-point Bézier curves spanning from hub to shroud. The baseline geometry for the analyses is based on a Bézier curve geometry that closely approximates the NAS R37 single-blade-row compressor geometry (see Figure 4.5).

#### 4.5.1.1 RBDO Formulation

We want to determine the values of the design variables that define the shape of a blade. These variables are explained in Section 4.5.1.2.



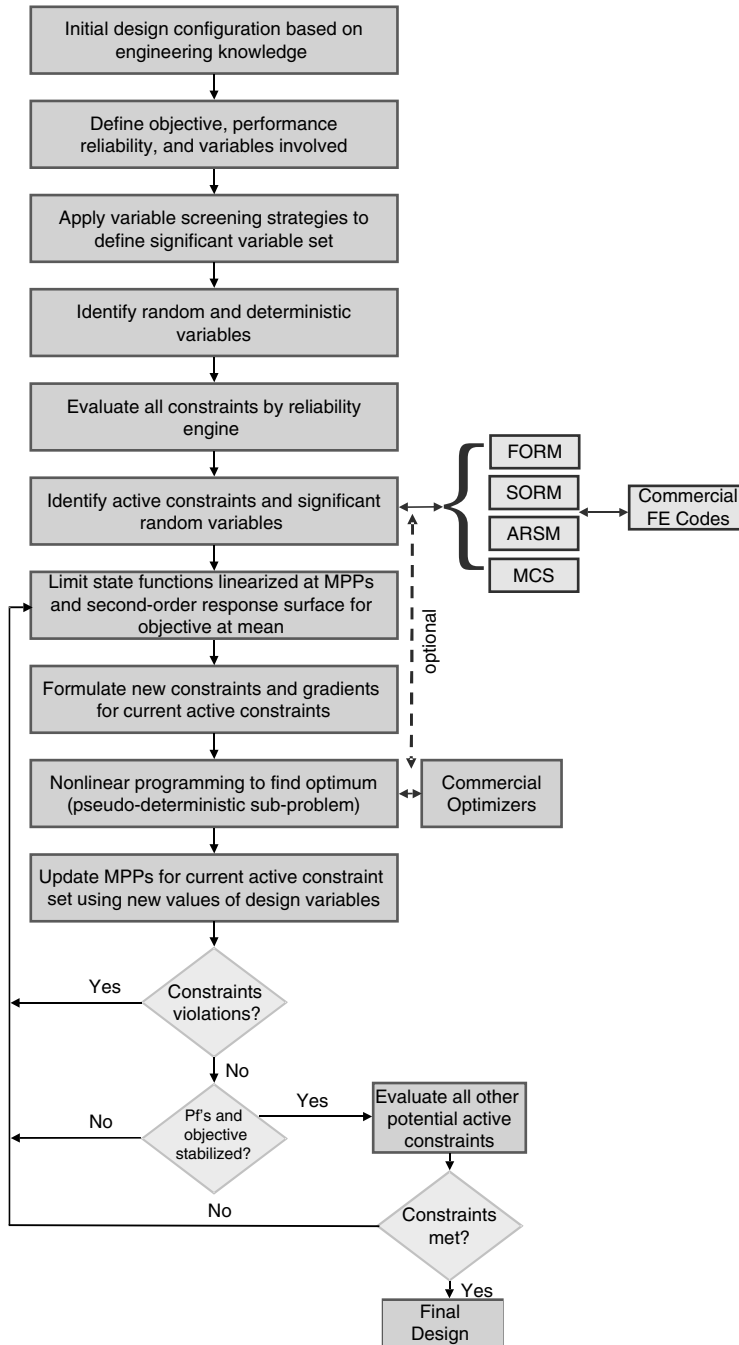


FIGURE 4.3 Flowchart for RBDO methodology.

Objective: minimize cost as a function of the blade weight and of the expected efficiency during cruise conditions.

Constraints:

- $P[\sigma_{max} < \sigma_y] \geq 0.999$
- $P[\sigma_c < \sigma_{cr}] \geq 0.999$



**FIGURE 4.4** Hub and shroud geometry for axial compressor example.

- $P[\text{blade extension in the radial direction} < 0.050 \text{ mm}] \geq 0.999$
- $P[\text{tip deflection in the axial direction} < 0.055 \text{ mm}] \geq 0.99$

The total cost is proportional to the inverse of the expected efficiency and a direct function of the weight. That is,

$$f = \frac{0.2}{E(\eta)} + C_w \quad (4.7)$$

where  $f$  is the objective function,  $\eta$  is the efficiency,  $C_w$  is the coefficient of weight, and  $E(\cdot)$  denotes the expected value of the enclosed quantity. The quantity 0.2 is a weighting factor that balances the relative contributions of the efficiency and weight terms to the overall cost.

The steady-state aerodynamic loads acting on the compressor blades as well as the blade row efficiency are determined using MTSB, a quasi-three-dimensional, inviscid turbomachinery analysis code [36]. The static response of the blade due to the aerodynamic and centrifugal loads is determined using NIKE3D, a nonlinear, implicit three-dimensional finite element code developed and distributed by Lawrence Livermore National Laboratory [37]. For this analysis, we couple the codes to account for the interaction between structural deflection and fluid load. Additionally, using a coupled analysis, the optimization provides the cold shape of the blade, which is required for manufacturing (i.e., an aerodynamics-only shape optimization produces the hot shape of the blade, and the cold shape would then be “backed out” by structural analyses).

#### 4.5.1.2 Design Variables and Random Variables

Three random shape-design variables shown in Table 4.1 are considered in the optimization. Two Bézier parameters define the blade twist distribution using the following three-point Bézier curve:

$$\beta(r) = \beta_0(1-r)^2 + 2\beta_1r(1-r) + \beta_2r^2 \quad (4.8)$$

where  $r$  denotes normalized radial station (i.e.,  $r = 0$  and  $r = 1$  correspond to the root and tip of the blade, respectively). The first Bézier twist parameter  $\beta_0$  is fixed at 50 degrees and controls the twist at the hub. The second and third Bézier twist parameters (i.e.,  $\beta_1$  and  $\beta_2$ ) are the random design variables with design ranges shown in Table 4.1.  $\beta_1$  and  $\beta_2$  are taken to be random variables due to uncertainties in the

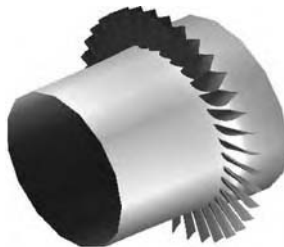


**FIGURE 4.5** Axial compressor geometry (NAS R37 single-blade-row compressor).

**TABLE 4.1** Random Design Variables for Axial Compressor Blade

Variable Name	Minimum	Maximum	Standard Deviation
Bézier twist parameter (degrees), $\beta_1$	-55	-35	3.0
Bézier twist parameter (degrees), $\beta_2$	0.25	1.0	3.0
Thickness scaling factor, $C_t$	0.75	1.25	0.05

manufacturing process. As a reasonable assumption, lognormal distributions with constant standard deviations of 3 degrees are used. The objective of RBDO is to optimize the mean values of  $\beta_1$  and  $\beta_2$ .

A blade thickness scaling factor  $C_t$  is taken to be the third random design variable and is used to linearly scale the thickness distribution of the blade, which is defined using the following three-point Bézier curve:

$$T(r) = T_0(1 - r)^2 + 2T_1 r(1 - r) + T_2 r^2 \quad (4.9)$$

where thickness parameters  $T_0$ ,  $T_1$ , and  $T_2$  are fixed at values of 0.250, 0.185, and 0.176, respectively. All of the design variables have a lognormal distribution. The uncertainty in the design variables simulates manufacturing uncertainty.

In addition to the design variables, the problem includes seven additional random variables. These variables are given in Table 4.2, along with their mean and coefficient of variation (COV). A lognormal distribution is assumed for each of these variables. Inaccuracies in the mechanical modeling are simulated by applying the random error factors shown in Table 4.2 to the analysis results. These random variables are included to recognize the fact that the aerostructural modeling and solution procedures are idealizations of real-world phenomena. The MTSB error factor is applied to the predicted blade-row efficiency; the NIKE3D error factor is applied to the predicted stress and displacement results. These scaling factors and the three material-property random variables are treated as single-occurrence random variables. Variations in the operational rotor speed  $V_0$  and uncertainties in the off-design or maximum rotor speed  $V_m$  represent two distinct random variables. Maximum off-design rotor speed uncertainty represents a single-occurrence random variable (since the maximum rotor speed occurs only once over the lifetime of the blade) that governs the constraints and therefore the reliability of the blade. Nominal rotor speed uncertainty represents an operational random variable that changes during a typical flight and affects the blade-row efficiency. Although it is possible to use a single experimental design to determine the blade response due to rotor speed, the design would need to cover a wide range to include the maximum rotor speed, and the accuracy of the resulting response-surface equations would likely be compromised. In order to properly simulate the effects of both single-occurrence and operational random variables, the nested-loop MCS algorithm described earlier is used.

**TABLE 4.2** Random Variables for Axial Compressor Blade

Variable Name	Mean	COV
Young's modulus (GPa)	81.4	0.10
Yield stress (MPa)	550	0.100
Endurance limit <sup>a</sup> (MPa)	138	0.125
MTSB model error	1.00	0.030
NIKE3D model error	1.00	0.060
Operational rotor speed (rpm)	9,330	0.018
Maximum rotor speed (rpm)	10,500	0.016

<sup>a</sup>Endurance limit ( $10^7$  cycles) taken from S-N diagram for Ti-6Al-4V at 482°C (900°F).

**TABLE 4.3** RBDO Results for Axial Compressor Blade

Case	$\beta_1$ (degrees)	$\beta_2$ (degrees)	$C_t$	$C_w$	$E(\eta)$	$f$
Baseline	-40.0	-30.0	1.00	0.243	0.921	0.460
Deterministic	-54.7	-39.8	0.750	0.182	0.944	0.394
Stochastic	-55.0	-40.0	0.882	0.214	0.942	0.427
Safety factor	-35.0	-40.0	1.25	0.304	0.904	0.525

#### 4.5.1.3 Results and Discussion

Results were obtained for four different cases:

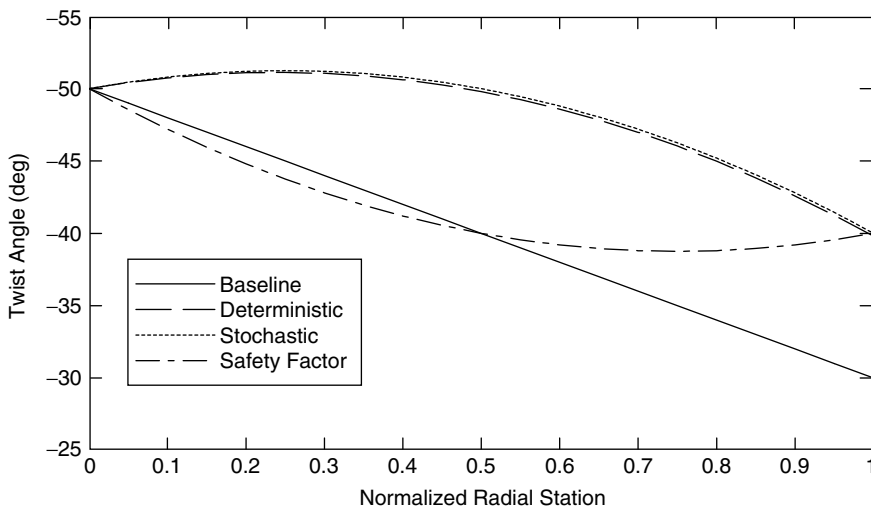
1. Baseline case representing the initial geometry of the axial compressor
2. Deterministic optimization
3. Stochastic optimization
4. Deterministic optimization using safety factors

For deterministic optimization (Cases 2 and 4), the random variables take on their mean values. The second deterministic optimization case (Case 4) was performed using a safety factor of 2.00 on the stress and fatigue constraints and a safety factor of 1.67 on the deflection constraints. That is,

$$\begin{aligned}\sigma_{\max} &< 0.5 \sigma_y \\ \sigma_c &< 0.5 \sigma_{cr} \\ \delta_R &< 0.030 \text{ mm} \\ \delta_A &< 0.033 \text{ mm}\end{aligned}$$

These safety factors introduce additional conservatism, in much the same way that a deterministic design would be performed in practice, by reducing the maximum allowable stresses and deflections by factors of 2 and 1.67, respectively.

The final numerical results for each case are summarized in Table 4.3. The final optimum values for  $\beta_1$ ,  $\beta_2$ , and  $C_t$  are tabulated along with the weight coefficient  $C_w$ , the expected efficiency  $E(\eta)$ , and the objective function value  $f$ . A plot of the twist distribution results is given in Figure 4.6, where the optimum twist angle is plotted as a function of the normalized radial position of the blade (i.e., 0 = blade root, 1 = blade tip). As shown in Table 4.3 and in Figure 4.6, the results for each case differ substantially from the baseline case and also from each other.

**FIGURE 4.6** Optimum twist angle vs. normalized radius.

Considering the deterministic optimization results first, the twist increases to its upper limit to improve the efficiency. The increase in twist at the end of the blade also serves to reduce the radial deflection and helps satisfy the tip-clearance constraint. The blade thickness decreases to its lower limit to reduce the weight. The deterministic optimization leads to a design where the objective function (total cost) is 14% less than the baseline case. However, this design will not be reliable under variable rotor speed conditions and manufacturing uncertainties. The design does satisfy the stress and fatigue reliability goals; however, it only achieves reliabilities of 0.854 (vs. 0.990) and 0.998 (vs. 0.999) for the axial deflection and tip-clearance constraints, respectively.

For the stochastic optimization, all of the stress and deflection constraints are now reliability based. As in the deterministic case, the twist increases to its upper limit to improve the efficiency and reduce the radial deflection. As shown in Figure 4.6, the optimal twist distribution for the stochastic case is essentially the same as that for the deterministic case. As shown in Table 4.3, the blade thickness once again decreases to reduce the weight. However, this time it stops at a value of 0.882, rather than decreasing to its lower limit of 0.750, in order to satisfy the reliability-based constraints for tip clearance and axial deflection. Note that it would be possible to reduce the axial deflection by reducing  $\beta_2$ ; however, this would significantly increase the radial deflection (which is more sensitive to  $\beta_2$ ) and violate the tip-clearance constraint. As such, the optimizer chooses to increase the thickness, at the expense of a higher blade weight, in order to maintain maximum efficiency and meet the deflection constraints. Ultimately, the stochastic optimization results yield a design with an overall cost that is 8% higher than the deterministic case. However, this design satisfies the specified reliability goals and should therefore perform reliably under extreme “off-design” variable rotor speed conditions and manufacturing uncertainties.

For the safety-factor case, the blade thickness increases to its upper limit to satisfy the tighter constraints on stress and deflection. However, this increase in thickness is not sufficient to satisfy the tip-clearance constraint. Thus, to reduce the radial deflection, the optimizer drives twist parameters  $\beta_1$  and  $\beta_2$  to their lower and upper limits, respectively. Although this twist configuration reduces the radial deflection by nearly 30%, it increases the axial deflection by almost 9%. Ultimately, even with this reduced twist and the thicker blade, the tip-deflection constraints are not completely satisfied: the axial and radial tip deflections exceed the limits by 37 and 31%, respectively. The reduced twist and larger weight of the safety-factor design lead to an overall cost that is 14% higher than the baseline case. This is because the safety factors used in this example were chosen somewhat arbitrarily, and they actually represent a solution that is more conservative with respect to the deflection constraints than the stochastic optimum. That is, the reliability levels for the stochastic optimum are 0.9996 for tip clearance and 0.990 for axial deflection, which match the target reliabilities of these constraints, whereas those for the safety-factor solution (which, in fact, did not meet the safety-factor goals due to bounds on the design variables) are 0.99996 for tip clearance and essentially 1.00 for axial deflection. Thus, the safety-factor solution is overdesigned for deflection.

## 4.5.2 Shape Optimization of an Airplane Wing

This example considers a detailed airplane wing design problem [38]. The baseline airplane is a Mach 0.3, 20-seat transport with a payload capacity on the order of 5000 lb.

### 4.5.2.1 RBDO Formulation

Objective: Maximize expected cruise range

Subject to reliability constraints:

$$P(\text{upper surface root stress } 1 \leq \text{yield}) \geq 99.0\%$$

$$P(\text{upper surface root stress } 2 \leq \text{yield}) \geq 99.0\%$$

$$P(\text{lower surface root stress } 1 \leq \text{yield}) \geq 99.0\%$$

$$P(\text{lower surface root stress } 2 \leq \text{yield}) \geq 99.0\%$$

$$P(\text{takeoff distance} \leq 3000 \text{ ft}) \geq 99.0\%$$

$$P(\text{wing area} \leq 600 \text{ ft}^2) \geq 50.0\%$$

**TABLE 4.4** Random Design Variables for Full-Featured Wing-Shape Optimization

Variable Name	Minimum	Maximum	COV
Aspect ratio, $AR$	6.0	12.0	0.0067
Taper ratio, $\lambda$	0.25	1.0	0.006
Semispan (ft), $b$	25.0	40.0	0.0002
Wingtip incidence (degrees), $i_{tip}$	-2	2	0.125
Structure skin thickness (in.)	0.07	0.12	0.01
Structure spar thickness (in.)	0.15	0.35	0.01
Wing sweep (degrees), $\Lambda_{LE}$	0.0	10.0	0.0002

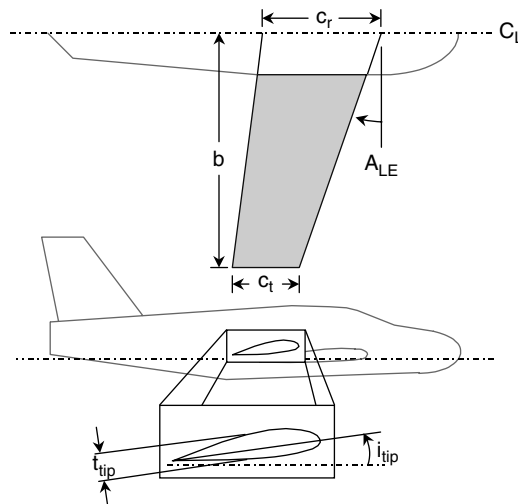
#### 4.5.2.2 Design and Other Random Variables

The wing design problem consists of random design variables, operational random variables, and single-occurrence random variables. In general, problems are formulated such that single-occurrence random variables affect constraint computations but not objective computations. The design variables themselves can be random, with the mean value being the designed value and the achieved value being a function of a random distribution about the designed mean.

The wing optimization example includes seven random design variables, given in Table 4.4. The table includes the minimum and maximum values as well as the coefficient of variation. All of the design variables have a normal distribution. The uncertainty in the design variables simulates manufacturing uncertainty. The skin thickness is the average thickness of the upper and lower wing skin, and is used as the thickness of all finite elements used to model the skin. The spar thickness is the average thickness of the wing spar, and is used as the thickness of all finite elements used to model the spar. The remaining variables are basic wing geometric parameters and are defined graphically in Figure 4.7.

In addition to the seven design variables, the problem includes ten additional random variables. These variables are given in Table 4.5 and are marked as being single-occurrence or operational.

A driver computer program called Cpanel manages the complete end-to-end deterministic analysis. Cpanel includes the following features: (1) geometry and grid generation subroutines to parametrically generate aerodynamic and structural grids for numerical methods; (2) a coupled aerostructural analysis

**FIGURE 4.7** Wing geometric parameters.

**TABLE 4.5** Random Variables for Full-Featured Wing-Shape Optimization

Variable Name	Mean	COV	Distribution
Single-occurrence			
Peak upward gust velocity (fps)	30.0	0.15	normal
Peak downward gust velocity (fps)	−30.0	0.15	normal
Skin Young's modulus (psf)	10.5 E+6	0.05	normal
Spar/rib Young's modulus (psf)	10.5 E+6	0.05	normal
Skin yield stress (psf)	5.76 E+6	0.10	lognormal
Material density (lb/in. <sup>3</sup> )	0.098	0.02	normal
Maximum takeoff altitude (ft)	4,000–6,000	0.20	truncated lognormal
Operational			
Cruise altitude (ft)	20,000–30,000	0.12	uniform
HP specific fuel consumption (lb/h/hp)	0.4–0.6	0.10	truncated lognormal
Payload (lb)	4,000–6,000	0.20	truncated lognormal

loop that uses aerodynamic and structural analysis programs to compute static aeroelastic deformation; and (3) analytic objective and constraint evaluation formulas.

The range objective is computed using the so-called constant-altitude, constant-airspeed flight program. The analytic function for this flight program requires the computation of maximum lift-to-drag ratio ( $E_{\max}$ ) as well as the lift-to-drag ratio ( $E_{\text{cruise}}$ ), and lift coefficient ( $C_{L,\text{cruise}}$ ) at the start of cruise. The latter is computed using the coupled aerostructural analysis code described later and is a direct function of the aircraft gross weight, the wing area, the Mach number, and altitude. All of these parameters are directly related to random design variables, operational random variables, and single-occurrence random variables, and so  $C_{L,\text{cruise}}$  is also random. In computing the lift-to-drag ratios, we assume a parabolic drag polar and a “typical” zero-lift drag coefficient of 0.025. We approximate an induced drag coefficient using the method of approximate spanwise efficiency and the method of leading-edge suction.

The wing design problem places probabilistic constraints on wing area, takeoff ground-roll distance at a maximum lifetime takeoff altitude, and wing root stress in a maximum lifetime upward or downward gust. We compute the takeoff ground roll distance using a piston-prop formula [39]. We select an approximate value of 2.0 for  $C_{L,\max}$  in the piston-prop formula, based on carpet plot data presented by Raymer [40].

The driver program, Cpanel, performs a static aeroelastic analysis by calling an external aerodynamics code and an external structural finite element analysis code. The coupled analysis predicts (a) the slope of the flexible wing lift curve,  $C_{L\alpha}$ , required for induced drag calculations and (b) the stress at four distinct points on the wing skin under maximum lifetime upward and downward gust loads.

Prior to driving the coupled analysis, Cpanel first generates structural and aerodynamic grids or meshes for the analyses. Once the geometry is meshed, Cpanel executes a sequential set of steps for each static coupled analysis, using the PMARC code [41] to compute pressure loads on the wing and COMET-AR [42] to compute deformation of the wing. The aerodynamic analysis is performed on the deformed shape in order to compute a lift coefficient for the flexible, deformed wing.

Stress values at the wing root are read from the COMET-AR results for two extreme loading conditions. Two upper-surface stresses are read for a maximum lifetime upward gust velocity. Two lower-surface stresses are read for a maximum lifetime downward gust velocity. Cpanel performs the coupled analyses for these extreme loading conditions at an adjusted angle of attack equal to the cruise angle of attack plus a perturbation due to a gust load perpendicular to the flight path. The analysis uses a gust alleviation factor described by Raymer [40] to account for the fact that the gust load is a transient effect that is not experienced instantaneously at full force.

**TABLE 4.6** RBDO Results for Full-Featured Wing-Shape Optimization

Variable Name	Initial	Case A	Case B	Case C
Aspect ratio, $AR$	9.0	12.0	12.0	10.98
Taper ratio	0.625	0.62	0.26	0.58
Semispan, $b$ (ft)	31.00	40.00	34.68	30.60
Wingtip incidence (degrees)	0.0	0.0	0.0	0.0
Structure skin thickness (in.)	0.095	0.070	0.0725	0.116
Structure spar thickness (in.)	0.25	0.35	0.35	0.26
Wing sweep (degrees)	5.0	5.0	5.0	5.0
Initial range (NM)	890.6	890.6	890.6	895.7
Optimal range (NM)	N/A	1024.7	984.7	974.9
Minimum constraint reliability (%)	99.9	38	96.0	99.0

#### 4.5.2.3 Results and Discussion

Three cases for a wing-shape optimization are selected as described below:

- Case A: six deterministic constraints with no safety factor on yield stress
- Case B: six deterministic constraints with safety factor of 1.5 on yield stress
- Case C: six probabilistic constraints (there are seven random design variables and ten nondesign random variables, as described)

The optimization results for all three cases are summarized in Table 4.6. The results indicate that the RBDO strategy is able to successfully find an optimum solution that effectively balances performance and reliability. Comparing the three cases, we see that while Case A provides the best performance, there is no safety factor applied, so the design will not be reliable. In fact, the final row in the table shows that the reliability of one of the stress constraints is only 38% (i.e., probability of exceeding yield stress is 62%), which is obviously unacceptable. Case B, with a safety factor of 1.5 on yield stress, is also able to improve on the original design while meeting the more stringent constraints; however, the safety factor of 1.5 is inadequate to ensure an acceptable reliability. The final row in the table shows that the reliability of the stress constraint is only 96% (still less than the required 99%). This illustrates the pitfall of using deterministic safety factors. There is no information on the true reliability of the structure. Hence, even though a safety factor has been applied, the wing is actually underdesigned relative to our required reliability of 99%. Case C, designed using the RBDO approach, is able to improve on the original design and still meet the reliability-based constraint. Although, for this problem, the RBDO results in a design that is more costly than the deterministic optimization (because the deterministic MDO [Multidisciplinary Design Optimization] does not meet the reliability goal), this will not be true for all cases. It is just as likely (perhaps even more likely) that the RBMDO could result in a less costly design.

Table 4.7 summarizes the values of stresses, takeoff distances, and wing areas at the optimums for the three cases. For Case A, the allowable stress is the yield stress of  $5.76 \times 10^6$  psf, and for Case B, the allowable stress is the yield stress divided by 1.5 (safety factor), or  $3.84 \times 10^6$  psf. The results for Case C

**TABLE 4.7** Information for Constraints at the Optimum Designs for Full-Featured Wing-Shape Optimization

Variable Name	Initial Design	Case A	Case B	Case C
Upper stress 1 ( $10^6$ psf)	−3.09	−5.74	−3.76	−3.66
Upper stress 2 ( $10^6$ psf)	−2.67	−4.99	−3.21	−3.18
Lower stress 1 ( $10^6$ psf)	1.16	1.53	1.38	1.65
Lower stress 2 ( $10^6$ psf)	1.06	1.40	1.25	1.47
Takeoff distance (ft)	1960.2	1404.6	2154.9	2751.2
Wing area (ft <sup>2</sup> )	427.1	533.3	400.9	340.9



are obtained by using the average values for the random design variables and mean values for the nondesign random variables. In addition to the advantages of the RBDO method discussed above, the RBDO approach also provides a better design than the one obtained with the deterministic approach (Case B). As can be seen from Table 4.7, the stress ranges at the upper and lower roots of the wing are narrower in Case C than in the first two cases. In other words, the load effects are more uniformly distributed to the components of the wing structures (skin and spar) compared with the deterministic design in Cases A and B. It can be seen from Table 4.6 that the skin and spar thicknesses are not as far apart as those in Cases A and B.

Thus, the RBDO results in a more balanced design. The objective is to maximize expected performance, accounting for all the uncertainties of the 17 random variables. This objective is subject to six probabilistic constraints, which again include the uncertainties of the random variables related to these constraints. Therefore, the final wing-shape configuration from the RBDO-based design procedure considers all uncertainties and provides the best performance in a sense of expectation, and it meets all the safety and serviceability criteria in a sense of probabilities. These conditions generally force a more balanced design because the aircraft must perform over a range of operating and extreme conditions, as represented by the random variables. On the other hand, the deterministic-based design procedure for Cases A and B maximizes the cruise range using seven design variables, while the other ten nondesign variables are set as constants (either reduced by a safety factor, set at the mean, or set at an upper/lower bound for the worst combinations). Therefore, the deterministic-based design procedure can drive the optimal point to an extreme location in the global design space, thus resulting in an unbalanced product configuration like that in Case B.

### 4.5.3 Optimization of an Integral Airframe Structure Step Lap Joint

An integral airframe structure (IAS) panel step lap joint [43] is considered in this example. Developed and tested by NASA and Boeing, this lap-joint design (see Figure 4.8) adopted a new concept that takes advantage of the monolithic construction process of the panel.

There are two main failure modes to be considered for the joints: longitudinal fatigue cracks due to high hoop stresses caused by internal pressurization and circumferential fatigue cracks due to vertical bending of the fuselage. However, the possibility of circumferential crack propagation at the top of the crown is fairly low, since a stronger butt splice is normally used for the circumferential skin splice. Hence, the longitudinal splice is the critical component. Therefore, the focus here was to perform a reliability-based fatigue analysis of the step lap joint and then attempt to improve the current design (redesign) using reliability-based optimization techniques.

The NASA Langley COMET-AR structural analysis code [42] was chosen to model and analyze this component during RBDO. For the fatigue life of the step lap joint, a cyclic stress to failure (S/N) approach

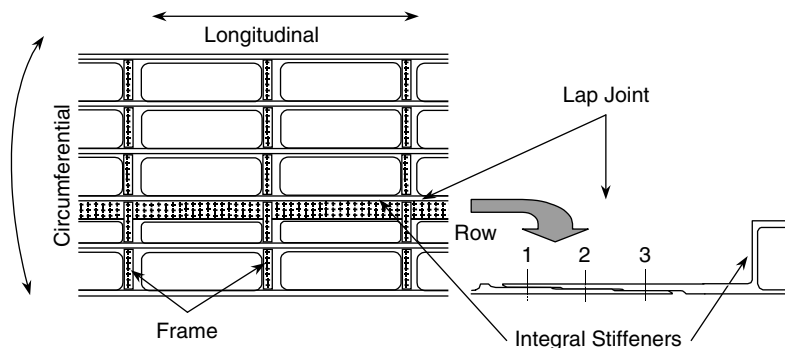


FIGURE 4.8 IAS panel with longitudinal lap joint.

**TABLE 4.8** Random Design Variables for Lap-Joint Optimization

Variable Name	Minimum	Nominal	COV
$lt_1$ (in.)	0.06	0.06	0.01
$lt_2$ (in.)	0.06	0.085	0.01
$lt_3$ (in.)	0.06	0.11	0.01
$lt_4$ (in.)	0.06	0.17	0.01
$rt_1$ (in.)	0.06	0.06	0.01
$rt_2$ (in.)	0.06	0.085	0.01
$rt_3$ (in.)	0.06	0.11	0.01
$rt_4$ (in.)	0.148	0.17	0.01

is used that applies the maximum stresses (stress concentrations) near the rivets to the corresponding fitted equation [MIL-HDBK] [44]:

$$\log(N_f) = 10.0 - 3.96 \log(S_{eq}) + \epsilon \quad (4.10)$$

where  $S_{eq} = S_{max} (1.0 - R)^{0.64}$ ,  $N_f$  is the number of cycles to failure, and  $R$  is the stress ratio of the minimum to maximum cyclic stresses.  $S_{max}$  is the applied maximum stress (ksi). The error in the failure life estimation is given by  $\epsilon$ .

#### 4.5.3.1 RBDO Formulation

Objective: Minimize the weight

Subject to reliability constraint:

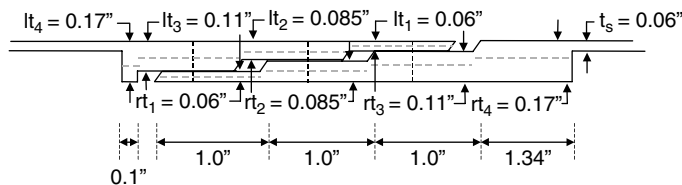
$$P(\text{Design life cycle} \geq 20,000) \geq 99.9\%$$

#### 4.5.3.2 Design and Other Random Variables

This lap-joint problem considers uncertainties in the fatigue life of the base material and elastic material properties, the loading conditions, and the manufacturing tolerances.

The stepped lap-joint optimization example includes eight random design variables for the thicknesses, given in Table 4.8 and depicted in Figure 4.9. The table includes the minimum and nominal values as well as the coefficient of variation. All of the design variables have a lognormal distribution. The uncertainty in the design variables simulates manufacturing uncertainty.

In addition to the random design variables, the problem includes four additional random variables. The uncertainty in the fatigue law (cycles to failure), as quantified by the parameter  $\epsilon$  (Equation 4.13), was obtained from the Military Handbook. The uncertainties for modulus ( $E$ ) and Poisson's ratio ( $\sigma$ ) were assumed to take on typical values of 5% coefficient of variation. The uncertainty of 5% on the load and of 1% on the thicknesses was obtained during discussions with the Boeing designers. All the random variables, with their mean values, coefficients of variation, and the distributions used for the analysis, are tabulated in Table 4.9.

**FIGURE 4.9** Current design dimensions of the stepped lap joint.

**TABLE 4.9** Input Random Variables for Lap-Joint Optimization

Input Variable	Mean	COV	Distribution
$\epsilon$	0.0	0.248 <sup>a</sup>	normal
$P_{\max}$	18.0 ksi	0.05	lognormal
$E$	$1.03 \times 10^7$ psi	0.05	lognormal
$n$	0.3205	0.05	lognormal

<sup>a</sup> Standard deviation.

#### 4.5.3.3 Results and Discussion

The optimized values are shown in Figure 4.10. The objective function  $f_1$  for the original design is 0.85, while the optimized objective function obtained was 0.631. The weight factor associated with the optimized design was 0.61104 (as opposed to the 0.7361 weight factor of the original design), which is a 17% reduction in the weight of the lap joint while maintaining the reliability requirement.

#### 4.5.4 Transport Aircraft Wing Optimization

The reliability-based structural optimization of a full-scale transport aircraft wing [45] is considered, and the optimized design and performance characteristics obtained using RBDO are compared with those from deterministic optimization. The ACT S/RFI composite wing box of the advanced composite technology (ACT) wing from the Boeing Company was used for the RBDO analysis. The baseline aircraft selected for this demonstration is the D-3308-4 configuration of the proposed Boeing 190-passenger, two-class transport aircraft.

The design weights for this aircraft are maximum takeoff gross weight (MTOGW) = 180 kips and maximum landing weight (MLW) = 167.5 kips. The critical design conditions for this composite wing box were derived from the DC-10-10 and MD-90-30 aircraft loads for 2.5-g positive balance flight maneuver (upbending). The semispan composite wing external loads are applied to eight discrete actuator load points on the test article shown in Figure 4.11. The discrete loads are adjusted to best approximate the shears, moments, and torques of the flight and ground conditions. The semispan test article consists of upper and lower cover panels and front and rear spars, ribs, and bulkheads, as shown in Figure 4.12. The major components are the cover panels. Each contains skin, stringers, spar caps, and intercostal clips. These subcomponents are stitched together to form a single dry-fiber preform, which is then filled with resin and cured by the resin film infusion (RFI) process.

##### 4.5.4.1 RBDO Formulation

Objective: Minimize expected weight of the wing

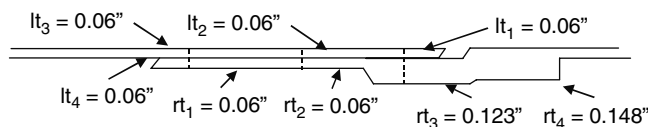
Subject to reliability constraints:

$$P(\text{maximum Von-Mises stress} \leq \text{yield}) \geq \text{target reliability}$$

$$P(\text{maximum wingtip displacement} \leq \text{tolerance}) \geq \text{target reliability}$$

##### 4.5.4.2 Design and Other Random Variables

Probabilistic constraints were evaluated with MSC/NASTRAN using the CAD/CAE interface capability built in ProFES/MDO. The finite element model of the wing is shown in Figure 4.13.

**FIGURE 4.10** Optimized design configuration of the stepped lap joint.

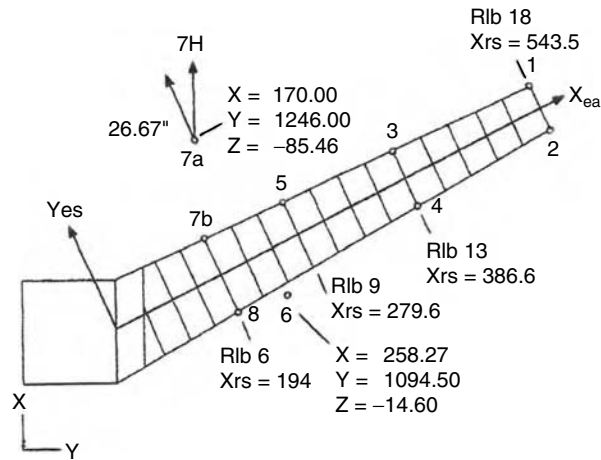


FIGURE 4.11 Actuator load points for semispan composite wing box.

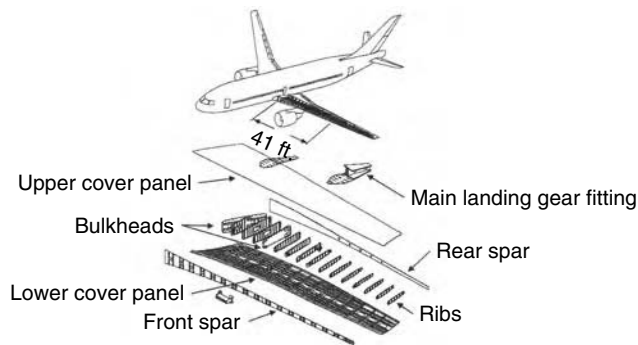
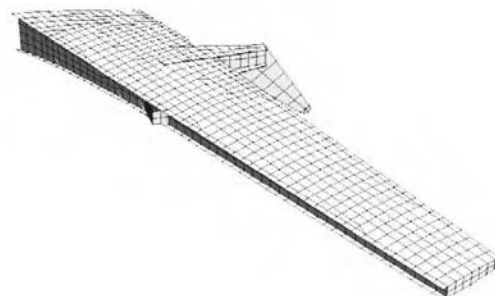


FIGURE 4.12 Baseline aircraft configuration and semispan structural arrangement.



3804 FE nodes  
 3770 FE elements (2222 Shells + 1548 Beams)  
 22 material properties  
 47 shell element properties (PSHELL)

FIGURE 4.13 Finite element model of transport aircraft wing.

**TABLE 4.10** Description of the Design Variables for Transport Aircraft Wing Optimization

Variable Name	Initial Design	Minimum	Maximum	Standard Deviation	Description
T1 (in.)	0.55	0.385	0.715	0.005	upper skin panel thickness
T2 (in.)	0.33	0.297	0.363	0.005	lower skin panel thickness
T3 (in.)	0.385	0.296	0.501	0.005	front spar panel thickness
T4 (in.)	0.385	0.296	0.501	0.005	rear spar panel thickness
T5 (in.)	0.149	0.104	0.194	0.005	rib panel thickness

The design random variables are chosen to be the thickness of the shell sections that contribute the most weight to the wing. The two design random variables T1 and T2 are the thickness of shell sections on the upper and lower skin panel, and they are the biggest weight contributors to the wing, with total weights of 251.38 and 152.44 lb, respectively. The other three random variables, T3, T4, and T5, are the respective thicknesses of shell section on the front spar panel, the rear spar panel, and on the rib panels. They are the next weight contributors to the wing in their corresponding sections, with total weights of 125.03, 116.36, and 59.08 lb, respectively. Table 4.10 shows the minimum and maximum values of the five design random variables as well as their coefficients of variation. All of the design variables have a normal distribution. The uncertainty in the design variables simulates manufacturing uncertainty.

In addition to the five design variables, the uncertainty on material property ( $E_{11}$ ) of the lower skin panels is considered, and it is shown in Table 4.11. For the material strength and displacement tolerances, the deterministic values are used. Figure 4.14 shows the finite elements in each section to which the design and random variables are assigned.

#### 4.5.4.3 Results and Discussion

Three cases for reliability-based optimization are selected as described below:

- Case A: Minimize the weight while keeping the same reliability as the one in the initial design
- Case B: Minimize the weight while increasing the reliability by a factor of 10
- Case C: Minimize the weight while increasing the reliability by a factor of 100

The optimization results for all three cases are summarized in Table 4.12.

The results in Table 4.12 show that the optimal design is achieved by transferring material to sections in the upper and lower skin panels from the rib and spar panels. It also shows that the optimal design reduces the weight by 25.02 lb from that of the initial design (i.e., 3.6% weight reduction in the five sections considered) while keeping the reliability of the new design the same as that of the initial design. From the results for Cases B and C, the optimal design still reduced the weight from that of the initial design while improving the reliability of the design by factors of 10 and 100, respectively.

Figure 4.15 shows a comparison of the initial design with the three optimal designs described above. The numbers in the figure show the ratio of the weight for the optimal design as compared with the initial design for various factors of improvement in reliability. The ratios shown in the figure are for the weight of the five sections in the initial design (with the total weight of 704.29 lb) and the weight of the same five sections in the optimal designs. We should note that in this study, the weight of these five sections constitutes only 8.5% of the total weight of the wing, and it would be a natural conclusion that more weight savings could be achieved if all shell sections as well as the beams in the model were treated as design random variables.

**TABLE 4.11** Description of the Random Variables for Transport Aircraft Wing Optimization

Variable Name	Mean	COV	Distribution	Description (unit)
R1	$1.21 \times 10^7$	$1.21 \times 10^5$	normal	$E_{11}$ of lower skin panels (psi)

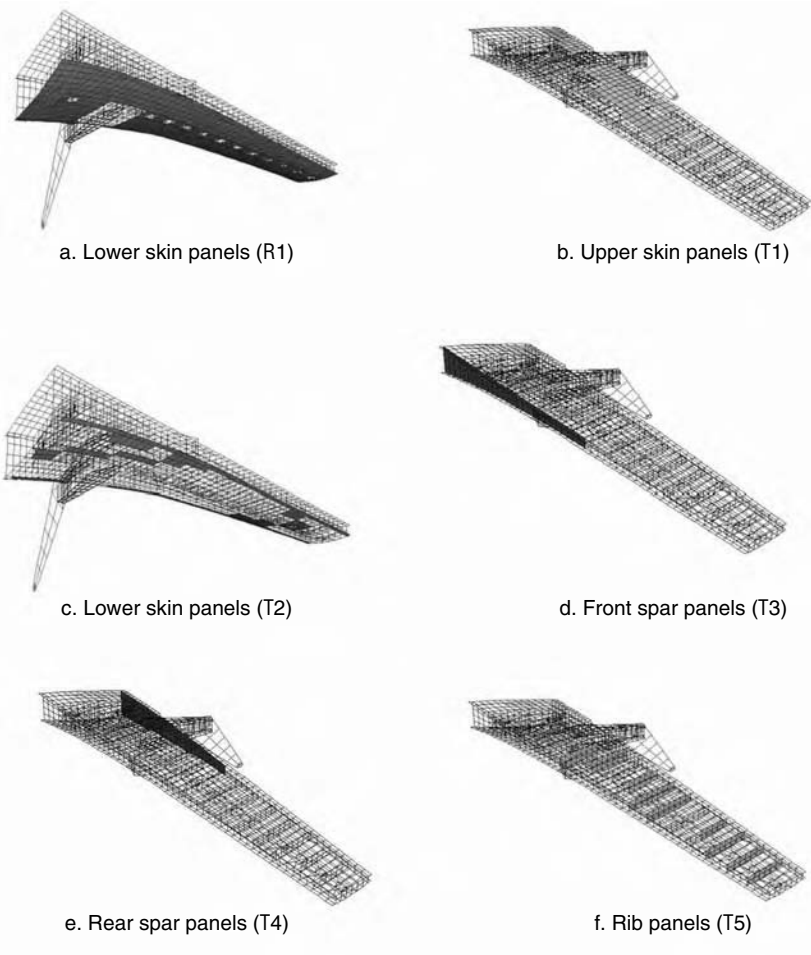


FIGURE 4.14 Design sections of transport aircraft wing.

## 4.6 Conclusions

Recent advances in reliability and RBDO computational methods have allowed designers to treat a wide range of application problems in many technical areas where there is a need to incorporate uncertainties into design optimization. This chapter summarized the methods, gave a brief overview of the RBDO

TABLE 4.12 Results of the ProFES/MDO for Transport Aircraft Wing Optimization

Variable Name	Initial Design	Optimal Design		
		Case A	Case B	Case C
T1 (in.)	0.55	0.5581	0.5512	0.5625
T2 (in.)	0.33	0.3328	0.3563	0.3630
T3 (in.)	0.385	0.3465	0.3465	0.3465
T4 (in.)	0.385	0.3465	0.3465	0.3466
T5 (in.)	0.149	0.1341	0.1341	0.1341
Objective (lb)	8275.22	8250.20	8257.90	8266.15
Weight of five sections (lb)	704.29	679.27	686.97	695.12

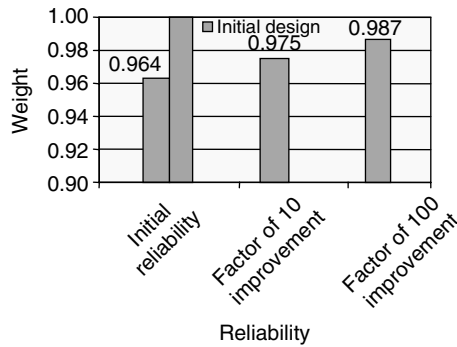


**FIGURE 4.15** Comparison of initial design with optimal designs using the RBDO methodology on the semispan composite wing box subjected to 2.5-g upbending load.

applications, and presented several examples with some details. These examples demonstrated that RBDO produced more cost-effective and reliable designs than the deterministic-based designs.

The field of optimization has seen rapid advancement from single-discipline optimization to multi-disciplinary optimization. However, even with efficient optimization/probabilistic-analysis algorithms and computational resources, the application of RBDO to large-scale multidisciplinary problems is still computationally demanding. Further research and development is needed to allow the practical incorporation of RBDO concepts to large-scale multidisciplinary optimization problems.

## References

1. Montgomery, D.C., *Design and Analysis of Experiments*, John Wiley and Sons, New York, 1991.
2. NIST/SEMATECH, e-Handbook of Statistical Methods, <http://www.itl.nist.gov/div898/handbook/>, 2004.
3. Fu, Y., Chuang, C.H., Li, G., and Yang, R.J., Reliability-Based Design Optimization of A Vehicle Exhaust System, 2004-01-1128, presented at SAE World Congress and Exhibition, Detroit, MI, 2004.
4. Li, G. and Yang, R.J., Recent Applications on Reliability-Based Optimization of Automotive Structures, 2003-01-0152, presented at SAE World Congress and Exhibition, Detroit, MI, 2003.
5. Madsen, H.O., Krenk, S., and Lind, N.C., *Methods of Structural Safety*, Prentice Hall, Englewood Cliffs, NJ, 1986.
6. Ang, A.H.S. and Tang, W.H., *Probability Concepts in Engineering Planning and Design*, Vol. II, *Decision, Risk, and Reliability*, John Wiley & Sons, New York, 1984.
7. Der Kiureghian, A., Lin, H.-Z., and Hwang, S.-J., Second-order reliability approximations, *J. Eng. Mech.*, 113 (8), 1208–1225, 1987.
8. Wen, Y.K. and Chen, H.C., On fast integration for time variant structural reliability, *Probabilistic Eng. Mech.*, 2 (3), 156–162, 1987.
9. Liu, P.L. and Der Kiureghian, A., Optimization Algorithms for Structural Reliability Analysis, report UCB/SESM-84/01, Dept. of Civil Engineering, University of California at Berkeley, 1986.
10. Kuschel, N., Rackwitz, R.R., and Pieracci, A., Multiple Points in Structural Reliability, presented at 3rd International Conference on Computational Stochastic Mechanics, Thera-Santorini, Greece, 1998.
11. Der Kiureghian, A. and Dakessian, T., Multiple design points in first- and second-order reliability, *Structural Safety*, 20, 37–49, 1998.
12. Fujita, M. and Rackwitz, R., Updating first- and second-order reliability estimates by importance sampling, *Structural Eng./Earthquake Eng.*, 5 (1), 53–59, 1988.

13. Hohenbichler, M. and Rackwitz, R., Improvement of second-order reliability estimates by importance sampling, *ASCE J. Eng. Mech.*, 114 (12), 2195–2199, 1988.
14. Au, S.K. and Beck, J.L., First-excursion probabilities for linear systems by very efficient importance sampling, *Probabilistic Eng. Mech.*, 16 (3), 193–207, 2001.
15. Au, S.K. and Beck, J.L., Estimation of small failure probabilities in high dimensions by subset simulation, *Probabilistic Eng. Mech.*, 16 (4), 263–277, 2001.
16. Wu, Y.-T. and Mohanty, S., Variable screening and ranking using several sampling based sensitivity measures, in *Proceedings of 44th Structures, Structural Dynamics, and Materials Conference*, AIAA/ASME/ASCE/AHS, Norfolk, VA, 2003; submitted to *Reliability Eng. System Safety*, 2003.
17. Yang, R.J. and Gu, L., Experience with approximate reliability-based optimization methods, in *Proceedings of 44th Structures, Structural Dynamics, and Materials Conference*, AIAA/ASME/ASCE/AHS, AIAA 2003–1781, Norfolk, VA, 2003.
18. Chen, X., Hasselman, T.K., and Neill, D.J., Reliability based structural design optimization for practical applications, in *Proceedings of 38th Structures, Structural Dynamics, and Materials Conference*, AIAA/ASME/ASCE/AHS, AIAA 97–1403, Kissimmee, FL, 1997.
19. Wu, Y.-T. and Wang, W., Efficient probabilistic design by converting reliability constraints to approximately equivalent deterministic constraints, *J. Integrated Design Process Sci. (JIDPS)*, 2 (4), 13–21, 1998.
20. Wu, Y.-T., Shin, Y., Sues, R.H., and Cesare, M.A., Safety-factor based approach for probability-based design optimization, in *Proceedings of 42nd Structures, Structural Dynamics, and Materials Conference*, AIAA 2001-1379, AIAA/ASCE/AHS/ASC, Seattle, WA, 2001.
21. Du, X. and Chen, W., Sequential Optimization and Reliability Assessment Method for Efficient Probabilistic Design, DETC2002/DAC-34127, presented at ASME Design Engineering Technical Conferences, Montreal, 2002.
22. Sues, R.H. and Rhodes, G.S., Portable Parallel Stochastic Optimization for the Design of Aeropropulsion Components, NASA-CR 195312, ARA Report No. 5786, 1993.
23. Sues, R.H., Oakley, D.R., and Rhodes, G.S., MDO of Aeropropulsion Components Considering Uncertainty, presented at the 6th AIAA/NASA/USAF Multidisciplinary Analysis and Optimization Symposium, Bellevue, WA, 1996.
24. Oakley, D.R., Sues, R.H., and Rhodes, G.S., Performance optimization of multidisciplinary mechanical systems subject to uncertainties, *Probabilistic Eng. Mech.*, 13 (1), 15–26, 1998.
25. Frangopol, D.M. and Maute, K., Life-cycle reliability-based optimization of civil and aerospace structure, *Comput. Struct.*, 81, 397–410, 2003.
26. Davidson, J.W., Felton, L.P., and Hart, G.C., On reliability-based structural optimization for earthquakes, *Comput. Struct.*, 12, 99–105, 1980.
27. Feng, Y.S. and Moses, F., Optimum design, redundancy and reliability of structural systems, *Comput. Struct.*, 24 (2), 239–251, 1986.
28. Yang, J.S. and Nikolaidis, E., Design of aircraft wings subjected to gust loads: a safety index based approach, *AIAA J.*, 29 (5), 804–812, 1991.
29. Pu, Y., Das, P.K., and Faulkner, D., A strategy for reliability-based optimization, *Eng. Struct.*, 19 (3), 276–282, 1997.
30. Stroud, W., Krishnamurthy, T., Mason, B., Smith, S., and Naser, A., Probabilistic design of a plate-like wing to meet flutter and strength requirements, in *Proceedings of 43rd Structures, Structural Dynamics, and Materials Conference*, AIAA 2002-1464, AIAA/ASCE/AHS/ASC, Denver, CO, 2002.
31. Pettit, C. and Grandhi R., Multidisciplinary Optimization of Aerospace Structures with High Reliability, in *Proceedings of 8th ASCE Joint Specialty Conference on Probabilistic Mechanics and Structural Reliability*, ASCE, Reston, VA, 2000.
32. Grandhi, R.V. and Wang, L., Reliability-based structural optimization using improved two-point adaptive nonlinear approximations, *Finite Elements Analysis Design*, 29, 35–48, 1998.



33. Yang, R.J., Gu, L., Tho, C.H., Choi, K.K., and Youn, B.D., Reliability-based multidisciplinary design optimization of a full vehicle system, in *Proceedings of 43rd Structures, Structural Dynamics, and Materials Conference*, AIAA 2002-1758, AIAA/ASCE/AHS/ASC, Denver, CO, 2002.
34. Sues, R.H., Oakley, D.R., and Rhodes, G.S., Portable Parallel Computing for Multidisciplinary Stochastic Optimization of Aeropropulsion Components, NASA contractor report 202307, NASA contract NAS3-27288, 1996.
35. Sues, R.H. and Cesare, M.A., An innovative framework for reliability-based MDO, in *Proceedings of 41st Structures, Structural Dynamics, and Materials Conference*, AIAA-2000-1509, AIAA/ASCE/AHS/ASC, Atlanta, GA, 2000.
36. Boyle, R.J., Haas, J.E., and Katsanis, T., Comparison between measured turbine stage performance and the predicted performance using quasi-3D flow and boundary layer analyses, *J. Propulsion Power*, 1, 242–251, 1985.
37. Hallquist, J., NIKE3D: an Implicit, Finite-Deformation, Finite Element Code for Analyzing the Static and Dynamic Response of Three-Dimensional Solids, report UCID-18822, Lawrence Livermore National Laboratory, University of California, Livermore, CA, 1984.
38. Xiao, Q., Sues, R.H., and Rhodes, G.S., Multi-disciplinary wing shape optimization with uncertain parameters, in *Proceedings of 40th Structures, Structural Dynamics, and Materials Conference*, AIAA 99-1601, AIAA/ASCE/AHS/ASC, St. Louis, MO, 1999.
39. Hale, F.J., *Aircraft Performance, Selection, and Design*, John Wiley & Sons, New York, 1984.
40. Raymer, D.P., *Aircraft Design: a Conceptual Approach*, AIAA Education Series, Reston, VA, 1992.
41. Ashby, D.L. et al., Potential Flow Theory and Operation Guide for the Panel Code PMARC, NASA TM-102851, 1991.
42. Stanley, G. et al., Computational Mechanics Testbed with Adaptive Refinement User's Manual, NASA contract report, 1998.
43. Fadale, T. and Sues, R.H., Reliability-based analysis and optimal design of an integral airframe structure lap joint, in *Proceedings of 9th International Space Planes and Hypersonic Systems and Technology Conference*, AIAA 99-1604, AIAA/ASCE/AHS/ASC, Norfolk, VA, 1999.
44. *Military Handbook 5G—Metallic Materials and Elements for Aerospace Vehicle Structures*, Vol. 1 and 2, 1994.
45. Aminpour, M.A., Shin, Y., Sues, R.H., and Wu, Y.-T., A framework for reliability-based MDO of aerospace systems, in *Proceedings of 43rd Structures, Structural Dynamics, and Materials Conference*, AIAA 2002-1476, AIAA/ASCE/AHS/ASC, Denver, CO, 2002.

# 5

## Probabilistic Progressive Buckling of Conventional and Adaptive Trusses

---

5.1	Introduction .....	5-1
5.2	Fundamental Approach and Considerations .....	5-2
	Finite Element Model • Buckling of Columns • Probabilistic Model • Probabilistic Progressive Buckling of Conventional Trusses	
5.3	Discussion of Results .....	5-5
	Probabilistic Progressive Buckling: First Buckled Member • Probabilistic Progressive Buckling: Second/Third/Fourth Buckled Members • Probabilistic Truss End-Node Displacements • Probabilistic Buckling Including Initial Eccentricity	
5.4	Adaptive/Smart/Intelligent Structures .....	5-15
5.5	Discussion of Results .....	5-18
	Adaptive Structure • Smart Structure • Intelligent Structure	
5.6	Summary.....	5-26
	References.....	5-26

Shantaram S. Pai

Christos C. Chamis

*NASA Glenn Research Center*

### 5.1 Introduction

---

It is customary to evaluate the structural integrity of trusses by using deterministic analysis techniques and appropriate load/safety factors. Traditionally, these factors are an outcome of many years of analytical, as well as experimental, experience in the areas of structural mechanics/design. Load factors are used to take into account uncertainties in many different operating conditions, including the maximum loads. Safety factors are used to account for unknown effects in analysis assumptions, fabrication tolerances, and material properties.

An alternative to the deterministic approach is the probabilistic analysis method (PSAM) [1]. This method formally accounts for various uncertainties in primitive variables (fundamental parameters describing the structural problem) and uses different distributions such as the Weibull, normal, lognormal, etc., to define these uncertainties. Furthermore, PSAM assesses the effects of these uncertainties on the scatter of structural responses (displacements, frequencies, eigenvalues). Thus, PSAM provides a more realistic and systematic way to evaluate structural performance and durability. A part of PSAM is a computer code NESSUS (numerical evaluation of stochastic structures under stress), which provides a choice of solution for static, dynamic, buckling, and nonlinear analysis [2, 3].

In the recent past, NESSUS has been used for the analysis of space shuttle main engine (SSME) components. Representative examples include a probabilistic assessment of a mistuned bladed disk assembly [4] and an evaluation of the reliability and risk of a turbine blade under complex service environments [5]. Furthermore, NESSUS has also been used to computationally simulate and probabilistically evaluate a cantilever truss typical for outer-space-type structures [6] and quantify the uncertainties in the structural responses (displacements, member axial forces, and vibration frequencies). The objective of this chapter is to develop a methodology and to perform probabilistic progressive buckling assessment of space-type trusses using the NESSUS computer code. The space trusses evaluated include trusses with and without adaptive structural concepts: specifically, adaptive, smart, and intelligent structures. The implementation of each of these is described in detail in the Section 5.4, which discusses adaptive/smart/intelligent structures.

## 5.2 Fundamental Approach and Considerations

One of the major problems encountered in the analysis of space-type trusses is to come up with a stable and optimum configuration for given loading conditions and to be able to probabilistically analyze them to take into account the probable uncertainties in the primitive variables typical for environment conditions in outer space. Presently, it is a practice to design these trusses with cross bracings, thereby increasing the overall weight of the truss, the cost of fabrication, and the effort to deploy in space. Furthermore, the presently available methods/programs do not easily allow us to identify any local instability in any of the internal members of the truss during probabilistic buckling (eigenvalue) analysis and to calculate overall margins of safety of the truss.

A probabilistic methodology for analyzing progressive buckling has been developed using the NESSUS code. The method is described in this chapter.

### 5.2.1 Finite Element Model

A three-dimensional, three-bay cantilever truss is computationally simulated using a linear isoparametric beam element based on the Timoshenko beam equations. The element is idealized as a two-noded line segment in three-dimensional space. The cantilever truss is assumed to be made from hollow circular pipe members. The members are made up of wrought aluminum alloy (616-W) with modulus of elasticity ( $E$ ) equal to 10 Mpsi. The outer and inner radii ( $r_o$  and  $r_i$ ) of the tube are 0.5 and 0.4375 in., respectively. All six degrees of freedom are restrained at the fixed end (left side) nodes. Each bay of the truss is 5 ft wide, 8 ft long, and 6 ft high (Figure 5.1). The overall length of the truss is 24 ft. Six vertical and two longitudinal loads

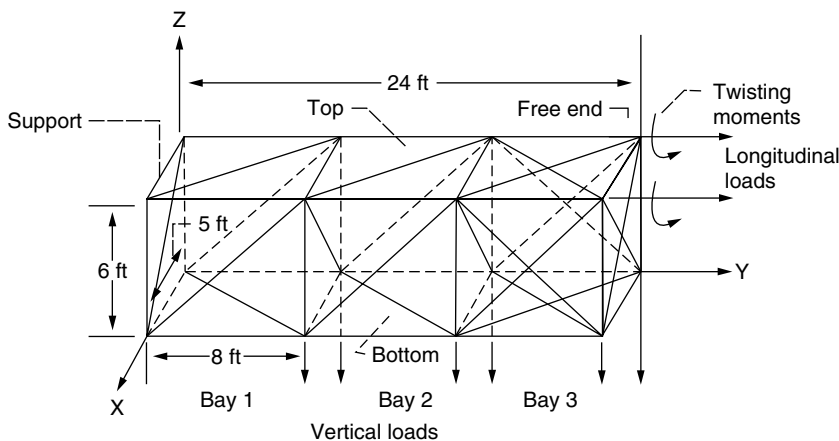


FIGURE 5.1 Solar-array panels mast — typical truss.

**TABLE 5.1** Primitive Variables and Uncertainties for Probabilistic Structural Analysis of a Space Truss

Primitive Variables		Distribution Type	Mean Value	Scatter, $\pm$ Percent
Geometry	Width	Normal	60 in.	0.5
	Length	Normal	96 in.	0.1
			192 in.	0.1
			288 in.	0.1
			72 in.	0.2
Loads	Vertical	Lognormal	20 lb	6.3
	Longitudinal	Lognormal	20 lb	2.5
	Twisting moment	Lognormal	50 lb-in.	6.3
Material property	Modulus	Normal	10 Mpsi	7.5
Tube radii	Outer radius	Normal	0.5 in.	7.5
	Inner radius	Normal	0.44 in.	7.5

Note: Random input data.

are applied. In addition, twisting moments are applied at the truss-end nodes. The directions of the forces and moments are shown in Figure 5.1, and mean values are given in Table 5.1. The applied loads and moments are selected to represent anticipated loading conditions for a typical space-type truss.

In general, the finite element equation for motion is written as:

$$[M]\{\ddot{u}\} + [C]\{\dot{u}\} + [K]\{u\} = F(t) \quad (5.1)$$

where  $[M]$ ,  $[C]$ , and  $[K]$  denote the mass, damping, and stiffness matrices, respectively. It is important to note that these matrices are calculated probabilistically in the NESSUS code. Furthermore,  $\{\ddot{u}\}$ ,  $\{\dot{u}\}$ , and  $\{u\}$  are the acceleration, velocity, and vectors at each node, respectively. The forcing function vector,  $\{F(t)\}$ , is time independent at each node.

In this discussion, the static case is considered by setting the mass and damping matrices to zero and considering the forcing function to be independent of time in Equation 5.1, such that

$$[K]\{u\} = \{F\} \quad (5.2)$$

It is important to note that in the NESSUS code, a linear buckling analysis is carried out using a subspace iteration technique to evaluate the probabilistic buckling load. The matrix equation for the buckling (eigenvalue) analysis for a linear elastic structure is as follows:

$$\{[K] - \lambda[K_g]\}\{\Phi\} = 0 \quad (5.3)$$

In Equation 5.3,  $[K]$  is the standard stiffness matrix,  $[K_g]$  is the geometric stiffness matrix,  $\lambda$  is the eigenvalue, and  $\Phi$  represents the eigenvectors.

Furthermore, the vibration frequency analysis is also carried out by setting only the damping matrix to zero and using the following equation:

$$\{[K] - \lambda^2[M]\}\{\Phi\} = 0 \quad (5.4)$$

Finally, the NESSUS/FPI (fast probability integration) module extracts the response variables (buckling loads, vibration frequencies, and member axial forces) to calculate respective probabilistic distributions and respective sensitivities associated with the corresponding uncertainties in the primitive variables. The mean, distribution type, and percentage variation for each of the primitive variables are given in Table 5.1.

### 5.2.2 Buckling of Columns

In slender columns, a relatively small increase in the axial compressive forces will result only in axial shortening of the member. However, the member suddenly bows out sideways if the load level reaches a certain critical level. Large deformations caused by an increase in the induced bending moment levels may lead to the collapse of the member. On the other hand, tension members as well as short stocky columns fail when the stress in the member reaches a certain limiting strength of the material. According to Chajes [7], “Buckling, however, does not occur as a result of the applied stress reaching a certain predictable strength of the material. Instead, the stress at which buckling occurs depends on a variety of factors, including the dimensions of the member, the way in which the member is supported, and the properties of the material out of which the member is made.” Chajes also describes the concept of neutral equilibrium that is being used to determine the critical load of a member such that, at this load level, the member can be in equilibrium both in the straight and in a slightly bent configuration. Furthermore, the Euler load (buckling load or critical load) is the smallest load at which a state of neutral equilibrium is possible or the member ceases to be in stable configuration. This above definition of buckling load is used to identify the probable truss members that contribute to the progressive buckling behavior of the cantilever truss.

### 5.2.3 Probabilistic Model

The following primitive variables are considered in the probabilistic analysis:

- Nodal coordinates ( $X, Y, Z$ )
- Modulus of elasticity ( $E$ )
- Outer radius of the tube ( $r_o$ )
- Inner radius of the tube ( $r_i$ )
- Vertical loads ( $V$ )
- Longitudinal loads ( $H$ )
- Twisting moments ( $M$ )
- Variables associated with adaptive/smart/intelligent structures, as described later

It is possible that the above primitive variables will vary continuously and simultaneously due to extreme changes in the environment when such trusses are used in upper Earth orbit for space-station-type structures. The normal distribution is used to represent the uncertainties in  $E$ ,  $r_o$ ,  $r_i$ , and  $X, Y, Z$  coordinates. The applied loads and moments are selected to represent an anticipated loading for a typical space-type truss. The scatter in these is represented by lognormal distributions. Initially, the NESSUS/FEM (finite element methods) module is used to deterministically analyze the truss for mean values of each of these primitive variables. In the subsequent probabilistic analysis, each primitive variable is perturbed independently and by a different amount. Usually, the perturbed value of the primitive variable is obtained by a certain factor of the standard deviation on either side of the mean value. It is important to note that, in the NESSUS code, a linear buckling analysis is carried out by making use of the subspace iteration technique to evaluate the probabilistic buckling load (see Equation 5.3). Finally, the NESSUS/FPI (fast probability integration) module extracts eigenvalues to calculate a probability distribution of the eigenvalues and to evaluate respective sensitivities associated with the corresponding uncertainties in the primitive variables. The mean, distribution type, and percentage variation for each of the primitive variables are given in Table 5.1.

### 5.2.4 Probabilistic Progressive Buckling of Conventional Trusses

Initially, the truss is deterministically analyzed for member forces and to identify the members in which the axial forces exceed the Euler load. These members are then discretized with several intermediate nodes, and a probabilistic buckling (eigenvalue) analysis is performed to obtain probabilistic buckling loads and respective buckled shapes. Furthermore, the sensitivity factors representing the impact of uncertainties in

the primitive variables on the scatter of response variable (eigenvalue) are evaluated. Finally, any members that have buckled are identified, and the probabilistic buckled loads/moments at each probability level are obtained by multiplying the respective eigenvalues with the applied loads and moments.

In the subsequent analyses, the buckled members are removed from the original truss configuration, and the above-described analysis steps are repeated until the onset of the collapse state. It is important to note that the mean values of the loads and moments are kept constant and are perturbed around their means during the probabilistic buckling analysis. The truss end-node displacements vs. the number of members removed are plotted to identify the onset of the truss collapse state. Finally, the minimum number of members needed to support the applied loads and moments are determined.

## 5.3 Discussion of Results

### 5.3.1 Probabilistic Progressive Buckling: First Buckled Member

Figure 5.2a through Figure 5.2f show the probabilistic progressive buckled mode shapes of the three-bay space truss as individual buckled members are sequentially removed from the original configuration until it reaches the onset of collapse. The probabilistic buckling analysis indicated that the first bay's front diagonal buckled first (Figure 5.2b). The corresponding probabilistic buckled loads and moments at 0.5 probability are shown in Figure 5.3. Probabilistic buckled loads and moments at different probability levels can also be obtained. Furthermore, Figure 5.4 shows a method of calculating the margin of safety (MOS) for a specified probability by using known distributions for applied loads and moments and corresponding cumulative distribution function curves obtained from PSAM.

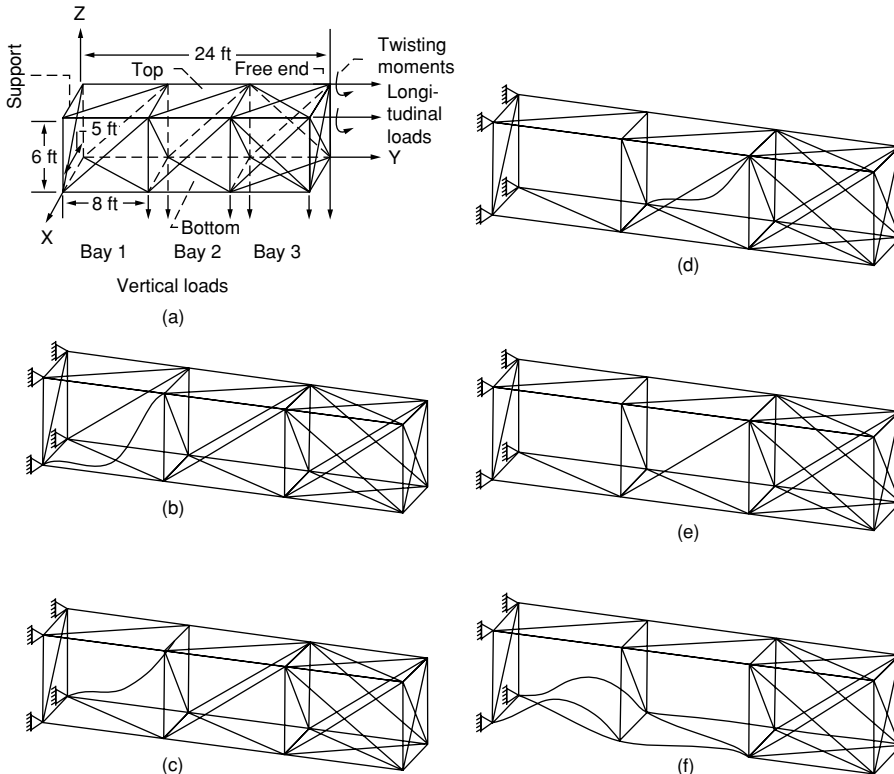
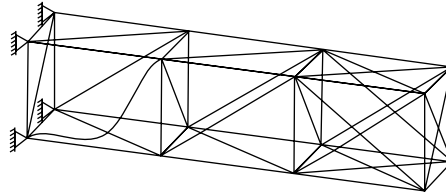


FIGURE 5.2 Probabilistic progressive buckling as buckled members are sequentially removed.

First buckled member — First bay front diagonal



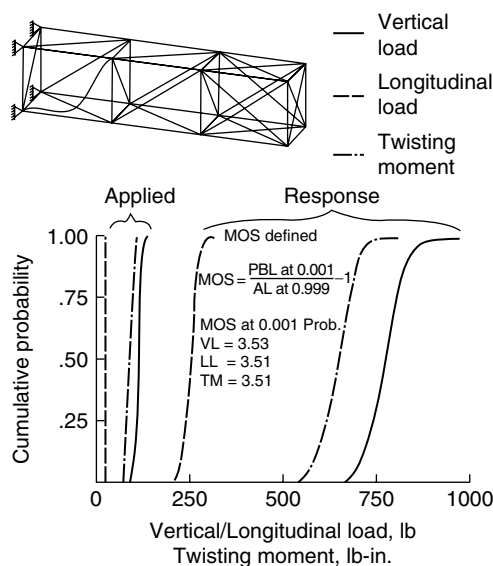
Probabilistic buckled loading condition (0.5 Prob.)

Vertical load	782 lb
Longitudinal load	260 lb
Twisting moment	651 lb-in.

**FIGURE 5.3** Probabilistic progressive buckling for first buckled member at 0.5 probability.

The sensitivity factors from Figure 5.5 suggest that the scatter in the bay length parameter (Y-coordinate) had the highest impact on the probabilistic distribution of the buckling load, followed by the bay height (Z-coordinate), bay width (X-coordinate), vertical and longitudinal loads, and finally twisting moments. Any slight variation in spatial (geometry) variables has a direct effect on the overall length of the members and thereby alters many terms in the stiffness matrix containing the length parameter. Finally, this has a definite effect on the probabilistic buckling loads that has been clearly observed in the results discussed above. However, it is important to note that even comparatively large variations in both member modulus (E) and area ( $r_o$  and  $r_i$ ) (see Table 5.1) had very negligible impact. Similar conclusions can also be drawn for the probabilistic member force in the first buckled member (see Figure 5.6).

The variation in the resistance (mean area  $\times$  mean yield strength) of the member was assumed to have a Weibull distribution and is shown in Figure 5.7. MOS calculations for stress exceeding strength using distribution curves for probabilistic member force and resistance as well as probabilistic buckling load and resistance indicate that the buckled member did satisfy the strength criteria condition. Therefore, it can be concluded from Figure 5.4 and Figure 5.7 that the member buckled when its axial force exceeded the Euler buckling load and when the stress due to tills load did not exceed the failure criteria.

**FIGURE 5.4** Probabilistic buckling load for first buckled member.

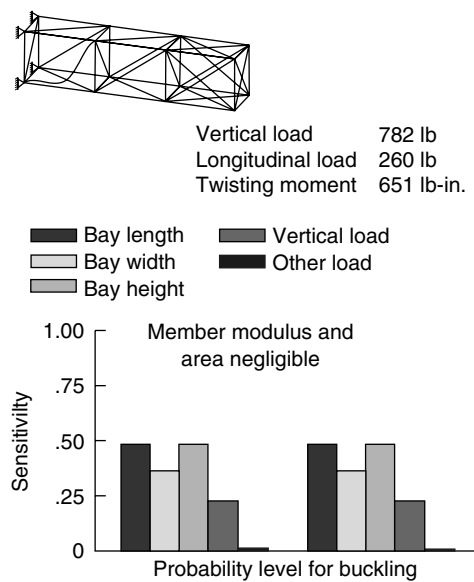


FIGURE 5.5 Sensitivity of probabilistic buckling load for first buckled member.

5.3.2 Probabilistic Progressive Buckling: Second/Third/Fourth Buckled Members

As described in the previous section, the deterministic analysis followed by the probabilistic analysis was performed with sequential removal of the first, second, third, and fourth buckled members from the truss. The probabilistic buckled loads and moments, sensitivity factors, and MOS values for stress were obtained for each stage.

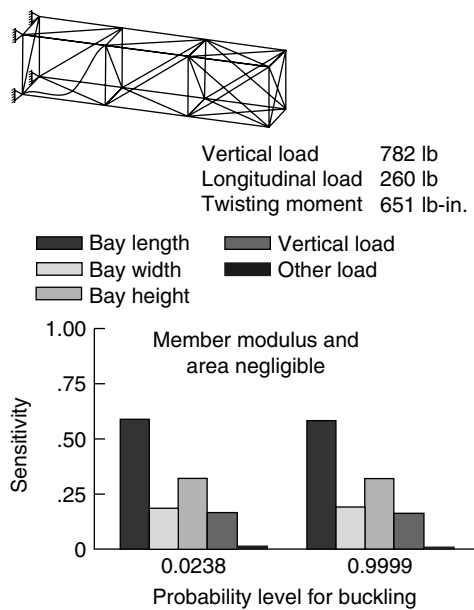


FIGURE 5.6 Sensitivity of probabilistic member force for first buckled member.



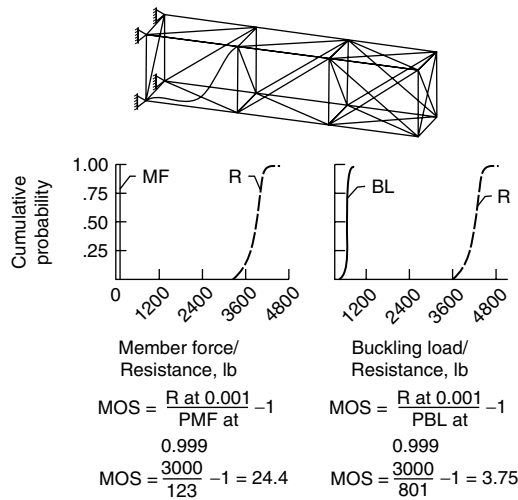


FIGURE 5.7 Probability of strength exceedence for first buckled member.

When the second member was buckled (see Figure 5.2c), the comparable results are shown in Figure 5.4 to Figure 5.6 and are described in Figure 5.8 to Figure 5.11. For these truss configurations, the MOS value decreased from 3.53 to 2.53. The similar details of the truss with the third buckled member (see Figure 5.2d) are given in Figure 5.12 to Figure 5.15. According to Figure 5.13, the MOS value further decreased to 1.62. Similarly, Figure 5.16 to Figure 5.19 present comparable results of the truss when the fourth member was buckled (see Figure 5.2e). It is important to note from Figure 5.18 and Figure 5.19 that the scatter in the bay height had much higher impact than scatter in either bay width or length on both the probabilistic buckling loads/moments and buckled member force.

Finally, the details of the onset of collapse state of the truss (Figure 5.2f) are shown in Figure 5.20 to Figure 5.22. When all the four buckled members were removed, the MOS value was equal to  $-3.75$ , which indicates that the onset of collapse was reached (Figure 5.21). Furthermore, the probabilistic buckling loads/moments at 0.001 probability value were equal to maximum applied loads/moments with assumed distributions (see Figure 5.20). In addition, at the collapse state, the uncertainties in both the bay length and bay height had sufficiently high impact on the distributions of the probabilistic buckling loads/moment (see Figure 5.22). In the various truss configurations discussed here, the uncertainties in the vertical loads had consistently the same impact on buckling loads/moment, whereas member modulus and area had negligible impact.

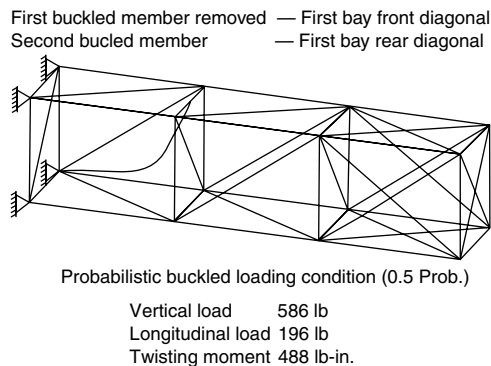


FIGURE 5.8 Probabilistic progressive buckling for second buckled member at 0.5 probability.

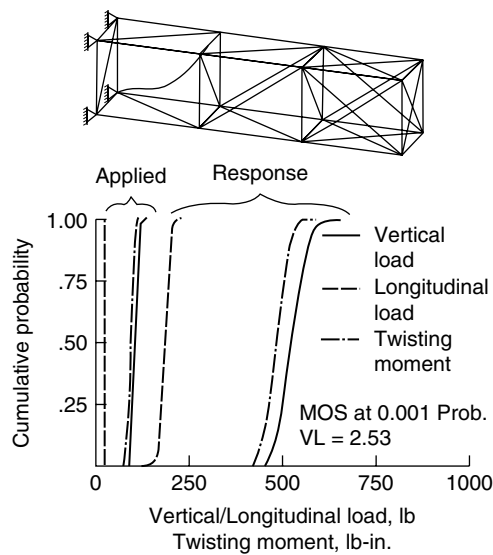


FIGURE 5.9 Probabilistic buckling load for second buckled member.

5.3.3 Probabilistic Truss End-Node Displacements

The truss end-node displacements (lateral and longitudinal) were also calculated during the deterministic analyses for each truss configuration, and these are shown in Figure 5.23. It is clear that there is no considerable change in either lateral or longitudinal displacement as each buckled member was sequentially removed. However, the truss end-node vertical displacement gradually increased up to the truss

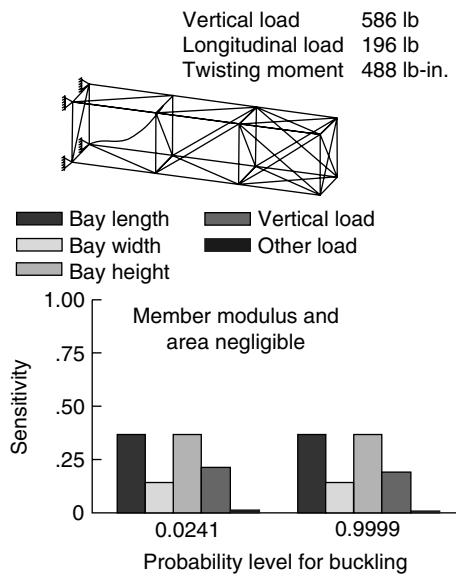


FIGURE 5.10 Sensitivity of probabilistic buckling load for second buckled member.

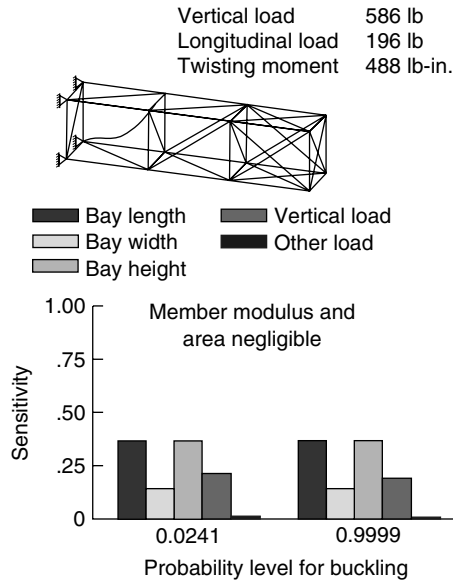


FIGURE 5.11 Sensitivity of probabilistic member force for second buckled member.

configuration with three buckled members removed, but it suddenly increased very rapidly when the fourth buckled member was removed, giving an indication of unbounded displacement growth, which suggests that the truss had reached the onset of its collapse state. This is due to the fact that the total vertical loads are six times higher than total longitudinal loads, and the perturbations in the vertical loads are higher than those of twisting moments.

Figure 5.24 and Figure 5.25 show, respectively, the relationships between the applied vertical loads and probabilistic buckling loads as well as probabilistic buckling loads and MOS values. The optimum truss configuration was reached with the fourth buckled member removed, whereby the probabilistic buckling load was equal to the applied vertical load at 0.001 probability level (see Figure 5.24). Similar conclusions can also be made for longitudinal loads and twisting moments. In addition, there is a gradual decrease

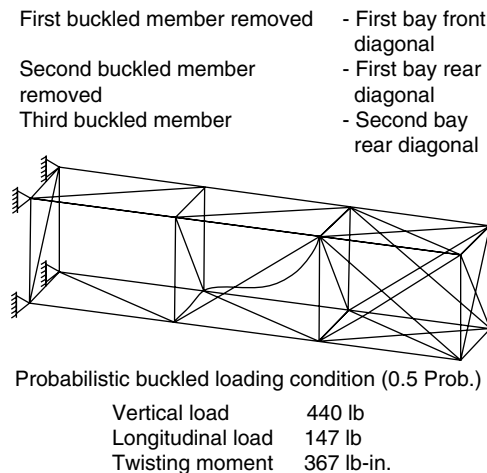


FIGURE 5.12 Probabilistic progressive buckling for third buckled member at 0.5 probability.

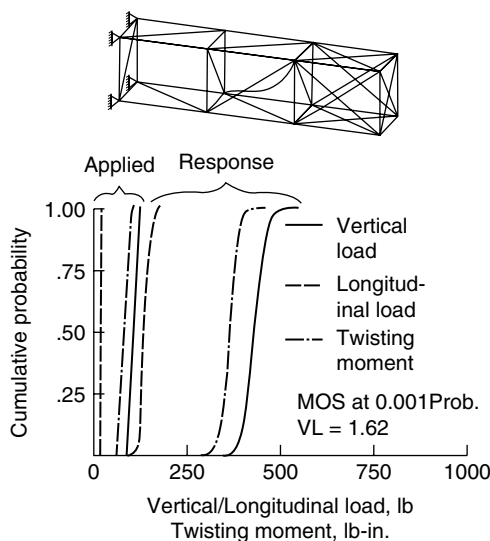


FIGURE 5.13 Probabilistic buckling load for third buckled member.

in the MOS values as buckled members were sequentially removed, reaching a zero value when the optimum truss configuration was reached (see Figure 5.25). Again, similar conclusions can also be made for longitudinal loads and twisting moments.

### 5.3.4 Probabilistic Buckling Including Initial Eccentricity

In the probabilistic progressive buckling methodology discussed here, all the members were assumed to be initially perfectly straight. The buckled members were sequentially removed with the assumption that once the member buckled, it would yield and could not resist any additional loading, and thereby would

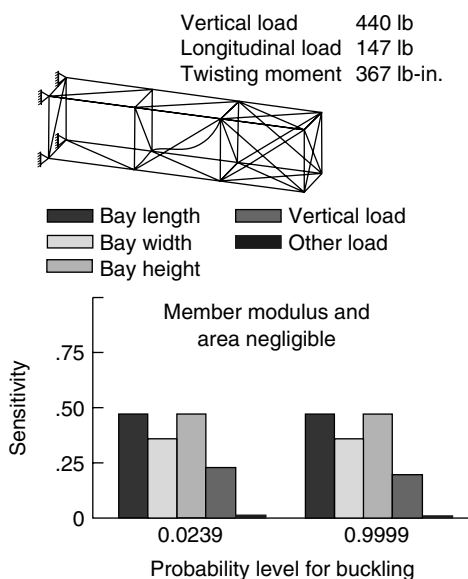


FIGURE 5.14 Sensitivity of probabilistic buckling load for third buckled member.

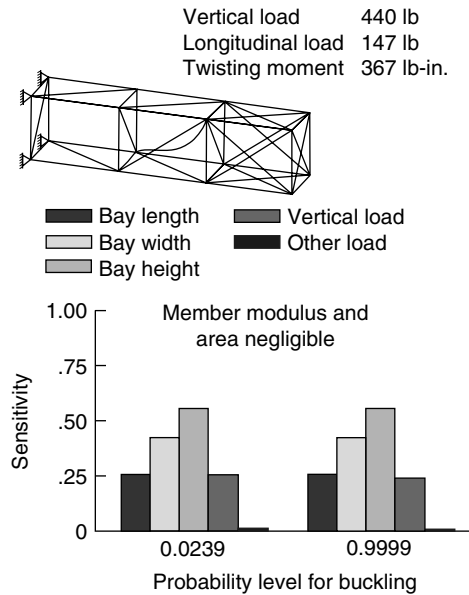


FIGURE 5.15 Sensitivity of probabilistic member force for third buckled member.

not contribute to the overall stiffness of the truss. In order to verify this assumption, we calculated the maximum eccentricity at which the yielding in the member (first-bay front diagonal) will take place due to the combined effects of axial and in-plane bending moments. Furthermore, this member was modeled to depict the buckled configuration of the member at which yielding will take place, using a parabolic distribution for the above-calculated eccentricity (see Figure 5.26).

The deterministic and subsequent probabilistic buckling analyses indicate, respectively, that the probabilistic buckling loads and moments did not change significantly from the original analysis (see Figure 5.3),

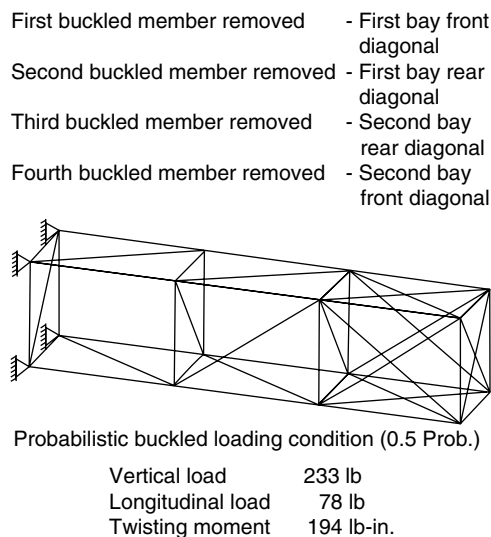


FIGURE 5.16 Probabilistic progressive buckling for fourth buckled member at 0.5 probability.

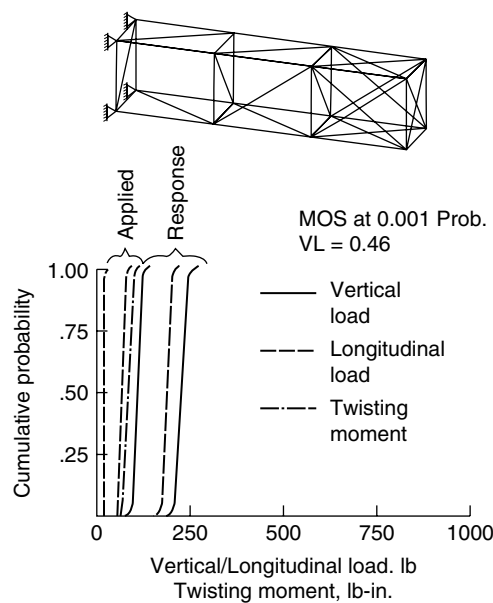


FIGURE 5.17 Probabilistic buckling load for fourth buckled member.

and that the first-bay rear diagonal has buckled (see Figure 5.27). However, as seen from Figure 5.5 and Figure 5.28 for probabilistic buckling loads and from Figure 5.6 and Figure 5.29 for probabilistic member forces, the sensitivity factors show some changes. Of particular note is the fact that the variation in bay width has the most dominant impact on both probabilistic buckling loads and moments (see Figure 5.28 and Figure 5.29). This is due to the fact that the member buckles in the plane perpendicular to the

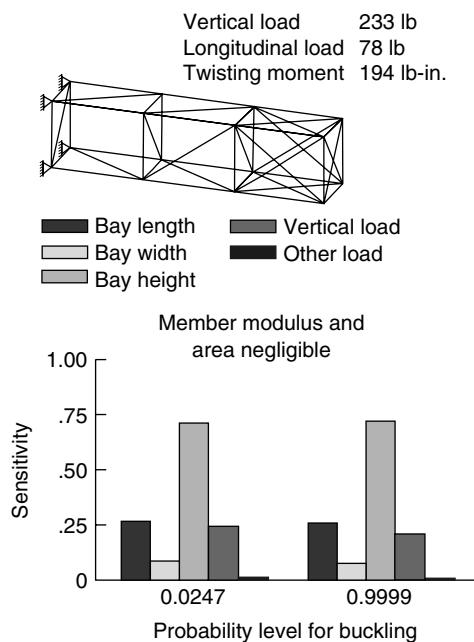
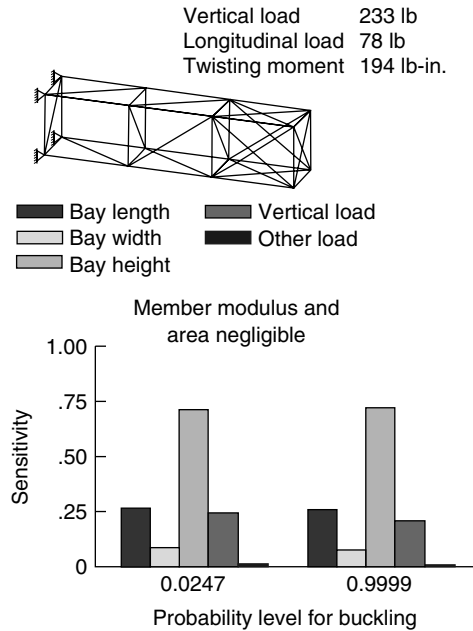
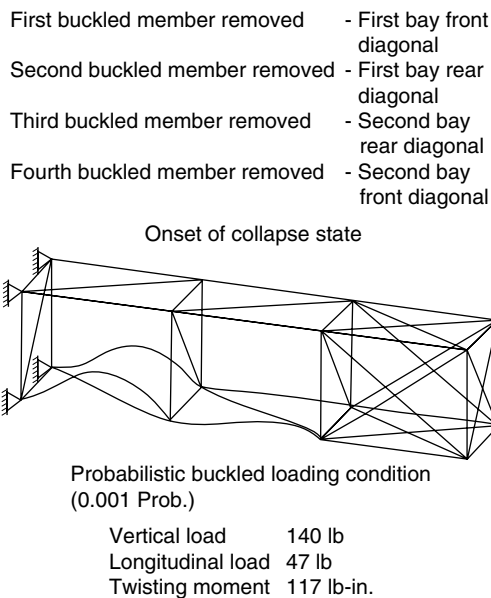


FIGURE 5.18 Sensitivity of probabilistic buckling load for fourth buckled member.



**FIGURE 5.19** Sensitivity of probabilistic member force for fourth buckled member.

direction of the loading. Nevertheless, it is important to note that the scatter in the spatial location accentuates the sensitivities of the bay length/width/height on the probabilistic load and diminishes that of vertical load. Once again, the variations in the member modulus and area have very negligible impact. These results justify the sequential removal of the buckled members during progressive buckling.



**FIGURE 5.20** Probabilistic progressive buckling for onset of collapse state at 0.001 probability.

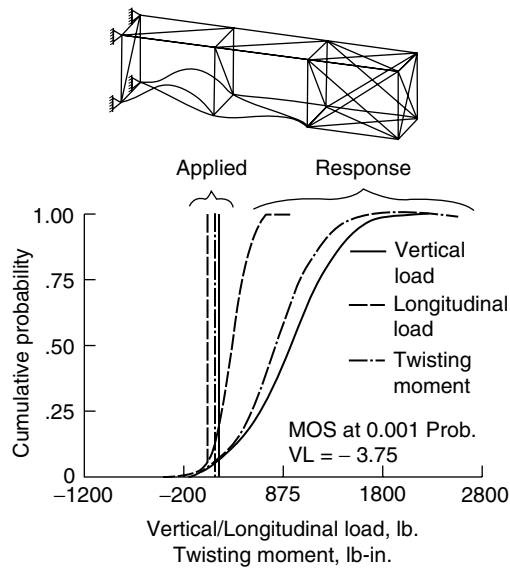


FIGURE 5.21 Probabilistic buckling load for onset of collapse state.

## 5.4 Adaptive/Smart/Intelligent Structures

NASA space missions have been advocating the use of adaptive/smart/intelligent structures for their spacecraft. These materials have great impact on the function of precision segmented reflectors, the control of large space truss structures, the manufacture of robotic assemblies/space cranes/manipulators, and the isolation of vibration frequencies. These materials also have a larger role in improving

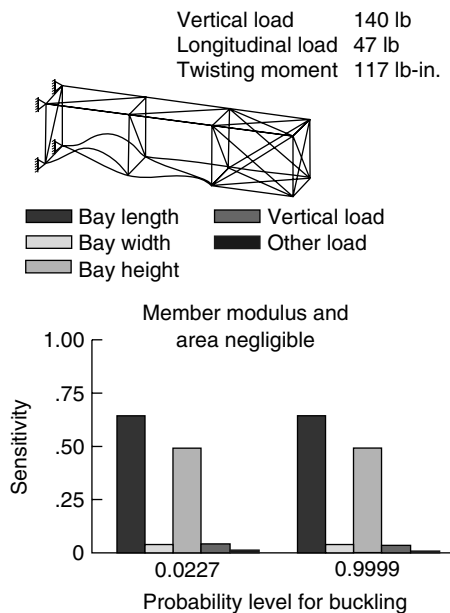


FIGURE 5.22 Sensitivity of probabilistic buckling load for onset of collapse state.



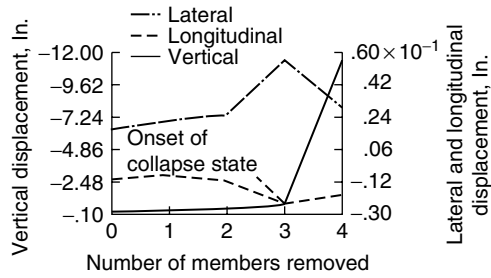


FIGURE 5.23 Progressive buckling leading to structural collapse, as indicated by unbounded displacement.

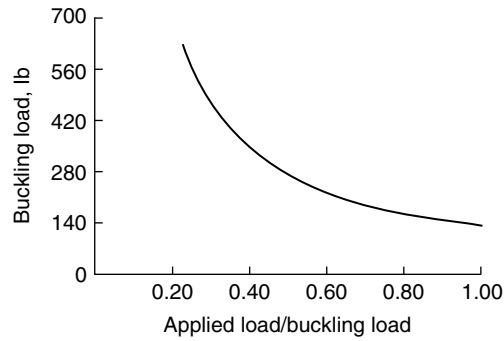


FIGURE 5.24 Buckling load vs. applied load/buckling load at 0.001 probability.

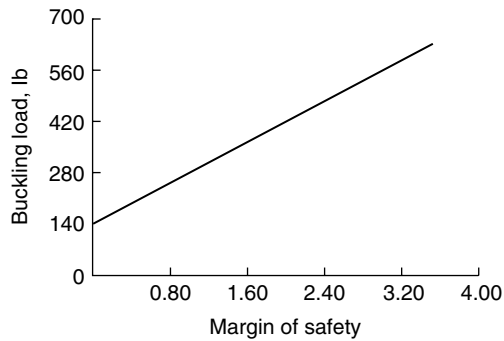


FIGURE 5.25 Buckling load vs. margin of safety at 0.001 probability.

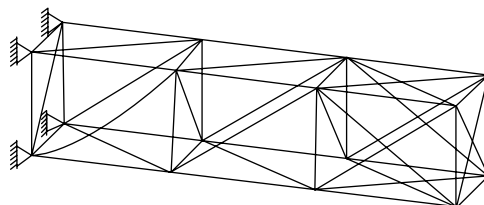


FIGURE 5.26 First-bay front diagonal with initial eccentricity.

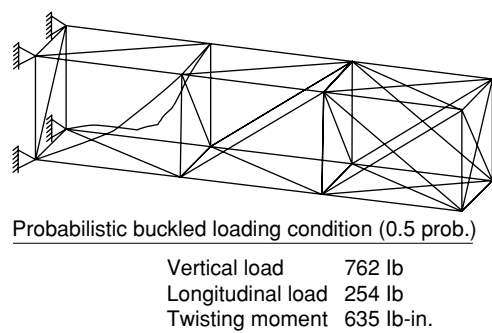


FIGURE 5.27 Probabilistic buckling: first-bay rear diagonal buckled.

the performance of aircraft and other commercial structures. However, the terminology, such as “adaptive,” “smart,” and “intelligent,” is being used loosely and interchangeably in the research community [8].

Ahmad [8] defines the intelligent/smart materials and systems as those having “built in or intrinsic sensors, processors, control mechanisms, or actuators making it capable of sensing a stimulus, processing the information, and then responding in a predetermined manner and extent in a short/appropriate time and reverting to its original state as soon as stimulus is removed.” Thus, the smart structures consist of sensors, controllers, and actuators. Furthermore, the intelligent materials usually respond quickly to environmental changes at the optimum conditions and modify their own functions according to the changes. Therefore, the intelligent truss structures are usually designed with active members early in the design process. In many instances, the trusses are designed with both active and passive members using an integrated design optimization procedure [9]. Finally, Wada [10] describes adaptive structures “as a structural system whose geometric and inherent structural characteristics can be beneficially changed to meet mission requirements either through remote commands and/or automatically in response to external stimulations.” It is important to note that these structures have an in-built capability to geometrically

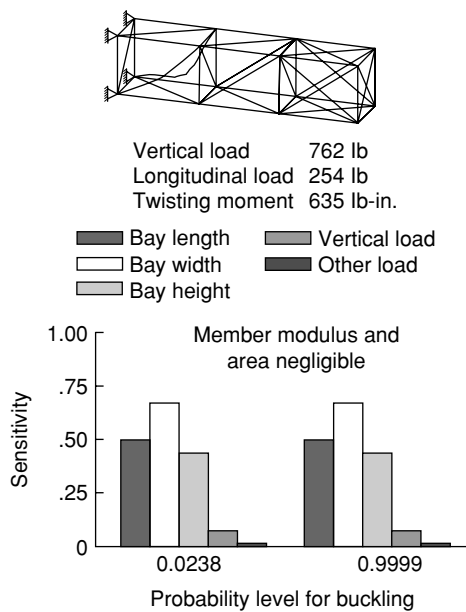


FIGURE 5.28 Sensitivity of probabilistic buckling load.

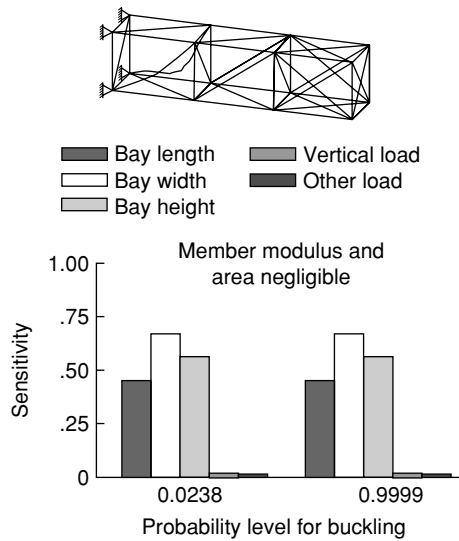


FIGURE 5.29 Sensitivity of probabilistic member force.

relocate critical points of the structure, when in space, to the desired positions through actuation of active members. Therefore, the configurations of such structures should have greater flexibility to move the critical locations.

For the evaluations performed herein, the following definitions are used:

1. When local instability is imminent, the length of that member is suitably controlled to prevent instability. This is referred to as an “adaptive structure.”
2. When local instability is imminent, a redundant member engages in load sharing without weight penalty. This is referred to as a “smart structure.”
3. When local instability is imminent as exhibited by bowing, the material induces a local restoring moment. This is referred to as an “intelligent structure” through the corresponding restoring action of the intelligent material.

The concepts discussed above are used for probabilistic structural analysis of adaptive/smart/intelligent structures typical for outer-space-type trusses using the NESSUS computer code. The individual analysis technique and respective results are discussed in the following section.

## 5.5 Discussion of Results

### 5.5.1 Adaptive Structure

The deterministic analysis indicated that the first sign of local buckling occurs in the first-bay front diagonal (Figure 5.30). Since buckling varies as the length squared, a decrease in length should prevent buckling at that load. Therefore, a suitable device or sensor can be attached to this truss member that will not only sense the local buckling in the member due to significantly high axial force, but also will automatically reduce the overall length of the member by a predetermined increment. Thus, this member acts like an adaptive member, whereby its geometrical parameters were changed accordingly.

Figure 5.30 through Figure 5.35 show the cumulative distribution functions (CDF) and corresponding sensitivities of the probabilistic buckling loads and vibration frequencies of the truss and axial forces in the diagonal (member). By reducing the length of the member by 6 in., the probabilistic buckling loads increased by 6% (Figure 5.30). The sensitivity factors from Figure 5.31 show that the uncertainties in the

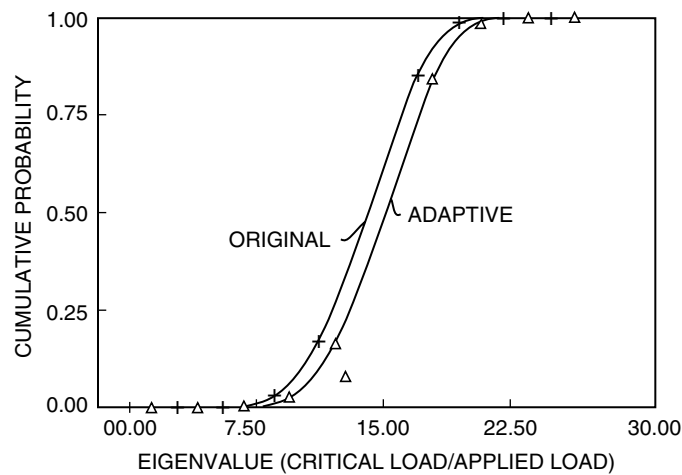


FIGURE 5.30 Probabilistic buckling load for adaptive structure.

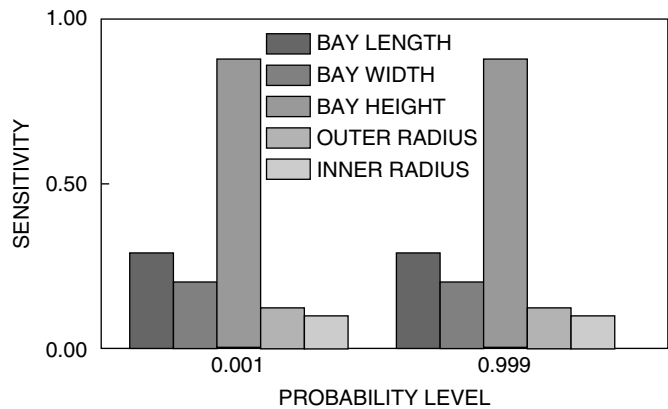


FIGURE 5.31 Sensitivity of probabilistic buckling load for adaptive structure.

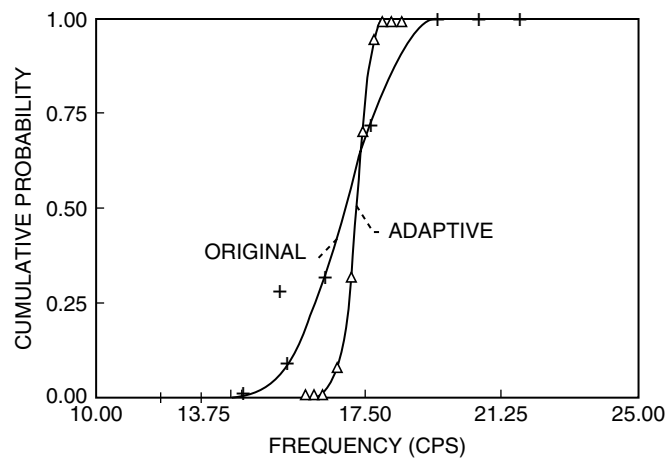


FIGURE 5.32 Probabilistic vibration frequency for adaptive structure.

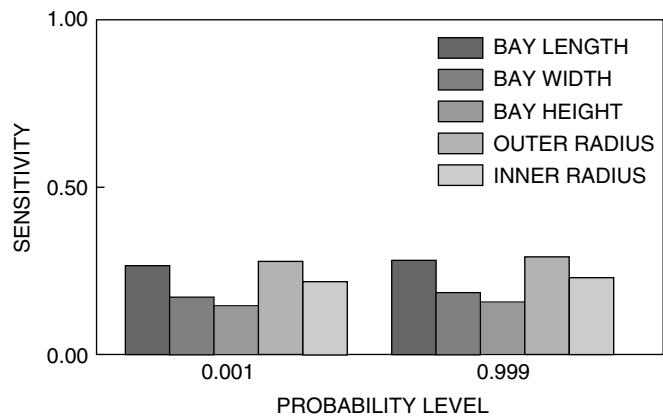


FIGURE 5.33 Probabilistic frequency sensitivities for adaptive structure.

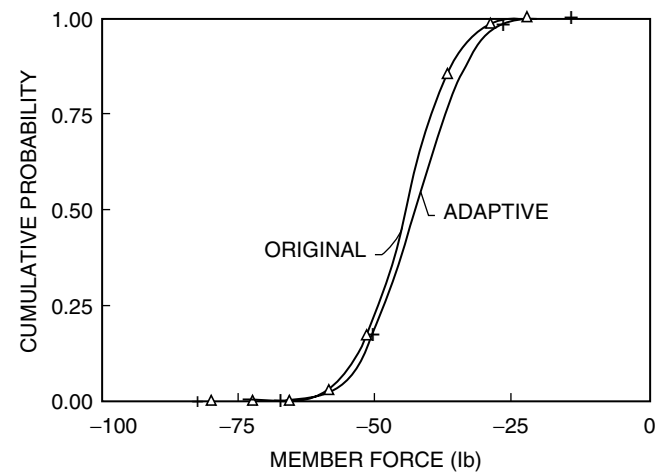


FIGURE 5.34 Probabilistic member force for adaptive structure.

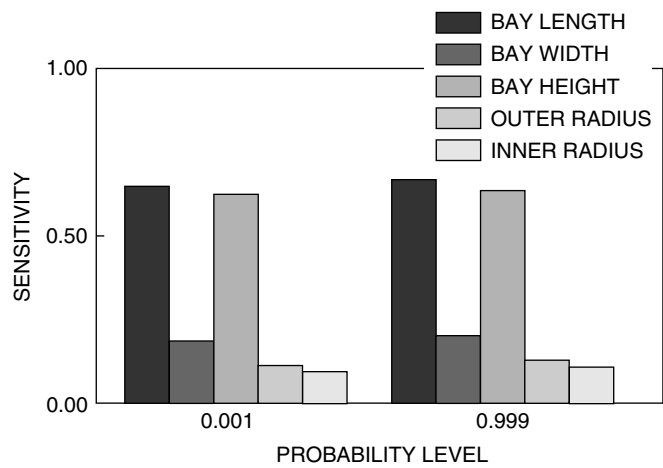


FIGURE 5.35 Sensitivity of probabilistic member force for adaptive structure.

bay height (Z-coordinate) had the highest impact on the probabilistic buckling loads. The probabilistic vibration frequencies increased by 25 to 35% for lower probability levels (Figure 5.32). The scatter in the tube radii had equally significant impact on the probabilistic vibration frequencies (Figure 5.33). The magnitude of the probabilistic member axial forces decreased by 5% (Figure 5.34), and the scatter in bay length had the highest impact on the probabilistic member axial forces, followed by bay height (Figure 5.35). Thus, the adaptive structures are effective in increasing the buckling loads and vibration frequencies as well as controlling the member axial forces.

## 5.5.2 Smart Structure

As mentioned earlier, in the case of a smart structure, the original single hollow member (diagonal) was replaced with two hollow tubes. Once again, the outer tube was made up of wrought aluminum alloy (616-W), and the outer and inner radii of the tube were 0.5 and 0.46875 in., respectively. However, the inlet (inner) tube was modeled using a high-modulus-fiber–intermediate-modulus-matrix composite with 60% fiber–volume ratio. For this tube, the modulus of elasticity was equal to 36 Mpsi with 0.421875 and 0.384375 in. outer and inner radii, respectively. It was assumed that the inner composite tube can be inserted inside the outer tube without affecting the details of the member end connections. It is important to note that the composite tube not only reduces the overall weight of the truss, but also increases the stiffness, and it is assumed that this tube was made with tight tolerance. Therefore, the scatter in  $E$  and tube radii are not considered in the probabilistic analysis. In addition, the aluminum tube is also useful in protecting the composite tube from possible damage from orbital environmental debris.

Figure 5.36 shows that the probabilistic buckling loads increased by almost 30% at several probability levels. The sensitivity factors show that the uncertainties in the bay height had the highest impact on the probabilistic buckling loads (Figure 5.37). The probabilistic frequencies increased by 15% (Figure 5.38). The scatter in the inner-tube radii had equally significant impact on the probabilistic frequencies (Figure 5.39). Similarly, the magnitude of the probabilistic member forces increased (Figure 5.40), and the scatter in the bay length and height had equally significant impact on the probabilistic member axial forces (Figure 5.41). Once again, the smart structures can also be used to increase the probabilistic buckling loads and frequencies and to control the forces in the member.

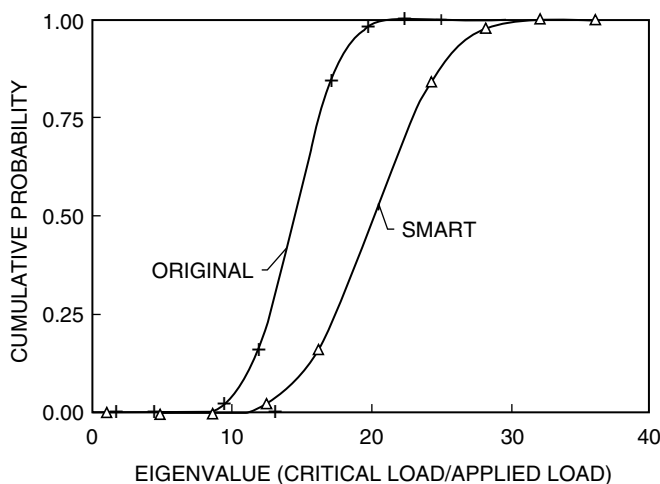


FIGURE 5.36 Probabilistic buckling load for smart structure.

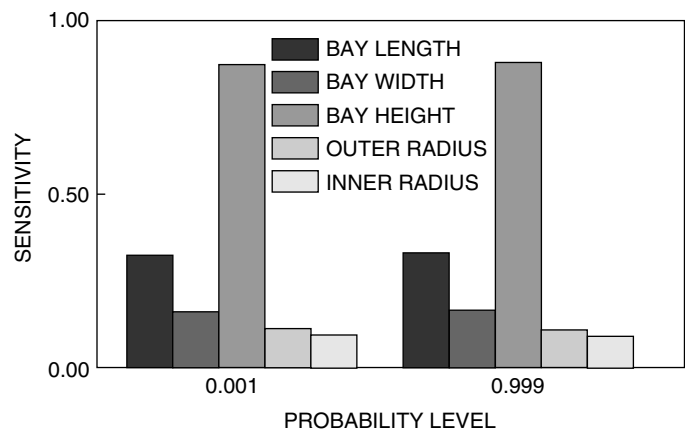


FIGURE 5.37 Sensitivity of probabilistic buckling load for smart structure.

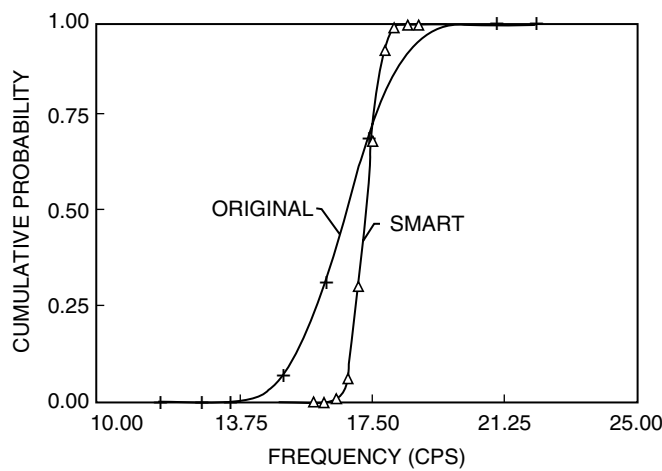


FIGURE 5.38 Probabilistic vibration frequency for smart structure.

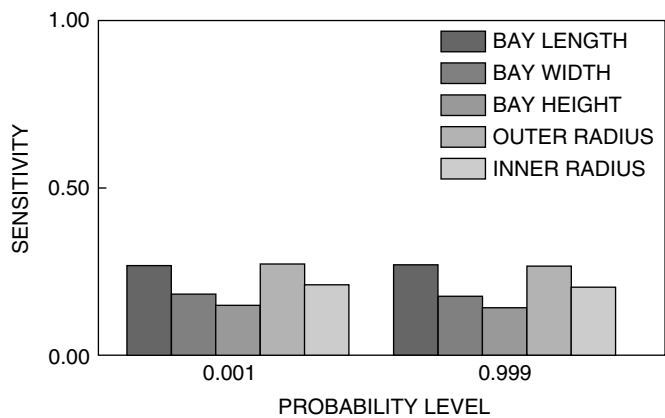


FIGURE 5.39 Probabilistic frequency sensitivities for smart structure.

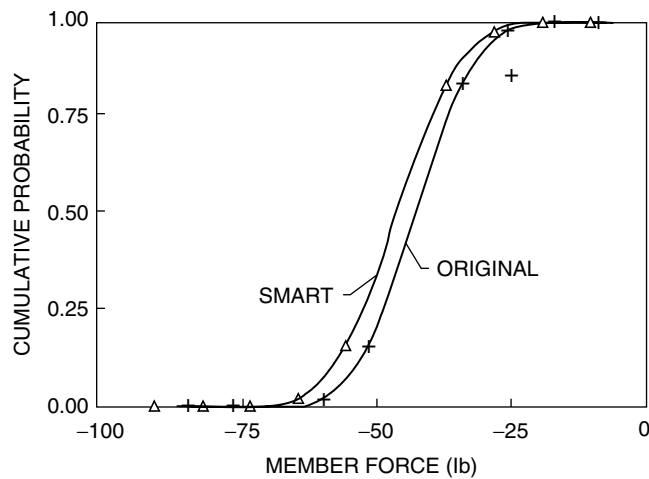


FIGURE 5.40 Probabilistic member force for smart structure.

5.5.3 Intelligent Structure

It is important to note that all of the truss members were assumed to be initially perfectly straight and that when any member buckled it would yield [5]. Therefore, the maximum eccentricity at which the yielding in the member (first-bay front diagonal) will take place due to the combined effects of axial and in-plane bending moments was calculated. Furthermore, this member (first-bay front diagonal) was modeled to represent the buckled configuration of the member at which yielding will take place by using a parabolic distribution with increased eccentricities. At the center of this diagonal (original shape), localized stress concentrators can be attached that will detect the local instability in the member and automatically apply a restoring moment of 15 lb-in. at the center of this diagonal. Thus, this diagonal acts like an intelligent structural member due to the action of intelligent material, and the loading parameters will be changed accordingly.

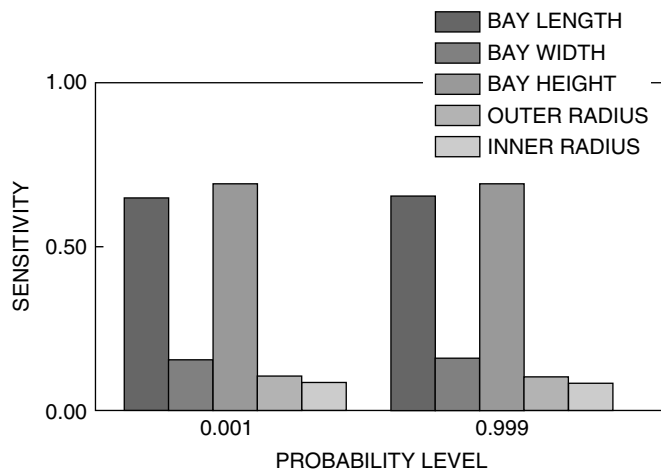
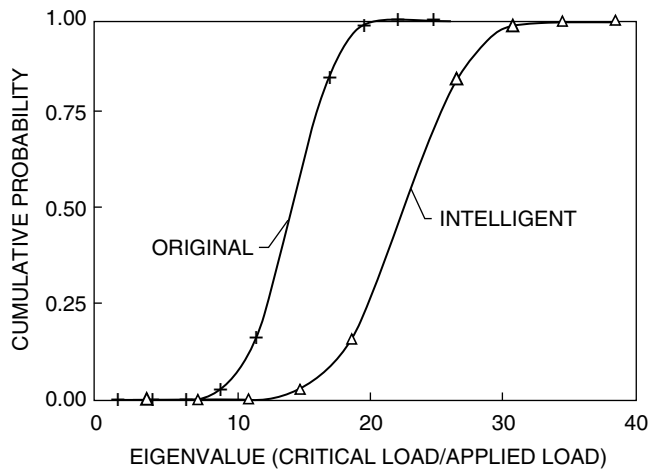


FIGURE 5.41 Sensitivity of probabilistic member force for smart structure.





**FIGURE 5.42** Probabilistic buckling load for intelligent structure.

It can be concluded that the probabilistic buckling loads increased by 50% (Figure 5.42) and that the scatter in the bay height had the highest impact on the probabilistic buckling loads (Figure 5.43). The probabilistic buckling frequencies increased by 20% only for the lower probability levels (Figure 5.44). Therefore, the level of scatter in the primitive variables did not increase the probabilistic frequencies at higher probability levels. The variations in the member radii had equally significant impact on the probabilistic vibration frequencies (Figure 5.45). The magnitude of the probabilistic member axial forces decreased by 40% (Figure 5.46), and the uncertainties in both bay length and bay height had a very significant impact on the probabilistic member forces (Figure 5.47). Finally, with the help of in-built intelligent materials, the intelligent structures are very useful in increasing the probabilistic buckling loads and decreasing the member axial forces.

Finally, the methodologies discussed above can be applied to more than one member at the same time, if the situation demands, and the probabilistic analysis can be carried out to evaluate various CDFs and determine the structural performance and durability of the truss.

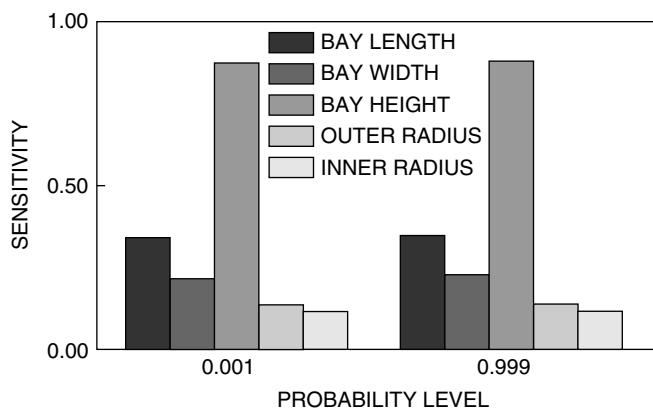


**FIGURE 5.43** Sensitivity of probabilistic buckling load for intelligent structure.

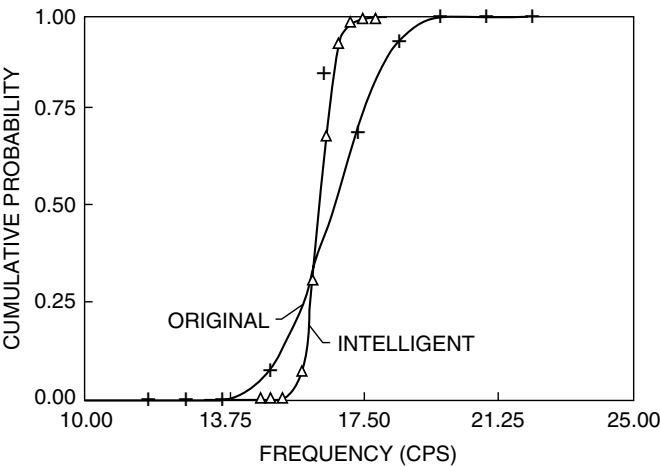


FIGURE 5.44 Probabilistic vibration frequency for intelligent structure.

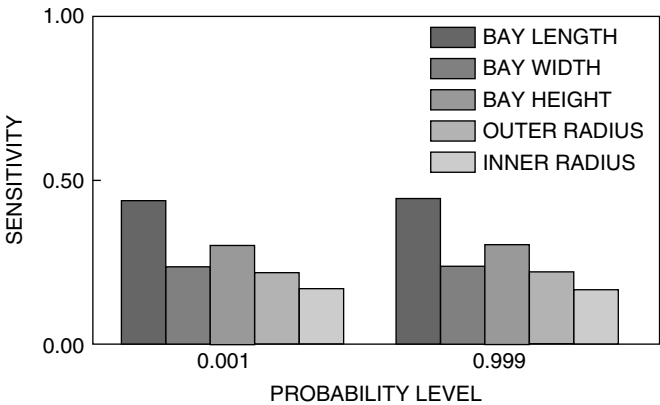


FIGURE 5.45 Probabilistic frequency sensitivities for intelligent structure.

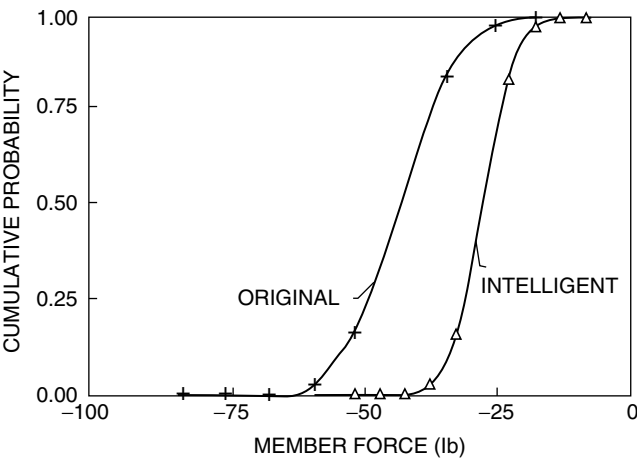


FIGURE 5.46 Probabilistic member force for intelligent structure.

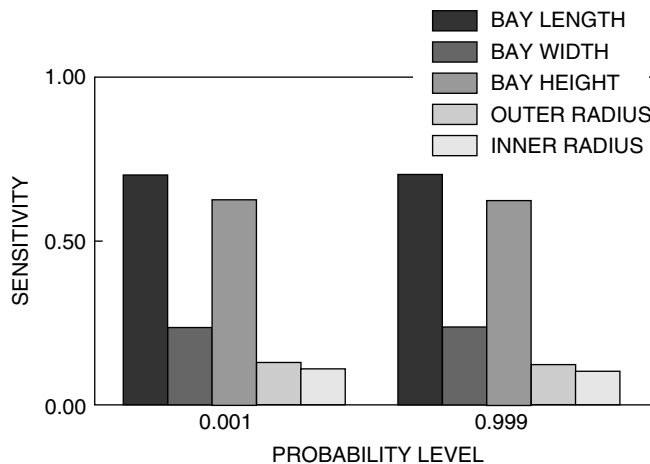


FIGURE 5.47 Sensitivity of probabilistic member force for intelligent structure.

## 5.6 Summary

The computational simulation of probabilistic evaluation for conventional and adaptive/smart/intelligent behavior of truss structures is demonstrated using the NESSUS computer code, and step-by-step procedures are outlined. Scatter of the probabilistic buckling loads, vibration frequencies, and member axial forces are evaluated, and the sensitivities associated with the uncertainties in the primitive variables are determined.

For the conventional truss, the results indicate that: (1) probabilistic buckling loads and margin-of-safety values decrease as buckled member(s) are sequentially removed; (2) the scatter in truss geometry (bay length/width/height) and vertical loads have considerable impact on the probability of the buckled load; (3) the member modulus and area parameters have negligible impact; and (4) initial eccentrics have negligible influence on the probabilistic buckling load but may influence the sensitivities.

For the adaptive/smart/intelligent truss, the results indicate that: (1) the probabilistic buckling loads and vibration frequencies increase for each truss classification; however, they increase significantly for the case of intelligent structure; (2) the magnitude of the probabilistic member axial forces increases for the smart structure and decreases for both adaptive and intelligent structures, with a considerable decrease for the intelligent structure; (3) for each structure, the scatter in the bay height has the highest impact on the probabilistic buckling loads; (4) the scatter in member area parameters has equally significant impact on the probabilistic frequencies; (5) the uncertainties in the bay length/height have equally significant effects on the probabilistic member forces.

Collectively, the results indicate that all three structures can be used to increase the probabilistic buckling loads. However, the intelligent structure gives the highest increase. Furthermore, both adaptive and smart structures are recommended for controlling the frequencies, but this is not true for intelligent structures. Finally, the adaptive/smart/intelligent structures are recommended for controlling the member axial forces. Collectively, the results demonstrate that the probability of collapse of space-type trusses can be reliably assessed by the procedure described herein.

## References

1. Chamis, C.C., Probabilistic structural analysis methods for space propulsion system components, in *Space System Technology Conference Proceedings*, AIAA, New York, 1986, pp. 133–144.
2. Dias, J.B., Nagtegaal, J.C., and Nakazawa, S., Iterative perturbation algorithms in probabilistic finite analysis, in *Computational Mechanics of Probabilistic and Reliability Analysis*, Liu, W.K. and Belytschko, Eds., ELME PRESS International, Lausanne, Switzerland, 1989, pp. 211–230.

3. Wu, Y.T., Demonstration of new, fast probability integration method for reliability analysis, in *Advances in Aerospace Structural Analysis, Proceedings of ASME Winter Annual Meeting*, Bumside, O.M., Ed., ASME, 1985, pp. 63–73.
4. Shah, A.R., Nagpal, V.K., and Chamis, C.C., Probabilistic analysis of bladed turbine disks and the effect of mistuning, in *Proceedings of 31st Structures, Structural Dynamics, and Materials Conference*, Part 2, AIAA, New York, 1990, pp. 1033–1038; also NASA TM-102564, NASA.
5. Shiao, M.C. and Chamis, C.C., A methodology for evaluating the reliability and risk of structures under complex service environments, in *Proceedings of 31st Structures, Structural Dynamics, and Materials Conference*, Part 2, AIAA, New York, 1990, pp. 1070–1080; also NASA TM-103244, NASA.
6. Pai, S.S., Probabilistic Structural Analysis of a Truss Typical for Space Station, NASA TM-103277, NASA, 1990.
7. Chajes, A., *Principles of Structural Stability Theory*, Prentice-Hall, Englewood Cliffs, NJ, 1974.
8. Ahmad, I., U.S.–Japan workshop on smart/intelligent materials and systems, *Onrasia Sci. Info. Bull.*, 15 (4), 67–75, 1990.
9. Manning, R.A., Optimum design of intelligent truss structures, in *Proceedings of 32nd Structures, Structural Dynamics, and Materials Conference*, Part 1, AIAA, New York, 1991, pp. 528–533.
10. Wada, B.K., Adaptive structures, in *Proceedings of 30th Structures, Structural Dynamics, and Materials Conference*, Part 1, AIAA, New York, 1989, pp. 1–11.



# 6

## Probabilistic Analyses of High-Speed Civil Transport (HSCT) Combustor Liner Components

---

Shantaram S. Pai

Pappu L.N. Murthy

*NASA Glenn Research Center*

6.1	Introduction .....	6-1
6.2	Fundamental Approaches and Considerations .....	6-2
6.3	Finite Element Model .....	6-2
6.4	Probabilistic Analysis .....	6-3
6.5	Discussion of Results .....	6-5
6.6	Conclusions .....	6-13
	References .....	6-14

### 6.1 Introduction

---

Aerospace propulsion systems are complex assemblages of structural components that are subjected to a variety of thermal and mechanical loading conditions involving uncertainties. Uncertainty in boundary or support conditions is also important. Furthermore, inherent variability in material properties and fabrication processes, as well as geometrical imperfections, introduce additional uncertainties. Deterministic structural analysis methods fail to address these issues. Consequently, these methods could lead to overly conservative designs or, sometimes, nonconservative designs.

Probabilistic structural analysis methods (PSAMs) were developed at NASA Lewis Research Center [1], which enable a formal assessment of the effect of uncertainties in loads, material property variations, and geometric imperfections on structural behavior (stability, natural frequencies, stresses, etc.). PSAMs also provide a systematic way to quantify sensitivities of system performance and reliability to the uncertainties in the design variables. The PSAM efforts have led to the development of the computer code NESSUS (Numerical Evaluation of Stochastic Structures Under Stress) [2, 3].

In the recent past, NESSUS has been used [4] to computationally simulate and probabilistically evaluate a typical hot structural component within an engine, such as a composite combustor liner. The probabilistic analysis results showed that the scatter in the combined stress is not uniform along the length of the combustor. Furthermore, the effects of the coefficient of thermal expansion, the hoop modulus of the liner material, and the thermal load profile on the stresses near the support and the midspan of the combustor liner dominate over other effects. This work was further extended [5] to evaluate the effects of uncertainties

of through-thickness thermal load gradients for a typical ceramic matrix combustor liner. The combustor was separately evaluated for local stresses using low, high, and mixed low/high moduli ceramic matrix composites (CMCs). The subsequent probabilistic analysis results indicated that the through-thickness gradients, the liner thickness, the coefficient of thermal expansion, and the axial and shear moduli had considerable impact on the combined stress, with the through-thickness thermal gradients having the most significant impact.

Currently, new concepts are being explored for combustor liners of an HSCT system that are subjected to complex environments and have to endure the applied loads for thousands of hours with assured reliability. In the past, several deterministic analyses, which included detailed heat transfer analyses to identify thermal profiles and deterministic stress analyses to identify critical locations of high stresses, and actual rig tests for segments, have been performed by simulating these loading situations as closely as possible. However, it is a well-known fact that many uncertainties do exist in loading (primary thermal loads due to heat transfer), boundary conditions (end fixity unknowns), and material properties (moduli, thermal expansion coefficients, and conductivities). The main objective of this chapter is to explain the computational simulations and probabilistic evaluation methodologies used for a single cup liner segment (typical combustor liner configuration) so as to account for the aforementioned uncertainties as well as other geometry- and material-related uncertainties in a formal way to assess the performance of a liner component under complex and uncertain loading conditions.

## 6.2 Fundamental Approaches and Considerations

One of the major problems encountered in the development of new concepts for hot section components in an engine, such as a combustor liner, is that it has to be economically viable considering its life-cycle costs, sufficiently assured reliable life, as well as environmental acceptability. Furthermore, the liner material should possess material characteristics to provide long-term durability as well as resistance to possible through-thickness and axial (along the length) high thermal gradients. In addition, the recommended ceramic matrix composite materials must have properly connected economical fabrication processes to minimize overall manufacturing costs. Users of available methods/programs for reliability analysis find it difficult to statistically quantify the uncertainties in the aforementioned uncertain variables. However, by using the NESSUS code, one can identify the dominant uncertain variables that affect significantly the natural frequencies, buckling loads, and combined stress values. This is important information because it allows designers to focus on collecting data to estimate the type of probability distributions and distribution parameters of these important random variables.

## 6.3 Finite Element Model

The finite element model of a single cup liner segment consists of a cylindrical liner segment with 660 nodes and 640 bilinear isoparametric variable-thickness shell elements based on Reissner–Mindlin plate and shell theories (see Figure 6.1). The liner is further subdivided into 33 ring sections, each with 22 nodes around

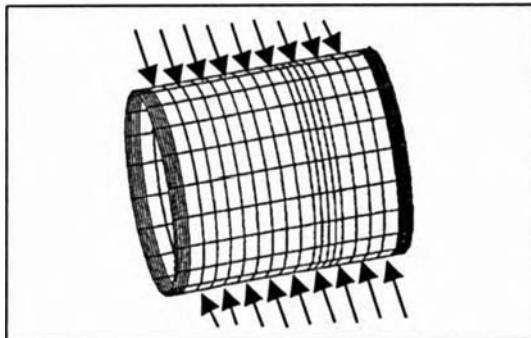


FIGURE 6.1 Finite element model of cylindrical liner segment.

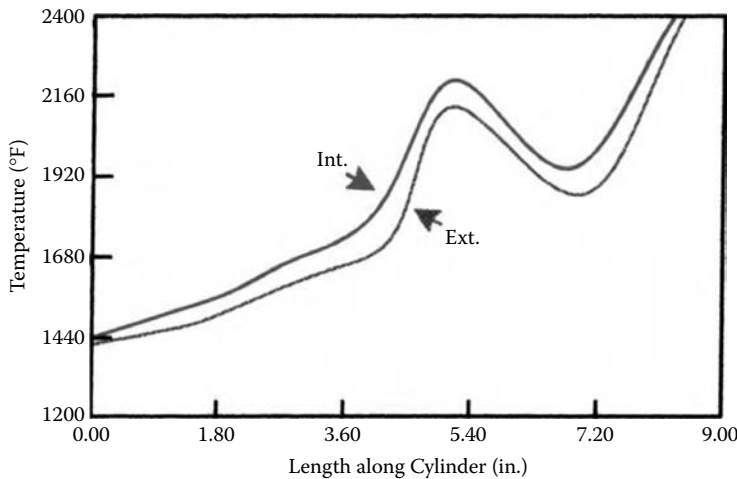


FIGURE 6.2 Thermal profile along the length of a cylindrical liner segment.

its circumference. The shell element is a four-noded quadrilateral in 3D space. The liner is made of a typical ceramic matrix composite material (SiC/SiC). As shown in Figure 6.1, the outer surface of the liner is exposed to uniform pressure loading. Heat transfer analyses are available in the form of thermal profiles (see Figure 6.2) and are used as a starting point for thermal loads. Furthermore, equivalent homogeneous, orthotropic properties of the liner material are obtained using the in-house composite mechanics code CEMCAN [6]. In addition, the temperature profiles, moduli, thermal expansion coefficients, and liner thicknesses are assumed to have known distributions and parameters such as standard deviations. In the initial finite element analysis it was assumed that all the nodes at the support locations were allowed to freely expand both in radial and circumferential directions, but were not allowed to move in the axial direction. However, all other nodes along its length were assumed to rotate freely and displace in all directions.

## 6.4 Probabilistic Analysis

Generally, in order to define completely a probabilistic model of a set of random variables, the joint probability density function of these random variables should be estimated. This is often impractical because: (1) there are few standard joint probability density functions and (2) a very large amount of data is required in order to construct a joint probability density function. To circumvent this difficulty, *primitive* random variables should be selected as inputs because these variables can be assumed to be mutually independent and the number of random variables needed to characterize uncertainty is minimized. In this case, only the marginal probability density functions of these variables need to be estimated. This strategy has been followed in the project described in this chapter.

The following input variables were considered to be random in the probabilistic analysis:

1. Density of the liner material
2. Coefficient of thermal expansion
3. Thickness of the liner
4. Pressure load
5. Through-thickness thermal loading along the length of the combustor liner
6. Material properties

In the case of the material properties, the stiffness parameters were considered random. In the present probabilistic analysis these material property variables were assumed to be normally distributed and mutually independent. Heat transfer analyses were available in the form of thermal profiles and were used as a starting point for thermal loads. Furthermore, the through-thickness thermal loads were used according



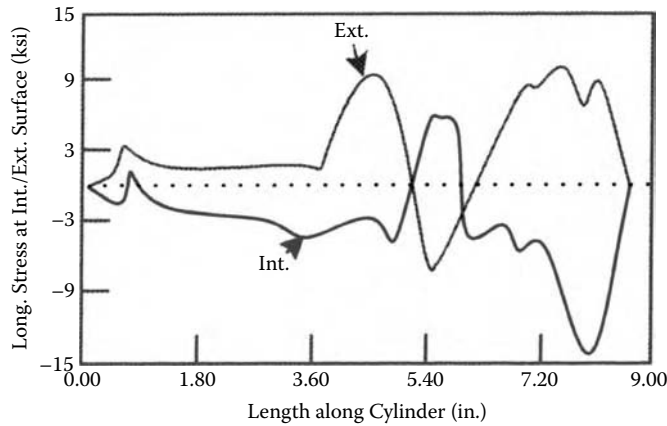


FIGURE 6.3 Longitudinal stress along the length of cylindrical liner segment.

to the thermal load profiles, both inside and outside of the liner (Figure 6.2). When the distribution type is considered important, sensitivity studies can be performed readily to assess the effect of the type of distribution on the performance of a design. Initially, the NESSUS/FEM module was used to analyze deterministically the combustor liner for the mean values of the primitive variables. The longitudinal and hoop stress values along the length of the cylindrical liner segment are shown in Figure 6.3 and Figure 6.4, respectively. In the subsequent probabilistic analyses, each primitive variable is perturbed independently and by a different amount. Usually, the perturbed value of the primitive variable is obtained by adding a certain factor of the standard deviation on either side of the mean values. Other details regarding probabilistic finite element analyses and sensitivity calculations are described in Reference 4. The primitive random variables and their mean values are presented in Table 6.1. All variables were assumed normal with standard deviations equal to 5% of their mean values.

In general, the finite element equation for motion is written as:

$$[M]\{\ddot{u}\} + [C]\{\dot{u}\} + [K]\{u\} = F(t) \quad (6.1)$$

where  $[M]$ ,  $[C]$ , and  $[K]$  denote the mass, damping, and stiffness matrices, respectively. These matrices are calculated in the NESSUS finite element analysis module. Furthermore,  $\{\ddot{u}\}$ ,  $\{\dot{u}\}$ , and  $\{u\}$  are the acceleration, velocity, and displacement vectors at each node, respectively.

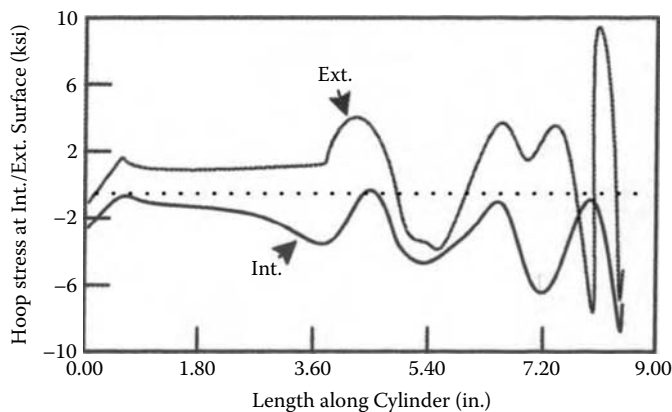


FIGURE 6.4 Hoop stress along the length of a cylindrical liner segment.

**TABLE 6.1** Primitive Variables and Uncertainties for Probabilistic Structural Analysis of Combustor Liner (random input data).

Primitive Variables	Mean Value
Density	0.1002 lbs.sec <sup>2</sup> /in <sup>4</sup>
Coefficient of thermal expansion	2.43×10 <sup>6</sup> in./in./°F
Thickness	0.8 in.
Pressure load	8.7 psi
Thermal load (inside)	1455–2400°F
Thermal load (outside)	1436–2386°F
Axial modulus	35.81 ksi
Hoop modulus	35.8 ksi
Poisson's contribution	5.37 ksi
Shear modulus	12.8 ksi
Shear modulus	10.2 ksi
Shear modulus	10.2 ksi

*Note:* All variables were assumed normal with standard deviations equal to 5% of their mean values.

In this chapter, the thermomechanical static case is considered by setting the mass and damping matrices equal to zero and considering the forcing function being independent of time in Equation 6.1 such that

$$[K]\{u\} = F \quad (6.2)$$

Using NESSUS, a linear buckling analysis was carried out by using the subspace iteration technique to evaluate the probabilistic buckling load. The corresponding matrix equation for the buckling (eigenvalue) analysis for a linear elastic structure is as follows:

$$([K] - \lambda [K_g]) \{\phi\} = 0 \quad (6.3)$$

In the preceding equation,  $[K]$  is the standard stiffness matrix,  $[K_g]$  is the geometric stiffness,  $\lambda$  is the eigenvalue, and  $\phi$  is the corresponding eigenvector.

Furthermore, the vibration frequency analysis is also carried out using the following equation:

$$([K] - \lambda^2 [M]) \{\phi\} = 0 \quad (6.4)$$

Finally, the NESSUS/FPI (Fast Probability Integration) module extracts the response variables (buckling loads, vibration frequencies, and stresses) to calculate the respective probabilistic distributions and the respective sensitivities associated with the corresponding uncertain random input variables.

## 6.5 Discussion of Results

The combustor liner has to satisfy all the structural reliability and safety requirements under the thermomechanical service loads. Initially, the liner was analyzed probabilistically to obtain the cumulative distribution functions (CDFs) of the probabilistic buckling loads for the first five modes (Figure 6.5). The eigenvalues (critical load/applied load) for the five modes are given in Table 6.2. The sensitivity factors from Figure 6.6 show that the uncertainty in the liner thickness has the highest impact on the probabilistic distribution of the buckling load for the first mode followed by the pressure load and hoop modulus of the liner material. Figure 6.7 through Figure 6.11 show the buckled mode shapes of the liner for modes 1 through 5, respectively. Figure 6.7 indicates rigid body motion, whereas Figure 6.8 and Figure 6.9 depict the edge buckling phenomena, which correspond to a pair of equal eigenvalues (Table 6.2).

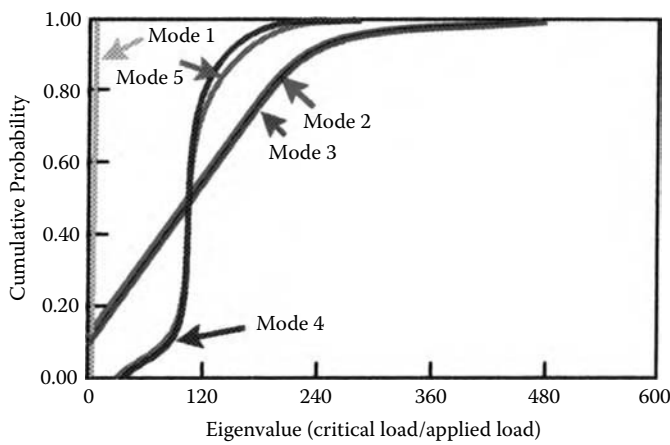


FIGURE 6.5 Cumulative distribution functions of cylindrical liner segment buckling loads.

TABLE 6.2 Probabilistic Buckling Analysis  
[single cup liner segment (pressure load —1 psi)]

Mode Number	Mean Values of Eigenvalue Critical Loads Normalized by the Applied Load
1	1.46
2	106.88
3	106.88
4	116.56
5	118.10

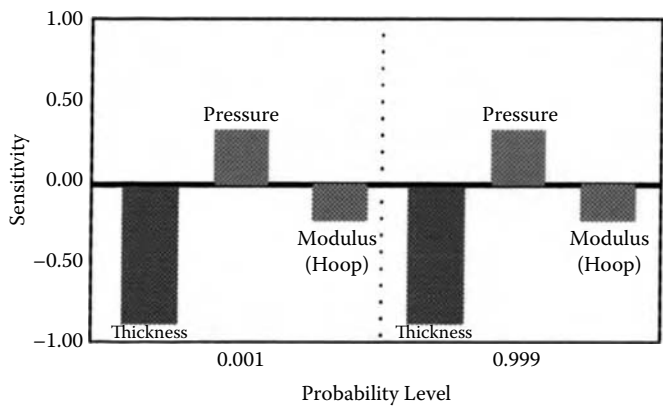


FIGURE 6.6 Probabilistic mode 1 buckling load sensitivities of a cylindrical liner segment.

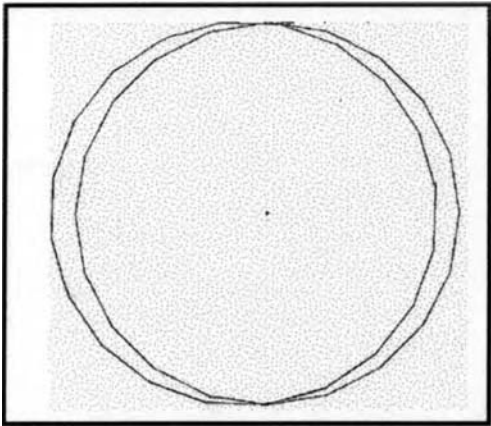


FIGURE 6.7 First buckling mode, indicating rigid body motion.

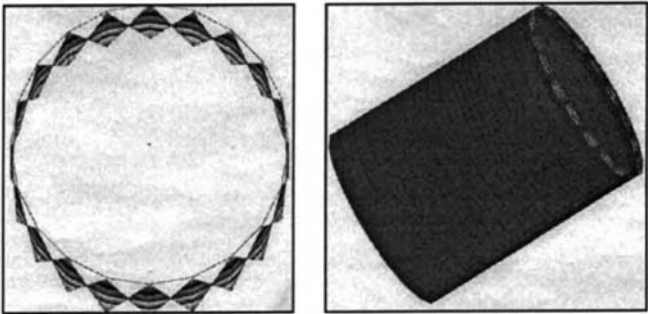


FIGURE 6.8 Mode 2, indicating edge buckling.

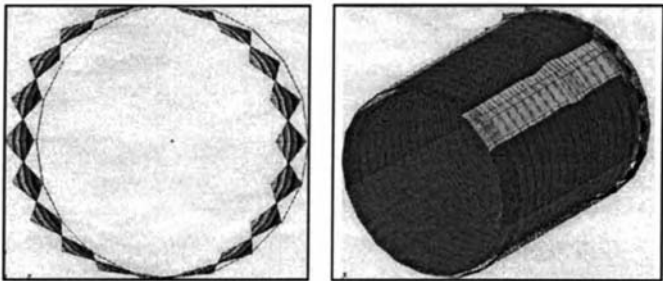
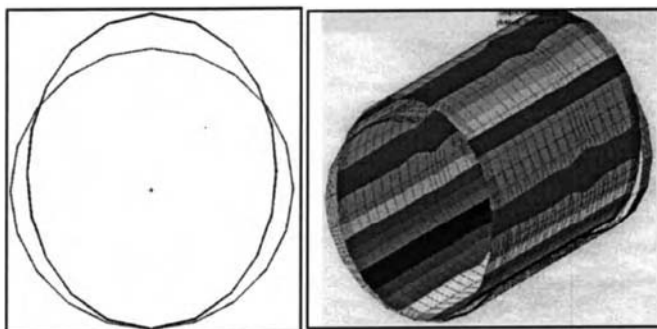


FIGURE 6.9 Mode 3, indicating edge buckling.



**FIGURE 6.10** Mode 4, indicating circumferential radial deformations.

On the other hand, modes 4 and 5, as shown in Figure 6.10 and Figure 6.11, exhibit a combination of circumferential/radial deformations that are typical for cylindrical shell structures. It is important to note that these mode shapes are due to the types of boundary conditions used at the support locations as well as the combination of pressure and thermal loads.

Subsequently, the liner was probabilistically analyzed to obtain the CDFs of the probabilistic vibration frequencies for the first five modes. These CDFs are shown in Figure 6.12. The mean values of the first five natural frequencies are shown in Table 6.3. According to Figure 6.13, the first natural frequency was very sensitive to the scatter in the following properties of the liner material; density, thickness, hoop modulus, and axial modulus. However, for higher probabilities of failure, the impact of the variation in the density of the liner material on the vibration frequencies for the first mode dominates. The respective first five mode shapes are shown in Figure 6.14 through Figure 6.18. The first mode appears to be a rigid body type, and modes 2 through 5 involve circumferential/radial deformations.

In addition to satisfying the design requirements about the allowable vibration frequencies and buckling loads, the stress level in the combustor liner should be below some critical stress level. Therefore, the probabilistic longitudinal stress at a critical location on the inside of the liner was determined for the thermomechanical loads (see Figure 6.19). Furthermore, this stress distribution showed a wide scatter between the lowest and highest longitudinal stresses. According to Figure 6.20, the longitudinal stress distributions were very sensitive to the scatter in the thermal load profile, the variations in the liner material thermal expansion coefficient, and axial modulus. However, the CDFs of the longitudinal stresses

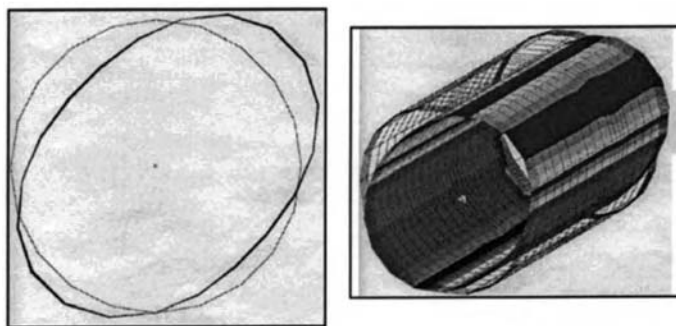


**FIGURE 6.11** Mode 5, indicating circumferential radial deformations.

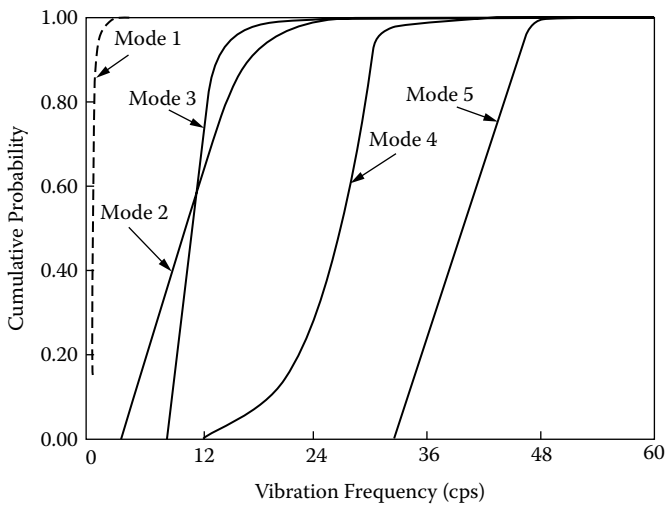


FIGURE 6.12 Cumulative distribution functions of cylindrical liner segment natural frequencies.

TABLE 6.3 Probabilistic Vibration Frequency Analysis  
[single cup liner segment (pressure load — 1 psi)]

Mode Number	Mean Values of Vibration Frequencies (cps)
1	0.97
2	11.08
3	18.97
4	36.43
5	61.17

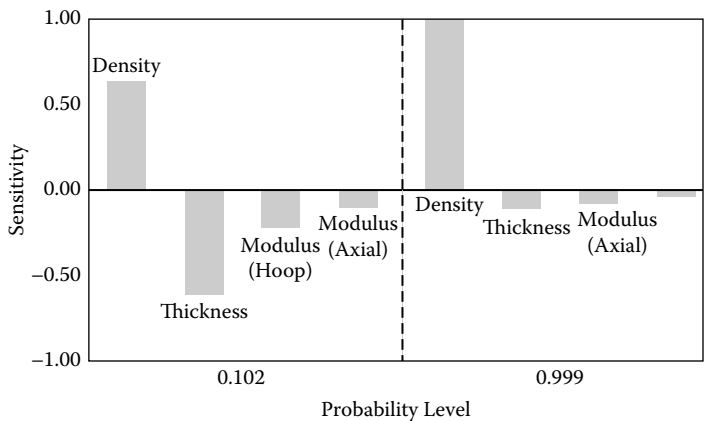


FIGURE 6.13 Probabilistic mode 1 vibration frequency sensitivities of a cylindrical liner segment.

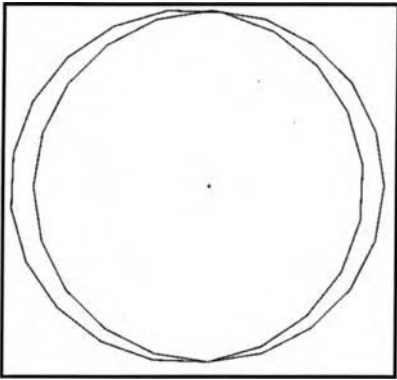


FIGURE 6.14 First vibration frequency, indicating rigid body motion.

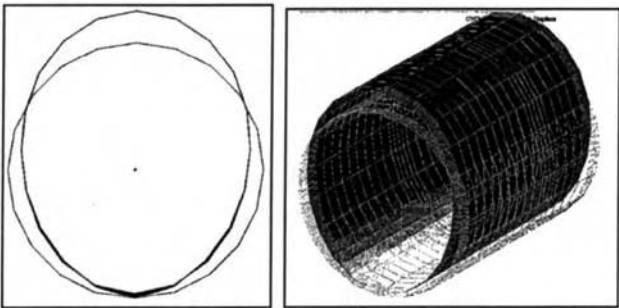


FIGURE 6.15 Second vibration frequency, indicating circumferential/radial deformations.

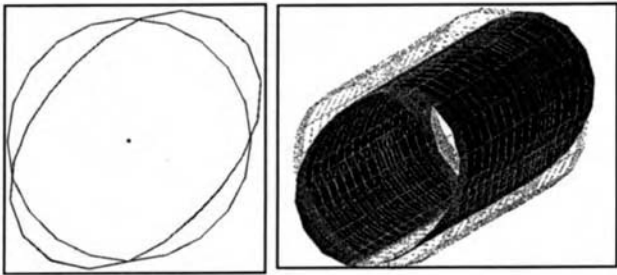


FIGURE 6.16 Third vibration frequency, indicating circumferential/radial deformations.

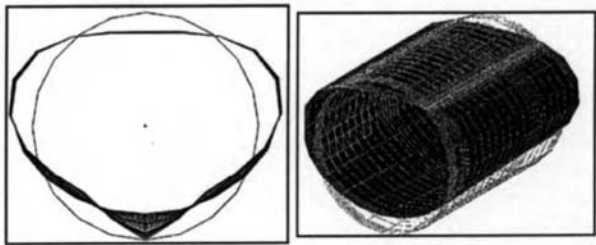


FIGURE 6.17 Fourth vibration frequency, indicating circumferential/radial deformations.

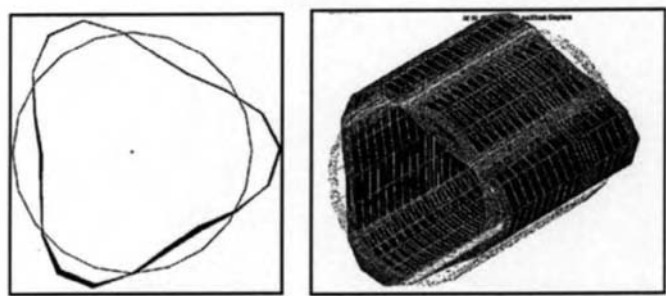


FIGURE 6.18 Fifth vibration frequency, indicating circumferential/radial deformations.

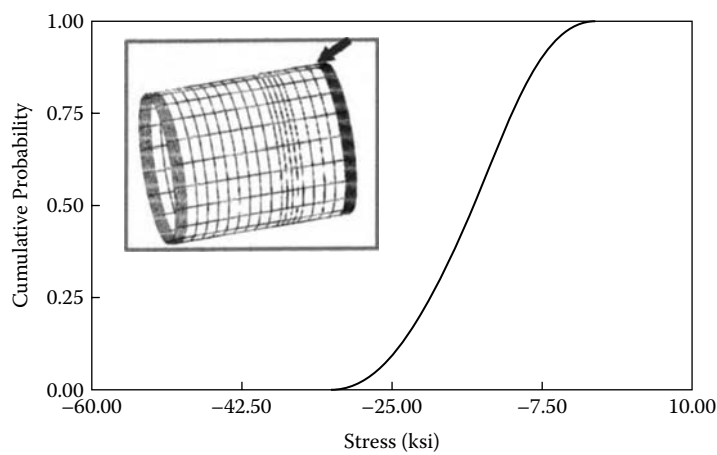


FIGURE 6.19 Cumulative distribution function of Node 441 longitudinal stress.

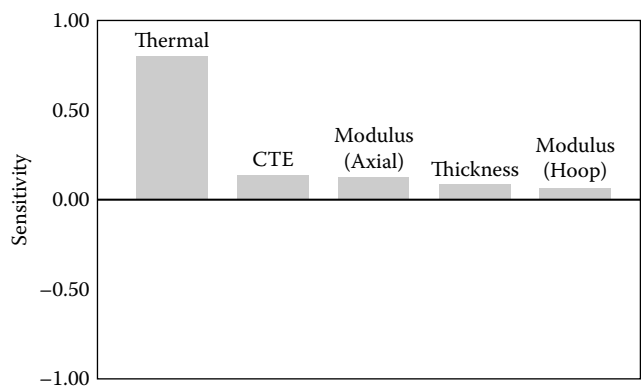
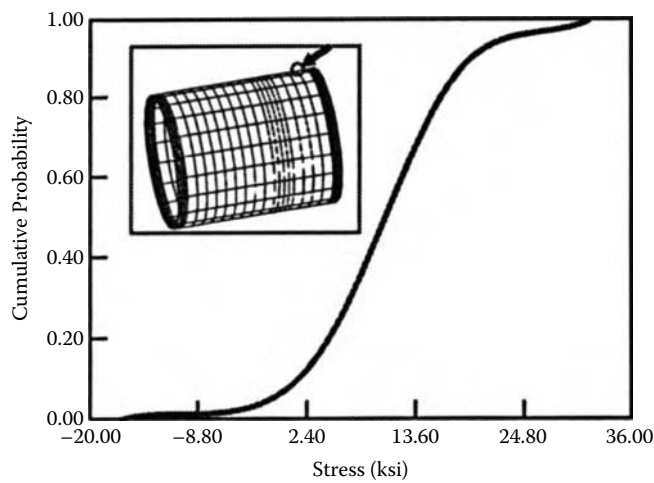


FIGURE 6.20 Probabilistic longitudinal stress sensitivities for Node 441 at 0.001 probability.





**FIGURE 6.21** Cumulative distribution function of Node 421 (outer surface of the liner) longitudinal stress.

for the outer surface of the liner (see Figure 6.21) clearly indicated that the stresses were compressive at the lower probability of failure level, whereas they were tensile at the remaining probability of failure level. Lastly, the probabilistic hoop stress at a critical location indicated the reversal of the stresses (from compressive to tensile) from lower to higher probability of failure levels (see Figure 6.22). Once again, the variation in the thermal load profile has the highest impact on the CDFs of the probabilistic hoop stress (see Figure 6.23). The CDFs of the probabilistic hoop stress at the critical location of the outside of the liner showed a wide variation, and the stress is reversible from the lower probability of failure levels to higher probability of failures (see Figure 6.24).

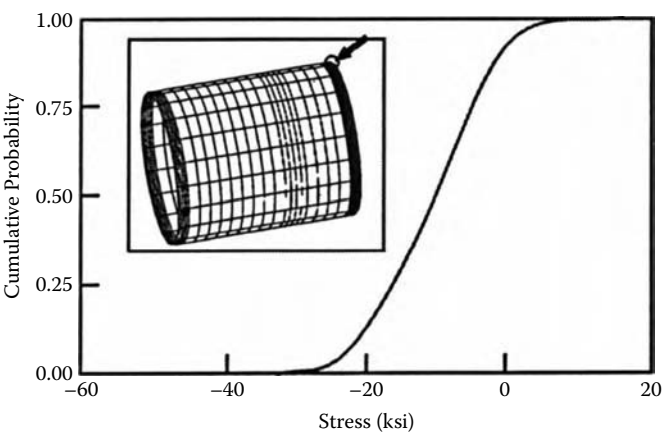


**FIGURE 6.22** Cumulative distribution function of Node 601 hoop stress.

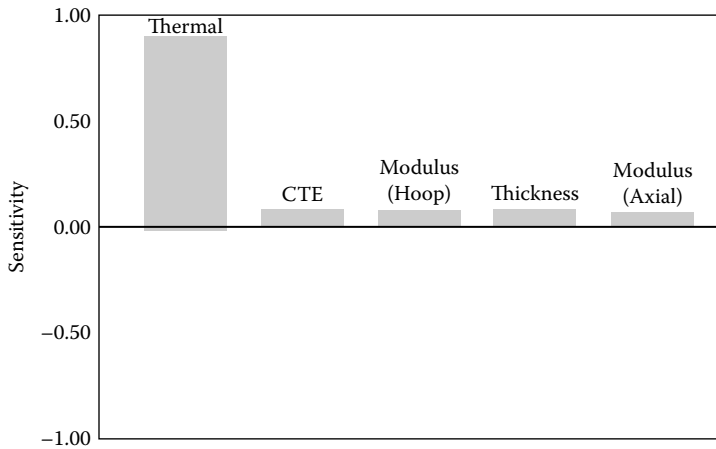


FIGURE 6.23 Probabilistic hoop stress sensitivities for Node 601 at 0.001 probability.

## 6.6 Conclusions

The computational simulation and probabilistic evaluation of a typical hot structural component within an engine, such as a ceramic composite combustor called a single cup cylinder, was demonstrated using the NESSUS code. The combustor liner was analyzed for compressive pressure loading and nonuniform thermal loading along its length as well as through the thickness of the liner. The cumulative distribution functions (CDFs) for buckling (eigenvalues), natural frequencies, and longitudinal and hoop stresses were evaluated. The results indicate that: (1) the variations in the liner thickness have the highest impact on the probability distribution of the buckling load for the first mode followed by the pressure load and the hoop modulus of the liner material; (2) at higher probability of failure levels, the scatter in the density of the liner material has the most significant impact on the probabilistic vibration frequencies for the first mode; (3) the nonuniform thermal load profile and the liner material thermal expansion coefficient

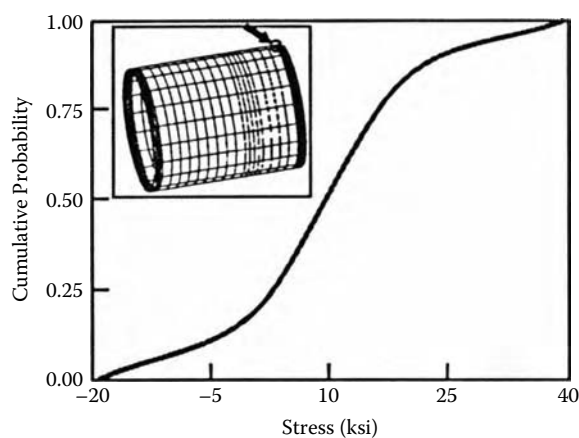


FIGURE 6.24 Cumulative distribution function of Node 461 (outer surface of the liner) hoop stress.

variations had significant impact on the probabilistic longitudinal and hoop stresses at critical locations along the length of the liner. Collectively, the results provide quantifiable guidance on dominant parameters for reliable/robust combustor liner design, including the support condition.

## References

1. Chamis, C.C.: "Probabilistic Structural Analysis Methods for Space Propulsion System Components," Space System Technology Conference, AIAA, New York, 1986, pp. 133–144.
2. Dias, J.B., Nagtegaal, J.C., and Nakazawa, S.: "Iterative Computational Mechanics of Probabilistic Finite Analysis," *Computational Mechanics of Probabilistic and Reliability Analysis*, edited by W.K. Liu and T. Belytschko, ELME Press International, Lausanne, Switzerland, 1989, pp. 211–230.
3. Wu, Y.T.: "Demonstration of New, Fast Probability Integration Method for Reliability Analysis," *Advances in Aerospace Structural Analysis; Proceedings of the Winter Annual Meeting*, edited by O.M. Burnside, ASME, New York, 1985, pp. 63–73.
4. Pai, S.S. and Chamis, C.C.: "Probabilistic Assessment of Combustor Liner Design," ASME TURBO EXPO'95, Land, Sea & Air, The 40th Gas Turbine and Aeroengine Congress/Users Symposium and Exposition, Houston, Texas, 1995.
5. Pai, S.S. and Chamis, C.C.: "Quantification of Thermal–Structural Uncertainties in Engine Combustor Liners," ASME TURBO EXPO'97 Symposium & Exposition, Orlando, Florida, 1997.
6. Mital, S.K. and Murthy, P.L.N.: "CEMCAN—Ceramic Matrix Composites Analyzer User's Guide—Version 2.0," NASA TM–107187, April 1996.

# Probabilistic Analysis and Design in the Automotive Industry

---

Zissimos P. Mourelatos

*Oakland University*

Jian Tu

*General Motors R&D Center*

Xuru Ding

*General Motors Corporation*

7.1	Introduction .....	7-1
7.2	Common Reliability Methods .....	7-2
	Component-Level Reliability Analysis • System-Level Reliability Analysis • Examples	
7.3	Nonparametric Metamodeling (Response Surface) Methods .....	7-10
	Parametric and Nonparametric Multiple-Regression Techniques • Uniform Sampling and Sample Partitioning in Computer Experiments • Cross Validation for Estimating Metamodel Prediction Error • Local Polynomial Fitting Using CVMLS Method • Variable Screening Based on CVMLS • Crash Safety Example for Illustrating CVMLS and Variable Screening	
7.4	Variation Reduction in Robust Engineering: an Automotive Example .....	7-19
7.5	Summary and Future Needs.....	7-22
	Acknowledgments.....	7-24
	References.....	7-24

## 7.1 Introduction

---

Delivering reliable, high-quality products at low cost has become the key to survival in today's global economy. The presence of uncertainty in the analysis and design of engineering systems has always been recognized. Traditional deterministic analysis accounts for these uncertainties through the use of empirical safety factors. These safety factors are derived from past experience and do not provide quantifiable measures of the frequency at which failure will occur.

Engineering design usually involves a trade-off between maximizing reliability at the component or system level while achieving cost targets. In contrast to the traditional deterministic design, probabilistic analysis provides the required information for optimum design and accomplishes both goals simultaneously. In the automotive industry, quality products are vehicles whose specifications, as manufactured, meet customer requirements. Given the uncertainties in loads, materials, and manufacturing, modern methods of reliability analysis should be used to ensure automotive quality in terms of reliability measures.

In large-scale systems, often encountered in the automotive and aerospace industries among others, reliability predictions based on expensive full-scale tests are not economically feasible. Efficient computational methods represent a far better alternative. The first requirement of a computational reliability analysis

is to develop a quantitative model of the behavior of interest. Subsequently, the statistical behavior is defined for all random variables involved in the limit-state function that separates the failure and the safe regions. Finally, the reliability is estimated using a variety of methods. Both analytical and simulation-based methods are available for reliability analysis. The analytical methods are generally simple and efficient, but for complex problems, their accuracy cannot be guaranteed. In simulation-based methods, the accuracy can be controlled, but the efficiency is generally not satisfactory. An overview of the reliability methods is given in Section 7.2. The commonly used analytical and simulation-based methods are described at both the component and system levels. Reliability examples involving an automotive liftgate and a glass-guidance design demonstrate how basic reliability principles are applied in automotive engineering.

To address the high computational costs associated with reliability and robust design assessment of complex automotive systems, the engineering community commonly relies on accurate metamodels, or response-surface models, as surrogates of the computationally demanding CAE models. Fast-running metamodels are typically developed to approximate the CAE model's input–output relationships from a set of pregenerated CAE simulations. Section 7.3 describes in detail the current state of the art of metamodeling in automotive reliability and robust design and illustrates the value of metamodeling with a practical automotive crash safety application.

The current competitive automotive market environment calls for high-quality vehicles in the presence of uncertainty in customer expectations, manufacturing tolerances, and operating conditions. Customers demand reliable and robust products. Robust design, originally proposed by Taguchi, is a method of improving the quality of a product by minimizing (without eliminating) the effect of the causes of variation. It is common to seek “robustness” of a design objective by simultaneously optimizing the mean performance and minimizing the performance variance. Although the importance of robust design has been recognized in the automotive industry, its high computational cost has hindered its wide-scale use by automotive designers. Section 7.4 highlights the importance and computational challenges of robust design by presenting a practical robust design procedure for an occupant-restraint system for frontal-impact performance.

The chapter closes with a summary of the presented work and some recommendations on reliability analysis needs from the automotive industry point of view.

## 7.2 Common Reliability Methods

---

Reliability analysis can be performed at either the component or the system level, depending on the number of limit states of the reliability problem. Analytical and simulation-based reliability methods are available for both component- and system-level reliability problems. The advantages and disadvantages of these methods are discussed in this section.

### 7.2.1 Component-Level Reliability Analysis

#### 7.2.1.1 Analytical Reliability Methods

For a limit-state function  $g$  with multiple random variables represented by a vector  $\mathbf{X}$ , whose joint probability density function is  $f_{\mathbf{x}}(\mathbf{x})$ , the probability of failure is defined as:

$$P_f = \int \cdots \int_{g(\mathbf{x}) < 0} f_{\mathbf{x}}(\mathbf{x}) d\mathbf{x} \quad (7.1)$$

In general, the exact calculation of the above multidimensional integral is difficult. Consequently, various analytical methods have been developed to estimate its value. They are mainly categorized as first-order reliability methods (FORM) or second-order reliability methods (SORM). FORM uses a linear approximation of the limit-state function at the most probable point (MPP), as shown in Figure 7.1. Consequently, for the nonlinear limit state shown, FORM will overestimate the probability of failure, since it considers the contribution of the region between the real limit state and the approximation in calculating the failure probability integral of Equation 7.1.

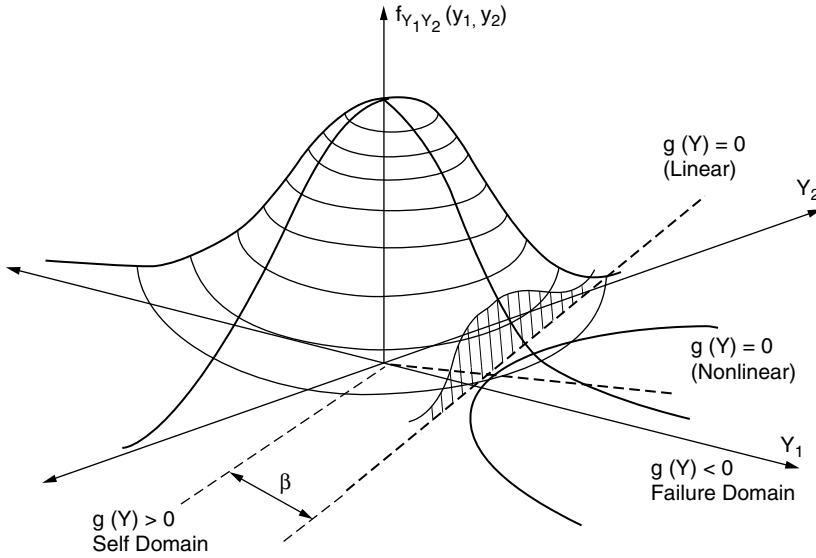


FIGURE 7.1 First-order reliability approximation.

In both FORM and SORM, the original random variables, which are generally nonnormal and correlated, are first transformed into an equivalent set of statistically independent normal variates. A general transformation for this purpose is the Rosenblatt transformation [1]. A two-parameter method suggested by Rackwitz and Fiessler [2] can also be used to find an equivalent set of normal variables. If the random variables are uncorrelated, the standard normal variables can be calculated as

$$Y = \frac{X - \mu_x}{\sigma_x} \quad (7.2)$$

where  $\mu_x$  and  $\sigma_x$  are the equivalent normal mean and standard deviation, respectively, of random variable  $X$ .

The first-order reliability method (FORM) finds the minimum-distance point on the limit state to the origin of the standard normal space by solving an optimization problem, and it subsequently estimates the failure probability based on the minimum distance. The minimum-distance point on the limit state is also called the most probable point (MPP). The first-order reliability estimate is computed as

$$P_f = \Phi(-\beta) \quad (7.3)$$

where  $\beta$  is the distance from the origin to MPP, and  $\Phi$  is the cumulative distribution function of a standard normal variable.

Various techniques can be used to calculate the most probable point (MPP). Rackwitz and Fiessler [2] used a Newton-type recursive formula to search for the MPP as

$$\mathbf{Y}_{k+1} = \frac{1}{|\nabla G(\mathbf{Y}_k)|^2} \{ \nabla G(\mathbf{Y}_k)^T \mathbf{Y}_k - \nabla G(\mathbf{Y}_k) \} \nabla G(\mathbf{Y}_k) \quad (7.4)$$

where  $\nabla G(\mathbf{Y}_k)$  is the gradient of the performance function at the  $k$ th iteration point  $\mathbf{Y}_k$ , defined in the standard normal space.

At each step of FORM, the sensitivity factors can be calculated as

$$\alpha_k = \left( \frac{\partial G(\mathbf{Y}_k)}{\partial y_k} \right) / |\nabla G(\mathbf{Y}_k)| \quad (7.5)$$

For problems with highly nonlinear limit states, the MPP search formula of Equation 7.4 may fail to converge. In such cases, other optimization methods can also be used to search for the MPP [3]. Among those, the sequential quadratic programming (SQP) is very common. In these methods, one needs to evaluate at least the first derivatives and, in some cases, the second derivatives, which brings additional computational cost for an implicit limit state containing a large number of random variables.

Even if the algorithm converges in searching for the MPP, the first-order reliability estimation may not be accurate for nonlinear limit states. Several more sophisticated reliability-analysis techniques have been developed to overcome the difficulty of FORM. The advanced mean value (AMV) method [4, 5] combines the information from the mean value first-order (MVFO) step and one additional deterministic analysis to obtain a substantially improved reliability estimate. Several second-order reliability methods (SORM) have also been developed [6–10]. In Breitung's SORM [6], the probability content in the failure domain is approximated using an asymptotic formula such as

$$P_f = \Phi(-\beta) \prod_{i=1}^{n-1} (1 + \beta \kappa_i)^{-1/2} \quad (7.6)$$

where  $\beta$  is the first-order reliability index, and  $\kappa_i$  represents the main curvatures of the failure surface at the design point.

Tvedt's SORM [8] improves over Breitung's method in two ways. First, it uses a full second-order Taylor series expansion at the design point to approximate the failure surface, and second, it numerically evaluates the probability content of the parabolic failure domain. Köylüoglu and Nielsen [7] proposed three closed-form approximations for SORM integrals, of which the one-term approximation is the simplest. Cai and Elishakoff [9] presented a refined second-order approximation, which is a series formula with three terms. Zhao and Ono [10] suggested a simple point-fitting SORM approximation and an empirical second-order reliability index for easy practical application of SORM.

### 7.2.1.2 Simulation-Based Reliability Methods

There is also a simulation-based category of reliability methods. The basic Monte Carlo method belongs in this category. It is simple to implement and can therefore be used for almost all problems, at any desired accuracy. However, the limit state needs to be evaluated a large number of times with randomly sampled input values of the design parameters, which can be time consuming and expensive for problems with implicit limit-state functions and high reliability. To address the high computational cost of the Monte Carlo method, several more-efficient simulation-based methods have been developed [11]. One of these is importance sampling.

The basic idea of importance sampling is to minimize the total number of sampling points by concentrating the sampling in the failure region. It can be reasonably efficient if a sampling density is used to generate sample points in the failure region, where the probability density is the greatest. However, in many cases, it is difficult to know the shape of the failure region in advance. To overcome this difficulty, the concept of adaptive importance sampling (AIS) has been proposed [12, 13].

The AIS is based on the idea that the importance-sampling density function can be gradually refined to reflect the increasing state of knowledge of the failure region. The sampling space is adaptively adjusted based on the generated sampling points. Two versions of AIS have been developed. The first version uses an adaptive surface to approximate the limit state. Based on different adaptive surfaces, a radius-based method, a plane-based method, and a curvature-based method have been developed [14]. The curvature-based method is generally the most efficient among the three, although its efficiency and robustness rely on the accuracy of the initial MPP. The second version of AIS is called multimodal adaptive importance sampling [13, 15, 16]. It uses a multimodal sampling density to emphasize all important sample points in the failure domain, each in proportion to the true probability density at the particular sampling point [15, 16]. This method was applied to component and system reliability analyses of large structures [16–18] with very satisfactory results.

## 7.2.2 System-Level Reliability Analysis

The search for computationally efficient procedures to estimate system reliability has resulted in several approaches, most of which belong to the enumeration and analytical bounds category and the efficient MCS (Monte Carlo simulation) category.

In the first category, the branch-and-bound method provides a systematic procedure to identify the various failure sequences of a system. It mainly involves the branching and the bounding operations. In the second category, several importance-sampling schemes developed over the last decade are used to estimate the system reliability. These schemes can be divided into direct methods [13, 19], updating methods [20–22], spherical schemes [23, 24], and adaptive schemes [15, 25]. All of the above methods, except the adaptive schemes, require prior knowledge of the failure region. System-reliability techniques, which account for progressive damage over time, have also been developed [26–28].

### 7.2.2.1 Analytical Methods for System-Reliability Analysis

The joint-failure probability of multiple failure events often needs to be computed during system-reliability analysis. Due to the difficulty in determining the joint-failure probabilities of more than two failures except through MCS, approximations using bounds were developed first. The simplest bounds are Cornell's first-order bounds [29]:

$$\max_{1 \leq i \leq n} P(E_i) \leq P\left(\bigcup_{i=1}^n E_i\right) \leq \sum_{i=1}^n P(E_i) \quad (7.7)$$

The general bimodal (second-order) bounds [30] can also be used to calculate the range of the system reliability as

$$P_1 + \max \left[ \sum_{i=2}^k \left\{ P_i - \sum_{j=1}^{i-1} P_{ij} \right\}; 0 \right] \leq P_f \leq \sum_{i=1}^k P_i - \sum_{i=2}^k \max_{j < i} P_{ij} \quad (7.8)$$

where  $P_1$  is generally selected as the maximum failure probability value among the  $k$  limit states, and  $P_{ij}$  is the joint probability of the  $i$ th and  $j$ th events. Ditlevsen [24] proposed a weakened version of the above bimodal bounds for Gaussian (normal) variables.

Hohenbichler and Rackwitz [20] and Gollwitzer and Rackwitz [31] developed numerical solutions for the multinormal integral that provide good approximations. Xiao and Mahadevan [27] proved that the upper bound for the intersection probability based on Ditlevsen's lower bound for the probability of union gives a rough upper bound, especially when the two least probable events are highly correlated. They also suggested that the numerical solutions of a multinormal integral be used if the reliability bounds do not have the desired accuracy.

### 7.2.2.2 Simulation-Based Methods for System-Reliability Analysis

In addition to enumeration methods, many simulation-based methods have been developed for system-reliability analysis. In general, the multimodal adaptive importance sampling [15, 18] and the sequential conditional importance sampling (SCIS) [32] have been found to be efficient. In SCIS, the multinormal distribution function is expressed as a product of  $m$  conditional probability terms:

$$\begin{aligned} \Phi_m(\mathbf{c}, \mathbf{R}) &= P \left[ (X_m \leq c_m) \mid \bigcap_{k=1}^{m-1} (X_k \leq c_k) \right] \\ &\quad \times P \left[ (X_{m-1} \leq c_{m-1}) \mid \bigcap_{k=1}^{m-2} (X_k \leq c_k) \right], \dots, \times \Phi(c_1) \\ &= \Phi(c_1) \prod_{k=2}^m E[I_k \mid I_1 = I_2 = \dots = I_{k-1} = 1] \end{aligned} \quad (7.9)$$



where  $\mathbf{R}$  is the covariance matrix,  $m$  is the number of random variables, and  $I_k$  is the indicator function ( $I_k = 1$  for  $X_k \leq c_k$ , else  $I_k = 0$ ). Equation 7.9 can be recast as a sequential simulation of random variables,  $X_k \leq c_k$  ( $k = 1, \dots, m$ ), from the conditional normal density function,  $\phi_k(x_k | x_1, \dots, x_{k-1})$ , provided that  $I_1 = I_2 = \dots = I_{k-1} = 1$ . This approach was found to lead to fairly accurate estimates of  $\Phi_m(\mathbf{c}, \mathbf{R})$  with a relatively small number of simulations. Pandey and Sarkar [33] proposed the following approximation:

$$P \left[ X_{m+1-p} \leq c_{m+1-p} \mid \bigcap_{k=1}^{m-p} (X_k \leq c_k) \right] \approx \Phi(c_{(m+1-p)|(m-p)}) \quad (7.10)$$

where  $c_{(m+1-p)|(m-p)}$  is a conditional normal fractile, leading to the following approximation for the multinormal distribution function:

$$\Phi_m(\mathbf{c}, \mathbf{R}) \approx \prod_{k=1}^m \Phi(c_{k|k-1}) \quad (7.11)$$

This is referred to as product of conditional marginals (PCM). Both SCIS and PCM are based on the multinormal integral, which requires that the random variables have normal distributions and the limit-state functions be linear. Transformations can be used to extend these methods to nonlinear limit states with nonnormal random variables.

### 7.2.3 Examples

The application of these basic reliability principles in the automotive industry is illustrated with two examples. In the first example, the reliability of an all-glass liftgate design is assessed using the probability of the maximum deflection exceeding a certain target value. The second example provides a reliability study of a cable-drive glass guidance system that is widely used as the mechanism to operate the window glass of a vehicle.

#### 7.2.3.1 Liftgate Reliability

The evenness and flushness of the gaps around the liftgate of a vehicle are important for the insulation of noise and water, as well as for customer-perceived quality. One source of variation in the gap flushness is the deflection of the liftgate panel. In this example, a method is presented for evaluating the reliability of the liftgate at the design stage, as it relates to the gap flushness.

Figure 7.2 shows the back view of a sport-utility type of vehicle, with a proposed all-glass liftgate design. The proposed liftgate is made of glass, with no metal frame around it. It is attached to the vehicle body with two hinges at the top. A pair of gas struts is glued to the liftgate to assist its opening. However, when the liftgate is closed, the gas struts exert a force on the liftgate, forcing it to deflect outward. This deflection increases the gap between the liftgate and the vehicle body, which may cause water leakage or an increased level of wind noise in the vehicle cabin.

The maximum deflection occurs where the gas struts are attached, and this can be evaluated using the ABAQUS commercial finite element code. The maximum deflection of the liftgate varies due to the variation of glue properties such as modulus of elasticity  $E_{glue}$  and Poisson ratio  $\mu_{glue}$ , the variation of the gas-strut forces due to temperature changes, and the variation of the glass modulus of elasticity  $E_{glass}$ . Our objective is to evaluate the reliability of the all-glass liftgate design, which is defined as the probability for the deflection not to exceed a certain maximum value. This reliability can be used as a performance measure to choose among alternative designs.

Figure 7.3 illustrates how the variation is transmitted. A linear static finite element model is created for predicting the deflections at the attachment locations of the gas struts. The parameters  $E_{glue}$ ,  $E_{glass}$ ,  $\mu_{glue}$ , and  $E_{steel}$  are assumed to be normally distributed, with means and standard deviations obtained from measurement data, best practices, or expert opinions.

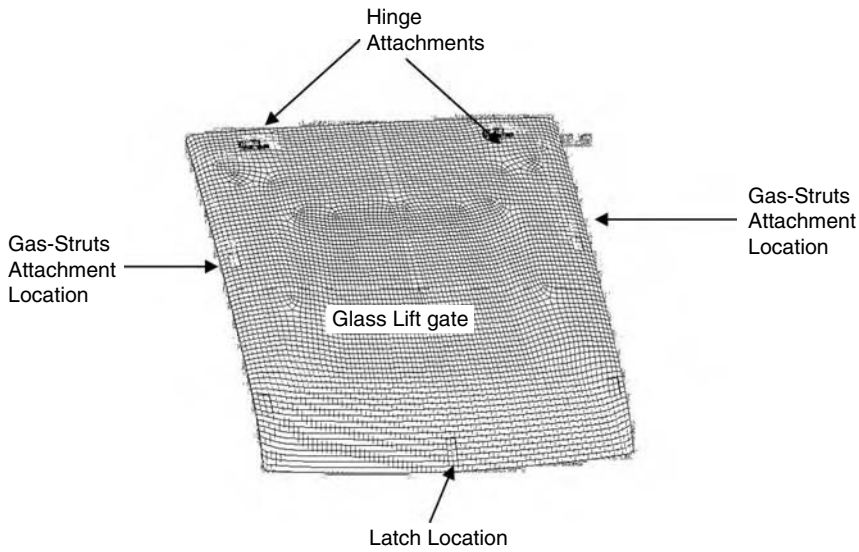


FIGURE 7.2 A CAD view of a glass liftgate at its closed position.

The limit-state function is defined by

$$d - D \leq 0, \quad (7.12)$$

where  $D$  is the target maximum displacement, and

$$d = f(E_{glue}, E_{glass}, \mu_{glue}, E_{steel}) \quad (7.13)$$

is the deflection at the gas-strut attachments when the liftgate is closed.

In this study, FORM was used to estimate the reliability of the design. Normal distributions were assumed, with large variation of the glue properties. For a target maximum displacement of  $D = 1$  mm, it was found that the probability of  $d$  being greater than  $D$  is 0.15. This means that the reliability of the proposed design is 0.85. The relatively low reliability is due to the large deflection  $d$  resulting from the fact

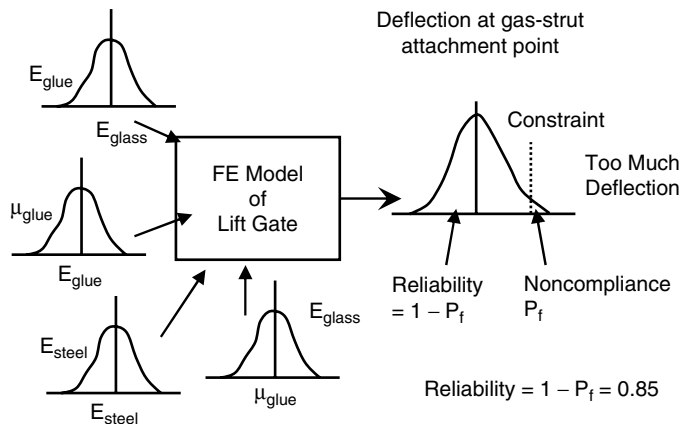


FIGURE 7.3 Schematic of liftgate reliability prediction.

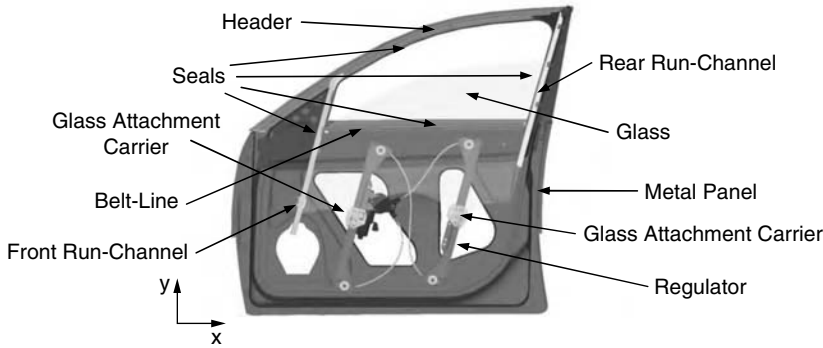


FIGURE 7.4 Schematic of a cable-driven glass guidance system.

that the nominal glass panel thickness does not provide adequate stiffness needed to counter the forces exerted by the struts. Another liftgate design, with a thin metal frame around the glass, was proposed as an alternative. Its reliability was found to be much higher than 0.85, and it was therefore chosen as the appropriate design.

In general, if an all-glass liftgate is preferred due to its aesthetic appeal, its reliability can be also improved by either increasing the thickness of the glass panel to provide more stiffness, or by reducing the gas-strut forces. The strut forces are designed to hold the liftgate at the open position at extremely low temperatures. A trade-off between the aesthetics and the hold-open requirement can be made to enable the use of an all-glass liftgate design.

### 7.2.3.2 Glass Guidance Design Reliability

A cable-drive glass guidance system [34–41], shown in Figure 7.4, is widely used as the mechanism to operate the window glass of a vehicle. This design has advantages in reducing weight and cost, compared with the commonly used cross-arm window-regulator design. However, the cable-drive design is more sensitive to system parameter variation. These variations affect the system reliability, which is traditionally assessed through hardware testing. Due to the complexity of the system integration, it is efficient and effective to use CAE simulations to assess the system reliability at the early stages of the product development process.

A glass guidance system consists of four major subsystems, the metal panel, seals, glass, and the regulator. The glass is driven by the regulator, which is powered by an electric motor. The motor torque is designed to overcome, first, the friction between the glass and the seal and, second, the glass weight. The required torque is therefore an important system performance metric. For a design to be valid, the available motor torque must be greater than the required torque to move the glass. Seal strips are attached to the metal panel in order to prevent airborne noise and water leakage. The window glass moves up and down through the space between the inner and outer belt-line seal lips, while its front and rear edges are embedded between the inner and outer seal lips of the run channels. The header seal provides insulation for the top edge of the glass at the fully up position. The glass movement is driven by a regulator subsystem through two attachment carriers, as shown in Figure 7.5. The carriers are driven by a cable along two guidance rails. An electric motor provides the torque needed to move the cable through a cable drum, as well as to overcome the friction between the cable and pulleys.

To analytically assess the reliability of the glass guidance system, a CAE model was created. A kinematic model was used to express the resultant forces at the two carriers,  $f_1$  and  $f_2$ , as

$$f_1 = f_1(\delta_1, \delta_2, \mu_s, k) \quad (7.14a)$$

$$f_2 = f_2(\delta_1, \delta_2, \mu_s, k) \quad (7.14b)$$

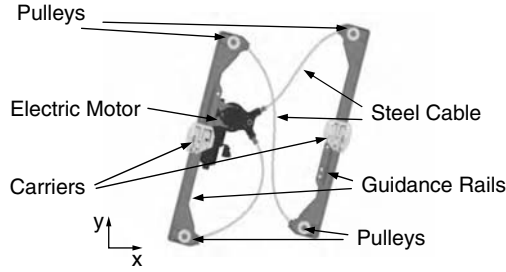


FIGURE 7.5 Schematic of a dual-cable regulator.

where  $\delta_1$  is the glass position in the cross-vehicle direction,  $\delta_2$  is the regulator position in the fore-aft direction,  $\mu_s$  is the seal friction coefficient, and  $k$  is the seal stiffness. The required system torque  $T$  can be subsequently expressed as

$$T = F(f_1, f_2, p, \mu_t) \quad (7.15)$$

where  $p$  is the regulator cable pre-tension, and  $\mu_t$  is the friction coefficient of the regulator components.

In order to handle the high computational cost associated with a reliability analysis, metamodels were developed for forces  $f_1$  and  $f_2$ . Using a design of experiment (DOE) matrix, a number of simulations using the CAE model were first performed. Since there is a nonlinear relationship between the carrier forces and design parameters, a quadratic regression model that includes interaction terms was used. For efficiency reasons, 25 runs were performed, corresponding to a fractional factorial central composite DOE with four variables and three levels [42]. The developed metamodels for  $f_1$  and  $f_2$  are as follows:

$$f_1(\delta_1, \delta_2, \mu_s, k) = 3.7 - 1.4\delta_1 - 0.1\delta_2 + 53.7\mu_s + 2.4k - 0.03\delta_1\delta_2 - 0.8\delta_1\mu_s + 8.9\delta_1k + 0.9\delta_2\mu_s + 0.1\delta_2k - 51.4\mu_s k - 1.6\delta_1^2 - 3.2\delta_2^2 - 51.4\mu_s^2 - 3.6k^2 \quad (7.16a)$$

$$f_2(\delta_1, \delta_2, \mu_s, k) = 40.6 - 2.5\delta_1 - 0.1\delta_2 - 45.3\mu_s + 3.8k + 0.02\delta_1\delta_2 + 8.8\delta_1\mu_s - 4.7\delta_1k - 1.1\delta_2\mu_s - 0.08\delta_2k + 283.6\mu_s k + 1.9\delta_1^2 + 2.6\delta_2^2 + 51.5\mu_s^2 + 0.7k^2 \quad (7.16b)$$

Note that the metamodels include all linear and interaction terms as well as all squared terms.

For estimating the reliability of the glass guidance system, the six input variables in Equation 7.15 and the torque  $T_0$  provided by the motor are considered normally distributed, independent random variables with means and standard deviations as given in Table 7.1. The probability distribution data have been obtained from the system manufacturers.

The limit-state function is given by  $T_0 - T \leq 0$ , where Equation 7.15 is used to calculate the motor torque  $T$ . For this particular example, the advanced mean value method (AMV) [4, 5] estimated the system reliability accurately and efficiently. Figure 7.6 shows the calculated cumulative distribution

TABLE 7.1 Description of Random Variables for the Glass Guidance System

Parameter	Assumed Distribution	Mean	Standard Deviation
Glass position, $\delta_1$	normal	0.0	0.45
Regulator position, $\delta_2$	normal	0.0	2.24
Seal friction coefficient, $\mu_s$	normal	0.2	0.04
Seal stiffness, $k$	normal	1.0	0.32
Cable pretension, $p$	normal	33.0	1.82
Friction coefficient of regulator, $\mu_t$	normal	0.1	0.03
Torque provided by motor, $T_0$	normal	7.0	0.5

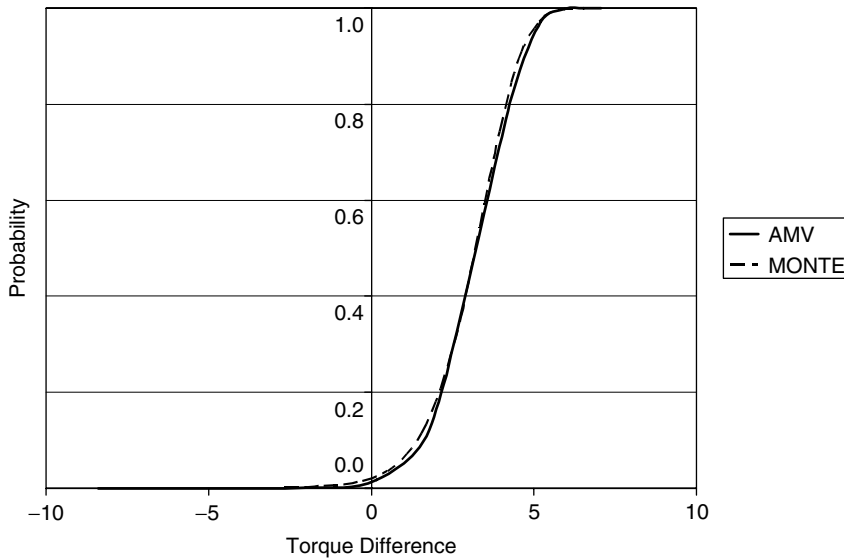


FIGURE 7.6 Reliability estimation for the glass guidance system.

function (CDF) with both the AMV and Monte Carlo methods, indicating the good accuracy of the AMV method.

If the estimated reliability is not satisfactory, a reliability-based design optimization (RBDO) [43–46] algorithm can be used to change the mean values of the six random variables so that the reliability requirement is met.

### 7.3 Nonparametric Metamodeling (Response Surface) Methods

Each probabilistic analysis of a CAE model often requires a large number of time-consuming CAE simulations. Moreover, each CAE simulation (such as a full-vehicle crash simulation using a large-scale finite element model) can be time consuming, even in the current high-performance computing environment. The broader applications of probabilistic analysis in engineering design [47, 48] only become feasible by using fast-running multivariate metamodels (also known as response-surface models or surrogate models) that can capture the generally nonlinear implicit input/output relationships in the time-consuming multidisciplinary CAE simulations [49, 50].

The traditional response-surface methodology using the design of experiments (DOE) techniques [51–54], such as fractional factorials, central composite, Plackett-Burman, and Box-Behnken designs, is usually computationally efficient. However, it often becomes inadequate in nonlinear multivariate metamodeling of complex CAE models. For this reason, some recent advances in nonparametric metamodeling are introduced in this section, along with the progressive space-filling sampling and variable screening techniques.

#### 7.3.1 Parametric and Nonparametric Multiple-Regression Techniques

The multivariate metamodeling provides efficient input–output relationships. CAE simulations are used to calculate the output values at various points of the input variable space. Subsequently, multiple-regression techniques are used to construct a metamodel for best fitting the provided set of output values.

In traditional parametric regressions, one assumes that the metamodel functional form is known (e.g., polynomials in the conventional least-squares regression). The goal of regression analysis is to determine

the parameter values of the assumed functional form, so that the generated metamodel best fits the provided data set. A linear or nonlinear parametric metamodel is likely to produce good approximations only when the assumed functional form is close to the true underlying function. For this reason, nonparametric regression techniques have attracted a growing interest [55–62]. They only use a few general assumptions about the functional form of the metamodel, such as its smoothness properties. The functional form is not prespecified, but determined instead from the available data. The nonparametric approach is therefore more flexible and is likely to produce accurate nonlinear approximations even if the true underlying function form is totally unknown.

Many nonparametric techniques have been proposed for univariate modeling, such as smoothing splines and local polynomial fitting [55–57]. They can be easily extended to multivariate cases. As a more general case of smoothing splines, nonparametric regression methods using Gaussian process models (similar to “kriging” in spatial statistics) and radial basis functions (RBF) have been used to fit data from computer experiments [58–60]. The local polynomial fitting and “kriging”/RBF techniques have demonstrated better predictive performance than the parametric regression techniques [61, 62]. Their main advantage is an automated metamodeling process, in which the hyperparameters in local polynomial fitting and “kriging” can be determined by minimizing the metamodel cross-validation error and maximizing the likelihood function, respectively [63–65]. The local polynomial fitting, using the cross-validated moving least-squares (CVMLS) method, is discussed in detail in Section 7.3.5.

### 7.3.2 Uniform Sampling and Sample Partitioning in Computer Experiments

Fractional factorial designs are the most popular sampling schemes in design of experiments (DOE) using the traditional parametric multiple-regression techniques. However, they are very often limited to two or three levels, even for a small number of input variables, due to the rapidly increasing number of required computer experiments with increasing number of inputs. In creating a metamodel of a CAE model, we want to use a modest number of computer experiments with many levels to explore potentially nonlinear input/output relationships. Previous studies [66, 67] have found that uniformity is the most important criterion and, moreover, that the space-filling uniform design is preferable for robust designs. The main advantage of the uniform design is its better representation of the input variable space with fewer samples for a large number of levels.

Perfectly uniform samples can be achieved by using a regular grid of sample points. However, the regular-grid sampling approach does not scale well to higher dimensions. In multivariate applications, random or quasi-random sampling techniques are therefore used to achieve optimum uniformity, which is commonly measured by a “minimum interpoint distance” criterion in terms of Euclidean distance normalized in  $[0, 1]^n$  space. Instead of searching for the minimum interpoint distance among all sample pairs, a function  $\varphi_p$  is used to conveniently assess the minimum interpoint distance for a set of  $N$  samples  $(\underline{x}^1 \dots \underline{x}^N)$ . The function  $\varphi_p$  is defined as  $\varphi_p = \sum_{(i,j)} (1/(d(\underline{x}^i, \underline{x}^j))^p)$ , where  $p \geq 1$ . Since the value of  $\varphi_p$  is mainly determined by the minimum interpoint distance, the criterion for optimum sample uniformity is equivalent to the minimization of  $\varphi_p$  ( $\varphi$  criterion).

The optimum uniform sample set is not necessarily unique and can be very difficult to find. It is, therefore, more practical to find the best sample set, in terms of the  $\varphi$  criterion, from a large number of either randomly or structurally generated sample sets. Although it is simple to find a better sample set by searching through a large number of randomly generated sample sets, the associated computing effort can be prohibitive. For this reason, some structured quasi-random sampling techniques, such as Latin hypercubes and randomized orthogonal arrays, have been used extensively in multivariate uniform sampling. The structured quasi-random samples are carefully constructed to give better uniform coverage of the sampled space while maintaining a reasonably random appearance. In Figure 7.7a, ten samples are randomly generated in a four-dimensional space, and their one-dimensional projections (normalized histogram plots on diagonal) and the two-dimensional projections (off-diagonal plots) are presented. As shown in Figure 7.7b, the quasi-random Latin hypercube (LH) sampling maintains the sample uniformity

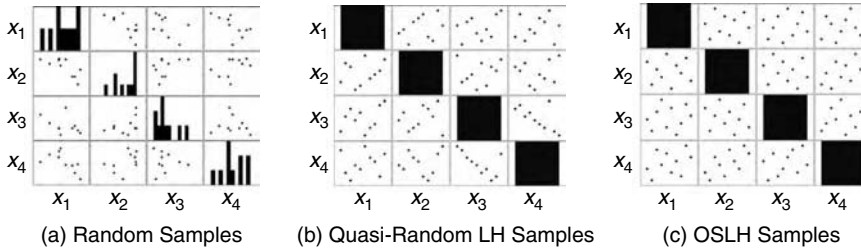


FIGURE 7.7 Comparison of uniform sampling techniques.

in their one-dimensional projection. For this reason, significantly less computing effort is required to find a much-improved sample set.

More recently, certain orthogonal properties were found in the so-called symmetric Latin hypercube (SLH) sampling, in which LH samples are constructed to be symmetric to the center of the sampled space. An efficient columnwise–pairwise exchange algorithm was proposed by Ye et al. [67] for finding optimal symmetric Latin hypercube (OSLH) samples in terms of certain uniformity criteria, such as the  $\phi$  criterion. As shown in Figure 7.7c, the OSLH sample set provides much better uniform coverage compared with both a random sample set (Figure 7.7a) and an arbitrary quasi-random LH sample set (Figure 7.7b).

Because the uniform designs avoid close sample pairs, they are also preferred in estimating the meta-model prediction error, using a “leave-one-out” cross-validation procedure. The entire uniform sample set is divided into several groups so that the samples in each group are evenly scattered in the sampled space. The union of any groups maintains the uniformity or space-filling property. An intergroup exchange algorithm is used to minimize the sum of within-group  $\phi$  measures. As shown in Figure 7.8, a 30-sample OSLH set in two dimensions is partitioned into two groups. Each group of samples uniformly covers the sampled space, even though it does not, in general, maintain the SLH properties by itself. The 30-sample OSLH set is the union of the two partitioned groups.

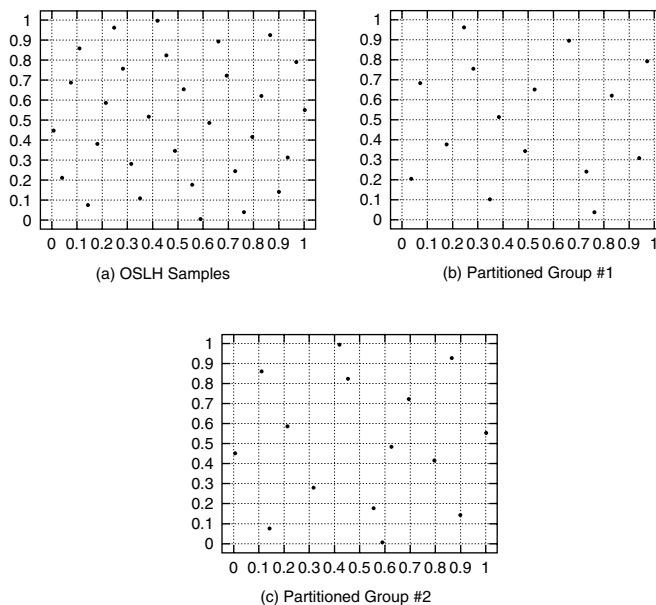


FIGURE 7.8 Illustration of uniform sample partitioning.

### 7.3.3 Cross Validation for Estimating Metamodel Prediction Error

For a given number of sample data, the metamodel prediction error can be reliably assessed using dedicated holdout samples. However, the holdout samples reduce the actual number of available samples for constructing the metamodel. For this reason, certain in-sample criteria are always used [52, 54].

To avoid overfitting in nonparametric regression techniques, cross validation and generalized cross validation [56, 68, 69] have been widely used for estimating metamodel prediction error. A  $K$ -fold cross-validation procedure is described in three steps. First, the known sample set is partitioned into  $K$  roughly equal-sized groups. Second, a metamodel is constructed using the union of  $K-1$  groups, and the prediction error is calculated for the  $K$ th group. Finally, the previous step is repeated for  $k = 2, \dots, K$ , and all prediction errors are combined to form the cross-validation error. To minimize the cross-validation overhead, a “leave-one-out” cross-validation procedure can be used, in which every known sample is left out successively, and then its value is predicted back.

Although the cross-validation procedure generally provides a good indicator of the metamodel accuracy, it is often necessary to also check the metamodel’s convergence with increasing sample size. We can generate a rather large uniform sample set and then uniformly partition it into many evenly scattered (space-filling) groups. All samples in each group are progressively evaluated using CAE simulations. Every time a new group of samples is added, the current metamodel’s prediction error on the new samples is calculated. Convergence is achieved when the improvement on the metamodel prediction error with the newly added group is small. This progressive sampling strategy can also be used for a converged variable-screening procedure.

### 7.3.4 Local Polynomial Fitting Using CVMLS Method

The moving least-squares (MLS) method originated in curve and surface fitting [70]. For a multivariate function  $f(\underline{x})$ , the notation  $\underline{x}^i = [x_1^i \ x_2^i \ \dots \ x_n^i]^T$  represents the  $i$ th point of  $N$  known sample points scattered in the  $n$ -dimensional space, where the sampling space is always normalized to the cube  $[0, 1]^n$ . The corresponding function value is denoted as  $f^i = f(\underline{x}^i)$  for  $i = 1, \dots, N$ . The function  $f(\underline{x})$  can generally be approximated by  $g(\underline{x})$ , using a linear combination of polynomial basis functions [57], as

$$f(\underline{x}) \approx g(\underline{x}) = \sum_{j=1}^m a_j \cdot b_j(\underline{x}) = \underline{a}^T \cdot \underline{b}(\underline{x}) \quad (7.17)$$

where the terms in  $\underline{b}(\underline{x})$  are the set of  $m = n + 1$  linear polynomials:

$$\underline{b}(\underline{x}) = [b_1(\underline{x}) \ b_2(\underline{x}) \ \dots \ b_m(\underline{x})]^T = [1 \ x_1 \ \dots \ x_n]^T. \quad (7.18)$$

It is assumed in MLS that the predicted function value at a point  $\underline{x}$  should be most strongly influenced by the values of  $f^i$  at those points  $\underline{x}^i$  that are closest to  $\underline{x}$ . This suggests that different weights should be assigned to each of the known sample points  $\underline{x}^i$  according to their distance to the prediction point  $\underline{x}$ . We can then choose the coefficients  $\underline{a}$  to minimize the weighted sum of residual-error squares:

$$E_{\underline{x}}(g) = \sum_{i=1}^N w^i(\underline{x}) \cdot (g(\underline{x}^i) - f^i)^2 \quad (7.19)$$

where the positive weight function  $w^i(\underline{x})$  has the property that its value decreases monotonically as the distance from  $\underline{x}$  to  $\underline{x}^i$  increases. A commonly used form for the weight function is

$$w(d(\underline{x}, \underline{x}^i)) = \exp(-\alpha(d(\underline{x}, \underline{x}^i))^2) = \exp\left(-\alpha \sum_{k=1}^n (x_k - x_k^i)^2\right) \quad (7.20)$$



where  $d(\underline{x}, \underline{x}^i)$  is a measure of the distance between  $\underline{x}$  and  $\underline{x}^i$ . The ordinary least-squares formulation is a special case in which the weight function  $w^i(\underline{x})$  is a constant. The nonnegative tuning parameter  $\alpha$  controls the degree of localization in MLS local polynomial regression by scaling the slope of the weight function.

Since the weight function is defined around the prediction point  $\underline{x}$  and its magnitude changes or “moves” with  $\underline{x}$ , the function that minimizes the error functional in Equation 7.19 is called the moving least-squares (MLS) approximation  $g_{mls}(\underline{x})$  of the original function  $f(\underline{x})$ . Because the weights  $w^i(\underline{x})$  are functions of  $\underline{x}$ , the polynomial basis function coefficients  $\underline{a}$  are also dependent on  $\underline{x}$ , i.e.,

$$f(\underline{x}) \approx g_{mls}(\underline{x}) = \sum_{j=1}^m a_j(\underline{x}) \cdot b_j(\underline{x}) = \underline{a}(\underline{x})^T \cdot \underline{b}(\underline{x}) \quad (7.21)$$

where the coefficients corresponding to any prediction point  $\underline{a}$  can be obtained by solving  $m$  normal equations  $\partial E_{\underline{x}}(g)/\partial a_j = 0$ , for  $j = 1, \dots, m$ . Details are given in the literature [57, 63–64].

The localized polynomial regression using the MLS procedure can be tuned by adjusting  $\alpha$  in Equation 7.20. However, because the performance function can have a very different relationship with each input variable, the Euclidean distance in Equation 7.20 can be replaced by the following general parameterized distance formula:

$$d(\underline{x}, \underline{x}^i) = \sqrt{\sum_{k=1}^n \theta_k (x_k - x_k^i)^2} \quad (7.22)$$

where  $\theta_1, \dots, \theta_n$  are  $n$  positive weight function parameters. Thus, the weight function of Equation 7.20 can be expressed as

$$w(d(\underline{x}, \underline{x}^i)) \Big|_{\theta_1, \dots, \theta_n} = \exp \left( - \sum_{k=1}^n \theta_k (x_k - x_k^i)^2 \right). \quad (7.23)$$

The  $n$  nonnegative weight function parameters  $\theta_1, \dots, \theta_n$  can be tuned automatically in the meta-modeling process by minimizing the metamodel cross-validation prediction error  $E^{CV}(\theta_1, \dots, \theta_n)$ , where either the cross-validation root mean square error (CV-RMSE) or the average absolute error (CV-AAE) can be used. If we let  $\hat{g}_{mls}^{-1}(\underline{x})$  denote the metamodel based on all data except the  $i$ th left-out sample, then

$$E_{RMSE}^{CV} = \sqrt{\frac{1}{N} \sum_{i=1}^N (\hat{g}^{-i}(\underline{x}^i) - f^i)^2} \quad (7.24a)$$

and

$$E_{AAE}^{CV} = \frac{1}{N} \sum_{i=1}^N |\hat{g}^{-i}(\underline{x}^i) - f^i| \quad (7.24b)$$

The resulting MLS metamodel will approximate the true performance function with minimum cross-validation prediction error based on available samples. This cross-validation-driven metamodeling technique is thus named the cross-validated moving least squares (CVMLS) method.

The leave-one-out cross-validation procedure effectively surveys the sampled space if the uniformity of the construction samples can be assured. However, the leave-one-out cross-validation procedure can be misleading if many samples appear in close pairs. When two samples are very close in input variable

space, their performance output will also be very similar. When one sample from the pair is left out, the remaining one will dominate the predicted-back performance value, thus leading to an unrealistically low cross-validation error. A generalized cross-validation procedure [56, 68–69] has also been widely used for estimating nonparametric metamodel prediction error. It should be noted that although the generalized cross-validation procedure is closely related to the cross-validation procedure, it is not a special case of cross validation. Instead, the generalized cross-validation procedure can be viewed as a weighted version of cross validation [56]. To ensure the robustness of the cross-validation error estimate, and also to avoid redundant samples, a uniformly spaced sampling structure, such as the optimal symmetric Latin hypercube (OSLH) of Section 7.3.2, is recommended.

### 7.3.5 Variable Screening Based on CVMLS

The goal of the metamodel is to mimic the output of a complex, slow-running model in as much detail as possible while running much faster. In practical applications, on the order of tens to a few hundred input variables are often need to be considered as likely contributors to the system performance. On the other hand, the number of metamodel samples obtained by expensive physics-based computer simulations is restricted by available computing resources and project time. While minimum sample requirements for constructing a numerically feasible metamodel with  $n$  inputs is  $m = n + 1$  for ordinary least-squares regression using linear polynomials,  $N$  generally needs to be many times of  $m$  in order to capture potential nonlinear performance behaviors through localized regression using CVMLS.

For a metamodel to better characterize the relationship of important input variables, it is thus necessary to eliminate insignificant inputs that are small contributors to the targeted performance measures. A metamodel that uses a subset of all inputs essentially lumps the effect of eliminated inputs into the metamodel approximation error. The purpose of eliminating insignificant inputs is to reduce the metamodel prediction error by focusing on major contributors. Here a process is described where the screening of input variables is not a separate preprocessing step but an integral part of the metamodeling process. When  $N$  is less than or close to  $n$  in size, a main-effects estimate procedure using the additive model with univariate CVMLS analysis is performed to eliminate insignificant inputs. Subsequently, if  $N$  is somewhat greater than the  $n$  and if the  $n$ -dimensional metamodel can be roughly constructed, a CVMLS backward-screening procedure is used for further input variable screening.

#### 7.3.5.1 Main-Effects Estimate Using a CVMLS Additive Model

In practical applications, a few hundred input variables can often be considered as likely contributors to the system performance. Meanwhile, the number of metamodeling samples obtained by expensive CAE simulations is restricted by available computing resources and project cadence. All multiple-regression techniques face the so-called curse of dimensionality, according to which the required sample size must increase exponentially with the number of input variables. However, some dimensionality-reduction processes, such as additive modeling and the more general projection-pursuit modeling, can be used to circumvent the problem [56–57].

The additive model assumes an additive approximation of the form [56–57]

$$f(\underline{x}) \approx g_{add}(\underline{x}) = f^{mean} + \sum_{j=1}^m f_j(x_j) \quad (7.25)$$

where  $f_j(x_j)$  are unknown univariate functions of a single input variable  $x_j$  with zero mean. Therefore, in Equation 7.25,  $f^{mean} = E[f]$ , where the superscript  $i$  ( $i = 1, \dots, N$ ) indicates the  $i$ th sample point. Thus, when the additive model is accurate, the following relationship holds:

$$g_{add}^{mee}(x_j) = \iint \cdots \int_{\underline{x}_{-j}} g_{add}(\underline{x}) d\underline{x}_{-j} - f^{mean} = f_j(x_j) \quad (7.26)$$

where “mee” stands for main-effects estimate. This suggests an iterative backfitting algorithm for computing all univariate functions, according to which a univariate CVMLS approximation can be used to fit  $f_j(x_j)$  from the partial residuals in Equation 7.26, given  $f_k(x_k)$ ,  $k \neq j$ . The best additive model is obtained by cycling the backfitting procedure until it converges.

Since only univariate regression is used, the additive model overcomes the *curse of dimensionality*. Moreover, the univariate components provide easily interpretable main-effects estimates. Unlike the least-squares linear regression, the main-effects estimates using the CVMLS additive model can capture highly nonlinear input/output relationships. Cross-validation error can be used to measure the accuracy, thus avoiding potential overfitting associated with high-order least-squares polynomial regression.

The CVMLS additive model is recommended for input screening only in cases where  $N$  is less than or close to  $n$  in size or when an  $n$ -dimensional metamodel cannot be reasonably constructed without excessive cross-validation error. For other cases, a more robust backward-screening procedure should be used. This procedure is introduced in the next subsection.

### 7.3.5.2 Elimination of Insignificant Input Variables Using CVMLS Backward Screening

The main-effects estimate, using the CVMLS additive model of the previous subsection, cannot identify cross effects among input pairs. Therefore, the significance of some closely coupled inputs can be underestimated. In cases when an  $n$ -dimension metamodel can be roughly constructed even with large cross-validation error, the goal of eliminating insignificant inputs can be accomplished by reducing the metamodel approximation error measured through cross validation. This can be accomplished by a backward-screening procedure that is described in the following three steps:

1. Construct the  $n$ -dimension CVMLS metamodel with all inputs and obtain its cross-validation error  $E^{CV}$ .
2. Construct leave-one-input-out metamodels for each input  $x_j$  ( $j = 1, \dots, n$ ) and calculate its cross-validation error  $E_{-j}^{CV}$ .
3. Compare  $E_{-j}^{CV}$  ( $j = 1, \dots, n$ ) with  $E^{CV}$ , and then remove any input  $x_k$  from CVMLS basis functions in Equation 7.18 if its impact index is negative, i.e.,  $E_{-k}^{CV} < E^{CV}$ .

The backward-screening process is more robust than “mee” because coupling effects, including cross effects among input pairs and other higher-order cross effects, are considered. Note that a leave-one-input-out metamodel ignores any potential effect from  $x_j$ . If  $x_j$  is an important contributor in  $g_{cvmls}(\underline{x})$ , the resulting approximation error in  $g_{cvmls}(\underline{x}_{-j})$  will increase significantly. Conversely, the resulting metamodel approximation error will either not change or slightly decrease if  $x_j$  is an insignificant factor. The small decrease here reflects the benefit of the improved sample-to-input ratio.

### 7.3.6 Crash Safety Example for Illustrating CVMLS and Variable Screening

The performance of a driver-restraint system in an NCAP (new car assessment program) crash test is considered. The test vehicle with a belted driver travels at 35 mph straight into a fixed rigid barrier that is perpendicular to the vehicle line of travel. The star rating of occupant-safety performance in NCAP is derived from a combined injury probability criterion  $P_{comb}$  based on two key injury numbers, HIC (head injury criteria) and Chest G (chest resultant acceleration in gs). The five-star rating is granted if  $P_{comb}$ , truncated to a full percentage point, is not more than 10%. Similarly, the four-star rating is granted if the  $P_{comb}$  number is larger than 10% but not more than 20%.

In this example, the vehicle-restraint system and occupant motion are simulated in Madymo (a multibody dynamics and nonlinear finite element analysis code) to assess the crash dummy's injury numbers, as illustrated in Figure 7.9. There are 20 Madymo parameters that can potentially impact  $P_{comb}$  and therefore the star rating. Among them, six parameters can be adjusted within rather wide design ranges and are denoted as design variables  $d_1$  to  $d_6$ . The other 14 variables are considered random noises and are denoted as random variables  $r_1$  to  $r_{14}$ . The random noises are associated with the restraint system,



**FIGURE 7.9** Model of occupant-restraint system.

test dummy setup, and vehicle deceleration pulse at any given design. The variation ranges for the 20 input variables are listed in Table 7.2. The outcomes of  $P_{comb}$  can be highly nonlinear in terms of input parameters.

Note that the Madymo simulation model is fundamentally deterministic. For a given set of inputs, the Madymo simulation produces a unique  $P_{comb}$  number, i.e.,

$$P_{comb} = P_{comb}(d_1, \dots, d_6; r_1, \dots, r_{14}) = P_{comb}(\underline{\mathbf{d}}; \underline{\mathbf{r}}) \quad (7.27)$$

We run 100 Madymo simulations in the 20-dimensional space using an optimal symmetric Latin hypercubes (OSLH) sampling design. The 100 Madymo samples will be used to demonstrate the main-effects estimate (“mee”) using the CVMLS additive model and the backward-screening procedure. For convenience of illustration, all variable ranges will be normalized into a 20-dimensional space cube  $[0, 1]^{20}$ .

### 7.3.6.1 Case A: Main-Effects Estimate Using CVMLS Additive Model

The main-effects estimate of each design variable is performed to provide an incomplete but intuitive view of the overall trend of  $P_{comb}$  with respect to each design variable in the variable space. Even in cases

**TABLE 7.2** Madymo Model Input Variables

Input Variable	Lower Design Bound	Upper Design Bound
$d_1$	3	6
$d_2$	2	6
$d_3$	24	28
$d_4$	600	1000
$d_5$	127	635
$d_6$	0.03	0.07
Random Noise Variable	Lower Variation Bound	Upper Variation Bound
$r_1$	−0.22	−0.18
$r_2$	12	14
$r_3$	58	72
$r_4$	28	52
$r_5$	120	140
$r_6$	3033	3057
$r_7$	455	479
$r_8$	0.3385	0.4255
$r_9$	24.4	27.4
$r_{10}$	0.9	1.1
$r_{11}$	0.55	0.65
$r_{12}$	0.185	0.215
$r_{13}$	0.185	0.215
$r_{14}$	0.046	0.054

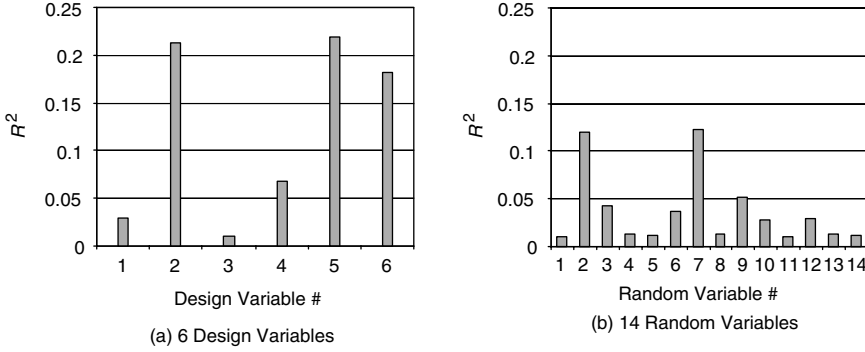


FIGURE 7.10  $R^2$  in CVMLS additive model of the NCAP example.

where the  $N$ -to- $n$  ratio is close to or less than 1, “mee” provides a basis for eliminating relatively unimportant input variables. The  $R^2$  results of six design variables and 14 random variables are compared in Figure 7.10a and Figure 7.10b, respectively. It shows clearly that design variables  $d_2$ ,  $d_5$ , and  $d_6$  are dominant controllable contributors to  $P_{comb}$ . Among the random variables,  $r_2$ ,  $r_7$ , and  $r_9$  have the most influence on  $P_{comb}$ .

When it is necessary to reduce inputs without regard to the controllability of the individual input, a threshold value, denoted as  $\bar{R}^2$ , can be specified. For instance, by setting  $\bar{R}^2 = 0.05$ , all inputs except a seven-dimensional subset  $[d_2, d_4, d_5, d_6, r_2, r_7, r_9]$  will be eliminated.

### 7.3.6.2 Case B: Backward Screening (BS) for Elimination of Insignificant Input Variables

In this example, the  $N$ -to- $n$  ratio is 5 prior to any input screening. This is generally adequate to construct a rough 20-dimensional metamodel. Because totally  $n+1$  metamodels need to be constructed in the backward screening, a fast variant of the CVMLS procedure that uses only one weight function parameter in Equation 7.23 by setting  $\alpha = \theta_1 = \dots = \theta_n$  is recommended. In the so-called  $\alpha$ -CVMLS procedure, the tuning of  $\alpha$  therefore becomes a one-dimensional optimization problem. Using the fast  $\alpha$ -CVMLS with linear polynomials, the baseline metamodel can be obtained with cross-validation average absolute error  $E^{CV} = 0.0559$ . The leave-one-input-out metamodels were constructed, and the impact index of the  $k$ th input variable was computed as

$$\text{Impact\_Index}(x_k) = (E_{-k}^{CV} - E^{CV}) / E^{CV} \quad (7.28)$$

As shown in Figure 7.11a and Figure 7.11b, the backward screening (BS) identifies that design variables  $d_2$  and  $d_5$  are the dominant factors related to the metamodel accuracy, while  $d_6$  has much less impact on

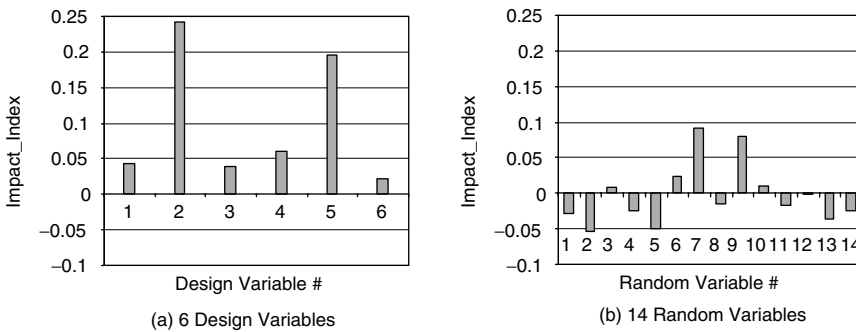


FIGURE 7.11 NCAP metamodeling using CVMLS.

**TABLE 7.3** NCAP Metamodeling Using CVMLS

Metamodel	20-D (Full Set)		7-D (MEE Subset)		6-D (MEE/BS Subset)	
CVMLS	CV-AAE	M-AAE	CV-AAE	M-AAE	CV-AAE	M-AAE
Error	0.0509	0.0505	0.0445	0.0448	0.0435	0.0442

the metamodel accuracy, even though it was suggested by “mee” as a significant variance contributor. This discrepancy implies that  $d_6$  is an important but rather noisy factor. Among the random variables, only  $r_7$  and  $r_9$  are identified as moderate positive factors in metamodeling. Note that  $r_2$  is closely associated with  $P_{comb}$ , but it has significant negative impact on metamodeling accuracy. Thus,  $r_2$  is likely a big noise factor, and its analytical relationship with others cannot be adequately represented in the CVMLS metamodel.

Considering the above,  $r_2$  can also be eliminated due to its negative impact on metamodeling accuracy. The resulting six-dimensional subset is  $[d_2, d_4, d_5, d_6, r_7, r_9]$ . In Table 7.3, the CVMLS metamodeling results using the full 20-dimensional set, the seven-dimensional mee subset, and the six-dimensional mee/BS subset inputs are obtained. For demonstration purpose, the true metamodeling errors in terms of M-AAE are obtained by comparing the metamodel results with new Madymo simulation results at 201 OSLH points in 20-dimensional input space that are different from the original 100 OSLH samples. Table 7.3 shows that metamodeling error decreases after elimination of insignificant or noisy input variables. Because of uniformly scattered and partitioned samples, CV-AAE is a close measure of M-AAE.

## 7.4 Variation Reduction in Robust Engineering: An Automotive Example

An automotive robust design example is presented in this section for the frontal-impact performance of an occupant-restraint system. It demonstrates how basic variation-reduction techniques can be used to achieve robust designs. An automotive occupant-restraint system consists of the air bag, seat belt, seat, steering wheel and column, knee bolster, as well as the driver or passenger. It is a very important part of the vehicle safety system, since it absorbs and dissipates energy in a crash situation to protect the occupant from severe injuries. The use of CAE models is common in the automotive industry for simulating a crash test. These models include dummies representing occupants of different sizes. The computer simulation helps in evaluating and improving the occupant-safety performance, which is measured by the “star rating,” among other technical specifications [71]. Figure 7.9 shows a typical occupant-restraint system.

The occupant-restraint system is affected by a variety of parameters, as shown in Table 7.4. Some of them can be changed by design, such as the air-bag size and the air-bag inflator output. These variables are called design variables. Others may vary randomly in a test, such as the dummy’s sitting position in the vehicle. These variables are called noise variables. Sometimes a design variable can also have small random variation around its nominal value. In that case, the nominal value is a design variable, and the

**TABLE 7.4** Typical Variables in Frontal Occupant-Restraint Systems

Air-bag size and shape	Seat-belt pretension firing time
Air-bag tether length	Knee-bolster stiffness
Air-bag vent area	Vehicle crash pulses
Air-bag inflator output	Air-bag firing time
Steering-column stroke	Dummy position and orientation
Twist-shaft level	Frictions between dummy and seat belt and air bag
Seat-belt pretension spool	Friction between seat belt and routing rings/buckles

**TABLE 7.5** Design Variables and Their Ranges

Variable	Range for Nominal
Air-bag tether-length scaling factor	0.86–1.48
Air-bag vent-area scaling factor	1.366–3.534
Twist-shaft-level scaling factor	0.62–1.49
Knee-bolster stiffness scaling factor	1.0–1.5
Air-bag inflation output scaling factor	1.0–1.4
Pretension spool scaling factor	2.0–4.4
Pretension firing-time scaling factor	0.5–1.0
Column strokes scaling factor	0.62–1.88

random variation around the nominal is a noise variable. The variation in the noise variables causes variation in safety performance, which can affect the “star rating” of the same vehicle model by one to two “stars.” It is, therefore, a challenge for automotive manufacturers to produce vehicles with consistent safety performance.

In this example, the design and noise variables and their ranges are listed in Table 7.5 and Table 7.6, respectively. The range for each design variable is determined from packaging constraints, availability, and other performance requirements. The range for the noise variables is determined from available data and expert opinions.

A robust design for the occupant-restraint system must meet all requirements from the following three load cases:

1. The frontal NCAP (new car assessment program) test for occupant-safety “star rating.” It is a test addressing 50th-percentile dummies, with the seat belt on, in both driver and passenger seats. The vehicle is crashed into a rigid barrier at 35 mph. Performance metrics include the head-injury criterion (HIC), chest acceleration (Chest G), and “star rating,” which is a function of HIC and Chest G. The best and worst “star ratings” are five and one, respectively.
2. U.S. federal government requirements from FMVSS (Federal Motor Vehicle Safety Standards) 208 [71] for frontal crash, with unbelted 50th-percentile dummies, crashed at 25 mph.
3. U.S. federal government requirements from FMVSS 208 [71] for frontal crash, with unbelted fifth-percentile dummies, crashed at 25 mph.

All three load cases have common design and noise variables. For the second and third load cases, there are a number of requirements on head injury, chest acceleration, and neck injury, among others. A complete list of the specifications is given in the Federal Motor Vehicle Safety Standards and Regulations [71].

In this example, an evaluation of the safety-performance variation is first performed, and a robust optimization procedure is subsequently used to improve the probability of achieving high safety performance. Since each occupant-restraint-system simulation is computationally intensive, it becomes impractical to directly apply any probabilistic method. For this reason, a high-fidelity response-surface model (RSM) is built. Due to the highly nonlinear behavior of the system and the restriction on computation time, advanced sampling methods are also required. In this example, a sequential optimum symmetric Latin hypercube (OSLH) sampling method is used (see Section 7.3.2). It provides “space-filling” properties, which are desirable if a restricted number of samples are available due to the high computational

**TABLE 7.6** Noise Variables and Their Ranges

Variable	Range
Air-bag firing time (sec)	$\pm 0.003$
Friction coefficient with dummy	$\pm 0.35$
Friction coefficient seat belt to buckle/ring	$\pm 0.2$
Dummy position and orientation	Per FMVSS test procedure
Column build load ( $N$ )	$\pm 444$

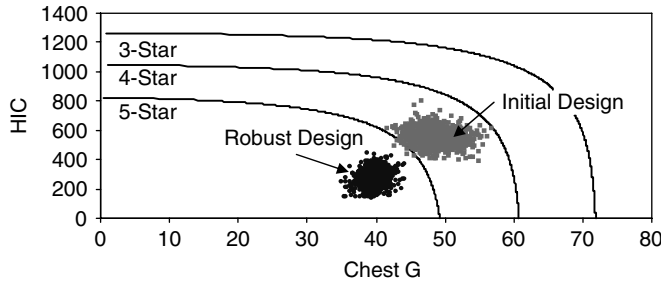


FIGURE 7.12 Comparison of the “star rating” ranges.

cost of the original simulation model. Nonlinear RSM techniques, such as stepwise regression [54] with nonlinear polynomials, kriging [72], and cross-validated moving least squares (see Section 7.3.4), can all generate response-surface models of decent fidelity. The required sample size is determined based on the needed accuracy, system nonlinear behavior, number of active variables in the range considered, sampling scheme, and the available computing resources. In this example, 150 simulations were first performed for each load-case using a Madymo model, and third-order polynomial stepwise regression RSM models were subsequently created for the key response metrics. All RSM models had a less than 5% average error.

The created RSM models are computationally efficient, since they are in polynomial form. Thus, Monte Carlo simulations were easily performed for evaluating the initial design performance. The used variation ranges for the design and noise variables, listed in Table 7.5 and Table 7.6, respectively, are based on test procedures, supplier tolerance specifications, test data, and engineering experience. All random variables were assumed to be uniformly distributed within their variation ranges. Monte Carlo simulations, with a 50,000 sample size, were used to assess the scatter in the safety performance. As shown in Figure 7.12, the “star rating” was mostly four star for the initial design.

The goal of this study was to produce a five-star design considering the variation in the design and noise variables. Therefore, the mostly four-star initial design “cloud,” shown in Figure 7.12, had to move within the five-star domain. One way to achieve such a robust design is to move the mean and simultaneously reduce the variation (scatter) around the mean, so that the final design “cloud” is within the five-star domain. Therefore, both the mean design and its variation must change simultaneously. This can be achieved by maximizing the  $(\text{mean} - 3\sigma)$  aggregate objective. If the  $(\text{mean} - 3\sigma)$  of the “star rating” is five, the final design will be mostly within the five-star rating domain, considering the variation in the design and noise variables. The  $(\text{mean} - 3\sigma)$  aggregate objective was mainly chosen for its simplicity. However, it was also chosen because the predictions of current CAE simulations of occupant-safety systems are not very accurate due to simplifying assumptions in the mathematical representation of the physical crash phenomena. Thus, a more rigorous reliability estimation using existing probabilistic techniques would not be meaningful [73].

The robust design is achieved by solving the following probability-based optimization problem:

$$\max_{\substack{\text{Design} \\ \text{Variables}}} (\mu_{\text{star}} - 3\sigma_{\text{star}}) \quad (7.29)$$

subject to other constraints and requirements, where  $\mu$  and  $\sigma$  denote the mean and standard deviation, respectively. Note that the “other constraints” can also be probability based. Due to the highly nonlinear behavior of the above objective, a global optimization search was utilized. A genetic algorithm was first used to identify the vicinity of a design point. A generalized reduced gradient algorithm was subsequently used to efficiently find the exact design point. For each function evaluation during the optimization process, 5000 Monte Carlo simulations were performed in order to evaluate the mean and standard deviation of the “star rating” and the constraints. The 5000 sample size for the Monte Carlo simulation provided adequate accuracy in estimating both the mean and the standard deviation. Then the design



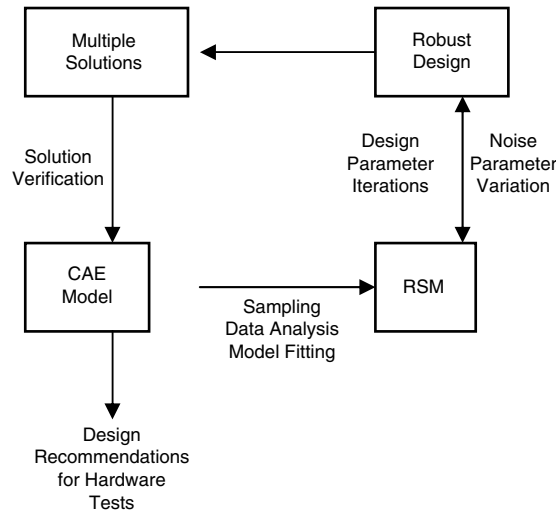


FIGURE 7.13 Process for robust design of occupant-safety system.

parameters are changed based on the search algorithm. This process usually requires hundreds to thousands of iterations. In the end, a new design is chosen as a robust design. Figure 7.12 shows the “cloud” of the final robust “star rating” design. The performance improvement between the initial and final designs is due to an increase in the mean and a decrease in the standard deviation of the “star rating.” The described optimization scheme produces multiple potential robust designs that are further evaluated using the original CAE simulation model.

The overall process to obtain a robust “star rating” design is summarized in Figure 7.13. It consists of the following steps.

1. Identify the design and noise variables and their ranges. Create sample points using space-filling sampling techniques, similar to those of Section 7.3.2. Use the CAE model of the occupant-restraint system to evaluate the response functions at all sample points.
2. Develop RSM models. Holdout samples are used to evaluate the accuracy of the developed RSM models.
3. Solve the robust optimization problem of Equation 7.29, using the RSM models.
4. Search for multiple alternative solutions.
5. Evaluate each alternative solution using the original CAE model.
6. Propose the best solution as the design recommendation.

In order to carry out the described robust design within the vehicle development process, it is essential to have numerically stable CAE models, high-fidelity RSM models, and an automated numerical process. The process automation is essential for fast execution and error avoidance for inexperienced engineers with minimal knowledge in sampling, RSM model generation, and optimization techniques.

## 7.5 Summary and Future Needs

This chapter presented an overview of the current state of the art in applying probabilistic methods in automotive engineering, and it described the commonly used reliability methods for addressing durability, performance, and quality issues. Some practical examples were used to demonstrate how the basic probabilistic design ideas are being used in the automotive industry to account for stochastic uncertainty. The automotive industry uses probabilistic methods mainly to improve vehicle quality and safety as well as to reduce inherent manufacturing variation in the context of robust engineering. The robust design

of an occupant-restraint system's frontal-impact performance was studied using basic variation-reduction techniques.

Most of the applications in the automotive industry require large-scale, computationally intensive CAE models. It is therefore necessary to develop accurate and efficient metamodels of the actual CAE models in order to reduce the high computational cost of probabilistic analysis. For this reason, the latest advances in nonparametric metamodeling methods were presented along with efficient structured uniform sampling techniques, such as optimum symmetric Latin hypercube (OSLH). Furthermore, efficient variable screening procedures were described for effective elimination of insignificant input variables in practical problems with a large number of inputs. These techniques were demonstrated using an automotive crash-safety example.

We believe that future research is needed in the areas of:

- Component and system reliability of complex systems with highly nonlinear limit states
- Computationally efficient reliability-based design optimization
- Multidisciplinary optimization under uncertainty
- Efficient sampling, metamodeling, and variable screening techniques
- Random fields
- Imprecision issues and uncertainty quantification and propagation with scarce data

For a variety of practical problems in the automotive industry, the failure domain is defined by highly nonlinear limit states. In such cases, the first-order reliability methods can overestimate or underestimate the true probability of failure. Thus, efficient simulation-based methods are needed instead of the commonly used approximate analytical methods. Some recent work in this area is reported by Zou [74, 75].

Reliability-based design optimization (RBDO) gradually becomes an important optimization tool in the presence of uncertainty [45, 46, 76] for automotive applications. However, the conventional double-loop approaches [43, 44, 46] are almost impractical due to the required excessive computational effort. Efficient RBDO algorithms are therefore needed. Advances in this area are reported in the literature [45, 77]. Furthermore, the design and development of complex automotive systems typically requires the integration of multiple disciplines and the resolution of multiple conflicting objectives in the presence of uncertainty. Although recent advances have been made [78–82], more research is needed in this area.

Almost exclusively, all probabilistic analysis and design methods in the automotive industry are “random variable” based. However, a “random process” approach must be used to characterize uncertainty for a variety of automotive applications. Examples include, among others, the random vehicle road excitation and the combustion excitation in an internal combustion engine. Random field models can be typically used to characterize random variations in space and time. Advanced engineering applications of random field analysis have been reported in industries such as aerospace [83]. However, the authors are not aware of similar applications in the automotive industry.

Classical probabilistic analysis is used in automotive applications when sufficient data are available to quantify uncertainty using probability distributions. However, when sufficient data are not available or when there is a lack of information due to ignorance, the classical probability methodology may not be appropriate. During the early stages of vehicle development, quantification of the product's reliability or compliance with performance targets is practically very difficult due to insufficient data for modeling the uncertainties. Formal theories, such as evidence theory (or Dempster–Shafer theory) [84, 85] and possibility theory [86], can be used to handle uncertainty quantification and propagation with scarce data. Although such theories have been recently applied to engineering applications [87, 88], they are not well known in the automotive industry. Fundamental and applied research is needed in this area with emphasis on large-scale automotive applications.

Resolution of trade-offs in multicriteria optimization problems is very common in automotive applications. The weighted-sum approach [89, 90] is commonly used for handling trade-offs, despite its serious drawbacks [91]. A multiobjective decision problem generally has a whole set of possible “best” solutions,

known as the Pareto set. A complete decision model, therefore, requires specification of the degree of compensation between conflicting criteria in order to select the best of all Pareto points [92]. A preference-aggregation method, based on a family of aggregation functions, is presented by Scott and Antonsson [92] to formally model all possible trade-offs in engineering design. An initial attempt has been recently made [93, 94] to extend the preference-aggregation methodology in the presence of uncertainty so that it can be used to handle robust design problems. More research is needed in this area.

## Acknowledgments

The authors would like to thank Raviraj Nayak, Chun-Liang Lin, and Donald Jones of General Motors Corporation for providing information on some of the examples presented in this chapter. The continuous support and enthusiasm of Robert Lust and Mary Fortier of General Motors Corporation throughout the preparation of this chapter is also acknowledged.

## References

1. Rosenblatt, M., Remarks on a multivariate transformation, *Ann. Mathematical Statistics*, 23 (2), 470-472, 1952.
2. Rackwitz, R. and Fiessler, B., Structural reliability under combined random load sequences, *Comput. Struct.*, 9 (5), 484-494, 1978.
3. Liu, P. and Der Kiureghian, A., Optimization algorithms for structural reliability, *Structural Safety*, 9, 161-177, 1991.
4. Cruse, T.A., Wu, Y.-T., Dias, J.B., and Rajagopal, K.R., Probabilistic structural analysis methods and applications, *Comput Struct*, 30, 163-170, 1988.
5. Wu, H., Millwater, R., and Cruse, T.A., Advanced probabilistic structural analysis method for implicit performance functions, *AIAA J.*, 28, 1663-1669, 1990.
6. Breitung, K. and Faravelli, L., Response surface methods and asymptotic approximations, in *Mathematical Models for Structural Reliability*, Casciati, F. and Roberts, J.B., Eds., CRC Press, Boca Raton, FL, 1996, chap. 5, pp. 237-298.
7. Köylüolu, H.U. and Nielsen, S.R.K., New approximations for SORM integrals, *Structural Safety*, 5, 119-126, 1988.
8. Tvedt, L., Distribution of quadratic forms in normal space-application to structural reliability, *ASCE J. Eng. Mech.*, 116 (6), 1183-1197, 1990.
9. Cai, G.Q. and Elishakoff, I., Refined second-order reliability analysis, *Structural Safety*, 14, 267-276, 1994.
10. Zhao, Y. and Ono, T., A general procedure for first/second-order reliability method (FORM/SORM), *Structural Safety*, 21 (2), 95-112, 1999.
11. Haldar, A. and Mahadevan, S., *Probability, Reliability and Statistical Methods in Engineering Design*, John Wiley & Sons, New York, 2000.
12. Bucher, C.G., Adaptive sampling—an iterative fast Monte Carlo procedure, *Structural Safety*, 5, 119-126, 1988.
13. Melchers, R.E., Improved importance sampling methods for structural system reliability calculation, in *Proceedings of International Conference on Structural Safety and Reliability (ICOSSAR)*, 1989, pp. 1185-1192.
14. Wu, Y.T., NESSUS/FPI User's and Theoretical Manuals, ver. 2.4, Southwest Research Institute, San Antonio, TX, 1998.
15. Karamchandani, A., Bjerager, P., and Cornell, C.A., Adaptive importance sampling, in *Proceedings of 5th International Conference on Structural Safety and Reliability*, Ang, A.H.-S., Shinozuka, M., and Schuëller, G.I., Eds., ASCE, New York, 1989, pp. 855-862.
16. Zou, T., Mahadevan, S., Mourelatos, Z., and Meernik, P., Reliability analysis of automotive body-door subsystem, *Reliability Eng. System Safety*, 78, 315-324, 2002.

17. Mahadevan, S. and Dey, A., Adaptive Monte Carlo simulation for time-variant reliability analysis of brittle structures, *AIAA J.*, 35 (2), 321–326, 1997.
18. Mahadevan, S. and Raghothamachar, P., Adaptive simulation for system reliability analysis of large structures, *Comput. Struct.* 77, 725–734, 2000.
19. Schuëller, G.I. and Stix, R., A critical appraisal of methods to determine failure probabilities, *Structural Safety*, 4 (4), 193–209, 1987.
20. Hohenbichler, M. and Rackwitz, R., A bound and an approximation to the multivariate normal distribution function, *Math. Japonica*, 30 (5), 821–828, 1985.
21. Fu, G. and Moses, F., Multimodal simulation method for system reliability analysis, *J. Eng. Mech.*, 119 (6), 1173–1179, 1993.
22. Fu, G., Reliability models for assessing highway bridge safety, in *Proceedings of International Conference on Structural Safety and Reliability (ICOSSAR)*, 1998, pp. 1883–1888.
23. Schuëller, G.I., Pradlwarter, H.J., and Bucher, C.G., Efficient computational procedures for reliability estimate of MDOF-systems, *Int. J. Nonlinear Mech.*, 26 (6), 961–974, 1991.
24. Ditlevsen, O., Narrow reliability bounds for structural systems, *J. Structural Mech.*, 7 (4), 453–472, 1979.
25. Wu, Y.-T., An adaptive importance sampling method for structural system reliability analysis and design, reliability technology 1992, in *Proceedings of ASME Winter Annual Meeting, AD-28*, Cruse, T.A., Ed., 1992, pp. 217–231.
26. Xiao, Q. and Mahadevan, S., Fast failure mode identification for ductile structural system reliability, *Structural Safety*, 13, 207–226, 1994.
27. Xiao, Q. and Mahadevan, S., Second-order upper bounds on probability of intersection of failure events, *J. Eng. Mech.*, 120 (3), 670–674, 1994.
28. Mahadevan, S. and Liu, X., Probabilistic optimum design of composite laminates, *J. Composite Mater.*, 32 (1), 68–82, 1998.
29. Cornell, C.A., Bounds on the reliability of structural systems, *J. Structural Div.*, 93 (ST1), 171–200, 1967.
30. Hunter, D., An upper bound for the probability of a union, *J. Appl. Probab.*, 3 (3), 597–603, 1976.
31. Gollwitzer, S. and Rackwitz, R., An efficient numerical solution to the multinormal integral, *Probabilistic Eng. Mech.*, 3 (2), 98–101, 1988.
32. Ambartzumian, R., Der Kiureghian, A., Ohanian, V., and Sukiasian, H., Multinormal probability by sequential conditioned importance sampling: theory and application, *Probabilistic Eng. Mech.*, 13 (4), 299–308, 1998.
33. Pandey, M.D. and Sarkar, A., Comparison of a simple approximation for multinormal integration with an importance sampling-based simulation method, *Probabilistic Eng. Mech.*, 17, 215–218, 2002.
34. Lin, C.-L., Virtual experimental design on glass guidance system with an integrated dual-cable regulator—Part I: CAE model validation, in *Proceedings of Seventh ISSAT International Conference on Reliability and Quality in Design*, ISSAT, 2001, pp. 237–241.
35. Lin, C.-L., Im, K.H., and Bhavsar, T.R., Virtual experimental design on glass guidance system with an integrated dual-cable regulator—Part II: design optimization, in *Proceedings of Eighth ISSAT International Conference on Reliability and Quality in Design*, ISSAT, 2002, pp. 287–291.
36. Lin, C.-L. and Im, K. H., System Design Process Integration of Cable-Drive Glass Guidance System Using Axiomatic Design, presented at Second International Conference on Axiomatic Design, Cambridge, MA, 2002.
37. Lin, C.-L., Virtual experimental design optimization on cable-drive glass guidance system, *Int. J. Reliability, Qual., Safety Eng.*, 9 (4), 317–328, 2002.
38. Chang, H.Y. and Song, J.O., Glass Drop Design for Automobile Windows—Design of Glass Contour, Shape, Drop Motion and Motion Guidance Systems, 951110, SAE, Warrendale, PA, 1995.
39. Singh, K., Zaas, C., and Newton, R., Engineering Moveable Glass Window Seals of Automotive Door Using Upfront CAE, 982382, SAE, Warrendale, PA, 1998.

40. Singh, K., Experimental Assessment of Door Window Glass Smooth Operation And Tracking, 1999-01-3161, SAE, Warrendale, PA, 1999.
41. Kanamori, M., Isomura, Y., and Suzuki, K., Dynamic Finite Element Analysis of Window Regulator Linkage System Using LS-DYNA, 980308, SAE, Warrendale, PA, 1998.
42. Lorenzen, T.J. and Anderson, V.L., *Design of Experiments*, Marcel Dekker, New York, 1993.
43. Reddy, M.V., Granhdi, R.V., and Hopkins, D.A., Reliability based structural optimization: a simplified safety index approach, *Comput. Struct.*, 53 (6), 1407–1418, 1994.
44. Wu, Y.-T. and Wang, W., A new method for efficient reliability-based design optimization, in *Proceedings of 7th Special Conference on Probabilistic Mechanics & Structural Reliability*, 1996, pp. 274–277.
45. Du, X. and Chen, W., Sequential optimization and reliability assessment method for efficient probabilistic design, in *Proceedings of ASME Design Automation Conference*, DETC-DAC34127, Montreal, Canada, 2002.
46. Choi, K.K. and Youn, B.D., Hybrid analysis method for reliability-based design optimization, in *Proceedings of ASME Design Automation Conference*, ASME, Pittsburgh, PA, 2001.
47. Tu, J., Choi, K.K., and Park, Y.H., A new study on reliability-based design optimization, *ASME J. Mechanical Design*, 121, 557–564, 1999.
48. Tu, J., Choi, K.K., and Park, Y.H., Design potential method for robust system parameter design, *AIAA J.*, 39 (4), 667–677, 2001.
49. Yang, R.J. et al., Metamodeling development for vehicle frontal impact simulation, in *Proceedings of 42nd Structures, Structural Dynamics, and Materials Conference*, AIAA/ASME/ASCE/AHS/ASC, 2001.
50. Gu, L., A comparison of polynomial based regression models in vehicle safety analysis, in *Proceedings of 42nd Structures, Structural Dynamics, and Materials Conference*, AIAA/ASME/ASCE/AHS/ASC, Seattle, WA, 2001.
51. Montgomery, D.C., *Design and Analysis of Experiments*, 5th ed., John Wiley and Sons, New York, 2001.
52. Myers, R.H., *Classical and Modern Regression with Application*, PWS-Kent, New York, 1990.
53. Myers, R.H. and Montgomery, D.C., *Response Surface Methodology: Process and Product Optimization Using Designed Experiments*, John Wiley and Sons, New York, 2002.
54. Draper, N.R. and Smith, H., *Applied Regression Analysis*, John Wiley and Sons, New York, 1981.
55. Stone, C.J., Consistent nonparametric regression, *Ann. Statistics*, 5, 595–645, 1977.
56. Eubank, R.L., *Spline Smoothing and Nonparametric Regression*, Marcel Dekker, New York, 1988.
57. Fan J. and Gijbels, I., *Local Polynomial Modeling and Its Applications*, Chapman & Hall, New York, 1996.
58. Sacks, J. et al., Design and analysis of computer experiments, *Statistical Sci.*, 4, 409–435, 1989.
59. Jones, D.R., A taxonomy of global optimization methods based on response surfaces, *J. Global Optimization*, 21, 345–383, 2001.
60. Dyn, N., Levin, D., and Rippa, S., Numerical procedures for surface fitting of scattered data by radial basis functions, *SIAM J. Scientific Statistical Computing*, 7, 639–659, 1986.
61. Jin, R., Chen, W., and Simpson, T.W., Comparative studies of metamodeling techniques under multiple modeling criteria, *Structural Multidisciplinary Optimization*, 23, 1–13, 2001.
62. Krishnamurthy, T. and Romero, V.J., Construction of response surface with higher order continuity and its application to reliability engineering, in *Proceedings of 43rd Structures, Structural Dynamics, and Materials Conference*, AIAA/ASME/ASCE/AHS/ASC, Denver, CO, 2002.
63. Tu, J., Cross-validated multivariate metamodeling methods for physics-based computer simulations, in *Proceedings of IMAC-XXI: A Conference and Exposition on Structural Dynamics*, 2003.
64. Tu, J. and Jones, D.R., Variable screening in metamodel design by cross-validated moving least squares method, in *Proceedings of the 44th Structure, Structural Dynamics, and Materials Conference*, AIAA-2003-1669, AIAA/ASME/ASCE/AHS/ASC, Norfolk, VA, 2003.
65. Tu, J. and Cheng, Y.-P., An Integrated Stochastic Design Framework Using Cross-Validated Multivariate Metamodeling Methods, 2003-01-0876, SAE, Warrendale, PA, 2003.

66. Bates, R.A., Buck, R.J., Riccomagno, E., and Wynn, H.P., Experimental design and observation for large systems, *J. Royal Statistical Soc. (Ser. B)*, 58, 77–94, 1996.
67. Ye, K.Q., Li, W., and Sudjianto, A., Algorithmic construction of optimal symmetric Latin hypercube designs, *J. Statistical Planning Inference*, 90, 145–159, 2000.
68. Stone, M., Cross-validatory choice and assessment of statistical predictions, *J. Royal Statistical Soc. (Ser. B)*, 36, 111–147, 1974.
69. Efron, B. and Tibshirani, R.J., *An Introduction to the Bootstrap*, Chapman & Hall, New York, 1993.
70. Lancaster, P. and Salkauskas, K., *Curve and Surface Fitting: an Introduction*, Academic Press, New York, 1986.
71. National Highway Traffic Safety Administration, Federal Motor Vehicle Safety Standards and Regulations, U.S. Department of Transportation, NHTSA, Washington, DC.
72. Jones, D.R., Schonlau, M., and Welch, W.J., Efficient global optimization of expensive black-box functions, *J. Global Optimization*, 13, 455–492, 1998.
73. Ding, X., Assessing Error in Reliability Estimates Obtained via CAE Simulations, 2003-01-0146, SAE, Warrendale, PA, 2003.
74. Zou, T., Mahadevan, S., Mourelatos, Z.P., and Meernik, P., Reliability analysis of automotive body-door subsystem, *Reliability Eng. System Safety*, 78 (3), 315–324, 2002.
75. Zou, T., Mourelatos, Z.P., Mahadevan, S., and Tu, J., Component and Monte Carlo approach, in *Proceedings of ASME Design Engineering Technical Conferences*, DETC2003/DAC-48708, ASME, 2003.
76. Yang, R.J., Gu, L., Tho, C.H., Choi, K.K., and Youn, B.D., Reliability-based multidisciplinary design optimization of a full vehicle system, in *Proceedings of 43rd Structures, Structural Dynamics, and Materials Conference*, AIAA/ASME/ASCE/AHS/ASC, Denver, CO, 2002.
77. Chen, X., Hasselman, T.K., and Neill, D.J., Reliability based structural design optimization for practical applications, in *Proceedings of 38th Structures, Structural Dynamics, and Materials Conference*, AIAA/ASME/ASCE/AHS/ASC, 1997.
78. Koch, P.N., Simpson, T.W., Allen, J.K., and Mistree, F., Statistical approximations for multidisciplinary design optimization: the problem of size, *J. Aircraft*, 36 (1), 275–286, 1999.
79. Oakley, D.R., Sues, R.H., and Rhodes, G.S., Performance optimization of multidisciplinary mechanical systems subject to uncertainties, *Probabilistic Eng. Mech.*, 13 (1), 15–26, 1998.
80. Padmanabhan, D. and Batill, S.M., Decomposition strategies for reliability based optimization in multidisciplinary system design, in *Proceedings of 9th AIAA/SSMO Symposium on Multidisciplinary Analysis and Optimization*, Atlanta, GA, 2002.
81. Du, X. and Chen, W., Collaborative reliability analysis for multidisciplinary systems design, in *Proceedings of 9th AIAA/SSMO Symposium on Multidisciplinary Analysis and Optimization*, Atlanta, GA, 2002.
82. Gu, X. and Renaud, J.E., Implementation study of implicit uncertainty propagation in decomposition-based optimization, in *Proceedings of 9th AIAA/SSMO Symposium on Multidisciplinary Analysis and Optimization*, Atlanta, GA, 2002.
83. Ghiocel, D.M., Stochastic field models for advanced engineering applications, in *Proceedings of 42nd Structures, Structural Dynamics, and Materials Conference*, AIAA/ASME/ASCE/AHS/ASC, Seattle, WA, 2001.
84. Klir, G.J. and Folger, T.A., *Fuzzy Sets, Uncertainty, and Information*, Prentice Hall, Englewood Cliffs, NJ, 1988.
85. Yager, R.R., Fedrizzi, M., and Kacprzyk, J., Eds., *Advances in the Dempster—Shafer Theory of Evidence*, John Wiley & Sons, New York, 1994.
86. Dubois, D. and Prade, H., *Possibility Theory*, Plenum Press, New York, 1988.
87. Wasfy, T.M. and Noor, A.K., Application of fuzzy sets to transient analysis of space structures, *AIAA J.*, 38, 1172–1182, 1998.
88. Akpan, U.O., Rushton, P.A., and Koko, T.S., Fuzzy probabilistic assessment of the impact of corrosion on fatigue of aircraft structures, in *Proceedings of 43rd Structures, Structural Dynamics, and Materials Conference*, AIAA/ASME/ASCE/AHS/ASC, Denver, CO, 2002.

89. Tang, X. and Krishnamurty, S., Performance estimation and robust design decisions, in *Proceedings of 41st Structures, Structural Dynamics, and Materials Conference*, AIAA/ASME/ASCE/AHS/ASC, Atlanta, GA, 2000.
90. Hacker, K. and Lewis, K., Robust design through the use of a hybrid genetic algorithm, in *Proceedings of 43rd Structures, Structural Dynamics, and Materials Conference*, AIAA/ASME/ASCE/AHS/ASC, Denver, CO, 2002.
91. Das, I. and Dennis, J., A closer look at drawbacks of minimizing weighted sums of objectives for Pareto set generation in multi-criteria optimization problems, *Structural Optimization*, 14 (1), 63–69, 1997.
92. Scott, M.J. and Antonsson, E.K., Aggregation functions for engineering design trade-offs, *Fuzzy Sets Systems*, 99 (3), 253–264, 1998.
93. Dai, Z., Scott, M.J., and Mourelatos, Z.P., Robust design using preference aggregation methods, in *Proceedings of ASME Design Engineering Technical Conferences*, DETC2003/DAC-48713, Chicago, IL, 2003.
94. Dai, Z., Scott, M.J., and Mourelatos, Z.P., Incorporating epistemic uncertainty in robust design, in *Proceedings of ASME Design Engineering Technical Conferences*, DETC2003/DAC-48715, Chicago, IL, 2003.

# 8

## Integrated Computer-Aided Engineering Methodology for Various Uncertainties and Multidisciplinary Applications

---

Kyung K. Choi

Byeng D. Youn

Jun Tang

*University of Iowa*

Jeffrey S. Freeman

*University of Tennessee*

Thomas J. Stadterman

Alan L. Peltz

*U.S. Army Materiel Systems  
Analysis Activity (AMSAA)*

William (Skip) Connon

*U.S. Army Aberdeen Test Center*

8.1	Introduction .....	8-1
8.2	Fatigue-Life Analysis and Experimental Validation .....	8-3
	Mechanical Fatigue Failure for Army Trailer Drawbar • Experimental Validation of Mechanical Fatigue • Design Optimization for Mechanical Fatigue	
8.3	Reliability Analysis and Reliability-Based Design Optimization.....	8-12
	Reliability Analysis for Durability-Based Optimal Design • Reliability-Based Design Optimization for Durability • Results of Reliability-Based Shape Design Optimization for Durability of M1A1 Tank Roadarm	
8.4	Conclusions .....	8-18
	Acknowledgments.....	8-19
	Nomenclature.....	8-19
	References .....	8-19

### 8.1 Introduction

---

Given the explosive growth in computational technology, computer-aided engineering (CAE) has long been used to analyze and evaluate product design. However, various uncertainties in an engineering system prevent CAE from being directly used for such purposes. Through the use of experimental validation and probabilistic methods, CAE will become an integral part of engineering product analysis and design. This chapter presents an advanced CAE methodology for qualitative, reliable, durable, and cost-effective product design under uncertainty that is composed of three key elements: CAE technology, experimental validation, and an uncertainty-based design [1–5].

CAE technology, such as simulation techniques, enables one to explore many different designs without building expensive prototype models. As shown in Figure 8.1, one must inevitably take account of physical



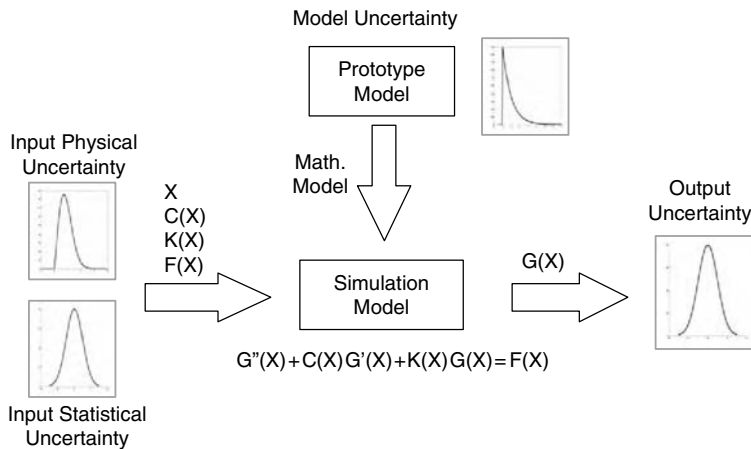


**FIGURE 8.1** Uncertainty types existing in computer-aided design.

input uncertainties, such as geometric dimensions, material properties, and loads. However, a simulation (or mathematical) model that departs from a prototype model introduces modeling uncertainty, uncertainty due to approximations in numerical algorithms, as well as any inherent physical uncertainty in the structure. It is not possible to completely eliminate model uncertainty. Instead it could be more practical to minimize modeling uncertainty through experimental validation. Moreover, while modeling physical uncertainty, a lack of statistical information can lead to statistical uncertainty, such as uncertainty of the distribution type and its parameters, which could be modeled using Bayesian probability or possibility or evidence theory [6, 7]. In fact, any engineering uncertainty can be categorized within three general types: physical uncertainty, model uncertainty, and statistical uncertainty [8].

This chapter presents an integrated CAE methodology based on experimental validation and an uncertainty-based design, as shown in Figure 8.2. Assuming that there is enough statistical information so that statistical uncertainty is minimal, an advanced CAE methodology can be presented with experimental validation and reliability-based design. As a result, a high-fidelity model and analysis can be created that takes physical and model uncertainties into account.

Mechanical fatigue subject to external and inertial transient loads in the service life of a mechanical system often leads to structural failure due to accumulated damage [9]. A structural-durability analysis that predicts the fatigue life of a mechanical component subjected to dynamic stresses and strains is an intensive and complicated multidisciplinary simulation process, since it requires the integration of several CAE tools and a large amount of data communication and computation. Uncertainties in geometric dimensions and material properties due to manufacturing tolerances result in an indeterministic nature of fatigue life for the mechanical component. The main objective of this chapter is thus to demonstrate the possibilities of using advanced CAE methodology to predict structural durability with experimental

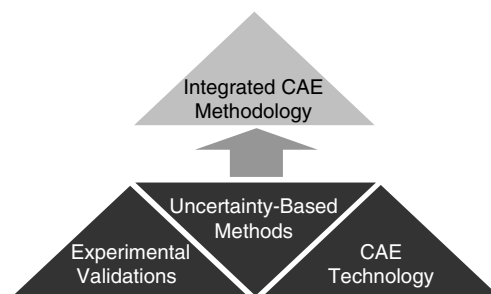


**FIGURE 8.2** Integrated computer-aided engineering methodology.

validation and reliability-based design. In this way, it is possible to determine whether the modeling and simulation are feasible and ascertain whether an optimal design is reliable. One of the primary challenges in developing an integrated CAE methodology is to produce effective reliability-based design optimization (RBDO) methods [1, 4, 5].

## 8.2 Fatigue-Life Analysis and Experimental Validation

### 8.2.1 Mechanical Fatigue Failure for Army Trailer Drawbar

The U.S. Army trailer encountered a mechanical failure due to damage accumulation after driving 1,671 miles on the Perryman course no. 3 at a constant speed of 15 mph. The failure is illustrated in Figure 8.3. This failure initiated further research using a physics-of-failure model of the U.S. Army trailer that involved the validation of the simulation model, dynamic analysis, and durability analysis. The goal was to further improve the trailer's design to extend its overall fatigue life and minimize its weight.

### 8.2.2 Experimental Validation of Mechanical Fatigue

#### 8.2.2.1 Validation of Simulation Model

The computer-aided design (CAD) model for the U.S. Army trailer is developed with Pro/Engineer to simulate a real trailer model (Figure 8.4). To achieve high fidelity, the CAD model goes through an experimental validation, which includes comparison of the mass/inertial properties and the natural frequencies and mode shapes of the model with physical measurements as seen in Figure 8.5a.

Table 8.1 shows the results of the modal analysis. The results indicate that the simulation results are close to the experimental results obtained from modal analysis as shown in Figure 8.5b. Meanwhile, other mechanical components — tire, axle, shock absorber, etc. — are appropriately modeled through experimental validation.



FIGURE 8.3 Army trailer and its structural failure.

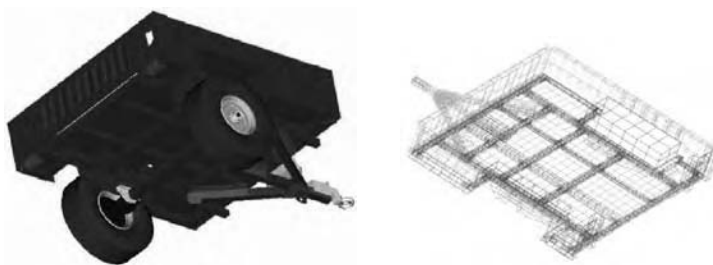
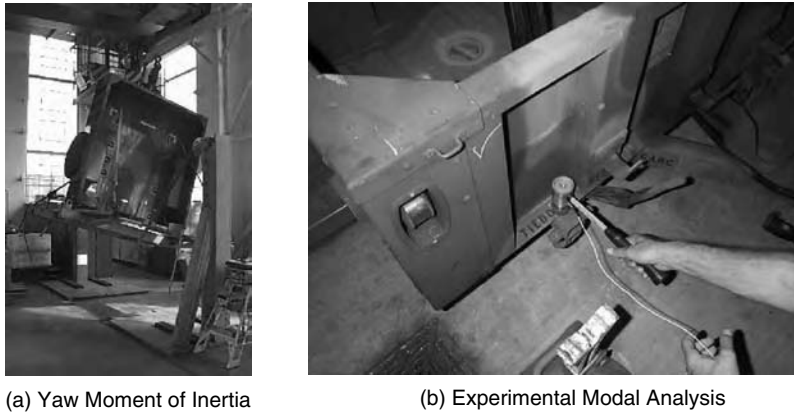


FIGURE 8.4 CAD and finite element models of trailer.



**FIGURE 8.5** Experimental validations: (a) yaw moment of inertia; (b) experimental modal analysis.

**TABLE 8.1** Results of Modal Analysis

Mode No.	Frequency (Simulation)	Frequency (Experiment)
1	18.92	17.73
2	21.55	22.14
3	26.30	29.07

### 8.2.2.2 Validation of Dynamic Analysis

A multibody dynamics model of HMMWV is created to drive the trailer on the Perryman course no. 3 at a constant speed of 15 mph (Figure 8.6). The trailer is modeled as a flexible dynamics model. A 30-sec dynamic simulation is performed with a maximum integration time step of 0.005 sec using the DADS dynamic analysis package [10]. To validate the dynamics model and analysis, dynamic strain (or stress) is measured by installing a (rosette) strain gauge at critical regions to collect strain time histories. As shown in Figure 8.7, a power spectral-density (PSD) curve of dynamic strain is used to compare testing data with simulation results, in addition to performing a statistical comparison of mean, root mean square, skewness, and kurtosis of the dynamic strain.

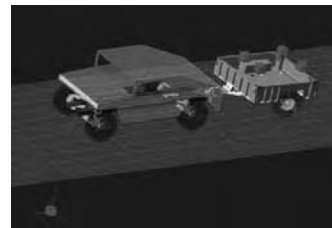


**FIGURE 8.6** Dynamic model and analysis of trailer.

### 8.2.2.3 Validation of Durability Analysis

For a durability analysis, the fatigue life for crack initiation is calculated at those critical regions in the mechanical system that experience a short life span. The fatigue-life analysis consists of two primary computations: dynamic stress and fatigue life computations (Figure 8.8). Dynamic stress can be obtained from either a hardware prototype experiment in which sensors or transducers are placed on the physical component, or from numerical simulation. Using simulation, a stress influence coefficient (SIC) [11] obtained from quasistatic finite element analysis (FEA) using MSC NASTRAN is superposed with dynamic analysis results (including external forces, accelerations, and angular velocities) to compute the dynamic stress history. This history is then used to compute the crack-initiation fatigue life of the component.

Durability analysis is carried out using durability analysis and reliability workspace (DRAW) programs developed at the University of Iowa [11]. A preliminary durability analysis is executed to estimate the fatigue life of the U.S. Army trailer and to predict the critical regions that experience a low fatigue life.

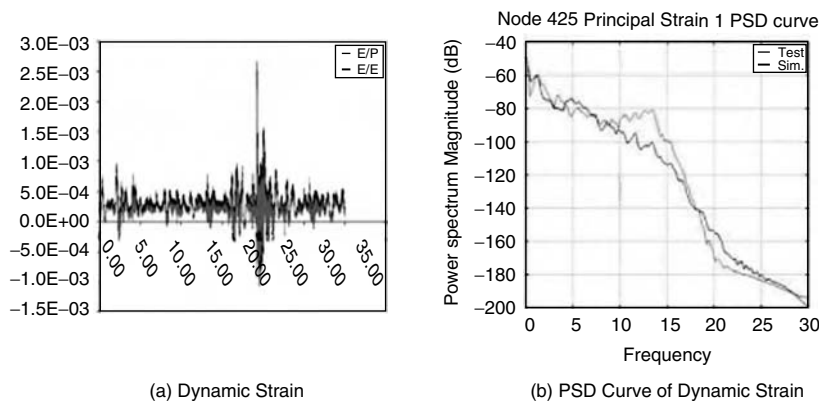


FIGURE 8.7 Validation of dynamic strain: (a) dynamic strain; (b) PSD curve of dynamic strain.

The critical regions on the drawbar assembly are clearly shown in Figure 8.9, excluding any fictitious critical regions that are the result of modeling imperfections due to applied boundary conditions. To compute the multiaxial crack initiation life of the drawbar, the equivalent von Mises strain approach is employed, which is described by the fatigue resistance and cyclic strength of the material as [12]

$$\frac{\Delta \epsilon}{2} = \frac{\sigma'_f}{E} (2N_f)^b + \epsilon'_f (2N_f)^c \quad \text{and} \quad \sigma = K'(\epsilon_p)^{n'} \quad (8.1)$$

with the empirical constants  $(\sigma', \epsilon', b, c, K', n')$ . Details on durability analysis are discussed in Refs. [11, 12].

### 8.2.3 Design Optimization for Mechanical Fatigue

Because damage accumulation leads to structural fatigue failure in the drawbar assembly, durability design optimization for the U.S. Army trailer drawbar was carried out to improve its fatigue life and to minimize weight. The critical region where mechanical fatigue failure occurs is now taken into account in conducting the design optimization process. The integrated design optimization process involves: design parameterization [13], design sensitivity analysis (DSA) [13], and design optimization [14]. Design parameters of the drawbar assembly are carefully defined, taking geometric and manufacturing restrictions into account.

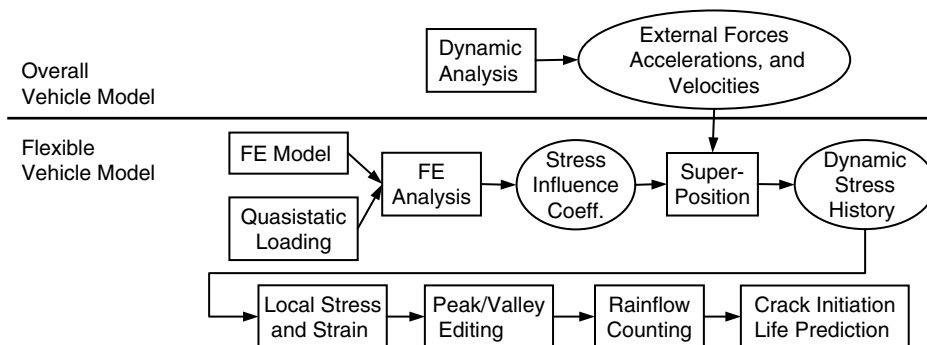


FIGURE 8.8 Computation process for fatigue life.

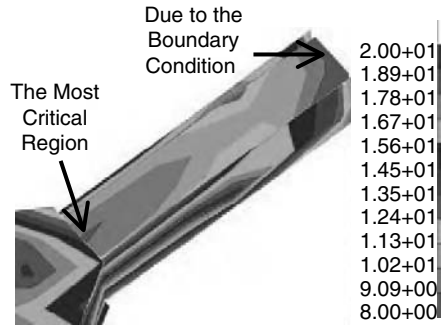


FIGURE 8.9 Fatigue-life contour of army trailer drawbar.

### 8.2.3.1 Design Parameterization

As shown in Figure 8.10, the drawbar assembly is composed of one central bar, two side bars, six side angles, two side attachments, and top and bottom plates. The optimum design of the drawbar assembly needs to be symmetric, and thus design parameterization is made to yield a symmetric design. Bars and attachments at the initial design have a uniform thickness. However, the thicknesses of those elements of the drawbar assembly that can be changed during the design optimization process are modeled as sizing design parameters. While maintaining the rectangular shape of the central and side bars, their height and width are considered as shape design parameters.

As shown in Table 8.2, seven design parameters are defined for the drawbar assembly. The first five are sizing design parameters, which include the thicknesses of the drawbar, side angles, and attachments. Two shape design parameters are defined as the width and height of the cross-sectional geometry of the drawbar.

### 8.2.3.2 Design Sensitivity Analysis for Fatigue Response

The sensitivity computational procedure for fatigue life is shown in Figure 8.11. First, quasistatic loadings need to be computed, which consist of inertial and reaction forces. For this problem, there are a total of 114 quasistatic loading cases. These cases are applied to the drawbar assembly to perform FEAs and to obtain the SICs, which are then used to compute a dynamic stress history of the current design. This dynamic stress history is used to predict the fatigue life of the perturbed design. A continuum-based DSA of the SICs is also carried out [13, 15], which is then used to predict the dynamic stress history of the perturbed design. This perturbed dynamic stress history is then used to predict the fatigue life of the

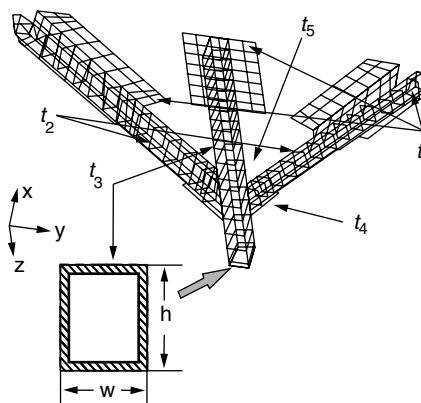


FIGURE 8.10 Design parameters of drawbar and attachments.

**TABLE 8.2** Design Parameters

Design	Symbol	Description
$d_1$	$t_1$	thickness of six side angles
$d_2$	$t_2$	thickness of two side bars
$d_3$	$t_3$	thickness of center bar
$d_4$	$t_4$	thickness of two side attachments
$d_5$	$t_5$	thickness of top and bottom plates
$d_6$	$w$	cross-sectional width of three bars
$d_7$	$h$	cross-sectional height of three bars

perturbed design. Finally, the design sensitivity of fatigue life is computed by taking a finite difference of the original and perturbed fatigue life.

### 8.2.3.3 Durability Design Optimization

The design objective is to increase the fatigue life of the drawbar while minimizing the weight of the trailer's drawbar assembly. Due to restrictions placed on manufacturing and assembling processes, side constraints are generally imposed on the design parameters. Therefore, the design optimization problem

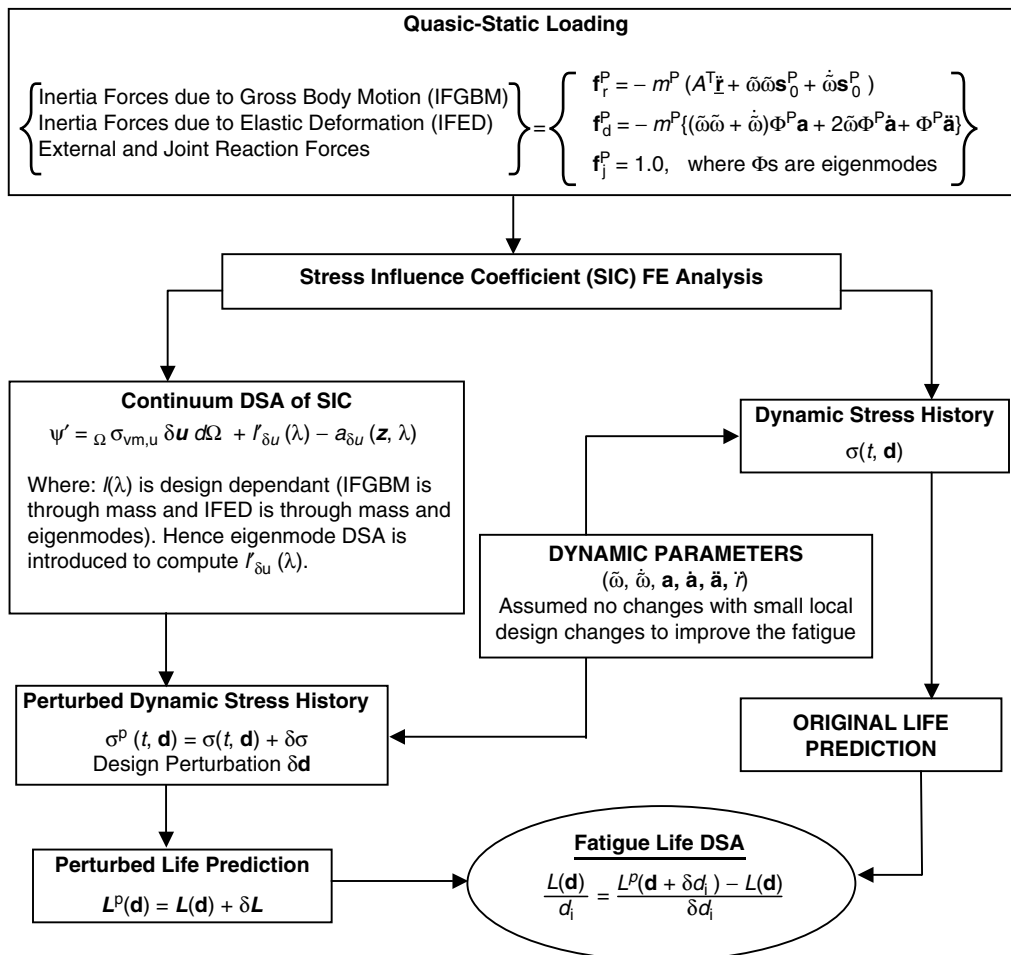


**FIGURE 8.11** Computational procedure for design sensitivity analysis of flexible structural systems.

**TABLE 8.3** Base Design and Its Bounds for Drawbar

Design Type	Design, $d_j$	Lower Bound, $\mathbf{d}^L$	Base Design	Upper Bound, $\mathbf{d}^U$
Sizing designs	$d_1$	0.100	0.250	0.500
	$d_2$	0.100	0.250	0.500
	$d_3$	0.100	0.250	0.500
	$d_4$	0.100	0.250	0.500
	$d_5$	0.100	0.250	0.500
Shape designs	$d_6$	1.000	2.000	5.000
	$d_7$	1.000	3.000	5.000

can be formulated as

$$\begin{aligned}
 &\text{Minimize } W(\mathbf{d}) \\
 &\text{Subject to } g_i = 1 - L_i(\mathbf{d})/L_{\min} \leq 0, \quad i = 1, \dots, nc \\
 &\quad \mathbf{d}^L \leq \mathbf{d} \leq \mathbf{d}^U, \quad \mathbf{d} \in R^{ndv}
 \end{aligned} \tag{8.2}$$

where  $W(\mathbf{d})$  is the weight of the drawbar assembly,  $L_i(\mathbf{d})$  is the fatigue life at the  $i$ th node,  $L_{\min}$  is the required minimum fatigue life,  $g_i$  is the  $i$ th design constraint, and  $\mathbf{d}^L$  and  $\mathbf{d}^U$  are lower and upper bounds of the design parameters, respectively. In Equation 8.2,  $nc$  is the number of design constraints, and  $ndv$  is the number of design parameters.

For the seven design parameters ( $ndv = 7$ ) defined in Table 8.2, the base design and design bounds are shown in Table 8.3. The side constraints need to be set by considering the restriction of manufacturing and assembling processes. For example, it is not possible for any upper bound of the sizing design parameter to be larger than half the size of a lower bound in the corresponding shape design parameter in the same cross section.

For optimization purposes, it will be extremely difficult to define fatigue-life constraints over the entire drawbar assembly in a continuum manner, since there could be an infinite number of design constraints. It is instead desirable to define a finite number of fatigue-life constraints that are limited to the critical regions. But if optimization is carried out only with respect to such critical regions, then it must be verified whether the fatigue life over the entire optimized drawbar assembly exceeds the required minimum fatigue life. As shown in Figure 8.12 and Table 8.4, the critical region is found on the central bar. Using symmetry, ten critical nodes ( $nc = 10$ ) are selected along the center of the top and bottom of the central bar. The required minimum fatigue life is set at  $3.0 \times 10^8$  cycles, which is more than 30 times the shortest life of the base design, which stands at  $9.425 \times 10^6$  cycles.

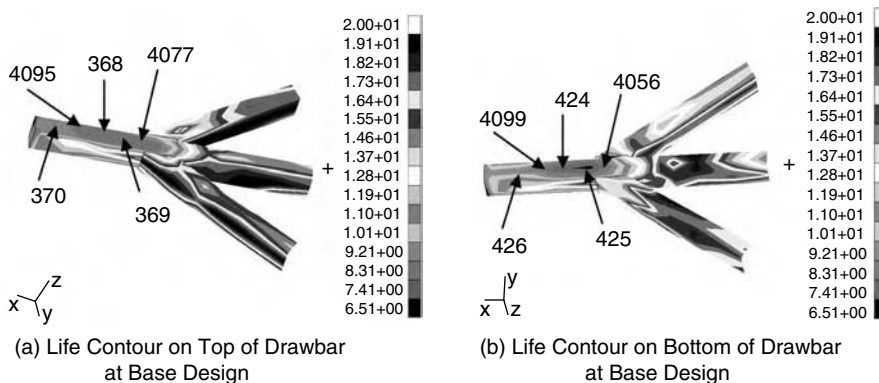


**FIGURE 8.12** Fatigue-life contour on drawbar at base design: (a) life contour on top of drawbar at base design; (b) life contour on bottom of drawbar at base design.

**TABLE 8.4** Critical Nodes at Base Design (Unit: Cycle)

Constraint ID	Node ID	Fatigue Life
1	425	$9.425 \times 10^6$
2	424	$7.148 \times 10^7$
3	426	$1.115 \times 10^{10}$
4	368	$4.927 \times 10^9$
5	369	$3.595 \times 10^9$
6	370	$3.056 \times 10^{10}$
7	4056	$9.775 \times 10^{11}$
8	4077	$2.161 \times 10^{11}$
9	4095	$5.581 \times 10^9$
10	4099	$6.137 \times 10^9$

As shown in Table 8.4, the fatigue life widely varies between  $10^7$  and  $10^{12}$  cycles, resulting in a large difference (even in order of magnitude) in design constraints during the design optimization process. Therefore, design constraints are normalized by using the required minimum fatigue life, as shown in Equation 8.2 [14]. For design optimization, a modified feasible direction method is used [14]. It should be noted that another seemingly critical region appears at the tip of the drawbar on the base design. However, due to the boundary condition imposed at the tip of the drawbar, this region is fictitious.

### 8.2.3.4 Results of Design Optimization

As shown in Table 8.5, the optimum design is obtained in four iterations. The total mass is reduced by about 40% of its original size (from 58.401 to 35.198 lb), while all fatigue-life constraints are satisfied. As shown in Figure 8.12, the critical region at the base design is spread out over the front of the central bar. Among ten design constraints, only the first and second constraints (at nodes 425 and 424) are violated or active at the base design. On the other hand, at the optimum design, the first, third, and sixth design constraints (nodes 425, 426, and 370) appear to be active, as shown in Table 8.6.

**TABLE 8.5** Design History in Optimization for HMT DRAW Durability Model

Iteration	Line Search	$W$	$d_1$	$d_2$	$d_3$	$d_4$	$d_5$	$d_6$	$d_7$
1	0	58.401	0.2500	0.2500	0.2500	0.2500	0.2500	2.0000	3.0000
	1	59.464	0.2494	0.2476	0.2762	0.2502	0.2503	1.9992	2.9966
	2	61.186	0.2485	0.2437	0.3186	0.2506	0.2507	1.9980	2.9910
	3	65.660	0.2462	0.2334	0.4297	0.2514	0.2519	1.9950	2.9764
	4	60.865	0.2487	0.2444	0.3107	0.2505	0.2506	1.9982	2.9920
2	0	65.656	0.2462	0.2334	0.4297	0.2514	0.2519	1.9950	2.9764
	1	35.712	0.1000	0.1011	0.3424	0.2283	0.2286	1.8110	2.5226
	2	24.990	0.1000	0.1000	0.2012	0.1910	0.1910	1.5134	1.7882
3	0	35.712	0.1000	0.1011	0.3424	0.2283	0.2286	1.8110	2.5226
	1	35.578	0.1000	0.1000	0.3417	0.2281	0.2284	1.8092	2.5183
	2	35.473	0.1000	0.1000	0.3405	0.2278	0.2281	1.8066	2.5115
	3	35.198	0.1000	0.1000	0.3375	0.2269	0.2272	1.7994	2.4937
	4	34.486	0.1000	0.1000	0.3297	0.2245	0.2248	1.7804	2.4471
	5	35.402	0.1000	0.1000	0.3405	0.2278	0.2281	1.8066	2.5115
4	0	35.198	0.1000	0.1000	0.3375	0.2269	0.2272	1.7994	2.4937
	1	19.704	0.1000	0.1000	0.1275	0.1622	0.1623	1.2888	1.2340
	2	24.044	0.1000	0.1000	0.1975	0.1837	0.1839	1.4590	1.6542
	3	29.212	0.1000	0.1000	0.2676	0.2053	0.2056	1.6292	2.0740
	4	32.190	0.1000	0.1000	0.3036	0.2164	0.2167	1.7168	2.2903
	5	34.649	0.1000	0.1000	0.3315	0.2250	0.2253	1.7848	2.4577
	6	34.713	0.1000	0.1000	0.3322	0.2252	0.2255	1.7864	2.4619
	7	34.900	0.1000	0.1000	0.3369	0.2267	0.2269	1.7976	2.4896
Optimum		35.198	0.1000	0.1000	0.3375	0.2269	0.2272	1.7994	2.4937



TABLE 8.6 Constraint History in Optimization for HMT DRAW Durability Model

Iteration	$G_1$	$G_2$	$G_3$	$G_4$	$G_5$	$G_6$	$G_7$	$G_8$	$G_9$	$G_{10}$
1	0	$9.42 \times 10^6$	$7.15 \times 10^7$	$1.11 \times 10^{10}$	$4.93 \times 10^9$	$3.59 \times 10^9$	$3.06 \times 10^{10}$	$9.77 \times 10^{11}$	$2.16 \times 10^{11}$	$5.58 \times 10^9$
	1	$2.09 \times 10^7$	$9.47 \times 10^8$	$3.26 \times 10^{10}$	$2.16 \times 10^{10}$	$1.88 \times 10^{10}$	$1.28 \times 10^{11}$	$2.49 \times 10^{12}$	$4.51 \times 10^{11}$	$8.73 \times 10^8$
	2	$5.90 \times 10^7$	$2.36 \times 10^9$	$1.06 \times 10^{11}$	$4.68 \times 10^9$	$1.07 \times 10^{11}$	$1.46 \times 10^{10}$	$9.62 \times 10^{12}$	$4.05 \times 10^{12}$	$6.17 \times 10^{10}$
	3	$1.07 \times 10^9$	$1.28 \times 10^{10}$	$2.09 \times 10^{11}$	$2.10 \times 10^{12}$	$1.13 \times 10^{13}$	$2.00 \times 10^{12}$	$2.08 \times 10^{14}$	$2.57 \times 10^{13}$	$8.48 \times 10^{11}$
	4	$5.18 \times 10^7$	$3.37 \times 10^8$	$4.56 \times 10^{10}$	$9.00 \times 10^{10}$	$3.67 \times 10^9$	$4.80 \times 10^{11}$	$8.01 \times 10^{12}$	$3.38 \times 10^{12}$	$2.02 \times 10^9$
2	0	$1.07 \times 10^9$	$1.28 \times 10^{10}$	$2.09 \times 10^{11}$	$2.10 \times 10^{12}$	$1.13 \times 10^{13}$	$2.00 \times 10^{12}$	$2.08 \times 10^{14}$	$2.57 \times 10^{13}$	$8.48 \times 10^{11}$
	1	$7.47 \times 10^9$	$1.25 \times 10^{13}$	$2.36 \times 10^9$	$2.00 \times 10^{13}$	$1.28 \times 10^{12}$	$9.76 \times 10^9$	$1.62 \times 10^{15}$	$1.00 \times 10^{13}$	$9.73 \times 10^{11}$
	2	$6.00 \times 10^4$	$1.47 \times 10^9$	$6.60 \times 10^5$	$5.22 \times 10^8$	$5.10 \times 10^6$	$1.13 \times 10^9$	$1.05 \times 10^9$	$6.77 \times 10^8$	$1.27 \times 10^{10}$
3	0	$7.47 \times 10^9$	$1.25 \times 10^{13}$	$2.36 \times 10^9$	$2.00 \times 10^{13}$	$1.28 \times 10^{12}$	$9.76 \times 10^9$	$1.62 \times 10^{15}$	$1.00 \times 10^{13}$	$9.73 \times 10^{11}$
	1	$5.08 \times 10^8$	$6.75 \times 10^{12}$	$4.18 \times 10^8$	$4.44 \times 10^{13}$	$3.86 \times 10^{10}$	$9.07 \times 10^{11}$	$5.79 \times 10^{15}$	$2.91 \times 10^{11}$	$1.60 \times 10^{13}$
	2	$2.11 \times 10^{10}$	$1.00 \times 10^{13}$	$2.70 \times 10^9$	$3.99 \times 10^{13}$	$1.75 \times 10^{11}$	$1.07 \times 10^{10}$	$9.03 \times 10^{14}$	$7.01 \times 10^{12}$	$4.15 \times 10^{10}$
	3	$8.99 \times 10^8$	$3.82 \times 10^{12}$	$1.19 \times 10^9$	$1.12 \times 10^{13}$	$3.05 \times 10^{11}$	$1.97 \times 10^9$	$1.78 \times 10^{14}$	$3.68 \times 10^{11}$	$7.43 \times 10^{12}$
	4	$2.06 \times 10^8$	$1.74 \times 10^{12}$	$4.02 \times 10^8$	$9.00 \times 10^{12}$	$1.64 \times 10^{11}$	$1.59 \times 10^{11}$	$4.53 \times 10^{13}$	$1.49 \times 10^{12}$	$5.34 \times 10^{12}$
	5	$4.59 \times 10^8$	$3.67 \times 10^{12}$	$3.66 \times 10^8$	$2.69 \times 10^{13}$	$6.23 \times 10^{11}$	$4.42 \times 10^{11}$	$1.87 \times 10^{15}$	$2.81 \times 10^{12}$	$1.69 \times 10^{13}$
4	0	$8.99 \times 10^8$	$3.82 \times 10^{12}$	$1.19 \times 10^9$	$1.12 \times 10^{13}$	$3.05 \times 10^{11}$	$1.97 \times 10^9$	$1.78 \times 10^{14}$	$3.68 \times 10^{11}$	$7.43 \times 10^{12}$
	1	$3.00 \times 10^4$	$1.79 \times 10^8$	$3.00 \times 10^4$	$1.50 \times 10^5$	$3.00 \times 10^4$	$7.11 \times 10^7$	$1.20 \times 10^5$	$1.08 \times 10^6$	$3.40 \times 10^7$
	2	$3.00 \times 10^4$	$1.29 \times 10^9$	$4.20 \times 10^5$	$4.79 \times 10^8$	$2.55 \times 10^6$	$8.49 \times 10^8$	$4.08 \times 10^8$	$3.05 \times 10^8$	$1.69 \times 10^{10}$
	3	$6.09 \times 10^6$	$7.42 \times 10^{10}$	$1.10 \times 10^7$	$9.06 \times 10^{10}$	$1.76 \times 10^9$	$3.65 \times 10^{10}$	$2.91 \times 10^{11}$	$8.49 \times 10^{10}$	$7.88 \times 10^9$
	4	$6.58 \times 10^7$	$4.04 \times 10^{11}$	$5.56 \times 10^7$	$3.65 \times 10^{12}$	$2.11 \times 10^{10}$	$7.27 \times 10^{10}$	$7.89 \times 10^{12}$	$6.80 \times 10^{10}$	$3.55 \times 10^{12}$
	5	$2.22 \times 10^8$	$1.84 \times 10^{12}$	$4.29 \times 10^8$	$1.23 \times 10^{13}$	$1.82 \times 10^{11}$	$1.43 \times 10^{11}$	$5.13 \times 10^{13}$	$1.57 \times 10^{12}$	$5.88 \times 10^{12}$
	6	$2.39 \times 10^8$	$1.94 \times 10^{12}$	$4.48 \times 10^8$	$7.19 \times 10^{11}$	$1.88 \times 10^{11}$	$1.54 \times 10^{11}$	$5.67 \times 10^{13}$	$1.68 \times 10^{12}$	$5.52 \times 10^{12}$
	7	$3.24 \times 10^8$	$2.21 \times 10^{12}$	$2.47 \times 10^8$	$8.25 \times 10^{11}$	$2.87 \times 10^{11}$	$2.22 \times 10^{11}$	$1.22 \times 10^{15}$	$6.30 \times 10^{12}$	$8.91 \times 10^{12}$
Optimum		$8.99 \times 10^8$	$3.82 \times 10^{12}$	$1.19 \times 10^9$	$1.12 \times 10^{13}$	$3.05 \times 10^{11}$	$1.97 \times 10^9$	$1.78 \times 10^{14}$	$3.68 \times 10^{11}$	$7.46 \times 10^{12}$
										$1.17 \times 10^{11}$

**TABLE 8.7** Design and Weight Changes between Base and Optimal Designs

Design	Base Design (in.)	Optimal Design (in.)	Change (%)
$t_1$	0.2500	0.1000	-60.0
$t_2$	0.2500	0.1000	-60.0
$t_3$	0.2500	0.3375	+35.0
$t_4$	0.2500	0.2269	-9.24
$t_5$	0.2500	0.2272	-9.12
h	2.0000	1.7994	-10.0
w	3.0000	2.4937	-16.9
Cost	Base Design (lb)	Optimal Design (lb)	Change (%)
Weight	58.401	35.198	-39.7

At the optimum design, all thicknesses decrease except for the central bar, and the width and height of all bars become smaller. Due to the decrease in some sizing design parameters and both shape parameters, about 40% of the mass is saved. The first two design parameters,  $b_1$  and  $b_2$ , decrease slowly at the beginning of the optimization process, and then they rapidly decrease to the lower bound, since more-rigid side bars and angles penalize the central bar, resulting in a decrease in its fatigue life. Moreover, increasing the thickness of the central bar by 35% ( $d_3$ : from 0.25 to 0.3375 in.) further reinforces its strength and produces a longer fatigue life. At the optimum design, the fourth and fifth design parameters (triangular plates and side attachments) are reduced by about 9%, since the weight can be effectively reduced without reducing the fatigue lives at critical regions. With respect to shape design parameters, the width and height are reduced by about 10 and 17%, respectively. These design changes are summarized in Table 8.7.

Because optimization only considers the critical regions, the optimized design must be confirmed through reanalysis to determine whether the fatigue life over the entire drawbar assembly exceeds the required minimum specifications. As shown in the optimal design in Figure 8.13, the original critical region (nodes 425 and 424) at the base design seems to bifurcate into an original region at node 425 and another region around node 426. Except for the tip of the central bar shown in Figure 8.13a, all other areas satisfy the minimum requirements for fatigue life. Similar to the base design, a fictitious critical region is detected at the tip of the drawbar. As explained earlier, it is suspected that the boundary condition at the tip causes this fictitious condition.

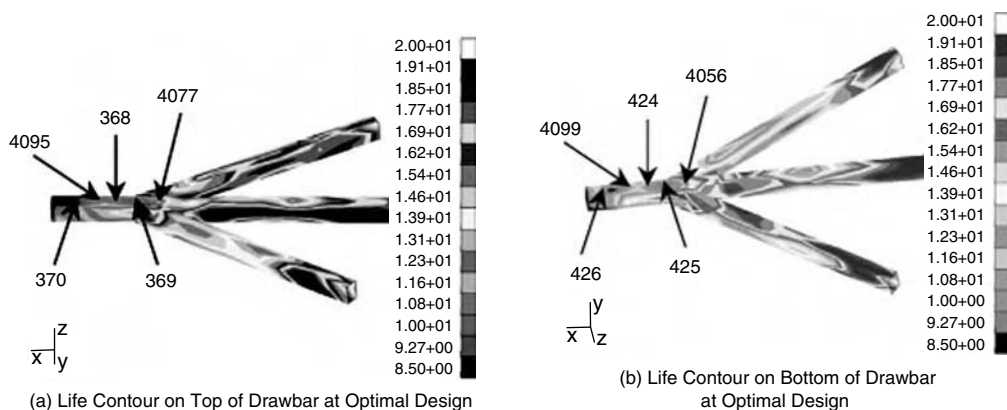


**FIGURE 8.13** Fatigue-life contour on drawbar at optimal design: (a) life contour on top of drawbar at optimum design; (b) life contour on bottom of drawbar at optimal design.

**TABLE 8.8** Fatigue Life with and without Considering Notch Effects

Predicted Fatigue Life		Without Considering Notch Effects	Considering Notch Effects
Base	Driving cycle (block)	$9.42 \times 10^6$	$1.44 \times 10^3$
	Driving mile (mile)	$1.18 \times 10^6$	180
	Driving time (hour)	78,500	12
Opt.	Driving cycle (block)	$8.99 \times 10^8$	$7.66 \times 10^4$
	Driving mile (mile)	$1.12 \times 10^8$	9,580
	Driving time (hour)	$7.49 \times 10^6$	638
Life extension (times)		95.4	53.2

### 8.2.3.5 Results of Design Optimization Considering Notch Effects [16]

Having identified the region near node 425 on the trailer drawbar as the location of the shortest fatigue life, it is now necessary to apply the fatigue-strength reduction factor ( $K_f$ ) to account for the effect of geometric discontinuities in the critical region, as shown in Table 8.8. A fatigue-strength reduction factor reduces the predicted fatigue life in a manner proportional to the severity of the geometric discontinuity.  $K_f$  is calculated from the stress intensity factor  $K_t$  and the notch-sensitivity factor  $q$ . Based on references in the literature [17], the values of  $K_t$  and  $q$  were estimated, and the associated  $K_f$  values were calculated to be 2.6. Using this  $K_f$ , the fatigue life on Perryman course no. 3 is estimated to be 9580 miles, which means that a fatigue crack will not initiate and grow to a 2-mm length until the trailer traverses 9580 miles of Perryman course no. 3 at 15 mph, or 638 h of continuous running. In contrast, the fatigue life of the base design was 180 miles or 12 h. This means that the fatigue life of the optimum design is 53.2 times greater than that of the base design. In this example we have tried to reduce the weight of the drawbar by imposing the constraint that the fatigue life be approximately equal to 30 times that of the baseline design (see Equation 8.2). A greater increase in fatigue life could be achieved if the fatigue life were constrained to be equal to that of the baseline.

## 8.3 Reliability Analysis and Reliability-Based Design Optimization

### 8.3.1 Reliability Analysis for Durability-Based Optimal Design

The reliability analysis of the durability-based optimum design is carried out to estimate the probability of failure as

$$P(L < 3 \times 10^8 \text{ cycles}) = \int \cdots \int_{L < 3 \times 10^8} f_{\mathbf{x}}(\mathbf{x}) d\mathbf{x} \quad (8.3)$$

For the reliability analysis, the uncertainty of each design parameter is modeled with a normal distribution and a 10% coefficient of variation. The optimal design turns out to be unreliable with a 49.7% ( $\beta = 0.073$ ) probability of failure through the reliability analysis. Considering the variability of the design that lays on the design constraint boundaries, as shown in Figure 8.14, it is reasonable that the deterministic optimal design has only about 50% reliability. Because the deterministic optimal design is unreliable, it is necessary to perform a reliability-based design optimization (RBDO) [1–5] for reliable and durable designs. Among all random parameters, uncertainty in the third random parameter (central bar thickness) has the most significant effect on the probability of failure. Thus, without a new reliability-based optimum design, the thickness of the central bar must be manufactured more accurately to increase reliability, which will significantly increase the manufacturing cost.

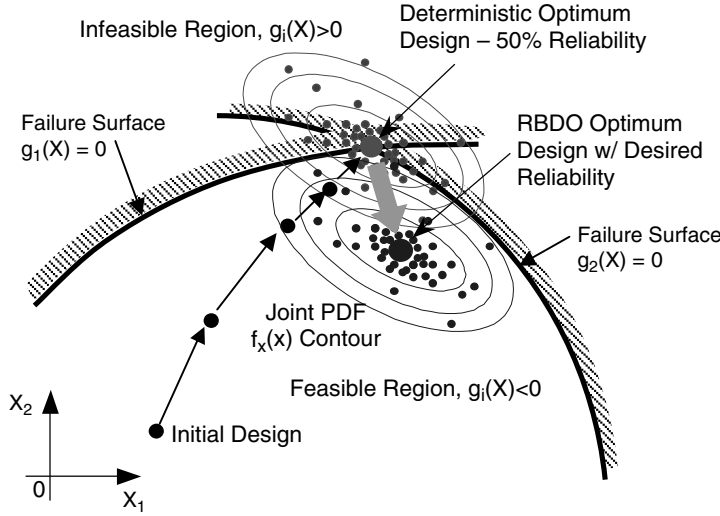


FIGURE 8.14 Overall procedure of PMA+ in RBDO.

### 8.3.2 Reliability-Based Design Optimization for Durability

As seen in the previous section, the various uncertainties in the mechanical system led to an unreliable deterministic design optimization. As shown in Figure 8.14, the design must move back to the feasible region to increase the reliability of design constraints while minimizing a design objective. The process is called reliability-based design optimization (RBDO), which will be explained in this section.

#### 8.3.2.1 RBDO Model of Performance Measure Approach (PMA)

For any engineering application, the RBDO model [1–5, 18–20] can generally be formulated as

$$\begin{aligned}
 &\text{minimize} \quad \text{Cost}(\mathbf{d}) \\
 &\text{subject to} \quad P(G_i(\mathbf{d}(\mathbf{X})) \leq 0) - \Phi(\beta_i) \geq 0, \quad i = 1, 2, \dots, nc \\
 &\quad \quad \quad \mathbf{d}^L \leq \mathbf{d} \leq \mathbf{d}^U
 \end{aligned} \tag{8.4}$$

where  $\mathbf{d} = [d_i^T] = \boldsymbol{\mu}(\mathbf{X}) \in R^{ndv}$  is the design vector;  $\mathbf{X} = [X_i]^T \in R^{nrv}$  is the random vector; and  $ndv$ ,  $nrv$ , and  $nc$  are the numbers of design parameters, random parameters, and probabilistic constraints, respectively. The probabilistic constraints are described by a probability constraint  $P(\bullet) \geq \Phi(\beta_i)$  for a safe event  $G_i(\mathbf{d}(\mathbf{X})) \leq 0$ .

The statistical description of the failure of the performance function  $G_i(\mathbf{d}(\mathbf{X}))$  is characterized by the cumulative distribution function,  $F_{G_i}(\bullet)$ , as

$$P(G_i(\mathbf{X}) \leq 0) = F_{G_i}(0) \geq \Phi(\beta_i) \tag{8.5}$$

where the reliability of failure is described as

$$F_{G_i}(0) = \int_{G_i(\mathbf{X}) \leq 0} \dots \int f_{\mathbf{X}}(\mathbf{x}) dx_1 \dots dx_n, \quad i = 1, 2, \dots, nc \tag{8.6}$$

In Equation 8.6,  $f_{\mathbf{X}}(\mathbf{x})$  is the joint probability density function of all random parameters. Its evaluation requires a reliability analysis where multiple integrations are involved, as shown in Equation 8.6.

Some approximate probability integration methods have been developed to provide efficient solutions, such as the first-order reliability method (FORM) [1–5, 8] or the asymptotic second-order reliability method (SORM) [21, 22], with a rotationally invariant measure as the reliability. FORM often provides adequate accuracy and is widely used for design applications. In FORM, the reliability analysis requires a transformation  $\mathbf{T}$  [23, 24] from the original random parameter  $\mathbf{X}$  to the standard normal random parameter  $\mathbf{U}$ . The performance function  $G(\mathbf{X})$  in  $X$ -space can then be mapped onto  $G(\mathbf{T}(\mathbf{X})) \equiv G(\mathbf{U})$  in  $U$ -space.

The probabilistic constraint in Equation 8.5 can be expressed as a performance measure through the inverse transformation of  $F^G(\bullet)$  as [1, 3–5, 18–20]:

$$G_{p_i}(\mathbf{d}(\mathbf{X})) = F_{G_i}^{-1}(\Phi(\beta_i)) \leq 0 \quad (8.7)$$

where  $G_{p_i}$  is the  $i$ th probabilistic constraint. In Equation 8.7, the probabilistic constraint in Equation 8.4 can be replaced with the performance measure. This is referred to as the performance measure approach (PMA) [1, 3–5, 18–20]. Thus, the RBDO model using PMA can be redefined as

$$\begin{aligned} & \text{minimize} \quad \text{Cost}(\mathbf{d}) \\ & \text{subject to} \quad G_{p_i}(\mathbf{d}(\mathbf{X})) \leq 0, \quad i = 1, 2, \dots, nc \\ & \quad \quad \quad \mathbf{d}^L \leq \mathbf{d} \leq \mathbf{d}^U \end{aligned} \quad (8.8)$$

### 8.3.2.2 Reliability Analysis Model of PMA

Reliability analysis in PMA can be formulated as the inverse of reliability analysis in the reliability index approach (RIA). The first-order probabilistic performance measure  $G_{p,\text{FORM}}$  is obtained from a nonlinear optimization problem in  $U$ -space, defined as

$$\begin{aligned} & \text{maximize} \quad G(\mathbf{U}) \\ & \text{subject to} \quad \|\mathbf{U}\| = \beta_i \end{aligned} \quad (8.9)$$

where the optimum point on the target reliability surface is identified as the most probable point (MPP)  $\mathbf{u}_{\beta=\beta_i}^*$  with a prescribed reliability  $\beta_i = \|\mathbf{u}_{\beta=\beta_i}^*\|$ . Unlike RIA, only the direction vector  $\mathbf{u}_{\beta=\beta_i}^* / \|\mathbf{u}_{\beta=\beta_i}^*\|$  needs to be determined by exploring the spherical equality constraint  $\|\mathbf{U}\| = \beta_i$ .

General optimization algorithms can be employed to solve the optimization problem in Equation 8.9. However, a hybrid mean value (HMV) first-order method is well suited for PMA due to its stability and efficiency [1, 3–5, 18–20].

### 8.3.2.3 Reliability Analysis Tools for PMA

Three numerical methods [1, 3–5, 18–20, 25] for PMA were used to solve Equation 8.9: the advanced mean value method [24] in Equation 8.10, the conjugate mean value method [1, 3–5, 18–20] in Equation 8.11, and the hybrid mean value (HMV) method [1, 3–5, 18–20] in Equation 8.12:

$$\mathbf{u}_{\text{AMV}}^{(1)} = \beta_i \mathbf{n}(\mathbf{0}), \quad \mathbf{u}_{\text{AMV}}^{(k+1)} = \beta_i \mathbf{n}(\mathbf{u}_{\text{AMV}}^{(k)}) \quad \text{where} \quad \mathbf{n}(\mathbf{u}_{\text{AMV}}^{(k)}) = \frac{\nabla_U G(\mathbf{u}_{\text{AMV}}^{(k)})}{\|\nabla_U G(\mathbf{u}_{\text{AMV}}^{(k)})\|} \quad (8.10)$$

$$\begin{aligned} & \mathbf{u}_{\text{CMV}}^{(0)} = \mathbf{0}, \quad \mathbf{u}_{\text{CMV}}^{(1)} = \mathbf{u}_{\text{AMV}}^{(1)}, \quad \mathbf{u}_{\text{CMV}}^{(2)} = \mathbf{u}_{\text{AMV}}^{(2)}, \\ & \mathbf{u}_{\text{CMV}}^{(k+1)} = \beta_i \frac{\mathbf{n}(\mathbf{u}_{\text{CMV}}^{(k)}) + \mathbf{n}(\mathbf{u}_{\text{CMV}}^{(k-1)}) + \mathbf{n}(\mathbf{u}_{\text{CMV}}^{(k-2)})}{\|\mathbf{n}(\mathbf{u}_{\text{CMV}}^{(k)}) + \mathbf{n}(\mathbf{u}_{\text{CMV}}^{(k-1)}) + \mathbf{n}(\mathbf{u}_{\text{CMV}}^{(k-2)})\|} \quad \text{for } k \geq 2 \quad \text{where} \quad \mathbf{n}(\mathbf{u}_{\text{CMV}}^{(k)}) = \frac{\nabla_U G(\mathbf{u}_{\text{CMV}}^{(k)})}{\|\nabla_U G(\mathbf{u}_{\text{CMV}}^{(k)})\|} \end{aligned} \quad (8.11)$$

$$\mathbf{u}_{\text{HVM}}^{(k+1)} = \begin{cases} \mathbf{u}_{\text{AMV}}^{(k+1)} \text{ in Eq. (36.8),} & \text{if } G(\mathbf{u}_{\text{HVM}}^{(k)}) \text{ is convex or } \text{sign}(\zeta^{(k+1)}) > 0 \\ \mathbf{u}_{\text{CMV}}^{(k+1)} \text{ in Eq. (36.9),} & \text{if } G(\mathbf{u}_{\text{HVM}}^{(k)}) \text{ is concave or } \text{sign}(\zeta^{(k+1)}) \leq 0 \end{cases}$$

$$\text{with } \zeta^{(k+1)} = (\mathbf{n}^{(k+1)} - \mathbf{n}^{(k)}) \cdot (\mathbf{n}^{(k)} - \mathbf{n}^{(k-1)}) \quad (8.12)$$

$$\text{sign}(\zeta^{(k+1)}) > 0: \text{ Convex type at } \mathbf{u}_{\text{HVM}}^{(k+1)} \text{ with respect to design } \mathbf{d}$$

$$\leq 0: \text{ Concave type at } \mathbf{u}_{\text{HVM}}^{(k+1)} \text{ with respect to design } \mathbf{d}$$

Although the advanced mean value method performs well for the convex performance function in PMA, it was found to have some numerical shortcomings, such as slow convergence, or even divergence, when applied to the concave performance function. To overcome this difficulty, the conjugate mean value method was proposed [1, 3–5, 18–20]. The conjugate steepest descent direction significantly improves the rate of convergence as well as stability, as compared with the advanced mean value method for the concave performance function. However, the conjugate mean value method is not as efficient as the advanced mean value method for the convex function. Consequently, the hybrid mean value (HVM) method was proposed to attain both stability and efficiency in the MPP search for PMA [1, 3–5, 18–20]. The HVM method employs the criterion for the performance function type near the MPP. Once the performance function type is identified, either the advanced mean value or conjugate mean value method is adaptively selected for the MPP search. The numerical procedure of the HVM method is presented with some numerical examples by Youn et al. [1].

### 8.3.3 Results of Reliability-Based Shape Design Optimization for Durability of M1A1 Tank Roadarm [14]

A roadarm of the military tracked vehicle shown in Figure 8.15 is employed to demonstrate the effectiveness of PMA for a large-scale RBDO application. A 17-body dynamics model is created to simulate the tracked vehicle driven on the Aberdeen Proving Ground 4 at a constant speed of 20 mph. A 20-sec dynamic simulation is performed with a maximum integration time step of 0.05 sec using the dynamic analysis package DADS.

As shown in Figure 8.16, 310 20-node isoparametric finite elements (STIF95) and four beam elements (STIF4) of ANSYS are used to create the roadarm finite element model, which is made of S4340 steel. Finite element analysis is performed to obtain the stress influence coefficient of the roadarm using ANSYS by applying 18 quasistatic loads. The empirical constants ( $\sigma'$ ,  $\epsilon'$ ,  $b$ ,  $c$ ,  $K'$ ,  $n'$ ) for fatigue material properties are defined in Table 8.9. It has been found [26] that geometric tolerances are normally distributed with about a 1% coefficient of variation (COV), while material properties are lognormally distributed with about 3% COV, except for negative quantities, such as the fatigue exponents  $b$  and  $c$ . The computation for fatigue-life prediction and for design sensitivity requires, respectively, 6950 and 6496 CPU sec (for eight design parameters) on an HP 9000/782 workstation.

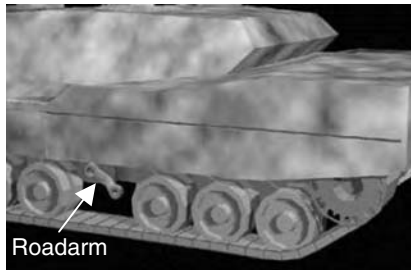


FIGURE 8.15 Military tracked vehicle.

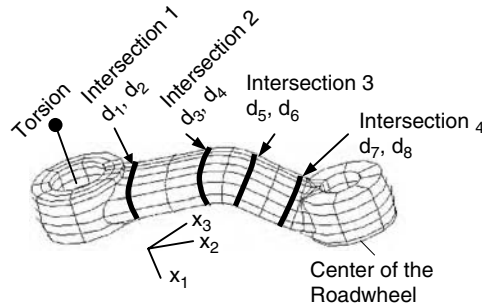


FIGURE 8.16 Random design parameters.

As shown in Table 8.9, eight design parameters are used to characterize the four cross-sectional shapes of the roadarm, while uncertainties in the dimensions and material properties of a structural component due to manufacturing tolerances are modeled using 14 random parameters. Vertical variations (in the  $x_1$ -direction) of cross-sectional shapes are defined as the random parameters  $d_1$ ,  $d_3$ ,  $d_5$ , and  $d_7$  for intersections 1 to 4, respectively, and side variations (moving in the  $x_3$ -direction) of cross sectional shapes are defined using the remaining four random variables.

In design optimization for fatigue life, the number of design constraints could be very large if a fatigue-life constraint were defined at every point of the structural component. To make the problem computationally feasible for structural durability analysis, a preliminary fatigue-life analysis for a crack initiation is carried out (as shown in Figure 8.17) to detect those critical spots that have a short fatigue life and to define the design constraints. A refined durability analysis using the critical-plane method is then carried out at these critical spots to accurately predict fatigue life. The design constraints for durability in Equation 8.4 are defined as

$$G_i(\mathbf{d}(\mathbf{X})) = 1 - L_i(\mathbf{d}(\mathbf{X}))/L_t \quad (8.13)$$

where  $L_i(\mathbf{d}(\mathbf{X}))$  is the crack-initiation fatigue life at the current design, and the target fatigue life  $L_t$  is set to 5 years. During this process, DRAW predicts the crack-initiation fatigue life, which is taken as the performance requirement.

TABLE 8.9 Definition of Random Parameters for Crack Initiation Fatigue-Life Prediction

Parameters		Lower Bound	Mean	Upper Bound	COV (%)	Distribution Type
Design/ random (geometric tolerance)	$d_1, X_2$	1.3776	1.8776	2.0000	1	normal
	$d_2, X_2$	1.5580	3.0934	2.0000	1	normal
	$d_3, X_3$	2.5934	1.8581	3.2000	1	normal
	$d_4, X_4$	2.7091	3.0091	3.2000	1	normal
	$d_5, X_5$	2.2178	2.5178	2.7800	1	normal
	$d_6, X_6$	4.6500	2.9237	5.0000	1	normal
	$d_7, X_7$	2.6237	4.7926	3.0500	1	normal
	$d_8, X_8$	2.5000	2.8385	3.0000	1	normal
Fatigue Material			Mean	COV (%)	Distribution Type	
Random (material parameter)	$X_9$	cyclic strength coefficient, $K'$	$1.358 \times 10^9$	3	lognormal	
	$X_{10}$	cyclic strength exponent, $n'$	0.12	3	lognormal	
	$X_{11}$	fatigue strength coefficient, $\sigma'$	$1.220 \times 10^9$	3	lognormal	
	$X_{12}$	fatigue strength exponent, $b$	-0.073	3	normal	
	$X_{13}$	fatigue ductility coefficient, $\epsilon'_f$	0.41	3	lognormal	
	$X_{14}$	fatigue ductility exponent, $c$	-0.60	3	normal	

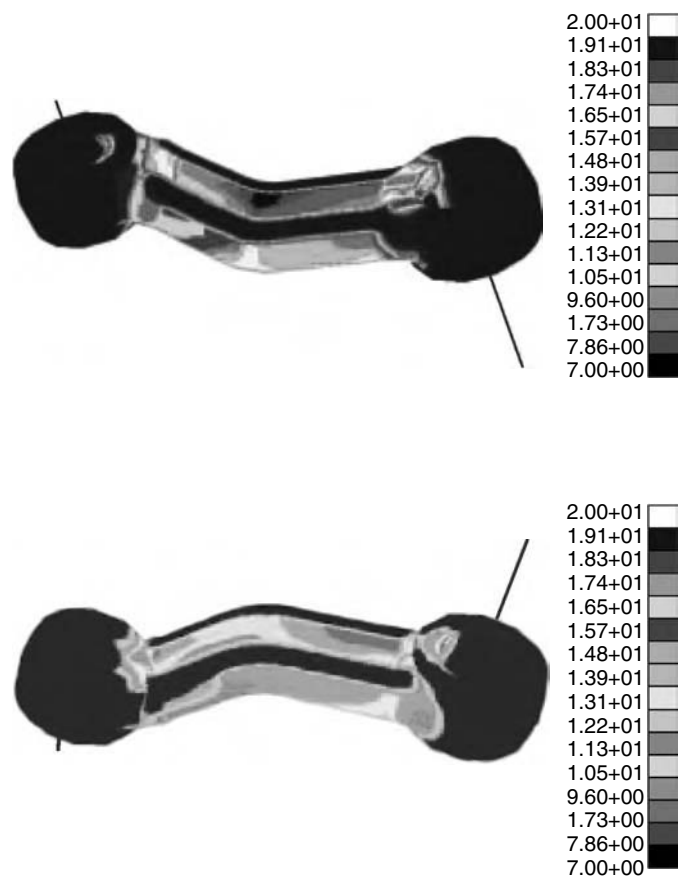


FIGURE 8.17 Preliminary fatigue-life analysis.

As illustrated in Figure 8.18, uncertainty of fatigue life is first determined only by considering uncertainty of geometric parameters, and then by considering uncertainty of both geometric and material parameters. It is shown that the RBDO process must consider uncertainty of material parameters, since it significantly affects uncertainty of the fatigue life [15]. Three- $\sigma$  RBDO results of durability for the M1A1 tank roadarm are shown in Figure 8.19 and Figure 8.20. Note that small design changes are made

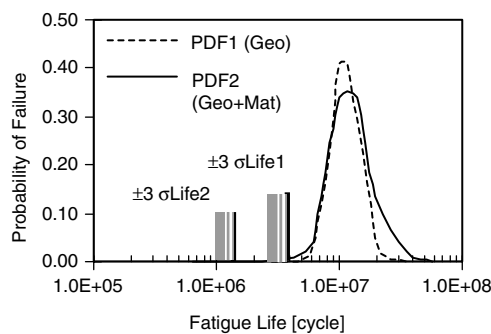
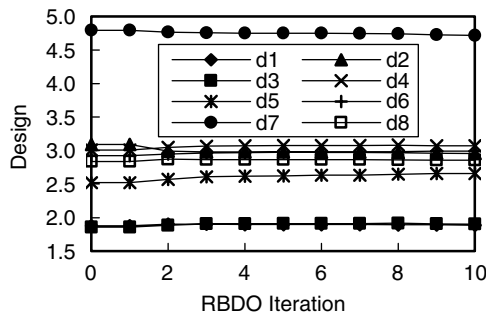
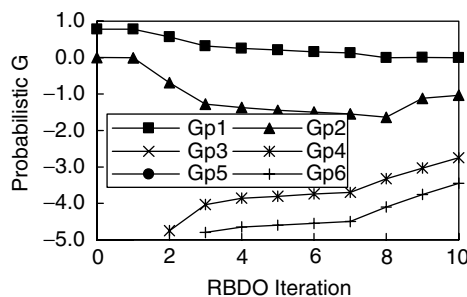
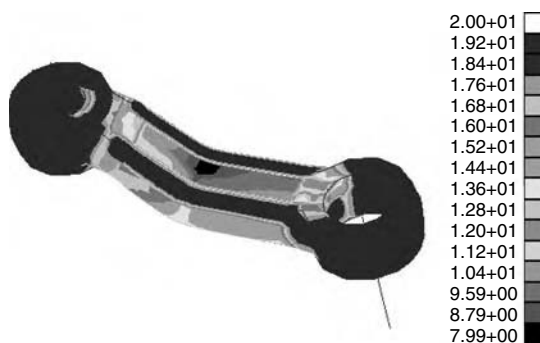


FIGURE 8.18 Uncertainty propagation to fatigue life.



FIGURE 8.19 Design history in 3- $\sigma$ .FIGURE 8.20 Probabilistic constraint history in 3- $\sigma$ .FIGURE 8.21 Fatigue-life contour at 3- $\sigma$  optimum design.

to satisfy the target fatigue life with target reliability levels, while increasing roadarm weight by 1%. The shortest fatigue life was 1.094 years at the initial design, but this increased to 5.017 years at the 3- $\sigma$  optimum design. Figure 8.21 illustrates the fatigue-life contour of a 3- $\sigma$  optimum design that has increased in overall fatigue life when compared with Figure 8.17.

## 8.4 Conclusions

This chapter presents the three key elements of an advanced CAE methodology: durability analysis, experimental validation, and an uncertainty-based design optimization. Since the CAE model is developed to simulate a prototype model, the former is exposed to a variety of natural uncertainties, which are categorized as model, physical, and statistical uncertainties. It was proposed that a high-fidelity model

and analysis through experimental validation is necessary to accurately characterize the effect of input uncertainty. Furthermore, the RBDO method must be incorporated into CAE to take physical uncertainties into account. A lack of statistical information in modeling physical uncertainty creates greater uncertainty that can be dealt with by using a Bayesian possibility or evidence theory.

It has been found that experimental validation should be conducted to obtain high-fidelity models and analyses. The structural durability of a trailer drawbar was used to demonstrate CAE with experimental validation, and optimization was then carried out to improve the fatigue life of the trailer drawbar while minimizing its weight. To develop accurate CAE models for multibody dynamics, FEA, and durability analysis, CAD models were carefully compared with experimental results. Design optimization successfully increased the fatigue life of the drawbar 53.2 times and reduced the weight 40% when considering notch effects due to rivet holes in the critical region. To validate the deterministic optimum design, a reliability analysis evaluates the reliability of fatigue failure under manufacturing tolerances. The fact that its probability of failure is 49.7% underscores the need for reliability-based design optimization (RBDO) for a reliable and durable optimum design. In addition to experimental validation, the RBDO method must be incorporated into advanced CAE methodology. One of the challenges in developing an advanced CAE methodology is to create an effective RBDO method. PMA was used to carry out the RBDO process for large-scale multidisciplinary applications (e.g., M1A1 tank roadarm durability), with emphasis on numerical efficiency and stability. Consequently, the advanced CAE methodology with experimental validation and uncertainty-based design optimization was successfully demonstrated by applying it to the computationally intensive and complicated multidisciplinary simulation process of predicting structural durability.

## Acknowledgment

Research is supported by the Physics of Failure project sponsored by U.S. Army Material Systems Analysis Activity (AMSAA).

## Nomenclature

$L$	crack initiation fatigue life
$W$	weight for design optimization
$\mathbf{d}$	design parameter; $\mathbf{d} = [d_1, d_2, \dots, d_n]^T$
$g(\mathbf{d})$	design constraint of design parameters
$\mathbf{X}$	random vector; $\mathbf{X} = [X_1, X_2, \dots, X_n]^T$
$\mathbf{x}$	realization of $\mathbf{X}$ ; $\mathbf{x} = [x_1, x_2, \dots, x_n]^T$
$G(\mathbf{X})$	constraint of random parameters
$\mathbf{U}$	independent and standard normal random parameter
$\mathbf{u}$	realization of $\mathbf{U}$ ; $\mathbf{u} = [u_1, u_2, \dots, u_n]^T$
$P_f$	probability of failure
$f_X$	probability density function of $X$
$\mu$	mean of random vector $\mathbf{X}$ ; $\mu = [\mu_1, \mu_2, \dots, \mu_n]^T$
$\beta$	reliability index
$K_f$	fatigue-strength reduction factor
$K_t$	stress intensification factor
$q$	notch sensitivity factor

## References

1. Youn, B.D., Choi, K.K., and Park, Y.H., Hybrid analysis method for reliability-based design optimization, *ASME J. Mechanical Design*, 125 (2), 221–232, 2003.
2. Enevoldsen, I. and Sorensen, J.D., Reliability-based optimization in structural engineering, *Structural Safety*, 15, 169–196, 1994.

3. Lee, T.W. and Kwak, B.M., A reliability-based optimal design using advanced first order second moment method, *Mech. Struct. Mach.*, 15 (4), 523–542, 1987/88.
4. Tu, J. and Choi, K.K., A new study on reliability-based design optimization, *ASME J. Mechanical Design*, 121 (4), 557–564, 1999.
5. Youn, B.D. and Choi, K.K., Selecting probabilistic approaches for reliability-based design optimization, *AIAA J.*, 42 (1), 124–131, 2004.
6. Shih, C.J., Chi, C.C., and Hsiao, J.H., Alternative  $\alpha$ -level-cuts methods for optimum structural design with fuzzy resources, *Comput. Struct.*, 81, 2579–2587, 2003.
7. Bae, H.R., Grandhi, R.V., and Canfield, R.A., Structural Design Optimization Based on Reliability Analysis Using Evidence Theory, SAE 03M-125, presented at SAE World Congress, Detroit, 2003.
8. Madsen, H.O., Krenk, S., and Lind, N.C., *Methods of Structural Safety*, Prentice-Hall, Englewood Cliffs, NJ, 1986.
9. Fuchs, H.O. and Stephens, R.I., *Metal Fatigue in Engineering*, John Wiley & Sons, New York, 1980.
10. CADSI Inc., DADS User's Manual, rev. 7.5, CADSI, Oakdale, IA, 1994.
11. Center for Computer-Aided Design, DRAW: Durability and Reliability Analysis Workspace, College of Engineering, University of Iowa, Iowa City, 1994.
12. Yu, X., Choi, K.K., and Chang, K.H., Probabilistic structural durability prediction, *AIAA J.*, 36 (4), 628–637, 1998.
13. Haug, E.J., Choi, K.K., and Komkov, V., *Design Sensitivity Analysis of Structural Systems*, Academic Press, New York, 1986.
14. Arora, J.S., *Introduction to Optimum Design*, McGraw-Hill, New York, 1989.
15. Chang, K.H., Yu, X., and Choi, K.K., Shape design sensitivity analysis and optimization for structural durability, *Int. J. Numerical Meth. Eng.*, 40, 1719–1743, 1997.
16. Choi, K.K., Youn, B.D., and Tang, J., Structural Durability Design Optimization and Its Reliability Assessment, presented at 2002 ASME Design Engineering Technical Conferences: 29th Design Automation Conference, Chicago, 2003.
17. Sines, G. and Waisman, J.L., *Metal Fatigue*, McGraw-Hill, New York, 1959.
18. Youn, B.D. and Choi, K.K., A new response surface methodology for reliability-based design optimization, *Comput. Struct.*, 82, 241–256, 2004.
19. Choi, K.K. and Youn, B.D., An Investigation of Nonlinearity of Reliability-Based Design Optimization Approaches, presented at ASME Design Engineering Technical Conferences, Montreal, 2002.
20. Youn, B.D., Choi, K.K., and Yang, R.-J., Efficient Evaluation Approaches for Probabilistic Constraints in Reliability-Based Design Optimization, presented at 5th WCSMO, Lido di Jesolo-Venice, Italy, 2003.
21. Breitung, K., Asymptotic approximations for multi-normal integrals, *ASCE J. Eng. Mech.*, 110 (3), 357–366, 1984.
22. Tvedt, L., Distribution of quadratic forms in normal space-application to structural reliability, *ASCE J. Eng. Mech.*, 116 (6), 1183–1197, 1990.
23. Rackwitz, R. and Fiessler, B., Structural reliability under combined random load sequences, *Comput. Struct.*, 9, 489–494, 1978.
24. Hohenbichler, M. and Rackwitz, R., Nonnormal dependent vectors in structural reliability, *ASCE J. Eng. Mech.*, 107 (6), 1227–1238, 1981.
25. Wu, Y.T., Millwater, H.R., and Cruse, T.A., Advanced probabilistic structural analysis method for implicit performance functions, *AIAA J.*, 28 (9), 1663–1669, 1990.
26. Rusk, D.T. and Hoffman, P.C., Component Geometry and Material Property Uncertainty Model for Probabilistic Strain-Life Fatigue Predictions, presented at 6th Joint FAA/DoD/NASA Aging Aircraft Conference, San Francisco, 2002.

# Reliability Assessment of Ships

---

9.1	Introduction.....	9-1
9.2	Historical Overview .....	9-2
9.3	Procedure for Reliability Assessment of Ships .....	9-3
9.4	Target Reliability for Ships against Hull Girder Collapse.....	9-4
9.5	Ultimate Limit-State Equations.....	9-5
9.6	Ultimate Hull Girder Strength Models .....	9-6
	Primary Failure Mode • Secondary Failure Mode • Tertiary Failure Mode • Quaternary Failure Mode • Effect of Corrosion • Effect of Fatigue Cracking • Effect of Local Denting • Effect of Combined Corrosion, Fatigue Cracking, and Local Denting	
9.7	Extreme Hull Girder Load Models.....	9-11
	Still-Water Bending Moment • Wave-Induced Bending Moment	
9.8	Prediction of Time-Dependent Structural Damage....	9-12
	Time-Dependent Corrosion Wastage Models • Time-Dependent Fatigue Crack Model	
9.9	Application to Time-Dependent Reliability Assessment of Ships.....	9-20
	Scenarios for Operational Conditions and Sea States • Scenarios for Structural Damage • Reliability Assessment • Some Considerations Regarding Repair Strategies	
9.10	Concluding Remarks .....	9-36
	References .....	9-37

**Jeom Kee Paik**

*Pusan National University, Korea*

**Anil Kumar Thayamballi**

*Chevron Texaco Shipping  
Company LLC*

## 9.1 Introduction

---

Failures in ship structures, including some total losses, continue to occur worldwide, in spite of continuous ongoing efforts to prevent them. Such failures can have enormous costs associated with them, including lost lives in some cases. One of the possible causes of such structural casualties is thought to be the inability of aging ships to withstand rough seas and weather, because the ship's structural safety decreases during later life, although it is quite adequate at the design stage and perhaps up to 15 years beyond. Corrosion and fatigue-related problems are considered to be the two most important factors potentially leading to such age-related structural degradation of ships and, of course, of many other types of steel structures. Local dent damage sometimes takes place in particular locations of certain merchant ships, e.g., inner bottom plates of bulk carriers.

In the design and operation of ship structures, there are a number of uncertainties that must be dealt with. Wherever there are uncertainties, a risk of failure exists. For a structure, the risk of failure for our purposes will be defined as the probability that the load-carrying capacity is smaller than the extreme or accidental load to which that the structure is subject. To minimize and prevent loss of life and financial exposure caused by ship structural casualties, it is of vital importance to keep the safety and reliability at an acceptable level.

It has been recognized that a reliability-based approach is potentially better than a deterministic approach for the design of ship structures as well as offshore platforms and land-based structures, since it can more rigorously deal with various types of uncertainties associated with the design variables [1]. The reliability-based approach is also equally useful in developing a damage-tolerant structure and for establishing strategies for repair and maintenance of age-degraded or otherwise damaged structural members.

The reliability of a structure is assessed based upon limit-state exceedence, which is defined as a condition in which the structure fails to perform an intended function. Four types of limit states can be considered, namely, serviceability limit state (SLS), ultimate limit state (ULS), fatigue limit state (FLS), and accidental limit state (ALS) [2]. SLS conventionally represents failure states for normal operations due to deterioration of routine functionality. ULS (also called ultimate strength) typically represents the collapse of the structure due to loss of structural stiffness and strength. FLS represents fatigue crack occurrence in structural details due to stress concentration and damage accumulation (crack growth) under the action of repeated loading. ALS represents excessive structural damage as a consequence of accidents, e.g., collisions, grounding, explosion, and fire, that affect the safety of the structure, environment, and personnel.

This chapter presents application examples for reliability assessment of merchant ships with the focus on hull girder ultimate limit state, taking into account the time-dependent effects of corrosion, fatigue cracking, and local denting. Some considerations for establishing a reliability-based repair and maintenance scheme are also made so as to keep ship hull girder strength reliability at an acceptable level, even in later life.

## 9.2 Historical Overview

---

The modern era of reliability-based structural design possibly started after World War II, when Freudenthal [3] suggested that statistical distributions of design factors should be taken into consideration when developing safety factors for engineering structures. Academic interest in structural reliability theory was further aroused in the 1960s, in part by the publication of another paper by Freudenthal [4].

The earliest works that used reliability-based methodologies in ship structural design were initiated by Mansour [5, 6] and Mansour and Faulkner [7]. Many such early efforts were primarily focused on developing reliability analysis methods [8–12], while the earliest applications to ship structures focused on the safety and reliability of ship hull girders subjected to wave-induced bending moments [10, 12–14].

The Ship Structure Committee (SSC; <http://www.shipstructure.org>) aims to promote safety, economy, education, and marine environment protection in the U.S. and Canadian maritime industries. Through its excellent research programs, which have been in place now for nearly 50 years, the SSC has devoted considerable effort to the advancement of the safety and integrity of marine structures. Under sponsorship of the SSC, a series of research and development projects in areas related to ship structural safety and reliability, among others, has been carried out [15–23]. An historical review of the R&D activities of the SSC in the area of reliability assessment of ship structures was made by Mansour et al. [23]. In addition, international effort has been made to develop ISO code 2394 [1], which deals with safety formats, partial load and resistance factors, load combinations, and properties of geometric and material parameters.

Ship structures are composed of individual structural components such as plating, stiffened panels, and support members. While some work continues in this area, there are today a number of useful methodologies for analyzing the safety and reliability of ship structural components. However, each structural component can fail in more than one way until the entire structure reaches the state where it fails to perform its intended function, and failure of a single structural component may or may not lead

to overall system collapse. One cannot achieve target reliabilities for the global system on the basis of individual component reliability alone because of the different ways in which such individual components may connect and interact prior to and during the failure process.

In order to appreciate whether ship failures achieve levels consistent with acceptable targets, it is of crucial importance to assess the safety and reliability of ship structures at the level of the global system. Application examples presented in this chapter focus on the ultimate hull girder strength reliability of ships at the global level.

### 9.3 Procedure for Reliability Assessment of Ships

The procedure for the reliability assessment of ship structures is similar to that adopted for other types of steel structures as presented elsewhere in this book. For our purposes, the associated risk can be written as follows:

$$\text{Risk} = P_f = \text{Prob}(C \leq D) \quad (9.1a)$$

where  $P_f$  = probability of failure,  $C$  = load-carrying capacity, and  $D$  = demand. To be safe, the following criterion should then be satisfied:

$$P_f \leq P_{f0} \quad (9.1b)$$

where  $P_{f0}$  = target value of risk or probability of failure.

The safety and reliability of a structure is the converse of the risk, i.e., the probability that it will not fail, namely,

$$\text{Reliability} = \text{Prob}(C > D) = 1 - P_f \quad (9.2)$$

The result of a standard reliability calculation, normally carried out after transformation of design variables into a standardized normal space, is a reliability index  $\beta$  that is related to the probability of failure  $P_f$  by

$$\beta = -\phi^{-1}(P_f) \quad (9.3a)$$

where  $\phi$  is the standard normal distribution function. To be safe, the following criterion should then be satisfied:

$$\beta \geq \beta_0 \quad (9.3b)$$

where  $\beta_0$  = target value of reliability index  $= -\phi^{-1}(P_{f0})$ . It should be emphasized that in order for Equation 9.3a and Equation 9.3b to be valid, all nonnormal variates should be transformed to normal variates when calculating the reliability indices.

It should be noted here that, broadly speaking, a formal risk assessment involves consideration of not only the probability of failure, but also the consequences of failure, ideally in quantitative terms (see for example [24, 25]). In this chapter, however, reliability assessment is taken as the converse of risk analysis. This practice has been common in the field of structural reliability for some time. A major aim of structural risk assessment for merchant cargo vessels is normally to determine (a) the level of risk in terms of probability as related to total loss from structural causes and, increasingly, (b) the possibility of environmental pollution. The main tasks needed for reliability assessment in a “design by analysis” approach are generally as follows:

1. Specify the required target value of the reliability index (or a target level of risk).
2. Identify all likely failure modes of the structure or fatal events.
3. Formulate a limit-state function for each failure mode identified in item 2.

4. Identify the probabilistic characteristics (mean, variance, distribution) of the random variables in each limit-state function.
5. Calculate the reliability for each limit state with respect to each failure mode of the structure.
6. Assess if the determined reliability is greater than or equal to the target reliability.

Repeat the above steps as required after changes to relevant design parameters.

## 9.4 Target Reliability for Ships against Hull Girder Collapse

The required level of structural safety and reliability may vary from one industry to another, depending on various factors such as the type of failure, the seriousness of its consequence, or perhaps even the cost of adverse publicity and other intangible losses. Appropriate values of target safety and reliability are not readily available and are usually determined by surveys or by examinations of the statistics of failures, although the fundamental difference between a risk assessment and a reliability analysis needs to be acknowledged when interpreting such results.

The methods to select the target safeties and reliabilities can be categorized into the following three groups:

1. Guesstimation: A reasonable value as recommended by a regulatory body or professionals on the basis of prior experience. This method can be employed for new types of structures for which a statistical database on past failures does not exist.
2. Analysis of existing design rules: The level of risk one has traditionally lived with is estimated by calculating the reliability that is implicit in existing design rules that have been successful. This method is often used for the revision of existing design rules, particularly from a traditional experience-based format to a reliability-based format.
3. Economic value analysis: The target value of safety and reliability is selected to minimize the total expected costs during the service life of the structure. This is perhaps the most attractive approach, although it is often difficult to undertake in practice.

Figure 9.1 shows the reliability indices of some types of ships based on data that have been obtained by different investigators using different calculation methods, as a function of the year of publication [26].

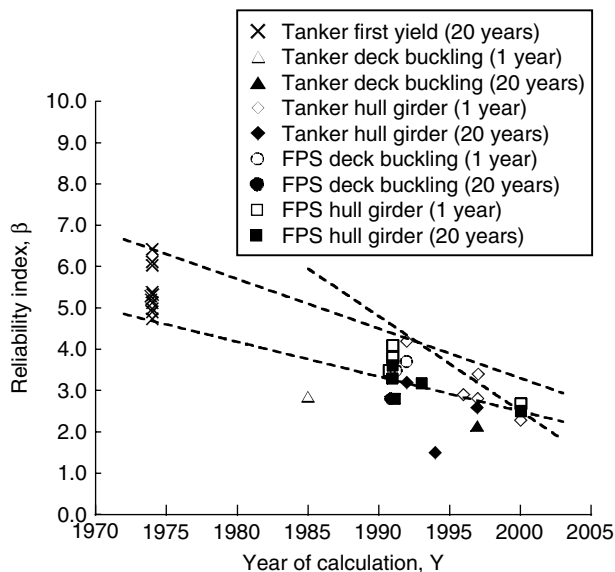


**FIGURE 9.1** Variation of the calculated notional reliability indices over the passage of the years for ships from 1974 to 2000 (FPS = floating, production, and storage unit).

The categories of vessels, governing failure modes, and service life are identified. For ships with 20 years of service life, the effect of corrosion damage was accounted for in calculating the  $\beta$  values. It is seen from Figure 9.1 that the calculated reliability index has decreased for the assessments conducted in more recent years. The trend shown in Figure 9.1 does not necessarily mean that vessels considered in more recent years are becoming less reliable, at least not to the extent implied by the trends shown. Of course, it is to be expected that ship structures have become more efficient over time because of the increasing availability of technology. Also, some of the calculated results are perhaps more notional than others, and the considered failure modes may be more sophisticated as well. It is true that most calculations tend to use a design wave environment based on nominal values and thus ignore actual experience that may be more benign. It is, of course, challenging to pin down the true wave environment for trading vessels.

An example is the calculations made by Mansour in 1974 [13]. His early results demonstrate higher notional  $\beta$  values. This appears to be mainly a consequence of obtaining the probability of failure under a wave load criterion that is different from, and less than, the lifetime extreme load. The same investigator has, over time, vastly refined and further developed his early calculation methodology, and has even successfully developed unified calculation procedures that are applicable to wave load criteria [23] ranging from a mild storm to the most severe during a vessel's life. Also, many early pioneering calculations typically used 'first yield' as the failure criterion.

The first-yield criterion ignores loss of plate effectiveness due to any propensity for buckling, and so the location of the neutral axis of a ship's hull girder during the actual ultimate failure process will not be correctly simulated. This can result in somewhat lower levels of stress being determined for the compression region of the hull girder in addition to the basic panel strength being too high in some cases, implying a higher predicted hull girder bending strength and similarly higher reliability when compared with a reliability based on a more refined prediction of ultimate hull girder bending strength.

Many of the prior studies ignore age-related degradation effects, which will decrease the  $\beta$  values further in comparative terms. Illustrations shown later in this chapter include such effects. That improvement notwithstanding, there is no escaping the fact that even today's calculations result in reliability indices that are not anything other than notional and comparative, mostly because of the uncertainties in the loads involved, and this situation is expected to continue into the foreseeable future. We can, however, improve the value of comparative and notional reliability measures further by appropriately taking advantage of continuing advances in load prediction and ultimate strength assessment procedures to higher levels of refinement, while also considering age-dependent strength degradation and other types of structural damage considered.

Regarding the more recent results of Figure 9.1, it is of some interest to note that whereas the  $\beta$  values determined in 1991 average around 3.5, those calculated in 2000 average 2.5. Based on the above varied results, and for purposes of use with evolving and recent (advanced) methodologies for ultimate hull girder strength calculations, it is considered that  $\beta = 2.5$  may be a speculative but good target reliability index to aim for in respect to ultimate hull girder strength. For a more elaborate description of how to determine a target value of reliability index for ship structures, the reader can refer to the SSC report by Mansour et al. [23].

## 9.5 Ultimate Limit-State Equations

For hull girder ultimate strength reliability assessment, we will define four levels of failure modes that need to be considered, which we will term the primary, secondary, tertiary, and quaternary failure modes.

The primary failure mode will be taken to represent a condition where hull girder collapse takes place, involving buckling collapse of the compression flange (i.e., deck panel in sagging or bottom panel in hogging) and yielding of the tension flange (i.e., bottom panel in sagging or deck panel in hogging). The secondary failure mode will be a condition wherein the flange (stiffened panel) in compression reaches its ultimate strength. The tertiary failure mode is one in which support members in the compression flange fail, e.g., lateral-torsional buckling or tripping of stiffeners. The quaternary failure mode is a condition



**TABLE 9.1** Samples of Means and COVs of Variables Related to Modeling Uncertainties and Load Combination Factors

Variable	Distribution	Mean	COV
$x_{iu}$	normal	1.0	0.1
$x_{sw}$	normal	1.0	0.05
$x_w$	normal	1.0	0.15
$k_{sw}$	fixed	1.0	—
$k_w$	fixed	0.9	—

when plating between support members in the compression flange reaches its ultimate strength. The last three failure modes do not necessarily result in the total loss of a ship, except in very special cases. However, a ship's function will be presumed to be totally lost if the primary failure mode occurs.

The ultimate limit-state equation for each failure mode noted above can be written as follows:

Primary failure mode:

$$F_I = x_{iu}M_{iu} - (x_{sw}k_{sw}M_{sw} + x_wk_wM_w) \leq 0 \quad (9.4a)$$

Secondary failure mode:

$$F_{II} = x_{2u}M_{2u} - (x_{sw}k_{sw}M_{sw} + x_wk_wM_w) \leq 0 \quad (9.4b)$$

Tertiary failure mode:

$$F_{III} = x_{3u}M_{3u} - (x_{sw}k_{sw}M_{sw} + x_wk_wM_w) \leq 0 \quad (9.4c)$$

Quaternary failure mode:

$$F_{IV} = x_{4u}M_{4u} - (x_{sw}k_{sw}M_{sw} + x_wk_wM_w) \leq 0 \quad (9.4d)$$

where  $M_{iu}$  = hull girder capacity for the  $i$ th failure mode;  $M_{sw}$  = still-water bending moment;  $M_w$  = wave-induced bending moment;  $k_{sw}$ ,  $k_w$  = load combination factors related to still-water bending moment and wave-induced bending moment, respectively, assuming that the corresponding variables they are applied to are the extreme values that do not necessarily occur simultaneously in time; and  $x_{iu}$ ,  $x_{sw}$ ,  $x_w$  = service-experience-dependent modeling parameters reflecting uncertainties associated with hull girder capacity, still-water bending moment, and wave-induced bending moment, respectively.

Table 9.1 proposes selected mean values and COVs (coefficients of variation) of variables related to modeling uncertainties and load combinations, broadly based on prior cited studies related to the reliability assessment of merchant cargo ships. The tabulated values will be used later in the illustrative examples of reliability analyses. It is to be noted that the mean values in particular have been mostly set to unity for convenience, although in particular studies they have been varied by investigators, and correctly so, depending on the particular circumstances involved. For purely illustrative purposes, all reliability calculations have been conducted with  $k_{sw} = 1.0$  and  $k_w = 0.9$  in this chapter.

## 9.6 Ultimate Hull Girder Strength Models

The largely simplified yet somewhat sophisticated formulations for predicting hull girder capacity are now presented for the four failure modes noted in Section 9.5. In predicting ultimate hull girder strength, two types of stiffened panel structural idealizations are relevant, namely the plate-stiffener combination model and the plate-stiffener separation model, as shown in Figure 9.2. The examples are selected from past work by the authors and also other investigators [2, 27, 28].

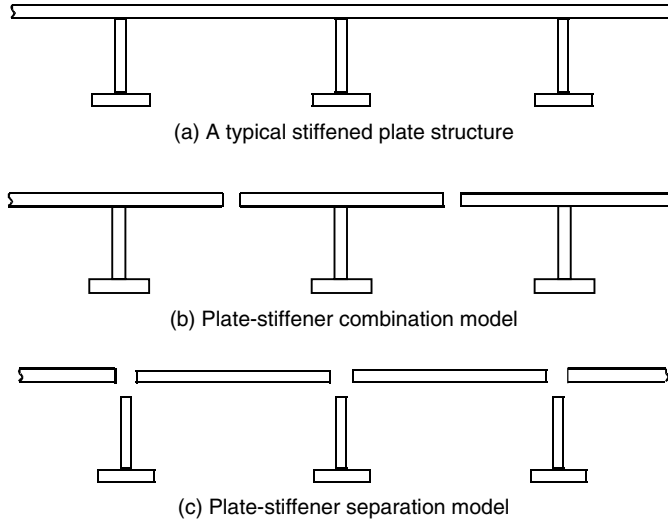


**FIGURE 9.2** Three types of structural idealizations for a stiffened panel. (From Paik, J.K. and Thayamballi, A.K., *Ultimate Limit State Design of Steel-Plated Structures*, John Wiley & Sons, Chichester, U.K., 2003. With permission.)

### 9.6.1 Primary Failure Mode

The ultimate bending moment capacity of a ship's hull (with positive sign for hogging and negative sign for sagging) will be calculated [2] by

$$M_{lu} = \sum_C \sigma_i A_{ei} (z_i - g_u) + \sum_T \sigma_j A_j (z_j - g_u) \quad (9.5)$$

where

$$g_u = [\sum_C \sigma_i A_{ei} z_i + \sum_T \sigma_j A_j z_j] / [\sum_C \sigma_i A_{ei} + \sum_T \sigma_j A_j]$$

$\sigma_i$  = longitudinal bending stress in the  $i$ th structural member, negative for compression and positive for tension, which is given by

$$\sigma_i = (z_i - g) \sigma_{yeq} / (D - g) \text{ for hogging}$$

$$\sigma_i = (g - z_i) \sigma_{yeqb} / g \text{ for sagging}$$

$z_i$  = coordinate of the  $i$ th element measured from the baseline ( $z_i = 0$  at the baseline)

$$g = \text{neutral axis, which is given as } g = [\sum_C A_{ei} z_i + \sum_T A_j z_j] / [\sum_C A_{ei} + \sum_T A_j]$$

$\sum_C()$ ,  $\sum_T()$  = summation for the part in compression or tension, respectively

$A_{ei}$  = effective cross-sectional area of the  $i$ th element in compression

$A_j$  = cross-sectional area of the  $j$ th element in tension

$\sigma_{yeq}$ ,  $\sigma_{yeqb}$  = average equivalent yield stresses at upper deck or outer bottom panels, respectively

$D$  = depth of the ship

In calculating the longitudinal bending stress value defined in Equation 9.5, the following criteria should be satisfied:

$$\sigma \leq \sigma_{yeq} \text{ for tension elements} \quad (9.6a)$$

$$|\sigma| \leq |\sigma_{lu}| \text{ for compression elements} \quad (9.6b)$$

where  $\sigma_{yeq}$  = equivalent yield stress for both plating and attached stiffeners and  $\sigma_{lu}$  = ultimate compressive stress of the structural element.

When a continuous, longitudinally stiffened plate structure is idealized as an assembly of plate-stiffener combination units, as shown in Figure 9.2b, the ultimate compressive strength of each element can be approximated by the so-called Paik-Thayamballi formula, as follows [2]:

$$\sigma_u = -\frac{\sigma_{Yeq}}{\sqrt{0.995 + 0.936\lambda^2 + 0.170\beta_x^2 + 0.188\lambda^2\beta_x^2 - 0.067\lambda^4}} \quad \text{and} \quad |\sigma_{1u}| \leq \frac{\sigma_{Yeq}}{\lambda^2} \quad (9.7)$$

where

$$\beta_x = \frac{b}{t} \sqrt{\frac{\sigma_Y}{E}}$$

$$\lambda = \frac{L}{\pi r} \sqrt{\frac{\sigma_{Yeq}}{E}}$$

with  $L$  = length of the unit,  $E$  = Young's modulus,  $r$  = radius of gyration of the plate-stiffener combination,  $b$  = breadth of plating between stiffeners,  $t$  = plate thickness, and  $\sigma_Y$  = yield stress of plating.

### 9.6.2 Secondary Failure Mode

The hull girder strength formula based on the secondary failure mode will be taken as

$$M_{2u} = \sigma_{2u} Z_e \quad (9.8)$$

where  $\sigma_{2u}$ ,  $Z_e$  = ultimate compressive strength and elastic section modulus, respectively, at the compression flange (stiffened panel) of the ship.

The ultimate compressive strength of the compression flange may again be predicted by Equation 9.7, assuming that the deck or bottom panel concerned is idealized as an assembly of plate-stiffened combination units, as shown in Figure 9.2b.

### 9.6.3 Tertiary Failure Mode

The hull girder strength formula based on the tertiary failure mode will be taken as

$$M_{3u} = \sigma_{3u} Z_e \quad (9.9)$$

where  $\sigma_{3u}$  = ultimate compressive strength of the stiffeners (support members) in the compression flange, and  $Z_e$  is as defined in Equation 9.8.

The ultimate compressive strength  $\sigma_{3u}$  in the tertiary failure mode is approximately represented by the elastic-plastic tripping strength of stiffeners in the compression flange. Useful closed-form formulae for predicting the tripping strength of typical stiffener profiles (e.g., flat-bar, angle and T-bar) can be found in the literature [2].

### 9.6.4 Quaternary Failure Mode

The hull girder strength formula based on the quaternary failure mode will be approximated by

$$M_{4u} = \sigma_{4u} Z_e \quad (9.10)$$

where  $\sigma_{4u}$  = ultimate compressive strength of plating between stiffeners in the compression flange, and  $Z_e$  is as defined in Equation 9.8.

The ultimate compressive strength of plating between stiffeners can be predicted by [29].

For  $\frac{a}{b} \geq 1$ :

$$\frac{\sigma_{4u}}{\sigma_Y} = \begin{cases} 0.032\beta_x^4 - 0.002\beta_x^2 - 1.0 & \text{for } \beta_x \leq 1.5 \\ -1.274 / \beta_x & \text{for } 1.5 < \beta_x \leq 3.0 \\ -1.248 / \beta_x^2 - 0.283 & \text{for } \beta_x > 3.0 \end{cases} \quad (9.11a)$$

For  $\frac{a}{b} < 1$ :

$$\frac{\sigma_{4u}}{\sigma_Y} = -\frac{a}{b} \frac{\sigma_{xu}}{\sigma_Y} - \frac{0.475}{\beta_y^2} \left( 1 - \frac{a}{b} \right) \quad (9.11b)$$

where

$\sigma_Y$  = yield stress of the plating

$$\beta_x = \frac{b}{t} \sqrt{\frac{\sigma_Y}{E}}$$

$$\beta_y = \frac{a}{t} \sqrt{\frac{\sigma_Y}{E}}$$

with  $a$  = plate length (in the ship's longitudinal direction), and  $b$  = plate breadth (in the ship's transverse direction). The term  $\sigma_{xu}$  is taken as  $\sigma_{xu} = \sigma_{4u}$ , but using Equation 9.11a together with replacement of  $\beta_x$  by  $\beta_y$ .

### 9.6.5 Effect of Corrosion

Corrosion wastage in ship plates can reduce their ultimate strength. Two types of corrosion damage are usually considered, namely, general (or uniform) corrosion and localized corrosion. General corrosion reduces the plate thickness uniformly, while localized corrosion such as pitting appears nonuniformly in selected regions such as the vessel bottom in cargo tanks of crude oil carriers.

The ultimate strength of a steel member with general corrosion can be easily predicted by excluding the plate thickness loss due to corrosion. On the other hand, it is proposed that the ultimate strength prediction of a structural member with pitting corrosion can be made using a strength-knockdown-factor approach. The following ultimate strength-knockdown factor may be relevant [30]:

$$R_r = \frac{\sigma_u}{\sigma_{uo}} = \left( \frac{A_0 - A_r}{A_0} \right)^{0.73} \quad (9.12)$$

where  $R_r$  = ultimate strength reduction factor due to pitting corrosion;  $\sigma_u$ ,  $\sigma_{uo}$  = ultimate compressive strengths for plating with and without (intact) pitting corrosion;  $A_0$  = cross-sectional area of the intact member; and  $A_r$  = largest cross-sectional area of plating lost to pitting corrosion (see Figure 9.3).

### 9.6.6 Effect of Fatigue Cracking

Under the action of repeated loading, fatigue cracks can be initiated at stress concentrations in the structure. Initial defects or cracks can also be formed in the structure by usual fabrication procedures and may conceivably remain undetected for some time. In addition to propagation under repeated cyclic

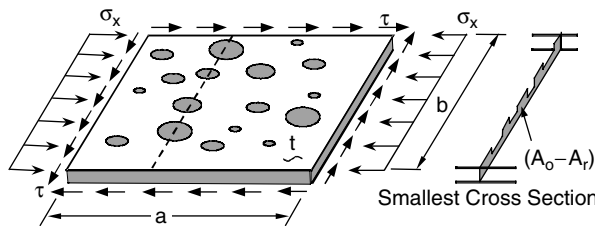


**FIGURE 9.3** A schematic for localized pitting corrosion and definition of the smallest cross-sectional area ( $A_0$  = cross-sectional area of the intact plate).

loading, cracks can also grow in an unstable way under monotonically increasing extreme loads, a circumstance that eventually can lead to catastrophic failure of the structure. This possibility is, of course, usually tempered by the ductility of the material involved and also by the presence of reduced-stress-intensity regions in a complex structure that can serve as crack arresters in an otherwise monolithic structure.

For residual strength assessment of aging steel structures under extreme loads as well as under fluctuating loads, it is thus often necessary to take into account a known or estimated crack as a parameter of influence. The ultimate strength of a structural member with fatigue cracking can be predicted, somewhat pessimistically, as follows [2]:

$$R_c = \frac{\sigma_u}{\sigma_{uo}} = \frac{A_o - A_c}{A_o} \quad (9.13)$$

where  $R_c$  = ultimate strength reduction factor due to fatigue cracking;  $\sigma_u$ ,  $\sigma_{uo}$  = ultimate tensile or compressive strengths for a cracked member or an intact (uncracked) member;  $A_o$  = cross-sectional area of the intact member; and  $A_c$  = cross-sectional area affected by fatigue cracking.

### 9.6.7 Effect of Local Denting

Plate panels in ships and offshore structures can suffer mechanical damage in many ways, depending upon where such plates are situated. At inner bottom plates of cargo holds of bulk carriers, mechanical damage can take place by indelicate loading or unloading of cargoes. Inner bottom plates can suffer mechanical damage during loading of iron ore when the iron ore strikes the plates. In unloading of bulk cargoes such as iron ore or coal, the excavators used can result in impacts to the inner bottom plates. Deck plates of offshore platforms may be subjected to impacts due to dropped objects from cranes. Such mechanical damage normally exhibits various features such as denting, cracking, residual stresses or strains due to plastic deformation, and coating damage.

In calculating ultimate hull girder strength, therefore, the effect of local denting of plating may need to be taken into account, where significant. An ultimate strength reduction factor for local denting is useful for this purpose, such as [31]

$$R_d = \frac{\sigma_u}{\sigma_{uo}} = C_3 \left[ C_1 \ln \left( \frac{D_d}{t} \right) + C_2 \right] \quad (9.14a)$$

where  $R_d$  = ultimate strength reduction factor due to local denting;  $\sigma_u$ ,  $\sigma_{uo}$  = ultimate compressive strengths of the dented member or the intact (undented) member;  $D_d$  = depth of the dent; and  $t$  = plate thickness. The coefficients  $C_1$  through  $C_3$  are empirically determined by regression analysis of computed results [31] as follows:

$$\begin{aligned} C_1 &= -0.042 \left( \frac{d_d}{b} \right)^2 - 0.105 \left( \frac{d_d}{b} \right) + 0.015 \\ C_2 &= -0.138 \left( \frac{d_d}{b} \right)^2 - 0.302 \left( \frac{d_d}{b} \right) + 1.042 \\ C_3 &= -1.44 \left( \frac{H}{b} \right)^2 + 1.74 \left( \frac{H}{b} \right) + 0.49 \end{aligned} \quad (9.14b)$$

where  $d_d$  = diameter of dent,  $b$  = plate breadth, and  $H = h$  for  $h \leq b/2$ ,  $H = b - h$  for  $h > b/2$ , and  $h$  =  $y$ -coordinate of the center of denting (Figure 9.4).

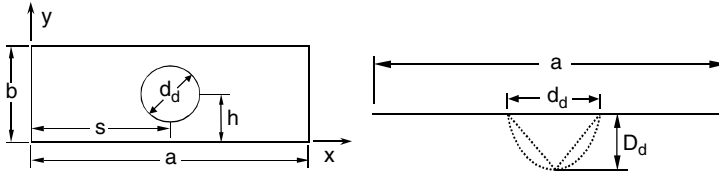


FIGURE 9.4 Geometric parameters for local denting on a plate surrounded by support members.

### 9.6.8 Effect of Combined Corrosion, Fatigue Cracking, and Local Denting

When pitting corrosion, fatigue cracking, and local denting exist simultaneously, the ultimate strength of a plate member is postulated to be given, again perhaps pessimistically (by virtue of a multiplicative model), as follows:

$$\sigma_u = R_r R_c R_d \sigma_{uo} \quad (9.15)$$

where  $R_r$ ,  $R_c$ ,  $R_d$  are as defined in Equation 9.12, Equation 9.13, and Equation 9.14, respectively.

## 9.7 Extreme Hull Girder Load Models

### 9.7.1 Still-Water Bending Moment

$M_{sw}$  in Equation 9.4 is taken as the maximum value of the still-water bending moment resulting from the worst load condition for a ship, considering both hogging and sagging. The related detailed distribution of the still-water moment along the ship's length can be calculated by double integration of the difference between weight and buoyancy, using simple beam theory.

For convenience, the mean value of  $M_{sw}$  will be taken from an empirical formula that has been suggested as a first-cut estimate of the maximum allowable still-water bending moment by some classification societies in the past. That approximate formula is given by

$$M_{sw} = \begin{cases} +0.015CL^2B(8.167 - C_b) \text{ (kNm)} & \text{for hogging} \\ -0.065CL^2B(C_b + 0.7) \text{ (kNm)} & \text{for sagging} \end{cases} \quad (9.16)$$

where

$$C = \begin{cases} 0.0792L & \text{for } L \leq 90 \\ 10.75 - \left( \frac{300 - L}{100} \right)^{1.5} & \text{for } 90 < L \leq 300 \\ 10.75 & \text{for } 300 < L \leq 350 \\ 10.75 - \left( \frac{L - 350}{150} \right)^{1.5} & \text{for } 350 < L \leq 500 \end{cases}$$

with  $L$  = ship length (m),  $B$  = ship breadth (m), and  $C_b$  = block coefficient at summer load waterline.

The COV associated with the still-water bending moment of a merchant cargo vessel is normally large, perhaps as high as 0.4 [32]. The variation in the still-water bending moment is usually assumed to follow the normal distribution.

### 9.7.2 Wave-Induced Bending Moment

For reliability assessment of newly built ships,  $M_w$  in Equation 9.4 is normally taken as the mean value of the extreme wave-induced bending moment that the ship is likely to encounter during its lifetime.

This is given for unrestricted worldwide service by IACS (International Association of Classification Societies), as follows:

$$M_w = \begin{cases} +0.19CL^2BC_b \text{ (kNm) for hogging} \\ -0.11CL^2B(C_b + 0.7) \text{ (kNm) for sagging} \end{cases} \quad (9.17)$$

where  $C$ ,  $L$ ,  $B$ ,  $C_b$  are as defined in Equation 9.16.

For the safety and reliability assessment of damaged ship structures in particular cases, short-term-based response analysis can be used to determine  $M_w$  when the ship encounters a storm of specific duration (e.g., 3 h) and with certain small encounter probability. The MIT sea-keeping tables developed by Loukakis and Chryssostomidis [33] are useful for predicting the short-term-based wave-induced bending moment of merchant cargo vessels, and these are used in our study. The MIT sea-keeping tables are designed to efficiently determine the root-mean-square value of the wave-induced bending moment given the values of significant wave height ( $H_s$ ),  $B/T$  ratio ( $B$  = ship breadth,  $T$  = ship draft),  $L/B$  ratio ( $L$  = ship length), ship operating speed ( $V$ ), the block coefficient ( $C_b$ ), and sea-state persistence time.

The most probable extreme value of the wave-induced loads,  $M_w$ , i.e., mode, which we may refer to as a mean for convenience, and its standard deviation,  $\sigma_w$ , can then be computed based on up-crossing analysis as follows [34]:

$$M_w = \left[ \sqrt{2\lambda_o \ln N} + \frac{0.5772}{\sqrt{2\lambda_o \ln N}} \right] \rho g L^4 \times 10^{-16} \text{ (GNm)} \quad (9.18a)$$

$$\sigma_w = \frac{\pi}{\sqrt{6}} \sqrt{\frac{\lambda_o}{2 \ln N}} \rho g L^4 \times 10^{-16} \text{ (GNm)} \quad (9.18b)$$

$$\text{COV} = \frac{\sigma_w}{M_w} \quad (9.18c)$$

where  $\sqrt{\lambda_o}$  is the nondimensional root-mean-square value of the short-term wave-induced bending moment process, which can be estimated using the MIT sea-keeping tables.  $N$  is the expected number of wave-bending peaks, which can be estimated as follows [34]:

$$N = \frac{S}{\sqrt{13H_s}} \times 3600 \quad (9.18d)$$

where  $H_s$  = significant wave height (m), and  $S$  = storm persistence time (h).

The USAS-L computer program, which automates the vertical bending moment calculation procedure using the MIT sea-keeping tables as well as by Equation 9.16 and Equation 9.17, can be downloaded from an Internet Web site [2]. The COV associated with the wave-induced bending moment can be defined by Equation 9.18c, on which the short-term response is based, although it is often assumed to be 0.1 when  $M_w$  is predicted from Equation 9.17.

## 9.8 Prediction of Time-Dependent Structural Damage

As a ship gets older, corrosion and fatigue cracking are expected to be the two most common types of structural degradations that will affect safety and reliability. Such strength degradations are time-dependent in nature. To make time-dependent reliability assessment possible under these circumstances, therefore, it is essential to establish time-dependent models for predicting corrosion and fatigue cracking.

This section presents some useful models for predicting the amount of corrosion and fatigue cracking, each as a function of time (ship age). While based largely on the authors' own related past work, the models presented do make use of several pertinent studies by other investigators as well. It should be noted that when time-dependent strength effects are considered, the loads used for reliability analysis in the illustrative examples presented herein are assumed to be time-independent. Also, it is assumed that local dent damage is not a function of time once it has occurred.

### 9.8.1 Time-Dependent Corrosion Wastage Models

The corrosion characteristics in a ship structure are influenced by many factors such as type of corrosion protection, type of cargo, temperature, humidity, and so on. This means that it should be possible to estimate corrosion depths for different structural members grouped by type and location for various types of ships or cargoes and other pertinent factors.

Figure 9.5 represents a plausible schematic of the proposed corrosion process model for a coated area in a marine steel structure. The corrosion behavior in this model is categorized into three phases: (a) corrosion on account of durability of coating, (b) transition to visibly obvious corrosion, and (c) progress of such corrosion [2]. The curve showing corrosion progression as indicated by the solid line in Figure 9.5 is convex, but it may in some cases be concave (dotted line). The convex curve indicates that the corrosion rate (i.e., the curve gradient) is initially relatively steep but decreases as the corrosion progresses. This type of corrosion process may be typical of a static immersion environment in seawater, because the relatively static corrosion scale at the steel surface tends to inhibit the corrosion progression. On the other hand, the concave curve represents a case where the corrosion rate is accelerating as the corrosion process proceeds. This type of corrosion progression may happen in changing immersion conditions at sea, particularly in dynamically loaded structures, where flexing continually exposes additional fresh surface to corrosion effects.

The life (or durability) of a coating will, in a specific case, correspond to the time when a predefined and measurable extent of corrosion starts after (a) the time when a newly built ship enters service, (b) the application of a coating to a previously bare surface, or (c) repair of a failed coating area in an existing structure to a good intact standard. The coating life typically depends on the type of coating system used, details of its application (e.g., surface preparation, film thickness, humidity and salt control during application, etc.), and relevant maintenance, among other factors. While the coating life to a predefined state of breakdown must essentially be a random variable, it is often treated as a constant parameter.

After the effectiveness of a coating is lost, some transition time, i.e., duration between the time of coating effectiveness loss and the time of corrosion initiation, can be considered to exist before the corrosion initiates over a large enough and measurable area. The transition time is often considered to be an exponentially distributed random variable.

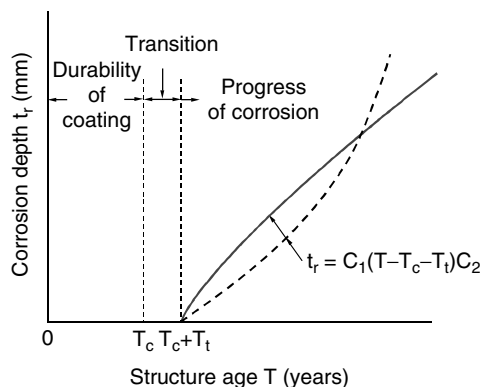


FIGURE 9.5 Schematic of a proposed corrosion process model for marine structures.



Three types of corrosion models, of perhaps increasing level of sophistication and sometimes increasing difficulty in use, have been suggested as follows:

Paik and Thayamballi [2, 35, 38, 39]:

$$t_r = C_1(T - T_c - T_t)^{C_2} \quad (9.19a)$$

$$r_r = C_1 C_2 (T - T_c - T_t)^{C_2-1} \quad (9.19b)$$

where  $t_r$  = depth of corrosion (mm);  $r_r$  = annualized corrosion rate (mm/year);  $T_c$  = coating life (year);  $T_t$  = transition time (year) between coating durability and corrosion initiation;  $T$  = structure age (year); and  $C_1, C_2$  = coefficients taking account of the characteristics of corrosion progress.

Guedes Soares and Garbatov [36]:

$$t_r = t_{r\infty} \left[ 1 - \exp\left(-\frac{T - T_c}{T_t}\right) \right] \quad (9.20a)$$

$$r_r = \frac{t_{r\infty}}{T_t} \exp\left(-\frac{T - T_c}{T_t}\right) \quad (9.20b)$$

where  $t_{r\infty}$  = depth (mm) of corrosion when the corrosion progress stops, with other terms as previously defined.

Qin and Cui [37]:

$$t_r = t_{r\infty} \left\{ 1 - \exp\left[-\left(\frac{T - T_{st}}{\eta}\right)^\alpha\right] \right\} \quad (9.21a)$$

$$r_r = t_{r\infty} \frac{\alpha}{\eta} \left(\frac{T - T_{st}}{\eta}\right)^{\alpha-1} \exp\left[-\left(\frac{T - T_{st}}{\eta}\right)^\alpha\right] \quad (9.21b)$$

where  $T_{st}$  = time (year) when accelerating of the corrosion process stops, and  $\alpha, \eta$  = coefficients to handle the corrosion decelerating, with the other terms as previously defined.

Figure 9.6A and Figure 9.6B show means and COVs of the coefficients  $C_1$  in Equation 9.19 for tanker corrosion groups (defined by location, category, and corrosion environment of member), when it is assumed that  $C_2 = 1$ ,  $T_t = 0$ , and  $T_c = 7.5$  years. Although proposed for double-hull tank vessels, the results were obtained by statistical analysis of corrosion measurement data of 230 aging single-hull tankers that carried crude oil or petroleum product oil. A total of 33,820 measurements for 34 different member groups, which comprised 14 categories of plate parts, 11 categories of stiffener webs, and 9 categories of stiffener flanges, were considered [38]. Figure 9.6A represents the most probable (average) value of the annualized corrosion rates, while Figure 9.6B gives the severe (95 percentile) values.

A similar model has also been proposed as being relevant for bulk carriers, as shown in Figure 9.7A and Figure 9.7B [39]. A total of 12,446 measurements for 23 different member groups (defined by location and category of member), which comprised 9 categories of plate parts, 7 categories of stiffener webs, and 7 categories of stiffener flanges, were obtained and made available for the statistical analysis. Figure 9.7A and Figure 9.7B show the means and COVs of the average and severe levels of the coefficient  $C_1$  for the 23 member location/category groups of a bulk carrier structure, respectively, when it is assumed that  $C_2 = 1$ ,  $T_t = 0$ , and  $T_c = 7.5$  years, except for IBP (inner bottom plating) and LSP (lower sloping plating), which may take a shorter coating life, i.e.,  $T_c = 5$  years.

With the coefficient  $C_1$  known, the corrosion depth of any structural member location in a tanker, a ship-type FPSO (floating, production, storage, and off-loading unit), or a bulk carrier can be predicted

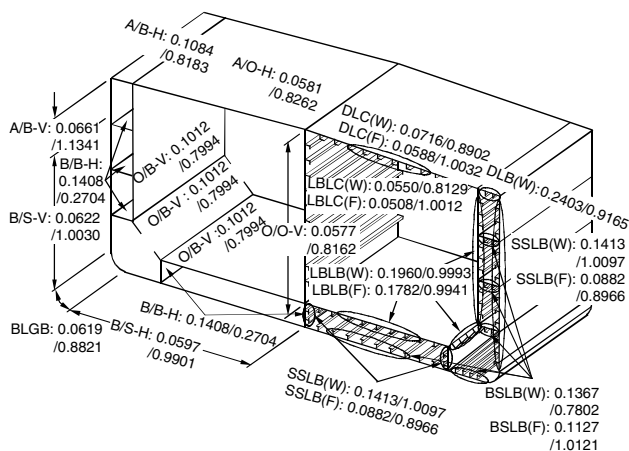


**FIGURE 9.6A** Means and COVs of the average (most probable) values of the coefficient  $C_1$  for the 34-member location/category groups, proposed for double-hull tanker or ship-shaped FPSO (floating, production, storage, and off-loading unit) structure. (From Paik, J.K. et al., *Marine Technol.*, 40 (3), 201–217, 2003. With permission.)

from Equation 9.19 as a function of ship age, assuming that  $C_2 = 1$ ,  $T_t = 0$ , and  $T_c = 7.5$  or 5 years, as specified.

## 9.8.2 Time-Dependent Fatigue Crack Model

Fatigue cracking is a primary source of costly repair work for aging ships. Crack damage is typically found in welded joints and in local areas of stress concentrations, e.g., in hull sides at the weld intersections of longitudinals, frames, and girders. Much of this is, of course, attributable to initial defects that can be formed in the structure by fabrication procedures and that conceivably remain undetected over time. Under cyclic loading or even large monotonic loading, cracking can originate and propagate from such defects and become larger with time.

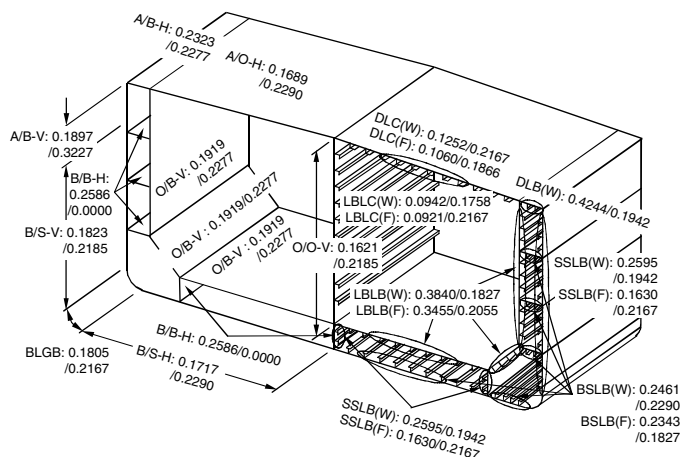


**FIGURE 9.6B** Means and COVs of the upper bound (severe) values of the coefficient  $C_1$  for the 34-member location/category groups, proposed for double-hull tanker or ship-shaped FPSO (floating, production, storage, and off-loading unit) structure. (From Paik, J.K. et al., *Marine Technol.*, 40 (3), 201–217, 2003. With permission.)

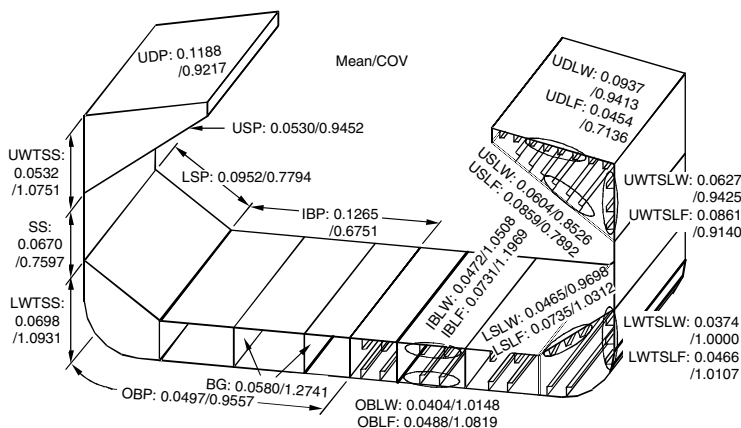


**FIGURE 9.7A** Means and COVs of the average levels of the coefficient  $C_1$  for the 23-member location/category groups of a bulk carrier structure. (From Paik, J.K. et al., *Int. J. Maritime Eng.*, 145 (A2) 61–87, 2003. With permission.)

Since cracks can conceivably lead eventually to catastrophic failure of the structure, it is essential to properly consider and establish relevant crack-tolerant design procedures for ship structures, in addition to implementation of appropriate close-up survey strategies and maintenance philosophies. For design-stage reliability assessment of an eventually aging ship structure under extreme loads, it is often necessary to include a known (existing or postulated or anticipated) crack as a parameter of influence in the ultimate limit-state analysis. To make this possible, it is necessary to develop a relatively simple time-variant fatigue-crack model that can predict crack damage in location and size as the ship gets older.

Figure 9.8 shows a schematic of fatigue-cracking progress as a function of time (age) in steel structures. The fatigue-cracking progress can be separated into three stages, namely the crack initiation stage (stage I), the crack propagation stage (stage II), and the failure (fracture) stage (stage III).

It is assumed in the model shown that no initial defects exist so that there is no cracking damage until the time  $T_f$ . While the fatigue damage is affected by many factors, for a given structural location, service profile, and other characteristics, the local stress concentration effects and the number of stress range cycles leading to detectable initiation of cracking can be evaluated by fatigue analysis. Fatigue analyses typically use small-specimen laboratory data in which the crack size at what we here call initiation is

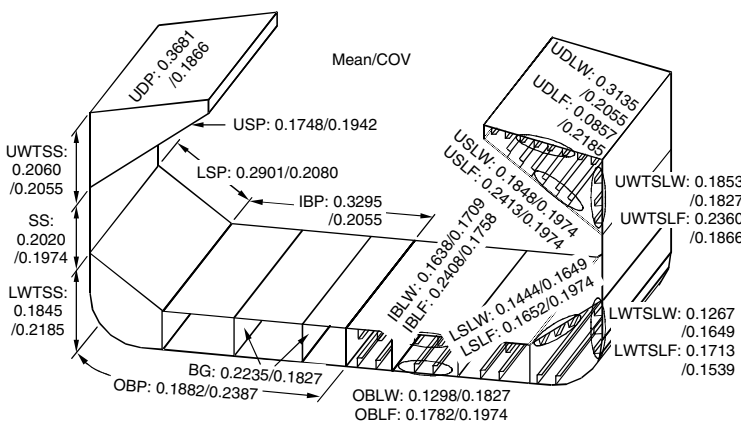


**FIGURE 9.7B** Means and COVs of the severe levels of the coefficient  $C_1$  for the 23-member location/category groups of a bulk carrier structure. (From Paik, J.K. et al., *Int. J. Maritime Eng.*, 145 (A2) 61–87, 2003. With permission.)

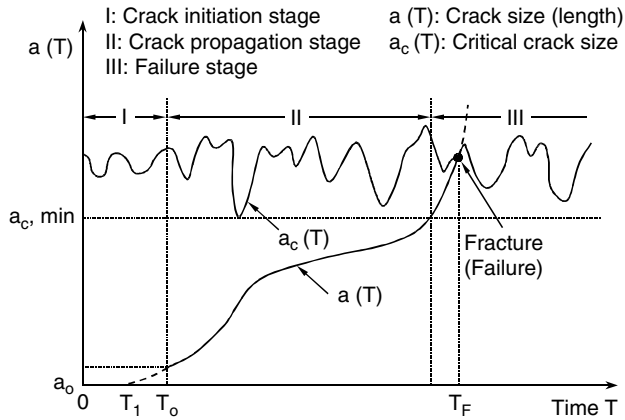


FIGURE 9.8 Schematic for crack initiation and growth in a steel structure with time.

typically not controlled or measured. On the other hand, when any crack is detected in an existing structure at time  $T_0$  during an inspection or survey process, it is normally of a size (length), denoted by  $a_0$  and called the initial crack size, that must be detectable.

For various reasons, there is the potential for mismatch between what the analysis predicts as “life to initiation” and the cracks that may be detected at the earliest survey in a real structure. For the assessment of time-dependent risks of a structure in the present illustrative examples, however, it is assumed that the initial crack size is small, say 1.0 mm. It should be noted that cracks of such a small size may not normally be detectable on structures in service using the predominantly visual inspection methods that are currently deployed.

Fatigue cracking will propagate with time. Crack propagation is mostly progressive in ductile materials but will be unstable in brittle materials. Crack propagation is in fact affected by many parameters, such as initial crack size, history of local nominal stresses, load sequence, crack retardation, crack closure, crack growth threshold, and stress intensity range, in addition to the stress intensity factor at the crack tip, which depends on material properties and geometry. Further, in seawater exposure situations, even the loading frequency and the form of loading may affect crack growth. The fracture-mechanics approach is often used to analyze the behavior of crack propagation, but usually in much simpler terms than reality.

As illustrated in Figure 9.8, the crack growth process with time can be categorized into three stages, namely crack initiation, propagation, and failure. In this regard, for purposes of predicting the effects of such a process on the structural capacity, the time-dependent cracking damage model can also be composed of three separate stage models as follows:

1. A model for crack initiation assessment and detected cracks
2. A model for crack growth assessment
3. A model for failure assessment

When a structure is designed, the crack initiation life at critical structural details is usually theoretically assessed using the S-N curve approach ( $S$  = fluctuating stress range,  $N$  = associated number of stress range cycles). In this approach, the so-called Palmgren-Miner cumulative damage rule can be applied together with the relevant S-N curve. This normally follows three steps, namely, (a) define the histogram of cyclic stress ranges, (b) select the relevant S-N curve, and (c) calculate the cumulative fatigue damage and judge whether the time to initiation of crack meets the required target fatigue-life value. In a reliability analysis involving this same phenomenon, the relevant design variables including the S-N parameters must be characterized by their probability distributions, including mean, COV, and form (type of distribution).

For an existing structure, cracking at critical joints and details is detected, and their size (length) denoted by  $a_0$  can be measured. Typically, the crack size that can be detected visually needs to be larger

than a certain amount, say 15 to 30 mm, or sometimes more. When the integrity of existing aged-ship structures is considered, it is assumed that the crack of length  $a_0$  at a critical joint or detail has initiated at a known ship age of  $T_0$  years.

The crack growth can in general be assessed by the fracture-mechanics approach. This considers one or more postulated cracks in the structure, and predicts the fatigue damage during the process of crack propagation, including any coalescence and through-thickness cracking propagation of a through-thickness crack, and subsequent failure. In this approach, a major task is to preestablish the relevant crack growth equations or 'laws' as a function of time (year).

Two types of fracture mechanics approaches can be considered, namely, physical and empirical models. In the physical model, which will be used in the present illustrative examples, the crack growth rate is expressed as a function of the stress intensity factor at the crack tip, under the assumption that the yielded area around the crack tip is relatively small. The so-called Paris-Erdogan law is often used for this purpose and is expressed as follows:

$$\frac{da}{dN} = C(\Delta K)^m \quad (9.22)$$

where the left-hand side of the equation represents the incremental growth per cycle of a crack of length  $a$ ;  $\Delta K$  = stress intensity factor range at the crack tip; and  $C$ ,  $m$  = material constants to be determined from tests.

For steel structures with typical types of cracks, stress-intensity-factor formulas can be found in the literature [2, 40]. In ship stiffened panels, cracks are observed along the weld intersections between plating and stiffeners. For a plate with a crack,  $\Delta K$  can be represented over a small enough period of time by

$$\Delta K = F\Delta\sigma\sqrt{\pi a} \quad (9.23)$$

where  $\Delta\sigma$  = stress range (or double amplitude of applied fatigue stress), and  $F$  is a geometric parameter depending on the loading type and configuration of the cracked body. For plates with typical types of cracks and under axial tension, as shown in Figure 9.9,  $F$  is approximately given as follows [2]:

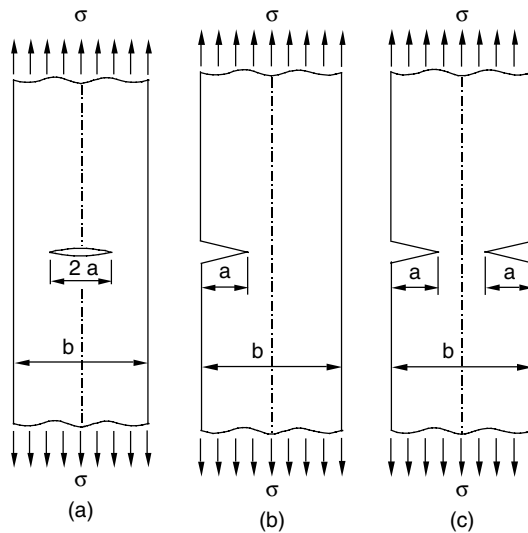


**FIGURE 9.9** Typical crack locations in a plate under tensile stress: (a) center crack, (b) crack to one side, (c) crack to both sides.

For a center crack as shown in Figure 9.9a:

$$F = \left( \sec \frac{\pi a}{b} \right)^{1/2} \quad (9.24a)$$

For a crack on one side as shown in Figure 9.9b:

$$F = 30.38 \left( \frac{a}{b} \right)^4 - 21.71 \left( \frac{a}{b} \right)^3 + 10.55 \left( \frac{a}{b} \right)^2 - 0.23 \left( \frac{a}{b} \right) + 1.12 \quad (9.24b)$$

For cracks on both sides as shown in Figure 9.9c:

$$F = 15.44 \left( \frac{a}{b} \right)^3 - 4.78 \left( \frac{a}{b} \right)^2 + 0.43 \left( \frac{a}{b} \right) + 1.12 \quad (9.24c)$$

It should be noted that the above simplified situations use idealized boundary conditions. The effect of stiffening is also neglected. There are other, more-refined stress-intensity-factor solutions and methods of calculating improved stress intensity factors in particular situations, e.g., by FEA or the Green's function technique [40].

The crack length,  $a(T)$ , as a function of time,  $T$ , can then be calculated by integrating Equation 9.22 with respect to stress range cycles,  $N$ . In the integration of Equation 9.22, it is sometimes assumed that the geometric parameter,  $F$ , is constant, i.e., assuming that the geometric parameter,  $F$ , is unchanged as the crack propagates. Note, however, that this assumption is only reasonable as long as the initial crack size,  $a_o$ , is small. In such a case, the integration of Equation 9.22 after substitution of Equation 9.23 results in

$$a(T) = \begin{cases} \left[ a_o^{1-m/2} + \left( 1 - \frac{m}{2} \right) C(\Delta\sigma F \sqrt{\pi})^m (T - T_o) \omega \right]^{\frac{1}{1-m/2}} & \text{for } m \neq 2 \\ a_o \exp \left[ C \Delta\sigma^2 F^2 \pi (T - T_o) \omega \right] & \text{for } m = 2 \end{cases} \quad (9.25)$$

where  $\omega$  = number of cycles per year. It is often considered in ships that a wave load cycle occurs (very approximately) once in every 6 to 10 sec, and hence  $N \approx (T - T_o) \times 365 \times 24 \times 60 \times 60/10 = \omega \times (T - T_o)$ , so  $\omega \approx 365 \times 24 \times 60 \times 60/10$ , where  $T$  = ship age in years, already defined above.

Figure 9.10 shows a sample application of Equation 9.25 and compares its results with results from a direct integration of Equation 9.22, which accounts correctly for the effect of crack growth on the geometric parameter,  $F$ . It is seen from Figure 9.10 that Equation 9.25 slightly overestimates the fracture life as the crack propagates, as would be expected because Equation 9.25 was derived under the assumption that the geometric parameter,  $F$ , remains constant over time. Notwithstanding, it is seen in this case that the difference for a small initial crack size is not significant, so Equation 9.25 apparently provides a reasonable tool for crack growth assessment.

In reliability analysis involving this same phenomenon, the relevant design variables, including the crack growth rate equation parameters, must be characterized by their probability distributions, including mean, COV, and form (type of distribution).

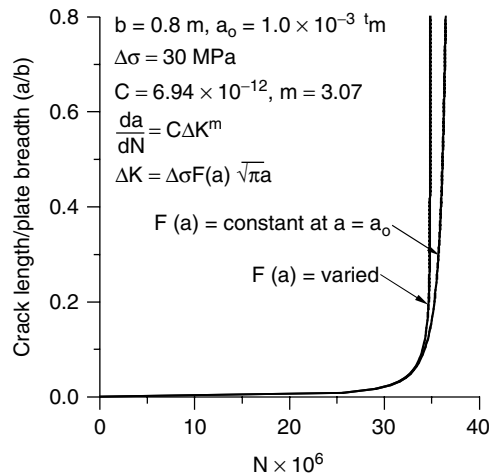


**FIGURE 9.10** A comparison of Equation 9.25 with a direct (numerical) integration of Equation 9.23 for a small initial crack size.

## 9.9 Application to Time-Dependent Reliability Assessment of Ships

The methodology of reliability assessment of ships described above was automated within the GUI-based computer program TRAAS (time-dependent reliability assessment of aging ships). The following subsections describe application examples of the time-dependent reliability assessment of three types of hull girders: a 105,000-dwt double-hull tanker, a 170,000-dwt bulk carrier, and a 113,000-dwt ship-shaped FPSO (floating, production, storage, and off-loading unit). The effects of age-related structural degradation (corrosion and fatigue cracking) and local denting are included. The purpose is to illustrate some of the previously discussed concepts. In the present application examples, only the primary failure mode among the four hull-girder failure modes previously described is considered. Figure 9.11A through Figure 9.11C show schematic representations of the mid-ship sections of the three ships considered. Table 9.2 indicates the principal dimensions of the ships.

### 9.9.1 Scenarios for Operational Conditions and Sea States

It is important to realize that hull girder loads depend on the operational conditions, vessel speed, vessel heading, and the sea states. Hence seamanship is a strong factor affecting hull girder loads in particular

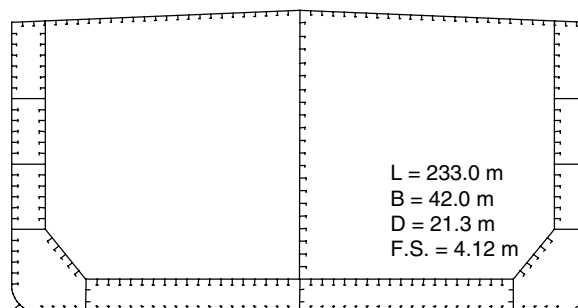


**FIGURE 9.11A** Mid-ship section of a hypothetical 105,000-dwt double-hull tanker with one center-longitudinal bulkhead (L = ship length, B = ship beam, D = ship depth, F.S. = frame spacing).

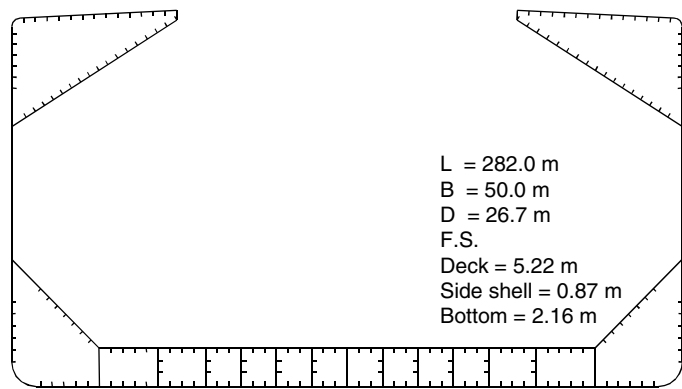


**FIGURE 9.11B** Mid-ship section of a 170,000-dwt single-sided bulk carrier (L = ship length, B = ship beam, D = ship depth, F.S. = frame spacing).

situations. In this regard, it is necessary to correctly establish relevant scenarios for operational conditions and sea states in predicting hull girder bending moments.

The still-water bending moments,  $M_{sw}$ , of the ships in this example are estimated from the empirical formula given as Equation 9.16. This, in a short-term sense, assumes that the vessels are loaded in the most onerous permitted still-water condition. Where long-term reliability analysis is planned, such as in a design context, the entire range of still-water bending moments possible and the effects of different types of hull behavior (hogging, sagging) must be correctly accounted for.

For the present illustrative purposes, on the other hand, the wave-induced bending moment,  $M_w$ , is predicted from Equation 9.18a using the short-term response analysis, which involves the operational conditions and sea states defined in Table 9.3. It is noted that for wave-load prediction purposes, the ship-shaped FPSO is assumed to have an equivalent operational speed of 10 knots in waves, while it usually remains at a specific location once installed.

The present scenarios associated with the operational conditions and sea states are adopted for illustrative purposes. The results of such reliability analyses are then indicative, i.e., only notional probabilities of failure, conditional on the specific storm condition noted above, and conditional on the vessel being loaded in that storm in the very onerous way, as also noted.

Figure 9.12A through Figure 9.12C show the variations of wave-induced bending moments as a function of significant wave height. Table 9.4 compares the wave-induced bending moments for the three

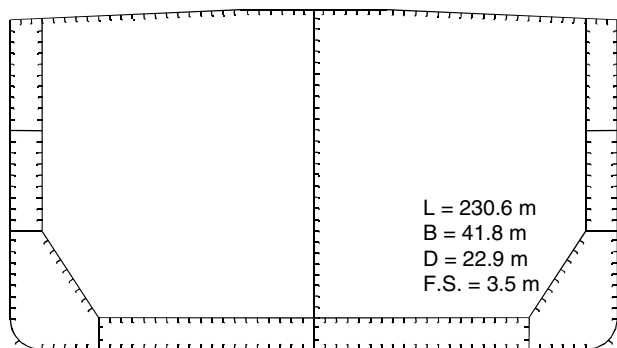


**FIGURE 9.11C** Mid-ship section of a 113,000-dwt ship-shaped FPSO (floating, production, storage, and offloading unit) (L = ship length, B = ship beam, D = ship depth, F.S. = frame spacing).



**TABLE 9.2** Hull Sectional Properties for the Three Example Vessels

Item		Double-Hull Tanker	Bulk Carrier	FPSO
LBP, $L$ (m)		233.0	282.0	230.6
Breadth, $B$ (m)		42.0	50.0	41.8
Depth, $D$ (m)		21.3	26.7	22.9
Draft, $d$ (m)		12.2	19.3	14.15
Block coefficient, $C_b$		0.833	0.826	0.831
Design speed (knots)		16.25	15.15	15.4
DWT or TEU (dwt)		105,000	170,000	113,000
Cross-sectional area ( $m^2$ )		5.318	5.652	4.884
Height to neutral axis from baseline (m)		9.188	11.188	10.219
$I$ ( $m^4$ )	vertical	359.480	694.307	393.625
	horizontal	1,152.515	1,787.590	1,038.705
$Z$ ( $m^3$ )	deck	29.679	44.354	31.040
	bottom	39.126	62.058	38.520
$\sigma_y$	deck	HT32	HT40	HT32
	bottom	HT32	HT32	HT32
$M_p$ (GNm)	vertical moment	11.930	20.650	12.451
	horizontal moment	19.138	31.867	19.030

Note: FPSO = floating, production, storage, and offloading system;  $I$  = moment of inertia;  $Z$  = section modulus;  $\sigma_y$  = yield stress;  $M_p$  = fully plastic bending moment; HT32 = high-tensile steel with  $\sigma_y = 32$  kgf/mm<sup>2</sup>; HT40 = high-tensile steel with  $\sigma_y = 40$  kgf/mm<sup>2</sup>; LBP = length between perpendiculars; TEU = twenty-foot equivalent unit.

**TABLE 9.3** Scenarios for Operating Conditions and Sea States of the Three Example Vessels

Parameter	Double-Hull Tanker	Bulk Carrier	FPSO
Operating speed	$0.6 \times \text{design speed} = 9.75$ knots	$0.6 \times \text{design speed} = 9.09$ knots	10 knots <sup>a</sup>
Significant wave height, $H_s$	$1.1\sqrt{L}$ , $L$ in ft = 9.27 m	$1.1\sqrt{L}$ , $L$ in ft = 10.198 m	$1.1\sqrt{L}$ , $L$ in ft = 9.222 m
Storm duration <sup>b</sup>	3 h ( $N \approx 1000$ )	3 h ( $N \approx 1000$ )	3 h ( $N \approx 1000$ )

<sup>a</sup> This is meant as an equivalent design speed, because an FPSO does not have an operating speed as such.

<sup>b</sup>  $N$  = number of wave peaks.

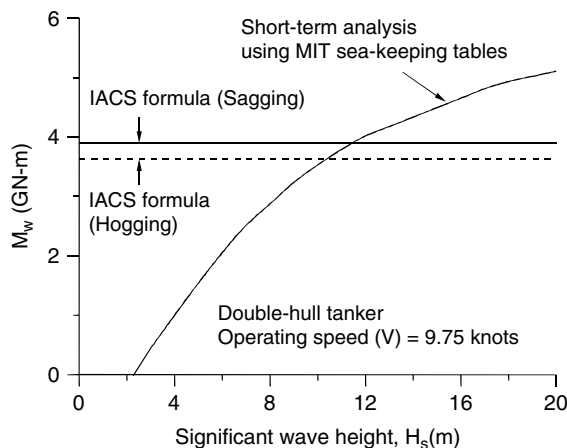


**FIGURE 9.12A** Variation of the wave-induced bending moment as a function of significant wave height for the 105,000-dwt double-hull tanker.

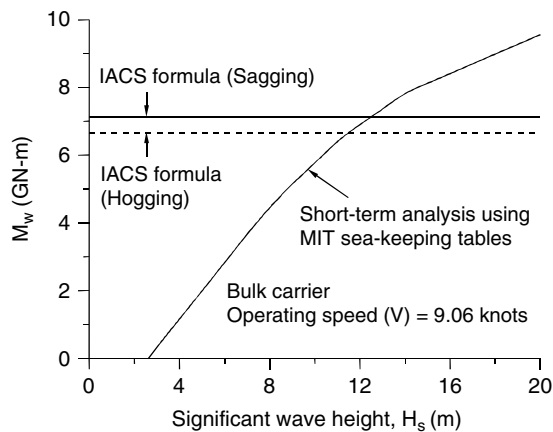


**FIGURE 9.12B** Variation of the wave-induced bending moment as a function of significant wave height for the 170,000-dwt bulk carrier.

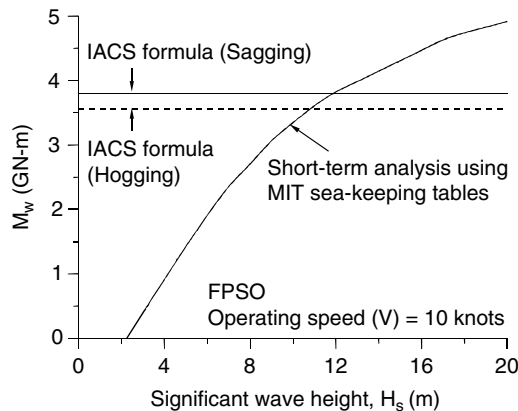


**FIGURE 9.12C** Variation of the wave-induced bending moment as a function of significant wave height for the 113,000-dwt ship-shaped FPSO.

ships computed by the IACS formula (Equation 9.17) with those computed by Equation 9.18a using the MIT sea-keeping tables. These tables are based on the short-term response during a storm persistence time of 3 h for a particular sea state, as noted above. While the IACS formula is independent of the operational conditions and sea states, it is seen from Table 9.4 that the IACS formula values are larger than the short-term-based calculations by 8 to 20% for the present specific scenarios. With different scenarios of operational conditions and sea states, the opposing trend can appear as well.

**TABLE 9.4** Wave-Induced Bending Moments,  $M_w$ , for the Three Example Vessels (GN · m)

$M_w$ (GN-m)	Double-Hull Tanker		Bulk Carrier		FPSO	
	Sagging	Hogging	Sagging	Hogging	Sagging	Hogging
IACS formula <sup>a</sup>	-3.895	3.634	-7.121	6.655	-3.805	3.564
MIT sea-keeping tables <sup>b</sup>	-3.352	3.352	-5.927	5.927	-3.172	3.172

<sup>a</sup> Based on a long-term analysis.

<sup>b</sup> Based on a short-term analysis.

## 9.9.2 Scenarios for Structural Damage

Age-related structural degradation and its effects need to be dealt with as a function of a ship's age, while mechanical damage can be considered to be time invariant. The results obtained from the present approach can be sensitive to the underlying assumptions. Specifically, the vessel is considered to be under the most onerous still-water condition and subject to the conditions of a given, reasonably severe, short-term storm; the vessel may be of varying age and subject to certain generic patterns of corrosion and certain idealized crack scenarios, as will be soon described below.

### 9.9.2.1 Corrosion Damage

In Section 9.8.1, corrosion wastage models for different structural member groups by type and location, considering plating, and stiffener webs and flanges, were presented. These models can be used to predict the corrosion depth in primary members as the ship ages. As previously noted, the corrosion-progress characteristics of a tanker structure are considered to be similar to those of a ship-shaped FPSO structure as long as the corrosion environment is similar.

In the present reliability assessment, a most probable (average) level of corrosion wastage is considered. While it is assumed that corrosion starts immediately after the breakdown of coating, the coating life of all structural members in the three ships considered is assumed to be 7.5 years, except for the inner bottom plating and the lower sloping plating of the bulk carrier, with coating lives of 5 years. Figure 9.13A and Figure 9.13B show the progress of corrosion depth for selected members as the vessels age. The figures neglect any effect of steel renewal after inspections and surveys; some consideration of repair of heavily corroded members is made in later illustrations.

As noted earlier, several types of corrosion are possible for mild- and low-alloy steels used in marine applications. While the so-called general (or uniform) corrosion, which reduces the member thickness over large areas, is normally regarded as an idealized type of corrosion in today's ships, localized corrosion such as pitting is more likely to be observed in ship structures. As discussed in Section 9.6.5, the ultimate strength behavior of ship structures with pitting corrosion is different from that of general corrosion. For more realistic assessment of the reliability, therefore, it is important to take into account pitting as well as general corrosion.

In the present reliability assessment, it is assumed that the most heavily pitted cross section of any structural member extends over the plate breadth. This may provide a somewhat pessimistic evaluation of residual strength, but it is a practical approach for the reliability assessment. The mean and COV

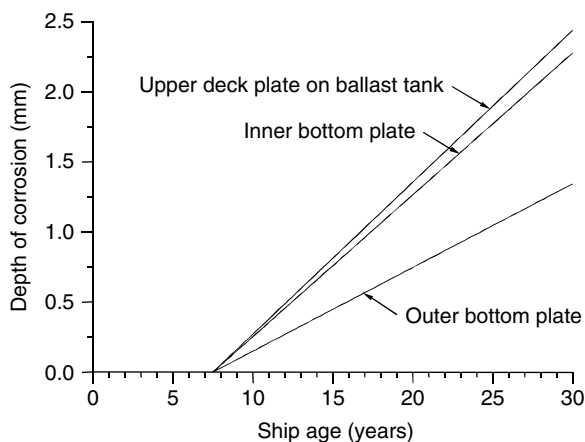


**FIGURE 9.13A** Progress of corrosion depth for selected members in the 105,000-dwt double-hull tanker and the 113,000-dwt FPSO.

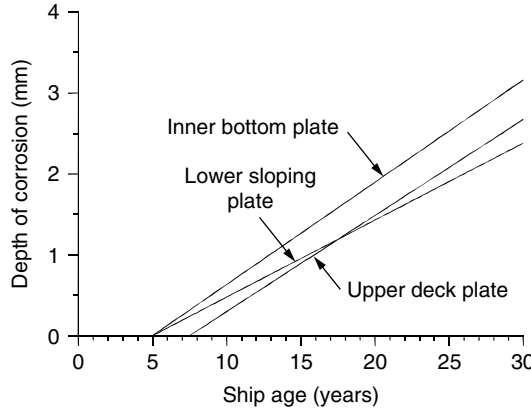


**FIGURE 9.13B** Progress of corrosion depth for selected members in the 170,000-dwt bulk carrier.

values of annualized corrosion rates for individual structural members are defined in Figure 9.6A, Figure 9.6B, Figure 9.7A, and Figure 9.7B. It should further be noted that, in reality, pits will be repaired once they reach certain depths and extents, regardless of the related strength criteria, and this is not accounted for in the present illustrative calculations.

### 9.9.2.2 Fatigue Cracking

In Section 9.8.2, a time-dependent fatigue cracking model was established. The crack length of any critical area is predicted by a closed-form formula as a function of ship age. In the present application examples, it is assumed that cracking initiates in all stiffeners and plating when the ship is 5 years of age. The initial crack size is considered to be 1.0 mm. These are simply assumptions for illustrative purposes, as previously discussed. Cracks normally start as surface cracks and then progress through the thickness of the plating. They certainly do not simultaneously occur at all stiffeners and plating. Also, it has been assumed that the structure had been designed based on the fatigue limit state using crack initiation technology to start with, and that they start at a specific time (namely 5 years in this case). While the constants of the Paris-Erdogan equation can usually be considered the same at all joints, the crack growth characteristics can be different because the stress ranges affecting the stress intensity factors at individual joints vary for reasons of geometry, location of crack, and any differences in load effects that may apply.

Fatigue loading characteristics are random in nature, and their sequence is normally unknown, while the long-term distribution of the fatigue loading is at most known. Therefore, some refined methodologies are used to generate a random loading sequence. With fatigue loading sequence and amplitude known, the dynamic stress range,  $\Delta\sigma_i$ , at the  $i$ th joint can then be given by

$$\Delta\sigma_i = 2 \times \sigma_{xi} \times SCF_i \times k_f = 2 \times \sigma_{xi}^* \times SCF_i \quad (9.26)$$

where  $\sigma_{xi}$  = cyclic ‘peak’ stress amplitude acting on the  $i$ th structural element, which can be given by  $M_w z / I$ ;  $M_w$  = wave-induced bending moment;  $I$  = time-dependent moment of inertia;  $z$  = distance from the time-dependent neutral axis to the point of stress calculation; and  $\sigma_{xi}^* = k_f \times \sigma_x$ .  $SCF_i$  in Equation 9.26 is the stress concentration factor at the  $i$ th critical joint. In the present illustrative examples, it is assumed that the  $SCF$  at all joints between plating and stiffeners (or support members) is 2.1, except for hold-frame connections to upper or lower wing tanks and the side shell of bulk carrier, where the  $SCF$  is 3.75, and hopper knuckle joints, where the  $SCF$  is much larger at 10.5. Note that more-refined calculations can be conducted to determine the  $SCF$  values for different joints. The  $SCF$  values used here are simply illustrative assumptions based on related proposals by some classification societies, e.g., Det Norske Veritas [41]. The variable  $k_f$  is a

**TABLE 9.5** Samples of the Probabilistic Characteristics for Random Variables at a Given Age of the Vessels

Parameter	Definition	Distribution Function	Mean	COV
$E$	elastic modulus	normal	205.8 GPa	0.03
$\sigma_y$	yield stress	lognormal	as for each member	0.10
$t_p$	thickness of plating	fixed	as for each member	—
$t_w$	thickness of stiffener web	fixed	as for each member	—
$t_f$	thickness of stiffener flange	fixed	as for each member	—
$T$	ship age	fixed	as for each age	—
$T_c$	coating life	normal	5.0 years	0.40
			7.5 years	0.40
$C_1$	corrosion rate	Weibull	as for each member	as for each member
$a_o$	initial crack size	normal	1.0 mm	0.20
$C$	$\frac{da}{dN} = C(\Delta K)^m$	lognormal	6.94E-12	0.20
$m$	$\frac{da}{dN} = C(\Delta K)^m$	fixed	3.07	—
$d_d$	diameter of local dent	normal	0.3 $b$	0.10
			0.5 $b$	0.10
			0.8 $b$	0.10
$D_d$	depth of local dent	normal	1.0 $t_p$	0.10
			2.5 $t_p$	0.10
			5.0 $t_p$	0.10

Note:  $a$  = crack size,  $b$  = plate breadth,  $N$  = number of stress cycles,  $\Delta K$  = stress intensity factor.

knockdown factor accounting for the dynamic stress cycles and is assumed to be 0.25 for the present illustrative purposes.

At a given age of the vessels, the ultimate strength of structural members with known (or assumed) fatigue cracking damage can be predicted by the strength-knockdown-factor approach, as previously noted, while it is considered that fracture takes place if the crack size (length) of the member reaches the critical crack size, which can be assumed to be the smaller of the plate breadth and the stiffener web height.

Table 9.5 indicates example probabilistic characteristics (mean, COV, distribution) of the random variables used for the present illustrative purposes. It is important to realize that the probabilistic characteristics of random variables will normally be different for different types of ship structures, operating scenarios, and applications.

### 9.9.2.3 Local Denting

Inner bottom plates of bulk carriers usually have local dent damage caused by mishandled loading and unloading of dense cargo such as iron ore, while other types of merchant ships such as tankers or FPSOs may not suffer such mechanical damage at the same or similar locations or of the same severity.

In this regard, it is assumed that inner bottom plating of only the bulk carrier has local dent damage after 5 years. The size of a local dent is assumed to be the same for all inner bottom plating, namely,  $D_d/t = 2.5$ ,  $d_d/b = 0.5$ , and  $h/b = 0.5$ , with the parameters as defined in Equation 9.14. The ultimate strength of plating with local dent damage is then predicted by the simplified formulas previously presented. The COVs associated with the local dent-related parameters are assumed as defined in Table 9.5.

### 9.9.3 Reliability Assessment

The ship hull ultimate strength formula is eventually expressed as a function of design parameters related to all relevant geometric and material properties. When time-variant structural degradation

(e.g., corrosion, fatigue cracking) and local denting areas are considered, the value of member thickness at any particular time is a function of such damage. Thus we have

$$M_{us} = M_{us}(E_i, \sigma_{Yi}, t_{pi}, t_{wi}, t_{fi}, T, T_{ci}, C_{li}, a_{oi}, C_i, m_i, D_{di}, d_{di}) \quad (9.27a)$$

$$M_{uh} = M_{uh}(E_i, \sigma_{Yi}, t_{pi}, t_{wi}, t_{fi}, T, T_{ci}, C_{li}, a_{oi}, C_i, m_i, D_{di}, d_{di}) \quad (9.27b)$$

where  $t_p$  = thickness of plating,  $t_w$  = thickness of stiffener web,  $t_f$  = thickness of stiffener flange,  $T$  = ship age,  $C_l$  = corrosion rate, and the other variables are as previously defined. The subscript  $i$  represents the  $i$ th member, and  $M_{us}$ ,  $M_{uh}$  = ultimate hull girder moments in sagging or hogging.

In a reliability assessment, all the parameters noted in Equation 9.27 are treated as random variables, with the probabilistic characteristics (i.e., mean, COV, and distribution function) as defined in Table 9.5. The structural-damage scenarios are divided into the following five groups:

1. Intact (undamaged)
2. Localized corrosion damage alone
3. Localized corrosion and local dent damage
4. Localized corrosion and fatigue cracking damage
5. Localized corrosion, fatigue cracking, and local dent damage

Local dent damage is considered only for the bulk carrier in hogging. Figure 9.14A through Figure 9.14D, Figure 9.15A through Figure 9.15D, and Figure 9.16A through Figure 9.16D show the effects of the above damage scenarios on the time-dependent characteristics of ultimate hull girder strength and reliability of the three object vessels when no repairs or renewals are made. As the vessels age, the corrosion depth and cracking size (length) increase, and thus the ultimate hull girder strength and reliability index decrease (or failure probabilities increase).

The reliability indices for the three vessels against hull girder collapse in the intact condition are about 2.5, which may be considered adequate in light of the target value previously noted for merchant cargo vessels. At the age of around 15 years, the safety and reliability of the three vessels reduce to less than 90% of the original (as-built) states. If repair and maintenance are not properly carried out, the levels of reliability can decrease rapidly.

### 9.9.4 Some Considerations Regarding Repair Strategies

To maintain the ship's safety and reliability at a certain target level or higher, a proper, cost-effective scheme for repair and maintenance must be established. In this regard, some considerations for repair strategies of structural members postulated to be heavily damaged by corrosion, fatigue cracking, and

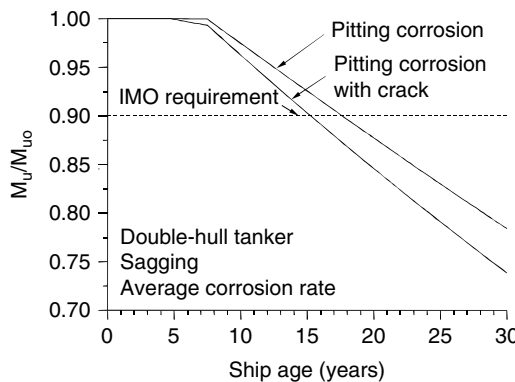


FIGURE 9.14A Time-dependent ultimate hull girder strength of the 105,000-dwt double-hull tanker in sagging.

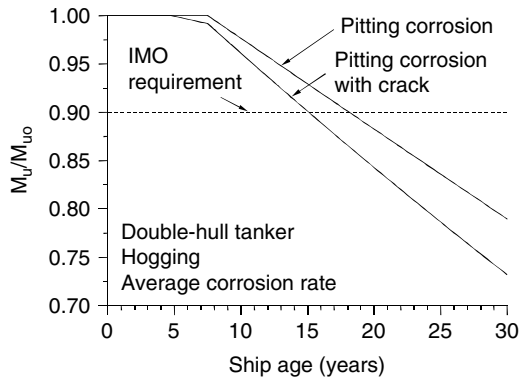


FIGURE 9.14B Time-dependent ultimate hull girder strength of the 105,000-dwt double-hull tanker in hogging.

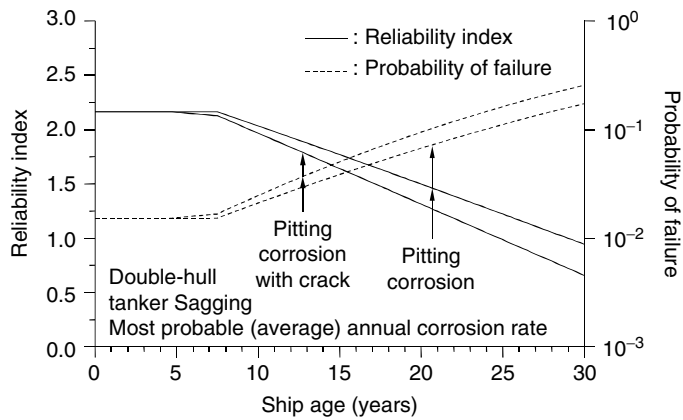


FIGURE 9.14C Time-dependent reliability of the 105,000-dwt double-hull tanker associated with hull girder collapse in sagging.

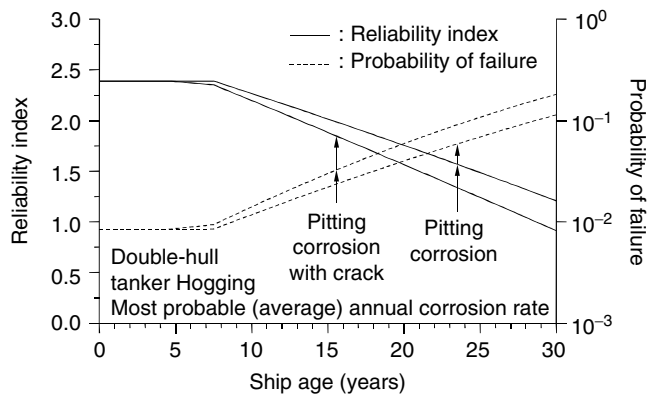


FIGURE 9.14D Time-dependent reliability of the 105,000-dwt double-hull tanker associated with hull girder collapse in hogging.

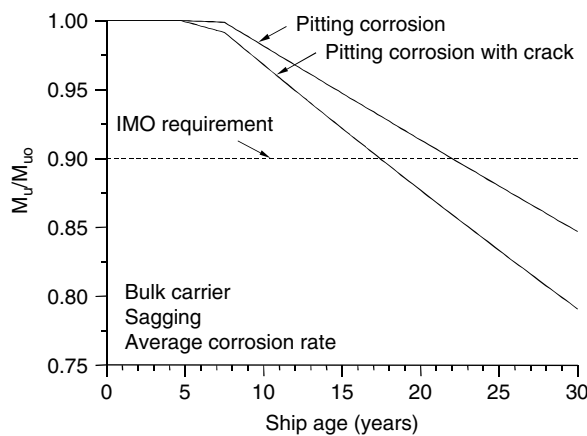


FIGURE 9.15A Time-dependent ultimate hull girder strength of the 170,000-dwt bulk carrier in sagging.

local denting are now illustrated. The International Maritime Organization (IMO) [42] requires that one should keep the longitudinal strength of an aging ship at the level of at least 90% of the initial state. While the IMO requirement is in fact based on the ship's section modulus, in the present illustrative examples it is extended as a device for establishing a more sophisticated maintenance and repair scheme based on hull girder ultimate strength. The aim of the illustrated scheme is that the ultimate hull girder strength of an aging ship must always be at least 90% of the initial, as-built vessel value.

Figure 9.17A through Figure 9.17D, Figure 9.18A through Figure 9.18D, and Figure 9.19A through Figure 9.19D show the time-dependent hull girder ultimate strength and reliability values for the object vessels after repair of postulated heavily damaged structural members so that the ultimate hull girder strength is always at least 90% of its original value. In these illustrations, the renewal criterion for any damaged member is based on the member's ultimate strength rather than member thickness, as is traditionally done. This is advantageous because the latter cannot reveal the effects of pitting corrosion, fatigue cracking, or local dent damage adequately, even though it may handle the thickness-reduction effects of uniform corrosion reasonably well. On the other hand, the former

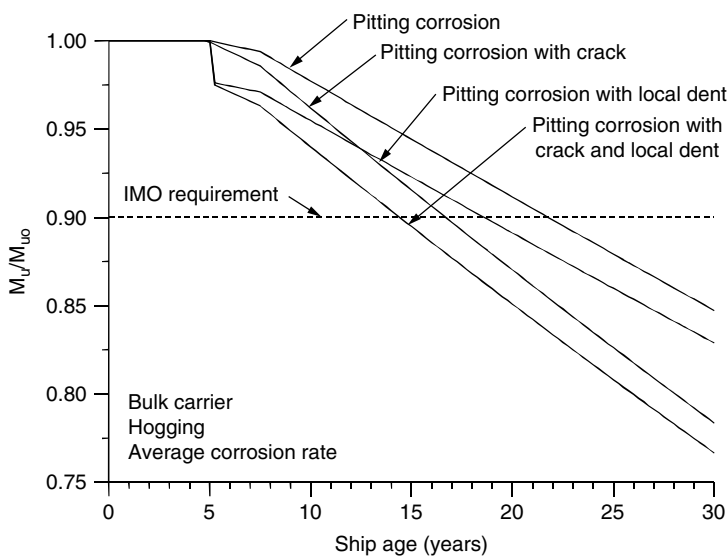


FIGURE 9.15B Time-dependent ultimate hull girder strength of the 170,000-dwt bulk carrier in hogging.



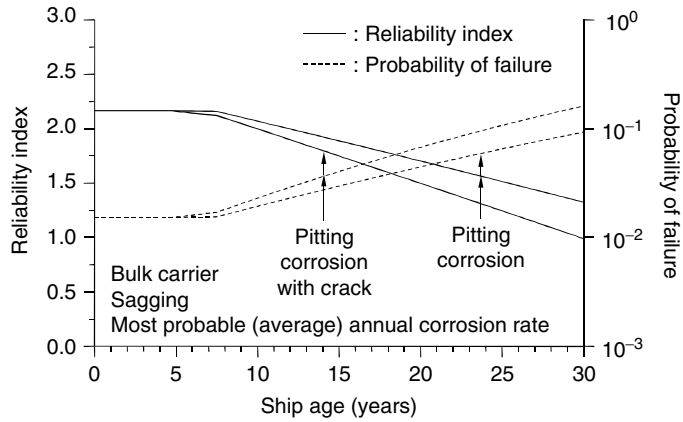


FIGURE 9.15C Time-dependent reliability of the 170,000-dwt bulk carrier associated with hull girder collapse in sagging.

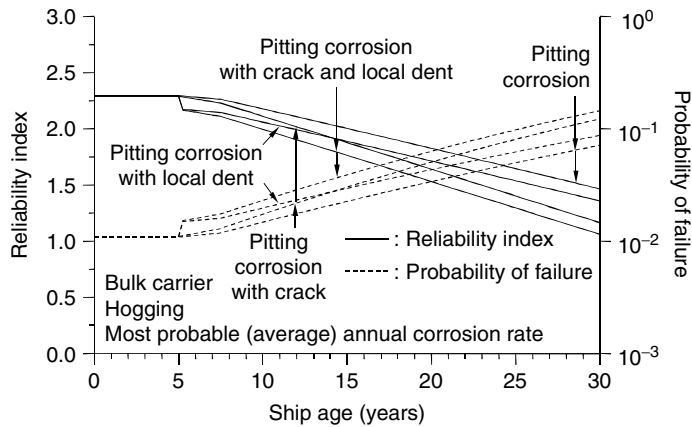


FIGURE 9.15D Time-dependent reliability of the 170,000-dwt bulk carrier associated with hull girder collapse in hogging.

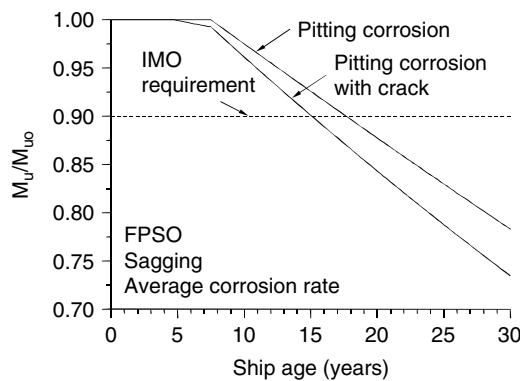


FIGURE 9.16A Time-dependent ultimate hull girder strength of the 113,000-dwt FPSO in sagging.

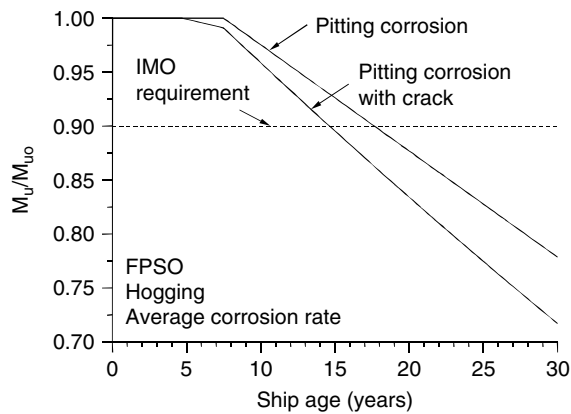


FIGURE 9.16B Time-dependent ultimate hull girder strength of the 113,000-dwt FPSO in hogging.

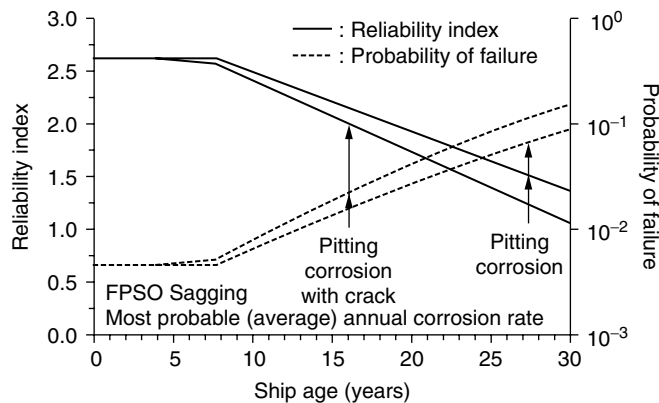


FIGURE 9.16C Time-dependent reliability of the 113,000-dwt FPSO associated with hull girder collapse in sagging.

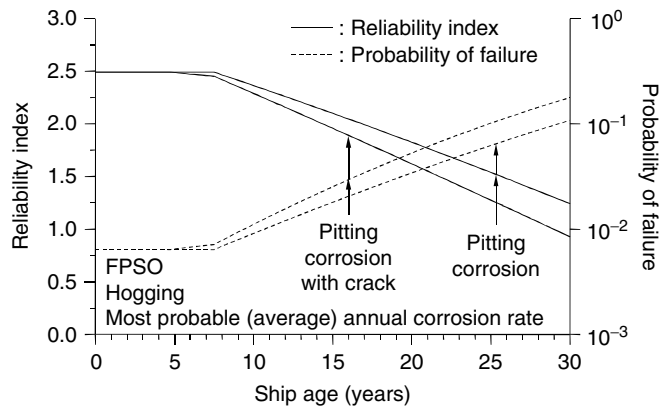
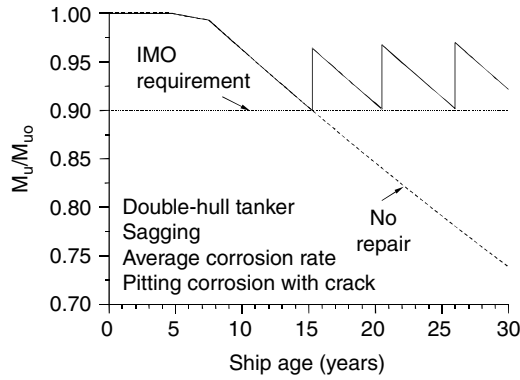
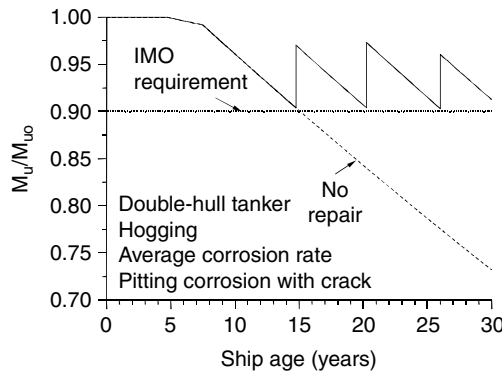


FIGURE 9.16D Time-dependent reliability of the 113,000-dwt FPSO associated with hull girder collapse in hogging.



**FIGURE 9.17A** Repairs and the resulting time-dependent ultimate hull girder strength of the 105,000-dwt double-hull tanker in sagging.



**FIGURE 9.17B** Repairs and the resulting time-dependent ultimate hull girder strength of the 105,000-dwt double-hull tanker in hogging.

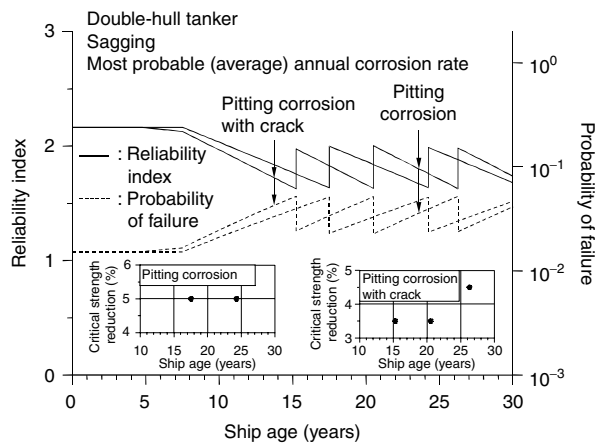


**FIGURE 9.17C** Repairs and the resulting time-dependent reliability of the 105,000-dwt double-hull tanker associated with hull girder collapse in sagging.

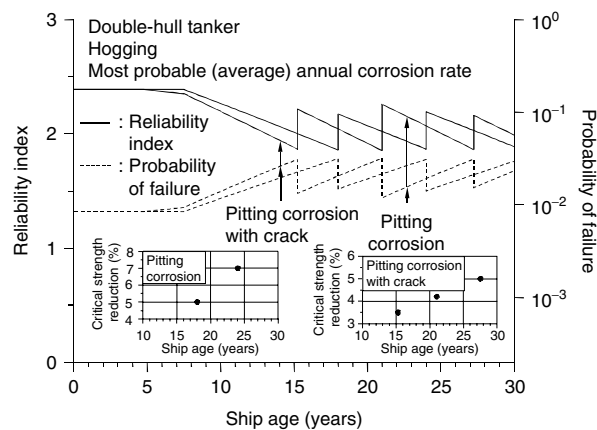


FIGURE 9.17D Repairs and the resulting time-dependent reliability of the 105,000-dwt double-hull tanker associated with hull girder collapse in hogging.

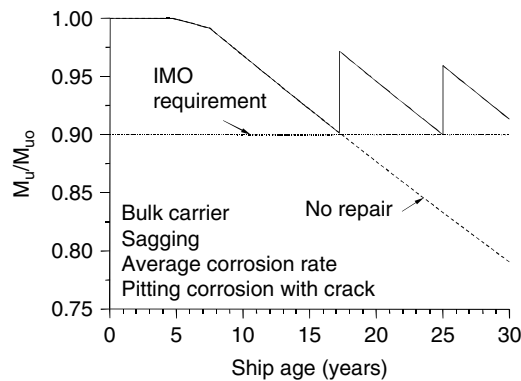


FIGURE 9.18A Repairs and the resulting time-dependent ultimate hull girder strength of the 170,000-dwt bulk carrier in sagging.

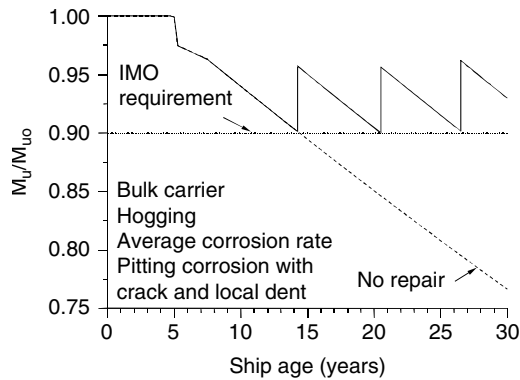
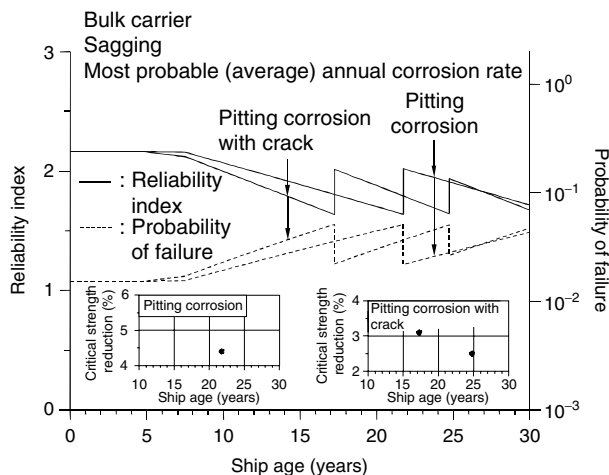


FIGURE 9.18B Repairs and the resulting time-dependent ultimate hull girder strength of the 170,000-dwt bulk carrier in hogging.



**FIGURE 9.18C** Repairs and the resulting time-dependent reliability of the 170,000-dwt bulk carrier associated with hull girder collapse in sagging.

(i.e., member's ultimate strength as defined) is adequate and better equipped to deal with all types of structural damage.

As the illustrations imply, the more heavily damaged members need to be renewed (or repaired) to their as-built states immediately, before the ultimate longitudinal strength of an aging ship reduces to a value less than 90% of the original ship.

It is evident from Figure 9.17 through Figure 9.19 that the structural safety and reliability of aging vessels can be controlled by proper repair and maintenance strategies. It is also seen that the repair criterion based on member ultimate strength can provide a potential improvement to better control the age-dependent degradation of a ship's longitudinal strength. It is seen in the illustrations that the percentage reduction in critical ultimate strength of structural members that need to be repaired is not constant, as might be expected, and is in the range of 2 to 7% of the as-built state.

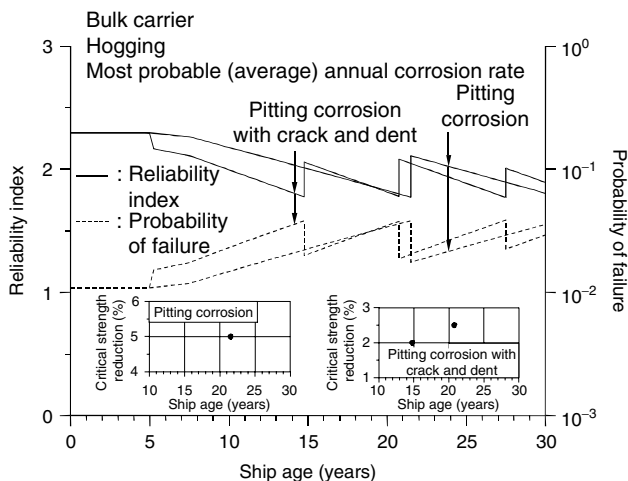


**FIGURE 9.18D** Repairs and the resulting time-dependent reliability of the 170,000-dwt bulk carrier associated with hull girder collapse in hogging.

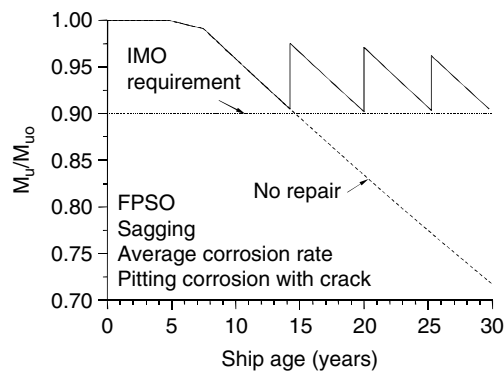


FIGURE 9.19A Repairs and the resulting time-dependent ultimate hull girder strength of the 113,000-dwt FPSO in sagging.

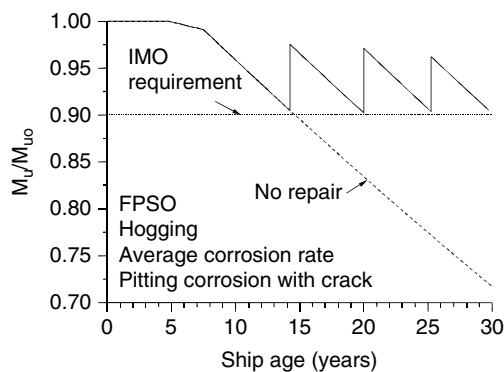


FIGURE 9.19B Repairs and the resulting time-dependent ultimate hull girder strength of the 113,000-dwt FPSO in hogging.

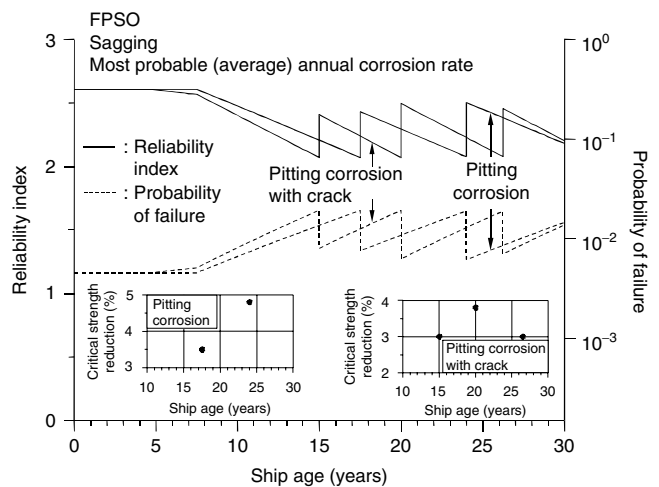
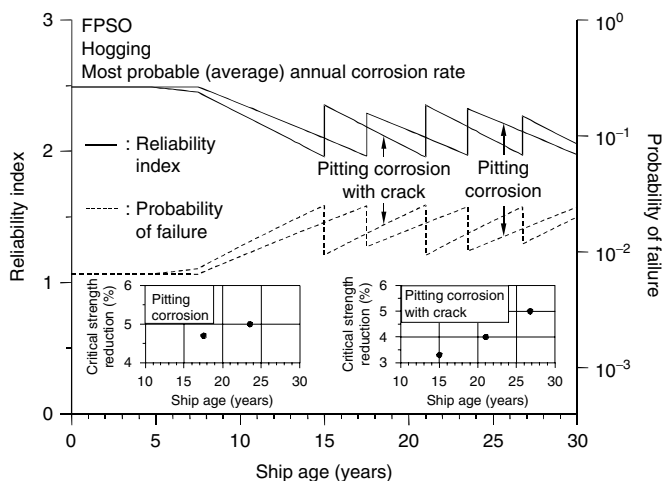


FIGURE 9.19C Repairs and the resulting time-dependent reliability of the 113,000-dwt FPSO associated with hull girder collapse in sagging.



**FIGURE 9.19D** Repairs and the resulting time-dependent reliability of the 113,000-dwt FPSO associated with hull girder collapse in hogging.

## 9.10 Concluding Remarks

It is recognized that reliability technology is a powerful tool for a more rigorous assessment of the integrity of ship structures as well as other types of steel structures such as offshore platforms and land-based structures. The use of reliability methods is required for many applications in the maritime industry [23]: (a) to develop probability-based design-code requirements, (b) to estimate reliability in existing ship structures, (c) to perform failure analysis that investigates the cause of structural failure, (d) to compare alternative designs that compete with existing or conventional design concepts, (e) to support economic value analysis (cost-benefit analysis) that identifies the trade-off between cost and risk so as to minimize total expected life-cycle cost, and (f) to develop optimal maintenance strategies of aging structures, leading to minimum cost without reducing the reliability below a specified level.

The present chapter describes a methodology for performing the reliability assessment of aging ships with the focus on hull girder ultimate limit state, accounting for corrosion, fatigue cracking, and local dent damage. Application examples of the methodology to two merchant cargo ships and one ship-shaped FPSO are presented. Time-dependent reliability indices with respect to ultimate strength limit state of three hull girders under a set of presumed damage scenarios are evaluated as they age, indicating that reliability methods can be very useful for identifying a realistic level of failure probability of hull girder collapse. It is also apparent that reliability methods are useful for establishing a cost-effective scheme for repair and maintenance of aging or damaged structures.

During the last two decades, significant developments in the reliability assessment of ships have been achieved. However, a number of problem areas still remain in applying reliability methods to ship structures, although it seems that the mathematical algorithms needed for such analysis have almost been established. These remaining problems are mainly due to the difficulties of quantifying probabilistic characteristics of random variables or the properties involved in structural reliability assessment, which include structural failure types, failure consequences, fabrication-induced initial imperfections, age-related damage (general or localized corrosion, fatigue cracking), mechanical damage (local denting), accident-induced damage (collision/grounding, fire, explosion), extreme sea states, and operational conditions. It is also not an easy task to determine relevant levels of target reliability index of ship structures for various types of limit states [2].

More effort to resolve such problem areas should be undertaken in this regard so that the reliability-based approach can be more widely employed in shipbuilding industry practice, in place of the deterministic approach currently used for ship structural design.

## References

1. ISO 2394, General Principles on Reliability for Structures, 2nd ed., International Organization for Standardization, Geneva, 1998.
2. Paik, J.K. and Thayamballi, A.K., *Ultimate Limit State Design of Steel-Plated Structures*, John Wiley & Sons, Chichester, U.K., 2003.
3. Freudenthal, A.M., The safety of structures, *Trans. ASCE*, 112, 125–180, 1947.
4. Freudenthal, A.M., Garrelts, J.M., and Shinozuka, M., The analysis of structural safety, *ASCE J. Structural Div.*, 92 (ST1), 267–325, 1966.
5. Mansour, A.E., Methods of computing the probability of failure under extreme values of bending moment, *J. Ship Res.*, 16 (2), 113–123, 1972.
6. Mansour, A.E., Probabilistic design concepts in ship structural safety and reliability, *SNAME Trans.*, 80, 64–97, 1972.
7. Mansour, A.E. and Faulkner, D., On applying the statistical approach to extreme sea loads and ship hull strength, *RINA Trans.*, 114, 273–314, 1972.
8. Ang, A.H.S., Structural risk analysis and reliability based design, *ASCE J. Structural Div.*, 100 (ST9), 1775–1789, 1973.
9. Ang, A.H.S. and Cornell, C.A., Reliability bases of structural safety and design, *ASCE J. Structural Eng.*, 100 (9), 1755–1769, 1974.
10. Stiansen, S.G., Mansour, A.E., Jan, H.Y., and Thayamballi, A.K., Reliability methods in ship structures, *RINA Trans.*, 121, 381–406, 1979.
11. Ayyub, B.M. and Haldar, A., Practical structural reliability techniques, *ASCE J. Structural Eng.*, 110 (8), 1707–1724, 1984.
12. White, G.J. and Ayyub, B.M., Reliability methods for ship structures, *ASNE Naval Engineers J.*, 97 (4), 86–96, 1985.
13. Mansour, A.E., Approximate probabilistic method of calculating ship longitudinal strength, *J. Ship Res.*, 18 (3), 201–213, 1974.
14. Mansour, A.E., Jan, H.Y., Zigelman, C.I., Chen, Y.N., and Harding, S.J., Implementation of reliability methods to marine structures, *SNAME Trans.*, 92, 353–382, 1984.
15. Kaplan, P., Benatar, M., Benton, J., and Acharides, T.A., Analysis and Assessment of Major Uncertainties Associated with Ship Hull Ultimate Failure, Ship Structure Committee report SSC-322, Washington, DC, 1984.
16. Mansour, A.E., An Introduction to Structural Reliability Theory, Ship Structure Committee report SSC-351, Washington, DC, 1990.
17. Nikolaidis, E. and Kaplan, P., Uncertainties in Stress Analysis on Marine Structures, Ship Structure Committee report SSC-363, Washington, DC, 1991.
18. Mansour, A.E., Lin, M., Hovem, L., and Thayamballi, A.K., Probability-Based Ship Design Procedures: a Demonstration, Ship Structure Committee report SSC-368, Washington, DC, 1993.
19. Pussegoda, L.N., Dinovitzer, A.S., and Malik, L., Establishment of a Uniform Format for Data Reporting of Structural Material Properties for Reliability Analysis, Ship Structure Committee report SSC-371, Washington, DC, 1993.
20. Mansour, A.E. and Thayamballi, A.K., Probability Based Ship Design; Loads and Load Combination, Ship Structures Committee report SSC-373, Washington, DC, 1994.
21. Hughes, O.F., Nikolaidis, E., Ayyub, B., White, G.J., and Hess, P.E., Uncertainty in Strength Models for Marine Structures, Ship Structure Committee report SSC-375, Washington, DC, 1994.
22. Basu, R.I., Kirkhope, K.J., and Srinivasan, J., Guideline for Evaluation of Finite Elements and Results, Ship Structure Committee report SSC-387, Washington, DC, 1996.



23. Mansour, A.E., Wirsching, P., Luckett, M., and Plumpton, A., Assessment of Reliability of Ship Structures, Ship Structure Committee report SSC-398, Washington, DC, 1997.
24. Ayyub, B.M., *Elicitation of Expert Opinions for Uncertainty and Risks*, CRC Press, Boca Raton, FL, 2001.
25. Ditlevsen, O. and Madsen, H.O., *Structural Reliability Methods*, John Wiley & Sons, New York, 1996.
26. Paik, J.K. and Frieze, P.A., Ship structural safety and reliability, *Progr. Structural Eng. Mater.*, 3 (2), 198–210, 2001.
27. Paik, J.K., Wang, G., Kim, B.J., and Thayamballi, A.K., Ultimate limit state design of ship hulls, *SNAME Trans.*, 110, 21.1–21.31, 2002.
28. Paik, J.K., A guide for the ultimate longitudinal strength assessment of ships, *Mar. Technol.*, 41 (3), 122–139, 2004.
29. Paik, J.K., Thayamballi, A.K., and Lee, J.M., Effect of initial deflection shape on the ultimate strength behavior of welded steel plates under biaxial compressive loads, *J. Ship Res.*, 48 (1), 45–60, 2004.
30. Paik, J.K., Lee, J.M., and Ko, M.J., Ultimate compressive strength of plate elements with pit corrosion wastage, *J. Eng. for the Maritime Environment*, 217 (M4), 185–200, 2003.
31. Paik, J.K., Lee, J.M., and Lee, D.H., Ultimate strength of dented steel plates under axial compressive loads, *Int. J. Mech. Sci.*, 45, 433–448, 2003.
32. Mansour, A.E. and Hovem, L., Probability based ship structural safety assessment, *J. Ship Res.*, 38 (4), 329–339, 1994.
33. Loukakis, T.A. and Chrysostomidis, C., Seakeeping series for cruiser stern ships, *SNAME Trans.*, 83, 67–127, 1975.
34. Paik, J.K. and Faulkner, D., Reassessment of the M.V. *Derbyshire* sinking with the focus on hull girder collapse, *Marine Technol.*, 40(4), 258–269, 2003.
35. Paik, J.K. and Thayamballi, A.K., Ultimate strength of ageing ships, *J. Eng. Maritime Environ.*, 216 (M1), 57–77, 2002.
36. Guedes Soares, C. and Garbatov, Y., Reliability of maintained, corrosion protected plates subjected to nonlinear corrosion and compressive loads, *Mar. Struct.*, 12, 425–445, 1999.
37. Qin, S.P. and Cui, W.C., Effect of corrosion models on the time-dependent reliability of steel plated elements, *Mar. Struct.*, 16, 15–34, 2003.
38. Paik, J.K., Lee, J.M., Hwang, J.S., and Park, Y.I., A time-dependent corrosion wastage model for the structures of single-and double-hull tankers and FSOs and FPSOs, *Mar. Technol.*, 40 (3), 201–217, 2003.
39. Paik, J.K., Lee, J.M., Park, Y.I., and Hwang, J.S., A time-dependent corrosion wastage model for bulk carrier structures, *Int. J. Maritime Eng.*, 145 (A2), 61–87, 2003.
40. Broek, D., *Elementary Engineering Fracture Mechanics*, Martinus Nijhoff, Dordrecht/Boston/Lancaster, 1986.
41. DNV, Fatigue Assessment of Ship Structures, classification notes 30.7, Det Norske Veritas, Høvik, Norway, January 2001.
42. IMO, SOLAS XI/2, Recommended Longitudinal Strength, MSC.108(73), Maritime Safety Committee, International Maritime Organization, London, 2000.

# 10

## Reliability Analysis of Composite Structures and Materials

---

10.1	Introduction .....	10-1
10.2	Strength Limit States (Laminate Theory) .....	10-2
	Ply-Level Limit States and Reliability • System Failure Probability • Numerical Example	
10.3	Strength Limit States (Three-Dimensional Analysis) .....	10-8
	Shear Deformation Theory and Analysis • Ply-Level Limit States • Stiffness Modification for Progressive Failure Analysis • Numerical Example (Composite Plate)	
10.4	Strength Limit State: Approximations .....	10-14
	Fast Branch-and-Bound Method • Deterministic Initial Screening • Weakest-Link Model • Critical Component Failure • Numerical Example: Aircraft Wing	
10.5	Fatigue Limit State: Material Modeling .....	10-18
	Fatigue Damage Modeling	
10.6	Multiaxial Fatigue .....	10-24
10.7	Fatigue Delamination Limit State .....	10-26
	Failure Mechanism and Model • Random Variables • Response Surface Modeling of the Limit State • Verification of Methodology	
10.8	Creep Limit State .....	10-30
	Creep of Undamaged Composites • Creep Analysis with Stochastic Fiber Fracture • Failure Criterion • Numerical Example	
10.9	Conclusion .....	10-36
	References .....	10-36

Sankaran Mahadevan  
*Vanderbilt University*

### 10.1 Introduction

---

Composite materials are being widely used in modern structures, such as aircraft and space vehicles, because of high performance, high temperature resistance, tailoring facility, and light weight. Considerable research on the design and failure analysis of composite structures is being conducted. The results of experiments and research into composite materials show large statistical variations in their mechanical properties. Therefore, probabilistic analysis has to play an important role in structural assessment. This chapter presents reliability analysis methods for composite structures, considering several types of failure criteria: ultimate strength, fatigue, delamination, and creep.

From the perspective of strength limit states, composite laminate failure may be considered in two major stages, first ply failure (FPF) and last ply failure (LPF). The FPF usually corresponds to the commencement of matrix cracking failure; structural ultimate failure or LPF consists of a series of ply-level component failures, such as matrix cracking, delamination, and fiber breakage, from the first one to last one. Well-known methods such as the first-order reliability method (FORM), second-order reliability method (SORM), or Monte Carlo simulation may be combined with finite element analysis to compute the component failure probability. The branch-and-bound method may then be employed to search for the significant system failure sequences. When each component failure occurs, the structural stiffness is modified to account for this damage and the damaged structure is reanalyzed. This continues until system failure occurs. Based on the identified significant failure sequences, the system failure probability is determined by means of bounding techniques. In the composite structure, multiple sequences are found to be highly correlated, leading to efficient approximations in the failure probability computation. Section 10.2 to Section 10.4 present these methods and illustrate them with simple examples, and then a practical application—a composite aircraft wing.

The characteristics of fatigue damage growth in composite materials are different from those of damage growth in homogeneous materials. Continuum damage mechanics concepts have been used to evaluate the degradation of composite materials under cyclic loading. Damage accumulation models that capture the unique characteristics of composite materials are presented in Section 10.5. The predictions from the models are compared with experimental data.

Because of the anisotropic properties of composite materials, the fatigue problem may need to be treated as multiaxial in some cases. There is extensive progress in multiaxial fatigue analysis of metals, but much effort is needed for composite materials. Section 10.6 develops a simple and versatile damage accumulation model for multiaxial fatigue in laminated composites. The model is extended to progressive failure of multidirectional laminates. The model parameters are obtained through analysis of test data on several unidirectional laminates. Monte Carlo simulation is used to calculate the distribution of fatigue life and reliability under different load amplitudes.

Fatigue leads to delamination in several laminated composite applications, affected by anisotropic material properties of various plies, ply thicknesses and orientations, the loads, and boundary conditions. The limit state may be formulated in terms of the strain energy release rate computed based on the virtual crack closure technique. The critical value of the strain energy release rate, obtained from test data, is seen to be a random function of life of the structure. Once the delamination initiation probability is estimated, the propagation life until system failure is estimated through the exploration of multiple paths through the branch-and-bound enumeration technique. The analysis is then repeated for multiple initiation sites, and the overall probability of failure is computed through the union of the multiple initiation/growth events. These techniques are presented and illustrated in Section 10.7 using a practical application—fatigue delamination analysis of a helicopter rotor component.

Composite materials are particularly attractive for high-temperature applications, as in engine components. Therefore, creep reliability models for high-temperature composites are presented in Section 10.8. Time-dependent reliability analysis, including the effect of broken fibers, is discussed. The final section discusses new research needs in composite materials and structural reliability.

## 10.2 Strength Limit States (Laminate Theory)

---

Several studies have developed static strength reliability assessment methods for fibrous composites [1, 2], using the FPF assumption; that is, if any of the plies in a laminate fails, the entire laminate is considered a failure. Other studies [3, 4] estimated ultimate strength reliability using the LPF assumption; that is, the laminate fails only if all plies fail. This latter analysis includes the search for the dominant failure sequences, and the laminate reliability is approximated through the union of the dominant failure sequences. Two options have been pursued in modifying the system definition during the progressive damage analysis. In the first option, a ply is completely removed from the system when it fails, because the material used in such a system is usually brittle [3]. The second option is to realistically consider the

consequence of different types of failures, such as matrix cracking and fiber breakage [4]. For instance, after the matrix failure of a ply occurs, the ply's stiffness along the matrix direction is reduced to zero, but the fiber is not yet broken and could have load-bearing capacity. If the fiber fails first, the ply's stiffness along the fiber direction is reduced to zero and the matrix is still able to carry the loading. Thus, if any one basic failure event occurs, then the corresponding stiffness matrix terms are modified; the ply is not removed until both matrix cracking and fiber failure occur.

A probabilistic progressive failure model may be developed as follows: FORM is used to compute the component reliability. The structural element stiffnesses are modified to reflect damage during the simulation of the progressive failure process. The significant failure sequences are identified based on the branch-and-bound method, and the system failure probability is determined as the failure probability of the union of the significant failure sequences.

### 10.2.1 Ply-Level Limit States and Reliability

In-plane failure of the ply can generally be classified into two major failures: matrix failure and fiber breakage. In this section, the following limit state functions are used:

Fiber failure [5]:

$$g_f = 1 - \{f_{11}\sigma_1^2 + f_1\sigma_1\} \quad (10.1)$$

Matrix failure, based on the Tsai–Wu criterion [6]:

$$g_m = 1 - \{f_{11}\sigma_1^2 + f_{22}\sigma_2^2 + f_{66}\sigma_{12}^2 + f_{12}\sigma_1\sigma_2 + f_1\sigma_1 + f_2\sigma_2\} \quad (10.2)$$

The coefficients  $f_{11}$ ,  $f_{22}$ , etc., in Equation 10.1 and Equation 10.2 are related to material strengths as

$$f_{11} = \frac{1}{(X_T \cdot X_C)}, \quad f_{22} = \frac{1}{(Y_T \cdot Y_C)}, \quad f_{66} = \frac{1}{S^2}$$

$$f_1 = \frac{1}{X_T} - \frac{1}{X_C}, \quad f_2 = \frac{1}{Y_T} - \frac{1}{Y_C}, \quad f_{12} = -\sqrt{f_{11} - f_{22}}$$

where  $X_T$  is the tension strength in the 1-1 direction;  $X_C$  is the compression strength in the 1-1 direction;  $Y_T$  is the tension strength in the 2-2 direction;  $Y_C$  is the compression strength in the 2-2 direction;  $S$  is the shear strength; and  $\sigma_1$ ,  $\sigma_2$ , and  $\sigma_{12}$  are stresses in the 1-1, 2-2, and 1-2 directions, respectively, as shown in Figure 10.1. The limit state functions in Equation 10.1 and Equation 10.2 imply failure when  $g_f \leq 0$  or  $g_m \leq 0$ .

In the reliability evaluation, the stress resultants  $\{N\}$  and the stress couples  $\{M\}$ , and the strength parameters  $X_T$ ,  $X_C$ ,  $Y_T$ ,  $Y_C$ , and  $S$  are considered as the basic random variables. These basic random variables are expressed as a vector  $X = \{X_1, X_2, \dots, X_m\}^T$ . In FORM, the component reliability index is obtained as  $\beta = (y^{*T} y^*)^{1/2}$ , where  $y^*$  is the point of minimum distance from the origin to the limit state  $G(Y) = 0$ , where  $Y$  is the vector of equivalent uncorrelated standard normal variables. The first-order approximation to the failure probability is computed as  $p_f = \Phi(-\beta)$ , where  $\Phi$  is the standard normal cumulative distribution function (CDF). The transformation of the random variables from the  $X$ -space to  $Y$ -space is achieved by any of the well-known methods [7].

The most probable failure point  $y^*$  is found using the following iterative formula proposed by Rackwitz and Fiessler [8]:

$$y_{i+1} = \left[ y_i^T \sigma_i + \frac{G(y_i)}{|\nabla G(y_i)|} \right] \alpha_i^T \quad (10.3)$$

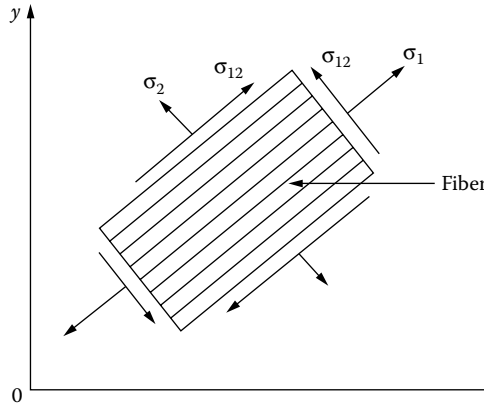


FIGURE 10.1 Laminate stresses.

where  $\nabla G(y_i)$  is the gradient vector of the limit state function at  $y_i$ , and  $\alpha_i$  is the unit vector normal to the limit state surface away from the origin. It has the following form:

$$\alpha_i = -\nabla G(y_i) / |\nabla G(y_i)| \quad (10.4)$$

The computation of  $\nabla G(y_i)$  is achieved by using the chain rule of differentiation on Equation 10.1 or Equation 10.2.

### 10.2.2 System Failure Probability

The laminate system is assumed to collapse only when all the plies have failed. Consider a laminate system that has  $n$  plies under the external loads  $\{N\}$  and  $\{M\}$ . Because there are two basic failure events for each ply (matrix cracking and fiber breakage),  $2n$  component failure events exist in the system. Based on the branch-and-bound concept, a procedure to identify the significant failure sequences for composite laminates may be formulated as follows:

- Step 1.* Suppose the laminate is originally in its intact state. For each basic event, compute its reliability index  $\beta$  using the component-level first-order reliability method (FORM) and then obtain its corresponding failure probability. Order the  $2n$  values of failure probabilities, and record the maximum value of failure probability as  $P_{f\max}^1$ . The superscript “1” means the first stage. Select the failure event that has the largest failure probability as the first one to occur. At the same time, the components that have failure probability greater than a specified fraction of  $P_{f\max}^1$  are saved for exploration (branching) and the other components that have failure probability less than the specified fraction of  $P_{f\max}^1$  are discarded.
- Step 2.* Modify the stiffness corresponding to the first failure event. If the event corresponds to matrix failure, the moduli  $E_2$  and  $G_{12}$  of the ply are reduced to zero. If the event corresponds to fiber failure, the modulus  $E_1$  of the ply is reduced to zero. The loads are globally redistributed in the damaged laminate in accordance with the modified stiffness. The same calculations as in step 1 are repeated. The event that has the largest path probability  $P_{f\max}^2$  at the second stage is taken as the next event to fail. This proceeds until the system failure occurs.
- Step 3.* After the first failure sequence is identified, step 2 is repeated to consider the other branched events until all the possible significant failure sequences are found. The failure sequences that have path probability lower than a prespecified value are considered insignificant and are not explored.

### 10.2.2.1 Single Failure Sequence

For one failure sequence with  $m$  individual failure events, the failure probability can be computed as

$$P_f^k = P\left(\bigcap_{j=1}^m E_j^k\right) \quad (10.5)$$

where  $E_j^k$  is the  $j$ th basic failure event along the  $k$ th failure sequence under the condition that the first  $(j-1)$  basic failure events have occurred.

In general, it is difficult to evaluate Equation 10.5 numerically when  $m \geq 3$ . In practical problems, approximate solutions may be obtained. The second-order upper bound suggested by Murotsu [9] is a good approximation for the estimation of the joint failure probability:

$$P\left(\bigcap_{j=1}^m E_j\right) \leq \min_{i \neq j} [P(E_i \cap E_j)] \quad (10.6)$$

In the case of composite structures, usually there are one or two components that have much smaller failure probabilities than others, as will be shown later in the numerical examples. In that case, a simpler formula [10] can be used to approximate the joint probability:

$$P\left(\bigcap_{j=1}^m E_j\right) \leq P(E_1 \cap E_2) \quad (10.7)$$

where  $E_1$  and  $E_2$  are the two least probable events in a failure sequence.

In general, some of the failure events are correlated; hence, the calculations of the joint probabilities in Equation 10.6 and Equation 10.7 remain difficult, especially when the basic random variables are nonnormal and the limit state functions are nonlinear. Mahadevan et al. [11] proposed an approximate method for this problem, as shown in Figure 10.2. The joint failure region is approximately bounded by the hyperplanes at the point  $y_{12}^*$ , which is the closest point (from the origin) on the intersection of the limit state surfaces  $G_1(y)=0$  and  $G_2(y)=0$  in the  $Y$ -space.  $y_{12}^*$  is found by solving the following optimization problem:

$$\text{minimize } \sqrt{Y^T Y} \quad (10.8)$$

$$\text{s.t. } G_1(Y) = 0$$

$$G_2(Y) = 0$$

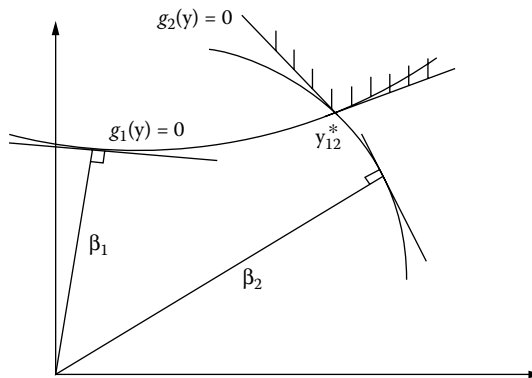


FIGURE 10.2 Joint failure probability with nonlinear limit states.

In the following discussion, sequential quadratic programming is used to solve this problem. After  $y_{12}^*$  is found, the limit states  $G_1(y)=0$  and  $G_2(y)=0$  are linearized at  $y_{12}^*$  so that the correlation coefficient between the two limit states  $\rho_{12}$  can be obtained as the product of the two unit gradient vectors,  $\alpha_1$  and  $\alpha_2$ , of the linear approximations at  $y_{12}^*$ . That is,

$$\rho_{12} = \sum_{r=1}^n \alpha_{1r} \alpha_{2r} \quad (10.9)$$

where  $\alpha_{1r}$  and  $\alpha_{2r}$  are the gradients similar to that defined in Equation 10.4, and  $n$  is the number of random variables. The joint failure probability is then calculated using the two-dimensional standard normal cumulative distribution as

$$P(E_1 \cap E_2) = \Phi(-\beta_1, -\beta_2, \rho_{12}) \quad (10.10)$$

### 10.2.2.2 Multiple Failure Sequences

As mentioned before, the overall failure probability requires the computation of the probabilities of the unions of multiple failure sequences. Because the performance functions of the failure sequences are not available, the Cornell first-order bound [12] is a suitable candidate for an approximate estimate. If  $l$  significant failure sequences are identified, the system failure probability,  $P_f$ , may be approximately computed as:

$$\max_{k=1, \dots, l} P_f^k \leq P_f \leq \sum_{k=1}^l P_f^k \quad (10.11)$$

In the case where all failure sequences are fully dependent, it follows directly that the weakest failure sequence will always be weakest. Hence, the system failure probability is equal to the lower bound in Equation 10.11. For mutually exclusive failure sequences, the system failure probability corresponds to the upper bound of Equation 10.11. Moreover, for statistically independent failure sequences with low probabilities (e.g.,  $10^{-4}$ ), the upper bound usually yields a good approximation of the system failure probability.

## 10.2.3 Numerical Example

A typical Graphite/Epoxy (T300/5208) laminate with configuration  $[90^\circ/45^\circ/45^\circ/0^\circ]$  and equal ply thickness of 0.25 mm is studied. This laminate system may be subjected to the stress resultants  $\{N\}$  and/or the stress couples  $\{M\}$  as shown in Figure 10.3. Two in-plane loading cases are considered for illustration: (1) uniaxial loading and (2) biaxial loading.

The material strength parameters  $X_T$ ,  $X_C$ ,  $Y_T$ ,  $Y_C$ ,  $S$  and loading  $\{N\}$ ,  $\{M\}$  are considered the basic random variables. In the current study, the strength parameters are assumed to have Weibull distributions, and the loads  $\{N\}$  and  $\{M\}$  are assumed to have Type-I extreme value distributions.

A cutoff value of 0.3 is used in the branch-and-bound search for the significant failure sequences; that is, components with failure probabilities greater than 0.3 of the maximum component failure probability are saved for exploration and others are discarded. For the laminate  $[90^\circ/45^\circ/45^\circ/0^\circ]$ , there are four plies with different orientations, and two basic events (matrix failure event and fiber breakage event) for each ply. Thus, there are eight basic events. Figure 10.4 shows the dominant failure sequences for the two loading cases. The failure events are denoted using ply orientation and the type of failure event. For example,  $90M$  stands for the matrix failure event of the  $90^\circ$  ply, and  $90F$  stands for its fiber breakage event.

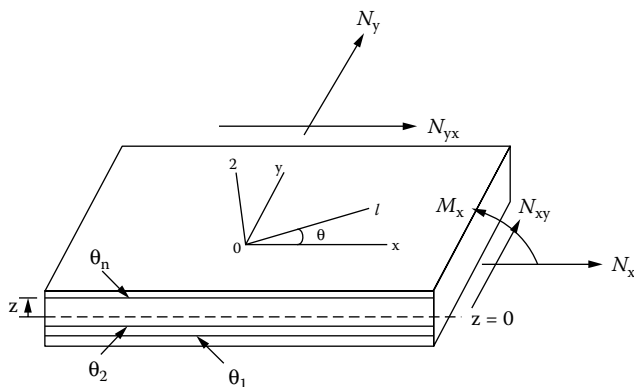
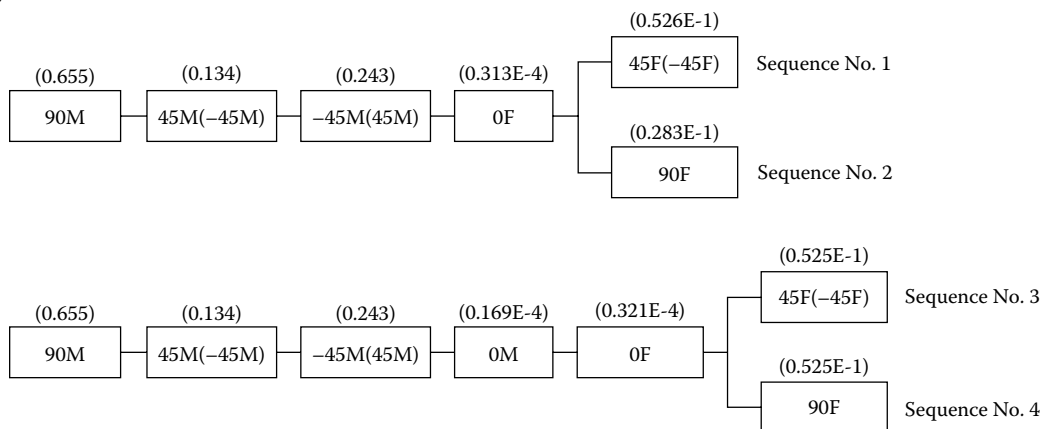


FIGURE 10.3 Composite laminate.

a)



b)

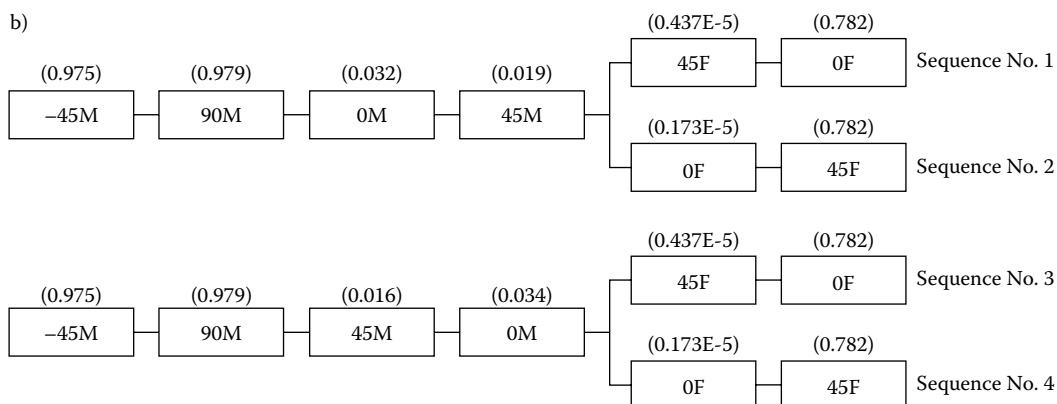


FIGURE 10.4 Dominant failure sequences: (a) axial loading only; (b) general in-plane loading.



(Refer to Reference [4] for details of this numerical example.) Three results are important for future discussion:

1. Figure 10.4 shows that, in general, for the same laminate configuration, different loading combinations have different significant failure sequences. That is because component failure probabilities depend on stress responses of components, which change with loading combinations. Also, it is seen from Figure 10.4 that matrix cracking failures usually occur first and then fiber failures occur. These kinds of failure sequences are consistent with experimental results.
2. The overall failure probability of a single sequence is found to greatly depend on the least probable event, owing to the strong correlation among the components in the sequence. The least probable event is usually the first failed fiber. This indicates that the failure of the first fiber can approximately be considered a system collapse.
3. The significant failure sequences under a given load are found to be quite similar. That implies strong correlations among the significant failure sequences. Therefore, considering multiple sequences, the system failure probability may be very close to the Cornell first-order lower bound. These observations are useful in devising computationally efficient schemes for larger systems considered in Section 10.3 and Section 10.4.

## 10.3 Strength Limit States (Three-Dimensional Analysis)

The analysis in Section 10.2 was based on classical laminate theory, and the composite laminate was considered a system consisting of individual plies as components. A general composite structure may consist of different laminate configurations in different parts of the structure, and may need to be analyzed using a finite element method and with a more advanced behavior model than classical laminate theory. Therefore, this section extends the probabilistic progressive failure analysis methodology to general three-dimensional composite structures, and presents several practical techniques to address issues with respect to system failure definition, progressive damage analysis, and probabilistic computation. The proposed methodology is applied to a numerical example of a composite plate.

### 10.3.1 Shear Deformation Theory and Analysis

The first-order shear deformation theory for laminated anisotropic plates is used in this section [13–15]; that is, normals to the centerplane are assumed to remain straight after deformation, but not necessarily normal to the centerplane.

The displacement field is of the form

$$\begin{aligned} u_x(x, y, z) &= u_0(x, y) + z\psi_x(x, y) \\ u_y(x, y, z) &= v_0(x, y) + z\psi_y(x, y) \\ u_z(x, y, z) &= w(x, y) \end{aligned} \quad (10.12)$$

where  $u_x, u_y$ , and  $u_z$  are the displacements in the  $x, y, z$  directions, respectively;  $u_0, v_0$ , and  $w$  are the associated midplane displacements; and  $\psi_x$  and  $\psi_y$  are the rotations of normals to midplane about the  $y$  and  $x$  axes, respectively. In the preceding equation, considering that the transverse normal stress is of the order  $(h/a)^2$  times the in-plane normal stresses, the assumption that  $w$  is not a function of the thickness coordinate is justified.

For any elastic body, the strain–displacement equations describing the functional relations between the elastic strains in the body and its displacements are given by

$$\epsilon_{ij} = \frac{1}{2}(u_{i,j} + u_{j,i}) \quad (10.13)$$

where  $i, j = x, y, z$  in a Cartesian coordinate system, and the comma denotes partial differentiation with respect to the coordinate denoted by the symbol after the comma. Explicitly, the relations are:

$$\begin{aligned}
 \varepsilon_x &= \frac{\delta u_x}{\delta x} \\
 \varepsilon_y &= \frac{\delta u_y}{\delta y} \\
 \varepsilon_z &= \frac{\delta w}{\delta z} \\
 \varepsilon_{xz} &= \frac{1}{2} \left( \frac{\delta u_x}{\delta z} + \frac{\delta w}{\delta x} \right) \\
 \varepsilon_{yz} &= \frac{1}{2} \left( \frac{\delta u_y}{\delta z} + \frac{\delta w}{\delta y} \right) \\
 \varepsilon_{xy} &= \frac{1}{2} \left( \frac{\delta u_x}{\delta y} + \frac{\delta u_y}{\delta x} \right)
 \end{aligned} \tag{10.14}$$

Substituting Equation 10.12 into Equation 10.14 results in:

$$\begin{aligned}
 \varepsilon_x &= \frac{\delta u_0}{\delta x} + z \frac{\delta \psi_x}{\delta x} = \varepsilon_x^o + z k_x \\
 \varepsilon_y &= \frac{\delta v_0}{\delta y} + \frac{\delta \psi_x}{\delta y} = \varepsilon_x^o + x k_y \\
 \varepsilon_x &= 0 \\
 \varepsilon_{xy} &= \frac{1}{2} \left( \frac{\delta u_0}{\delta y} + \frac{\delta v_0}{\delta x} \right) + \frac{z}{2} \left( \frac{\delta \psi_x}{\delta y} + \frac{\delta \psi_y}{\delta x} \right) = \varepsilon_{xy}^o + z k_{xy} \\
 \varepsilon_{xz} &= \frac{1}{2} \left( \psi_x + \frac{\delta w}{\delta x} \right) \\
 \varepsilon_{yz} &= \frac{1}{2} \left( \psi_y + \frac{\delta w}{\delta y} \right)
 \end{aligned} \tag{10.15}$$

For a plate of constant thickness  $h$  and composed of thin layers of orthotropic material, the constitutive equations can be derived [16], under the assumption that each layer possesses a plane of elastic symmetry parallel to the  $x$ - $y$  plane, as

$$\begin{Bmatrix} \sigma_1 \\ \sigma_2 \\ \sigma_6 \end{Bmatrix} = \begin{bmatrix} Q_{11} & Q_{12} & 0 \\ Q_{12} & Q_{22} & 0 \\ 0 & 0 & 2Q_{66} \end{bmatrix} \begin{Bmatrix} \varepsilon_1 \\ \varepsilon_2 \\ \varepsilon_6 \end{Bmatrix} \tag{10.16}$$

$$\begin{Bmatrix} \sigma_4 \\ \sigma_5 \end{Bmatrix} = \begin{bmatrix} 2Q_{44} & 0 \\ 0 & 2Q_{55} \end{bmatrix} \begin{Bmatrix} \varepsilon_{23} \\ \varepsilon_{31} \end{Bmatrix} \tag{10.17}$$

where all the foregoing quantities are in the principal material directions (1,2,3) of the layer. To relate these relationships to the  $x$ - $y$ - $z$  coordinate system, a transformation is performed. The result is

$$\begin{Bmatrix} \sigma_x \\ \sigma_y \\ \sigma_{xy} \end{Bmatrix} = \begin{bmatrix} Q_{11} & Q_{12} & \overline{2Q_{16}} \\ Q_{12} & Q_{22} & \overline{2Q_{26}} \\ Q_{16} & Q_{26} & \overline{2Q_{66}} \end{bmatrix} \begin{Bmatrix} \varepsilon_x \\ \varepsilon_y \\ \varepsilon_{xy} \end{Bmatrix} \quad (10.18)$$

$$\begin{Bmatrix} \sigma_{yz} \\ \sigma_{xz} \end{Bmatrix} = \begin{bmatrix} 2\overline{Q}_{44} & 2\overline{Q}_{45} \\ 2\overline{Q}_{45} & 2\overline{Q}_{55} \end{bmatrix} \begin{Bmatrix} \varepsilon_{yz} \\ \varepsilon_{xz} \end{Bmatrix} \quad (10.19)$$

The ply stresses along the material axes can be obtained using finite element analysis. Then, they are substituted into a suitable strength failure criterion for reliability analysis of ply-level component failure modes.

### 10.3.2 Ply-Level Limit States

Failure criteria are based on four types of theories: (1) limit theory, (2) polynomial theory, (3) strain energy theory, and (4) direct mode determining theory. The limit theory compares the value of each stress or strain component to a corresponding ultimate value. The polynomial theory uses a polynomial of stress terms to describe the failure surface. The strain energy theory uses a nonlinear energy-based criterion to define failure. Finally, the direct mode determining theory uses polynomials of stress terms and uses separate equations to describe each mode of failure. In progressive failure analysis, the direct mode determining failure criteria are most widely used because they automatically determine the mode of failure (for instant, matrix cracking failure mode) so that the stiffness can be reduced in the correct manner. However, it is to be noted that the direct failure criteria are based mainly on empirical reasoning. In this chapter, Lee's [13] simple empirical criteria are used to derive component performance functions for the sake of illustration, as follows:

For fiber breakage:

$$\begin{aligned} g_f &= 1 - \sigma_1 / X_T, & \sigma_1 > 0 \\ g_f &= 1 + \sigma_1 / X_C, & \sigma_1 < 0 \end{aligned} \quad (10.20)$$

For matrix cracking:

$$g_m = 1 - \left[ \frac{\sigma_2^2}{Y_T Y_C} + \frac{\sigma_{12}^2}{S^2} \right] \quad (10.21)$$

For delamination:

$$g_d = 1 - \left( \frac{1}{S_z} \right)^2 (\sigma_{23}^2 + \sigma_{31}^2) \quad (10.22)$$

In the foregoing equations,  $X_T$  and  $X_C$  are the tensile and compressive strengths in the fiber direction;  $Y_T$  and  $Y_C$  are the tensile and compressive strengths in the direction transverse to fibers; and  $S$  and  $S_z$  are the shear strengths in the  $x$ - $y$  plane and in the  $z$  direction, respectively. As in Section 10.2,  $g < 0$  indicates the failure of the component.

### 10.3.3 Stiffness Modification for Progressive Failure Analysis

Once the ply-level failure probabilities are determined using the limit states in Equation 10.20 to Equation 10.22 are obtained, the significant sequences to laminate (system) failure are identified using the branch-and-bound technique. This requires progressive failure analysis similar to that in Section 10.2.2. The stiffness matrix terms corresponding to each type of failure are modified as follows.

When fiber failure occurs, the ply stiffness terms contributed by the fiber (related to material direction “1”), i.e.,  $E_{11}$ ,  $G_{12}$ , and  $G_{31}$ , are reduced to zero, and  $[Q]$  becomes

$$\begin{bmatrix} 0 & 0 & 0 & 0 & 0 \\ 0 & E_{22} & 0 & 0 & 0 \\ 0 & 0 & 0 & 0 & 0 \\ 0 & 0 & 0 & 2G_{23} & 0 \\ 0 & 0 & 0 & 0 & 0 \end{bmatrix} \quad (10.23)$$

When matrix cracking occurs, the ply stiffness terms related to material direction “2,” i.e.,  $E_{22}$ ,  $G_{12}$ , and  $G_{23}$ , are reduced to zero, and  $[Q]$  becomes

$$\begin{bmatrix} E_{11} & 0 & 0 & 0 & 0 \\ 0 & 0 & 0 & 0 & 0 \\ 0 & 0 & 0 & 0 & 0 \\ 0 & 0 & 0 & 0 & 0 \\ 0 & 0 & 0 & 0 & 2G_{31} \end{bmatrix} \quad (10.24)$$

When delamination failure occurs, the ply stiffness terms related to material direction “3,” i.e.,  $G_{23}$  and  $G_{31}$ , are reduced to zero, and  $[Q]$  becomes

$$\begin{bmatrix} E_{11} & E_{12} & 0 & 0 & 0 \\ E_{12} & E_{22} & 0 & 0 & 0 \\ 0 & 0 & 2G_{12} & 0 & 0 \\ 0 & 0 & 0 & 0 & 0 \\ 0 & 0 & 0 & 0 & 0 \end{bmatrix} \quad (10.25)$$

### 10.3.4 Numerical Example (Composite Plate)

This example deals with a simply supported square cross-ply laminated plate subjected to a uniform pressure  $p_0$ . The structure and configuration are shown in Figure 10.5. The composite material is a 0/90/90/0 Graphite/Epoxy (T300/5208). There are totally 18 basic random variables. They are strength properties  $X_T$ ,  $X_C$ ,  $Y_T$ ,  $Y_C$ ,  $S$ , and  $S_Z$ ; material properties  $E_X$ ,  $E_Y$ ,  $E_Z$ ,  $G_{XY}$ ,  $G_{YZ}$ , and  $G_{ZX}$ ;  $\nu_{XY}$ , the loading  $p_0$ ; and the configuration properties (ply orientations and thicknesses). (See Reference [10] for details of this numerical example.) All the variables are assumed to be normally distributed, for the sake of illustration. This is not a limitation of the method. Other types of distributions can also be used.

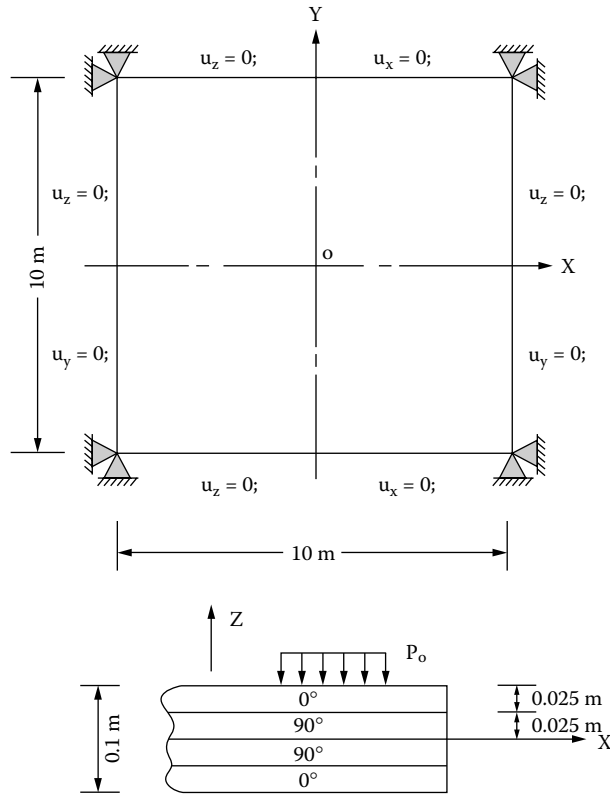


**FIGURE 10.5** Composite plate with transverse loading.

The stresses are computed using finite element stress analysis, using the software ANSYS. The 8-node shell element SHELL99 is used, which is capable of modeling the multiple plies in the laminate. The stresses,  $\sigma_X$ ,  $\sigma_Y$ ,  $\sigma_Z$ ,  $\sigma_{XY}$ ,  $\sigma_{YZ}$ , and  $\sigma_{ZX}$ , used in the failure criteria are average values of stresses at the element nodes in the middle of each layer. The component performance functions in Equation 10.20 to Equation 10.22 are used, corresponding to the three ply failure modes of fiber breakage, matrix cracking, and delamination.

The first-order reliability method using the Rackwitz–Fiessler algorithm is used to estimate the failure probability of each component. In searching for the significant failure sequences, the branch-and-bound method is employed and a cutoff value of  $= 0.5$  is selected. System failure (structure collapse) is assumed if fiber breakages take place across the entire width of the plate.

Figure 10.6 and Figure 10.7 show the structural damage in the most dominant failure sequence and the corresponding failure probabilities, respectively. It is seen that the damage of the composite plate begins with matrix cracking in some plies and elements. After some damage accumulation, the first fiber breakage failure occurs. Further structural damage becomes faster because of higher failure probabilities of the failed components after the first fiber breaks. When the second fiber breaks, the structural damage becomes much faster because of much higher failure probabilities. When the third fiber breaks, the whole structure is regarded as failed because fiber failures have crossed the entire width of the plate at this state. Figure 10.7 shows that component failure probability changes with progressive structural damage. It can be seen that after each fiber failure, the failure probability of the next component shows a remarkable increase. This is consistent with the fact that fiber failure is a major failure event, leading rapidly to overall structural system failure.

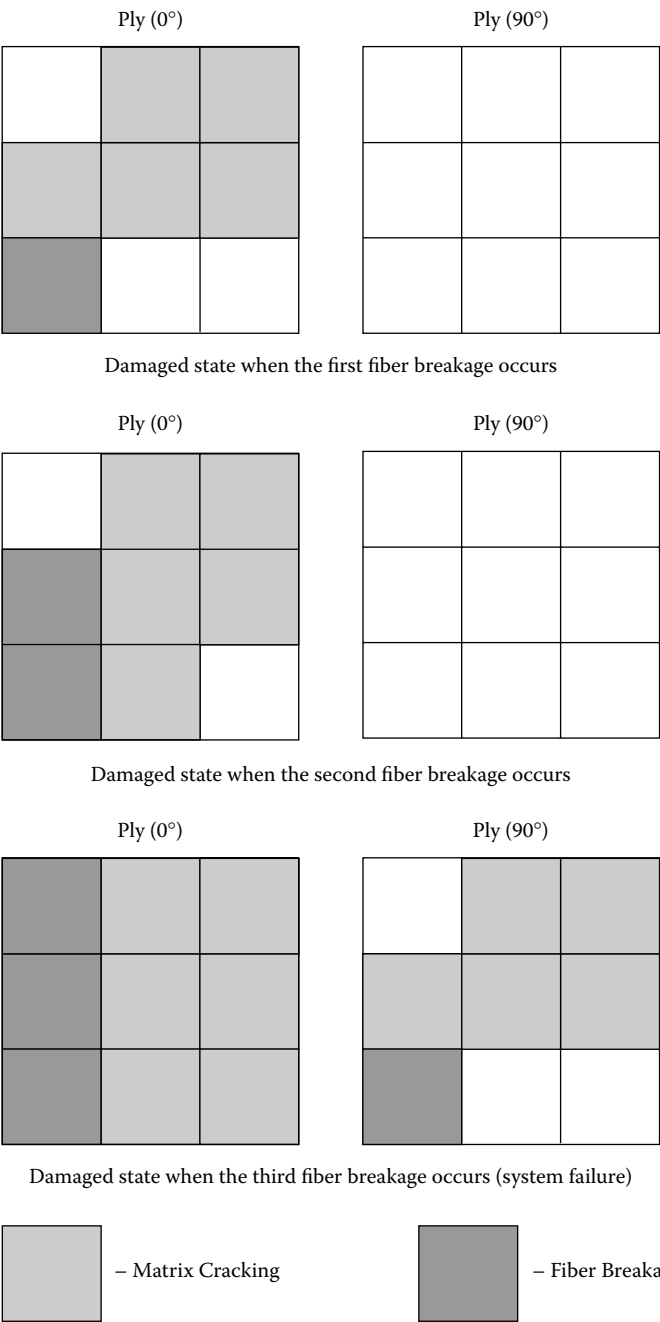


FIGURE 10.6 Progressive damage in a composite plate.

Several other significant sequences are also obtained, but it is seen that they are very similar to the first identified failure sequence. The computed results indicate that these significant sequences consist of common components with slight changes in the order of failed components. Thus, it is reasonable to assume that there are high correlations among these failure sequences and that the overall system failure probability may be approximated by the probability of the first identified failure sequence.

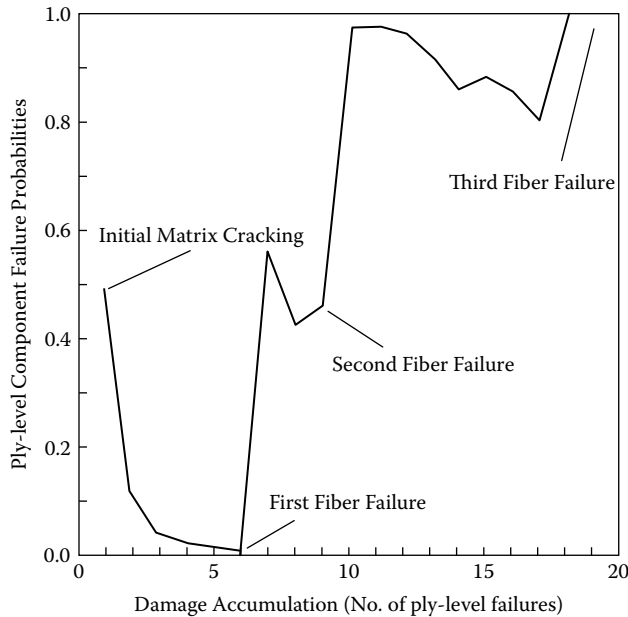


FIGURE 10.7 Ply-level failure probability change with progressive damage.

## 10.4 Strength Limit State: Approximations

The reliability method followed in Section 10.2 and Section 10.3 is applicable in general to the probabilistic ultimate strength analysis of any structure. However, this procedure is computationally time consuming for large structures with many components, where the structural analysis is carried out through a finite element code with numerous finite elements. In the case of composite structures, the brittleness of the failures and the correlation between different failures and sequences can be used advantageously to introduce several techniques and approximations that make the method efficient and practical for ultimate strength reliability analysis. These are discussed in this section.

### 10.4.1 Fast Branch-and-Bound Method

When there are a large number of components in a structural system, which is the case for composite structures, the basic branch-and-bound method described in Section 10.2 becomes time consuming and tedious. In the original method, only one component failure is imposed at each damaged stage so that a large number of steps is required to complete a failure sequence. This makes the basic branch-and-bound method difficult to apply in practice.

The following strategy may be used to speed up the enumeration procedure. The different component limit states share many common random variables related to loading and material properties. Therefore, the component limit state functions in any structure are correlated. This implies that if a component fails, then the probability is high that other components that are highly correlated with this component may also fail subsequently. Therefore, in the failure sequence enumeration, several component failures (instead of only one failure) may be imposed together as a group at each damage stage.

For a group of strongly correlated components, the component having the highest failure probability is selected to be representative of the group at the current damage state. Other components in the group are identified using a conditional probability criterion:

$$P(E_i/E_k) \geq \lambda_0 \quad i = k+1, \dots, n \quad (10.26)$$

where  $\lambda_0$  is a chosen cutoff value;  $E_k$  stands for the event of failure of the component  $k$ ;  $E_i$  denotes the event of failure in the  $i$ th component among the remaining  $n-k$  components; and  $P(E_i/E_k)$  is the probability of event  $E_i$  given that the event  $E_k$  has occurred. The failure probability for the group of components is approximated by the failure probability of the representative component. All the components in the group are removed at the same time, and the structure is reanalyzed with the remaining components.

The other steps in the failure sequence search are the same as those in the original branch-and-bound method. This concept of grouping can drastically reduce the number of damage states and, hence, the number of structural reanalyses. Therefore, this method may be referred to as a fast branch-and-bound method. Xiao and Mahadevan [18], who proposed this method, found that for even a small problem with 18 possible component failures, the fast branch-and-bound method requires only 0.6% of the computational time taken by the original branch-and-bound method. The savings in computational time grows with the size of the problem.

### 10.4.2 Deterministic Initial Screening

Any component failure could be the starting point of a failure sequence. However, in the branch-and-bound enumeration, only component failures with high probability of occurrence are generally the starting points of the dominant failure sequences. The computation of the probability  $P(g < 0)$  corresponding to each component failure involves several iterations of structural analysis to find the minimum distance point, if FORM or SORM are used. (Monte Carlo simulation requires many more structural analyses.) For large structures with numerous components, this first step in failure sequence enumeration is quite time consuming. Therefore, an efficient idea is to observe that the components with higher failure probabilities are in general likely to have the  $g$  values closer to zero, when the structure is analyzed at the mean values of the random variables. Therefore, the starting points of the dominant failure sequences may be selected using deterministic structural analysis at the mean values, and by choosing only those component failures with  $g$  values below a cutoff value. Note that this strategy is simply to select the starting points of the sequences, not for the final probability computation. Therefore, it will provide significant reduction in computational effort, with minimal impact on the accuracy of the probability result.

Note that the probability-based criterion for all component failures is much more rigorous and accounts for the variation in random variable sensitivities; that is, some component failures that may appear insignificant with a deterministic criterion may become significant with a probabilistic criterion. Therefore, the deterministic screening should be done carefully, so that probabilistically significant events do not get discarded. Mahadevan and Liu [19] adopted the following strategy. The limit state value, calculated at the mean values of the random variables, is used for selecting the 20 most likely component failures at each stage. Then, the 20 component failures are subjected to probabilistic analysis, and only the component failure with the highest probability among these 20 is used to start the fast branch-and-bound enumeration of the most probable failure sequence. Thus, the failure sequence enumeration is in fact probabilistic, except for the initial screening where component failures are ignored based on their  $g$  values instead of their probabilities.

### 10.4.3 Weakest-Link Model

As seen in Section 10.2, the various significant failure sequences are very similar in the list of failed components, which implies that there are strong correlations among these failure sequences. When the sequences are very similar, the system failure probability may be approximated using the most probable sequence, i.e., by Cornell's first-order lower bound. In that case, only one significant failure sequence might provide an adequate estimate of system failure probability. Therefore, instead of enumerating many failure sequences, it may be adequate to stop after the first significant failure sequence is identified. This provides tremendous savings in the computational effort of structural reanalysis corresponding to numerous steps of progressive failure in multiple sequences.



#### 10.4.4 Critical Component Failure

Strictly speaking, a structural system failure is defined to be the collapse of the entire structure. Section 10.3 has shown that a failure sequence from initial failure to system final failure involves a large number of ply-level components. Thus, the search for even a single complete sequence is quite time consuming. Therefore, Mahadevan and Liu [19] proposed another approximation to avoid tedious and expensive computation.

It is assumed that there exists a critical component for the structure. This critical component should have a failure probability much lower than the other components that fail after the critical component. The components with higher failure probabilities will easily fail once the critical one fails. In other words, the critical component failure is not far from the entire system failure. As a result, the structural system failure can be approximately defined to be the failure of the critical component.

The assumption of a critical failure to approximate system failure is quite reasonable for laminated composites. The overall probability of the sequence is computed as the probability of the intersection of the component events in that sequence. The probability of the intersection of several events is dominated by the low-probability events [17], which are usually present before the first critical failure. After this critical failure, the probabilities of subsequent failures are much higher, and thus do not make a significant contribution to the probability computation. As an example, consider the plate structure made of composite laminates considered in Section 10.3. It is seen that after the first fiber failure (which has the lowest probability), the probabilities of the subsequent events are significantly increased. The overall probability of the sequence is dominated by the low-probability events up to the first fiber failure, and is closely approximated by the probability of the intersection of the first fiber failure and a few matrix cracking failures immediately preceding it. Therefore, considering probability computation, it appears adequate to terminate the exploration of the failure sequence at the first critical failure.

With the preceding assumption, a large amount of computation after the failure of the critical component can be avoided, and the prediction of ultimate failure probability will have adequate accuracy. The grouping concept, deterministic screening, and the weakest-link approximations of the previous subsections provide additional computational efficiency. Thus, the approximations may be summarized as follows:

1. Start from the intact structure. Calculate the values of the performance functions ( $g$  functions) for all the components, and sort the values in descending order. Select the first several components with small  $g$  values to be explored, using a suitable cutoff value for  $g$  (deterministic initial screening).
2. Estimate the failure probabilities of the selected components, and arrange them in descending order of probability values. Select the component with the highest failure probability and other components with high correlation to this first component (fast branch-and-bound).
3. Simulate failure of the selected components by modifying the corresponding structural stiffness terms, and reanalyze the damaged structure to compute the failure probabilities of the remaining components.
4. Repeat steps 2 and 3 until the critical component fails.
5. Approximate system failure probability using the failure probability of the sequence identified in steps 2, 3, and 4.

#### 10.4.5 Numerical Example: Aircraft Wing

An aircraft composite wing composed of skin and stringer components and consisting of center, leading edge, and trailing edge is shown in Figure 10.8. The stringer is constructed in both longitudinal and transverse directions. The data for this example were taken from Shiao and Chamis [1], who computed FPF probability. Mahadevan and Liu [19] computed the system failure probability using the methods in this section.

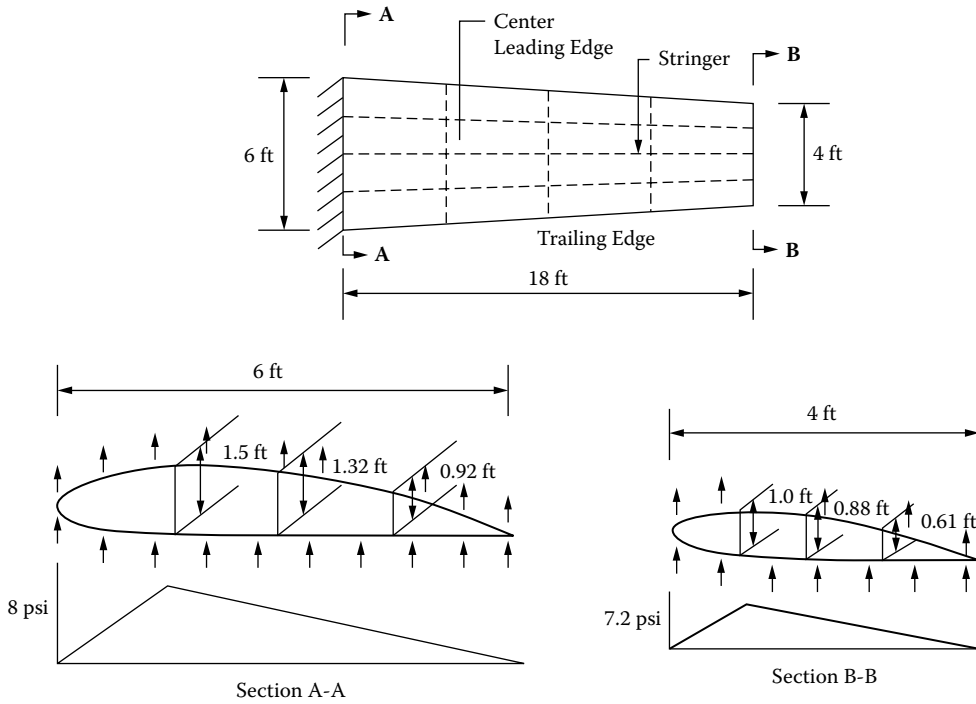


FIGURE 10.8 Composite aircraft wing: geometry and loading.

In Figure 10.8, the left end (section A-A) is fixed, and the right end (section B-B) is free. The air pressure is assumed to be triangularly distributed along the transverse direction of the wing, and linearly distributed along the longitudinal direction. The ply-level stiffness properties, material strengths, ply thicknesses and orientations, and the pressure loads are all assumed to be random variables. A laminate configuration of  $[0^\circ/-45^\circ/90^\circ/45^\circ/0^\circ]$  is used for the skin and  $(0^\circ)_5$  for the stringer. The statistical distribution of a variable is assumed to be lognormal for the strength parameters and normal for the rest, with a coefficient of variation of 0.10. A standard deviation of  $2^\circ$  is used for the ply angles. See Reference [19] for detailed data, finite element modeling, and results of this numerical example.

For the fast branch-and-bound method,  $\lambda = 0.4$  is used in this example, only for the sake of demonstration. The choice of  $\lambda$  has to be based on a trade-off between accuracy and efficiency. A larger value of  $\lambda$  reduces the number of failures in the grouping operation, and therefore makes the computation more expensive, but more accurate. For specific applications, the variation of failure probability estimate and computational effort with  $\lambda$  may be investigated, and an optimum value may be chosen.

The first significant failure sequence identified using the fast branch-and-bound method is used for ultimate strength failure probability estimation, using the weakest-link model. The following notation is used to identify the ply-level failures: for example,  $85_{2M}$  stands for finite element number 85, ply number 2, and matrix cracking failure mode;  $37_{1F}$  stands for finite element number 37, ply number 1, and fiber breakage failure mode. The computed results are summarized in Table 10.1.

At each stage of damage, a few highly correlated components are chosen to fail together. Structural failure proceeds through progressive damage accumulation as shown in Table 10.1. Damage accumulates in the zones near the fixed end and at the center of the skin. The structure experiences eight stages of damage before undergoing the first fiber failure. In the damage process, the failure probability of each damage stage decreases with damage accumulation up to the first fiber breakage occurrence. Probabilistic analysis was also carried out for the ninth damage stage. Its representative failure probability was increased to 0.028, which is much higher than the one prior to it. This indicates that the first fiber failure is likely to be a severe or critical failure

**TABLE 10.1** Structural Progressive Damage Stages

Damage Stage	Failed Components	Representative Failure Probability
1st	85 <sub>2M</sub> , 85 <sub>4M</sub> , 86 <sub>4M</sub> , 86 <sub>2M</sub>	0.2820
2nd	37 <sub>2M</sub> , 37 <sub>4M</sub> , 87 <sub>4M</sub> , 38 <sub>2M</sub> , 73 <sub>2M</sub> , 97 <sub>4M</sub>	0.0903
3rd	87 <sub>2M</sub> , 49 <sub>4M</sub> , 97 <sub>2M</sub> , 25 <sub>4M</sub> , 98 <sub>2M</sub>	0.0451
4th	98 <sub>4M</sub> , 25 <sub>2M</sub> , 50 <sub>4M</sub> , 49 <sub>2M</sub> , 26 <sub>4M</sub> , 73 <sub>4M</sub> , 26 <sub>2M</sub> , 38 <sub>4M</sub>	0.0338
5th	74 <sub>2M</sub> , 85 <sub>3M</sub> , 39 <sub>2M</sub> , 74 <sub>4M</sub> , 88 <sub>4M</sub> , 89 <sub>2M</sub> , 88 <sub>2M</sub> , 86 <sub>3M</sub>	0.0156
6th	99 <sub>4M</sub> , 39 <sub>4M</sub> , 50 <sub>2M</sub>	0.0036
7th	51 <sub>4M</sub> , 13 <sub>2M</sub> , 13 <sub>4M</sub>	0.0029
8th	37 <sub>3M</sub> , 14 <sub>4M</sub> , 75 <sub>2M</sub> , 14 <sub>2M</sub> , 27 <sub>4M</sub> , 85 <sub>1F</sub> , 89 <sub>4M</sub> , 85 <sub>5F</sub>	0.0010

for the entire structure. After this critical event, the structure will rapidly proceed to final failure. This implies that the exploration of the failure sequence may be terminated after this first severe failure.

Three damage levels with the lowest failure probabilities, namely the sixth, seventh, and eighth damage levels, dominate the computation of the system failure probability. The computed correlation coefficient matrix between the limit states representing these three events is:

$$[\rho_{ij}] = \begin{bmatrix} 1 & \cdots & Sym \\ 0.99 & 1 & \cdots \\ 0.71 & 0.70 & 1 \end{bmatrix} \quad (10.27)$$

The corresponding individual event failure probabilities and the two-event joint failure probabilities are obtained as:

$$[P_{ij}] = \begin{bmatrix} 0.0036 & \cdots & Sym \\ 0.0026 & 0.0029 & \cdots \\ 0.0003 & 0.0003 & 0.001 \end{bmatrix} \quad (10.28)$$

where  $P_{ij}$  refers to the joint probability of the  $i$ th and  $j$ th failures (the off-diagonal terms in the matrix). The diagonal terms in the matrix ( $i = j$ ) refer to the individual failure probabilities.

Using only the two-event joint probabilities, the second-order upper bound formula suggested by Murotsu [9] is used to estimate the system failure probability as

$$P_f = 2.977 \times 10^{-4} \quad (10.29)$$

Using the three-event joint probability, the third-order estimate for the system failure probability is obtained as

$$P_f = 2.957 \times 10^{-4} \quad (10.30)$$

These two results are quite close to each other, as expected. For this reason, most system reliability studies report only second-order estimates.

## 10.5 Fatigue Limit State: Material Modeling

Many applications of composite materials involve components that are subjected to cyclic loading. Cyclic loading causes damage and material property degradation in a cumulative manner. Considerable research on fatigue behavior has been carried out for monolithic materials such as metals, and progress has been

made in devising fatigue-resistant materials as well as in developing methodologies for life prediction. For composite materials, fatigue analysis and consequent life prediction become difficult because the material properties of the constituents of the composite are quite different. The fatigue behavior of one constituent may be significantly affected by the presence of other constituents and the interfacial regions between the fibers and matrix. Fatigue properties of composites may vary significantly because of the large difference in the properties between the fibers and matrix of the composite and the composition of constituents.

Fatigue analysis of composite materials is difficult because of several basic characteristics of the composite material. However, many attempts have been made for fatigue modeling and life prediction of fiber-reinforced polymers. Degrieck and Van Paepegem [20] classify existing fatigue models into three categories: fatigue life models (S-N curves), residual strength or residual stiffness models, and progressive damage models.

The fatigue life model is established based on S-N curves or Goodman diagrams. This approach does not consider the details of the damage mechanism. It is entirely empirical and needs a lot of experimental data. For every variation in laminates (different stacking sequence and ply orientation), a new set of specimens is needed to develop the S-N curves, thus making this approach expensive and time consuming. However, this methodology is easy to apply, and many commercial software packages are available for use. The failure criteria mimic the form of static strength criteria, based on two major failure modes (fiber failure and matrix failure) [21, 22]:

$$\sigma_1 = \sigma_1''$$

$$\left( \frac{\sigma_2}{\sigma_2''} \right)^2 + \left( \frac{\tau}{\tau''} \right)^2 = 1 \quad (10.31)$$

where  $\sigma_1$  and  $\sigma_2$  are the stresses along the fiber direction and transverse to the fiber direction, respectively, and  $\tau$  is the shear stress.  $\sigma_1''$ ,  $\sigma_2''$ , and  $\tau''$  are the ultimate strengths of the three stress components. These strengths are functions of the stress level, stress ratio, and the number of stress cycles. The relationship is expressed in S-N curves from previous experimental data.

Wu [23] and Jen and Lee [24] proposed different failure criteria based on the Tsai–Hill criterion. Philippidis and Vassilopoulos [25] proposed a failure criterion based on the Tsai–Wu criterion. All these methods use the fatigue strength (corresponding to a given N, from the S-N curves) instead of the ultimate strength in the Tsai–Hill or Tsai–Wu criteria.

Other researchers directly use the family of S-N curves to calculate the fatigue life [26–28]. The family of S-N curves includes stress ratio, load frequency, and other factors affecting the shape of the S-N curves. The main objective is to use the same computing methodology to account for different loading conditions.

The residual strength or residual stiffness model is based on damage mechanics, which relates fatigue failure to the damage evolution process. The degradation of stiffness or strength is correlated with a damage variable (damage index). Different damage evolution functions [29–35] have been suggested based on some assumptions or experimental results. The failure is assumed to occur when the cumulative damage reaches a critical value (usually unity). The general form of the damage accumulation rule is:

$$\frac{dD}{dN} = f(D, \sigma_i, \epsilon_i, N \dots) \quad (10.32)$$

where  $D$  is the damage index,  $\sigma_i$  and  $\epsilon_i$  are the stress and strain components, and  $N$  is the number of load cycles. The parameters in the damage model are calibrated through experimental observations or through assumptions based on experience and judgment.

Unlike the preceding two approaches in fatigue analysis, which are at the macroscopic level, the progressive failure model considers local damage mechanisms, such as delamination, local ply buckling,

and fiber breakage. All these local damage mechanisms lead to damage accumulation in the macroscopic material. Global failure occurs once the damage introduced by the local failure exceeds the global allowable level. This method is computationally complicated because it accounts for many failure mechanisms and is also related to damage accumulation. Tserpes et al. [36] derived a progressive damage model that includes seven local failure modes, including material stiffness degradation.

The fatigue life model is easy to use and has an experimental database. Also, commercial software is available to calculate the fatigue life. However, this model requires a lot of experimental work, the cost of which is sometimes prohibitive. Most of the fatigue life models do not consider damage accumulation and are difficult to extend to complicated loading conditions.

The residual strength and the stiffness model consider damage accumulation. The idea of the residual strength model is simple and easy to apply. However, the damage evolution function is assumed and calibrated through constant amplitude tests. For composite materials, the damage mechanism is different under different stress levels and also depends on the load sequence. It is hard to use a simple damage accumulation rule to describe the damage evolution under complicated loading conditions.

The progressive model seems to be more accurate because it accounts for the detailed failure mechanism of the composite material. However, for accurate analysis, this model requires that the damage introduced by local failure be correlated with the material properties' degradation. A quantitative relationship in this regard is difficult to find and needs extensive experimental data. Also, this model is computationally expensive and complicated, and thus is difficult to apply directly to engineering designs.

Many experimental studies have been reported for obtaining the fatigue properties of different types of composite materials since the 1960s. Based on these experimental results, empirical S-N curves have been derived between stress and fatigue life. These relationships have been suggested for use in design [37]. Both linear and nonlinear S-N curves have been proposed based on the experimental results [38–40]. A nonlinear curve between strain and fatigue life is also used to predict the fatigue life of composite materials [41–43]. The following relationship is widely used:

$$S = m \log N + b \quad (10.33)$$

where  $m$  and  $b$  are parameters related to material properties.

With the predicted fatigue life under constant cyclic loading, fatigue damage can be evaluated after a given number of cycles with a fatigue damage accumulation model. The composite is assumed to fail when the accumulated damage exceeds the critical level of damage.

### 10.5.1 Fatigue Damage Modeling

For homogeneous, or monolithic, materials with isotropic material properties, damage is accumulated at a low growth rate in the beginning, and a single crack propagates in a direction perpendicular to the cyclic loading axis. On the other hand, in composite materials, especially for structures with multiple plies and laminates, the fracture behavior is characterized by multiple damage modes, such as crazing and cracking of the matrix, fiber/matrix decohesion, fiber fracture, ply cracking, delamination, void growth, and multidirectional cracking. These modes appear rather early in the fatigue life of composites.

The mechanisms of crack initiation and crack growth are quite complex for composite materials. Even for unidirectional reinforced composites under the simple loading case such as tension along the direction of fibers, cracks can initiate at different locations and in different directions. Cracks can initiate in the matrix, perpendicular to the direction of loading. Cracks can also initiate in the interface along the directions of fibers between the fibers and matrix due to debonding. Many experimental fatigue tests have been carried out to study crack growth in composites when there is only one dominant crack that is propagating. The crack propagates in the same plane and direction as the initial crack. Paris' law has been used to describe this fatigue crack propagation behavior, but this is limited to unidirectional aligned fiber reinforced composites. For more general laminates, a similar mode of crack propagation cannot be

obtained even under simple loading. Thus, traditional fracture mechanics cannot be used for fatigue analysis of composite materials.

The concept of damage accumulation may be used as a more suitable approach to predicting the fatigue life of structures of composite materials. However, fatigue damage cannot be measured directly. Therefore, for quantitative evaluation of fatigue damage, change in Young's modulus or stiffness is often used to evaluate the fatigue damage due to cyclic loading. For example, fatigue damage may be defined in terms of Young's modulus as [44]:

$$D = \frac{E_0 - E}{E_0 - E_f} \quad (10.34)$$

where  $D$  is the accumulated fatigue damage (also called damage index),  $E_0$  is the initial Young's modulus of the undamaged material,  $E_f$  is the Young's modulus when fracture occurs, and  $E$  is the Young's modulus at any stage. According to Equation 10.34, the accumulated damage will be in the range between 0 and 1.

As previously mentioned, the complexity of composites leads to the presence of many modes of damage. These modes appear at the early stages of the fatigue life. The damage accumulates rapidly during the first few cycles. During this stage, microcracks initiate in multiple locations in the matrix. Debonding occurs at the weak interfaces between fibers and matrix. Also, some fibers with low strength may break during this stage. The next stage shows a slow and steady damage growth rate. Finally, the damage again grows rapidly during the last stage before the fracture occurs. Figure 10.9 shows schematically a comparison of damage accumulation in composite materials and homogeneous materials as a function of the fatigue cycle ratio. The Young's modulus measured from fatigue tests also shows the same characteristics of damage accumulation [45–47]. Figure 10.9 is plotted in terms of the damage index versus cycle ratio, where the damage index is defined in Equation 10.34. The cycle ratio is the number of cycles at a given instant divided by the fatigue life.

A linear damage summation model was first used to evaluate the fatigue behavior of composite materials by Nicholas and Russ [48]. Halverson et al. [45] used a power function in terms of the cycle ratio to evaluate the remaining strength of the material and to calculate the fatigue life:

$$F_r = 1 - (1 - F_a) \left( \frac{n}{N} \right)^j \quad (10.35)$$

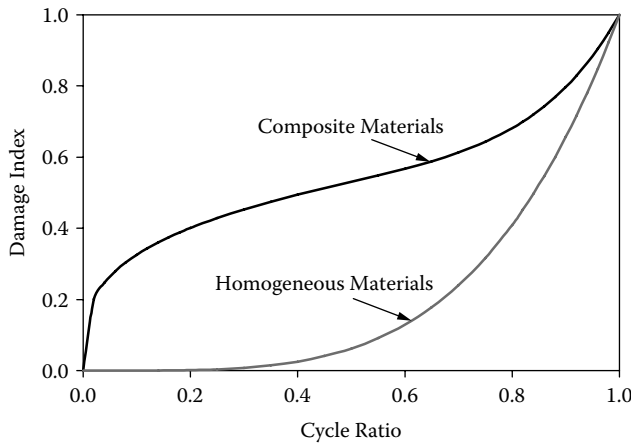


FIGURE 10.9 Fatigue damage accumulation: metals vs. composites.

where  $F_r$  is the normalized remaining strength (normalized by the undamaged static strength),  $F_a$  is the normalized applied load (also normalized by the undamaged static strength),  $j$  is a material constant, and  $n$  is the number of cycles of applied load.  $N$  is the fatigue life of a constant load. Then, according to the definition of damage in Equation 10.32, the mathematical function for damage accumulation will also be a power function of the cycle ratio:

$$D = (1 - F_a) \left( \frac{n}{N} \right)^j \quad (10.36)$$

Once the residual strength is computed, the degradation of the material can be described with Equation 10.34 or Equation 10.35. Other nonlinear damage accumulation functions have also been used. These nonlinear damage accumulation functions are able to capture the characteristics of rapid damage growth either at the early stages of life or near the end of life, but not both. For example, the damage model of Subramanian et al. [42] explains the fast damage growth during early loading cycles but does not accurately describe the rapid damage growth close to the material fracture. Halverson et al. [45] model the characteristics of rapid damage growth at the end of fatigue life of the material. But the model is not accurate during the early loading cycles.

Mao and Mahadevan [44] proposed a versatile new damage accumulation model for accuracy in both the early and final stages of life as

$$D = q \left( \frac{n}{N} \right)^{m_1} + (1 - q) \left( \frac{n}{N} \right)^{m_2} \quad (10.37)$$

where  $D$  is the normalized accumulated damage;  $q$ ,  $m_1$ , and  $m_2$  are material-dependent parameters;  $n$  is the number of applied loading cycles; and  $N$  is the fatigue life at the corresponding applied load level. The characteristics of rapid damage accumulation during the first few cycles can be captured with the first term, with  $m_1 < 1.0$ . The second term shows the fast damage growth at the end of fatigue life with  $m_2 > 1.0$ .

The parameters in Equation 10.37 are defined in terms of fatigue life of interest as

$$q = \frac{A \left( \frac{N_0}{N} \right)^\alpha}{1 - (1 - A) \left( \frac{N_0}{N} \right)^\alpha} \quad (10.38)$$

$$m_1 = \left( \frac{N_0}{N} \right)^\beta \quad (10.39)$$

$$m_2 = \left( \frac{N}{N_0} \right)^\gamma \quad (10.40)$$

where  $N_0$  is the reference fatigue life. The parameters  $\alpha$ ,  $\beta$ , and  $\gamma$  are material-dependent constants. These parameters can be obtained with fatigue experimental data. Once the damage indices are obtained during the fatigue tests, regression analysis can be carried out to obtain the parameters  $q$ ,  $m_1$ , and  $m_2$ . Then, parameters  $\alpha$ ,  $\beta$ , and  $\gamma$  can be calculated using Equation 10.38 to Equation 10.40.

Two sets of experimental results were used by Mao and Mahadevan [44] to demonstrate the performance of the damage accumulation model in Equation 10.35. The first set was with 810 O laminates (Subramanian et al. [42]), and the second one was with a woven composite. The Young's moduli of the

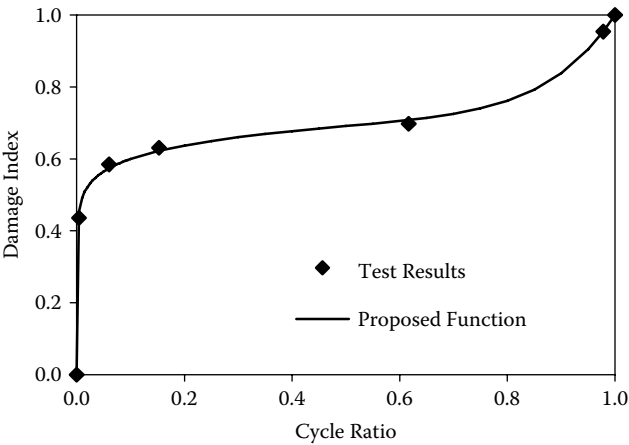


**FIGURE 10.10** Experimental observation and model prediction of damage index for 810 O laminates (75% loading level).

laminated composite were measured after different numbers of cycles of tensile fatigue loading, and the corresponding damage indices were computed according to Equation 10.34.

The experimental results and the proposed model showed excellent agreement, as seen in Figure 10.10. Next, parameters for the damage model at the 80% loading level were obtained with the values of  $\alpha$ ,  $\beta$ , and  $\gamma$  obtained at the 75% loading level. Again, the predicted damage results agreed very well with the experimental results, as seen in Figure 10.11.

Kumar and Talreja [47] conducted tension-tension fatigue experiments on the AS4/PR500 5 harness satin weave composite laminates at a frequency of 10 Hz and  $R$  ratio of 0.1 to study the fatigue behavior of the composite material. Tension fatigue tests were conducted on the symmetric  $(0/90_{2w})$  laminates. Two types of specimens, unaged and 6000 hours aged, were tested. Young’s modulus of the material was measured after different numbers of fatigue cycles. For this material also, the damage accumulation model of Equation 10.35 did an excellent job of capturing the characteristics of the damage evolution, as seen in Figure 10.12. (See Mao and Mahadevan [44] for details.)

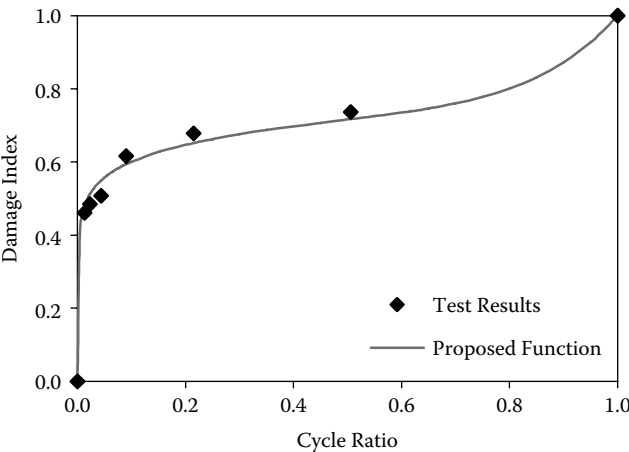


**FIGURE 10.11** Experimental observation and model prediction of damage index for 810 O laminates (80% loading level).



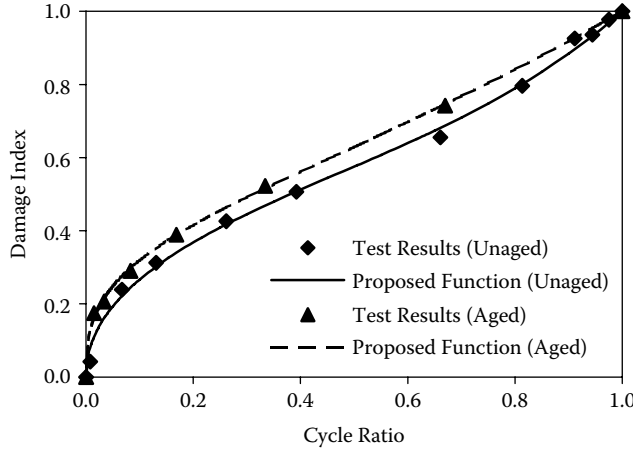


FIGURE 10.12 Experimental observation and model prediction for AS4/PR500 woven composite.

## 10.6 Multiaxial Fatigue

A simple and versatile model based on damage mechanics was suggested by Liu and Mahadevan [49] for the multiaxial fatigue life prediction of laminated composites. It is basically an S-N curve-based fatigue progressive damage model and ignores the detailed analysis of the local failure. It uses fatigue data from the family of S-N curves and uses a special damage variable to account for the multiaxial fatigue in each ply.

For general fatigue calculation using S-N curves, first, a set of experiments is conducted considering different stress levels and specimen geometries. Then, the fatigue life and applied stress level are plotted together. A curve-fitting method is used to find the relation between the fatigue life and stress level. The empirical relationship is then used to predict the fatigue life of the real structure [50]. In this study, the maximum cyclic stress is used to correlate with the fatigue life under different stress ratios. The general formula is:

$$S_{\max} = A_R \cdot \log(N) + B_R$$

$$R = \frac{S_{\max}}{S_{\min}} \quad (10.41)$$

where  $S_{\max}$  and  $S_{\min}$  are the maximum and minimum cyclic stresses,  $R$  is the stress ratio,  $N$  is the fatigue life, and  $A_R$  and  $B_R$  are the strength coefficients corresponding to the stress ratios. Actually, Equation 10.41 is a family of S-N curves, which are expressed in a semi-log manner.

The foregoing description is for one-dimensional constant-amplitude loading. The damage concept is needed for multidimensional complicated loading conditions. In damage mechanics, damage evolution is expressed through the material property degradation process. When the damage reaches unity, the whole material is assumed to fail. The damage increases monotonically as the loading history increases. Under cyclic fatigue loading, the damage is usually expressed as the fraction of the number of failure cycles. A linear damage accumulation function, Miner's rule, is popularly used:

$$D = \sum_{i=1}^K D_i = \sum_{i=1}^K \frac{n_i}{N_{fi}} = 1 \quad (10.42)$$

where  $K$  is the number of variable loading stages,  $D_i$  is the damage caused in each loading stage,  $n_i$  is the number of cycles in the  $i$ th loading stage, and  $N_{fi}$  is the constant amplitude fatigue life estimated from Equation 10.41.

For multidirectional composite laminates, each ply is generally under a multiaxial stress. One way to calculate the fatigue life is to perform the fatigue experiment under different stress states to get the S-N curves. Because of the large number of possible combinations of each stress component, this method is impractical. Therefore, a new damage index is suggested based on the Tsai–Hill static strength failure criterion, for which only the experiment for unidirectional laminates is required and the fatigue life for a general stacking sequence and ply orientation can be predicted based on the model. The Tsai–Hill criterion is for a single ply in the form of Equation 10.43 [51]:

$$\frac{\sigma_1^2}{F_1^2} + \frac{\sigma_2^2}{F_2^2} + \frac{\tau_6^2}{F_6^2} - \frac{\sigma_1\sigma_2}{F_1^2} = 1 \quad (10.43)$$

where  $\sigma_1$  and  $\sigma_2$  are the stresses along the fiber direction and transverse to the fiber direction respectively;  $\tau_6$  is the shear stress; and  $F_1, F_2$ , and  $F_6$  are the static strengths of different directions.

The damage in a single ply caused in one cycle under the stress state  $(\sigma_1, \sigma_2, \tau_6)$  is assumed to have the form:

$$D_i = \sqrt{\frac{1}{(N_{fi}^1)^2} + \frac{1}{(N_{fi}^2)^2} + \frac{1}{(N_{fi}^6)^2} + \frac{1}{N_{fi}^1 N_{fi}^2}} \quad (10.44)$$

where  $N_{fi}^1, N_{fi}^2$ , and  $N_{fi}^6$  are the fatigue lives estimated for unidirectional laminates under pure stress components  $\sigma_1, \sigma_2$ , and  $\tau_6$ , respectively. The sign for the normal stress interactive term is chosen as positive in considering the monotonically increasing damage. As shown in Equation 10.44, the fatigue experiments are only needed along the longitudinal direction, along the transverse direction, and under shear loading for unidirectional laminates.

Using the new damage index, Miner's rule is rewritten as:

$$D = \sum_{i=1}^K D_i = \sum_{i=1}^K n_i \sqrt{\frac{1}{(N_{fi}^1)^2} + \frac{1}{(N_{fi}^2)^2} + \frac{1}{(N_{fi}^6)^2} + \frac{1}{N_{fi}^1 N_{fi}^2}} \quad (10.45)$$

Equation 10.45 is the general form for multiaxial fatigue damage accumulation. The ply is assumed to fail if the accumulated damage index exceeds unity.

The foregoing discussion is easily extended to a laminate with multiple plies, along the following steps. Divide the total loading history into several blocks. In each block, check the failure of each ply using Equation 10.45. If no failure occurs, accumulate the fatigue damage for each ply caused in this block and progress to the next step. If failure occurs, assume that the ply strength and stiffness decrease to zero. Then update the global stiffness matrix and progress to the next step. The computation is continued until the entire laminate fails. The number of loading cycles to failure is the fatigue life of the composite laminate.

The foregoing discussion was limited to deterministic considerations. Owing to the high randomness inherent in the composite fatigue problem [52], it is more appropriate to use a probabilistic approach to evaluate the fatigue life and reliability of the structure.

This methodology can be easily extended to probabilistic analysis. First, the material properties are treated as random variables and are randomized based on the scatter in the experimental data or on appropriate assumptions. The geometric properties of the laminate, such as the thickness and the orientation of the laminate, are also treated as random variables. Monte Carlo simulation is used to calculate the fatigue life distribution. Under different load levels, a certain number of Monte Carlo samples are used to calculate the fatigue lives. The fatigue lives are plotted and fitted to a probabilistic distribution. Once the fatigue life distribution is obtained, it is easy to calculate the reliability at the different number of loading cycles.

Liu and Mahadevan [49] validated the foregoing model for various orientations of a glass-fiber-based composite D155, available from the U.S. Department of Energy/Montana State University (DOE/MSU) Composite Materials Fatigue Database [53]. The model prediction showed excellent agreement with the experimental data in the database. The reliability calculations were demonstrated for a balanced angle laminate ( $[\pm 45]_3$ ), using 5000 Monte Carlo simulations with four different stress levels.

## 10.7 Fatigue Delamination Limit State

Fatigue loads can initiate progressive failure in a composite laminate in various ways such as successive delamination, matrix cracking, and fiber waviness. A probabilistic analysis framework to predict the fatigue delamination reliability of composite structures may be developed along the following lines. Finite element analysis is used to compute the global and ply-level responses of the structure at the damage sites. A suitable failure model is used to evaluate the fatigue delamination limit state. A response surface approximation is constructed for the limit state, in terms of basic random variables related to input loads, material properties, and geometry. This response surface is then used with FORM, SORM, or Monte Carlo simulation to estimate the failure probability.

### 10.7.1 Failure Mechanism and Model

Consider a helicopter rotor hub test specimen shown in Figure 10.13. Hingeless, bearingless helicopter rotor hubs are being designed using laminated composite materials to reduce weight, drag, and the number of parts in the hub. During flight, the rotor hub arm experiences centrifugal loads as well as bending in the flapping flexure region. An effective elastic hinge is designed integrally to the composite rotor yoke by incorporating a tapered region between the thick and thin regions. The varying thickness of the tapered region is achieved by dropping internal plies, as shown in Figure 10.13. The thick-taper-thin geometry is tailored to give the proper flapping flexure.

Generalized test specimens have been developed to understand the basic response of the composite rotor hub yoke [54]. The specimens are geometrically simple with thick, thin, and tapered regions, as shown in Figure 10.13, and approximately one-quarter symmetry of the geometry of section A-A is considered for analysis. The specimens consist of an outside fabric layer denoted as F, continuous  $0^\circ$  belt plies denoted as B1 through B5, and discontinuous  $\pm 45^\circ$  plies denoted by D1 through D4. The specimens are subjected to a constant axial tensile load ( $P$ ) to simulate the centrifugal load, and a cyclic bending load ( $V$ ) to simulate the interaction of the rotor passage with the fuselage. The cyclic load ( $V$ ) induces an angular displacement ( $q$ ) that simulates the flexural bending in the yoke.

The ply drop in the laminate creates geometrical and material discontinuities that cause large interlaminar stresses and initiate delamination. The failure mechanism observed from this type of loading is an initial tension crack between the internal delamination at the thick-to-taper transition, where internal ply dropoffs occur.

Numerous studies have investigated computational models for delamination failure. The following discussion is limited to tapered laminates. Some studies have used stress-based criteria for modeling delamination failure [55–58]. Others have used a strain energy release rate approach [59–64]. Most of these studies have only considered delamination under pure tension, bending, or torsion loads. Very few studies have considered the combined effect of bending and tension on delamination of tapered laminated composites [54, 65].

The strain energy release rate  $G$  computed in these studies is associated with edge delamination. Finite element analysis has been used to show that once the delamination progresses beyond a distance equal to the thickness of a few plies from the edge,  $G$  reaches a constant plateau [66]. However, delamination in composite laminates may interact with other damage mechanisms such as matrix cracking and fiber bridging, and result in stable growth behavior [67]. Because a delamination is constrained to grow between individual plies, both interlaminar tension and shear stresses are commonly present at the delamination front. Therefore, delamination is often a mixed-mode fracture process. The strain energy release rate,  $G$ , generally equals the sum of  $G_I$ ,  $G_{II}$ , and  $G_{III}$ , which are interlaminar tension, sliding shear,

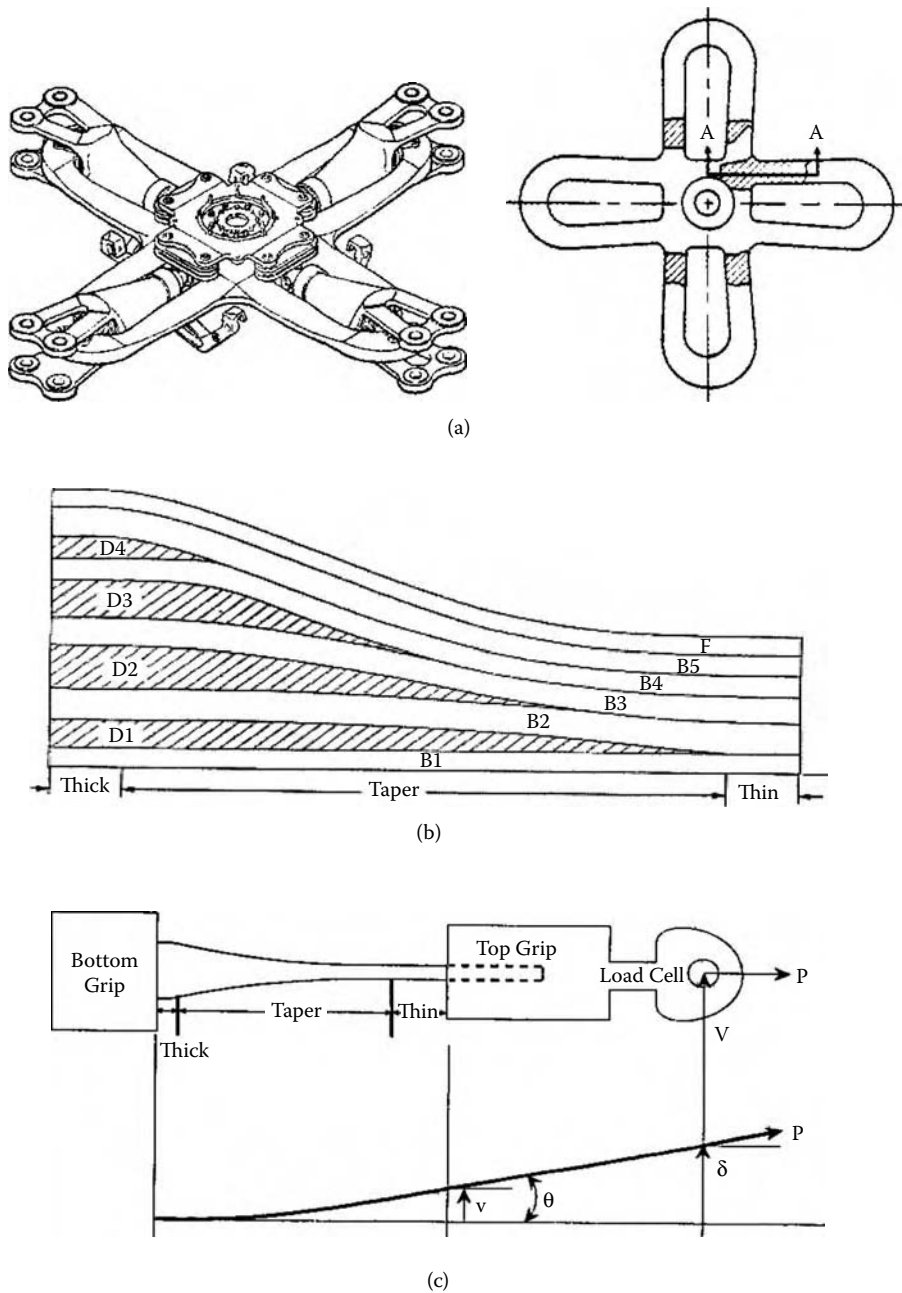


**FIGURE 10.13** Composite helicopter rotor: (a) rotor hub assembly; (b) half of the symmetric section of the test specimen; (c) typical test setup.

and scissoring shear, respectively. The effect of  $G_{III}$  is assumed to be small and may be ignored, following Murri et al. [54].

A virtual crack closure technique (VCCT) is used to calculate  $G$  at the delamination tip as shown in Figure 10.14 [68,69] such that

$$G = G_I + G_{II} \quad (10.46)$$

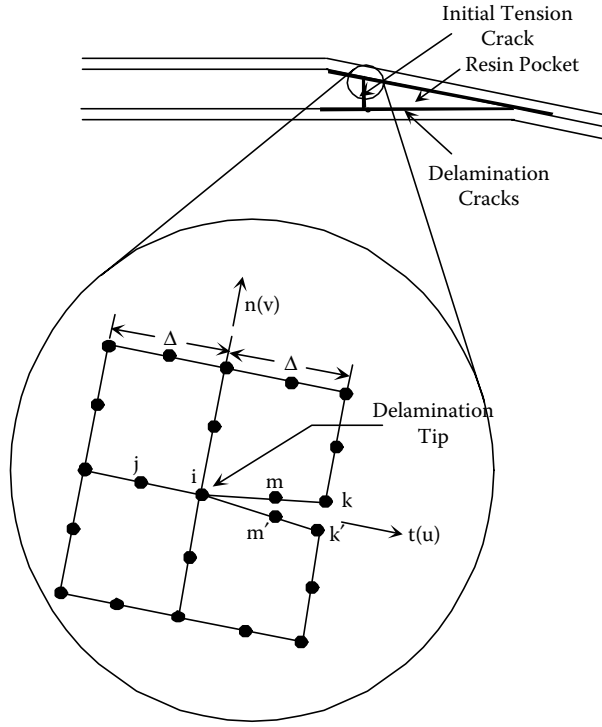


FIGURE 10.14 Computation of strain energy release rate.

where  $G_I$  and  $G_{II}$  are the mode I and mode II strain energy release rates, computed as

$$G_I = -\frac{1}{2\Delta} [F_m(v_k - v_{k'}) + F_{mj}(v_m - v_{m'})]$$

$$G_{II} = -\frac{1}{2\Delta} [F_u(u_k - u_{k'}) + F_{uj}(u_m - u_{m'})]$$

where  $u$  and  $v$  are tangential and perpendicular nodal displacements, respectively, and  $F_t$  and  $F_n$  are the tangential and perpendicular nodal forces, respectively, computed from finite element analysis. Here,  $t$  refers to the direction tangential to the crack, and  $n$  refers to the direction perpendicular to the crack. In Figure 10.14, node  $i$  is the delamination tip, and node  $j$  is the next node to which the delamination will advance.

Delamination onset is assumed to occur when the calculated  $G$  exceeds a critical value  $G_{crit}$  derived from material coupon delamination tests [54, 59, 60]. See Reference [70] for details of finite element stress analysis and estimation of the delamination probability. A few pertinent observations are summarized in the following text.

### 10.7.2 Random Variables

Based on the material data, seven random variables were identified for probabilistic analysis with the finite element model of the helicopter rotor hub. These are material property variables  $E_{11}$ ,  $E_{22}$  (elastic moduli along directions 1 and 2),  $\nu_{13}$  (Poisson ratio), and  $G_{13}$  (shear modulus); the oscillatory bending angle  $\theta$  caused by the cyclic loading; the magnitude of the axial load  $P$ ; and the limiting value of the strain energy release rate  $G_{crit}$ . All the random variables are assumed to follow Gaussian (normal) distributions. No statistical correlation is assumed among the material property variables. (This is not realistic;

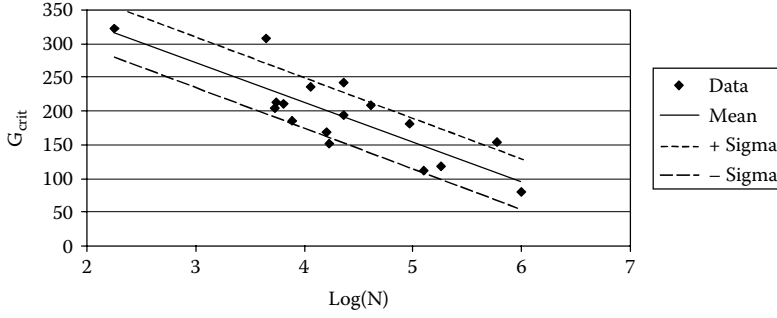


FIGURE 10.15 Relationship between  $G_{crit}$  and cycles of life.

however, as shown by the analysis results, only  $E_{I1}$  is significant. Therefore this assumption is not critical in this problem.) The seventh variable,  $G_{crit}$ , is discussed in the following text.

The objective is to estimate the probability of initiation of delamination at the required life. This is assumed to occur when the strain energy release rate exceeds the limiting value  $G_{crit}$ , which is a function of load cycles,  $N$ . Figure 10.15 shows the plot of  $G_{crit}$  vs.  $N$  obtained from material test data. Figure 10.15 also shows the best-fit line through the data, assuming  $G_{crit}$  is a linear function of  $\text{Log}_{10}(N)$ . This is shown by the solid line denoting “Mean.” The lines corresponding to mean plus and minus one standard deviation are shown above and below this line, denoted “+Sigma” and “-Sigma,” respectively. For the given data, the relationship between  $G_{crit}$  and  $N$  is obtained using regression analysis as

$$G_{crit} = 448.56 - 58.571 \text{Log}_{10}(N) \quad (10.47)$$

where  $G_{crit}$  has units of  $\text{J}^2/\text{m}$ . Based on statistical analysis of the  $G_{crit}$  vs.  $N$  data, it was determined that  $G_{crit}$  is a Gaussian (normal) random variable with its mean value described by Equation 10.47 and a constant standard deviation of  $36.6 \text{ J}^2/\text{m}$ . The corresponding performance function is

$$g = G_{crit} - G \quad (10.48)$$

In this case, both  $G_{crit}$  and  $G$  are random variables that are dependent on the basic random variables such as material properties, geometric properties, and loading conditions, which have inherent scatter in their definitions.

### 10.7.3 Response Surface Modeling of the Limit State

The limit state function in Equation 10.48 is not available as a closed-form function of the basic random variables. It can only be computed through a nonlinear finite element stress analysis, combining several analysis codes. Thus, it is an implicit function of the random variables. In such a case, the response surface approach may be used to develop an approximate closed-form expression of the limit state function, and then the first-order reliability method (FORM) can be used to estimate the delamination probability.

The literature on design of experiments is quite vast, and many methods are available [71, 72]. Using a central composite design of experiments, the following second-order approximation of the limit state function is constructed for illustration:

$$g = G_{crit} - G = G_{crit} - 175.344(0.569 - 0.0861E_{I1} + 0.0231P - 0.117\theta - 0.000546P^2 + 0.00376\theta^2 + 0.0046P\theta) \quad (10.49)$$

where the units of  $G$  and  $G_{crit}$  are  $\text{J}/\text{m}^2$ .

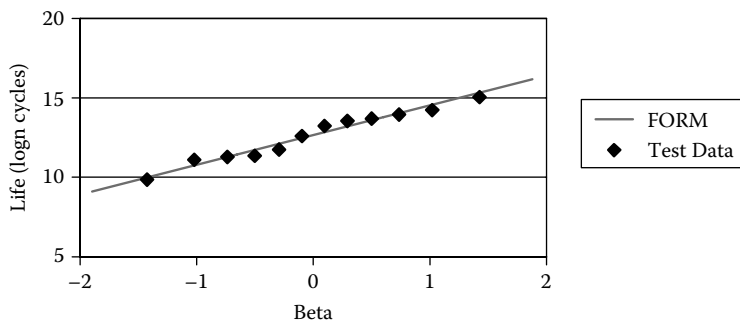


FIGURE 10.16 Predicted fatigue delamination life vs. test data.

### 10.7.4 Verification of Methodology

Having developed and implemented the probabilistic analysis framework, the next step is to compare the predicted results with test data and to validate the proposed method. Twelve test specimens were tested by Bell/Textron Helicopter, which gave a mean life of  $\mu = 1,559,694$  cycles and standard deviation of  $\sigma = 7,725,401$  cycles, which gives a large coefficient of variation of 4.95. The life data from the 12 specimens were plotted on lognormal probability paper, and compared with the FORM reliability analysis with the response surface in Equation 10.49.

Figure 10.16 shows that the statistical distribution of the life predicted by the reliability analysis is in excellent agreement with the test data. The reliability analysis predicts a nominal life similar to the experimental observations. However, currently available deterministic analysis may be capable of predicting nominal behavior. What is more important is that the reliability analysis also predicts a lognormal distribution with a coefficient of variation similar to the experimental observations (5.66 vs. 4.95). Zhang and Mahadevan [73] developed a Bayesian validation technique for model-based reliability prediction and found that the data gave strong support for the model. Using the same data, Mahadevan and Zhang [74] also developed a test-planning methodology that integrates both model-based and test-based information. Such a methodology was found to offer significant savings in testing cost.

## 10.8 Creep Limit State

In certain elevated temperature applications, composites undergo creep deformation, which is a function of loading, operating environments, and the properties of the constituents. Creep is one of the principal damage mechanisms for materials operating at elevated temperatures. If the temperature is less than about 30% of the melting temperature of the fiber material, creep of fibers can be neglected. The composite longitudinal creep behavior is largely controlled by the fracture behavior of the fibers. It has been shown [75] that, at a low applied load in the fiber direction, very few fibers fracture during creep. The composite creep strain is limited by the elastic strain of the fibers. However, when a relatively large load is applied, a substantial number of fibers can fracture, and damage is initiated during the initial loading and creep of the matrix. In addition, some defects introduced during the manufacture of fibers can also cause fracture. When fibers break, the load on the cross section is redistributed. The load shed by the broken fibers is shared by the intact fibers and the matrix, which increases the creep strain and causes more fibers to break.

A number of experimental and theoretical studies have been conducted on the creep of composites. Cell models have been widely used to study the creep behavior of composites [76–83]. Bullock et al. [83] proposed an analytical model to predict the creep rate by assuming that both the fibers and matrix creep according to a power law. McLean [84] proposed a model assuming that the composite consists of a creeping matrix and elastic fibers. In this model, the effect of the broken fibers is ignored. A simple model that accounts for fiber breakage in a uniaxial tension test has been presented by McLean [85]. Goto and McLean [77] also modified the preceding model by introducing a strain-hardening third phase at the

interface, deforming according to a power law. The McLean model gives very accurate predictions [86] for undamaged composites compared to finite element analysis results. Theoretical studies on the fiber failure within the framework of global load sharing, whereby the load shed from broken fibers is shared nearly equally among all intact fibers, have been carried out by Curtin [87] for composites with a weak interface. Du and McMeeking [80] used Curtin's results and studied the effects of fiber breakage and the consequential stress relaxation in the broken fibers. The simulation method is also used to predict the lifetime of composites with broken fibers [88, 89]. The foregoing models are limited to longitudinal creep behavior. There are also some studies carried out theoretically and experimentally on the transverse creep behavior of composites [90–93]. Song analyzed the effect of transverse loading and plasticity of matrix on the longitudinal creep behavior. It was observed that the applied transverse tension can reduce the composite creep strain and the normal stress in the fibers; and the applied transverse compression will increase the creep strain and the normal stress in the fibers.

All of these models were developed to carry out the deterministic stress and strain analysis of the composites, or to predict the creep life of the composites. However, it is well known that there exists large scatter in the material strength and other mechanical properties. The strength of the fibers is usually described with the weakest-link model, and the Weibull distribution is also commonly used.

The purpose of this section is to develop a method for the probabilistic analysis of longitudinal reinforced composites under creep, with and without fiber breaks. Sensitivity analysis is also carried out to investigate the importance of different stochastic parameters on the failure probability of composites. First, the time-dependent creep behavior of longitudinal composites without broken fibers is discussed, followed by creep behavior of composites with fiber fractures. Next, different limit state functions (failure criteria) are established for the reliability analysis of composites.

### 10.8.1 Creep of Undamaged Composites

Fiber-reinforced composites exhibit creep deformation at high temperatures [85, 94]. In the range of operating temperatures, the fibers may not creep, but the matrix can. In this section, it is assumed that the composite consists of elastic fibers and a creep matrix. It is assumed that the fibers neither creep nor fracture, and deform elastically at a rate governed by the surrounding creep matrix. The total strain includes elastic, plastic, and creep strains. Previous experience [86] shows that matrix plasticity has a very limited effect on the creep behavior of composites. Therefore, the plasticity effect is not included here.

The governing equations for the longitudinal stress and strain in the composite can be expressed as

$$\sigma_f = E_f \varepsilon \quad (10.50)$$

$$\dot{\varepsilon} = \frac{\dot{\sigma}_m}{E_m} + B \sigma_m^n \quad (10.51)$$

$$\sigma = f \sigma_f + (1 - f) \sigma_m \quad (10.52)$$

where  $\sigma_f$  and  $\sigma_m$  are the fibers and matrix stresses, respectively;  $E_f$  and  $E_m$  are the Young's moduli of the fibers and the matrix, respectively;  $f$  is the fiber volume fraction;  $\varepsilon$  and  $\dot{\varepsilon}$  are the strain and strain rate of the composite, respectively; and  $n$  and  $B$  are the creep exponent and creep constant of the matrix, respectively.

The performance of the composite can be evaluated based on this model. Assume that the composite is subjected to a fixed stress loading. Solving Equation 10.50 to Equation 10.52, the stress in the matrix is given by

$$\sigma_m(t) = \left[ \left( \frac{E}{E_m \sigma} \right)^{n-1} + \frac{f(n-1)E_f E_m B t}{E} \right]^{-\frac{1}{n-1}} \quad (10.53)$$



The stress in the fibers is given by

$$\sigma_f = \frac{\sigma}{f} - \frac{1-f}{f} \left[ \left( \frac{E}{E_m \sigma} \right)^{n-1} + \frac{f(n-1)E_f E_m Bt}{E} \right]^{-\frac{1}{n-1}} \quad (10.54)$$

The strain is given by

$$\varepsilon = \frac{\sigma}{fE_f} - \frac{1-f}{fE_f} \left[ \left( \frac{E}{E_m \sigma} \right)^{n-1} + \frac{f(n-1)E_f E_m Bt}{E} \right]^{-\frac{1}{n-1}} \quad (10.55)$$

And the strain rate is

$$\dot{\varepsilon} = \frac{(1-f)E_m B}{E} \left[ \left( \frac{E}{E_m \sigma} \right)^{n-1} + \frac{f(n-1)E_f E_m Bt}{E} \right]^{-\frac{n}{n-1}} \quad (10.56)$$

In this model, as time proceeds, the fibers increasingly sustain the loads formerly carried by the creeping matrix. Eventually, when the matrix stress is completely relaxed, all of the loads are carried by the intact fibers and the strain approaches a steady state. The creep strain rate decreases as the stress in the matrix relaxes because of the matrix creep. For the situation where the composite is subjected to a low level of stress, the foregoing model predicts creep strain with reasonable success [86]. However, when a relatively large load is applied to the composite, damage is initiated in the form of isolated or localized fiber breaks [75, 94]. In addition, the defects introduced in the fibers during manufacturing can also cause fibers to break. McLean's model ignores these effects and therefore underestimates the creep strain and fails to predict the creep ruptures resulting from the failures of fibers. Therefore, creep analysis with fiber break is considered next.

### 10.8.2 Creep Analysis with Stochastic Fiber Fracture

The randomness in the strength of the fibers may be modeled using the Weibull distribution, which is an extreme-value distribution of the smallest values, following the weakest-link approach. For a composite with the stress in fibers,  $\sigma_f$ , some of the fibers will break. The failure probability of the fibers can be estimated by

$$p = 1 - \exp \left( - \left( \frac{\sigma_f}{\sigma_c} \right)^m \right) \quad (10.57)$$

where  $m$  is referred to as the Weibull modulus that characterizes the shape of the distribution, and  $\sigma_c$  is the characteristic strength of the fibers.

Here,  $p$  can be considered as the fraction of the broken fibers. For small absolute values of the exponent (e.g.,  $10^{-1}$ ) Equation 10.57 can be approximated and simplified as

$$p \cong \left( \frac{\sigma_f}{\sigma_c} \right)^m \quad (10.58)$$

For a composite with broken fibers, near the end of the fiber break, the load carried by the fiber is released and transferred to the matrix and the intact fibers through the interface. The stress in the fiber increases from zero to the nominal stress from the end of a broken fiber to a certain length, which is known as

the stress recovery length. The shear stress is set equal to the yield stress of the interface  $\tau_y$  at the end of the fiber break. The stress recovery length can be obtained by the equilibrium condition. The average fiber stress over the stress recovery length is given by

$$\bar{\sigma}_f = \left(1 - \frac{1}{2}p\right)\sigma_f \quad (10.59)$$

From Equation 10.50, Equation 10.58, and Equation 10.59, the average stress in the fibers is obtained as

$$\bar{\sigma}_f = \left(1 - \frac{1}{2}\left(\frac{E_f \epsilon}{\sigma_c}\right)^m\right) E_f \epsilon \quad (10.60)$$

From Equation 10.52, the matrix stress is obtained as

$$\sigma_m = \frac{1}{1-f} \left( \sigma - f \left(1 - \frac{1}{2}\left(\frac{E_f \epsilon}{\sigma_c}\right)^m\right) E_f \epsilon \right) \quad (10.61)$$

and the matrix stress rate as

$$\dot{\sigma}_m = \frac{-f}{1-f} \left(1 - \frac{1+m}{2}\left(\frac{E_f \epsilon}{\sigma_c}\right)^m\right) E_f \dot{\epsilon} \quad (10.62)$$

By substitution of the matrix stress and matrix stress rate into Equation 10.51, the creep strain rate is obtained as

$$\dot{\epsilon} = \frac{B \left( \sigma - f \left(1 - \frac{1}{2}\left(\frac{E_f \epsilon}{\sigma_c}\right)^m\right) E_f \epsilon \right)^n}{\left(1 + \frac{f}{1-f} \left(1 - \frac{1+m}{2}\left(\frac{E_f \epsilon}{\sigma_c}\right)^m\right) \frac{E_f}{E_m}\right) (1-f)^n} \quad (10.63)$$

The creep behavior of the composite is governed by Equation 10.60 to Equation 10.62. The strain is a function of time. It can be obtained from the integration of Equation 10.63. However, analytical integration is difficult; instead, a numerical solution may be obtained. The applied external stress produces an initial instantaneous elastic response. The instantaneous elastic strain of the composite is obtained as

$$\epsilon_0 = \frac{\sigma}{fE_f + (1-f)E_m} \quad (10.64)$$

The corresponding instantaneous stresses in the fibers and the matrix are

$$\sigma_{f0} = \frac{E_f \sigma}{fE_f + (1-f)E_m} \quad (10.65)$$

$$\sigma_{m0} = \frac{E_m \sigma}{fE_f + (1-f)E_m} \quad (10.66)$$

The creep strain rate at time  $t_0$  is obtained from Equation 10.63.

With broken fibers taken into account, it can be seen that the average fiber stress is not only a function of the strain of composites and the Young's modulus of fibers but also a function of the Weibull distribution parameters of the fiber strength. Because of the broken fibers, the stress in the remaining fibers in the cross section is larger than the average stress. If we assume that the load previously carried by the broken fibers is shared by the intact fibers in the cross section, then the stress in the intact fibers may be estimated as

$$(\sigma_f)_{\max} = \frac{\sigma_f \sigma_c^m}{\sigma_c^m - \sigma_f^m} \quad (10.67)$$

### 10.8.3 Failure Criterion

In order to evaluate the failure probability of composites at different service times, it is necessary to establish limit state functions based on the failure criteria for the composite. Failure criteria can be established in a simple manner, based on strength or deformation. Here, two models may be postulated based on the fiber stress or the strain. In one model, the composite is assumed to fail when the fiber stress exceeds the allowable stress. This can be termed as the stress-based failure model. The limit state function can be given as:

$$g(\sigma_f, \sigma_{f\_lim}) = \sigma_{f\_lim} - \sigma_f \quad (10.68)$$

where  $\sigma_{f\_lim}$  is the limiting strength of the fibers.

In this formula, when the fiber stress is larger than the limiting value,  $g(\sigma_f, \sigma_{f\_lim}) < 0$  denotes the failure of the composite. When the fiber stress is less than the limiting value,  $g(\sigma_f, \sigma_{f\_lim}) > 0$  denotes that the composite is safe. The equation  $g(\sigma_f, \sigma_{f\_lim}) = 0$  is known as the limit state that separates the safe and failure states. The probability of failure of the composite is

$$p_f = P(\sigma_{f\_lim} < \sigma_f) = P(g(\sigma_f, \sigma_{f\_lim}) < 0) \quad (10.69)$$

For the composite without fiber fracture, the function  $g(\sigma_f)$  may be written as

$$g(\sigma_f, \sigma_{f\_lim}) = \sigma_{f\_lim} - \left\{ \frac{\sigma}{f} - \frac{1-f}{f} \left[ \left( \frac{E}{E_m \sigma} \right)^{n-1} + \frac{f(n-1)E_f E_m B t}{E} \right]^{-\frac{1}{n-1}} \right\} \quad (10.70)$$

For the composite with broken fibers taken into account, the function  $g(\sigma_f, \sigma_{f\_lim})$  may be written as

$$g(\sigma_f, \sigma_{f\_lim}) = \sigma_{f\_lim} - \frac{\sigma_f \sigma_c^m}{\sigma_c^m - \sigma_f^m} \quad (10.71)$$

The second model assumes that the composite fails when the strain exceeds the limiting value. This is termed the strain-based failure model. The corresponding limit state function is written as

$$g(\epsilon, \epsilon_{lim}) = \epsilon_{lim} - \epsilon \quad (10.72)$$

where  $\epsilon_{lim}$  is the limiting value of the composite strain.

The probability of failure of the composite with this limit state function is

$$p_f = P(\epsilon_{lim} < \epsilon) = P(g(\epsilon, \epsilon_{lim}) < 0) \quad (10.73)$$

For the composite without fiber fractures, the function  $g(\varepsilon, \varepsilon_{\text{lim}})$  may be written as

$$g(\varepsilon, \varepsilon_{\text{lim}}) = \varepsilon_{\text{lim}} - \left( \frac{\sigma}{fE_f} - \frac{1-f}{fE_f} \left[ \left( \frac{E}{E_m \sigma} \right)^{n-1} + \frac{f(n-1)E_f E_m B t}{E} \right]^{-\frac{1}{n-1}} \right) \quad (10.74)$$

For the composite with broken fibers taken into account, the function  $g(\varepsilon, \varepsilon_{\text{lim}})$  may be written as

$$g(\varepsilon, \varepsilon_{\text{lim}}) = \varepsilon_{\text{lim}} - \varepsilon \quad (10.75)$$

where  $\varepsilon$  is obtained by integrating Equation 10.63.

#### 10.8.4 Numerical Example

In this example, the probabilistic creep analysis of SiC fiber-reinforced Ti-6Al-4V matrix metal–matrix composite is demonstrated with the stress-based failure criterion. The constituent properties of the composite are obtained from experimental data on the specimen. The limiting fiber strength, and the Young's moduli of the fibers and the matrix, are treated as random variables. Other constituent properties of the composite are taken as deterministic (e.g., the volume fraction of the composite, creep exponent [ $n = 3$ ] and creep constant of the matrix  $B = 4.12 \times 10^{-31} \text{ Pa}^{-3} \text{ s}^{-1}$ ). The reliability indices at different times for composites with different fiber volume fractions and different shape parameters of the Weibull distribution of the fiber strength are calculated. (See Mao and Mahadevan [95] for details of the numerical example.)

First, the reliability indices at different time instants are calculated with FORM. The effect of broken fibers on the reliability is investigated. Figure 10.17 presents the reliability index  $\beta$  vs. time with and without considering the effect of broken fibers. From the results, it can be seen that the broken fibers make large contribution to the reduction of reliability index. Also, the degradation in reliability over time is larger when the broken fibers are considered.

In Figure 10.17, the reliability index decreases slowly at first, followed by a rapid decrease in the second stage, and a slow decrease in the third stage. At the initial time, all of the loads are carried by both fibers and matrix, and there are no broken fibers. Therefore, the composite creeps slowly. After some fibers break, the load previously carried by broken fibers is shared by intact fibers and the matrix, the composite

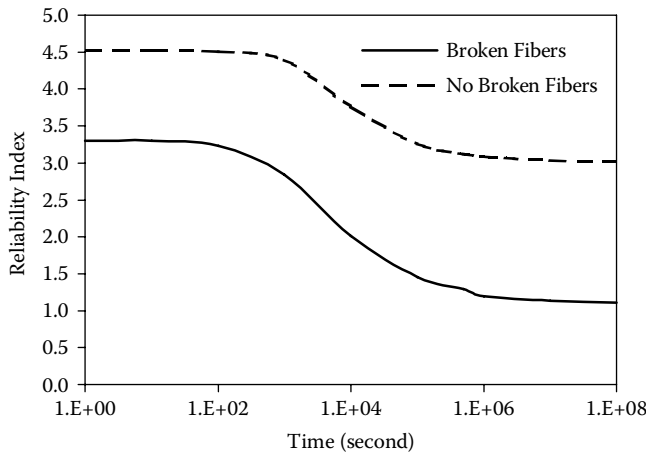


FIGURE 10.17 Creep reliability vs. time.

creeps faster, and the stress in the fiber consequently increases. As more loads are sustained by fibers, the creep rate decreases. The reliability index still decreases, but more slowly. After a certain time, the reliability index almost ceases to decrease. At this stage, most of the stress is carried by fibers. The stress in the matrix is so small that the creep strain rate is very low, and the stress increase in the fibers is also very slow and can be neglected.

Mao and Mahadevan [95] also observed that the applied load, fiber volume fraction, and the Weibull strength parameters  $m$  and  $\sigma_c$  in Equation 10.57 all had a strong effect on the reliability of the material. The larger the load is, the lower is the reliability of the material, and the earlier is the start of the rapid degradation stage. When the volume fraction is small ( $f = 0.1$ ), the reliability index starts low and begins to decrease rapidly (which means the failure probability increases rapidly), and fracture will occur in a short time. When the fiber volume fraction is large, fracture may not happen for the same applied load.

It can be seen that the fiber characteristic strength has the most influence on the reliability of the material. When the reliability is estimated at different service times, the sensitivity indices show that the fiber characteristic strength has even more effect on the reliability, with increasingly longer service time, while the sensitivity indices for Young's moduli of fiber and matrix become much smaller. Therefore, for reliability estimation after a long lifetime, the Young's moduli of fiber and matrix may be treated as deterministic parameters.

The characteristic strength of the fiber follows the Weibull distribution, which is described by two parameters: characteristic value and shape parameter. A lower value of the shape parameter  $m$  gives a higher failure probability under the same load. Also, the reliability index was observed to decrease rapidly slightly earlier for a lower value of  $m$  [95].

## 10.9 Conclusion

This chapter discussed reliability evaluation methods for composite structures under strength (matrix cracking and fiber breakage), fatigue, delamination, and creep limit states. In all cases, the essential steps of individual limit state reliability evaluation are: structural analysis, failure definition, data collection about the random variables, uncertainty propagation through the structural and limit state models, and reliability analysis. For multiple limit states, the overall failure probability may be computed through the union of individual failures. In the case of progressive damage, dominant failure sequences are identified, and the system failure is computed through the union of the failure sequences. Several approximations to reduce the computational effort, based on practical considerations, were identified and illustrated.

Most of the discussion in this chapter was focused on laminated composites, partly owing to the widespread use and availability of data for such materials. As composite material technology expands with increased use of other materials such as woven composites and particulate composites, reliability evaluation methods will also follow. However, the essential steps are similar to those outlined in this chapter.

One important need that has not been addressed yet is the effect of interaction between different failure mechanisms on reliability. This requires development of physics models first. For example, creep-fatigue interaction modeling has been developed for metallic materials [96]. Similar models are yet to be explored for composite materials. The progressive failure analysis of Section 10.2 to Section 10.4 considers the effect of multiple limit states on system reliability, but all of them are related to strength, and it is therefore easy to compute the effect of one failure on another through structural reanalysis. The interaction of qualitatively different mechanisms such as creep and fatigue should be studied both experimentally and analytically before reliability methods can be applied to such situations.

## References

1. Shiao, M.C. and Chamis, C.C., Reliability of Composite Structures with Multi-Design Criteria, in *Proceedings of the 35th AIAA/ASME/ASCE/AHS/ASC Structures, Structural Dynamics, and Materials Conference*, Hilton Head, 1994, 606.
2. Murotsu, Y. and Miki, M., Reliability design of fiber reinforced composites, *Structural Safety*, 15, 1–2, 35, 1994.

3. Zhao, H. and Gao, Z., Reliability analysis of composite laminate by enumerating significant failure modes, *Journal of Reinforced Plastics and Composites*, 14, 427, 1995.
4. Mahadevan, S., Liu, X., and Xiao, Q., A probabilistic progressive failure model of composite laminates, *Journal of Reinforced Plastics and Composites*, 16, 11, 1020, 1997.
5. Tan, S.C., A Progressive failure model for composite laminates containing openings, *Journal of Composite Materials*, 25, 557, 1991.
6. Tsai, S.W. and Wu, E.M., A general theory of strength for anisotropic materials, *Journal of Composite Materials*, January, 58, 1971.
7. Haldar, A. and S. Mahadevan, *Probability, Reliability, and Statistics in Engineering Design*, John Wiley, New York, 2000.
8. Rackwitz, R. and Fiessler, B., Structural reliability under combined random load sequences, *Computers & Structures*, 484, 1978.
9. Murotsu, Y. et al., Reliability Assessment of Redundant Structures, in *Proceedings of the 3rd International Conference on Structural Safety and Reliability*, ICOSAR Norway, Trondheim, 1981, 315.
10. Liu, X. and Mahadevan, S., Ultimate strength failure probability estimation of composite structures, *Journal of Reinforced Plastics and Composites*, 19, 5, 403, 2000.
11. Mahadevan, S. et al., Structural Reanalysis for System Reliability Computation, in *Reliability Technology 1992*, AD-Vol. 28, ASME Winter Annual Meeting, Anaheim, 1992, 169.
12. Cornell, C.A., Bounds on the reliability of structural systems, *Journal of the Structural Division*, ASCE, 93, 171, 1967.
13. Lee, J. D., Three dimensional finite element analysis of damage accumulation in composite laminate, *Computers & Structures*, 15, 3, 335, 1982.
14. Reddy, Y.S. and Reddy, J.N., Three-dimensional finite element progressive failure analysis of composite laminates under axial extension, *Journal of Composites Technology and Research*, 15, 2, 73, 1993.
15. Cruse, T.A., Review of Recent Probabilistic Design in Composite Structures, CAME, Consultants in Applied Mechanics and Engineering, Nashville, Tennessee, 1994.
16. Vinson, J.R. and Sierakowski, R.L., *The Behavior of Structures Composed of Composite Materials*, Martinus Nijhoff Publishers, Netherlands, 1986.
17. Xiao, Q. and Mahadevan, S., Second-order upper bounds on probability of intersection of failure events, *Journal of Engineering Mechanics*, 120, 3, 670, 1994.
18. Xiao, Q., and Mahadevan, S., Fast failure mode identification for ductile structural system reliability, *Structural Safety*, 13, 4, 207, 1994.
19. Mahadevan, S. and Liu, X., Probabilistic analysis of composite structure ultimate strength, *AIAA Journal*, 40, 7, 1408, 2002.
20. Degrieck, J., and Van Paepegem, W., Fatigue damage modelling of fibre-reinforced composite materials: Review, *Applied Mechanics Reviews*, 54, 4, 279–300, 2001.
21. Hasin, Z. and Rotem, A., A fatigue criterion for fiber reinforced composite material, *Journal of Composite Materials*, 7, 448–464, 1973.
22. Reifsnider, K.L. and Gao, Z., A micromechanics model for composite under fatigue loading, *International Journal of Fatigue*, 13, 149–156, 1991.
23. Wu, L., Thermal and mechanical fatigue analysis of CFRP laminates, *Composite Structures*, 25, 339–344, 1993.
24. Jen, M.H.R and Lee C.H., Strength and life in the thermaloplastic composite laminates under static and fatigue loads, *International Journal of Fatigue*, 20, 605–615, 1998.
25. Philippidis, T.P. and Vassilopoulos, R.P, Fatigue strength prediction under multiaxial stress, *Journal of Composite Materials*, 33, 1578–1599, 1999.
26. Fawaz, Z. and Ellyin, F., Fatigue damage model for fiber-reinforced materials under general loading conditions, *Journal of Composite Material*, 28, 1432–1451, 1994.
27. Haris, B., Fatigue Behavior of Polymer-Based Composite and Life Prediction Methods, AIB-Vincotte Leerstoel, 2 maart 1995, Belgium, National Fonds voor Wetenschappelijk Onderzoek, 28 p, 1985.

28. Bond, I.P., Fatigue life prediction for GRP subjected to variable amplitude loading, *Composite Part A, Applied Science and Manufacturing*, 30, 363–367, 1999.
29. Hwang, W. and Han, K.S., Cumulative models and multi-stress fatigue life prediction, *Journal of Composite Materials*, 20, 125–153, 1986a.
30. Hwang, W. and Han, K.S., Fatigue of composite of fatigue modulus concepts and life prediction, *Journal of Composite Material*, 20, 154–165, 1986b.
31. Sidoroff, F. and Subagio, B., Fatigue damage modeling of composite materials from bending tests, in *Proceedings of the Sixth International Conference on Composite Materials (ICCM-VI) & Second European Conference on Composite Materials (ECCM-II)*, Vol. 4, 20–24, pp. 432–439, July 1987, London.
32. Van Paepegem, W. and Degrieck, J., Numerical Modelling of Fatigue Degradation of Fibre-Reinforced Composite Materials, in *Proceedings of the Fifth International Conference on Computational Structures Technology, Volume F: Computational Techniques for Materials, Composites and Composite Structures*. Leuven, Belgium, 6–8 September 2000, Civil-Comp Press, pp. 319–326, 2000.
33. Caprino, G., DiAlmore, A., and Facciolo, F., Fatigue sensitivity of random glass fibre reinforced plastics, *Journal of Composite Material*, 32, 1203–1220, 1999.
34. Whitworth, H.A., Evaluation of the residual strength degradation in composite laminates under fatigue loading, *Composite Structures*, 48, 262–264, 2000.
35. Yao, W.X. and Himmel, N., A new cumulative damage model for fiber-reinforced plastics, *Composite Science and Technology*, 60, 59–64, 2000.
36. Tserpes, K.I., Papanikos, P., Labeas, G., and Pantelakis, S.P., Fatigue damage accumulation and residual strength assessment of CFRP laminates, *Composite Structures*, 63, 2, 219–230, 2004.
37. Harris, B. et al., Constant-stress fatigue response and life-prediction for carbon-fiber composites, in *Progress in Durability Analysis of Composite Systems*, Cardon, A.H., Fukuda, H., and Reifsnider, K., Eds., A.A. Balkema Publisher, Rotterdam, Netherlands, 1995, 63.
38. Yang, J., Fatigue and residual strength degradation for graphite/epoxy composite under tension-compression cyclic loading, *Journal of Composite Materials*; 12, 1, 19, 1978.
39. Nicholas, S., An approach to fatigue life modeling in titanium-matrix composites, *Materials Science and Engineering A*, 200, 29, 1995.
40. Cardon, A.H., Fukuda, H., and Reifsnider, K., Eds., *Progress in Durability Analysis of Composite Systems*, A.A. Balkema Publisher, Rotterdam, Netherlands, 1995.
41. Halford, G.R. et al., Proposed framework for thermomechanical fatigue life prediction of metal-matrix composites (MMCs), in *Thermomechanical Fatigue Behavior of Materials*, Sehitoglu, H., Ed., ASTM STP 1186, American Society for Testing and Materials, Philadelphia, 1993, 176.
42. Subramanian, S., Reifsnider, K.L., and Stinchcomb, W.W., A Cumulative damage model to predict the fatigue life of composite laminates including the effect of a fiber-matrix interphase, *International J. of Fatigue*, 17, 5, 343, 1995.
43. Reifsnider, K., Case, S., and Duthoit, J., The mechanics of composite strength evolution, *Composites Science and Technology*, 60, 2539, 2000.
44. Mao, H. and Mahadevan, S., Fatigue damage modeling of composite materials, *Composite Structures*, 58, 405, 2002.
45. Halverson H.G., Curtin W.A., and Reifsnider K.L., Fatigue life of individual composite specimens based on intrinsic fatigue behavior, *International Journal of Fatigue*, 19, 5, 269, 1997.
46. Chawla, K.K., *Composite Materials—Science and Engineering*, 2nd ed., Springer-Verlag, New York, 1998.
47. Kumar, R. and Talreja, R., Fatigue Damage Evolution in Woven Fabric Composites, 41st AIAA/ASME/ASCE/AHS/ASC structures, Structural Dynamics, and Materials Conferences and Exhibit, Atlanta, 2000.
48. Nicholas, S. and Russ, R., Elevated temperature fatigue behavior of SCS-6/Ti-24Al-11Nb, *Material Science Engineering A*, 153, 514, 1992.
49. Liu, Y., and Mahadevan, S., Probabilistic fatigue life prediction of multidirectional composite laminates, *Composite Structures*, 69, 11–19, 2005.

50. Suresh, S., *Fatigue of Materials*, 2nd ed., Cambridge University Press, New York, 1998.
51. Daniel, I.M., and Ishai, O., *Engineering Mechanics of Composite Materials*, Oxford University Press, New York, 1994.
52. Diao, X., Lessard, L.B., and Mahmood, M.S., Statistical model for multiaxial fatigue behavior of unidirectional plies, *Composites Science and Technology*, 59, 13, 2025–2035, 1999.
53. Mandell, J.F. and Samborsky, D.D., DOE/MSU Composite Materials Fatigue Database: Test Methods, Materials, and Analysis, Sandia National Laboratories, Albuquerque, NM, February, 2003.
54. Murri, G.B., O'Brien, T.K., and Rousseau, C.Q., Fatigue Life Prediction of Tapered Composite Laminates, in *53rd Annual Forum, April–May*, American Helicopter Society, Virginia Beach, 1997.
55. Fish, J.C. and Lee, S.W., Tensile Strength of Tapered Composite Structures, AIAA Paper No. 88-2252, in *Proceedings of the 30th AIAA/ASME/ASCE/AHS SDM Conference*, Williamsburg, VA, 1988, pp. 324.
56. Hoa, S.V., Daoust, J., and Du, B.L., Interlaminar stresses in tapered laminates, *Polymer Composites*, 9, 5, 337, 1988.
57. Llanos, A.S., Lee, S.W., and Vizzini, A.J., Delamination Prevention in Tapered Composite Structures under Uniaxial Tensile Loads, AIAA, in *Proceedings of the 31st AIAA/ASME/ASCE/AHS SDM Conference*, Paper No. 90-1063, Long Beach, CA, 1242, 1990.
58. Hoa, S.V. and Daoust, J., Parameters affecting interlaminar stresses in tapered laminates under static loading conditions, *Polymer Composites*, 10, 5, 374, 1989.
59. Murri, G.B., Salpekar, S.A., and O'Brien, T.K., Fatigue delamination onset prediction in unidirectional tapered laminates, in *Composite Materials: Fatigue and Fracture*, Vol. 3, ASTM STP 1110, O'Brien, T. K., Ed., ASTM, Philadelphia, PA, 1991, 312.
60. Murri, G.B., O'Brien, T.K., and Salpekar, S.A., Tension fatigue of glass/epoxy and graphite/epoxy tapered laminates, *Journal of the American Helicopter Society*, 38, 1, 29, 1993.
61. Winsom, M. R., Delamination in tapered Unidirectional Glass Fibre-Epoxy Under Static Tension Loading, AIAA Paper No. 91-1142, in *Proceedings of the 32nd AIAA/ASME/ASCE/AHS SDM Conference*, Baltimore, MD, 1991, 1162.
62. Trethewey, B.R. Jr., Gillespie, J.W. Jr., and Wilkins, D.J., Interlaminar Performance of Tapered Composite Laminates, in *Proceedings of the American Society for Composites, 5th Technical Conference*, East Lansing, MI, 1990, 361.
63. Armanios, E.A. and Parnas, L., Delamination analysis of tapered laminated composites under tensile loading, in *Composite Materials: Fatigue and Fracture*, Vol. 3, in ASTM STP 1110, O'Brien, T.K., Ed., ASTM, Philadelphia, PA, 1991, 340.
64. Salpekar, S.A., Raju, I.S., and O'Brien, T.K., Strain Energy Release Rate Analysis of Delamination in a Tapered Laminate Subjected to Tension Load, in *Proceedings of the American Society for Composites, 3rd Technical Conference*, Seattle, WA, 1988, 642.
65. O'Brien, T.K. et al., Combined tension and bending testing of tapered composite laminates, *Applied Composite Materials*, 1, 6, 401, 1995.
66. Rybicki, E.F., Schmueser, D.W., and Fox, T., An energy release rate approach for stable crack growth in the free-edge delamination problem, *Journal of Composite Materials*, 11, 470, 1977.
67. Russell, A.J. and Street, K.N., Delamination and debonding of materials, *ASTM STP 876*, 349, 1985.
68. Rybicki, E.F. and Kanninen, M.F., A finite element calculation of stress-intensity factors by a modified crack-closure integral, *Engineering Fracture Mechanics*, 9, 931, 1977.
69. Raju, I.S., Calculation of strain energy release rates with higher order and singular finite elements, *Engineering Fracture Mechanics*, 28, 251, 1987.
70. Mahadevan, S. et al., Reliability analysis of rotorcraft composite structures, *Journal of Aerospace Engineering*, ASCE, 14, 4, 140, 2001.
71. Myers, R.H. and Montgomery, D.C., *Response Surface Methodology: Process and Product Optimization Using Designed Experiments*, John Wiley, New York, 1995.
72. Khuri, A. and Cornell, J.A., *Response Surfaces: Design and Analyses*, Marcel Dekker, New York, 1997.
73. Zhang, R. and Mahadevan, S., Bayesian methodology for reliability model acceptance, *Reliability Engineering and System Safety*, 80, 95, 2003.



74. Mahadevan, S. and Zhang, R., fatigue test planning using reliability and confidence simulation, *International Journal of Material and Product Technology*, 16, 4–5, 317, 2001.
75. Ohno, N. et al., Creep behavior of a unidirectional SCS-6/Ti-15-3 metal matrix composite at 450°C, *Journal of Engineering Materials and Technology*, ASME, 116, 208, 1994.
76. Dragone, T.L. and Nix, W.D., Geometric factors affecting the internal stress distribution and high temperature creep rate of discontinuous fiber reinforced metals, *Acta Metallurgica Materialia*, 38, 10, 1941, 1990.
77. Goto, S. and McLean, M., Role of interfaces in creep of fiber reinforced metal matrix composites-II. Short fibers, *Acta Metallurgica Materialia*, 39, 2, 165, 1991.
78. Bao, G., Hutvnhinson, J.W., and McMeeking, R.M., Partical reinforcement of ductile matrices against plastic flow and creep, *Acta Metallurgica Materialia*, 39, 8, 1871, 1991.
79. McMeeking, R.M., Power law creep of a composite material containing discontinuous rigid aligned fibers, *International Journal of Solids and Structures*, 30, 1807, 1993.
80. Du, Z.Z. and McMeeking, R.M., Creep models for metal matrix composites with long brittle fibers, *Journal of Mechanics and Physics of Solids*, 43, 5, 701, 1995.
81. Aravas, N., Cheng, C., and Ponte Castaneda, P., Steady-state creep of fiber-reinforced composites: Comstitutive equations and computational issues, *International Journal of Solids and Structures*, 32, 15, 2219, 1995.
82. Cheng, C. and Aravas, N., Creep of metal-matrix composites with elastic fibers—Part I: Continuous aligned fibers, *International Journal of Solids and Structures*, 34, 31–32, 4147, 1997.
83. Bullock, J., McLean, M., and Miles, D.E., Creep behavior of a Ni-Ni<sub>3</sub>Al-Cr<sub>3</sub>C<sub>2</sub> eutecti composite, *Acta Metallurgica Materialia*, 25, 333, 1977.
84. McLean, M., Creep deformation of metal matrix composites, *Composite Science and Technology*, 23, 37, 1985.
85. McLean, M., *Directionally Solidified Materials for High Temperature*, The Materials Society, London, 1989.
86. Song, Y., Bao, G., and Hui, C.Y., On creep of unidirectional fiber composites with fiber damage, *Acta Metallurgica Materialia*, 43, 7, 2615, 1995.
87. Curtin, W.A., Theory of mechanical properties of ceramic matrix composites, *Journal of American Ceramic Society*, 74, 11, 2837, 1991.
88. Ibnabdeljalil, M. and Phoenix, S., Creep rupture of brittle matrix composites reinforced with time dependent fibers: Scalings and Monte Carlo simulations, *Journal of Mechanics and Physics of Solids*, 43, 6, 897, 1995.
89. Iyengar, N. and Curtin, W.A., Time-dependent failure in fiber-reinforced composites by matrix and interface shear, *Acta Materialia*, 45, 8, 3419, 1997.
90. Binienda, W.K. and Robinson, D.N., Creep model for metallic composites based on matrix testing, *Journal of Engineering Mechanics*, 117, 624, 1991.
91. Lee, S.C. et al., Modeling of transverse mechanical behavior of continuous fiber reinforced metal-matrix composites, *Journal of Composite Materials*, 25, 536, 1991.
92. Chun, H.J. and Daniel, I.M., Creep characterization of unidirectional SiC/Al under transverse loading in Proceeding of SEM, 1995, 279.
93. Chun, H.J. and Daniel, I. M., Transverse creep behavior of a unidirectional metal matrix composite, *Mechanics of Materials*, 25, 37, 1997.
94. Weber, C.H., Du, Z.Z., and Zok, F.W., High temperature deformation and fracture of a fiber reinforced Titanium matrix composite, *Acta Materialia*, 44, 2, 683, 1996.
95. Mao, H. and Mahadevan, S., Probabilistic analysis of creep of metal-matrix composites, *Journal of Reinforced Plastics and Composites*, 21, 7, 587, 2001.
96. Mahadevan, S., Mao, H., and Ghiocel, D., Probabilistic Simulation of Engine Blade Creep Fatigue Life. Paper No. AIAA 2002-1384. *Proceedings, 43rd AIAA/ASME/ASCE/AHS/ASC Conference on Structures, Dynamics and Materials*, Denver, Colorado, 2002.

# 11

## Micromechanics Modeling and Reliability Analysis of Carbon Nanocomposite Structures

---

11.1	Introduction .....	11-1
	Background and Motivation • Literature Review • Scope and Objectives • New Developments in the Study of This Chapter • Chapter Outline	
11.2	Micromechanical Modeling of Carbon Nanotube/Nanofiber Composites .....	11-7
	Introduction • Mori–Tanaka Method • Failure Analysis of Plates Made of Nanocomposite Materials Using Results From the Micromechanical Model • Example	
11.3	An Encapsulated Inclusion Model for Interface Modeling of Carbon NT/NF Composites .....	11-17
	Introduction • Step 1: Finding the Properties of the Inclusion • Step 2: Finding the Matrix of Elastic Constants of the Nanocomposite • Examples	
11.4	Probabilistic and Reliability Analysis of Nanocomposites.....	11-30
	Introduction • Probabilistic Analysis of Nanocomposite Materials • Numerical Example • Reliability Analysis • Numerical Example	
11.5	Conclusion .....	11-38
	Acknowledgments.....	11-39
	References .....	11-39

Srikanth Pilla\*  
*University of Wisconsin*

Aaron Hammitt  
Efstratios Nikolaidis  
*University of Toledo*

### 11.1 Introduction

---

#### 11.1.1 Background and Motivation

Carbon nanofibers (CNFs) and carbon nanotubes (CNTs), which were discovered in the 1980s, and 1990s, respectively, have attracted considerable attention because of their outstanding physical properties.

---

\*The work presented in this chapter was done when the first author was a graduate student in the Mechanical Industrial and Manufacturing Engineering Department at the University of Toledo, in Toledo, Ohio.

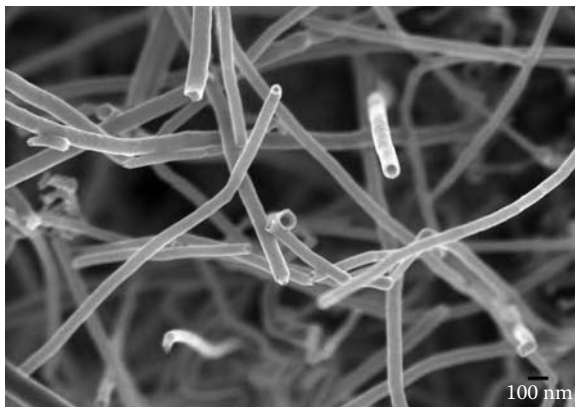


**FIGURE 11.1** SEM image of carbon nanofibers.

In addition to their small size, CNTs and CNFs are half as dense as aluminum, have high tensile strength, elastic modulus, high electric conductivity, current-carrying capacity, and transmit heat twice as well as pure diamond.<sup>12</sup> For example, the strength of CNFs can be 100 times that of steel, and the elastic modulus can be as high as 1000 GPa. CNTs and CNFs are used in a variety of applications, such as chemical and genetic probes, field emission tips, mechanical memory, ultrafine sensors, hydrogen and ion storage, scanning probe microscope tips, and structural components.<sup>12</sup>

Figure 11.1 shows multiple CNFs imaged by a scanning electron microscope (SEM). The diameter of a CNF is in the range of 60 to 200 nm and the length in the range of 20 to 100  $\mu\text{m}$ . Figure 11.2 is a high-resolution transmission electron microscope (TEM) image of the wall of a single CNF. The CNF consists of conical carbon layers. Both figures are original images provided by Dr. Arunan Nadarajah of the Department of Chemical and Environmental Engineering at The University of Toledo. CNTs consist of a graphite sheet rolled up into a cylinder. CNTs have diameters in the range of 1 to 10 nm.

Composites made of CNTs/CNFs embedded in a polymer matrix have attracted the attention of many researchers recently.<sup>11</sup> Reinforcing nano-structured material in polymers provides better mechanical properties compared to large-scale reinforcements that are currently used for aerospace applications, such as carbon fibers.<sup>49</sup> For example, adding 1% CNFs to polymers increases their stiffness significantly (e.g., by 10%) and their resistance to fracture. Falling costs of CNFs/CNTs have further increased demand for these materials.

It is important to develop constitutive relationships that predict the bulk mechanical properties of nanostructured materials as a function of the properties of the polymer, reinforcement, and their interface. These constitutive relationships will help design these materials before they are synthesized.

Figure 11.3 illustrates the importance of an analytical model for understanding the behavior of matter and developing a theory for this behavior. As discussed in Reference 51, first, the material behavior is investigated experimentally. Experimental data are collected, and models are developed for predicting the observed behavior. The models are necessary to develop a theory for the material behavior. Then simulation studies are performed using the developed models to predict the behavior of the material analytically. The predicted behavior is then compared to observed behavior from experiments. This comparison serves to either validate the theory, or to provide a feedback loop to improve the theory using modeling data. Therefore, the development of a validated theory for describing the structure and behavior of materials requires accurate modeling and simulation techniques.

This chapter focuses on the development of a micromechanical model and a probabilistic model for nanocomposites consisting of CNT/CNF embedded in a polymer matrix. The micromechanical model predicts the stiffness of the nanocomposite material based on the properties of the individual phase (base) materials. This model accounts for the interface between the CNT/CNF and polymer matrix. The probabilistic model considers the variation in the properties of base materials and predicts the resulting uncertainty in the overall properties of the nanocomposites. Additionally, it performs sensitivity analysis

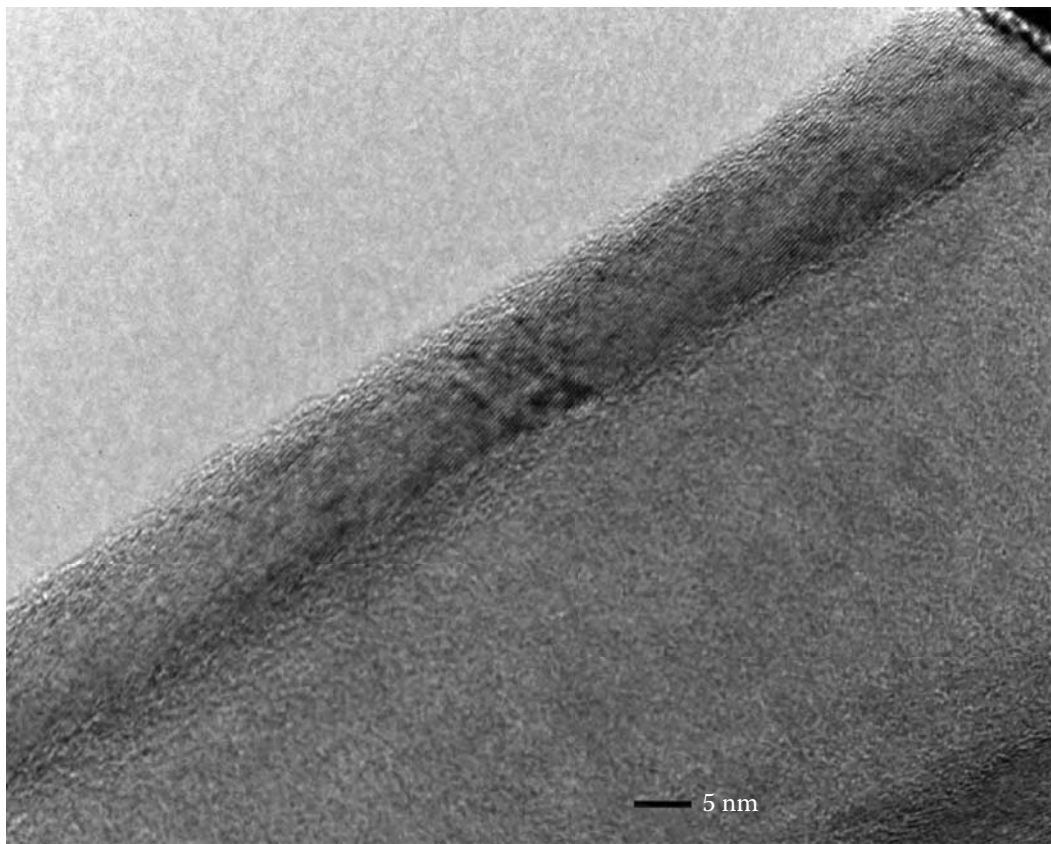


FIGURE 11.2 TEM image of a carbon nanofiber showing conical layers.

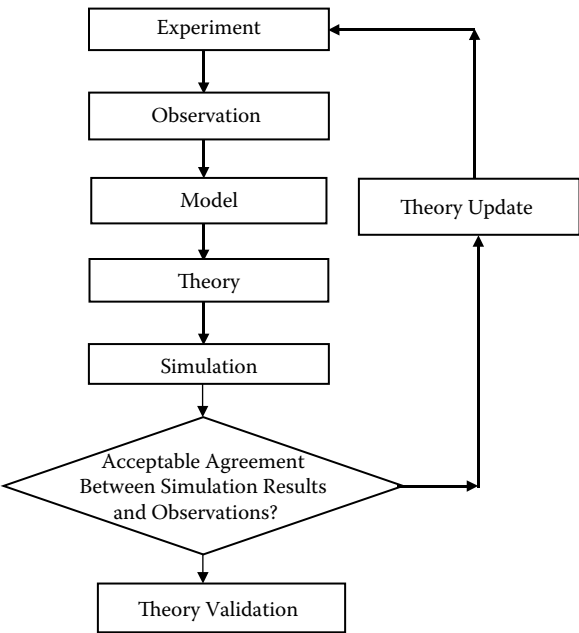


FIGURE 11.3 Schematic of the process of developing and validating a theory using experimental data.

to determine the most important uncertainties affecting the mechanical properties of nanocomposites and performs reliability analysis to determine the reliability of a structure made of nanocomposites. Although the models developed in this study represent reinforcements by solid cylinders, these models are applicable to both CNFs and CNTs.

## 11.1.2 Literature Review

There are many publications on various aspects of this study, including stiffness prediction of conventional composites, stiffness prediction of nanocomposites, modeling of the interface between the nanofiber/nanotube and polymer matrix, failure analysis of structures, and probabilistic analysis of nanocomposites. A literature review for nanocomposites and probabilistic analysis of nanocomposites is presented here. For a review on other aspects of this study, refer to Hammitt<sup>21</sup> and Pilla.<sup>37</sup>

### 11.1.2.1 Nanocomposites

A review of experimental work on polymer nanocomposites has been presented by Jordan et al.<sup>31</sup> Qian et al.,<sup>40</sup> and Andrews et al.<sup>5</sup> showed experimentally that small amounts of CNTs/CNFs substantially improve the properties of a composite material compared to the properties of the polymer matrix. This inference has been theoretically supported by Sheng et al.,<sup>44</sup> Fisher,<sup>17</sup> and Shi et al.<sup>45</sup> These researchers used the Mori–Tanaka (M-T) method to model the behavior of nanocomposites. The M-T method predicts the average stress fields and overall effective stiffness of a composite with a nondilute concentration of inclusions. Sheng et al.<sup>44</sup> performed stiffness analysis of polymer/clay nanocomposites. They calculated the nanocomposite stiffness by considering multiscale micromechanical models accounting for the hierarchical morphology of the nanocomposite. They compared the results from their finite element model (FEM) to results from the Halpin–Tsai and M-T methods. A principal conclusion of their study was that the modulus of clay particles has a significant effect on the modulus of a nanocomposite. Additionally, they compared results from their FEM and the M-T and Halpin–Tsai methods with experimental results, and found that the latter method overestimates the nanocomposite stiffness, whereas the FEM and M-T methods agreed well with experiments. The FEM results agreed better with experimental results than those of the M-T method. However, the latter method provides a reasonably accurate analytical estimate for the nanocomposite modulus. Fisher<sup>17</sup> studied the effect of the waviness of nanofibers using finite element analysis and incorporated this effect into the M-T micromechanical method. Shi et al.<sup>45</sup> also studied analytically the effect of the nanofiber waviness. Both models by Fisher<sup>17</sup> and Shi et al.<sup>45</sup> assume perfect bonding between CNF/CNT and consequently yield an upper bound of the properties of a nanocomposite.

The bonding between the reinforcement and matrix significantly affects the mechanical properties of nanocomposite materials. For CNT/CNF-reinforced composites, the high surface area of CNTs/CNFs creates a large interfacial region that has properties different from the bulk matrix. Therefore, it is important to account for the degree of adhesion of the reinforcement to the matrix to improve the accuracy of a micromechanics model. Pukanszky<sup>39</sup> studied the interface of multicomponent materials. Wagner et al.,<sup>52</sup> Lourie and Wagner,<sup>34</sup> and Jia et al.<sup>29</sup> studied the effect of interfacial bonding on the mechanical properties of CNT-reinforced composites experimentally. Shi et al.<sup>46</sup> modified their approach for stiffness prediction of nanocomposites in Reference 45 by including the effect of the interface. They considered the interface as a third phase (an inclusion with a different modulus from that of the nanotube) and used the multiphase M-T micromechanical method to estimate the stiffness of the composite. They justified their assumption that the foregoing multiphase model can describe the effect of the interface by citing Reference 8. Although the results of Shi et al.'s approach in Reference 46 are plausible, the assumption that the composite consists of the nanotube and the interface dispersed randomly in the matrix has not been justified adequately in the opinion of the authors of this chapter. Odegard et al.<sup>36</sup> developed a model for analyzing the interface effect on nanocomposites, but their model considers spherical reinforcements. When the authors of this chapter modified this model for cylindrical reinforcements and tested it for unidirectional composites, they did not obtain satisfactory results. Specifically, although, the variation in the Young's modulus of the composite with the volume fraction of the reinforcement seemed reasonable,

very little difference was found in the longitudinal and transverse moduli. This result is counterintuitive for unidirectional composites. Therefore, the authors believe that although the model presented by Odegard et al.<sup>36</sup> considers the physics of the problem, it is not valid for cylindrical CNTs/CNFs.

### 11.1.2.2 Probabilistic and Reliability Analysis of Nanocomposites

In engineering problems, uncertainties can be classified as random and epistemic. Random uncertainty, or variability, refers to inherent randomness in natural phenomena or processes. Random uncertainty is also called irreducible uncertainty, because it cannot be reduced by acquiring knowledge. Epistemic uncertainty is due to lack of knowledge; it is also called reducible uncertainty because it can be reduced by collecting data. Probabilistic analysis accounts for both variability and epistemic uncertainty.

The modulus of the nanotubes/nanofibers cannot be estimated accurately. As a result, the modulus is specified in terms of upper and lower bounds, which are far apart. Moreover, there is uncertainty and variability in the moduli of the matrix and the interface between the nanotubes/nanofibers and the matrix. It is important to account for the variability and uncertainty in the moduli of the constituent materials of nanocomposites using probabilistic analysis because uncertainty and variability significantly affect the composite material properties. Probabilistic analysis provides a probability distribution of the modulus of the composite. This information is more useful for making design decisions than a single value of the modulus obtained by deterministic analysis because it shows the confidence in the estimate of the modulus. Many researchers, cited in Reference 21, developed methods for probabilistic analysis and reliability analysis of conventional composites. Thostenson and Chou<sup>50</sup> used probabilistic models to account for the distribution of the diameters of CNTs/CNFs. However, there is no literature in the public domain on probabilistic analysis of nanocomposites and of structures made of nanocomposites that accounts for the variability and uncertainty in the moduli of the constituent materials.

### 11.1.3 Scope and Objectives

As mentioned in Section 11.1.2, there has been significant work in the areas of stiffness analysis of conventional composites and nanocomposites, and in reliability methods. What is lacking, however, is an integrated methodology for deterministic and probabilistic analysis of nanocomposite materials and structures made of these materials. The deterministic micromechanical model predicts the stiffness of nanocomposite materials when the properties of the CNT/CNF and polymer matrix are known. The failure analysis model predicts the load-deflection behavior of a structure made of nanocomposite materials. The probabilistic model determines the probability density function (PDF) of the modulus of the nanocomposite and the sensitivity of the nanocomposite modulus to uncertainties in the moduli of the phase materials, and the reliability model predicts the probability of failure of structures made of nanocomposite materials.

This chapter presents a study whose objective is to develop a methodology for probabilistic and reliability analysis of structures made of nanocomposite materials. This methodology is developed by integrating three models: one for predicting the stiffness of nanocomposites, a second model for failure analysis of structures made of nanocomposites, and a method for probabilistic and reliability analysis of materials and structures.

Inputs to the micromechanical model are the properties of the phase materials (CNT/CNF, matrix, and interface) and their volume fractions. The phase material properties can be estimated from experiments or from molecular dynamics models. Inputs to the probabilistic model are the probability distributions of the properties of the constituent materials of a nanocomposite material. Output of the methodology includes the following: (1) the matrix of the elastic constants of the nanocomposite, histograms, and estimates of the mean values and standard deviations of these constants; (2) load-deflection data for a plate under axial or transverse loading; and (3) the probabilities of the important failure modes and the sensitivity of these failure probabilities to the input parameters.

In this chapter, the nanofibers/nanotubes are assumed straight. Agglomeration of the fibers is not considered, so the nanocomposite is assumed macroscopically homogeneous. In the encapsulated inclusion interface model, the interface is assumed to surround the CNT/CNF only on the circumference, but not on the circular ends.

### 11.1.4 New Developments in the Study of This Chapter

There are three new developments in this study. The first is an integration of the following four models:

1. A model for predicting the stiffness of nanocomposites with and without considering the CNT/CNF–matrix interface
2. A model for probabilistic analysis of nanocomposites
3. A model for predicting the strength and for performing failure analysis of plates made of nanocomposites
4. A model for reliability analysis of plates made of nanocomposites.

The second development is the encapsulated inclusion model that accounts for the interface between the nanofiber (NF)/nanotube (NT) and the polymer matrix. This encapsulated model can be used to predict the stiffness of the nanocomposite. This model is an extension of the model presented by Shi et al.<sup>46</sup>

The third development is the tool for probabilistic analysis of nanocomposites materials and structures. This analysis, in addition to accounting for the variability and uncertainty in the phase material properties, performs sensitivity analysis to identify those properties whose variation has the highest impact on the mechanical properties of a nanocomposite material and on the reliability of a structure made of a nanocomposite material. This is valuable information to a designer because it helps him or her identify those properties that must be controlled most carefully to improve performance and reliability.

A custom FORTRAN 90 code was developed by the authors for predicting the mechanical properties of nanocomposite materials, and existing in-house codes were used for the strength and reliability models. The in-house codes provide the user with more flexibility than commercial codes and facilitate the exchange of information between the models (Figure 11.4).

This study lays a foundation for future work on modeling spatial variation of material properties. The in-house code can be modified to include new information about the behavior of nanocomposites. The

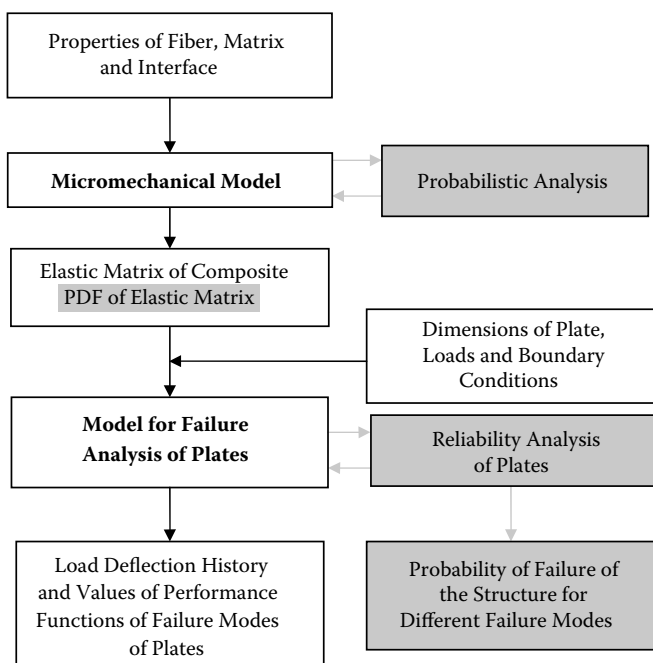


**FIGURE 11.4** Flow of information between various models and methods for deterministic and probabilistic analyses of plates made of conventional composites and nanocomposites. Tools and results of the probabilistic part of this study are highlighted in gray.

method could also be used to analyze continuous-fiber composite laminates where a carbon nanofiber composite is used as the matrix material, and conventional carbon fibers are added to further enhance structural strength and performance.

### 11.1.5 Chapter Outline

Section 11.2 focuses on micromechanical modeling of NF/NT composites using M-T<sup>35</sup> theory. It is assumed that the NFs/NTs and matrix are perfectly bonded. A numerical example is presented that integrates the M-T method and the failure analysis model for predicting the load-deflection history of a structure made of nanocomposite materials.

Section 11.3 presents a model for predicting the stiffness of nanocomposites by considering the reinforcement–matrix interface. A modified two-step approach, which uses two concentric cylinders encapsulated in the matrix, is developed based on the models by Whitney and Riley,<sup>54</sup> Agarwal and Broutman,<sup>4</sup> and Mori and Tanaka.<sup>35</sup> This approach yields a continuum-based constitutive model for predicting the matrix of the elastic constants of nanocomposites. The model assumes that the CNT/CNF, interface, and matrix are continuous and perfectly bonded to each other. It further assumes that the *inclusion* (the two concentric cylinders representing the CNT/CNF and the interface) is embedded into the matrix. This model computes the elastic modulus of nanocomposites in two steps. First, a mechanics approach<sup>54</sup> is used to compute the properties of the inclusion whose physical structure is similar to the three-phase unit cell model presented in literature.<sup>46</sup> In the second step, the M-T<sup>35</sup> model is employed to estimate the elastic properties of the composite from those of the inclusion and matrix. The developed approach is demonstrated with examples.

In Section 11.4, a methodology for probabilistic analysis of nanocomposites is presented. The methodology consists of a probabilistic model, which uses Monte Carlo simulation,<sup>41</sup> for estimation of the PDF of the modulus of a nanocomposite given the PDFs of the properties of the constituent materials. This PDF is used for reliability analysis of nanocomposites. Numerical examples for both analyses are presented.

The conclusions of this study are presented in Section 11.5.

## 11.2 Micromechanical Modeling of Carbon Nanotube/Nanofiber Composites

---

### 11.2.1 Introduction

A theory for predicting the effective properties of NF/NT-reinforced polymers is needed in order to understand better the mechanical behavior of these materials. The theory can be developed using modeling methods, such as those shown in Figure 11.5. These modeling methods span a wide range of length scales from  $10^{-10}$  to 1 m. These methods can be categorized into “discrete molecular” and “continuous molecular” in terms of the way they represent a structure. Computational chemistry modeling methods are suitable for discrete molecular representation of structures, whereas computational mechanics methods are suitable for continuous molecular representation. Both modeling methods are based on thoroughly established principles developed in science and engineering, and these methods can predict the atomic structure and mechanical behavior of materials and structures, respectively. For the intermediate length and time scales, multiscale modeling techniques are employed, which use a combination of tools from both computational chemistry and computational mechanics.<sup>51</sup>

As shown in Figure 11.5, each modeling method is associated with modeling techniques. Quantum mechanical and nanomechanical modeling tools are applicable to discrete molecular structures, whereas micromechanical and structural mechanics tools are applicable to materials that can be assumed continuous.

Figure 11.5 shows the relationship of specific modeling techniques in computational mechanics and computational chemistry. The continuum-based methods are classified as micromechanics and structural mechanics. The former category of methods is further subdivided into (1) analytical micromechanics,



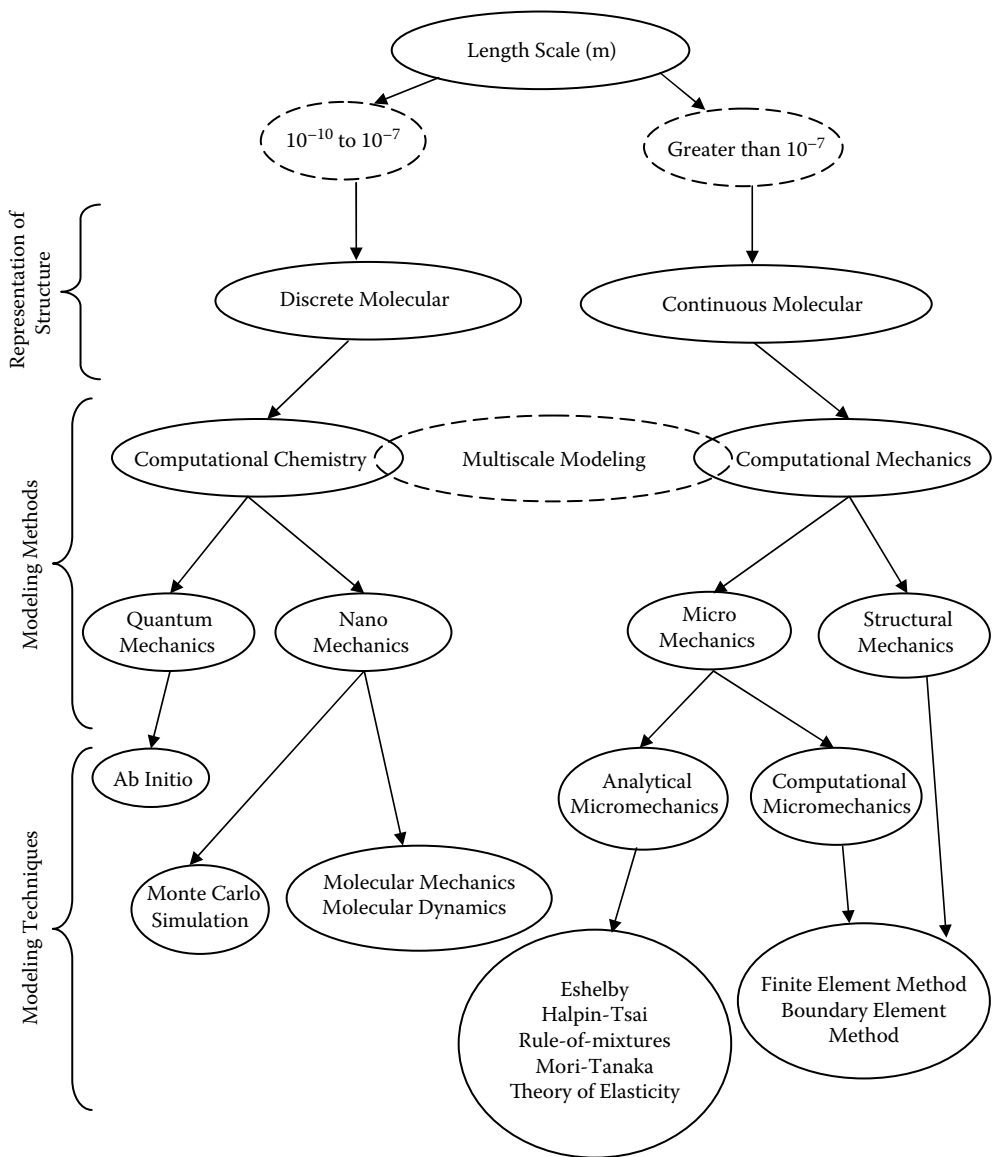


FIGURE 11.5 Various modeling methods and techniques used to develop a theory.

which includes the M-T, Eshelby, Halpin-Tsai methods, and (2) computational micromechanics, which include the finite element method (FEM) and the boundary element method (BEM).<sup>1,7,10,16,22–26,35</sup> Molecular modeling techniques include molecular dynamics, Monte Carlo simulation, and techniques based on first principles. This study assumes that the material is continuous and uses the M-T method to predict the mechanical behavior of nanocomposites given the mechanical properties of the constituent materials.

11.2.2 Mori-Tanaka Method

The M-T micromechanical method has been used by many researchers<sup>18,45</sup> to model the effective behavior of nanocomposites. This model determines the average stress field and overall effective stiffness of a

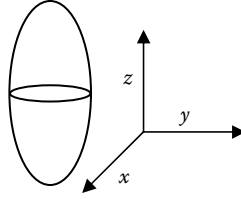


FIGURE 11.6 Inclusion of an elliptical shape.

composite with a nondilute concentration of inclusions. The model has been extended by Benveniste<sup>8</sup> and Weng<sup>53</sup> for composites with multiple inclusion phases and by Tandon et al.<sup>48</sup> and Weng<sup>53</sup> for randomly orientated inclusions.

In this study, M-T solution for a two-phase composite is of interest. One phase is the inclusion (NF/NT, assumed to be straight) and the other is the polymer matrix. First, the case where the inclusions are aligned within the matrix is considered. Then the solution is extended to composites with randomly oriented inclusions, using averaging techniques. The derivation of the matrix of elastic constants of a nanocomposite material with aligned and randomly oriented inclusions is presented briefly in the following sections.

#### 11.2.2.1 Mori–Tanaka Method for Aligned Inclusions

Consider a composite material consisting of straight, aligned inclusions (reinforcements) embedded in a matrix. Let  $C_m$  and  $C_r$  denote the stiffness tensors and  $V_m$  and  $V_r$  the volume fractions of the matrix and the reinforcement materials, respectively. Assume that the inclusions and matrix are perfectly bonded and they are linearly elastic and isotropic. The inclusions are ellipsoids with circular cross section and they are oriented in the  $z$ -direction (Figure 11.6).

The objective is to find the stiffness tensor of the composite in terms of the stiffness of the inclusion and matrix, and their volume fractions. To derive the stiffness tensor of the composite material, consider two models as shown in Figure 11.7, one representing the multiphase composite material and another the matrix material.

Both materials (models) are subjected to a displacement resulting in a uniform far-field strain described by matrix  $\epsilon_u$ . The stresses required to produce this strain in the two models are

$$\bar{\sigma} = C\epsilon_u, \quad \sigma_m = C_m\epsilon_u \quad (11.1)$$

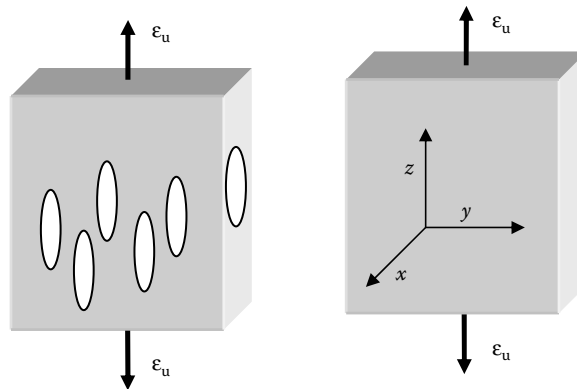


FIGURE 11.7 Models of reinforced composite material (left cube) and matrix material (right cube) used for derivation of stiffness tensor.

where an overscore represents the volume average of the stated quantity. Symbols  $\bar{\sigma}$  and  $\sigma_m$  are the stresses and  $C$  and  $C_m$  the stiffness tensors of the two models (composite and matrix, respectively) in Figure 11.7.

The average stress in the composite model is equal to the sum of the weighted average stresses in the matrix and reinforcement,

$$\bar{\sigma} = V_m \bar{\sigma}_m + V_r \bar{\sigma}_r \quad (11.2)$$

where  $\bar{\sigma}_m$  and  $\bar{\sigma}_r$  are the average stresses in the matrix and inclusion, respectively.

If the volume fraction of the inclusion is small, then the strain in the matrix is equal to the far-field strain  $\epsilon_u$ . Otherwise, the average strain in the matrix is different from the far-field strain because of the inclusions. The average stress in the matrix of the composite material can be expressed as

$$\bar{\sigma}_m = C_m \bar{\epsilon}_m \quad (11.3)$$

where  $C_m$  and  $\bar{\epsilon}_m$  are the stiffness tensor and average strain of the matrix, respectively. Similarly, the average stress of the inclusions can be expressed in terms of its stiffness and average strain as

$$\bar{\sigma}_r = C_r \bar{\epsilon}_r \quad (11.4)$$

In order to find the stiffness of the composite, we need to find the average stress of the inclusions. Eshelby derived the following equation for the average stress of a single ellipsoidal inclusion embedded in an infinite matrix using theory of elasticity:

$$\bar{\epsilon}_r = A_r^{dil} \epsilon_u \quad (11.5)$$

where  $A_r^{dil}$  is the tensor of the dilute strain concentration factors of the reinforcement and  $\epsilon_u$  the far-field strain. An expression for this tensor will be presented in the following paragraphs. However, this equation cannot be used directly to find the strain in the inclusions because the strain in the matrix is not equal to  $\epsilon_u$ . The M-T model assumes that the inclusion sees a far-field strain  $\bar{\epsilon}_m$ . Therefore, the average strain in the inclusion is

$$\bar{\epsilon}_r = A_r^{dil} \bar{\epsilon}_m \quad (11.6)$$

The far-field strain  $\epsilon_u$  is equal to the sum of the average weighted strains in the matrix and reinforcement:

$$\epsilon_u = V_m \bar{\epsilon}_m + V_r \bar{\epsilon}_r \quad (11.7)$$

A relation between the average strain in the matrix and the far-field strain can be derived by plugging Equation 11.6 in Equation 11.7 and solving for  $\bar{\epsilon}_m$ :

$$\begin{aligned} \epsilon_u &= V_m \bar{\epsilon}_m + V_r A_r^{dil} \bar{\epsilon}_m \\ \Rightarrow \bar{\epsilon}_m &= A_0 \epsilon_u \end{aligned} \quad (11.8)$$

In Equation 11.8,  $A_0$  is the strain concentration tensor of the matrix and it is equal to  $(V_m I + V_r A_r^{dil})^{-1}$ .

The stiffness tensor of the composite material is found by plugging Equation 11.3, Equation 11.4, Equation 11.6 and Equation 11.7 in Equation 11.2:

$$C = V_m C_m A_0 + V_r C_r A_r^{dil} A_0 \quad (11.9)$$

or

$$C = \left( V_m C_m + V_r C_r A_r^{dil} \right) \left( V_m I + V_r A_r^{dil} \right)^{-1} \quad (11.10)$$

The dilute strain concentration factor of the reinforcement is given by the following equation for ellipsoidal reinforcements in a matrix:

$$A_r^{dil} = \left[ I + S_r C_m^{-1} (C_r - C_m) \right]^{-1} \quad (11.11)$$

where  $I$  is the fourth-order identity tensor. Symbol  $S_r$  denotes the Eshelby tensor for ellipsoidal inclusions. A cylindrical inclusion can be approximated by an ellipsoid with circular cross section and very large aspect ratio. The components of this tensor for an ellipsoidal inclusion with an infinite aspect ratio ( $l/d \rightarrow \infty$ ) parallel to the  $z$ -axis are<sup>18</sup>

$$\begin{aligned} S_{3333} &= S_{3311} = S_{3322} = 0 \\ S_{1111} &= S_{2222} = \frac{5 - 4\nu_m}{8(1 - \nu_m)} \\ S_{1122} &= S_{2211} = \frac{4\nu_m - 1}{8(1 - \nu_m)} \\ S_{1133} &= S_{2233} = \frac{\nu_m}{2(1 - \nu_m)} \\ S_{1212} &= \frac{3 - 4\nu_m}{8(1 - \nu_m)} \\ S_{3131} &= S_{3232} = \frac{1}{4} \end{aligned} \quad (11.12)$$

where  $\nu_m$  is Poisson's ratio of the matrix.

Equation 11.10 for the stiffness tensor has been reported in References 18 and 35.

### 11.2.2.2 Mori–Tanaka Method for Randomly Oriented Inclusions

In this section we consider composites with randomly oriented inclusions. The term *randomly oriented inclusion* means that an inclusion has same probability of being oriented in any direction. This can be achieved by taking orientational averages of the appropriate quantities. Thus, Equation 11.2 can be written as

$$\bar{\sigma} = V_m \bar{\sigma}_m + V_r \{ \bar{\sigma}_r \} \quad (11.13)$$

The curly brackets  $\{ \}$  represent the orientational average (the average over all possible orientations of the fiber). Because the matrix is isotropic, its stiffness and strain concentration tensors are orientation independent.

The equations for the stress and strain become

$$\bar{\sigma} = \left[ V_m C_m + V_r \left\{ C_r A_r^{dil} \right\} \right]^{-1} A_0 \epsilon_u \quad (11.14)$$

$$\epsilon_u = \left[ V_m I + V_r \left\{ A_r^{dil} \right\} \right]^{-1} \quad (11.15)$$

The stiffness tensor for randomly oriented fibers is

$$C = \left( V_m C_m + V_r \left\{ C_r A_r^{dil} \right\} \right) \left( V_m I + V_r \left\{ A_r^{dil} \right\} \right)^{-1} \quad (11.16)$$

This equation is similar to Equation 11.10 except that appropriate averaging is calculated here to account for the orientation of inclusions.

The orientational average of a tensor is calculated by transforming the tensor from a global to a local coordinate system obtained by rotating the global coordinate system and integrating the transformed tensor over the orientational space. The equations for transformation of tensors and calculation of orientational average are given in Section 11.2.2.3 below.

### 11.2.2.3 Euler Angles and Tensor Transformations

As seen in Equation 11.16, orientational averages of tensors have to be calculated in order to determine the effective properties of a nanocomposite with randomly oriented inclusions. This section highlights the tensor transformations and Euler angles necessary for orientational average. For detailed analysis consult Reference 17.

Assume the local axes of the inclusion are denoted by  $x'_1$ ,  $x'_2$ , and  $x'_3$  and the global axes by  $X'_1$ ,  $X'_2$ , and  $X'_3$  (Figure 11.8). Also assume the inclusion is parallel to the  $x'_3$ -axis.

The objective is to develop the transformation matrix  $a_{ij}$  that maps vector  $v_j^i$  in the local coordinate system to coordinates  $v^i$  in the global coordinate system:

$$v^i = a_{ij} v_j^i \quad (11.17)$$

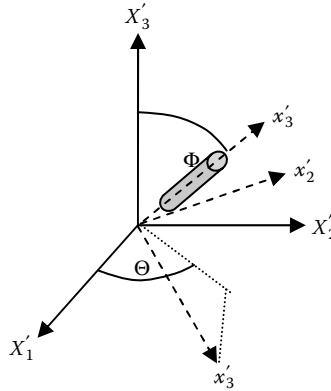


**FIGURE 11.8** Relationship between the local and global coordinate systems. The local coordinate system is obtained by rotating the global one by angle  $\Theta$  about  $X'_3$  and then by angle  $\Phi$  about  $x'_2$ .

In general, it is necessary to specify three Euler angles to describe the orientation of an inclusion, but here, because the inclusion is assumed cylindrical, it is enough to specify only angles  $\Theta$  and  $\Phi$  in Figure 11.8.

Following the transformations (rotation of axes with respect to the angles specified), the local and global vectors are related by Equation 11.18:

$$\begin{bmatrix} X_1 \\ X_2 \\ X_3 \end{bmatrix} = \begin{bmatrix} ab & -c & ad \\ bc & a & cd \\ -d & 0 & b \end{bmatrix} \begin{bmatrix} x'_1 \\ x'_2 \\ x'_3 \end{bmatrix}$$

$$a = \cos \Theta, \quad b = \cos \Phi, \quad c = \sin \Theta, \quad d = \sin \Phi \quad (11.18)$$

Equation 11.18 can also be written as

$$X_i = A_{ij} x'_j \quad (11.19)$$

where  $A_{ij}$  represents the transformation matrix for three-dimensional space.

For higher-order tensor transformations, the usual tensor transformation laws are performed. Thus the transformation of a fourth-order stiffness tensor  $C_{ijkl}$  from local to global coordinates can be written as

$$C_{ijkl}(\Theta, \Phi) = A_{ir} A_{js} A_{kt} A_{lu} C'_{rstu} \quad (11.20)$$

Given Equation 11.20, the orientational average of a fourth-order tensor in three-dimensional (3D) space is,

$$\{C_{ijkl}\} = \frac{1}{2\pi} \int_0^\pi \int_0^\pi C_{ijkl}(\Theta, \Phi) \sin(\Phi) d\Phi d\Theta \quad (11.21)$$

where the transformation matrix for three-dimensional space from Equation 11.19 is used in Equation 11.20 and the term  $\sin(\Phi)$  accounts for the surface area of a sphere.

For a 3D random orientation of inclusions, the stiffness tensor transformations in contracted notation can be written in matrix form as

$$\begin{bmatrix} \{C_{11}\} \\ \{C_{22}\} \\ \{C_{33}\} \\ \{C_{12}\} \\ \{C_{21}\} \\ \{C_{13}\} \\ \{C_{31}\} \\ \{C_{23}\} \\ \{C_{32}\} \\ \{C_{44}\} \\ \{C_{55}\} \\ \{C_{66}\} \end{bmatrix} = \frac{1}{120} \begin{bmatrix} 9 & 45 & 24 & 5 & 5 & 6 & 6 & 10 & 10 & 10 & 6 & 5 \\ 9 & 45 & 24 & 5 & 5 & 6 & 6 & 10 & 10 & 10 & 6 & 5 \\ 64 & 0 & 24 & 0 & 0 & 16 & 16 & 0 & 0 & 0 & 16 & 0 \\ 3 & 15 & 8 & 15 & 15 & 2 & 2 & 30 & 30 & -10 & 2 & -5 \\ 3 & 15 & 8 & 15 & 15 & 2 & 2 & 30 & 30 & -10 & 2 & -5 \\ 8 & 0 & 8 & 0 & 40 & 12 & 32 & 20 & 0 & 0 & -8 & 0 \\ 8 & 0 & 8 & 40 & 0 & 32 & 12 & 0 & 20 & 0 & -8 & 0 \\ 8 & 0 & 8 & 0 & 40 & 12 & 32 & 20 & 0 & 0 & -8 & 0 \\ 8 & 0 & 8 & 40 & 0 & 32 & 12 & 0 & 20 & 0 & -8 & 0 \\ 8 & 0 & 8 & 0 & 0 & -8 & -8 & 0 & 0 & 10 & 14 & 20 \\ 8 & 0 & 8 & 0 & 0 & -8 & -8 & 0 & 0 & 10 & 14 & 20 \\ 3 & 15 & 8 & -5 & -5 & 2 & 2 & -10 & -10 & 10 & 2 & 5 \end{bmatrix} \begin{bmatrix} C_{11} \\ C_{22} \\ C_{33} \\ C_{12} \\ C_{21} \\ C_{13} \\ C_{31} \\ C_{23} \\ C_{32} \\ C_{44} \\ C_{55} \\ C_{66} \end{bmatrix} \quad (11.22)$$

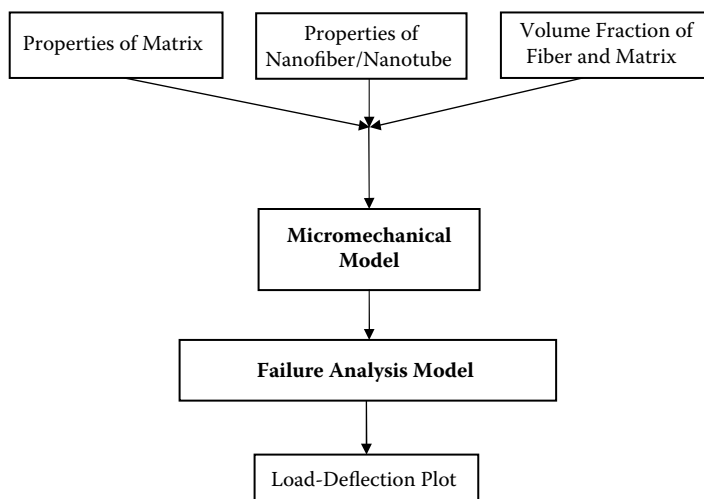


FIGURE 11.9 Flowchart of micromechanical and deterministic failure analysis models.

### 11.2.3 Failure Analysis of Plates Made of Nanocomposite Materials Using Results from the Micromechanical Model

Figure 11.9 explains the interaction between the micromechanical model, which predicts the matrix of elastic constants of a nanocomposite material, and the failure analysis model. The properties of the NF/NT and polymer matrix and their respective volume fractions are the inputs to the micromechanical model. The output of the micromechanical model is the matrix of the elastic constants of the nanocomposite. This matrix is input to the failure analysis model of a plate made of the nanocomposite material. The output of the failure analysis model is the load-deflection history of the nanocomposite plate and the strain distribution in the plate. This information is used to determine if the plate has failed using some criteria for excessive deflection and strain that are specified by the user.

## 11.2.4 Example

### 11.2.4.1 Predicting the Properties of Nanocomposite Materials

A nanocomposite material consisting of unidirectional and randomly oriented straight CNFs is considered. The moduli of the matrix and the reinforcement are 1.9 GPa and 200 GPa, respectively. The effective elastic modulus of the nanocomposite is calculated using Equation 11.10 and Equation 11.16, for unidirectional and randomly oriented fibers, respectively.

Figure 11.10 and Figure 11.11 show the variation of a composite modulus with the volume fraction of the inclusions for unidirectional and randomly oriented fibers, respectively. These results suggest that small amounts of CNF can significantly increase the stiffness of the matrix. For example, an addition of a small amount of CNF with volume equal to 1% of the volume of the composite to the matrix increases the longitudinal modulus of the composite with unidirectional reinforcements from 2 GPa (modulus of the matrix) to 5.5 GPa (Figure 11.10). On the other hand, the presence of CNF does not significantly affect the transverse modulus of the composite. It is also observed that the effect of the CNF decreases with their volume fraction and that there is a point of diminishing returns for this effect that corresponds to a volume fraction of about 15%.

The NFs also significantly increase the modulus of the composite with randomly oriented fibers; the modulus increases from 2 to 2.6 GPa by adding an amount of CNFs to the matrix, whose volume is 1% of the composite. Moreover, the model shows that the modulus increases linearly with the volume fraction of the CNFs. The significant increase in the modulus of nanocomposites has also been observed experimentally by researchers mentioned in the literature.<sup>6,19,40,42,43</sup> However, micromechanics models overestimate

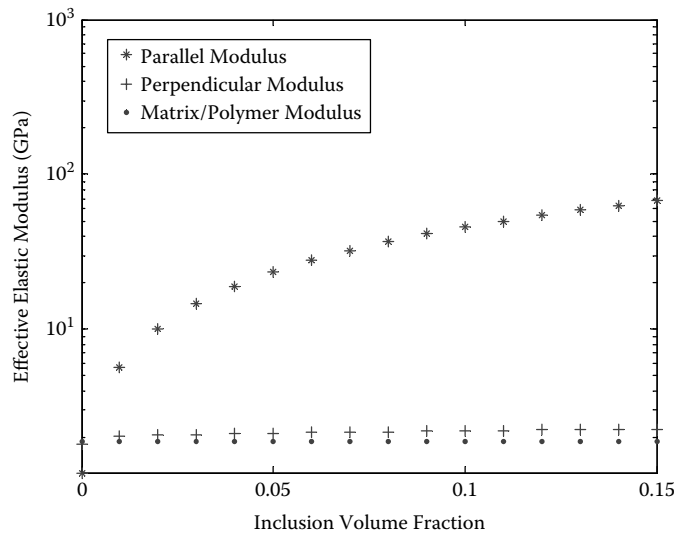


FIGURE 11.10 Effect of volume fraction on elastic modulus of a nanocomposite material with unidirectional straight inclusions.

the modulus of nanocomposites because these models neglect the agglomeration and waviness of CNFs and the flexibility of the interface of the NTs and the matrix.<sup>18</sup> Moreover, the increase in the modulus of the nanocomposites with randomly oriented fibers is expected to decrease with the volume fraction because of the foregoing deficiencies of the micromechanics models.

11.2.4.2 Failure Analysis of Plates Made of Nanocomposite Materials

The matrix of elastic constants of a nanocomposite, computed from Equation 11.10 or Equation 11.16, was input to the failure analysis model. Here, we briefly explain this model, which is presented in detail by Hammitt.<sup>21</sup>

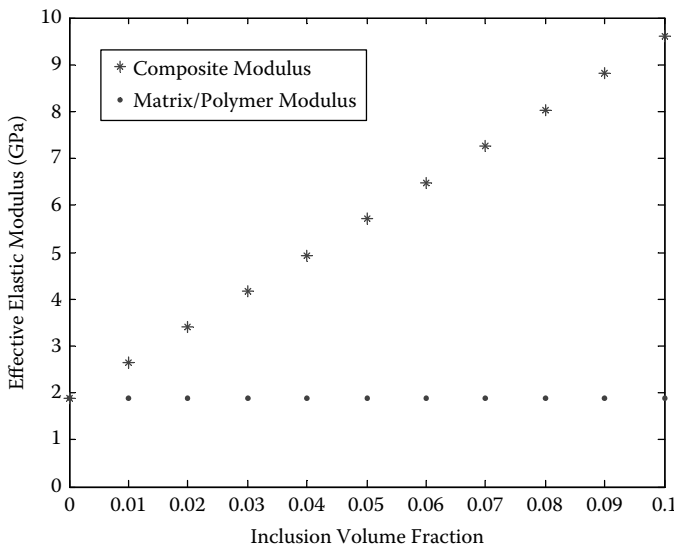
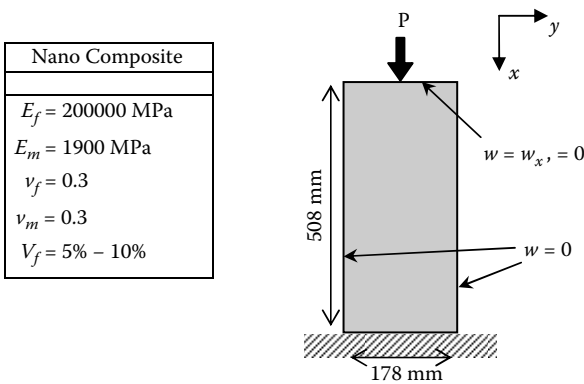


FIGURE 11.11 Effect of volume fraction on elastic modulus of a nanocomposite material with randomly oriented straight inclusions.





**FIGURE 11.12** Properties and geometry of graphite epoxy plate. (Note:  $w$  is the displacement in the  $z$ -direction, and  $w_x$  is the derivative of this displacement with respect to  $x$ .)

In this method, plates are modeled by 20-degree-of-freedom, four-noded rectangular finite elements. A large-displacement formulation that is capable of modeling geometric and material nonlinearity was developed to facilitate the simulation of load-deflection behavior in the postbuckling regime. To calculate the postbuckling response of plates, it was also necessary to use a time-stepping algorithm that is able to traverse limit points in the load deflection history. This was accomplished by an arc-length control algorithm, as described by Hammitt.<sup>21</sup>

To induce buckling in a finite element model of a flat plate, transverse loading, eccentric axial loading, or initial imperfections must be introduced. Because one objective of the study (Hammitt<sup>21</sup>) was to investigate the sensitivity to initial imperfections, a method was developed for introducing an imperfection profile into the model. This profile was assumed to be a linear combination of the first three buckling mode shapes (i.e., eigenvectors of the stiffness matrix) of the plate.

The postbuckling response of a flat rectangular graphite-epoxy plate was analyzed. Figure 11.12 shows the properties and geometry of the plate. The finite element mesh consisted of 12 elements in the  $x$ -direction and 6 elements along the  $y$ -direction. The load was distributed across the edge of the plate. The CNFs were randomly oriented in the polymer matrix. The total applied load is 2100 N.

Figure 11.13 shows the postbuckling response of plates with volume fractions of CNFs of 5 and 10%. As expected, the plate with a higher volume fraction of the CNFs exhibits greater strength than the plate with lower volume fraction.

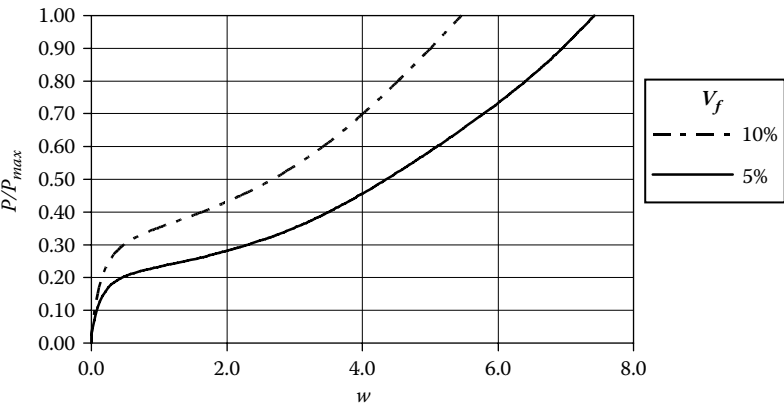


**FIGURE 11.13** Load-deflection curve for a nanocomposite plate with postbuckling strength (assuming perfect bonding between inclusions and matrix).

## 11.3 An Encapsulated Inclusion Model for Interface Modeling of Carbon NT/NF Composites

### 11.3.1 Introduction

A continuum-based micromechanical model is presented in this section that accounts for the interface between the CNT/CNF and matrix to compute the overall nanocomposite elastic modulus. The model assumes that each CNT/CNF is encapsulated in a hollow cylinder (Figure 11.14a). This outer cylinder is called *interface*, and its properties can be obtained either by experiments or molecular dynamics. The model assumes that a CNT/CNF is perfectly bonded to the hollow cylinder and that the inclusion (the cylinder comprising the CNT/CNF and interface) is perfectly bonded to the polymer matrix (Figure 11.14b). The analysis for prediction of the modulus of a nanocomposite is performed in two steps. In the first step, the effective elastic modulus of the inclusion is calculated by considering the inclusion as a long-fiber composite. The calculated modulus of the inclusion is then used as input in the second step, where the elastic modulus of the nanocomposite is calculated considering the inclusion and matrix as two phases.

It is assumed that (a) the CNT/CNF's are straight; (b) the inclusions can be aligned or randomly oriented in the polymer matrix; and (c) the properties of the materials of the CNT/CNF, the interface, and the matrix are linear elastic.

### 11.3.2 Step 1: Finding the Properties of the Inclusion

Consider a two-phase concentric cylinder model shown in Figure 11.14a. In this step, the fiber and interface are aligned, and they can be considered together as a composite with an aligned long fiber. The effective modulus of this composite can be calculated using any of the following three methods:

1. A method based on mechanics<sup>54</sup>
2. The M-T method<sup>35</sup>
3. An approach that uses a rule of mixtures for the longitudinal modulus and Poisson's ratio, and the Halpin–Tsai empirical equations for the transverse and shear moduli. This approach will be called the *conventional method* in the rest of the section.

This section focuses on the mechanics method. The other aforementioned methods will be used to compare the results from the first method. The M-T method<sup>35</sup> yields the stiffness tensor of the inclusion, which can be used as input for step 2, whereas in the mechanics and conventional methods, the moduli of the interface are estimated separately and the stiffness tensor is formed by assuming a transversely isotropic matrix for the inclusion. This assumption is realistic because a fiber exhibits transversely isotropic properties.

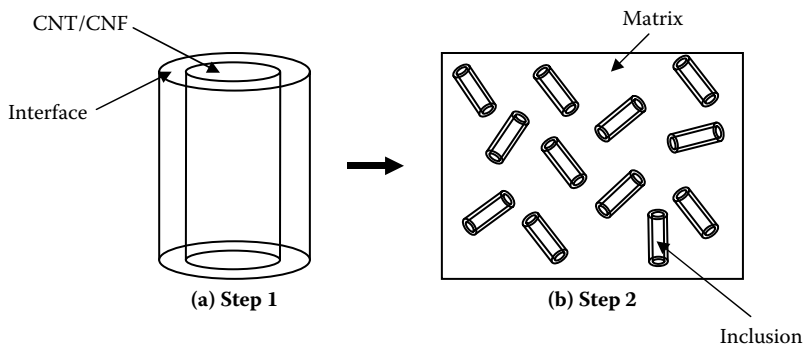


FIGURE 11.14 Two-step approach with inclusions randomly oriented in step 2.

### 11.3.2.1 Mechanics Method

Assuming the composite material to be macroscopically homogeneous and to obey Hooke's law, the stress-strain relationships from theory of elasticity are<sup>32</sup>

$$\begin{aligned}
 \varepsilon_{xx} &= (1/E_T)(\sigma_{xx} - \nu_{yx}\sigma_{yy}) - (\nu/E_L)\sigma_{zz} \\
 \varepsilon_{yy} &= (1/E_T)(\sigma_{yy} - \nu_{yx}\sigma_{xx}) - (\nu/E_L)\sigma_{zz} \\
 \varepsilon_{zz} &= (1/E_L)[\sigma_{zz} - \nu(\sigma_{yy} + \sigma_{xx})] \\
 \gamma_{yz} &= (1/G)\tau_{yz} \\
 \gamma_{xy} &= [2(1 - \nu_{yx})/E_T]\tau_{yz} \\
 \gamma_{xz} &= \tau_{xz}/G
 \end{aligned} \tag{11.23}$$

The orientation of the axes is shown in Figure 11.15. In Equation 11.23, there are five independent elastic constants, which, according to Whitney et al.,<sup>54</sup> and Hashin and Rosen,<sup>23</sup> are longitudinal modulus,  $E_L$ ; transverse modulus,  $E_T$ ; major Poisson's ratio,  $\nu$ ; shear modulus,  $G$ ; and Poisson's ratio in the  $x$ - $y$  plane,  $\nu_{yx}$ .

Whitney et al.<sup>54</sup> and Hashin and Rosen<sup>23</sup> have derived equations for the five constants in Equation 11.23 for conventional, long-fiber composites. These studies did not consider the effect of the matrix-fiber interface; rather, they modeled the matrix and fiber as two concentric cylinders. However, the equations derived (Whitney et al.<sup>54</sup> and Hashin and Rosen<sup>23</sup>) can still be applied to find the five constants for the concentric cylinders representing CNT/CNF and the interface in this study.

It is assumed that the CNT/CNF and interface are isotropic. In the following, the approach by Whitney et al.<sup>54</sup> is summarized:

1. Longitudinal modulus: Consider a cross section of a concentric cylinder composite element as shown in Figure 11.16. The composite element consists of the CNT/CNF and interface. Let an axial force be applied to this element so that the axial strain  $\varepsilon$  of the composite is constant. Consider an Airy stress function as in Equation 11.24,

$$\nabla^4 \bar{\phi} = \frac{d^4 \bar{\phi}}{dr^4} + \frac{2}{r} \frac{d^3 \bar{\phi}}{dr^3} - \frac{1}{r^2} \frac{d^2 \bar{\phi}}{dr^2} + \frac{1}{r^3} \frac{d\bar{\phi}}{dr} = 0 \tag{11.24}$$

Equation 11.24 has the form of the Euler differential equation, the solution of which is given by

$$\bar{\phi} = c_1 \log r + c_2 r^2 \log r + c_3 r^2 + c_4 \tag{11.25}$$

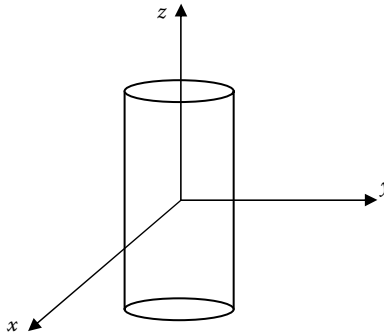
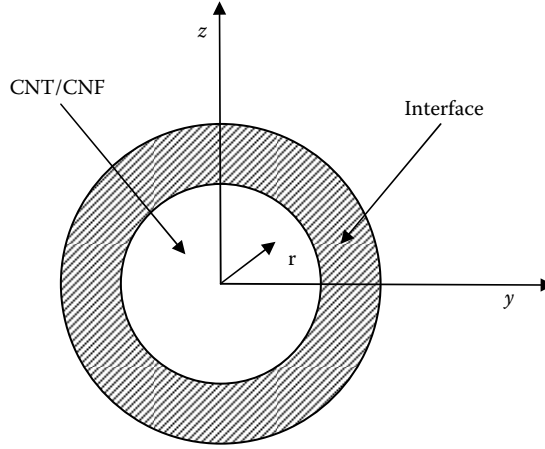


FIGURE 11.15 CNF/CNT orientation.



**FIGURE 11.16** Composite element of inclusion.

Using a stress function for both the CNT/CNF and the interface and applying different boundary conditions to solve for the constants in Equation 11.25 will yield the stresses in the CNT/CNF and the interface. The elastic modulus,  $E_L$ , is now obtained by an energy balance.

$$E_L = \frac{2(\nu_f - \nu_i)^2 E_f E_i (1 - V_f) V_f}{E_i (1 - V_f) L' + [L V_f + (1 + \nu_i)] E_f} + E_i + (E_f - E_i) V_f$$

where  $L' = 1 - \nu_i - 2\nu_i^2$  and  $L = 1 - \nu_f - 2\nu_f^2$  (11.26)

The first term of Equation 11.26 is not significant for most composites.<sup>54</sup> Therefore, the longitudinal modulus can be estimated from the following equation:

$$E_L = E_i + (E_f - E_i) V_f \quad (11.27)$$

The preceding equation is the rule of mixtures.

2. Major Poisson's ratio: The major Poisson's ratio,  $\nu$ , can be found from the calculation of the longitudinal modulus. Considering the radial contraction of the composite, Poisson's ratio is given by

$$\nu = \nu_i - \frac{2(\nu_i - \nu_f)(1 - \nu_i^2) E_f V_f}{E_i (1 - V_f) L' + [L V_f + (1 + \nu_i)] E_f} \quad (11.28)$$

3. Transverse modulus: For the same concentric cylinder model (Figure 11.16), in order to find the transverse modulus, a radial pressure is applied to the surface of the composite cylinder. It is also assumed that an axial stress is applied to the composite cylinder such that the axial strain is zero. The bulk modulus,  $k$ , of the cylinder can be found by considering change in volume caused by the pressure:

$$1 + \Delta V = (1 + \epsilon_z)(1 + \epsilon_y) \quad (11.29)$$

Neglecting second-order terms, we obtain

$$\Delta V = \epsilon_z + \epsilon_y \quad (11.30)$$

Using stress–strain relationships, the bulk modulus will be

$$k = \frac{E_L E_T}{2[(1 - \nu_{yx})E_L - 2E_T \nu^2]} \quad (11.31)$$

$E_T$  needs to be evaluated using Equation 11.31, which in turn needs the bulk modulus to be evaluated using the following stress–strain relationships:

$$\begin{aligned} \sigma_x^f &= \nu^f (\sigma_r^f + \sigma_\theta^f) \\ \sigma_x^m &= \nu^m (\sigma_r^m + \sigma_\theta^m) \end{aligned} \quad (11.32)$$

Applying the boundary conditions and solving for the constants yield

$$\begin{aligned} k &= \frac{(k_f + G_i)k_i - (k_f - k_i)G_i V_f}{(k_f + G_i) - (k_f - k_i)V_f} \\ k_f &= \frac{E_f}{2(1 - \nu_f - 2\nu_f^2)} \text{ and } k_i = \frac{E_i}{2(1 - \nu_i - 2\nu_i^2)} \end{aligned} \quad (11.33)$$

As an approximation,  $\nu_{yx}$ , as given by rule of mixtures, is assumed to be

$$\nu_{yx} = \nu_f V_f + \nu_i (1 - V_f) \quad (11.34)$$

The transverse modulus is obtained by substituting Equation 11.27, Equation 11.33, and Equation 11.34 in Equation 11.31 and solving for  $E_T$ :

$$E_T = \frac{2k(1 - \nu_{yx})E_L}{E_L + 4k\nu^2} \quad (11.35)$$

4. Shear modulus: In the composite element shown in Figure 11.16, the Cartesian equations of elasticity reduce to<sup>23</sup>

$$\nabla^2 u_i = 0 \quad (11.36)$$

where  $i = 1, 2, 3$ , and  $\nabla^2$  is the three-dimensional Laplacian. For the preceding problem, the simple-displacement solution in cylindrical coordinates is as follows:

$$\begin{aligned} u_1 = u_z &= \left( Ar + \frac{B}{r} \right) \cos \theta \\ u_r &= Cz \cos \theta \\ u_\theta &= -Cz \sin \theta \end{aligned} \quad (11.37)$$

where  $A$ ,  $B$ , and  $C$  are arbitrary constants. After calculating the stresses associated with these solutions and applying boundary conditions, the shear modulus can be computed as

$$G = \frac{[(G_f + G_i) + (G_f - G_i)V_f]G_i}{[(G_f + G_i) - (G_f - G_i)V_f]} \quad (11.38)$$

In the preceding equation,  $E_f$ ,  $\nu_f$ , and  $G_f$  are the modulus, Poisson's ratio, and shear modulus of the CNT/CNF;  $E_i$ ,  $\nu_i$ , and  $G_i$  are the corresponding quantities of the interface; and  $V_f$  is the volume fraction of the CNT/CNF. The user of this method needs to specify the foregoing quantities.

### 11.3.2.2 Mori–Tanaka Method

The composite model described in Section 11.2.2.1 can be thought of as a nanocomposite with the CNT/CNF and interface as two phases. One can use the M-T model described in Section 11.2.2.1 to predict the stiffness tensor of an inclusion. Only those expressions from the method that are of interest are highlighted here. For a complete description of the M-T method, refer to Section 11.2.2. The stiffness tensor  $C$  for the inclusion is

$$C = (V_i C_i + V_f C_f : A) : (V_i I + V_f A)^{-1} \quad (11.39)$$

where  $I$  is the fourth-order identity tensor, and  $A$  is the fourth-order dilute strain concentration tensor that relates average strains  $\epsilon_f$  and  $\epsilon_i$ . This relation is as follows:

$$\epsilon_f = A : \epsilon_i \quad (11.40)$$

where

$$A = [I + S : (C_i)^{-1} : (C_f - C_i)]^{-1} \quad (11.41)$$

and  $S$  is the standard Eshelby tensor.<sup>16,18,45</sup> A colon between two tensors denotes contraction (inner product) over two indices. Subscripts  $i$  and  $f$  stand for the interface and reinforcing phase.  $V_i$  and  $V_f$  denote the volume fractions, and  $C_i$  and  $C_f$  denote the tensors of elastic moduli of the corresponding phases.

Even though the M-T method has been developed specifically for discontinuous fibers, its analytical derivation does not distinguish between long and short fibers. To apply this method, the interface properties should be assumed isotropic.

The user of this method needs to specify the following input parameters:

1. Five independent elastic constants if the CNT/CNF is transversely isotropic, as shown in Table 11.1, and two independent constants if it is isotropic.
2. The volume fraction of the CNT/CNF or the interface.
3. The elastic modulus and Poisson's ratio of the interface.

### 11.3.2.3 The Conventional Approach

A CNT/CNF surrounded by the interface can be considered a conventional composite. Hence, the rule of mixtures and Halpin–Tsai empirical relations can be used to find the moduli in different directions, which can then be used to construct a stiffness matrix for the inclusion. This information will be input in step 2. In contrast to the M-T method, the Halpin–Tsai method distinguishes between long and short fibers and uses different equations for each type of fiber.

To apply this method, the CNT/CNF and interface properties should be assumed to be isotropic. According to Equation 11.23, five independent elastic constants are required, but because there are only

**TABLE 11.1** Compliance Matrices for Transversely and Isotropic Materials for Inclusion

Transversely Isotropic  
(for fiber oriented in  $z$ -direction in Figure 11.15)  
 $E_T, \nu_T$ —Modulus and Poisson's ratio in the  $x$ - $y$  symmetry plane  
 $E_L, \nu_{LT}, G_{LT}$ —Elastic modulus, Poisson's ratio, and shear modulus in  $z$ -direction

$$\begin{bmatrix} \frac{1}{E_T} & -\frac{\nu_T}{E_T} & -\frac{\nu_{LT}}{E_L} & 0 & 0 & 0 \\ -\frac{\nu_T}{E_T} & \frac{1}{E_T} & -\frac{\nu_{LT}}{E_L} & 0 & 0 & 0 \\ -\frac{\nu_{LT}}{E_T} & -\frac{\nu_{LT}}{E_T} & \frac{1}{E_L} & 0 & 0 & 0 \\ 0 & 0 & 0 & \frac{1}{2G_{LT}} & 0 & 0 \\ 0 & 0 & 0 & 0 & \frac{1}{2G_{LT}} & 0 \\ 0 & 0 & 0 & 0 & 0 & \frac{1+\nu_T}{E_T} \end{bmatrix}$$

Isotropic  
 $E, \nu$ —Elastic modulus and Poisson's ratio

$$\frac{1}{E} \begin{bmatrix} 1 & -\nu & -\nu & 0 & 0 & 0 \\ -\nu & 1 & -\nu & 0 & 0 & 0 \\ -\nu & -\nu & 1 & 0 & 0 & 0 \\ 0 & 0 & 0 & 1+\nu & 0 & 0 \\ 0 & 0 & 0 & 0 & 1+\nu & 0 \\ 0 & 0 & 0 & 0 & 0 & 1+\nu \end{bmatrix}$$

four in Halpin–Tsai empirical relations, the out-of-plane shear modulus is assumed to be equal to the in-plane shear modulus. Then, if Equation 11.23 is written in matrix form, the compliance matrix can be rewritten as:

$$\begin{bmatrix} \frac{1}{E_T} & -\frac{\nu_T}{E_T} & -\frac{\nu_{LT}}{E_L} & 0 & 0 & 0 \\ -\frac{\nu_T}{E_T} & \frac{1}{E_T} & -\frac{\nu_{LT}}{E_L} & 0 & 0 & 0 \\ -\frac{\nu_{LT}}{E_T} & -\frac{\nu_{LT}}{E_T} & \frac{1}{E_L} & 0 & 0 & 0 \\ 0 & 0 & 0 & \frac{1}{2G_{LT}} & 0 & 0 \\ 0 & 0 & 0 & 0 & \frac{1}{2G_{LT}} & 0 \\ 0 & 0 & 0 & 0 & 0 & \frac{1}{2G_{LT}} \end{bmatrix} \quad (11.42)$$

The following equations estimate moduli in different directions. The rule of mixtures is used to estimate the longitudinal modulus:

$$E_L = E_f V_f + E_i V_i \quad (11.43)$$

where  $E_f$ ,  $V_f$ ,  $E_i$ , and  $V_i$  are the moduli of elasticity and volume fractions of the fiber and interface materials, respectively.

The transverse modulus,  $E_T$ , is estimated using the Halpin–Tsai empirical relations:

$$\frac{E_T}{E_i} = \frac{1 + \xi \eta V_f}{1 - \eta V_f} \quad \text{where, } \eta = \frac{\left(\frac{E_f}{E_i}\right) - 1}{\left(\frac{E_f}{E_i}\right) + \xi} \quad (11.44)$$

The constant,  $\xi$ , is equal to 2 for fibers with circular or square cross section, and it is equal to  $2\frac{a}{b}$  for fibers with rectangular cross section. The fraction  $\frac{a}{b}$  is the rectangular cross-sectional aspect ratio, where the dimension  $a$  is taken in the direction of loading.

The shear modulus ( $G_{LT}$ ) is also estimated by an empirical relation by Halpin–Tsai:

$$\frac{G_{LT}}{G_i} = \frac{1 + \xi \eta V_f}{1 - \eta V_f} \quad \text{where } \eta = \frac{\left(\frac{G_f}{G_i}\right) - 1}{\left(\frac{G_f}{G_i}\right) + \xi} \quad (11.45)$$

where  $\xi = 1$  as suggested by Halpin and Tsai.

The three Poisson's ratios can be calculated from the following equations:

The Poisson's ratio in the  $x$ - $y$  symmetry plane can be obtained by solving the equation for the definition of the shear modulus:

$$\nu_T = \frac{E_T}{2G_{LT}} - 1 \quad (11.46)$$

Poisson's ratio in the 3-direction is given by:

$$\nu_{LT} = \nu_f V_f + \nu_i V_i \quad (11.47)$$

Also,

$$\frac{\nu_{TL}}{E_T} = \frac{\nu_{LT}}{E_L} \quad (11.48)$$

The matrix of elastic constants,  $C$ , is obtained by inversion of the compliance matrix in Equation 11.42:

$$C = [\text{Compliance Matrix}]^{-1} \quad (11.49)$$

The user of the Halpin–Tsai method needs to specify the following input parameters:

1. Two independent constants (modulus and Poisson's ratio) since the CNT/CNF are assumed isotropic.
2. The volume fraction of fiber or the interface.
3. The elastic modulus and Poisson's ratio of the interface.



This section described three alternative methods that can be used for step 1 of the encapsulated inclusion model. The following section describes step 2 of the same model where the M-T method is used to calculate the modulus of the nanocomposite given the properties of the matrix and inclusion.

### 11.3.3 Step 2: Finding the Matrix of Elastic Constants of the Nanocomposite

After the elastic matrix of the inclusion has been computed, the mechanical behavior of the nanocomposite (consisting of the matrix and inclusion) is predicted using the M-T micromechanical model.<sup>18,45</sup> This model is more suitable than the Halpin–Tsai model for nanocomposites, because the latter model assumes long fibers. For a nanocomposite with inclusions aligned in a polymer matrix, the stiffness matrix is calculated by Equation 11.39 to Equation 11.41 with subscript  $i$  for the interface replaced by subscript  $m$  for the matrix, and subscript  $f$  for the fiber replaced by subscript  $r$  for the inclusion. For a nanocomposite with randomly oriented inclusions, the stiffness tensor  $C$  is given by:

$$C = (V_m C_m + V_r \{C_r : A\}) : (V_m I + V_r \{A\})^{-1} \quad (11.50)$$

The curly brackets  $\{ \}$  represent the orientational average of the quantity within the brackets<sup>45</sup> (average over special orientations), and  $V_r$  represents the volume fraction of the inclusion (CNT/CNF + matrix).

#### 11.3.4 Examples

A nanocomposite with randomly oriented CNFs is analyzed. In step 1, the matrix of elastic constants of the inclusion is computed using the mechanics (Equation 11.23), M-T (Equation 11.39), and conventional (Equation 11.42) methods. In step 2, the M-T method (Equation 11.48) is applied.

Six cases are studied in which the mechanics, M-T, and conventional approaches are employed in step 1. The results are compared with those obtained by ignoring the effect of the interface, to assess the effect of the interface on the overall composite modulus. These results are also compared with published experimental results.<sup>6</sup>

##### Case 1: Mechanics Method in Step 1

The CNT/CNF is isotropic with two independent elastic constants shown as follows:

$E_f$	Elastic modulus of CNT/CNF	200 GPa
$\nu_f$	Poisson's ratio of CNT/CNF	0.3

The properties of the interface can be estimated using a molecular dynamics model or by comparing the predictions of a model for estimating the properties of a nanocomposite with experimental results and tuning the parameters of the interface to make the model predictions approach the experimental results. In the latter approach, the model should be validated using new measurements that were not used for tuning the model. In this example, we assume that the Young's modulus and Poisson's ratio of the interface are equal to those of the matrix. The volume fraction of the interface is assumed to be 0.1. The interface properties are presented as follows:

$\nu_i$	Poisson's ratio of interface	0.3
$E_i$	Young's modulus of interface	2 GPa
$V_i$	Volume fraction of interface	0.1

First, Equation 11.23 was applied, which yields the constants of the inclusion. Then Equation 11.50 was applied to determine the matrix of elastic constants of the overall CNT/CNF composite. Figure 11.17 shows the modulus of elasticity of the composite as a function of the volume fraction of the inclusion.

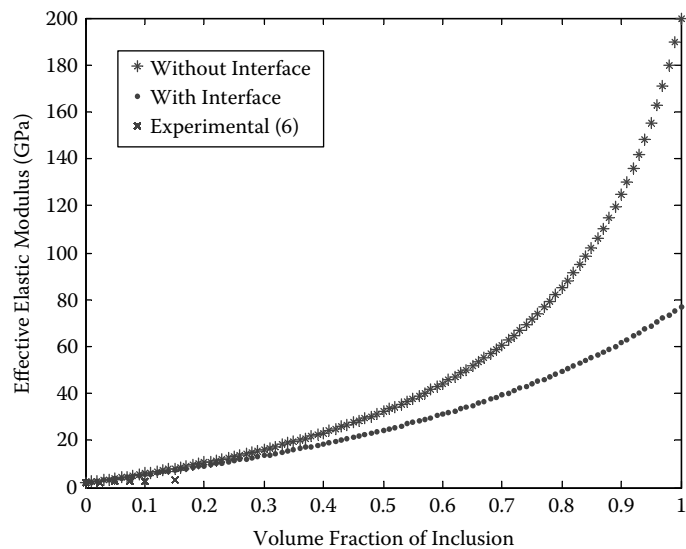


FIGURE 11.17 Variation of  $E$  with volume fraction of inclusion using the mechanics method in step 1.

It is observed that when the volume fraction of the inclusion is zero, then, as expected, the modulus of the composite is equal to the modulus of the matrix (Figure 11.17). When the volume fraction of the inclusion is one, the modulus of the composite is equal to the modulus of the CNT/CNF. The modulus of the composite when the effect of the interface is taken into account is considerably lower than that when the effect of the interface is ignored. For example, for a volume fraction of 0.08 the modulus of the composite is 44.7% lower than the modulus when the effect of the interface is ignored.

The effect of the volume ratio of the inclusion is linear for volume fractions in the range from 0 to 0.2 (Figure 11.18). The modulus increases at a higher rate for larger volume fraction coefficients (Figure 11.18). However, this result will change when one accounts for agglomeration in fibers for higher volume fractions.

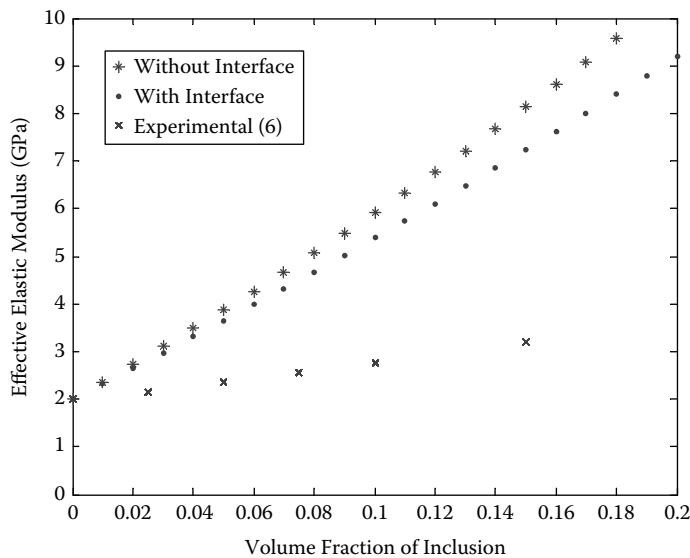


FIGURE 11.18 Variation of  $E$  with volume fraction of inclusion using the mechanics method in step 1.

It is also observed that the model predictions are much higher than experimental measurements. This can be due to deficiencies in the model of the interface, errors in the values of the interface parameters, and agglomeration of the fibers.

### Case 2: M-T Method in Step 1

The CNT/CNF is transversely isotropic and is specified in terms of five independent elastic constants. These elastic constants ( $k$  to  $p$ ) are known as Hill's elastic moduli<sup>45</sup> and are defined as follows:

$k$	Plane-strain bulk modulus normal to the CNT/CNF direction	30 GPa
$n$	Uniaxial tension modulus in CNT/CNF direction	450 GPa
$l$	Associated cross modulus	10 GPa
$m, p$	Shear moduli in planes normal and parallel to the CNT/CNF direction	1 GPa

The matrix of the elastic constants of the CNT/CNF can be determined using these constants, as shown in Equation 11.51 can be determined using these above-mentioned constants as follows

$$C = \begin{bmatrix} k+m & l & l & 0 & 0 & 0 \\ l & n & k-m & 0 & 0 & 0 \\ l & k-m & n & 0 & 0 & 0 \\ 0 & 0 & 0 & \frac{n-l}{2} & 0 & 0 \\ 0 & 0 & 0 & 0 & p & 0 \\ 0 & 0 & 0 & 0 & 0 & p \end{bmatrix} \quad (11.51)$$

As in case 1, we assume that the properties of the interface are the same as those of the matrix. The volume fraction of the interface was assumed to be 0.1. The interface properties are presented as follows:

$\nu_i$	Poisson's ratio of interface	0.3
$E_i$	Young's modulus of interface	2 GPa
$V_i$	Volume fraction of interface	0.1

The matrix properties are as follows:

$\nu_m$	Poisson's ratio of matrix	0.3
$E_m$	Young's modulus of matrix	2 GPa

First, Equation 11.39 was applied, which yielded the constants of the inclusion. Then, Equation 11.50 was applied to determine the matrix of elastic constants of the overall CNF composite. Figure 11.19 shows the modulus of elasticity of the composite as a function of the volume fraction of the inclusion. The modulus of the composite when the effect of the interface is taken into account is considerably lower than that when the effect of the interface is ignored. For example, for a volume fraction of 0.08, the modulus of the composite is 8.2% lower than that when the effect of the interface is ignored.

The effect of the volume ratio of the inclusion is linear for volume fractions in the range from 0 to 0.2. The modulus increases at a higher rate for larger volume fraction coefficients. However, this result will change when one accounts for agglomeration in fibers for higher volume fractions.

It is also observed that the model predictions are much higher than experimental measurements. Again, this could be due to deficiencies in the model of the interface, errors in the values of the interface parameters, and agglomeration of the fibers.

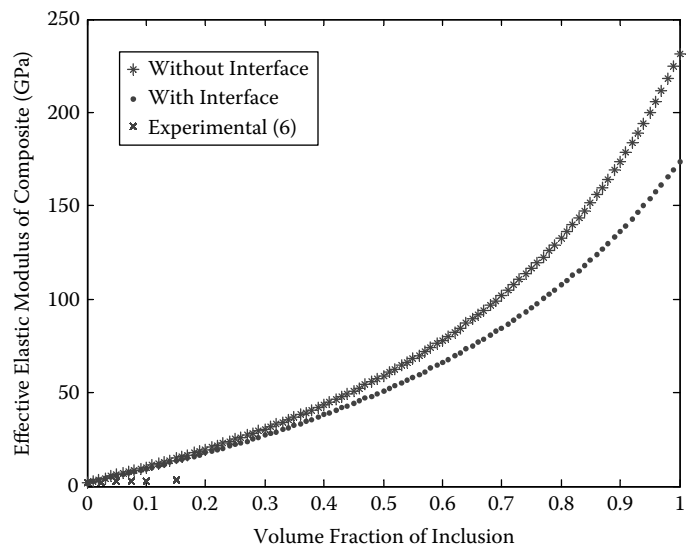


FIGURE 11.19 Variation of composite modulus with volume fraction of inclusion using the M-T method in step 1.

Case 3: Conventional Method Is Used in Step 1

Here, the conventional method is used to estimate the elastic moduli of the inclusion in step 1 instead of the mechanics or M-T method. The CNT/CNF is assumed to be isotropic. The properties of the CNT/CNF, interface, and matrix are the same as in case 1.

Figure 11.20 shows the variation of the modulus of the composite with the volume fraction of the inclusion. The modulus of the composite when the effect of the interface is taken into account is considerably lower than that when the effect of the interface is ignored. For example, for a volume fraction of 0.08, the modulus of the composite is 7.6% lower than that when the effect of the interface is ignored.

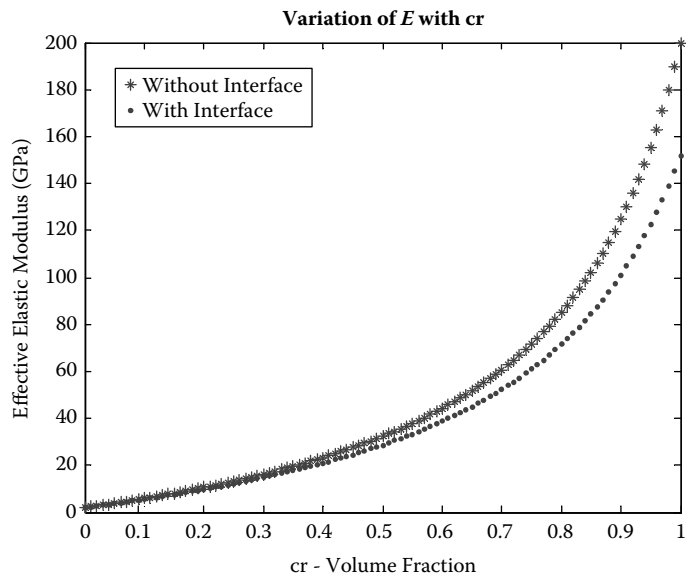


FIGURE 11.20 Variation of composite modulus with volume fraction of inclusion using the conventional method in step 1.

#### 11.3.4.4 Case 4: Comparison of Methods That Use the Mechanics, M-T, and Conventional Methods in Step 1

Here, the moduli predicted by the developed encapsulated approach using the mechanics, M-T, and conventional methods in step 1 are compared.

The CNT/CNF and the matrix properties are the same as in case 1. The interface properties are as follows:

$\nu_i$	Poisson's ratio of interface	0.3
$E_i$	Young's modulus of interface	2 GPa
$V_i$	Volume fraction of interface	0.1

Figure 11.21 and Figure 11.22 compare different methods for calculating the matrix of elastic constants for the inclusion in step 1 for different values of the volume fraction of the inclusion. Figure 11.21 shows that the three methods yield significantly different results. However, as Figure 11.22 indicates, in practical applications where the volume fraction ranges from 0 to 0.2, the results of the three methods are close to each other.

The estimates of the elastic modulus of the composite from the conventional method are higher than those of the M-T method. The reason is that the M-T method assumes discontinuous short fibers in step 1 (estimation of the modulus of the inclusion), whereas the conventional method assumes long fibers in step 1. The conventional method is more realistic for the interface than the M-T method because the CNF/CNT is a long fiber when the inclusion is considered in isolation (Figure 11.14a).

The mechanics method underestimates the elastic modulus compared to the conventional method, which uses Halpin–Tsai empirical equations. The authors believe that the results of the mechanics method are more accurate than those of the conventional method because the mechanics method is based on first principles, whereas Halpin–Tsai method is empirical.

Because the M-T method is not suitable for long-fiber composites, and because the inclusion is a long-fiber composite when considered in isolation, the mechanics method should be the most suitable of the three methods.

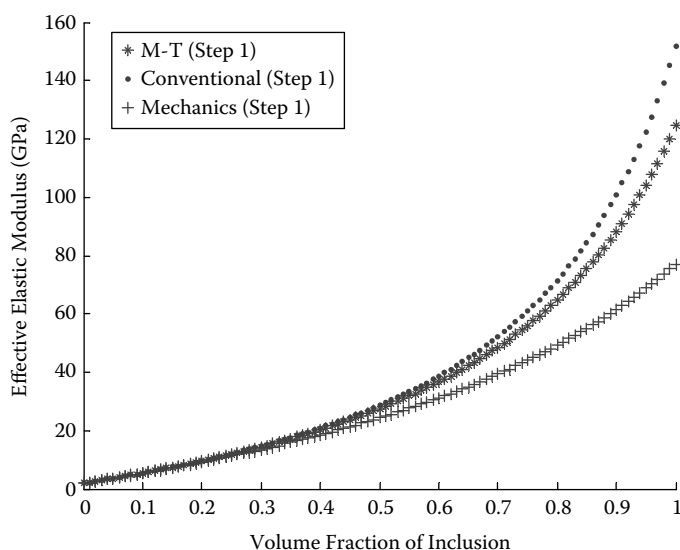


FIGURE 11.21 Comparison of mechanics, M-T, and conventional methods.

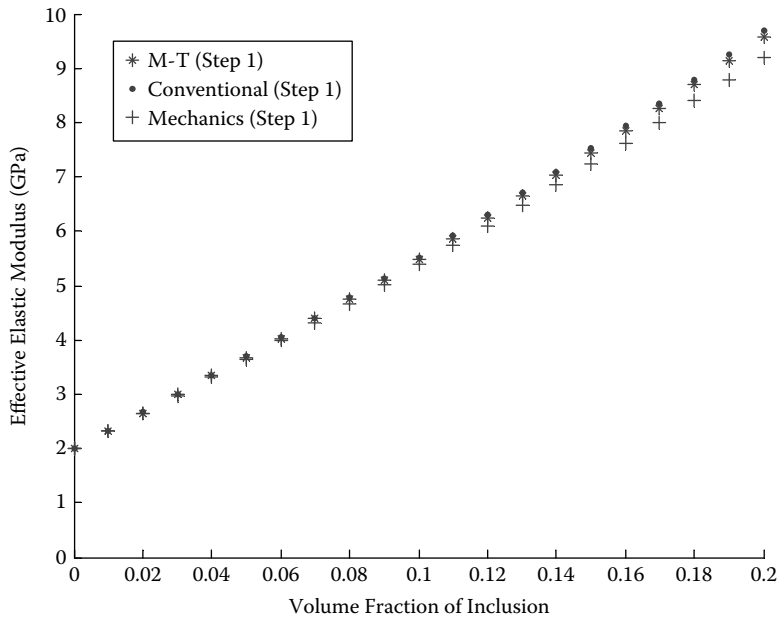


FIGURE 11.22 Comparison of mechanics, M-T, and conventional methods.

### Postbuckling Response of a Rectangular Graphite–Epoxy Plate

The computed matrix of elastic constants of a nanocomposite with interface in Equation 11.50 is used as input to the failure analysis model presented in Section 11.2.4.2. The same example problem presented in Section 11.2.4 and Pilla et al.<sup>38</sup> is solved for the load-deflection history.

The postbuckling response of a flat rectangular graphite–epoxy plate was analyzed. Figure 11.23 presents the properties and geometry of the plate. The NFs/NTs are randomly oriented in the polymer matrix. The total applied load is 2100 N.

Figure 11.24 shows the postbuckling response for plates with volume fractions of NF/NT of 5 and 10%. As expected, the plate with a higher volume fraction of fiber exhibits greater strength than the plate with less fiber.

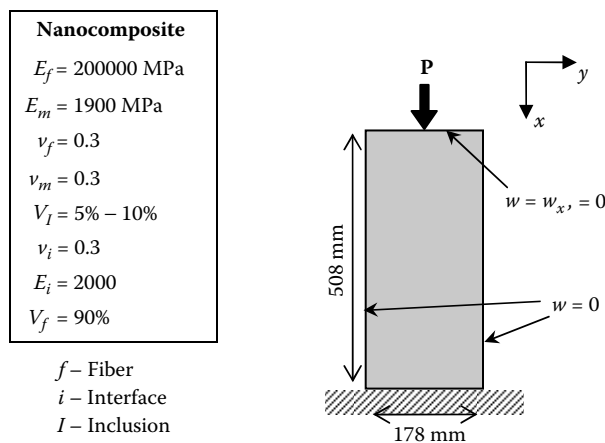
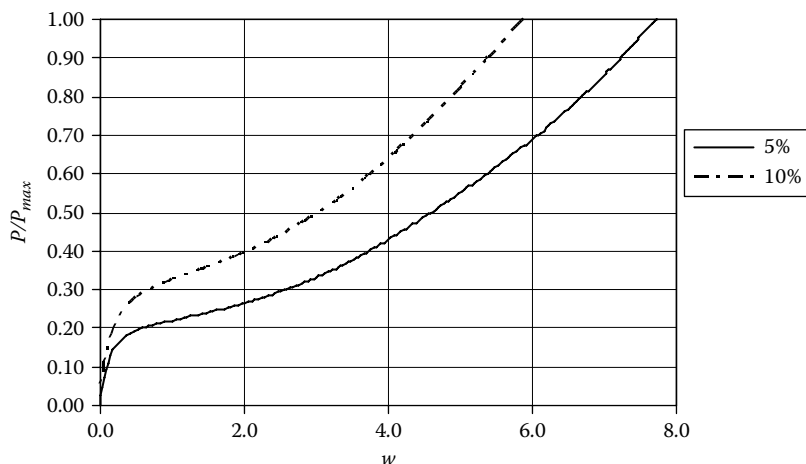


FIGURE 11.23 Properties of graphite–epoxy plate.



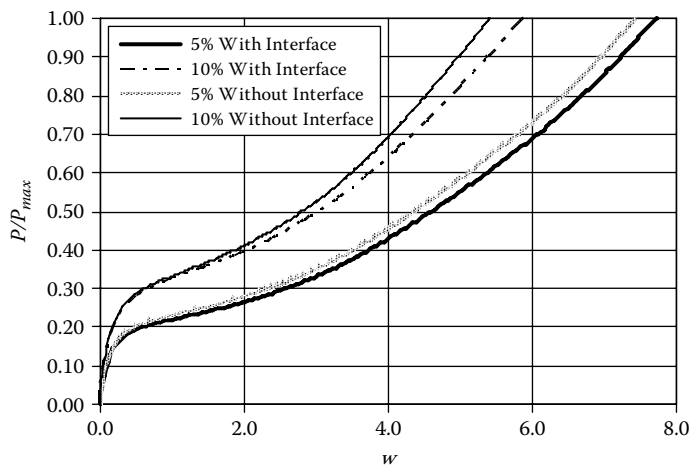
**FIGURE 11.24** Load-deflection curve for a nanocomposite plate with postbuckling strength (with interface).

Figure 11.25 combines the results presented in Figure 11.13 and Figure 11.24 and compares the postbuckling responses of plates with and without considering the effect of interface and for varied volume fractions. It is observed that the deflection of the plate is underestimated significantly when the CNT/CNF is assumed to be perfectly bonded to the matrix in both cases where the volume fraction of the CNF/CNT is 5 and 10%.

## 11.4 Probabilistic and Reliability Analysis of Nanocomposites

### 11.4.1 Introduction

There is great uncertainty in the properties of CNT/CNFs because it is difficult to measure them. For example, Young's modulus is often measured by performing nanoindentation experiments, which entail large errors. Jacobsen et al.<sup>28</sup> estimated the Young's modulus of vapor-grown carbon NFs by measuring the natural frequency of NFs. The values of Young's modulus reported by Jacobsen et al.<sup>28</sup> ranged from



**FIGURE 11.25** Comparison of load-deflection curves for a nanocomposite plate with postbuckling strength for cases of with and without interfaces.

190 to 950 GPa. Moreover, there is significant uncertainty in analytical models for predicting the properties of nanocomposite materials because of approximations in these models. For example, models for predicting the effects of the CNF–matrix interface, agglomeration, and waviness of the CNFs on the properties of a composite material are often based on strong assumptions. It is important to predict the uncertainty in the properties of a nanocomposite material and assess the contribution of different types of uncertainty to the uncertainty in the material properties of the nanocomposite. A methodology is presented in this section that accounts for the uncertainty and variability in the properties of the constituent materials of a CNT/CNF composite and computes the PDF of the composite modulus.

In addition to uncertainty in material properties of nanocomposites, variation in manufacturing processes for structures induces variation in the geometry of these structures. This variation should be considered when analyzing the performance and safety of a structure. When there is uncertainty and variability, the safety of a structure is usually quantified by the reliability (one minus the probability of failure) of the structure.

This section presents two methods, one using Monte Carlo simulation and the other using first-order, reliability methods (FORM), for finding the probability of failure of a plate made of nanocomposite materials. Input to these methods is the PDF of the modulus of the nanocomposite material, which is calculated by the methodology for probabilistic analysis of Young's modulus of nanocomposite materials.

### 11.4.2 Probabilistic Analysis of Nanocomposite Materials

As mentioned earlier, there is great uncertainty in the properties of CNT/CNFs because it is difficult to measure them. A methodology has been developed that accounts for the uncertainty and variability in the moduli of the constituent materials of a CNT/CNF composite and estimates the PDF of the overall composite modulus.

#### Approach

First, the PDFs of the elastic constants of the constituent materials of a nanocomposite are estimated. There are little data regarding the modulus of CNF/CNT because it is difficult to measure this modulus experimentally. When there is large uncertainty in a random variable, it is often assumed that the variable follows a uniform probability distribution. This is justified by the principle of insufficient reasoning—there is no reason to assume that some values are more likely than others. Also, it is easier for a designer to estimate upper and lower bounds for a variable than its mean value, standard deviation, and/or percentiles. In this study it is assumed that the modulus of CNT/CNF, interface, and matrix follow uniform distributions.<sup>41</sup>

Once the PDFs of the moduli of the constituent materials are established, Monte Carlo simulation is used to generate a sample of values of the moduli of the CNT/CNF, interface, and matrix. For each sample value, the modulus of the composite is calculated using one of the micromechanical models described in Section 11.3.2 and Section 11.3.3.

The user of this method needs to specify the following input parameters:

1. Lower and upper bounds for the modulus of CNT/CNF
2. Lower and upper bounds or the mean value and standard deviation of the moduli of the interface, and matrix
3. Poisson's ratios of the CNT/CNF, interface, and matrix.

Output of the method includes histograms of the elastic constants of the nanocomposite, and estimates of the distribution parameters of these constants. A PDF is selected for each elastic constant and is fitted to the histogram of this constant. This PDF can be used for reliability analysis of nanocomposites.<sup>21,38</sup>

### 11.4.3 Numerical Example

A nanocomposite with randomly oriented inclusions (CNF plus the CNF–matrix interface) is analyzed to determine the PDF of the modulus. The analysis is performed twice, first by considering the effect of



the interface and then by neglecting it. Information about the material properties needed for probabilistic analysis is presented in the following table:

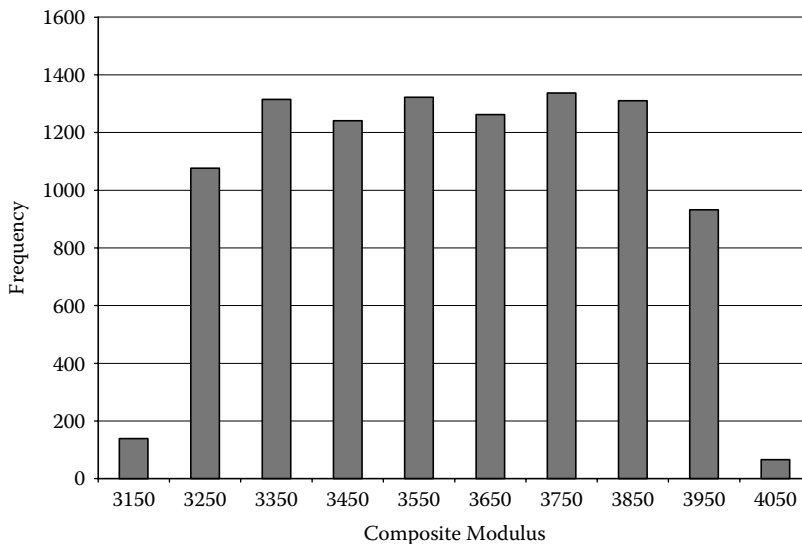
$E_f(\text{lower})$	Lower bound of modulus of CNT/CNF	150 GPa
$E_f(\text{upper})$	Upper bound of modulus of CNT/CNF	250 GPa
$\nu_f$	Volume fraction of CNT/CNF considered part of the inclusion	0.9
$V_f$	Volume fraction of inclusion	0.05
$E_m(\text{lower})$	Lower bound of modulus of matrix	1.85 GPa
$E_m(\text{upper})$	Upper bound of modulus of matrix	1.95 GPa
$E_i(\text{lower})$	Lower bound of modulus of interface	1.50 GPa
$E_i(\text{upper})$	Upper bound of modulus of interface	2.50 GPa
$\nu_i, \nu_f, \nu_m$	Poisson's ratio of CNT/CNF, interface and matrix	0.3

In this example, the modulus of the CNT/CNF is two orders of magnitude greater than that of the matrix. The volume of the CNT is only 4.5% of the volume of the composite.

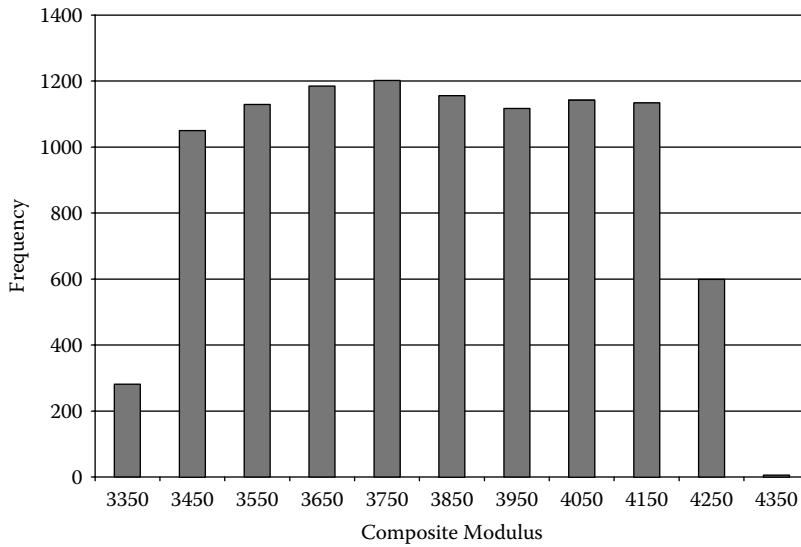
The mechanics method was used to determine the properties of the inclusions when considering the CNF–matrix interface (Section 11.3.2.1) whereas the M-T method was used to determine the composite properties (Section 11.2.2.2 and Section 11.3.3). As mentioned earlier, for a nanocomposite with interface, the mechanics approach is believed to be more realistic than the conventional and M-T methods.

Figure 11.26 and Figure 11.27 show the histograms of the modulus of the composite for the cases where the CNF–matrix interface is considered and neglected, respectively. The descriptive statistics of the data for the two cases (with and without interface respectively) are shown in Table 11.2 and Table 11.3. These results were obtained using 10,000 simulations.

The presence of the CNF/CNT dramatically increases the nanocomposite modulus. Although the volume of the CNF/CNT is only about 5% of that of the composite, the addition of the CNF/CNT stiffness increases the modulus of the composite by about 80% of that of the matrix. It is observed from Table 11.2 and that the variability in the nanocomposite elastic modulus is relatively low; the standard deviation of the modulus is about 7% of the mean. The variability would increase for higher volume fractions of the CNT/CNF. The histograms in Figure 11.26 and Figure 11.27 seem to follow a uniform distribution. This can be attributed to the fact that CNT/CNF, whose randomness dominates (Figure 11.28), was assumed uniformly distributed.



**FIGURE 11.26** Histogram of modulus of composite when the interface between CNT/CNF and matrix is assumed flexible (the modulus is expressed in MPa).



**FIGURE 11.27** Histogram of modulus of composite when CNF and matrix are assumed perfectly bonded (the modulus is expressed in MPa).

The importance of the uncertainties can be assessed from Figure 11.28. Three pairs of bars are shown in this figure. The light gray bars show the variance in the modulus of the composite when one of the three random variables is considered deterministic, whereas the dark gray bars show the variance in the modulus when all three variables are random. The larger the reduction in the variance is when a variable is assumed deterministic, the more important is that variable. Clearly, the uncertainty in the CNT/CNF modulus dominates. If this uncertainty were eliminated, then the uncertainty in the composite modulus would be greatly reduced. This shows the importance of modeling accurately the uncertainty in the CNT/CNF modulus.

#### 11.4.4 Reliability Analysis

The probabilistic analysis performed in Section 11.4.2 yields the PDF of the modulus of the nanocomposite. The output from the probabilistic analysis is input to the reliability analysis model. Here, we present briefly the reliability analysis model. For a detailed discussion the reader is referred to Hammitt.<sup>21</sup>

The primary components of the reliability analysis model are: (1) PDFs for random input parameters (e.g., elastic modulus, yield strength, initial imperfections); (2) performance functions that quantify the

**TABLE 11.2** Descriptive Statistics for Nanocomposite Modulus when the Interface between CNT/CNF and Matrix Is Assumed to Be Flexible

Quantity	Value
Mean (GPa)	3.542
Median (GPa)	3.543
Standard Deviation (GPa)	0.225
Kurtosis	-1.1569
Skewness	-0.009
Minimum (GPa)	3.097
Maximum (GPa)	3.985

**TABLE 11.3** Descriptive Statistics for Nanocomposite Modulus when the CNT/CNF Is Assumed to Be Perfectly Bonded to the Matrix

Quantity	Value
Mean (GPa)	3.767
Median (GPa)	3.765
Standard deviation	0.252
Kurtosis	-1.148
Skewness	0.0105
Minimum (GPa)	3.283
Maximum (GPa)	4.254

point at which failure occurs (and in some cases the “nearness” to failure); and (3) a deterministic model for calculating the value of the performance functions for a given set of input parameters. Random input is generated and passed to the deterministic model, which calculates a value for each performance function. This process is repeated several times to generate data from which the likelihood of failure and the sensitivity to variation in the input parameters can be calculated. There are many algorithms for controlling this iterative process, including Monte Carlo simulation, FORM, and second-order reliability method (SORM). These methods vary in complexity and computational expense, as discussed in Hammitt.<sup>21</sup>

Figure 11.29 shows the flow of information between the models for probabilistic, micromechanics, and reliability analyses for nanocomposite plates.

### 11.4.5 Numerical Example

The example problem presented in Section 11.2.4 is considered here, but now the modulus of the nanocomposite, load factor, yield strength, and imperfection are random variables. For the nanocomposite, the inclusion is assumed to be randomly oriented in the polymer matrix. As in the example in

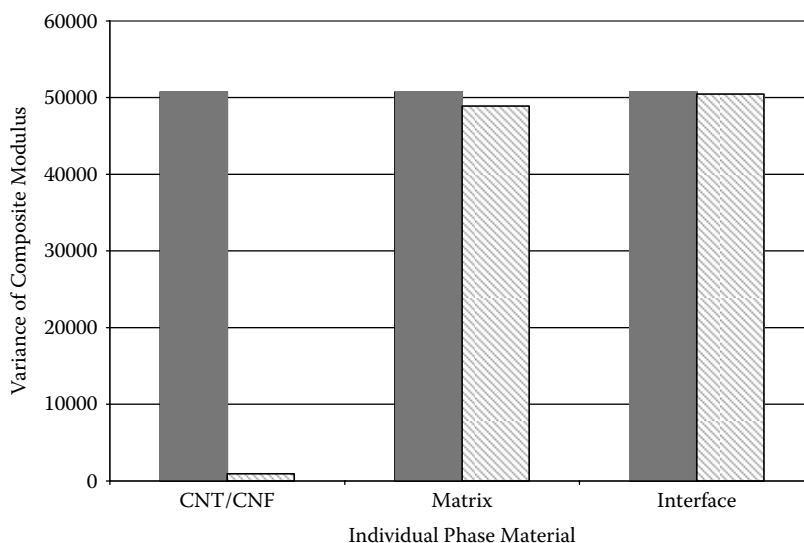


**FIGURE 11.28** Sensitivity of overall composite modulus to constituent materials.

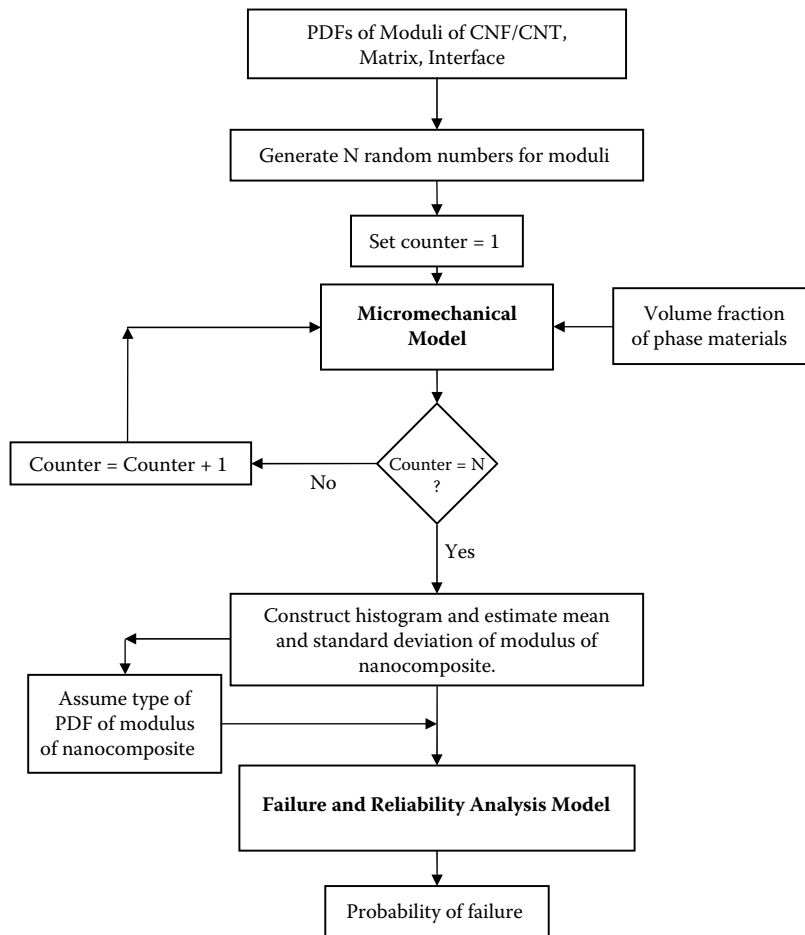


FIGURE 11.29 Monte Carlo simulation for estimation of probability of failure of a nanocomposite plate.

Section 4.3, the reliability of the plate was calculated for two cases in which (1) the CNT/CNF is assumed perfectly bonded to the matrix and (2) the interface between the CNT/CNF and the matrix is considered flexible. Figure 11.30 shows the plate geometry and input parameters for both problems. The plate has two failure modes: excessive displacement and excessive strain. The maximum allowable displacement was set at 42 mm, and the maximum allowable strain was set at 0.5 mm/mm.

Table 11.4 shows the PDF of the modulus,  $E$ , of the nanocomposite. The mean values and standard deviation of  $E$  are equal to the corresponding descriptive statistics obtained from the probabilistic analysis in Section 11.4.3.

The probabilities of failure of the modes of the plate were calculated using Monte-Carlo simulation and a FORM method. In the latter method, both the Hasofer–Lind and the gradient projection algorithms were employed to determine the most probable point.<sup>34</sup> Although importance sampling could be employed for Monte-Carlo simulation, it is not used in the examples presented here because the failure probabilities were high.

The failure probabilities of the modes for both cases where the interface between the matrix and CNT/CNF is considered flexible and rigid are shown in Figure 11.31 and Figure 11.32, respectively. The vertical axis represents the probability of failure, and the horizontal axis represents various analytical and simulation techniques. Good agreement is observed among the methods, except for the results of

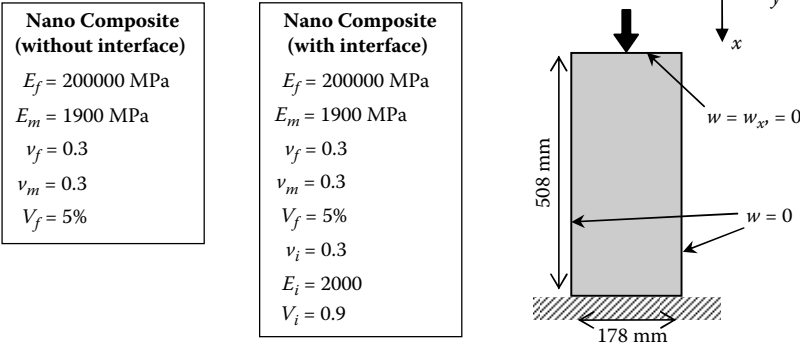


FIGURE 11.30 Geometry and input parameters for graphite-epoxy plate.

the Monte Carlo simulation with 100 replications. Mode 1 (failure due to excessive deflection) is more important than mode 2 (failure due to straining). Note that the computed probabilities of failure are high, and would not be acceptable in practice. They are acceptable, however, for demonstrating the methodology.

The histograms of Young’s modulus,  $E$ , in Section 11.4.3 suggest that Young’s modulus of the nano-composite,  $E$ , follows a uniform distribution. In order to investigate the effect of the type of PDF of Young’s modulus on the calculated probabilities of failure, the failure probabilities of the modes were computed twice, assuming uniform and normal PDFs for Young’s modulus. The results of the reliability analysis in Table 11.5 show that if  $E$  is assumed to follow a normal distribution, the failure probabilities of the two failure modes do not change significantly compared to the estimates corresponding to a uniform distribution.

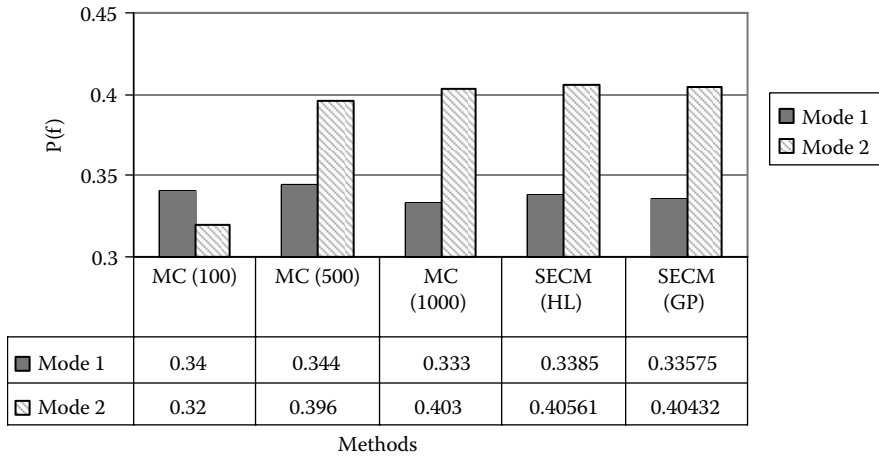
**11.4.5.1 Effect of the CNF/CNT–Matrix Interface on the Probability of Failure of Nanocomposite Plates**

In this section the probabilities of failure obtained by reliability analysis of nanocomposite plates for the cases where (1) the CNF/CNT is perfectly bonded to the matrix and (2) the interface between the CNF/CNT and matrix is flexible. The same example shown in Figure 11.30 is solved. Figure 11.33 and Figure 11.34 compare the calculated failure probabilities for mode 1 (excessive deflection) and mode 2 (excessive straining).

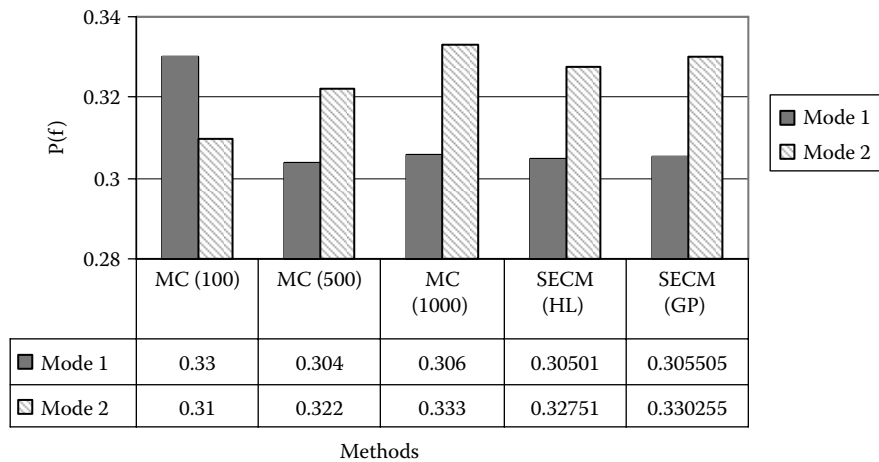
As expected, for both failure modes the probability of failure is higher when the interface between CN to CNF and matrix is considered flexible than when it is assumed to be rigid. The probabilities of failure can be underestimated considerably in the latter case. This suggests that it is important to consider the flexibility of the interface in reliability analysis.

TABLE 11.4 Random Input Variables

Property	True Distribution		Variable Type	Unit
	Mean	SD		
$E$ (with interface)	3.543	0.225	Normal	GPa
$E$ (without interface)	3.767	0.252	Normal	GPa
Yield strength	0.25	0.025	Normal	GPa
Load factor	1.0	0.3	Lognormal	



**FIGURE 11.31** Probability of failure computed by Monte Carlo simulation and FORM (the interface between CNT/CNF and matrix is assumed to be flexible).



**FIGURE 11.32** Probability of failure computed by Monte Carlo simulation and FORM (CNF/CNT is assumed to be perfectly bonded to the matrix).

**TABLE 11.5** Comparison of Probability of Failure for Uniform and Normal Distributions of  $E$  (CNF/CNT is perfectly bonded to the matrix)

Method	Mode 1 $P(f)$	Mode 2 $P(f)$	PDF of Young's Modulus
MC (100)	0.33	0.31	Normal
MC (100)	0.34	0.34	Uniform
MC (500)	0.304	0.322	Normal
MC (500)	0.3	0.32	Uniform
MC (1000)	0.306	0.333	Normal
MC (1000)	0.31	0.332	Uniform

Note: MC ( $X$ ): Monte Carlo simulation for  $X$  random values.

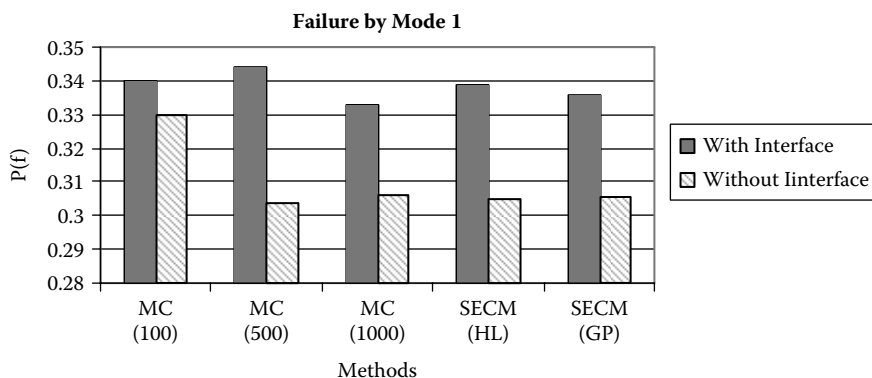


**FIGURE 11.33** Comparison of probability of failure of nanocomposite plates with and without interface for failure mode 1.

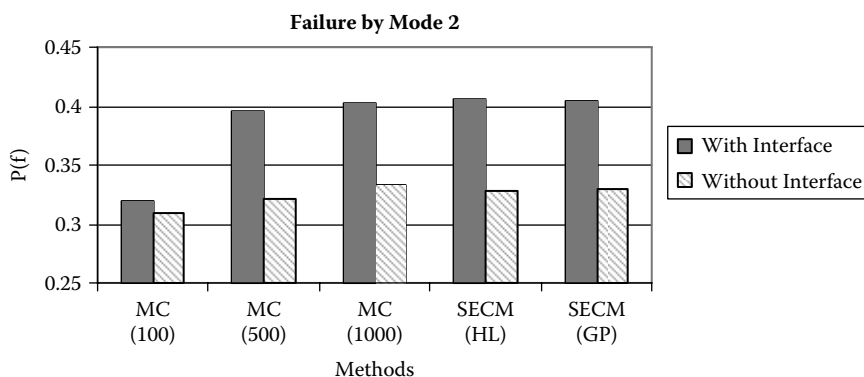


**FIGURE 11.34** Comparison of probability of failure of nanocomposite plates with and without interface for failure mode 2.

## 11.5 Conclusion

A method for calculating the matrix of the elastic constants of nanocomposite materials consisting of carbon nanotubes or nanofibers (CNTs/CNFs) embedded in a matrix has been presented. The method considers the flexibility of the interface between the reinforcement and the matrix. A method for predicting the probability distribution of the elastic constants of nanocomposites by using Monte Carlo simulation has been developed. These two methods have been integrated with a method for failure analysis of structures into a methodology for predicting the load-deflection history and probability of failure of plates made of nanocomposite materials.

The methodology presented in this chapter incorporates the following components:

1. A micromechanics model for nanocomposite materials: A model has been presented for stiffness analysis of nanocomposites. This includes an encapsulated inclusion model to account for the flexibility of the interface between the CNT/CNF and the matrix. For this purpose, the latter model uses three alternative methods, which are based on principles of mechanics or empirical methods, such as the rule of mixtures, and the Halpin-Tsai and Mori-Tanaka models.

The micromechanics models have been demonstrated on examples. It has been shown that the addition of small amounts of CNT/CNF can dramatically increase the stiffness of a nanocomposite material. The reason is that the stiffness of CNT/CNF can be about two orders of magnitude

higher than that of a polymer matrix. It has also been shown that the flexibility of the interface between the reinforcement and matrix can considerably reduce the stiffness of a nanocomposite material.

The micromechanics model was integrated with a method for strength/failure analysis of structures. The resulting method can compute the load-deflection history of a plate and determine if it can fail under a given applied load.

2. A methodology for probabilistic analysis of nanocomposites and reliability analysis of structures: A methodology has been presented for (1) assessing the uncertainty in the modulus of a nanocomposite material due to uncertainties in the moduli of the constituent materials, and (2) determining the sensitivity of effect of the modulus of the material to the uncertainties in the properties of the constituent materials.

In the particular example considered, the modulus of the composite was found to be sensitive only to the uncertainty in the CNT/CNF modulus. The reason is that there is very high uncertainty in the CNT/CNF modulus because it is difficult to measure it. Therefore, it is important to develop methods for measuring the elastic modulus of CNT/CNFs, estimating the uncertainty in the measurements, and estimating the variability in the modulus.

The method for probabilistic analysis has been integrated with a method for reliability analysis of plates. A suite of tools for reliability analysis, such as Monte Carlo simulation and second moment methods, is available. The method for reliability analysis has been demonstrated with an example. The results suggest that the flexibility of the CNT/CNF interface can significantly affect the reliability of a structure.

## Acknowledgments

---

The study presented in this chapter was funded in part by the U.S. Army Research Laboratory (contract number: W911NF-05-1-0542, project manager Dr. Mark VanLandingham). The support is gratefully acknowledged. Such support does not, however, constitute an endorsement by the funding agency of the opinions expressed in the chapter.

Dr. Leslie Berhan, Dr. Ali Fatemi, and Dr. Arunan Nadarajah of the University of Toledo reviewed the work on the micromechanics model and strength analysis of plates in this study and provided valuable suggestions to the authors.

## References

1. Aboudi, J., 1991, *Mechanics of Composite Materials: a Unified Micromechanical Approach*, Elsevier, Amsterdam.
2. Agarwal, B. D., Lifshitz, J. M., and Broutman, L. J., 1974, "Elastic-Plastic Finite Element Analysis of Short Fiber Composites," *Fiber Science Technology*, 7 (1), pp. 45–62.
3. Agarwal, B. D., and Bansal, R. K., 1977, "Plastic Analysis of Fiber Interactions in Discontinuous Fiber Composites," *Fiber Science Technology*, 10 (4), pp. 281–297.
4. Agarwal, B. D., and Broutman, L. J., 1990, *Analysis and Performance of Fiber Composites*, John Wiley & Sons, New Jersey.
5. Andrews, R., Jacques, D., Rao, A. M., Rantell, T., Derbyshire, F., Chen, Y., Chen, J., and Haddon, R. C., 1999, "Nanotube composite carbon fibers," *Applied Physics Letters*, 75(9), pp. 1329–1331.
6. Andrews, R., Jacques, D., Minot, M., and Rantell, T., 2002, "Fabrication of carbon multiwalled nanotube/polymer composites by shear mixing," *Macromolecular Materials and Engineering*, 287(6), pp. 395.
7. Benveniste, Y., 1987, "A new approach to the application of Mori–Tanaka's theory in composite materials," *Mechanics of Materials*, 6, pp. 147–157.
8. Benveniste, Y., Dvorak, G. J., and Chen, T., 1989, "Stress fields in composites with coated inclusions," *Mechanics of Materials*, 7, pp. 305.



9. Broutman, L. J., and Agarwal, B. D., 1974, "A theoretical study of the effect of an interfacial layer on the properties of composites," *Polymer Engineering Science*, 14 (8), pp. 581–588.
10. Budiansky, V., 1965, "On the elastic moduli of some heterogeneous materials," *Journal of the Mechanics and Physics of Solids*, 13, pp. 223–227.
11. Calvert, P., 1999, "Nanotube composites: A recipe for strength," *Nature (London)*, 399, pp. 210–211.
12. Collins, P. G., and Avouris P., 2000, "Nanotubes for electronics," *Scientific American*, pp. 62–69.
13. Daniel, I. M., and Ishai, O., 1994, *Engineering Mechanics of Composite Materials*, Oxford University Press, New York.
14. Dunn, M. L., Ledbetter, H., 1995, "Elastic moduli of composites reinforced by multiphase particles," *Journal of Applied Mechanics*, 62(4), pp. 1023–1028.
15. Elseifi, M., 1998, A New Scheme for the Optimum Design of Stiffened Composite Panels with Geometric Imperfections, Ph.D. Dissertation, Department of Aerospace and Ocean Engineering, Virginia Polytechnic Institute and State University, Blacksburg, Virginia.
16. Eshelby, J. D., 1957, "The determination of the elastic field of an ellipsoidal inclusion and related problems," *Proceedings of the Royal Society of London, Series A*, 241, pp. 376–396.
17. Fisher, F. T., 2002, Nanomechanics and the viscoelastic behavior of carbon nanotube-reinforced polymers, Ph.D. Dissertation, Department of Mechanical Engineering, Northwestern University, Evanston/Chicago, Illinois.
18. Fisher, F. T., Bradshaw, R. D., and Brinson, L. C., 2003, "Fiber waviness in nanotube-reinforced polymer composites: I. Modulus predictions using effective nanotube properties," *Composites Science and Technology*, 63 (11), pp. 1689–1703.
19. Gong, X., Liu, J., Baskaran, S., Voise, R. D., and Young, J. S., 2000, "Surfactantassisted processing of carbon nanotube/polymer composites," *Chemistry of Materials*, 12, pp.1049.
20. Halpin, J. C., and Tsai, S. W., 1969, "Effects of Environmental Factors on Composite Materials," *AFML-TR*, 67, pp. 423.
21. Hammitt, A., 2005, Failure and reliability analysis of nanocomposite plates with variability in material and geometric properties, MS. Thesis, Mechanical, Industrial and Manufacturing Engineering Department, The University of Toledo, Toledo, Ohio.
22. Hashin, Z., 1962, "The elastic moduli of heterogeneous materials," *Journal of Applied Mechanics*, 29, pp. 143–150.
23. Hashin, Z., and Rosen, B.W., 1964, "The elastic moduli of fiber reinforced materials," *Journal of Applied Mechanics*, 31, pp. 1–9.
24. Hill, R., 1963, "Elastic properties of reinforced solids: Some theoretical principles," *Journal of the Mechanics of Physics and Solids*, 11, pp. 357–372.
25. Hill, R., 1964, "Theory of mechanical properties of fiber-strengthened materials: I. Elastic Behaviour," *Journal of the Mechanics of Physics and Solids*, 12, p. 199.
26. Hill, R., 1965, "A self-consistent mechanics of composite materials," *Journal of the Mechanics of Physics and Solids*, 13(4), pp. 213–222.
27. Iijima, S., 1991, "Helical microtubes of graphitic carbon," *Nature (London)*, 354, pp. 56–58.
28. Jacobsen, R. L., Tritt, T. M., Guth, J. R., Ehrlich, A. C., and Gillespie, D. J., "Mechanical Properties of Vapor-Grown Carbon Fiber," *Carbon*, Vol. 33, No. 9, pp. 1217–1221.
29. Jia, Z. J., Wang, Z., Xu, C., Liang, J., Wei, B., Wu, D., and Zhu, S., 1999, "Study on poly (methyl methacrylate)/carbon nanotube composites," *Material Science Engineering A*, 271, pp. 395–400.
30. Jones, R. M., 1999, *Mechanics of Composite Materials*, Taylor and Francis, London.
31. Jordan, J., Jacob, K. I., Tannenbaum, R., Sharaf, M. A., and Jasiuk, I., 2005, "Experimental trends in polymer nanocomposites—a review," *Material Science and Engineering A—Structural Materials Properties Microstructure and Processing*, 393 (1–2), pp. 1–11.
32. Lekhnitskii, S.G., 1963, *Theory of Elasticity of an Anisotropic Body*, Chapter 1, pp. 38, Holden-Day, San Francisco, California.
33. Liu, P.-L., and A. Der Kiureghian 1990, "Optimization algorithms for structural reliability," *Structural Safety*, Vol. 9(3), 161–177.

34. Lourie, O., and Wagner, H. D., 1998, "Transmission electron microscopy observations of single-wall carbon nanotubes under axial tensile," *Applied Physics Letters*, 73(24), pp. 3527–3529.
35. Mori, T., and Tanaka, K., 1973, "Average stress in the matrix and average elastic energy of materials with misfitting inclusions," *Acta Metallurgica*, 21, pp. 571–574.
36. Odegard, G.M., Clancy, T.C., and Gates T.S., 2005, "Modeling of the mechanical properties of nanoparticle/Polymer composites," *Polymer*, 46, no. 2, pp. 553–562.
37. Pilla, S. 2005, "Integration of micromechanical and probabilistic analysis models of nanocomposites," MS. Thesis, Mechanical, Industrial and Manufacturing Engineering Department, The University of Toledo, Toledo, Ohio.
38. Pilla, S., Hammitt, A., and Nikolaidis, E., 2005, "A methodology for strength and reliability analysis of carbon nanofiber and conventional composite plates," *Proceedings of 20th American Society for Composites (ASC) Technical Conference*, September 7–9, Philadelphia, PA.
39. Pukanszky, B., 2005, "Interfaces and interphases in multicomponent materials: past, present, future," *European Polymer Journal*, 41 (4), pp. 645–662.
40. Qian, D., Dickey, E. C., Andrews, R., and Rantell, T., 2000, "Load transfer and deformation mechanisms in carbon nanotube-polystyrene composites," *Applied Physics Letters*, 76(20), pp. 2868.
41. Ranganathan, R., 2000, *Structural Reliability—Analysis and Design*, Jaico, Bombay, India.
42. Schadler, L. S., Giannaris, S. C., and Ajayan, P. M., 1998, "Load transfer in carbon nanotube epoxy composites," *Applied Physics Letters*, 73(26), p. 3842.
43. Shaffer, M. S. P., and Windle, A. H., 1999, "Fabrication and characterization of carbon nanotube/poly(vinyl alcohol) composites," *Advanced Materials*, 11(11), p. 937.
44. Sheng, N., Boyce, M. C., Parks, D. M., Rutledge, G. C., Abes, J. I., Cohen, R. E., 2004, "Multiscale micromechanical modeling of polymer/clay nanocomposites and the effective clay," *Polymer*, 45 (2), pp. 487–506.
45. Shi, D. L., Feng, X. Q., Huang, Y., Hwang, K. C., and Gao, H., 2004, "The effect of nanotube waviness and agglomeration on the elastic property of carbon nanotube reinforced composites," *Journal of Engineering Materials and Technology*, 126, pp. 250–257.
46. Shi, D. L., Feng, X. Q., Huang, Y., and Hwang, K. C., 2004, "Critical evaluation of the stiffening effect of carbon nanotubes in composites," *Key Engineering Materials*, 261–263, pp. 1487–1492.
47. Starnes, J. H., Jr., and Rouse, M., 1981, "Postbuckling and Failure Characteristics of Selected Flat Rectangular Graphite-Epoxy Plates Loaded in Compression," AIAA Paper, 81–0543.
48. Tandon, G. P., and Weng G. J., 1986, "Average stress in the matrix and effective moduli of randomly orientated composites," *Composites Science and Technology*, 27, pp. 111–132.
49. Thostenson, E.T., Ren, Z., and Chou, T. W., 2001, "Advances in the science and technology of carbon nanotubes and their composites: a review," *Composites Science and Technology*, 61(13), pp. 1899–912.
50. Thostenson, E.T., Chou, T.W., 2003, "On the elastic properties of carbon nanotube-based composites: modeling and characterization," *Journal of Physics D: Applied Physics*, 36(5), pp. 573–582.
51. Valavala, P.K., and Odegard, G.M., 2005, "Modeling techniques for determination of mechanical properties of polymer nanocomposites," *Reviews on Advanced Materials Science*, 9, pp. 34–44.
52. Wagner, H. D., Lourie, O., Feldman, Y., and Tenne, R., 1998, "Stress-induced fragmentation of multiwall carbon nanotubes in a polymer matrix," *Applied Physics Letters*, 72(2), pp. 188–190.
53. Weng, G. J., 1990, "The theoretical connection between Mori-Tanaka's theory and the Hashin-Shtrikman-Wadpole bounds," *International Journal of Engineering Science*, 28(11), pp. 1111–1120.
54. Whitney, J.M., and Riley, M.B., 1966, "Elastic properties of fiber reinforced composite materials," *AIAA Journal*, 4, pp. 1537–1542.



2024-T3  
  crack nucleation in, 2–12  
  cyclic stress-strain curves for, 2–8  
    adjusted, 2–10  
  pit-growth model for, 2–30  
  pitting corrosion models of, 2–22  
  stochastic variability of corrosion in, 2–23  
  use of CCCF model to compute corrosion-fatigue life of, 2–39  
  variability of fatigue-crack growth rate in, 2–17

## A

---

A-basis allowable, 2–7  
ABAQUS finite element analysis, 1–4, 7–6  
Accidental limit state. *See* ALS  
Adaptive importance sampling. *See* AIS  
Adaptive structures, 5–15  
  buckling in, 5–18  
  definition of, 5–17  
Additive model, CVMLS, main-effects estimate using, 7–15, 7–17  
Advanced mean value method. *See* AMV method  
Aero damping, effect of geometric variability of blades on, 3–10  
Aerospace Industries Association. *See* AIA  
Age-related degradation effects, ship structures, 9–5  
AIA, damage tolerance strategy of, 3–4  
Air Transport Association. *See* ATA  
Aircraft maintenance  
  risk-based approach to, 2–5  
  use of NDI methods for, 2–2  
Aircraft structural failure, maximum acceptable frequency of, 2–5  
Aircraft structural integrity program. *See* ASIP  
Aircraft wing  
  shape optimization of using RBDO, 4–12  
  system failure probability of, 10–17  
  transport, optimization of using RBDO, 4–18  
Aircraft-structure joints, failure of, 2–2  
AIS, 7–4  
Aligned inclusions, use of M-T method to determine stiffness for nanocomposites with, 11–9  
ALS, 9–2  
Aluminum alloys. *See also* 2024-T3  
  crack nucleation in, 2–12  
  pitting corrosion of, 2–21  
  stochastic variability of corrosion in, 2–23  
AMV method, 7–4, 7–9, 8–14  
AMV+ method, 1–19

Analysis steps, risk/reliability-based condition assessment, 2–36  
Analytical reliability methods, 7–2  
Anomalies, assessing fracture risks associated with, 1–6  
Anomaly fatigue behavior, 3–5  
ANSYS, 10–12  
Approximation models, 4–3  
ASIP, 2–5  
ATA, consensus structure, 3–3  
Automotive industry  
  engineering design, uncertainty in, 7–1  
  failure domain in, 7–23  
  NCAP star rating, 7–16  
  reliability analysis  
    liftgate example, 7–6  
    maximum deflection example, 7–6  
Axial compressor blade, shape optimization of using RBDO, 4–7

## B

---

B-basis allowable, 2–7  
Backward screening, elimination of insignificant input variables using, 7–16, 7–18  
Bayesian analysis, 3–18  
Bayesian probability, 8–2  
Bending moment  
  capacity, 9–7  
  still-water, 9–11  
  wave-induced, 9–11  
Blade-to-blade vibratory stress variation, parametric model for, 3–13  
Blades  
  axial compressor, shape optimization of using RBDO, 4–7  
  design of, use of maximum vibratory stresses in, 3–8  
  failure probability calculation for, 3–16  
  geometric variability of, 3–10  
  integral-order stimuli of, 3–8  
  probabilistic analysis of frequency, 3–12  
  resonant-mode vibration as a cause of failure of, 3–7  
Bottom-up reliability roll-up, 3–4  
Bounds, approximation using, 7–5  
Box-Benkehn DOE method, 4–3, 7–10  
Branch-and-bound method, 7–5, 10–2  
  fast, 10–14, 10–17  
Buckling  
  columns, 5–4  
  load, 5–4  
  local ply, 10–19

- nanocomposite plates, 11–16
- progressive
  - probabilistic analysis of, 5–2, 5–4, 5–11
  - removal of buckled members during, 5–5, 5–7, 5–14
- relationship of loads to, 5–10
- single cup combustor liner, 6–5
- Bulk carriers
  - corrosion of, 9–14
  - local denting of, 9–26
- Burst design, use of probabilistic models for, 3–7

## C

### CAE

- incorporation of RBDO into, 8–19
  - (*See also* RBDO)
- prediction of structural durability using, 8–2
- simulation model for mechanical fatigue, experimental validation of, 8–3
- uniform sampling in, 7–11
- use of for engineering product analysis and design, 8–1
- CAE simulations, 7–8
  - disadvantages of, 7–10
- Campbell diagram, 3–8
  - probabilistic, blade frequency, 3–12
- Cantilever trusses, buckling of, 5–2
- Carbon nanofibers. *See* CNFs
- Carbon nanotubes. *See* CNTs
- CCCF model, 2–28, 2–31
  - comparison with WCF model, 2–33
  - use of to compute corrosion-fatigue life, 2–39
- CEMCAN, 6–3
- Central composite DOE technique, 7–10
- Centrifugal stiffening, 3–8
- Ceramic matrix composites, evaluation of stresses of, 6–1
- Cervical spine injuries, impact assessments, 1–20
- CFD models, 4–2
- CNFs, physical properties of, 11–1
- CNT/CNF-reinforced composites, 11–4
  - interface modeling of, 11–17
  - micromechanical modeling of, 11–7
- CNTs, physical properties of, 11–1
- Coatings, corrosion of on marine structures, 9–13
- Columbia Space Shuttle Launch Vehicle, debris transport modeling, 1–14
- Columns, buckling of, 5–4
- Combustor liners, probabilistic analysis of stress on, 6–1
- COMET-AR, 4–14, 4–16
- Component failures. *See also* Failure, sequences for composite laminates
  - critical, 10–16
  - failure sequences and, 10–15
- Component risk/reliability-based condition assessment, 2–35
- Component-level reliability analysis, 7–2
- Composite laminates
  - creep behavior of, 10–30
  - failure criterion for, 10–34
  - failure of
    - probability of, 10–4
    - stages of, 10–2

- fatigue analysis for, 10–19
- fatigue delamination limit state of, 10–26
- mechanisms of crack initiation and growth in, 10–20
- shear deformation theory for, 10–8
- undamaged, creep behavior of, 10–31
- use of probabilistic analysis to determine fatigue life of, 10–25
  - with stochastic fiber fracture, creep behavior, 10–32
- Composites, CNT/CNF-reinforced, 11–4
  - M-T method for aligned inclusions, 11–9
  - M-T method for randomly-oriented inclusions, 11–11
- Compressors
  - axial blades, shape optimization of using RBDO, 4–7
  - resonant-mode vibration of, 3–7
- Computational chemistry, 11–7
- Computational fluid dynamics models. *See* CFD models
- Computational mechanics, 11–7
- Computer-aided engineering simulations. *See* CAE simulations
- Condition assessment
  - analysis and modeling steps for, 2–36
  - risk-based approach to, 2–5
  - risk/reliability-based approach to, 2–35
- Conditional events, modeling, 1–17. *See also* Probabilistic analysis
- Conjugate mean value method, 8–14
- Conjugate pairs, 3–18
- Containment vessels, use of in high explosion experiments, 1–18
- Continuum damage mechanics, 10–2
- Cornell's first order bounds, 7–5, 10–8, 10–15
- Correlation length, 2–18
- Corroded surface topography, 2–27
- Corrosion, 2–1, 9–24
  - effect of, 9–9
  - effects, types of, 2–28
  - in ships, 9–1
  - pitting
    - models of, 2–22
    - stochastic variability of in aluminum alloys, 2–23
  - random effects, 2–41
  - time-dependent wastage models, 9–13
  - types of, 2–21
  - use of NDI to find, 2–4
- Corrosion-fatigue damage modeling, 2–8, 2–28, 2–41
  - comparative results for, 2–31
- Cpanel, 4–13
- Crack initiation, 2–8, 2–28. *See also* Fatigue cracking
  - fatigue life for, durability analysis of, 8–4, 8–16
  - mechanisms of in composite materials, 10–20
  - model for assessment of, 9–17
  - stochastic variability in, 2–12
- Crack probabilities, 3–6
- Crack propagation, 2–8, 2–29, 9–17. *See also* Fatigue cracking
  - crack-closure model of, 2–16
  - estimation of, 2–26
  - Forman model of, 2–15
  - hyperbolic sine equation model of, 2–16
  - mechanisms of in composite materials, 10–20
  - model for assessment of, 9–18

modified sigmoidal equation model of, 2–16  
 stochastic variability in, 2–17  
 use of LEFM theory to model, 2–14

Crack sizing, errors, 2–37

Crack-closure corrosion-fatigue model. *See* CCCF model

Crack-closure model, 2–16

Crack-growth analysis, 2–2

Cracking  
   deterministic analysis of, 1–24, 2–2  
   premature, use of field-management risk assessments for, 3–7

Crashworthiness  
   characteristics, 1–11  
   use of RBDO in studies of, 4–6

Creep  
   analysis with stochastic fiber fracture, 10–32  
   behavior in composite laminates, 10–30  
   use of probabilistic models for, 3–7

Creep limit state, 10–30

Critical component failure, 10–16

Critical load, 5–4

Critical regions, design optimization and, 8–9, 8–11

Critical stress, determination of, 2–6

Cross-validated moving least squares method. *See* CVMLS method

Cross-validation procedures, 7–13

Cumulative damage models, fatigue cracking, 2–11, 2–14

CVMLS, 7–21  
   additive model, main-effects estimate using, 7–15, 7–17  
   backward screening, elimination of insignificant input variables using, 7–16, 7–18  
   local polynomial fitting using, 7–13  
   variable screening based on, 7–15  
   crash safety example, 7–16

CVMLS method, 7–11

Cycle ratio, 10–21

Cyclic loading, 10–18

Cyclic-symmetry models, 3–13

## D

DADS dynamic analysis package, 8–4

Damage accumulation models, 10–2, 10–21, 10–23

Damage curve approach, 2–12

Damage tolerance analysis  
   use of DARWIN for, 1–3  
   use of NESSUS for, 1–25

Damage tolerance strategy, aerospace industry consensus for, 3–4

Damage-tolerance analysis, requirements for, 3–4

Damping, 3–14

DARWIN, 1–3, 3–6  
   fracture risk assessment using, 1–7  
   gas turbine engine rotor risk assessment using, 1–9  
   general probabilistic framework for risk prediction, 1–8  
   overview of, 1–6

Debris analysis, 1–14  
   uncertainties affecting transport, 1–16

Delamination, 10–2, 10–10, 10–19  
   failure, 10–26  
   stiffness modification for, 10–11

Dent damage in ships, 9–1

Denting, local, effect of, 9–10

Department of Energy. *See* DOE

Design  
   optimization, 8–5, 8–7, 8–9, 8–19  
   parameterization, 8–6  
   uncertainties in, 7–1

Design Assessment of Reliability with INspection. *See* DARWIN

Design rules analysis, selection of target safeties and reliabilities using, 9–4

Design sensitivity analysis, fatigue response, 8–6

Design-of-experiment methods, 4–3, 7–10. *See also* specific methods  
   fractional factorial designs, 7–11

Detection probability, 2–37

Deterministic analysis techniques  
   evaluation of structural integrity of trusses using, 5–1  
   micromechanical model, 11–5

Deterministic fracture mechanics analysis, 1–24, 1–29

Deterministic initial screening, 10–15

Deterministic optimization, 4–12, 4–15

Direct mode determining theory, 10–10

Discrete source damage, 2–5

Disk modes, 3–14

Displacement, 10–8

DOE, Stockpile Stewardship program, 1–1

Double damage curve approach, 2–12

Double-loop optimization, 4–2, 4–5, 7–23

DRAW programs, 8–4

Durability analysis, 8–16  
   validation of, 8–4

Durability analysis and reliability workspace programs. *See* DRAW programs

Durability design optimization, 8–7

Durability-based optimal design, reliability analysis for, 8–12

DYNA3D, use for numerical simulation, 1–18

Dynamic analysis, validation of, 8–4

Dynamic stress history, 8–6

## E

Eccentricity, initial, progressive probabilistic buckling and, 5–11

Economic value analysis, selection of target safeties and reliabilities using, 9–4

Eddy current, 2–39, 2–52  
   use of to find corrosion, 2–4

Edge buckling phenomena, 6–5

Edge delamination, 10–26

EFH, reliability predictions based on, 3–4

Elastic matrix of inclusion, 11–24

Encapsulated inclusion model, interface modeling of CNT/CNF composites with, 11–17

Engine flight hours. *See* EFH

Engineering design  
   automotive industry, uncertainties in, 7–1  
   use of CAE for, 8–1

Equivalent stress, 3–15

Eshelby tensor, 11–21

Eularian hydrodynamics code, use of for numerical simulation, 1–18  
 Euler angles, 11–12  
 Euler load, 5–4  
 Evidence theory, 8–2  
 Excitation frequencies, 3–8  
 Exfoliation, 2–21  
 Experimental validation, 8–2, 8–18  
   fatigue-life analysis and, 8–3  
 Extreme load models, hull girders, 9–11

## F

### FAA

Advisory Circular 33.14-1, 1–9, 3–4  
 Turbine Rotor Material Design program, 1–1

Factorial design method, 4–3

### Failure

composite laminate, stages of, 10–2  
 criteria for composites, 10–34  
 critical component, 10–16  
 definition of, 3–2  
 effect of CNF/CNT-matrix interface on probability of, 11–36  
 model for assessment of due to cracking, 9–18  
 probability computation, 10–2  
 risk of, definition of, 9–2  
 sequences for composite laminates, 10–4, 10–8, 10–12, 10–17  
 theories, 10–10

Failure analysis model, 11–5

### Failure criteria

local, selection of, 2–6  
 uncertainty in, 2–7

Failure hazards, 3–2

Failure modes, hull girders, 9–5

Failure modes effects and criticality analysis.

*See* FMECA

Failure probabilities, 2–55

calculation of, 3–16  
 updating predictions of, 3–18

FALSTAFF, 2–13

Fans, resonant-mode vibration of, 3–7

Fast branch-and-bound method, 10–14, 10–17

FASTRAN, 2–16

use of with CCCF model, 2–39

Fatigue, 2–1

analyses, 9–16  
 cycle ratio, 10–21  
 damage growth in composite materials, 10–2  
 damage modeling, 2–8, 10–20  
 delamination limit state, 10–26  
 in ships, 9–1  
 risk-based maintenance analysis of, 2–43  
 use of probabilistic models for, 3–7

Fatigue cracking, 1–25, 9–25. *See also* Crack propagation

crack-closure model of, 2–16  
 effect of, 9–9

Forman model of, 2–15

hyperbolic sine equation model of, 2–16

modified sigmoidal equation model of, 2–16

time-dependent model of, 9–15

ultimate strength of structural member with, 9–10

Fatigue limit state. *See* FLS

Fatigue loading, 9–25

Fatigue-crack growth rate. *See* FCGR

Fatigue-crack-propagation models, 2–41

Fatigue-life analysis

defining constraints for optimization, 8–8

design optimization for, 8–16

experimental validation and, 8–3

FCGR, variability of in aluminum alloys, 2–17

FEA, 10–12

single cup combustor liner segment, 6–2

stress analyses using, 1–21

truss buckling using probabilistic methodology, 5–2

Federal Aviation Administration. *See* FAA

Fiber breakage, 10–2, 10–6, 10–10

creep and, 10–30

stiffness modification for, 10–11

stochastic, creep analysis with, 10–32

Fiber characteristic strength, 10–36

Field-expansion models, 2–28

Field-management risk assessments, 3–7

Finite element analysis. *See* FEA

Finite element model, modeling behavior of nanocomposites with, 11–4

First ply failure. *See* FPF

First-order reliability method. *See* FORM

First-yield criterion, 9–5

Flexible dynamics modeling, 8–4

Flowliner Fatigue Life, 1–25

FLS, 9–2, 10–18

FMECA, 3–4

Forced response, effect of geometric variability of blades on, 3–10

Forced-response vibratory stress prediction, 3–9, 3–14

Foreign object damage, 3–19

FORM, 4–4, 7–2, 7–7, 8–14, 10–2

Forman model, 2–15, 2–41

FPF, 10–2

Fractional factorial designs, 7–11

Fracture analysis, probabilistic, 1–27

use of PROF software for, 2–5

Fracture mechanics, 9–18

probabilistic, 3–4

Fracture probabilities. *See* Probability of fracture

Fracture reliability, space shuttle main engine flowliner, 1–24

Fracture risk, use of DARWIN for assessment of, 1–6

Fracture toughness, 2–7

Frequency placement, 3–8

## G

Gas turbine engines

design of, use of probabilistic methods for, 3–1

rotors, fracture risk assessment of, 1–9

General corrosion, 2–21, 9–9, 9–24

Glass guidance system, design reliability of, 7–8

Global response-surface models, 4–5

Goodman diagrams, transforming fatigue-curve data to, 3–15  
 Guesstimation, selection of target and safety reliabilities using, 9–4

## H

Halpin-Tsai empirical relations, 11–21, 11–23  
 Hard-alpha inspection programs, use of field-management risk assessments for, 3–7  
 Heat transfer analyses, use of in probabilistic analysis of single cup liner segment, 6–3  
 Helicopter rotor hubs, failure mechanism and model of, 10–26  
 High explosion experiments, use of containment vessels for, 1–18  
 High-cycle fatigue  
   failure probability  
     calculation of, 3–16  
     influence of variation in blade response on, 3–13  
     updating predictions of, 3–18  
   field effects on, 3–19  
   resonant-mode vibration as a cause of blade failure in, 3–7  
   use of probabilistic analyses for, 3–9  
 Hill's elastic moduli, 11–26  
 HMMV first-order method, 8–14  
 Hogging, 9–5, 9–7, 9–12, 9–23  
 Hoop stress, probabilistic, 6–12  
 Hull girders  
   extreme load models, 9–11  
   failure modes of, 9–5  
   load factors, 9–20  
   primary failure mode, 9–7  
   quaternary failure mode, 9–8  
   repair strategies for, 9–29  
   secondary failure mode, 9–8  
   target reliability against collapse, 9–4  
   tertiary failure mode, 9–8  
   ultimate strength models, 9–6  
 Hybrid mean value first-order method. *See* HMMV first-order method  
 Hyperbolic sine equation model, 2–16

## I

IAS, step lap joint, optimization of using RBDO, 4–16  
 Importance sampling, 7–4  
   sequential conditional, 7–5  
 Importance-sampling density function, 7–4  
 In-service inspection of military engines, use of field-management risk assessments for, 3–7  
 Inclusion model  
   elastic matrix of, 11–24  
   interface modeling of CNT/CNF composites with, 11–17  
   use of M-T method to predict stiffness tensor of, 11–21  
 Inclusion probabilities, 3–5  
 Inner-loop reliability analysis, 4–2  
 Input uncertainty propagation, 1–2

Insignificant input variables, elimination of using CVMLS backward screening, 7–16, 7–18  
 Inspection intervals, 2–3  
 Instantaneous failure probabilities, 2–54, 3–4  
 Integral airframe structure. *See* IAS  
 Integral-order blade stimuli, 3–8  
 Intelligent structures, 5–15  
   probabilistic buckling loads in, 5–23  
 Intelligent systems, definition of, 5–17  
 Intergranular corrosion, 2–21  
 Irreducible uncertainty, 11–4

## J

Joint failure probability, 10–5  
 Joint probability density function, 6–3  
 Joint-failure probabilities, 7–5

## K

Karhunen-Loeve series expansion, 2–28  
 Kriging techniques, 7–11, 7–21

## L

Laminate systems  
   failure probability, 10–4  
   shear deformation theory for, 10–8  
 Laminate theory, 10–2  
 LANL  
   dynamic experiment containment vessel, 1–18  
   PREDICT system, 3–9  
 Last ply failure. *See* LPF  
 Latin hypercubes, 7–11  
 LCF lifing methods, 3–16  
 Leave-one-out cross validation procedure, 7–12, 7–14  
 Limit state. *See also* specific limit states  
   response surface modeling of, 10–29  
 Limit theory, 10–10  
 Limit-state exceedance, 9–2  
 Linear damage summation model, 10–21  
 Linear elastic fracture mechanics, 2–6  
   use of for crack propagation modeling, 2–14  
 Linear-damage rule, 2–11  
 Load modeling  
   composite laminates, 10–6  
   multidimensional, 10–24  
   probabilistic, 1–27  
     buckling, 5–3, 5–6  
     random-amplitude, changes in crack growth due to, 2–20  
 Local denting, 9–26  
   effect of, 9–10  
 Local failure criteria, selection of, 2–6  
 Local ply buckling, 10–19  
 Local polynomial fitting, 7–11  
   CVMLS method for, 7–13  
 Local strain-life method, 2–8  
 Localized corrosion, 9–9  
 Longitudinal strength, IMO requirements for, 9–29



Longitudinal stress  
 composites, **10–31**  
 probabilistic, **6–8**  
 Los Alamos National Laboratory. *See* LANL  
 LPE, **10–2**

## M

M-T method  
 failure analysis of plates made of nanocomposites using, **11–15**  
 modeling behavior of nanocomposites with, **11–4, 11–7**  
   aligned inclusions, **11–9**  
   randomly-oriented inclusions, **11–11**  
   use of to predict stiffness tensor of an inclusion, **11–21**  
 Madymo, **7–16**  
 Main-effects estimate, use of a CVMLS additive model for, **7–15, 7–17**  
 Maintenance inspections. *See also* Aircraft maintenance;  
   NDI  
   uncertainties of, **2–37**  
 Margin of safety, calculating, **5–6**  
 Material modeling, **10–18**  
 Material nonhomogeneity, crack growth and, **2–19**  
 Matrix cracking failure, **10–6, 10–10**  
   correspondence of FPF with, **10–2**  
   stiffness modification for, **10–11**  
 Maturity, **3–4**  
 Maximum deflection, reliability analysis for, **7–6**  
 Mean value first order. *See* MVFO  
 Mechanical fatigue, **8–2**  
   design optimization for, **8–5**  
   experimental validation of, **8–3**  
 Metamodeling  
   cross validation for estimating prediction error in, **7–13**  
   multivariate, **7–10**  
 Micromechanical modeling of CNT/CNF composites, **11–7**. *See also* M-T method  
 Miner's rule, **2–12**  
 Mistuning, **3–9**  
   effect of geometric variability of blades on, **3–10, 3–13**  
 MIT sea-keeping tables, use of to predict wave-induced  
   bending moment, **9–12**  
 MLS method, **7–13**  
 Model approximation methods, **4–3**  
 Model validation studies, **1–24**  
 Modeling steps, risk/reliability-based condition  
   assessment, **2–36**  
 Modeling uncertainty, **8–2**  
 Modified Morrow correction, **2–10**  
 Modified sigmoidal equation model, **2–16**  
 Monte Carlo simulations, **7–4, 7–21, 10–2**  
   modeling vibratory stress with, **3–13, 3–17**  
   use of in RBDO, **4–2**  
 Mori-Tanaka Micromechanical Method. *See* M-T method  
 Morrow correction, **2–9**  
   modified, **2–10**  
 Most probable point. *See* MPP  
 Moving least squares method. *See* MLS method  
 MPP, **4–4, 7–2, 8–15**  
   calculation of, **7–3**

MSD, **2–5, 2–39**  
 MSO shell code, **4–6**  
 MTSB, **4–9**  
 Multiaxial fatigue, **10–2, 10–24**  
 Multibody dynamics modeling, **8–4**  
 Multicriteria optimization, resolution of trade-offs in  
   automotive applications, **7–23**  
 Multidisciplinary stochastic optimization shell code. *See*  
   MSO shell code  
 Multimodal adaptive importance sampling, **7–4**  
 Multiple failure sequences for composite laminates,  
   **10–6**  
 Multiple site damage. *See* MSD  
 Multivariate metamodeling, **7–10**  
 MVFO, **7–4**

## N

Nanocomposites  
   effect of CNF/CNT-matrix interface on probability of  
     failure, **11–36**  
   failure analysis of plates made of, **11–15**  
   literature review, **11–4**  
   matrix of elastic constants of, **11–24**  
   modulus of, **11–15**  
   predicting properties of, **11–14**  
   probabilistic and reliability analysis of, **11–4, 11–30**  
 NASA, probabilistic shuttle debris transport modeling for,  
   **1–14**  
 NCAP, star rating of occupant safety performance  
   in, **7–16**  
 NDE tests, **2–38**  
   crack detection using, **2–52**  
   effect of operator skill on success of, **2–53**  
 NDI  
   crack discovery using, **2–2**  
   quantification of capabilities of, **2–4**  
   techniques for, **2–37**  
 NESSUS, **1–2, 5–1, 6–1**  
   analysis of single cup combustor liner using, **6–4**  
   capabilities of, **1–4**  
   Debris Transport Analysis equation database, **1–16**  
   GUI, **1–5**  
   integration of Flowliner Fatigue Life software with, **1–25**  
   model mapping facility, **1–19**  
   overview of, **1–3**  
   stochastic crashworthiness model, **1–11**  
   use of for probability analysis of progressive buckling,  
     **5–3**  
   vehicle system reliability improvement study, **1–13**  
 Net section stress, **2–6**  
 Neural networks, **4–3**  
 New car assessment program. *See* NCAP  
 New parts, probabilistic life analysis for, **3–5**  
 NIKE3D, **4–9**  
 Nominal blade frequency, use of in probabilistic analysis,  
   **3–13**  
 Nondestructive evaluation tests. *See* NDE tests  
 Nondestructive inspections. *See* NDI  
 Nonlinear damage accumulation functions, composite  
   materials, **10–22**

Nonparametric metamodeling methods, 7–10. *See also*  
 Response-surface models  
 Nonparametric multiple-regression techniques, 7–10  
 Notch effects, consideration of in design optimization,  
 8–12  
 NRC, 1–1  
 Nuclear Regulatory Commission. *See* NRC  
 Numerical Evaluation of Stochastic Structures Under  
 Stress. *See* NESSUS  
 Numerical simulation, 1–1

## O

Occupant safety performance, 7–16  
 robust design example, 7–19  
 Offshore structures, effect of local denting, 9–10  
 Operational conditions, hull girder loads and, 9–21  
 Optimal symmetric Latin hypercube sampling. *See* OSLH  
 sampling  
 Optimization methods, 7–4  
 OSLH sampling, 7–12, 7–15, 7–20

## P

PARADYN, use of for structural response simulation, 1–18  
 Parametric models, 1–21, 1–24  
 Parametric multiple-regression techniques, 7–10  
 Paris-law model, 2–20, 2–29, 2–41, 9–18  
 PCA, 3–11  
 PDF, 2–36, 2–39, 2–50, 11–5  
 nanocomposites, 11–31, 11–33  
 Performance measure approach. *See* PMA  
 Physics-based reliability engineering approach, 2–35  
 Pit curves, computation of, 2–47  
 Pitting corrosion, 2–21, 2–28, 9–9, 9–24  
 CCCF model of, 2–31  
 corroded surface topography, 2–27  
 power-law pit model, 2–22  
 risk-based maintenance analysis of, 2–43  
 SCF model of, 2–31  
 stochastic variability of in aluminum alloys, 2–23  
 WCF model of, 2–29  
 Wei pit model, 2–22  
 Plackett-Burman DOE technique, 7–10  
 Plane-strain fracture toughness, 2–7  
 Plate-stiffener combination model, 9–6  
 ultimate compressive strength, 9–8  
 Plate-stiffener separation model, 9–6  
 Ply-level limit states, 10–3, 10–10  
 PMA  
 RBDO model of, 8–13  
 reliability analysis model of, 8–14  
 reliability analysis tools for, 8–14  
 PMARC, 4–14  
 Polymers, use of carbon nanofibers and nanotubes  
 in, 11–2  
 Polynomial theory, 10–10  
 Power-law pit model, 2–22  
 Primitive variables  
 probabilistic analysis of single cup liner segment, 6–3  
 probabilistic analysis of trusses, 5–4

scatter in, 5–24  
 uncertainties in, 5–2  
 Principal component analysis. *See* PCA  
 Probabilistic analysis, 1–1. *See also* NESSUS  
 application of to large-scale numerical  
 models, 1–18  
 automotive industry, 7–23  
 computation of corrosion-fatigue life, 2–45  
 creep in composite laminates, 10–35  
 damage tolerance, 1–25  
 fatigue life of composite laminates, 10–25  
 life assessment for new parts, 3–5  
 longitudinal composites under creep, 10–31  
 methods for, 1–2  
 nanocomposites, 11–4, 11–31  
 RBDO and, 4–2  
 response metric for, 1–19  
 rotor design/fracture dynamics, 3–4  
 shuttle debris transport modeling, 1–14  
 uncertainties affecting, 1–16  
 use of for assessing aircraft safety, 2–5  
 Probabilistic fracture mechanics  
 risk assessments based on, use of DARWIN  
 for, 1–7  
 use of NESSUS for analysis of, 1–27  
 Probabilistic life prediction, 2–39  
 Probabilistic models  
 blades, effect of geometric variability of, 3–10  
 crack growth, 2–39  
 fatigue, 2–13  
 use of for biological systems, 1–21, 1–24  
 validation/calibration of, 3–6  
 vibratory stresses, 3–9  
 Probabilistic progressive failure model, 10–3  
 Probabilistic redesign, use of NESSUS for, 1–13  
 Probabilistic structural analysis methods. *See* PSAM  
 Probability densities. *See* PDF  
 Probability of detection curves, 2–2, 2–38  
 Probability of failure, 8–12  
 Probability of fracture, 3–5  
 sensitivity of, 3–6  
 Probability of fracture software. *See* PROF software  
 Probability-based design optimization, 4–1  
 PROF software, 2–5  
 ProFES/MDO, 4–7  
 Progressive damage analysis, 10–2  
 Progressive failure analysis, 10–10, 10–19  
 stiffness modification for, 10–11  
 Proper orthogonal decomposition, 2–28  
 PSAM, 5–1  
 buckling loads  
 single cup combustor liner, 6–5  
 trusses, 5–10  
 development of, 6–1  
 space trusses, 5–18  
 variables, 5–4

## Q

Quasi-random samples, 7–11

**R**

Radial basis functions, 7–11  
 Random fatigue-limit model, 3–15  
 Random uncertainty, 11–4  
 Random variables  
   transformation of, 7–3  
   use of for probabilistic analysis of composite material delamination, 10–28  
 Randomly-oriented inclusions, use of M-T method for nanocomposites with, 11–11  
 RBDO, 4–1, 7–10, 8–12  
   applications of, 4–5  
   approximation methods for, 4–5  
   effectiveness of PMA for, 8–15  
   flowchart for, 4–8  
   model of performance measure approach, 8–13  
   optimization of a transport aircraft wing using, 4–18  
   optimization of an IAS step lap joint using, 4–16  
   shape optimization of an airplane wing using, 4–12  
   shape optimization of axial compressor blades using, 4–7  
   use of in automotive industry, 7–23  
 Redesign analysis, use of NESSUS for, 1–13  
 Reduced-order models, 3–13  
 Reducible uncertainty, 11–4  
 Regression analysis, 7–10  
 Rejectable crack size, 2–37  
 Reliability  
   comparative and notional measures of, 9–5  
   definition of, 3–2  
   ply-level limit states and, 10–3  
 Reliability analysis, 2–35  
   component-level, 7–2  
   durability-based optimal design, 8–12  
   in PMA, 8–14  
   liftgate, 7–6  
   nanocomposites, 11–4, 11–33  
   options, 2–37  
   risk-based, 2–43  
   simulation-based, 7–4  
   system-level, 7–5  
   use of in automotive design, 7–1  
 Reliability approximation methods, 4–3. *See also* RBDO  
 Reliability assessment  
   ship structures, 9–3, 9–26  
   time-dependent, 9–12, 9–20  
 Reliability engineering, traditional approaches, 3–2  
 Reliability index approach, 8–14  
 Reliability metrics, 2–36  
 Reliability-based design, 4–1, 8–2, 9–2  
   corrosion considerations in, 9–14  
   (*See also* Corrosion)  
   fatigue cracking considerations in, 9–16  
   (*See also* Fatigue cracking)  
 Reliability-based design optimization. *See* RBDO  
 Repair strategies, ships, 9–27  
 Residual strength, 2–6, 10–19  
   assessment of aging steel structures, 9–10  
 Resonant-mode vibration, 3–7  
   calculating, 3–12

Response metric for probabilistic analysis, 1–19  
 Response surfaces, 4–3  
 Response-surface models, 4–5, 7–10. *See also*  
   Nonparametric metamodeling methods  
     high-fidelity, 7–20  
     limit state, 10–29  
 Risk assessment  
   field-management, 3–7  
   ship structures, 9–3  
 Risk-based approach to aircraft management, 2–5  
   maintenance analysis, 2–43  
 Risk-based maintenance analysis, 2–39  
 Robust design, 4–2, 7–2  
 Robust engineering, variation reduction in, automotive example, 7–19  
 Rosenblatt transformation, 7–3  
 Rule of mixtures, 11–19, 11–21

**S**

S-N curves, use of for modeling fatigue in composites, 10–19, 10–24  
 Safety-factor-based design, 4–1, 7–1  
 Sagging, 9–5, 9–7, 9–12, 9–23  
 Sample partitioning, 7–11  
 Sampling strategies  
   progressive, 7–13  
   uniform, 7–11  
 Scatter, 5–1, 5–4, 5–14, 5–21, 5–24  
   in single cup combustor liner material, 6–8  
 SCF model, 2–28, 2–31  
   comparison with other corrosion-fatigue damage models, 2–34, 2–41  
 SCIS, 7–5  
 Sea states, hull girder loads and, 9–21  
 Second-order central composite design, 4–3  
 Second-order reliability method. *See* SORM  
 Sensitivity factors, probabilistic, 1–27, 5–6  
 Sequential conditional importance sampling. *See* SCIS  
 Sequential optimization and reliability assessment method.  
   *See* SORA  
 Sequential quadratic programming. *See* SQP  
 Serviceability limit state. *See* SLS  
 Shear deformation theory, 10–8  
 SHELL99, 10–12  
 Ship Structure Committee. *See* SSC  
 Ships  
   corrosion of, 9–13  
   effect of local denting, 9–10  
   fatigue cracking of, 9–15  
   repair strategies for, 9–27  
   structural damage scenarios, 9–24  
   structures of, 9–2  
   target reliability for against hull girder collapse, 9–4  
   time-dependent reliability assessment of, 9–20  
   ultimate bending moment capacity, 9–7  
 Shuttle debris transport modeling, 1–14  
   uncertainties affecting, 1–16  
 Simulation techniques, 8–1  
 Simulation-based reliability methods, 7–4  
 Simultaneous corrosion fatigue model. *See* SCF model

Single cup liner segment, finite element model of, 6–2  
 Single failure sequence for composite laminates, 10–5  
 SLH sampling, 7–12  
 SLS, 9–2  
 Small-crack-growth modeling, 2–14. *See also* Crack initiation  
 Smart structures, 5–15  
   probabilistic buckling loads in, 5–21  
 Smart systems, definition of, 5–17  
 Smiths-Watson-Topper (SWT) procedure, 2–10  
 Smoothing splines, 7–11  
 SORA, 4–5  
 SORM, 4–4, 7–2, 7–4, 8–14, 10–2  
 Southwest Research Institute. *See* SwRI  
 Space truss structures, control of with adaptive/smart/intelligent structures, 5–15  
 Spatial statistics analysis. *See* SSA  
 SQP, 7–4  
 SSA, 3–11  
 SSC, 9–2  
 Statistical uncertainty, 8–2  
 Statistics, condition assessment, 2–36  
 Step lap joint, optimization of using RBDO, 4–16  
 Stepwise regression, 7–21  
 Stiffness, 3–13, 5–6  
   model, 10–19  
   modification for progressive failure analysis, 10–11  
   nanocomposites, 11–5  
     use of M-T method for aligned inclusions, 11–9  
   structural, composite laminate failure and, 10–2  
   use of for quantifying fatigue damage in composites, 10–21  
 Still-water bending moment, 9–11, 9–21  
 Stochastic crashworthiness model, 1–11  
 Stochastic fiber fracture, creep analysis with, 10–32  
 Stochastic optimization, 4–12  
 Stochastic variability  
   corrosion in aluminum alloys, 2–23  
   crack initiation, 2–12  
   crack propagation, 2–17  
 Strain energy release rate, 10–2, 10–26  
 Strain energy theory, 10–10  
 Strain gauges, 3–9  
 Strain-displacement equations, 10–8  
 Strain-life modeling, 2–8  
 Strength limit states, 10–2, 10–8, 10–36  
   approximations for, 10–14  
 Strength reliability assessment methods, laminate materials, 10–2  
 Strength-knockdown factor, 9–9, 9–26  
 Stress analysis, use of finite element analysis for, 1–21  
 Stress corrosion cracking, 2–21  
 Stress influence coefficient, 8–4  
   use of to compute dynamic stress history, 8–6  
 Stress intensity factors, calculation of, 9–18  
 Stress-strain curves  
   modeling, 2–8  
   selection of local failure criteria using, 2–6  
 Structural damage  
   age-related, 9–24  
   time-dependent, prediction of, 9–12

Structural failure, 10–17  
   aircraft, maximum acceptable frequency of, 2–5  
 Structural fatigue, 8–2  
 Structural reliability theory, 2–35, 9–2  
 Structural risk assessment, ship structures, 9–3  
 Structural ultimate failure, 10–2  
 Structural-durability analysis, 8–2  
 Subsystem reliability, 3–2  
 SwRI, 1–2, 3–6  
 Symmetric Latin hypercube sampling. *See* SLH sampling  
 System failure probability, 10–2  
 System reliability analysis  
   analytical methods for, 7–5  
   use of NESSUS for, 1–13  
 System-level reliability, 3–2

## T

Tankers, corrosion of, 9–14  
 Target safeties and reliabilities, selection of, 9–4  
 Taylor's series expansion method, 4–3  
 Tension fatigue tests, 10–23  
 Tensors  
   modeling of stiffness of for nanocomposites, 11–9, 11–11, 11–21  
   transformation of, 11–12  
 Theory validation, 11–3  
 Thermal gradients, through-thickness, 6–1  
 Thermal load profiles, use of in probabilistic analysis of single cup liner segment, 6–3  
 Three-dimensional analysis, 10–8  
 Through-thickness thermal gradients, 6–1  
 Time-dependent reliability assessment of aging ships. *See* TRAAS  
 Time-dependent structural damage, prediction of, 9–12  
 Titanium alloys, hard-alpha anomaly distributions for, 3–5  
 TRAAS, 9–20  
 Transport aircraft wing, optimization of using RBDO, 4–18  
 Trusses  
   end-node displacements, 5–9  
   intelligent, design of, 5–17  
   probabilistic analysis of progressive buckling of, 5–4  
     collapse states, 5–8  
     initial eccentricity and, 5–11  
   space  
     control of with adaptive/smart/intelligent structures, 5–15  
     probabilistic structural analysis of, 5–18  
     structural integrity of, 5–1  
 Tsai-Hill static strength failure criterion, 10–25  
 Turbine blades  
   internal cooling-air passages in, 3–10  
   resonant-mode vibration of, 3–7

## U

U.S. Department of Defense, damage-tolerance design best practices, 3–5  
 U.S. Department of Energy. *See* DOE  
 ULS, 9–2

equations, failure modes, 9–6  
 reliability, 10–2  
 repair strategies to maintain, 9–29  
 Ultimate bending moment capacity, 9–7  
 Ultimate compressive strength, 9–8  
 Ultimate limit state. *See* ULS  
 Ultimate strength. *See* ULS  
 Ultrasound, use of to find corrosion, 2–4  
 Uncertainties, 6–2  
   characterization of for the automotive industry, 7–23  
   in CAE, 8–2  
   modeling of for hull girder failure modes, 9–6  
   ship design and operation, 9–2  
   simulation of, 1–2  
 Uncertainty-based design, 8–2  
 Uniform sampling, 7–11  
 United States Air Force. *See* USAF  
 Unsteady pressure field variation, 3–14  
 Updating distributions, 3–18  
 USAF  
   aircraft structural integrity program (ASIP), 2–5  
   crack growth analysis, 2–2  
   maximum acceptable frequency of aircraft structural failure, 2–5  
   PROF software, 2–5

## V

---

Validation/calibration of probabilistic methods, 3–6  
 Variability, 11–4  
 Variable screening, 7–16  
   based on CVMLS, 7–15  
 VCCT, 10–27  
 Veering region, 3–14  
 Vehicle reliability, analysis of, 1–11  
 Vibration frequencies

cumulative distribution functions of, 6–8  
 isolation of in NASA spacecraft, 5–15  
 Vibratory stresses, 3–8  
   allowable, 3–9  
   forced-response prediction of, 3–9  
 Virtual crack closure technique. *See* VCCT  
 Von Mises strain approach, 8–5

## W

---

Wastage models, time-dependent, 9–13  
 Wave-induced bending moment, 9–11, 9–21  
 WCF model, 2–29  
   comparison with CCCF model, 2–33  
   comparison with SCF model, 2–41  
 Weakest link model, 10–15, 10–17  
 Wei corrosion-fatigue model. *See* WCF model  
 Wei pit model, 2–22, 2–47  
 Weibull analysis, 3–4  
 Weibull failure models, physics-based, 2–37  
 WFD, 2–5, 2–39  
 Widespread fatigue damage. *See* WFD  
 Wing design, shape optimization using RBDO, 4–12

## X

---

X-rays, use of to find corrosion, 2–4

## Y

---

Yield strength, 2–7  
 Young's modulus, 11–30  
   use of for quantifying fatigue damage in composites, 10–21

# ENGINEERING DESIGN RELIABILITY APPLICATIONS

In the current, increasingly aggressive business environment, crucial decisions about product design often involve significant uncertainty. Highlighting the competitive advantage available from using risk-based reliability design, ***Engineering Design Reliability Applications: For the Aerospace, Automotive, and Ship Industries*** provides an overview of how to apply probabilistic approaches and reliability methods to practical engineering problems using real-life engineering applications. A one-step resource, the book demonstrates the latest technology, how others have used it to increase their competitiveness, and how you can use it to do the same.

The book makes the case for accurate assessment of the reliability of engineering systems, simple, complex, or large-scale. It presents two computer programs for reliability analysis and demonstrates these programs on aircraft engines, structures used for testing explosives, medical and automotive systems. The focus then shifts to aircraft and space systems, including lap joints, gas turbines, and actively controlled space structures. The editors provide analytical tools for reliability analysis, design optimization, and sensitivity analysis of automotive systems. They include a general methodology for reliability assessment of ship structures and highlight reliability analysis of composite materials and structures.

Delineating generic tools and computer programs applicable to any situation, the book shows you how to quantify, understand, and control uncertainties, reduce risk, and increase reliability using real-life examples. Engineers from the industry and national labs as well as university researchers present success stories and quantify the benefits of reliability design for their organizations. They demonstrate how to convince colleagues and management of the potential benefits of these approaches in allowing their organizations to gain significant benefits and dramatically increase their competitiveness.

51326



**CRC Press**

Taylor & Francis Group  
an informa business

[www.taylorandfrancisgroup.com](http://www.taylorandfrancisgroup.com)

6000 Broken Sound Parkway, NW  
Suite 300, Boca Raton, FL 33487  
270 Madison Avenue  
New York, NY 10016  
2 Park Square, Milton Park  
Abingdon, Oxon OX14 4RN, UK



[www.crcpress.com](http://www.crcpress.com)